

# **Identification, characterization and optimization of peptide ligands for therapeutic applications**

Inaugural-Dissertation

zur Erlangung des Doktorgrades  
der Mathematisch-Naturwissenschaftlichen Fakultät  
der Heinrich-Heine-Universität Düsseldorf

vorgelegt von

**Marc Michael Sevenich**  
aus Frechen

Jülich, Juli 2022

aus dem Institut für Physikalische Biologie  
der Heinrich-Heine-Universität Düsseldorf

Gedruckt mit der Genehmigung der  
Mathematisch-Naturwissenschaftlichen Fakultät der  
Heinrich-Heine-Universität Düsseldorf

Berichtersteller:

1. Prof. Dr. Dieter Willbold
2. Prof. Dr. Wolfgang Hoyer
3. Prof. Dr. Peter Bayer

Tag der mündlichen Prüfung: 14.02.2023

We are all apprentices in  
a craft where no one ever  
becomes a master.

*Ernest Hemingway*



## **Part 1**

**Stabilization of monomeric  $\alpha$ -synuclein by all-D-enantiomeric peptide ligands  
as therapeutic strategy for Parkinson's disease**

## **Part 2**

**Kinetic characterization of the SARS-CoV-2 spike interaction with hACE2 and  
identification of spike protein binding inhibitors of complex formation**

# Table of contents

<b>Table of contents</b> .....	<b>i</b>
<b>List of abbreviations</b> .....	<b>iii</b>
<b>List of patent applications</b> .....	<b>v</b>
<b>List of conference contributions and oral presentation</b> .....	<b>vi</b>
<b>List of publications</b> .....	<b>vii</b>
<b>List of figures</b> .....	<b>viii</b>
<b>Abstract</b> .....	<b>ix</b>
<b>Kurzzusammenfassung</b> .....	<b>xi</b>
<b>1 Introduction</b> .....	<b>1</b>
<b>1.1 Part I: Stabilization of monomeric <math>\alpha</math>-synuclein by all-D-enantiomeric peptide ligands as therapeutic strategy for Parkinson’s disease</b> .....	<b>1</b>
1.1.1 Parkinson’s disease .....	1
1.1.1.1 Epidemiology.....	1
1.1.1.2 Clinical features.....	1
1.1.1.3 Neuropathology .....	2
1.1.2 $\alpha$ -synuclein .....	3
1.1.2.1 Structure and physiological role .....	3
1.1.2.2 $\alpha$ -syn aggregation .....	4
1.1.2.3 Structure and toxicity of $\alpha$ -syn oligomers, protofibrils and fibrils.....	7
1.1.2.3.1 Oligomers and protofibrils.....	7
1.1.2.3.2 Fibrils.....	10
1.1.2.4 Cell-to-cell transmission and seeding of $\alpha$ -syn: PD as a prion-like disease	12
1.1.3 PD therapy.....	13
1.1.3.1 Symptomatic treatment.....	13
1.1.3.2 $\alpha$ -syn as a pharmacological target.....	14
1.1.3.3 Direct elimination of toxic oligomers and seeding competent fibrils as anti-prionic strategy against neurodegenerative diseases .....	16
<b>1.2 Part II: Kinetic characterization of the SARS-CoV-2 spike protein interaction with hACE2 and identification of spike protein binding inhibitors of complex formation</b> .....	<b>19</b>
1.2.1 SARS-CoV-2 and COVID-19 .....	19
1.2.1.1 Coronaviruses .....	19
1.2.1.2 Epidemiology.....	19
1.2.1.3 Pathogenesis .....	20
1.2.2 SARS-CoV-2 replication cycle .....	20
1.2.3 The SARS-Cov-2 spike protein: structure and function.....	22
1.2.4 The RBD – hACE2 interface for SARS-CoV-2 and VOCs .....	24
1.2.5 Current medical treatment options for COVID-19.....	25

1.2.6	Targeting the SARS-CoV-2 spike protein – hACE2 interaction as therapeutic strategy for COVID-19 .....	26
<b>1.3</b>	<b>Peptides as therapeutics .....</b>	<b>28</b>
1.3.1	Therapeutic peptides throughout the years .....	28
1.3.2	Peptide optimization strategies for improved pharmacokinetics, membrane penetrance and enhanced target binding affinity and specificity .....	29
<b>1.4</b>	<b>Phage display selection .....</b>	<b>32</b>
<b>1.5</b>	<b>Aim of this work.....</b>	<b>35</b>
<b>2</b>	<b>Published Manuscripts.....</b>	<b>37</b>
2.1	Direct disassembly of $\alpha$ -syn preformed fibrils into native $\alpha$ -syn monomers by an all-D-peptide.....	37
2.2	A so-far overlooked secondary conformation state in the binding mode of SARS-CoV-2 spike protein to human ACE2 and its conversion rate is crucial for estimating infectivity efficacy of the underlying virus variant.....	86
2.3	Phage Display-Derived Compounds that Displace hACE2 from Its Complex with SARS-CoV-2 Spike Protein.....	98
2.4	Development of an $\alpha$ -synuclein fibril and oligomer specific tracer peptide for diagnosis of Parkinson’s disease, dementia with Lewy bodies and multiple system atrophy 122	
2.5	Discovery of all-D-peptide inhibitors of SARS-CoV-2 3C-like protease.....	133
2.6	Ligand-Induced Stabilization of the Native Human Superoxide Dismutase 1.....	150
2.7	In vitro reconstitution of the highly active and natively folded human superoxide dismutase 1 (hSOD1) .....	160
2.8	Alpha-Synuclein-specific naturally occurring antibodies prevent aggregation in vitro and in vivo .....	167
<b>3</b>	<b>Global discussion .....</b>	<b>181</b>
3.1	Optimization of the phage display selection protocol.....	181
3.2	<i>In vitro</i> screening and characterization .....	182
3.3	A general procedure for the identification of D-enantiomeric peptide compounds by phage display selection.....	184
<b>4</b>	<b>Summary .....</b>	<b>187</b>
<b>5</b>	<b>References.....</b>	<b>189</b>
	<b>Acknowledgements.....</b>	<b>204</b>
	<b>Eidesstattliche Erklärung.....</b>	<b>205</b>
	<b>Printing Permissions.....</b>	<b>206</b>

## List of abbreviations

Abbreviation	Meaning
3CL <sup>pro</sup>	Chymotrypsin-like protease
aa	Amino acid
ALS	Amyotrophic lateral sclerosis
ARDS	Respiratory distress syndrome
ARS	Angiotensin-renin system
A $\beta$	Amyloid- $\beta$
CPPs	Cell-penetrating peptides
CZSB, CTSL	Cathepsin B and L
ED	Electron diffraction
EM	Electron microscopy
EPR	Electron paramagnetic resonance
ER	Endoplasmic reticulum
ERGIC	(ER)-to Golgi compartment
hACE2	Human angiotensin converting enzyme 2
hSOD1	Human superoxide dismutase 1
HSP	Heat shock proteins
LB	Lewy Bodies
LN	Lewy Neurites
MERS-CoV	Middle east respiratory syndrome coronavirus
MOF	Multiple organ failure
MSA	Multiple system atrophy
M <sub>w</sub>	Molecular weight
NAC	Non-amyloid component
NGS	Next generation sequencing
NHC	$\beta$ -D-hydroxycystidine
NRP1	Neuropilin-1
nsp	Non-structural proteins
ORFs	Open reading frames
PD	Parkinson's disease
PEG	Polyethylene glycol
PL <sup>pro</sup>	Papain-like protease
PoC	Proof of concept
PrP	Prion protein
PrP <sup>C</sup>	Cellular prion protein
PrP <sup>Sc</sup>	Scrapie prion protein
PRRAR	Furin polybase cleavage site
RBD	Receptor binding domain

RBM	Receptor binding motif
RdRp	RNA-dependent RNA polymerase
RTC	Reverse transcription complex
SARS-CoV	Severe acute respiratory syndrome coronavirus
SNpc	Substantia nigra pars compacta
TMPRSS2	Transmembrane protease serine kinase 2
TRS	Transcription regulatory sequences
VOC	Variant of concern
$\alpha$ -syn	Alpha-synuclein

## List of patent applications

1. Willbold D., Mohrlüder J., **Sevenich M.**, Altendorf T., Santur K.B. „Verwendung von D-enantiomeren Peptidliganden von monomerem  $\alpha$ -synuclein für die Therapie verschiedener Synucleinopathien.“, 22.03.2021, DE 102021107061.9
2. Willbold D., Mohrlüder J., Altendorf T., **Sevenich M.**, Santur K.B. „Verwendung von D-enantiomeren Peptidliganden von monomerem Tau für die Therapie verschiedener Tauopathien.“, 25.03.2021, DE 102021107546.7
3. Willbold D., Mohrlüder J., Santur K.B., Altendorf T., **Sevenich M.** „Verwendung von L-enantiomeren Peptidliganden von nativ gefalteter humaner Superoxiddismutase 1 (SOD1) für die Therapie von Amyotropher Lateralsklerose (ALS)“, 22.03.2021, DE 102021107051.1
4. Willbold D., Mohrlüder J. **Sevenich M.** „Entwicklung eines  $\alpha$ -syn Amyloidtracers“, 15.02.2021, Patentantrag eingereicht an das Deutsche Patent- und Markenamt (DPMA)
5. Willbold D., Mohrlüder J. **Sevenich M.** „Hemmung der Interaktion von viralen Spike Proteinen von SARS-CoV-2 und dem humanen Angiotensin-konvertierenden Enzym 2 (hACE2)“, 25.11.2021, Patentantrag eingereicht an das Deutsche Patent- und Markenamt (DPMA)

## List of conference contributions and oral presentation

1. **Marc Sevenich**, Wolfgang Hoyer, Jeannine Mohrlüder and Dieter Willbold "Stabilization of monomeric  $\alpha$ -syn by all-D enantiomeric peptide ligands as therapeutic strategy for Parkinson's disease ". Düsseldorf-Jülich Symposium on Neurodegenerative Diseases: Formation, aggregation and propagation of amyloids (2017; Düsseldorf, Germany). Poster presentation.
2. **Marc Sevenich**, Wolfgang Hoyer, Jeannine Mohrlüder and Dieter Willbold "Stabilization of monomeric  $\alpha$ -syn by all-D enantiomeric peptide ligands as therapeutic strategy for Parkinson's disease ". PRION 2018 (2018; Santiago de Compostela, Spain). Poster presentation.
3. **Marc Sevenich** "SPR - Surface plasmon resonance" International Helmholtz Research School of Biophysics and Soft matter – Standard Techniques in Biochemistry and Biophysics (2019; Jülich, Germany). Oral presentation.
4. **Marc Sevenich**, Ian Gering, Madita Vollmer, Markus Tusche, Matthias Stoldt, Antje Willuweit, Janine Kutzsche, Gültekin Tamgüney, Jeannine Mohrlüder and Dieter Willbold "Stabilization of monomeric  $\alpha$ -syn by all-D enantiomeric peptide ligands as therapeutic strategy for Parkinson's disease ". Düsseldorf-Jülich Symposium on Neurodegenerative Diseases: Formation, aggregation and propagation of amyloids (2021; Düsseldorf, Germany). Poster presentation – 2<sup>nd</sup> poster-prize winner Alzheimer Forschung Initiative e.V.
5. **Marc Sevenich**, Ian Gering, Madita Vollmer, Markus Tusche, Matthias Stoldt, Antje Willuweit, Janine Kutzsche, Gültekin Tamgüney, Jeannine Mohrlüder and Dieter Willbold "Stabilization of monomeric  $\alpha$ -syn by all-D enantiomeric peptide ligands as therapeutic strategy for Parkinson's disease ". AD/PD (2022; Barcelona, Spain) Poster presentation.

## List of publications

1. **Sevenich, M.**; Gering, I.; Vollmer, M., Aghabashlou Saisan, S.; Tusche, M.; Kupreichyk, T.; Pauly, T., Stoldt, M.; Hoyer, W.; Willuweit, A.; Kutzsche, J.; Lakomek, N.A.; Nagel-Steger, L.; Gremer, L.; Tamgüney, G.; Mohrlüder, J.; Willbold, D. *Direct disassembly of  $\alpha$ -syn preformed fibrils into native  $\alpha$ -syn monomers by an all-D-peptide*. Submitted to Journal of American Chemical Society.
2. **Sevenich, M.**; van den Heuvel, J.; Gering, I.; Mohrlüder, J.; Willbold, D. *A so far overlooked secondary conformation state in the binding mode of SARS-CoV-2 spike protein to human ACE2 and its conversion rate is crucial for estimating infectivity efficacy of the underlying virus variant*. Journal of Virology, 2022: <https://doi.org/10.1128/jvi.00685-22>.
3. **Sevenich, M.**; Thul, E.; Lakomek, N.-A.; Klünemann, T.; Schubert, M.; Bertoglio, F.; van den Heuvel, J.; Petzsch, P.; Mohrlüder, J.; Willbold, D. *Phage Display-Derived Compounds Displace hACE2 from Its Complex with SARS-CoV-2 Spike Protein*. Biomedicines 2022, 10, 441: <https://doi.org/10.3390/biomedicines10020441>.
4. **Sevenich, M.**; Honold D.; Willuweit A.; Kutzsche J.; Mohrlüder J.; Willbold D. *Development of an  $\alpha$ -synuclein fibril and oligomer specific tracer peptide for diagnosis of Parkinson's disease, dementia with Lewy bodies and multiple system atrophy*. Neurochemistry International 2022, 161: <https://doi.org/10.1016/j.neuint.2022.105422>.
5. Eberle, R.; **Sevenich, M.**; Gering, I.; Scharbert, L.; Strodel, B.; Lakomek, N.A.; Santur, K. B.; Mohrlüder, J.; Coronado, M.; Willbold, D. *Discovery of All-D-Peptide Inhibitors of SARS-CoV-2 3C-like Protease*. ACS Chemical Biology 2023: <https://doi.org/10.1021/acscchembio.2c00735>.
6. Santur, K; Reinartz, E.; Lien Y; Tusche, M; Altendorf, T.; **Sevenich, M.**; Gültekin, T., Mohrlüder, J.; Willbold, D. *Ligand-induced Stabilization of the Native Human Superoxide Dismutase 1*. ACS Chemical Neuroscience 2021, 12, 13: <https://doi.org/10.1021/acscchemneuro.1c00253>.
7. Santur, K\*, **Sevenich, M.**\*, Schwarten, M.; Nischwitz, V.; Willbold, D., Mohrlüder, M. *In Vitro Reconstitution of the Highly Active and Natively Folded Recombinant Superoxide Dismutase 1 Holoenzyme*. ChemistrySelect 2018, 3, 26: <https://doi.org/10.1002/slct.201801319>; (\* shared first authorship).
8. Braczynski, A.K.; **Sevenich, M.**; Gering, I.; Kupreichyk, T.; Agerschou, E.D.; Kronimus, Y.; Habib, P.; Stoldt, M.; Willbold, D.; Schulz, J.B.; Bach, J.-P.; Falkenburger, B.H.; Hoyer, W. *Alpha-Synuclein-Specific Naturally Occurring Antibodies Inhibit Aggregation In Vitro and In Vivo*. Biomolecules 2022, 12, 469: <https://doi.org/10.3390/biom12030469>.

## List of figures

<b>Figure 1:</b> Characteristic structural elements of $\alpha$ -syn.....	3
<b>Figure 2:</b> Aggregation pathway of $\alpha$ -syn.....	5
<b>Figure 3:</b> Mechanism of the seeding process of monomeric $\alpha$ -syn resulting in fibril mass growth and the formation of oligomers and protofibrils. ....	6
<b>Figure 4:</b> Three-dimensional structure of $\alpha$ -syn off-pathway oligomers.....	8
<b>Figure 5:</b> Toxic effects exerted by $\alpha$ -syn oligomers. ....	9
<b>Figure 6:</b> Characteristic structure of $\alpha$ -syn fibril filaments. ....	11
<b>Figure 7:</b> Potential intervention points of $\alpha$ -syn aggregation and prion-like propagation of seeding species.....	15
<b>Figure 8:</b> Anti-prionic MoA in prion-like diseases. ....	17
<b>Figure 9:</b> Viral replication cycle of SARS-CoV-2.....	21
<b>Figure 10:</b> The SARS-CoV-2 spike protein structure and function.. ....	23
<b>Figure 11:</b> Molecular interaction sites of SARS-CoV-2 RBD and hACE2.....	24
<b>Figure 12:</b> MoA of RBD targeting spike – hACE2 inhibitors of complex formation. ....	27
<b>Figure 13:</b> Fields of peptide drug optimization and corresponding strategies.....	30
<b>Figure 14:</b> Retro-inverso peptide optimization strategy for phage display derived L-enantiomeric peptide sequences.....	31
<b>Figure 15:</b> Principle of M13 phage display selection.. ....	33
<b>Figure 16:</b> Mirror-image phage display selection.. ....	34
<b>Figure 17:</b> Schematic representation for the development of therapeutic and diagnostic peptide compounds. ....	185

## Abstract

The identification, characterization and optimization of therapeutic agents are key issues for today's pharmaceutical industry. In particular, innovative treatment and development strategies are required that either target diseases which are considered incurable or provide short development times in response to novel emerging diseases. In this work, phage display selection was performed as a starting point for the development of peptide drugs against the two target diseases, Parkinson's disease (PD) as well as coronavirus disease 2019 (COVID-19).

PD is the most common neurodegenerative movement disorder worldwide. A central feature is the progressive degeneration of dopaminergic neurons, which is associated with the accumulation of cytosolic inclusions called Lewy bodies. These consist largely of the pre-synaptically located, physiologically intrinsically unfolded and monomeric protein alpha-synuclein ( $\alpha$ -syn), which, under disease-promoting conditions, associates with itself and deposits in structured biopolymers, called fibrils. During aggregation of  $\alpha$ -syn, soluble oligomers are formed, which are thought to be the key-factor for neurodegeneration. In addition, it is hypothesized that prion-like  $\alpha$ -syn structures can spread between cells and induce aggregation in recipient cells, ultimately leading to spread of neuropathology and disease progression. In this work, mirror-image phage display on the D-enantiomeric full-length  $\alpha$ -syn was performed for the identification of all-D-enantiomeric peptides that bind to the unstructured monomer with high affinity, thereby stabilizing the physiological status and preventing aggregation. In addition, initial sequence optimizations were investigated with respect to their ability to eliminate  $\alpha$ -syn oligomers and thus recover active monomer.

Another target disease addressed in this work is caused by the beta-coronavirus severe respiratory syndrome coronavirus 2 (SARS-CoV-2), first identified in Wuhan (China) in 2019. The high transmission efficiency between humans has resulted in a worldwide pandemic, with the disease primarily affecting the upper respiratory tract as well as the lung epithelium. Severe courses of coronavirus disease 2019 (COVID-19) can result in systemic inflammatory responses eventually leading to multi-organ failure (MOF). The SARS-CoV-2 replication cycle is a multi-step process initiated by cell contact of the viral spike protein and human angiotensin converting enzyme 2 (hACE2). To lay a foundation for the subsequent project, the interaction of the SARS-CoV-2 spike protein with hACE2 was first kinetically characterized in a separate project, where a secondary binding state within the already formed complex could be identified. This increases the affinity of the virus on the cell surface and is a potential factor that can be modulated among the currently circulating variants of concern (VOC). Based on these findings, phage display selection was performed on the receptor binding domain (RBD) of the SARS-CoV-2 spike protein to identify peptide ligands that block association with hACE2 and displace the receptor from the already formed complex. For this purpose, the interaction kinetics of the peptides with the spike protein were investigated and validated with respect

to inhibition of hACE2 binding. Rational design using the combination of sequences in divalent approaches led to improved inhibitory effects.

To address the previously alluded projects, a novel phage display selection protocol was developed that introduces control selections and a next generation sequencing (NGS)-based sequence analysis to specifically identify sequence variants that exhibit binding to the respective target protein. This protocol was also applied to the target proteins SARS-CoV-2 3C-like protease (3CL<sup>Pro</sup>, COVID-19) and hSOD1 (human superoxide dismutase, Amyotrophic lateral sclerosis (ALS)) in separate projects. Here, the screening protocol also led to the identification of peptide ligands that can be considered for therapeutic applications after appropriate optimization. In addition, the use of fibrillar  $\alpha$ -syn as a target, demonstrates the development of peptide ligands for diagnostic purposes.

In summary, the combined results of the different projects allow the derivation of a general approach for the development of therapeutic and diagnostic peptide ligands.

## Kurzzusammenfassung

Die Identifizierung, Charakterisierung und Optimierung von therapeutischen Wirkstoffen ist ein Schlüsselthema für die heutige Pharmaindustrie. Insbesondere werden innovative Behandlungs- und Entwicklungsstrategien für jene Erkrankungen benötigt, die entweder als unheilbar gelten, oder kurze Entwicklungszeiten als Reaktion auf neu auftretende Krankheiten bieten. In dieser Arbeit wurde eine Phagen-Display-Selektion als Ausgangspunkt für die Entwicklung von Peptidmedikamenten gegen die beiden Zielkrankheiten, die Parkinson-Krankheit (PD) und die Coronavirus-Erkrankung 2019 (COVID-19), durchgeführt.

PD ist die weltweit am häufigsten auftretende neurodegenerative Bewegungsstörung. Ein zentrales Merkmal ist die fortschreitende Degeneration dopaminergischer Neuronen, die mit der Ansammlung von zytosolischen Einschlüssen, den so genannten Lewy-Körpern, einhergeht. Diese bestehen größtenteils aus dem präsynaptisch gelegenen, physiologisch intrinsisch ungefaltetem und monomeren Protein alpha-Synuclein ( $\alpha$ -syn), das unter krankheitsfördernden Bedingungen mit sich selbst assoziiert und sich in strukturierten Biopolymeren, den sogenannten Fibrillen, ablagert. Bei der Aggregation von  $\alpha$ -syn werden lösliche Oligomere gebildet, die als Schlüsselfaktor für die Neurodegeneration gelten. Darüber hinaus wird angenommen, dass sich Prionen-ähnliche  $\alpha$ -syn-Strukturen zwischen Zellen ausbreiten und in den Empfängerzellen Aggregation auslösen können, was letztlich zur Ausbreitung der Neuropathologie und zum Fortschreiten der Krankheit führt. In dieser Arbeit wurde ein Spiegelbild Phagen-Display gegen das Volllänge D-Enantiomer von  $\alpha$ -syn durchgeführt, um vollständig D-Enantiomere-Peptide zu identifizieren, die mit hoher Affinität an das unstrukturierte Monomer binden und dadurch den physiologischen Zustand stabilisieren sowie Aggregation verhindern. Darüber hinaus wurden erste Sequenzoptimierungen im Hinblick auf die Eigenschaft untersucht,  $\alpha$ -syn-Oligomere zu eliminieren und somit das aktive Monomer wiederherzustellen.

Eine weitere in dieser Arbeit behandelte Zielkrankheit wird durch das Beta-Coronavirus schweres respiratorisches Syndrom Coronavirus 2 (SARS-CoV-2) verursacht, das 2019 erstmals in Wuhan (China) identifiziert wurde. Die hohe Übertragungseffizienz zwischen Menschen hat zu einer weltweiten Pandemie geführt, wobei die Krankheit vor allem die oberen Atemwege sowie das Lungenepithel befällt. Schwere Verläufe der Coronavirus-Krankheit 2019 (COVID-19) können zu systemischen Entzündungsreaktionen und schließlich zu Multiorganversagen (MOF) führen. Der Replikationszyklus von SARS-CoV-2 ist ein mehrstufiger Prozess, der durch den Zellkontakt des viralen Spike-Proteins und des humane Angiotensin-konvertierende Enzyme 2 (hACE2) eingeleitet wird. Um eine Grundlage für das nachfolgende Projekt zu schaffen, wurde die Interaktion des SARS-CoV-2-Spike-Proteins mit hACE2 in einem separaten Projekt zunächst kinetisch charakterisiert, wobei ein sekundärer Bindungszustand innerhalb des bereits gebildeten Komplexes identifiziert werden konnte. Dieser erhöht die Affinität des Virus an der Zelloberfläche und ist ein potenzieller Faktor, der

bei den derzeit zirkulierenden besorgniserregenden Varianten (VOC) moduliert werden kann. Auf Basis dieser Erkenntnisse wurde eine Phage-Display-Selektion an der Rezeptorbindungsdomäne (RBD) des SARS-CoV-2-Spike-Proteins durchgeführt, um Peptidliganden zu identifizieren, die die Assoziation mit hACE2 blockieren und den Rezeptor aus dem bereits gebildeten Komplex verdrängen könnten. Zu diesem Zweck wurde die Interaktionskinetik der Peptide mit dem Spike-Protein untersucht und im Hinblick auf die Hemmung der hACE2-Bindung validiert. Rationales Design unter Verwendung der Kombination von Sequenzen in divalenten Ansätzen führte zu verbesserten Hemmwirkungen.

Um die zuvor erwähnten Projekte anzugehen, wurde ein neuartiges Phagen-Display-Selektionsprotokoll entwickelt, das Kontrollselektionen sowie eine auf Next Generation Sequencing (NGS) basierende Sequenzanalyse vorsieht, um speziell Sequenzvarianten zu identifizieren, die eine Bindung an das jeweilige Zielprotein aufweisen. Dieses Protokoll wurde auch auf die Zielproteine SARS-CoV-2 3C-ähnliche Protease (3CL<sup>pro</sup>, COVID-19) und hSOD1 (humane Superoxid-Dismutase, amyotrophe Lateralsklerose (ALS)) in separaten Projekten angewendet. Auch hier führte das Screening-Protokoll zur Identifizierung von Peptidliganden, die nach entsprechender Optimierung für den therapeutischen Einsatz in Frage kommen. Zusätzlich wird, durch die Verwendung von fibrillärem  $\alpha$ -syn als Zielstruktur, die Entwicklung von Peptidliganden für diagnostische Zwecke demonstriert.

Zusammenfassend ermöglichen die kombinierten Ergebnisse der verschiedenen Projekte die Ableitung eines allgemeinen Ansatzes für die Entwicklung therapeutischer und diagnostischer Peptidliganden.

## **1 Introduction**

### **1.1 Part I: Stabilization of monomeric $\alpha$ -synuclein by all-D-enantiomeric peptide ligands as therapeutic strategy for Parkinson's disease**

#### **1.1.1 Parkinson's disease**

##### **1.1.1.1 Epidemiology**

Parkinson's disease (PD) is the most common neurodegenerative movement disorder and the second most common degenerative disease of the central nervous system [1]. It affects the general population with a prevalence of 0.3 % and an overall risk of 2.0 % for men and 1.6 % for women of developing PD during their lifetime [2]. The incidence in the population over 60 years of age is 1.0 %, increasing to 4.0 % in those over 80 years of age [3, 4]. The incidence ranges from 10 to more than 20 individuals per 100,000 per year. In 2009, the total number of PD cases worldwide was estimated at 4 million. This number is expected to double to more than 9 million cases by 2030, mainly due to the demographic increase in the age of the world population [5].

##### **1.1.1.2 Clinical features**

PD is characterized by both motor and non-motor features [6]. Motor cardinal symptoms were first recognized by James Parkinson in 1817 and are defined as tremor, rigidity, bradykinesia/akinesia, and postural instability [7]. The clinical diagnosis of PD is made by the presence of bradykinesia and an additional cardinal motor feature (rigidity or tremor), as well as additional supportive and exclusionary criteria [8].

Motor symptoms can occur throughout the course of the disease, with an average onset in the late fifties. Early-onset PD is defined by an onset of motor symptoms before the age of 45, with 10 % of patients having a genetic predisposition [9]. By the time the first motor deficits are noted, 50-70 % of dopaminergic neurons have already been lost. The average life expectancy from this point is between 15 and 20 years [10, 11].

Non-motor symptoms include cognitive impairment, autonomic dysfunction, sleep disturbances, depression, and hyposmia [12]. Some of these symptoms may precede cardinal motor symptoms by years or even decades (prodromal PD) [13].

### 1.1.1.3 Neuropathology

PD is characterized by progressive neurodegeneration in a specific brain region, the substantia nigra pars compacta (SNpc). A key feature of SNpc dopaminergic neurons is their steady, autonomic pacing, which is critical for the sustained release of dopamine needed by target structures such as the striatum to plan and initiate motor functions [14].

Dopaminergic neurodegeneration is associated with the formation of intracellular protein accumulations, called Lewy bodies (LB) and Lewy neurites (LN). Therefore, a common method of determining disease progression is to divide the disease into Braak stages based on the distribution of LB and LN, known as Lewy pathology. While Braak stages 1 and 2 are presymptomatic, Braak stages 3 and 4 involve the midbrain and basal forebrain, eventually extending to regions of the neocortex in Braak stages 5 and 6 [15]. Recent research has shown that inclusions of  $\alpha$ -synuclein ( $\alpha$ -syn) can already be observed in the peripheral nervous system and caudal brainstem before parkinsonism and neurodegeneration occur in SNpc [16]. LB are inclusion bodies formed in the cytoplasm of neurons, whereas LN are typically found in the axons of neurons. Both consist of a granular core formed by a large number of nitrated [17], phosphorylated and ubiquitinated [18] proteins that are involved in cellular processes like several heat-shock proteins, neurofilaments, lysosomal proteins and ubiquitin as well as lipids. The core is surrounded by filamentous halo up to 10 nm in size, which is mainly composed of  $\alpha$ -syn. Although Lewy pathology is a hallmark of PD, it can also be found in other neurodegenerative diseases such as dementia with Lewy bodies (DLB), the Lewy body variant of Alzheimer's disease (AD) and multiple system atrophy (MSA).

Hereditary forms of PD account for 5-10 % of all cases. Genetic defects in genes associated with PD can trigger neuropathology [19] that resembles sporadic PD including impaired  $\alpha$ -syn homeostasis, impaired mitochondrial function, oxidative stress, calcium homeostasis, axonal transport and neuroinflammation [20]. In addition to mutations in the *SNCA* locus encoding  $\alpha$ -syn, a variety of loci have been identified as risk factors for PD over the past three decades [19]. To date, 15 genes responsible for monogenic forms of PD have been identified, including *PRKN*, *PINK1*, and *DJ-1*, as well as autosomal dominant mutations in the *LRRK2* gene [21].

## 1.1.2 $\alpha$ -synuclein

### 1.1.2.1 Structure and physiological role

The protein  $\alpha$ -syn was first isolated from synaptic vesicles in the *Torpedo* fish and termed “synuclein”. Later, a homologous protein was identified in rat neuronal synaptic vesicles and nuclear envelopes [22]. Human  $\alpha$ -syn was first identified in the context of Alzheimer’s disease (AD) and later named NACP, the precursor of the non-amyloid beta component of AD [23]. Together with  $\beta$ - and  $\gamma$ -synuclein, it belongs to the synuclein family, with  $\alpha$ -syn being the only member associated with the adaptation of pathological structures [24].

$\alpha$ -syn is a 14.46-kDa protein with 140 residues that occurs predominantly in the presynaptic regions of the central nervous system. The majority of  $\alpha$ -syn is located in the cytoplasm of dopaminergic neurons, where it is present as an intrinsically disordered protein (IDP) associated with the regulation of neurotransmitter release, but is also found in other cell and tissue types such as red blood cells, muscle, liver, lung and heart [25, 26]. The primary sequence of  $\alpha$ -syn can be divided into three distinct regions, each playing a critical role in its physiological and pathophysiological behavior: the repeat-rich N-terminus (residues 1-60), the “non-amyloid component” (NAC) domain (residues 61-95), and the C-terminal region (residues 96-140).

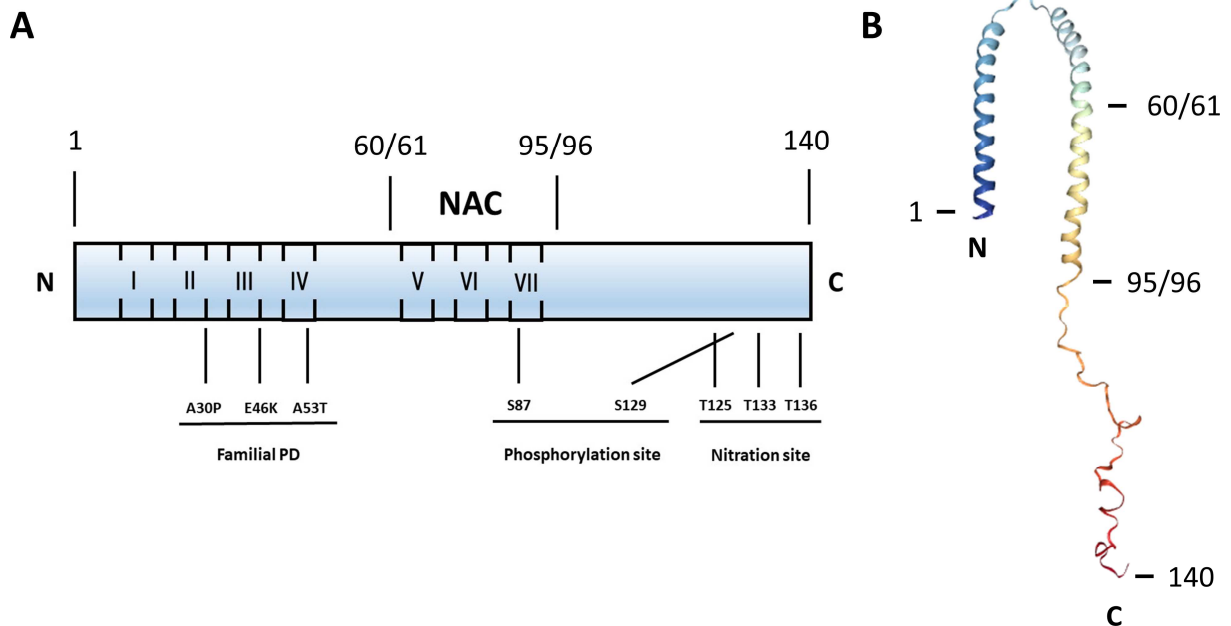


**Figure 1: Characteristic structural elements of  $\alpha$ -syn.** (A) Schematic representation of the structural elements of  $\alpha$ -syn, the distribution of the repetitive motifs (I-VII) and PD-related point mutations as well as phosphorylation and nitration sites (adapted and changed from Cheng et al., 2011 [27]). (B) Protein structure showing  $\alpha$ -syn with alpha helical secondary structural elements (which  $\alpha$ -syn adopts in membrane bound state) located at positions 1 – 95, (PDB: 1XQ3, [28]).

## Introduction

The repeat-rich N-terminus (residues 1-60) as well as the "non-amyloid component" (NAC) domain (residues 61-95) adopt alpha-helical substructures upon interaction with lipid membranes, allowing regulation of vesicle trafficking [29, 30]. The N-terminal region harbors most of the seven imperfect 11-mer repeats carrying a highly conserved hexameric "KTKEGV" motif. The 11-mer repeats consist of a conserved apolipoprotein-like class A2 helix that mediates the binding of  $\alpha$ -syn to phospholipid vesicles [31]. Four repeats are located in the N-terminal region, while three are localized in the NAC region [32, 33]. The NAC region is highly hydrophobic and acidic and acts as a lipid 'sensor' that mediates specificity for binding to synaptic vesicles. In addition,  $\alpha$ -syn is involved in synaptic maintenance and assembly of SNARE proteins and acts as a chaperone, enabled by transient molecular interactions inherent to IDPs [34, 35].  $\alpha$ -syn is associated not only with the synaptic vesicle pool but also with mitochondria, where both loss and overexpression can lead to mitochondrial dysfunction [36]. Finally, the C-terminal portion (residues 96-140) remains unstructured and highly flexible in almost all conformations and carries 15 negatively charged residues that provide chaperone activity along with the ability to bind metals, polyamines, and positively charged proteins such as tau [29, 34, 37, 38].

### 1.1.2.2 $\alpha$ -syn aggregation

In recent decades, there has been a heated debate about whether  $\alpha$ -syn exists as a disordered monomer or a folded helical tetramer under physiological conditions. However, a growing body of evidence, such as in-cell nuclear magnetic resonance (NMR), shows that  $\alpha$ -syn indeed behaves like a disordered monomeric protein in its native state [39-42]. During PD pathogenesis,  $\alpha$ -syn loses its IDP status and undergoes structural rearrangements that eventually results in the formation of oligomers, protofibrils and mature fibrils (Fig. 2).

## Introduction

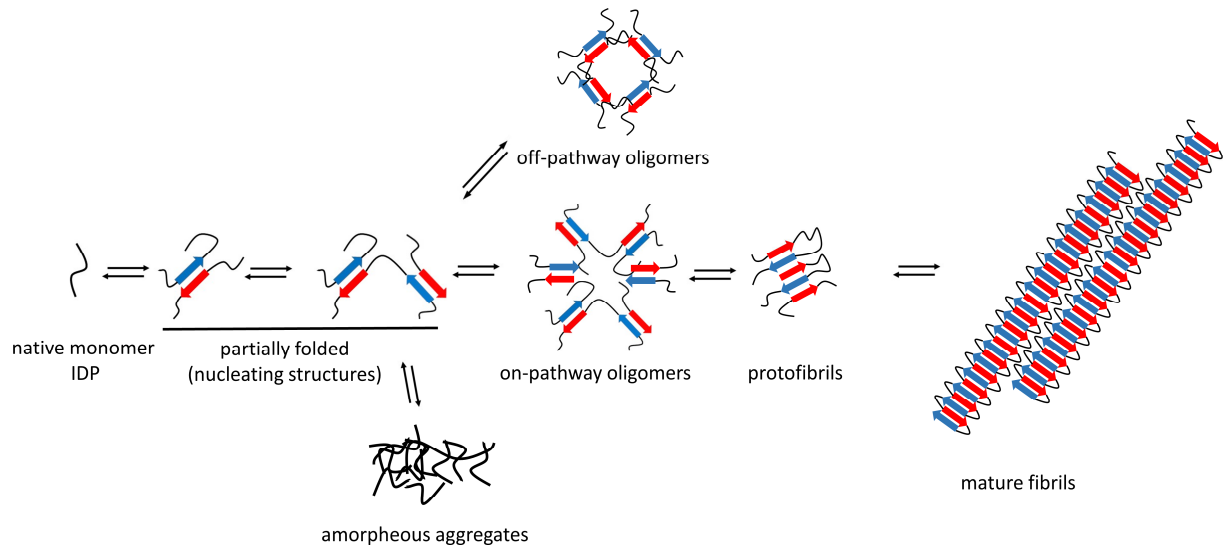


**Figure 2: Aggregation pathway of  $\alpha$ -syn.** Upon nucleation events, the monomeric  $\alpha$ -syn undergoes structural rearrangements that will lead to the formation of partially folded, nucleating structures, followed by the formation of on- and off-pathway oligomers as well as amorphous aggregates. While off-pathway oligomers are to convert into fibrils, on-pathway oligomer assemblies have the ability to undergo structural rearrangements that result in the formation of protofibrils which will elongate into highly ordered cross- $\beta$ -sheet mature fibrils by the recruitment of monomeric  $\alpha$ -syn (adapted and changed from Mehra et al., 2019; [43]).

Monomeric  $\alpha$ -syn has a dynamic structure and populates an ensemble of conformational states under solution conditions [44, 45]. In order to form well-defined interactions with physiological binding partners,  $\alpha$ -syn exposes amino acid stretches and adopts compatible conformations [28, 29, 34, 46]. Similarly, monomeric  $\alpha$ -syn is able to self-associate and form dimeric, trimeric structures, and higher order conformers, eventually leading to the formation of stable fibrillar structures. Normally, the Gibbs free energy of monomer transition from the solution phase to the aggregated phase is positive and thus kinetically unfavorable [47]. However, stable aggregation nuclei can form under supersaturated conditions, which can be caused by a sudden change in temperature, pH, or dilution in aqueous solution. The formation of stable aggregates is the result of a selection process that favors thermodynamically stable conformers capable of further alignment of monomeric  $\alpha$ -syn. Therefore, conformations that are thermodynamically unstable and lack the ability to self-propagate are excluded during the selection process. What remains is an ensemble of fibrils with high stability, while the dominant morphology is the conformer that is most populated under certain solution conditions and/or the fibril morphology that can grow the fastest [48]. In addition to the kinetic selection process, proteolytic selection [49, 50], in which the fibril morphology with the highest proteolytic resistance is selected, and cofactor-dependent selection [51], in which cofactors stabilize the preferred fibril morphology, have also been proposed.

Once primary nucleation has occurred and protofibrils have formed, the process of  $\alpha$ -syn aggregation becomes autocatalytic, such that (i) fibrils are able to recruit further  $\alpha$ -syn by

elongating fibril ends, (ii) secondary nucleation occurs at fibril surfaces, and (iii) fibril fragmentation leads to the formation of additional fibril ends that can be further elongated (Fig. 3; [52]). In this context, the relationship between the processes induced by elongation or secondary nucleation has been found to be highly pH dependent, with fibril elongation being the dominant process at neutral pH and secondary nucleation at intermediate acidic pH [52]. In addition to primary nucleation, secondary nucleation is the mechanism that critically contributes to the formation of additional oligomeric and proto-fibrillary conformers during aggregation and thus is the central mechanism contributing to autocatalytic self-amplification [47, 53]. While fibril elongation follows a linear growth rate that slows as monomer depletion progresses, secondary nucleation events exhibit many features known from Michaelis-Menten kinetics of enzyme activity, in which the rate of conversion in the unsaturated region depends on monomer concentration and becomes independent at saturating monomer concentrations [54].

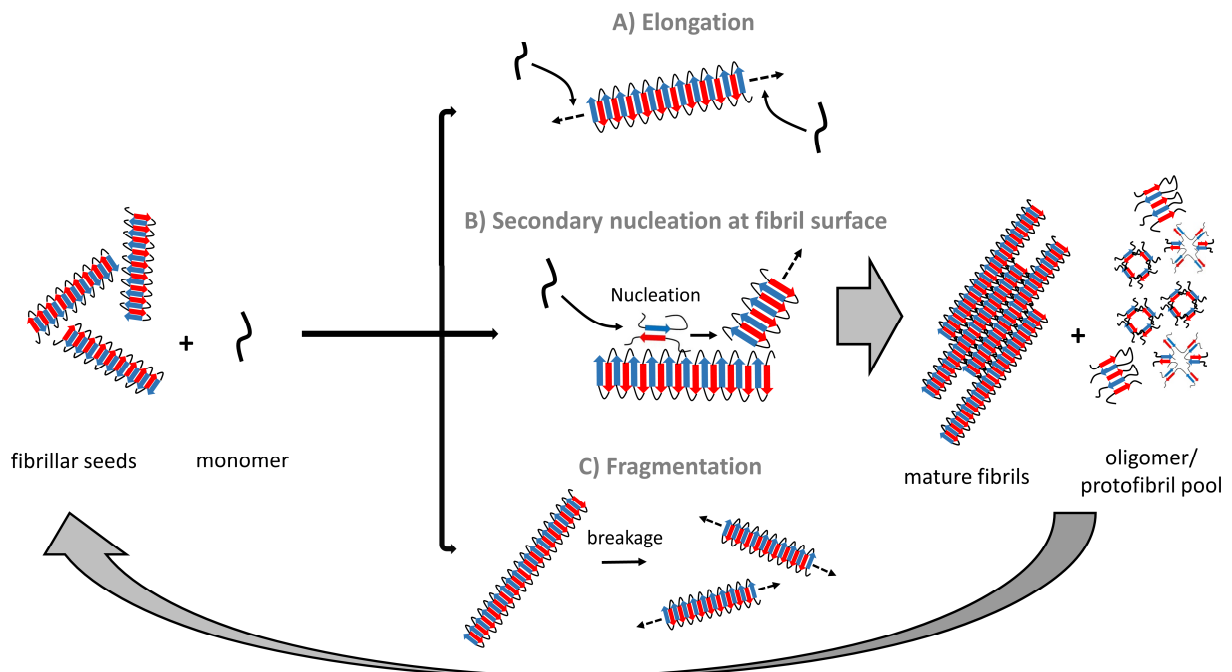


**Figure 3: Mechanism of the seeding process of monomeric  $\alpha$ -syn resulting in fibril mass growth and the formation of oligomers and protofibrils.** Starting with seeds, growth of fibril mass can occur via three distinct mechanics together with monomeric  $\alpha$ -syn. A) Fibril elongation: monomeric  $\alpha$ -syn is recruited to the fibril ends and fibrils grow in both directions. B) Secondary nucleation: monomeric  $\alpha$ -syn attaches to fibril surfaces and undergoes structural rearrangements that result in the formation of novel aggregation nuclei. C) Fibril fragmentation: fragmentation of fibrils during the aggregation process results in the creation of novel fibril ends which can be elongated by the recruitment of monomeric  $\alpha$ -syn analogous to (A).

The concept that  $\alpha$ -syn is part of PD etiology was first proposed when mutations in the *SNCA* gene were associated with rare familial cases of PD that resembled symptoms of sporadic PD [55]. In addition, enhanced genetic dosage by duplication or triplication of the *SNCA* gene also

results in familial forms of the disease. In the context of the thermodynamically driven selection process described, it is hypothesized that PD-associated point mutations of the SNCA gene alter the distribution of  $\alpha$ -syn conformations such that the thermodynamic barrier to the formation of kinetically stable and self-replicating self-assemblies is lowered [56]. Similarly, increased gene dosage leads to an overpopulation of such conformations by simply increasing the total protein concentration. In contrast, sporadic cases of PD lack the link between direct changes in the SNCA locus and  $\alpha$ -syn nucleation. Primary nucleation can occur throughout the solution (homogeneous nucleation) or at a surface (heterogeneous nucleation) and was found to be highly dependent on solution conditions, such as pH and salt concentration [52], air-water interfaces [57, 58], the presence of polyvalent heavy metal ions and polycationic molecules like putrescine or spermidine [59], anionic surfactants including SDS-micelles [60, 61] as well as oxidative modifications [62]. In addition, to accelerate the rate of aggregation, the introduction of artificial surfaces and mechanical actions such as stirring and shaking have proven to be extremely effective [63].

### **1.1.2.3 Structure and toxicity of $\alpha$ -syn oligomers, protofibrils and fibrils**

#### **1.1.2.3.1 Oligomers and protofibrils**

The term oligomer is a widely used to describe soluble aggregated species that have not yet adopted a fibrillar conformation. On the way to fibril formation, prefibrillar oligomeric species are formed, which, similar to fibrils, occur in different structures, molecular weights and morphologies ranging from mainly  $\beta$ -sheet to  $\alpha$ -helical secondary structures with different proportions of disordered regions [64, 65]. Due to their transient nature, these conformations are difficult to study. However, trapping of intermediate structures by inhibition of the elongation of certain oligomer types, using compounds as epigallocatechin (EGCG, [66]), covalent cross-linking with glutaraldehyde [67] and formaldehyde [68] as well as stabilization by additives such as heme [69], catecholamines [70] and by certain flavonoids like baicalein [71] have helped to elucidate and characterize the structural diversity of  $\alpha$ -syn oligomers behaving "on-pathway". On the other hand, certain "off-pathway" oligomeric conformers, which lack the ability to grow into mature fibrils, have shown to be kinetically stable without the addition of additives [72], allowing for more detailed structural investigation.

Depending on the protocol used for oligomer preparation,  $\alpha$ -syn oligomers exhibit different structural features and functional properties. One of the most commonly used methods for the preparation of kinetically stable  $\alpha$ -syn "off pathway" oligomer samples is lyophilization of monomeric  $\alpha$ -syn, followed by incubation of 12 mg/ml protein at physiological pH and ionic strength without addition of supplements [72, 73]. The effect of lyophilization on oligomer

formation can be attributed to a combination of factors, including a significant increase of the solvent/air ratio and decrease of the molecular distance during the process [74].

The oligomers thus produced have been shown to contain largely antiparallel  $\beta$ -sheet structures and to have an approximate size of 30  $\alpha$ -syn monomer units, corresponding to an  $M_w$  of ~450 kDa [72, 75-77]. It has been suggested that the NAC region, together with an N-terminal portion (residues 39 to 89), generates the ellipsoidal core structure of the oligomers [78], which is surrounded by disordered protein proportions (Fig. 4; [72, 73, 79]). These oligomer preparations have found to be remarkably stable at extreme pH and temperature conditions, dissociating into monomers only at very high urea concentrations [80].

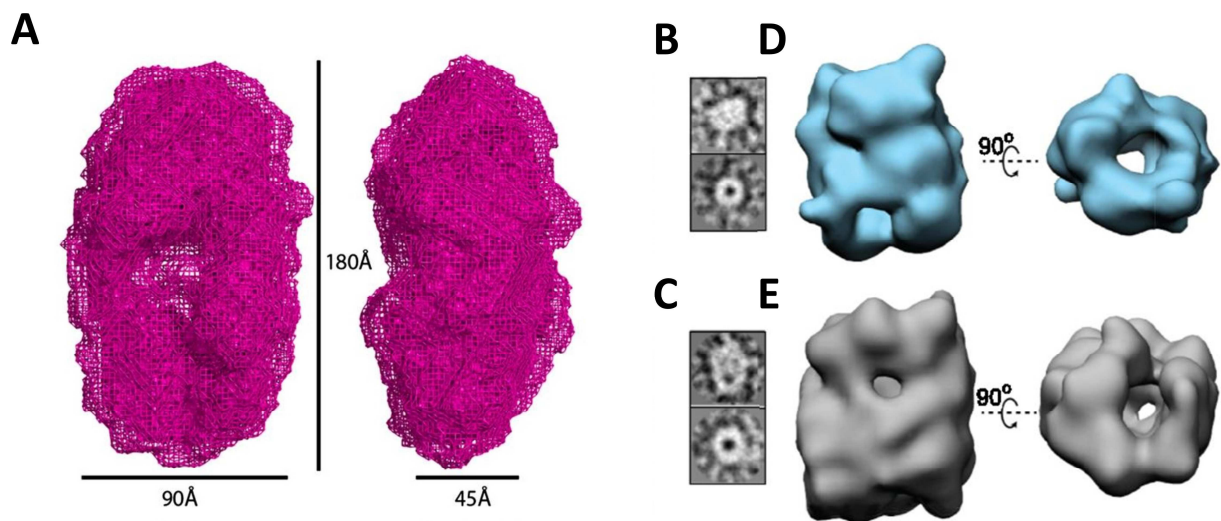


**Figure 4: Three-dimensional structure of  $\alpha$ -syn off-pathway oligomers.** (A) Low resolution SAXS model of  $\alpha$ -syn off-pathway oligomers. The average structure (mesh representation) and the filtered averaged structure (surface representation) are displayed and superimposed. The model is shown in two orientations along the longitudinal axis (adapted from Giehm et al, 2011; [81]). (B-E) Cryo-electron microscopy (EM) image and structure of two subgroups (10S (B/D) and 15S (C/E) oligomers) identified in the  $\alpha$ -syn off-pathway oligomer preparation. (B/C) Representative Cryo-EM images of side view (top) and end-on view (bottom) of the two oligomer subgroups. (D/E) 3D reconstitution of the average structure of the orthogonal views, side (left) and end-on (right) of the two oligomer subgroups (adapted from Chen et. al, 2015; [82]).

Over the last decades, evidence has accumulated to demonstrate that aggregated  $\alpha$ -syn is toxic in its oligomeric form. Toxic properties have been demonstrated in both *in vitro* studies and *in vivo* models of PD [83-85]. When pre-formed  $\alpha$ -syn oligomers were applied to cell cultures or formed due to overexpression, they were shown to cause cell death [86-89]. Moreover,  $\alpha$ -syn rationally designed to form oligomeric structures, rather than converting to mature fibrils, was shown to induce cell death when applied to immortalized cell lines, primary cultures of rat neurons, or dopaminergic neurons from *C. elegans* and *Drosophila* [85]. In contrast, a  $\alpha$ -syn construct that rapidly forms fibrils showed no toxicity [90].

## Introduction

In the past, several possible pathways have been proposed to explain the mechanism of the observed toxic effects of  $\alpha$ -syn oligomers (Fig. 5).

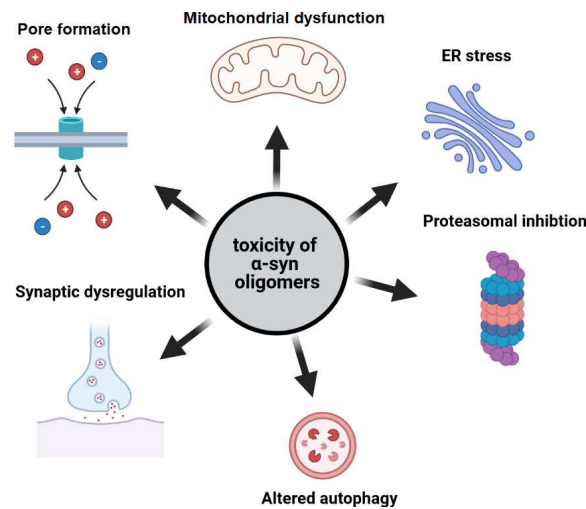


**Figure 5: Toxic effects exerted by  $\alpha$ -syn oligomers (adapted and changed from Alam et. al, 2019; [48], created with BioRender).**

Several observations suggest that oligomers can disrupt cellular homeostasis by forming pores in the cell membrane [87, 91, 92]. This leads to an increased influx of ions from the extracellular space and an impairment of cellular integrity. As described previously,  $\alpha$ -syn is thought to be involved in the regulation of synaptic trafficking and association with the SNARE complex at synapses [93]. Indeed,  $\alpha$ -syn oligomers added to rat hippocampal slices were found to have an effect on neuronal signaling, and tissues pre-incubated with  $\alpha$ -syn oligomers showed an increase in synaptic transmission, resulting in suppression of the long-term potentiation [94]. Moreover,  $\alpha$ -syn oligomers generated by strong sonication of fibrils showed a negative effect on neuronal excitability [95]. The formation of  $\alpha$ -syn oligomers might also be implicated in the failure of protein degradation pathways, such as the ubiquitin-proteasome system or the autophagy-lysosomal pathway. One study found a connection between inhibition of the lysosomal pathway by bafilomycin, which was accompanied by an increased cellular toxicity, and reduced fibril formation. Instead, the proportion of smaller, soluble species increased [96]. Another mechanism that may be involved in the toxicity of  $\alpha$ -syn oligomers is the phagocytosis of oligomeric species by microglia and astrocytes and their subsequent degradation, which may be related to the prevention and/or elimination of oligomer formation. Here, microglia from adult mice were shown to exhibit less efficient uptake and clearance of oligomeric  $\alpha$ -syn compared to younger mice [97]. Overexpression of  $\alpha$ -syn A53T and A30P in human neuroblastoma cells was found to lead to increased formation of  $\alpha$ -syn oligomers in mitochondria. The affected mitochondria showed decreased transmembrane potential and impaired cellular respiration [98]. In

addition, it was shown that  $\alpha$ -syn oligomers can prevent protein import into mitochondria by interacting with the translocase TOM20. This interaction may be associated with a decreased concentration of the complex I subunit Ndufs3, which was also observed in the SNpc of PD patients [99]. Regarding the association of endoplasmic reticulum (ER) and  $\alpha$ -syn oligomers, it has been shown that oligomers and protofibrils can accumulate in the ER and trigger a stress response, possibly contributing to neurodegeneration [100]. Previous studies have shown that aggregated extracellular species can cause inflammation and degeneration of affected neurons, possibly mediated by generation of reactive oxygen species through activation of NADPH oxidase [101] or activation of signaling pathways involving p38, ERK1/2 MAP kinases and NF- $\kappa$ B [102].

### 1.1.2.3.2 Fibrils

Several structures of different fibrillar  $\alpha$ -syn polymorphs have been published. Different polymorphs have shown different seeding capacities *in vitro* and *in vivo*, which may be associated with different types of synucleinopathies that resemble the rate of progression of each pathophenotype. The amino acid proportions which are exposed on the fibril surface of the different polymorphs define the potential interactions which will impact their specific physiochemical properties: (i) formation of fibril bundles, (ii) formation of macromolecular structures, (iii) resistance to degradation and protein clearance, (iv) post-translational modifications, (v) interactions at neuronal plasma membranes, (vi) interactomes with neuronal cell's cytosol, (vii) escaping rate from endolysosomal compartments after their cell entry, (viii) transportation within neurons and their (ix) export from cells, thereby allowing spread from cell-to-cell.

Negative stain electron microscopy (EM) of fibrils extracted from PD and MSA patients revealed different polymorphs with either 10 nm wide straight or twisted filaments and a smaller population with 5 nm wide straight filaments [103, 104]. Another EM study using recombinant  $\alpha$ -syn yielded similar polymorphisms, where each of the 10 nm wide filaments consisted of a bundle of two  $\alpha$ -syn filaments [105]. When brain-derived  $\alpha$ -syn was used for seeding monomeric  $\alpha$ -syn, a correlation between the origin of the different synucleinopathies and the seeding capacity of the different fibril polymorphs was found [106]. Similarly, two polymorphs generated *in vitro* exhibited different toxicity and *in vitro* and *in vivo* seeding properties [107, 108].

Several structural studies (hydrogen/deuterium exchange NMR, electron paramagnetic resonance spectroscopy (EPR), microelectron diffraction (microED), solid-state NMR (ssNMR), and cryo-EM) on  $\alpha$ -syn fibrils have shown that a central region (aa 44 - 96) forms the fibril core, which is flanked by N- and C-terminal residues. While the fibril core region is completely

## Introduction

buried and exhibits a highly ordered, homogeneous packing, the N-terminal region is structurally more heterogeneous and the C-terminal domain retains its structural flexibility [109].

Regarding the structural details of the core hydrophobic region, two regions, namely the preNAC region ( $_{47}\text{GVVHGVTTVA}_{56}$ ) and the NACore region ( $_{68}\text{GAVVTGVTAVA}_{78}$ ), were identified as critical for fibril formation and cytotoxicity, both containing a pair of parallel in-register  $\beta$ -sheets forming a steric zipper (Fig. 6, [110]). In addition, structural analysis by ssNMR allowed the identification of a Greek  $\beta$ -sheet motif in the hydrophobic core of each filament, which is stabilized by multiple hydrophobic and ionic interactions [38]. Recent studies have shown that, although the fibril structure has a conserved core interface for different polymorphs (rod and twister filaments), single point mutations can affect the core regions, leading to the formation of different polymorphs with different seeding capacity and toxic properties [111].

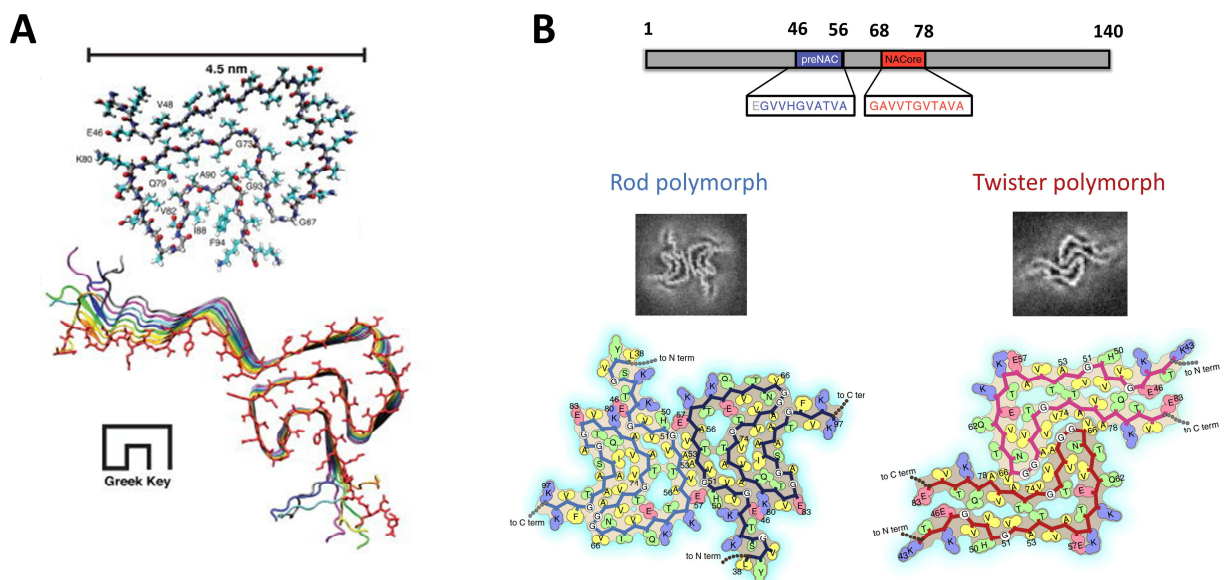


**Figure 6: Characteristic structure of  $\alpha$ -syn fibril filaments.** (A) View of central monomer from residues 44 to 96 looking down the fibril axis showing the Greek-key motif (top) and stacked monomers showing the side chain alignment between each monomer down the fibril axis as determined by ssNMR (bottom; adapted from Tuttle et al., 2016; [38]). (B) Location of the preNAC and NACore region within the full-length  $\alpha$ -syn sequence (top), Cryo-EM cross-section view of the two polymorphs (middle) and residue interactions of two asymmetric units in two opposing protofilaments (bottom, viewed down fibril axis). Residues are colored by hydrophobicity (yellow: hydrophobic; green: polar; red: negative charge; blue: positive charge; adapted and changed from Li et al., 2018 [111].)

Similar to the previously described toxic spectrum of  $\alpha$ -syn oligomers (Fig. 5), a variety of toxic effects have also been described for fibrillary or proto-fibrillary  $\alpha$ -syn.  $\alpha$ -syn fibrillary species have been reported to contribute to neurodegeneration by affecting cellular homeostasis, impairing cellular proteostasis, and compromising the integrity of cytosolic organelles such as

ER, Golgi, mitochondria, and lysosomes [112]. Moreover, the process of fibril formation has been shown to accelerate neurodegeneration due to chronic inflammation [113-116]. While oligomeric  $\alpha$ -syn exhibits a broader range of toxic functions and higher robustness compared to  $\alpha$ -syn fibrils, interneuronal spread of aggregated  $\alpha$ -syn species in terms of seeding effects has been mainly demonstrated for fibrillary conformers [108, 117-119]. Therefore, fibrillar species with low  $M_w$  or protofibrils are the most promising candidates for interneuronal propagation of disease pathology in PD and other synucleinopathies.

### 1.1.2.4 Cell-to-cell transmission and seeding of $\alpha$ -syn: PD as a prion-like disease

“Prion” is a term coined by Stanley Prusiner in 1982. It is used for the definition of “proteinaceous infectious particle” that are able to adopt different conformations, thereby seed their endogenous counterparts and induce further aggregation [120, 121]. In a departure to the status quo during this time, which was mainly based on the “one protein, one structure” hypothesis, prions can adopt different morphologies of misfolding that give rise to different disease-related features. Several prion diseases based on misfolding of the same prion protein (PrP), such as Kuru, Creutzfeldt-Jacob disease, and Gerstmann-Sträussler-Scheinker syndrome, have been identified in humans, but there are also a number of other prion diseases not associated with humans [122-124]. In prion diseases, PrP<sup>C</sup> (cellular PrP) misfolds into the pathogenic form PrP<sup>Sc</sup> (scrapie PrP), which forms aggregates that will spread disease pathology further into the brain and induce neurodegeneration [120]. The spread of neurodegeneration by misfolded PrP<sup>Sc</sup> is realized by two basic mechanisms. First, nuclei form *de novo* upon misfolding events and induce an aggregation downstream cascade that amplifies itself auto-catalytically within a donor cell by further recruitment of endogenous PrP as previously described for  $\alpha$ -syn (Fig. 3). Second, on-pathway misfolded species act as template and interact with the native protein of recipient cells which results in the conversion of the natively folded protein into its pathological counterpart. Both mechanisms lead to the pathological spread within the same organism, but can also infect other organisms by breaking the species barrier [125].

Similar to prion diseases, several other neurodegenerative diseases are associated with prion-like protein misfolding and templating [126]. The concept of a “prion-like” disease was first demonstrated with amyloid- $\beta$  (A $\beta$ ), where Alzheimer's brain homogenates were able to induce cerebral  $\beta$ -amyloidosis in transgenic mice [127]. To date, the concept of “prion-like” disease mechanism has been extended to many other neurodegenerative diseases such as tauopathies, poly-Q diseases, ALS and PD as already mentioned [128-130].

First evidence that  $\alpha$ -syn might be involved in a prion-like disease propagation emerged when grafted neuronal cells were transplanted to recipients in an attempt to restore dopaminergic neurotransmission. Findings of histological studies on post-mortem tissue revealed LB-like

inclusions within the transplanted dopaminergic neurons of eight patients that died more than a decade after surgery. Interestingly, the LB in the grafts shared classic features with those of the SNpc of the host [131-133]. This observation was further verified when PD brain cell homogenate or LB extracts were injected intracerebral in the recipient mouse brain and induced similar pathology and spread as that of the host [119, 134]. The observation that Lewy disease progression occurs in a sequential order in different brain regions, which has been defined as the aforementioned "Braak staging," highlights the potential prion-like spread of misfolded  $\alpha$ -syn species [15]. However, a recent study has shown that the spread of  $\alpha$ -syn pathology does not always occur along the connectome as suggested by "Braak staging," which may be explained by the presence of intra-astrocytic  $\alpha$ -syn pathology [135]. In addition, it has been suggested that  $\alpha$ -syn pathology could originate in the gut and travel retrograde to the brain via the vagus nerve, or alternatively originate from the vagus nerve and spread to the gut via anterograde movement [136, 137].

As shown by the identification of  $\alpha$ -syn in human cerebrospinal fluid (CSF) and plasma as well as in the medium of several neuronal culture models,  $\alpha$ -syn is able to access the extracellular space [138-140]. Even  $\alpha$ -syn oligomers have been identified in CSF [141]. However, the exact mechanism by which misfolded  $\alpha$ -syn leaves cells, is transported between cells, and is eventually internalized in a recipient cell to trigger aggregation is still under investigation. Several lines of evidence suggest that exocytosis is involved in the release of  $\alpha$ -syn species by cells, as  $\alpha$ -syn can be detected in the lumen of vesicles isolated from rat brain or neuroblastoma cells [140, 142]. In addition, export of  $\alpha$ -syn to exosomes has been shown to be upregulated under conditions that promote its aggregation, potentially allowing the cell to remove misfolded species [142]. After release into the extracellular space, the next critical step for cell-to-cell transfer of  $\alpha$ -syn is the uptake into the recipient cell. While monomeric  $\alpha$ -syn is thought to passively cross the membrane, internalization of larger aggregated  $\alpha$ -syn species such as fibrils or oligomers most likely requires an endocytic process or receptor-mediated transport [143, 144].

### **1.1.3 PD therapy**

#### **1.1.3.1 Symptomatic treatment**

Since the pathology of PD is not yet fully understood, existing therapeutic strategies are primarily limited to the treatment of symptoms. The loss of dopaminergic neurons in the SNpc, leading to striatal dopamine depletion, is the main reason for the cardinal symptoms of PD. The loss of dopaminergic neurons in the SNpc, leading to striatal dopamine depletion, is the main reason for the cardinal symptoms of PD. For this reason, one of the most important

therapeutic strategies and the gold standard for the treatment of PD remains the substitution of dopamine loss by administration of the dopamine precursor amino acid L-DOPA [145]. Catechol-O-methyltransferase [146] and Monoamine oxidase type B [147] inhibitors have been shown to be advantageous when administered together with L-DOPA in order to increase its bioavailability and half-life. However, due to the development of motor complications, long-term L-DOPA (also known as Levodopa) treatment is limited in use [148]. In addition to dopamine-related targets, treatment of non-motor symptoms such as cognitive dysfunction, depression, and autonomic dysfunction has been shown to improve patients' quality of life [149]. The breakthrough in symptomatic treatment of Parkinson's disease occurred in 1993, when the subthalamic nucleus was identified as a new target. Here, deep brain stimulation (DBS), which uses implanted electrodes for high-frequency stimulation of specific brain targets to mimic the clinical effect of lesioning, established as an evidence-based therapy for motor fluctuations and dyskinesia in patients with advanced PD [150]. However, all of the above therapeutic options are symptom-based and therefore unable to halt or reverse the progression of PD.

### 1.1.3.2 $\alpha$ -syn as a pharmacological target

To date, there are no disease-modifying therapies for PD. As described earlier,  $\alpha$ -syn and its ability to form toxic aggregates that can self-replicate and spread from cell-to-cell in a prion-like manner make it a highly attractive target for drug development to intervene at various stages of  $\alpha$ -syn-induced pathology (Fig.7).

As a result of the observed intercellular propagation of  $\alpha$ -syn aggregation, several therapeutic approaches aim to block the process of cellular secretion, transport, and uptake of the aggregated species (Fig. 7 (a)). For example, one strategy aims to block the cell surface receptor protein LAG3, which has been shown to be involved in the exocytic process of  $\alpha$ -syn release [151]. Indeed, an anti-LAG3 directed antibody reduced misfolded  $\alpha$ -syn induced toxicity and transmission in cell cultures [151].

As described previously, gene duplications and triplications of the *SNCA* locus lead to heritable forms of PD by increasing  $\alpha$ -syn protein levels. Therefore, one of the possible treatment strategies aims at reducing  $\alpha$ -syn biosynthesis by RNA interference (RNAi), using gene silencing mechanisms targeting  $\alpha$ -syn mRNA [152] or by modulation of  $\alpha$ -syn transcription via regulation of histone deacetylase (HDAC) activity at the  $\alpha$ -syn promoter and enhancer regions (Fig. 7 (b); [153]). One of the major drawbacks of this therapeutic approach is that the physiological role of  $\alpha$ -syn is not fully understood and reducing the total  $\alpha$ -syn concentration could lead to undesirable side effects.

## Introduction

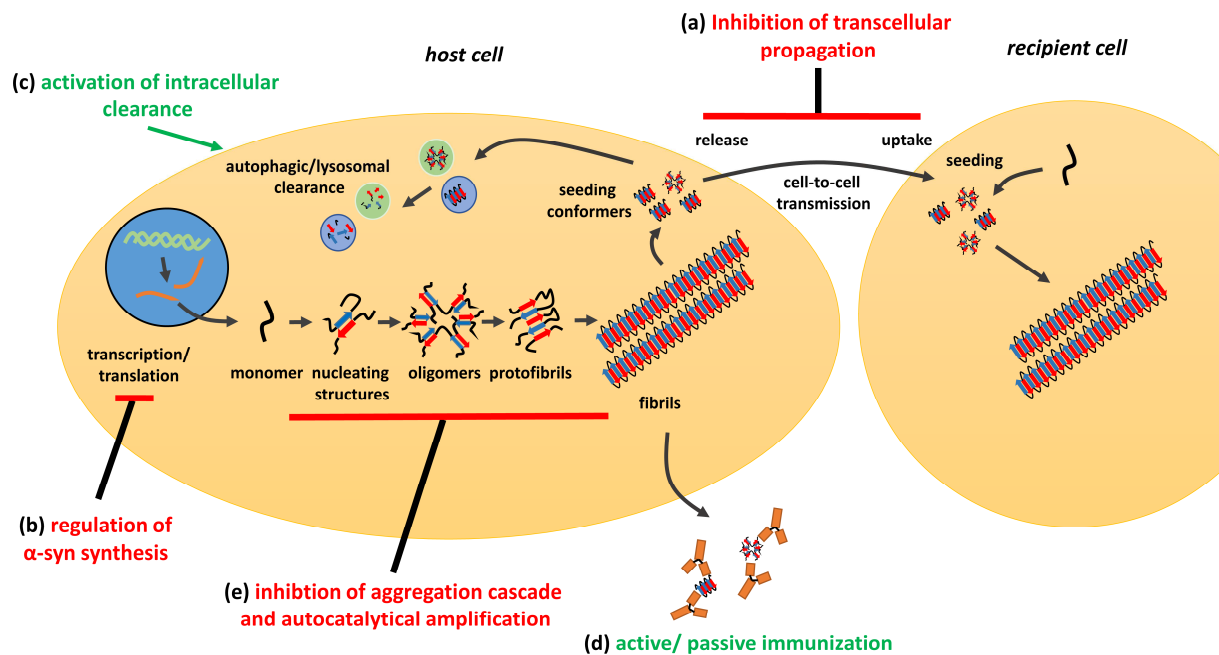


**Figure 7: Potential intervention points of  $\alpha$ -syn aggregation and prion-like propagation of seeding species.** Different therapeutic strategies aim for (a) inhibition of host cell release, intercellular translocation and recipient cell uptake of seeding  $\alpha$ -syn fibrillary or oligomeric species; (b) regulation of  $\alpha$ -syn synthesis by modulation of transcription and translation processes; (c) activation of autophagic/ lysosomal pathways for intracellular degradation of toxic and or seeding species (d) active or passive immunization strategies that target for elimination of seeding conformers; (e) inhibition of aggregation starting with the first nucleating events and continuing with the formation of oligomers, protofibrils and fibrils; (adapted and changed from Fields et al., 2019 [154] and Mehra et al., 2019 [43]).

To date, the majority of therapeutic PD approaches related to  $\alpha$ -syn target the different stages of the aggregation process, aiming either at inhibition of aggregation or cellular elimination of misfolded species (Fig. 7 (c - e)).

Activation of proteasomal degradation or autophagy is one of the most important strategies to enhance the elimination of aggregated species. (Fig. 7 (c)). Autophagy is thought to play an important role in the intracellular degradation of aggregated  $\alpha$ -syn species [155]. The mammalian target of rapamycin (mTOR) was identified as essential for the regulation of cell apoptosis and autophagy [156]. Rapamycin and its mTOR inhibiting analogs were shown to reduce the burden of misfolded  $\alpha$ -syn by increasing autophagic clearance [155-159]. Similar to autophagy or the proteasomal machinery, heat shock proteins (HSP) are one of the main target proteins in order to prevent misfolding of  $\alpha$ -syn and enhance cellular degradation of already aggregated species [160]. Because HSPs were found to be trapped in aggregated protein assemblies during the process of  $\alpha$ -syn aggregation, modulation of HSP expression levels was proposed as a therapeutic strategy [161].

Another possible therapeutic approach is the immunotherapy through passive and active immunization specifically targeting epitopes of misfolded  $\alpha$ -syn (Fig. 7 (d)). Here, the

humanized IgG1 antibody PRX002, which binds epitopes near the C-terminus of  $\alpha$ -syn, has shown to decrease the concentration of  $\alpha$ -syn in serum by  $\sim 97\%$  [162]. However, a disadvantage of full-length antibodies used for passive immunization strategies is that their limited penetration of the blood-brain barrier (BBB) means that they have an inadequate effect on the target. Other passive immunization approaches using compounds such as intra- or nanobodies are more likely to pass the BBB and, have a similar binding profile to their full-length counterparts, making them more attractive vaccines. Another promising therapeutic alternative for active immunization strategies is the administration of short peptide fragments that mimic misfolded  $\alpha$ -syn-related epitopes [163].

The final class of  $\alpha$ -syn targeting therapeutic strategies aims for the direct interaction with misfolded  $\alpha$ -syn at various stages of aggregation to inhibit the formation of cytotoxic conformers like oligomers or fibrillar species (Fig. 7 (e)). One of the most promising candidates is the small molecule compound Anle138b, which was originally identified by a library screening to inhibit the formation of PrP and  $\alpha$ -syn oligomers [164]. In subsequent experiments with A30P- $\alpha$ -syn transgenic mice, the compound showed a reduction in disease progression, even when treatment was started after disease onset [165]. Interestingly, no direct interaction with monomeric  $\alpha$ -syn was detected, while the compound showed affinity for fibrillar species [166], which suggests that the underlying mechanism mode of action (MoA) is realized by a reduction of secondary nucleation at the fibril surface [47]. Another prominent compound targeting  $\alpha$ -syn to prevent the formation of toxic conformations is NPT200-11, a small molecule identified by dynamic molecular modeling using  $\alpha$ -syn protein sequences critical for oligomer and protofibril formation. Although positive effects on reducing  $\alpha$ -syn pathology were demonstrated when the compound was administered to  $\alpha$ -syn-overexpressing transgenic mice, evidence of interaction and stabilization of monomeric  $\alpha$ -syn is still lacking [167].

### **1.1.3.3 Direct elimination of toxic oligomers and seeding competent fibrils as anti-prionic strategy against neurodegenerative diseases**

$\alpha$ -syn aggregates have not only been identified as the most promising particles when it comes to the etiology of PD and disease pathology in different brain regions, but they also represent the species most likely to directly trigger neuronal cell death during neurodegeneration. The major challenge for scientists in treating prion-like diseases is the strain polymorphism that occurs in both, fibril and oligomer formation. Therefore, strategies targeting disease-related structures may eliminate only a particular sub-polymorph, leaving the remaining strains unaffected. In support of this assumption, it has been observed in prion diseases that elimination of certain fibril strains leads to promotion of other, drug resistant, strains [168, 169]. This implies that the most promising strategy is not to target disease-related structures

but rather to stabilize the physiological native state. Drugs following this MoA can act independently of the disease-related conformer and independently of the patient's immune system (Fig. 8). Monomer stabilization inhibits all processes during the aggregation cascade that require further consumption of monomer, such as primary nucleation, elongation, and secondary nucleation. Thus, the prion-like autocatalytic amplification cycle is efficiently interrupted. Most importantly, a drug that exerts this "anti-prionic" MoA has the potential to halt disease progression and eliminate toxic components from already affected cells.

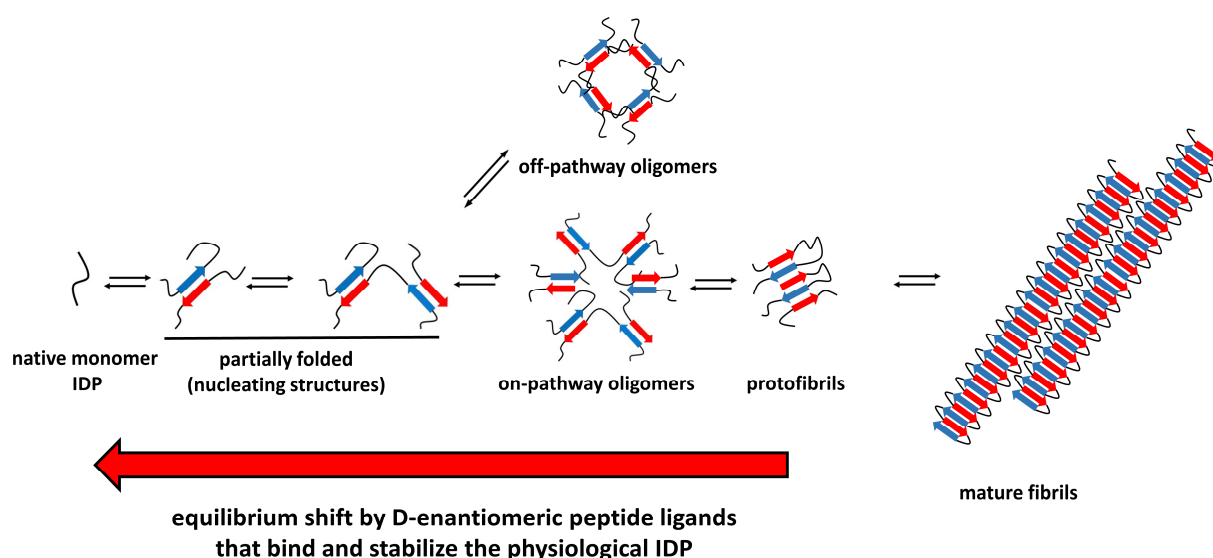


**Figure 8: Anti-prionic MoA in prion-like diseases.** The compound binds the monomeric IDP with high affinity and shifts the equilibrium from the aggregated status to the physiological monomer. Toxic oligomers as well as seeding competent structures are progressively eliminated. In addition, all aggregation processes that require the further consumption of monomer will be inhibited (adapted and changed from Mehra et al., 2019; [43]).

This therapeutic concept has already been shown to be valid for the prion-like disease Alzheimer's disease and its target molecule A $\beta$  [170]. Similar to  $\alpha$ -syn, the IDP A $\beta$  is able to aggregate in the form of fibrils and soluble oligomers after proteolytic cleavage by  $\gamma$ - and  $\beta$ -secretase [171]. The resulting aggregated species, which are either fibrillar or oligomeric, were found to be capable of seeding aggregation and inducing intercellular disease progression and neuronal cell death. Consistent with the previously outlined anti-prionic MoA, the all-D enantiomeric peptide compound RD2 [172] (derivative of D3, which was selected by mirror-image phage display on A $\beta$  monomer [173]) was designed to stabilize monomeric A $\beta$  and destabilize and disintegrate pre-existing aggregates. D3 and its derivative RD2 were able to eliminate preformed oligomeric species *in vitro* [174], as well as from brain homogenates of transgenic mice [175]. Interestingly, RD2 was able to restore cognitive abilities in mice in which AD pathology was already full-blown, suggesting successful elimination of toxic components under pathological *in vivo* conditions [172, 175].

## Introduction

Considering these promising results, the aim of this work is to apply this MoA, which has been successfully applied to AD, to another prion-like neurodegenerative disease, namely PD with its target protein  $\alpha$ -syn.

## **1.2 Part II: Kinetic characterization of the SARS-CoV-2 spike protein interaction with hACE2 and identification of spike protein binding inhibitors of complex formation**

### **1.2.1 SARS-CoV-2 and COVID-19**

#### **1.2.1.1 Coronaviruses**

Coronaviruses (CoV) belong to a diverse family of single-stranded positive-sense RNA viruses that can infect mammals such as humans as well as avian species. They are divided into the families of alpha, beta, gamma, and delta coronaviruses, of which alpha and beta coronaviruses exclusively infect mammals, while gamma and delta coronaviruses exert wider host ranges [176, 177]. Coronaviruses have long been known to circulate in populations as endemic viral strains such as HCoV-HKU1, HCoV-OC43, HCoV-NL63, or HCoV-229E, causing mainly mild symptoms commonly known as the "seasonal cold" [177]. Three of the seven coronaviruses known to include humans in their host range cause more severe symptoms by infecting upper respiratory tract cells, bronchial epithelial cells, and pneumocytes. Infections with severe acute respiratory syndrome coronavirus (SARS-CoV, 2002), Middle East coronavirus (MERS-CoV, 2012), and SARS-CoV-2 (2019) are known to cause life-threatening respiratory illness and lung injury for which no therapeutic treatment is yet available [178]. Among the three epidemics caused by these viruses, the current epidemic caused by SARS-CoV-2 occupies a prominent position due to its widespread and persistent global impact.

#### **1.2.1.2 Epidemiology**

Severe acute respiratory syndrome coronavirus 2 (SARS-CoV-2), first detected in Wuhan, China, in December 2019, is the causative agent of 2019 coronavirus disease (COVID-19) [179]. As of January 10, 2022, more than 312 million people have been infected with the virus, according to the World Health Organization (WHO), of whom 5.5 million have died as a result of the severe course of COVID-19 disease [180]. The virus has spread across the world with high transmission efficiency, affecting more than 222 countries, and was classified as a global pandemic by the WHO in March 2020. Since then, the virus has severely affected social and economic systems around the world. After infection, replication of SARS-CoV-2 occurs mainly in the upper and lower respiratory tract, so human-to-human transmission most commonly occurs via respiratory droplets and aerosols [181]. Replication in the upper respiratory tract has been identified as a major cause of increased infectivity of SARS-CoV-2, favoring transmission by asymptomatic individuals [182]. The median incubation period until the onset of the first symptoms is 5.7 days after primary infection, whereas transmissibility was detected

at much shorter intervals before the onset of the first symptoms [183]. Susceptibility to severe disease progression of SARS-CoV-2 increases with age, particularly affecting males older than 70 years [184]. The basic reproduction number ( $R_0$ ) of the SARS-CoV-2 ancestral strain ranges in between 2.39 to 3.34 in a naïve population where no preventive measures are taken [185]. However, studies suggest that  $R_0$  is highly dependent on population density and human behavior, which explains the different courses of the pandemic across different countries and regions [185]. Compared with previous epidemics such as the SARS-CoV epidemic in 2002 ( $R_0 = 2.5$ ) and the influenza pandemics of 1918 ( $R_0 = 2.0$ ) and 2012 ( $R_0 = 1.7$ ), the SARS-CoV 2 virus proved to be more transmissible, highlighting the prominent role of the current pandemic [186].

### 1.2.1.3 Pathogenesis

Human-to-human transmission of SARS-CoV-2 occurs primarily via droplets expelled from the respiratory tract of an infected individual. The virus then penetrates the mucous membrane, particularly the nasal and laryngeal mucosa, infects the lung tissue, and eventually reaches the bloodstream [187]. Initial replication of the virus in the lung tissue is accompanied by rather mild symptoms like fever, cough, myalgia or fatigue, sore throat, and headache. Worsening of symptoms can occur 7 to 14 days after disease onset [188]. Disease progression is divided into three distinct phases: pulmonary, proinflammatory, and prothrombotic. The first phase, the pulmonary phase, is characterized by decreased expression of human angiotensin converting enzyme 2 (hACE2) on lung and tissue cells. This disrupts the angiotensin-renin system (ARS), which in turn leads to acute respiratory distress syndrome (ARDS) and increased inflammation [189]. In the next phase, the pro-inflammatory phase, the immune system responds to infection with an overproduction of cytokines, in some cases leading to acute lung injury (ALI) and a cytokine storm via systemic inflammation. In the final phase, the prothrombotic phase, platelet aggregation and thrombosis can lead to coagulopathy and multiple organ failure (MOF) [190]. Compared to the SARS-CoV 2002 (9.6 %) and MERS-CoV (34.4 %) epidemics, the ancestral strain of SARS-CoV-2 resulted in a substantially lower case fatality rate (CFR) of 3–4 % [191].

### 1.2.2 SARS-CoV-2 replication cycle

Replication of SARS-CoV-2 is a balanced multistep process that begins with attachment of the viral particle to the host cell surface, followed by membrane fusion and release of viral RNA into the host cell cytoplasm (Fig. 9). This first step is mediated by the interaction of the spike glycoprotein (S) located on the viral membrane surface, which interacts with human angiotensin converting enzyme 2 (hACE2) via a specific receptor binding motif (RBM) [192,

193]. Priming of the spike protein, which ultimately leads to membrane fusion with the host cell, is initiated by the cellular transmembrane protease serine kinase 2 (TMPRSS2) and can be further facilitated by the endosomal/lysosomal cysteine proteases cathepsin B and L (CZSB, CTSL) [194]. Tissue tropism and infection efficiency are further influenced by the presence of furin protease (acting on a SARS-CoV-2-specific furin polybasic cleavage site (PRRAR)) together with neuropilin-1 (NRP1), which both increase viral infectivity but also provide a pathway for central nervous system infection [195].

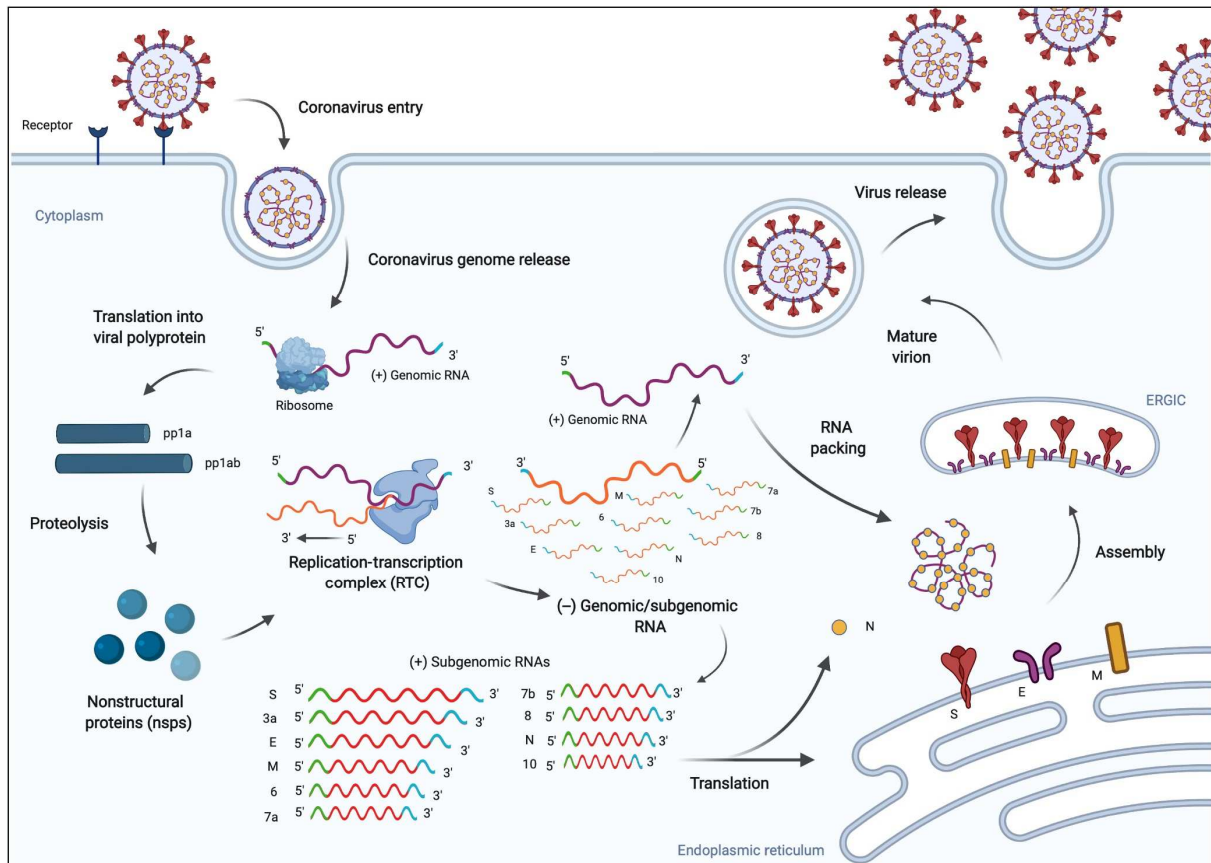


**Figure 9: Viral replication cycle of SARS-CoV-2.** The viral replication cycle starts with association of the viral spike (S) protein to the host cell surface, followed by cell fusion and release of the genomic RNA into the cytoplasm. The translation of the viral polyprotein follows the proteolytic cleavage by 3CL<sup>pro</sup> into non-structural proteins (nsps), which in turn form the reverse transcription complex (RTC). The RTC uses genomic (+) RNA as template to produce either copies that are packaged into maturing virions or sub-genomic mRNAs that are further translated into structural and accessory proteins. Finally, structural proteins are assembling at the (ER)-to Golgi compartment (ERGIC), followed by release of the mature virion via exocytosis (adapted from Zafferani et al, 2021, [196]).

Injection of viral RNA follows a highly regulated cascade of viral protein expression that begins with the translation of ORF1a and ORF1b producing two polyproteins pp1a and pp1b [197]. After proteolytic cleavage by the two cysteine proteases papain-like protease (PL<sup>pro</sup>) and chymotrypsin-like protease (3CL<sup>pro</sup>) [196], 16 non-structural proteins (nsp1-16) are released

from the polyproteins, which either directly contribute to the viral reverse transcription complex (RTC) or provide the necessary environment for the RTC [198]. The functioning RTC is responsible for replication of genomic RNA, which either serves as a template for synthesis of additional copies or is packaged into new virions. During the synthesis process of negative-stranded RNA, the RTC interrupts transcription when it reaches transcription regulatory sequences (TRSs) that induce the formation of a series of subgenomic mRNAs, which are then translated into structural and accessory proteins [199]. Open reading frames (ORFs) encoding structural proteins (spike protein (S), envelope protein (E), membrane protein (M), and nucleocapsid protein (N)) self-assemble and support the process of formation and budding of new virions, which takes place in the (ER)-to-Golgi compartment (ERGIC) [200]. This process results in the release of the mature virions into the extracellular space by exocytosis. The mRNA ORF of the structural proteins are interspersed by so-called accessory proteins (ORF3a, ORF6, ORF7a, ORF 7b and ORF8), which display a high variability among the different coronavirus groups. Accessory proteins are not required for viral replication *in vitro*, and although their role is not fully elucidated, they are thought to have important functions in host interactions, e.g., as interferon antagonists [201, 202].

Understanding of the SARS-CoV-2 replication cycle, gene function, and host interaction is still evolving and may lead in the future to a better understanding of why certain viral alterations of VOCs are associated with a more or less severe course of COVID-19 disease.

### **1.2.3 The SARS-Cov-2 spike protein: structure and function**

The SARS-CoV-2 S protein is a 1273 aa long, highly glycosylated trimer that facilitates attachment of the virus to the host cell surface through interaction with hACE2. It contains several functional regions that collectively contribute to the process that ultimately leads to fusion of the viral membrane with the host membrane and subsequent injection of genomic RNA into the host cell cytoplasm (Fig. 10).

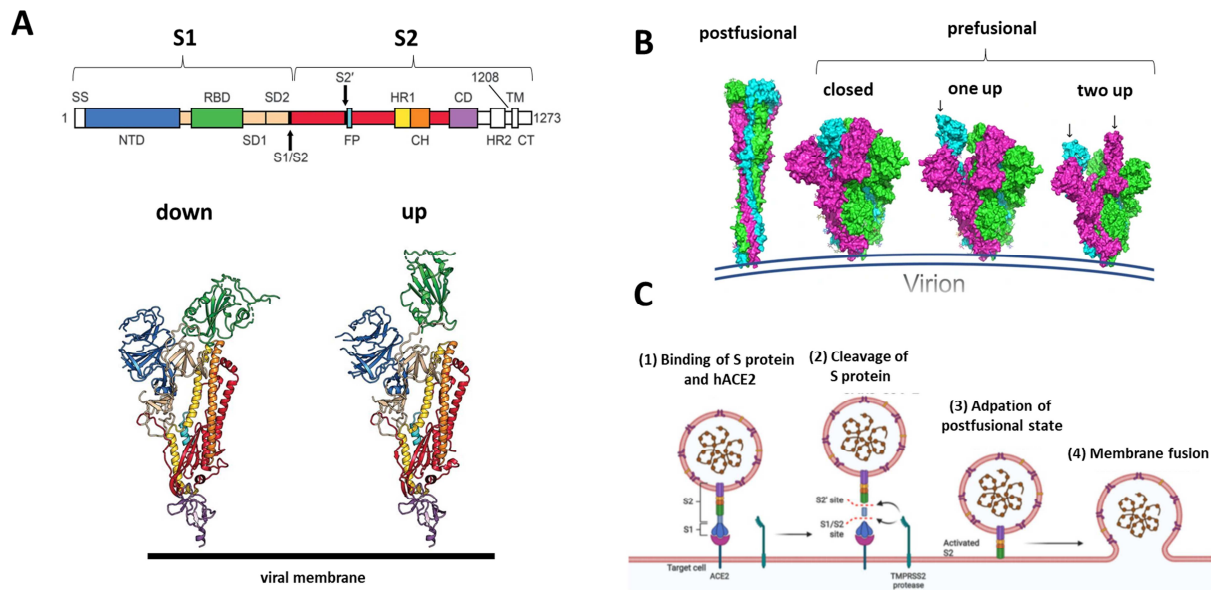


**Figure 10: The SARS-CoV-2 spike protein structure and function. (A)** The subunits and functional domains of the viral S protein (upper part) and the folding of the monomeric spike protein adopting down and up conformation (lower part, adapted from Wrapp et al., 2020 [203]). **(B)** The prefusional and postfusional states of the trimeric S protein (adapted from Ismail et al., 2020 [204]). **(C)** The stages of viral attachment to the host cell and subsequent membrane fusion (adapted from Gupta et al., 2021 [205]).

The S protein is divided into two subunits: the more variable S1 (residues 14-685) and the more conserved S2 (residues 686-1273, Fig. 10 A). The S1 subunit comprises the receptor binding domain (RBD, residues 319-541), which enables attachment of the virus to the cell surface by specific binding of the host cell surface membrane protein hACE2 via a defined receptor binding motif (RBM, residues 424 - 494). The S2 subunit comprises the fusion peptide (FP, residues 788-806), heptapeptide sequences 1 and 2 (HR1 and HR2, residues 912-984 and 1163 - 1213, respectively), as well as the transmembrane domain (TM, residues 1213-1237) and the cytoplasmic domain (CP, residues 1237-1273) [206].

The S protein adopts two isoforms, classified as prefusional and postfusional depending on the state of viral binding (Fig. 10 B [204]). During the prefusional state, the three RBDs of each trimer are present either in a "down" conformation, in which the major hACE2 interaction sites of the RBM are obscured by interaction with the NTD, or in an "up" conformation, in which the RBM is accessible for interaction with hACE2 [203]. In addition, cryo-EM experiments have shown that in the closed conformation all three RBDs are in the "down" state, whereas in the open conformation either one or two RBDs occupy the "up" state (Fig. 10 B [204]). After association with hACE2, the conformation of the S protein changes and facilitates the availability of the S2' and S1/S2 cleavage sites for proteolytic cleavage by TRMPSS2, followed by insertion of the FP domain into the host cell membrane. In the postfusional state the S1 subunit dissociates and refolding events of the remaining S2 unit

efficiently bring the viral and host cell membranes together, ultimately leading to membrane fusion (Fig. 10 C [207]).

### 1.2.4 The RBD – hACE2 interface for SARS-CoV-2 and VOCs

The hACE2 protein is the main receptor targeted by the SARS-CoV-2 S protein. Its main function is to negative regulate and thus maintain the renin-angiotensin system (RAS), which is crucial for physiological and pathological regulation in various organs such as the heart, kidney and lung [208]. The RBD core of SARS-CoV-2 consists of five antiparallel beta strands ( $\beta 1$ ,  $\beta 2$ ,  $\beta 3$ ,  $\beta 4$ , and  $\beta 7$ ) connected by helices and loops (Fig. 11 A).  $\beta 4$  and  $\beta 7$  are connected via an elongated insertion called RBM (residues 424-494), which interacts with the  $\alpha 2$ -helix of hACE2 mainly via hydrophilic contacts (Fig. 11 B – C; [209]).

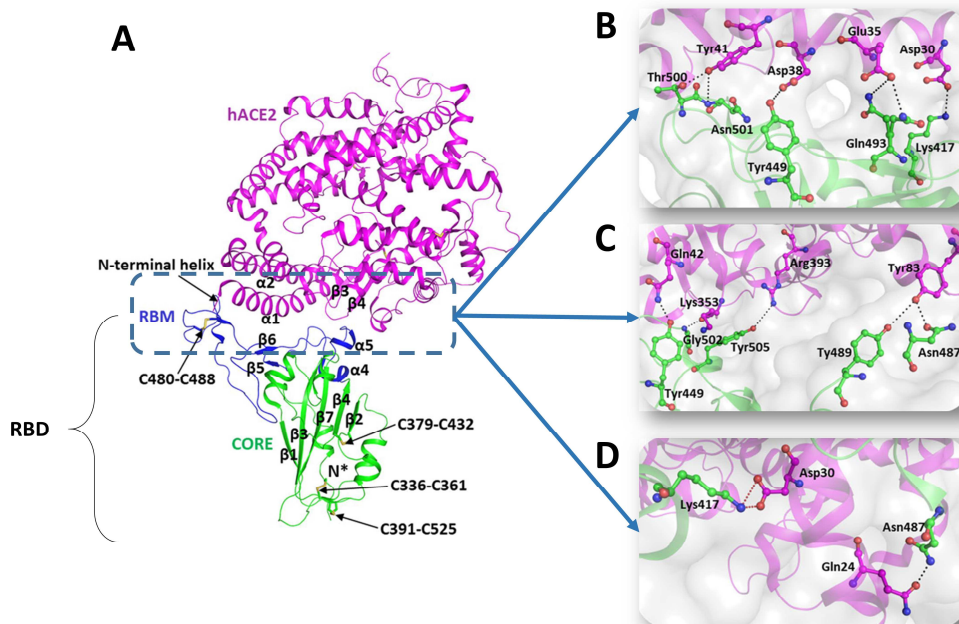


**Figure 11: Molecular interaction sites of SARS-CoV-2 RBD and hACE2.** (A) SARS-CoV-2 RBD (green) interacts via a defined RBM (blue) with the N-terminal proportion of hACE2 (magenta; PDBID: 6M0J). (B–D) The interaction of the N-terminal  $\alpha$ -helix of hACE2 and the RBM is stabilized by mainly hydrophilic interactions (marked by dotted lines).

During the course of the pandemic, several VOCs emerged which exhibited enhanced infectivity and immune defense properties. Analysis of the corresponding genetic sequences led to the identification of numerous mutations in the S protein, some of which are considered essential for the observed increased viral fitness. One of the dominant mutations of the S protein associated with higher infectivity, transmissibility and stability was identified at

position 614 outside the RBD - hACE2 interface, where aspartate was replaced by glycine (D614G; [210]). This substitution is present in almost all B-lineage VOCs, such as the  $\alpha$ - (B.1.1.7),  $\beta$ - (B.1.351),  $\gamma$ - (P.1),  $\delta$ - (B.1.617.2), and o-variant (B.1.1.529). Cell culture experiments with pseudo-typed viruses have shown that the mutation leads to reduced shielding of the S1 subunit, resulting in increased viral infectivity [211]. Another conspicuous mutation that also occurs in the above VOCs (apart from the  $\delta$ -variant) is the N501Y substitution, in which the RBM-resident asparagine (Fig. 11 B) is replaced by tyrosine. This substitution strengthens intermolecular hydrogen bonding with hACE2 and has been shown to directly contribute to increased affinity of the RBD with hACE2, leading to increased viral infectivity [212]. Other mutations like K417N [213], N439K [214], S477N [215] and S494P [216] have also shown to singularly or cooperatively affect the binding affinity of the S protein with hACE2. In addition, other mutations of the S protein are associated with either a change in the spike protein immunogenicity like E484K/Q [217], N440K [218] and L453R [219] or facilitation of the transformation process from prefusional to postfusional state, such as H655Y and P681H/R [220], both of which are located at the polybasic TMPRSS2 cleavage site.

Continuous emergence of novel VOCs with distinct traits concerning their infectious efficacy as well as immune evasive traits will require the development of adapted vaccines and medications in the future.

### 1.2.5 Current medical treatment options for COVID-19

Severe progression of COVID-19 disease results in increased systemic inflammatory responses in response to progressive lung tissue damage. Therefore, medical intervention has mainly relied on inflammatory management to prevent MOF using anti-inflammatory agents so far. Fortunately, the rapid spread of SARS-CoV-2 has not only triggered the development of highly effective mRNA-based vaccines, but one of the major goals of current research is to identify and develop antiviral therapies for acute COVID-19 treatment.

Therapeutic strategies used for the development of tailored SARS-CoV-2 antivirals can be classified into two approaches, which either target for direct interference with the virus or modulation of the immune system. The latter include therapeutic measures in which, for example, blood plasma [221] or monoclonal antibodies [222], are administered in order to neutralize the virus.

Other strategies deal with the impairment of the viral replication cycle (Fig. 9). Here, various stages offer attractive therapeutic targets like (i) the process of viral attachment to the host cell surface, (ii) fusion and endocytosis, (iii) RNA replication, (iv) protein maturation by viral proteases, and (v) virus packaging [206].

More recently, efforts to develop 3CL<sup>pro</sup> inhibitors have led to the development of the small molecule compound Paxlovid (Nirmatrelvir, Pfizer), which binds and blocks the active site of the main protease, effectively inhibiting further maturation of pp1a and pp1b polyproteins [223]. According to a recently published large phase 2/3 study, Paxlovid is 89 % effective in preventing hospitalization or death in patients at risk of severe disease [224]. Another compound, targeting viral replication cycle impairment is Molnupiravir (Lagevrio, Merck). The MoA is the induction of RNA mutagenesis during the viral transcription process. The RNA-dependent RNA polymerase (RdRp), which is part of the RTC, uses an intermediate of the prodrug Molnupiravir,  $\beta$ -D-hydroxycystidine (NHC), as substrate instead of cytidine triphosphate or uridine triphosphate. When the resulting RNA is used as template by the RdRp, NHC incorporation leads to mutated RNA products, which in turn inhibits the RNA replication and synthesis of structural and accessory proteins [225]. Like Molnupiravir, the drug Remdisivir (Gilead Sciences) targets the RdRp by being incorporated into the viral RNA. However, unlike Molnupiravir, the transcription complex is stalled when the compound is incorporated, preventing further RNA elongation [226].

Although extensive research for acute COVID-19 drugs has already led to the identification and development of first antivirals, it cannot be excluded that, given the high mutation rate of SARS-CoV-2, their efficacy against emerging VOCs will be reduced due to escape mutations. Therefore, the development of tailored antiviral agents with innovative modes of action will continue to be necessary in the future.

### **1.2.6 Targeting the SARS-CoV-2 spike protein – hACE2 interaction as therapeutic strategy for COVID-19**

One of the potential strategies to inhibit the replication cycle of SARS-CoV-2 is to target the interaction of the viral spike protein to the cellular human receptor hACE2. Inhibition of the primary step of viral replication can be achieved by developing agents that target the interface between hACE2 and spike protein and interact with both components. However, agents targeting hACE2 have the major disadvantage of potentially interfering with the physiological function of hACE2, leading, for example, to an imbalanced ARS homeostasis. Therefore, a more favorable strategy for inhibitor development is to target of the SARS-CoV-2 spike protein and, in particular, the RBD with the RBM.

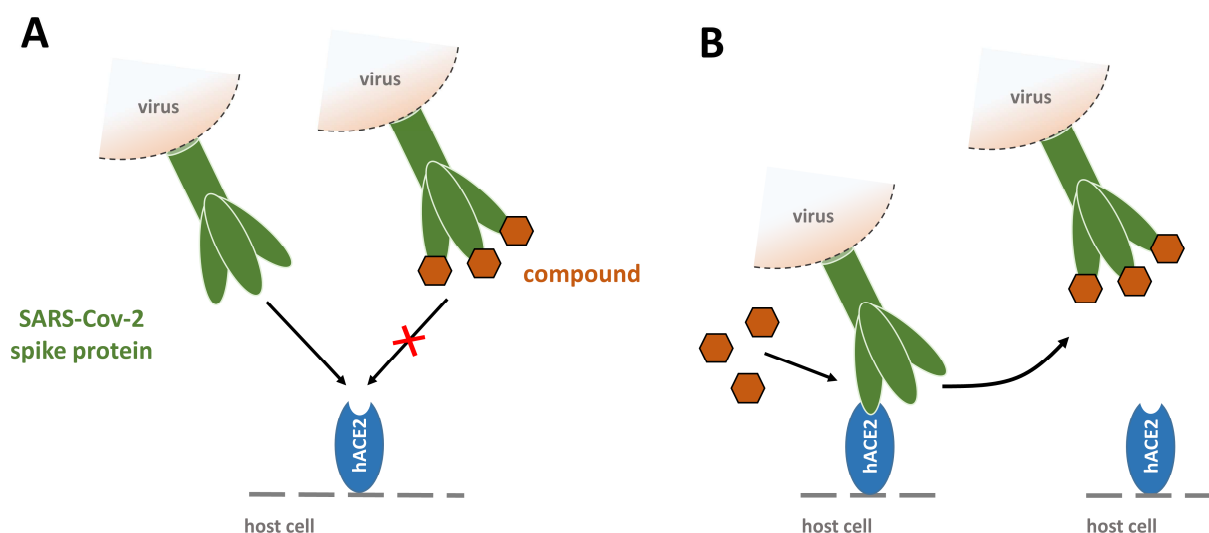


**Figure 12: MoA of RBD targeting spike – hACE2 inhibitors of complex formation.** (A) The SARS-CoV-2 spike protein has not formed a complex. In this preset, a compound targeting the RBD binds the spike protein and prevents association with hACE2 by shifting the equilibrium towards the unbound spike. (B) In the second preset, the spike protein is already bound to hACE2. Here, a compound targeting the RBD should displace hACE2 from the spike protein by shifting the equilibrium towards the hACE2-unbound form (adapted and changed from Sevenich et. al, 2022, [227]).

Compounds targeting with high affinity the parts of SARS-CoV-2 relevant to the hACE2 interaction are in principle not only able to prevent complex formation before binding to the viral cell surface (Fig. 12 A), but also to displace the spike protein from the complex before the transition to the postfusional state occurs. This MoA shifts the equilibrium toward the hACE2-unbound form of the spike protein, leading to a reduction in membrane fusion events (Fig. 12 B). In principle, the design of compounds that inhibit complex formation with the cellular receptor can be accomplished by identifying new interaction partners or by using the binding moieties relevant to hACE2 as scaffolds. With the latter option, however, there is a risk of generating compounds that have undesirable side effects under physiological conditions. For this reason, the identification of hACE2-independent compounds is the more attractive approach. Following this principle, the success of antiviral "binding inhibitors" has already been demonstrated for HIV, where, among others, the small molecule compound Fostemsavir (ViiV Healthcare) binds to the viral surface protein gp120 and prevents interaction with the cellular receptor CD4 [228].

Overall, the development of binding inhibitors targeting the RBD of SARS-CoV-2 represents a promising strategy for the development of tailored antiviral agents against COVID-19. In particular, the combined administration of antivirals acting at different stages of the viral life cycle is very promising in terms of efficacy and circumvention of possible escape mutations [229].

## 1.3 Peptides as therapeutics

### 1.3.1 Therapeutic peptides throughout the years

Peptides are a unique class of therapeutics that are of intermediate  $M_w$ , between small molecules and proteins. The history of therapeutically used peptides dates to the first half of the 20th century, when peptides were mainly used to supplement hormones, whose endogenous levels were found to be insufficient or nonexistent. One example is the treatment of diabetes with insulin in the 1920s [230]. While the first use of therapeutic peptides was limited to the isolation of hormones from natural sources, new strategies emerged when the chemical synthesis of peptides became possible in the 1950s [231, 232]. Soon, the isolation of natural products became a popular strategy for the identification of novel peptide therapeutics [233] and the progressive decoding of the human genome contributed to the identification of new promising receptor targets for peptide ligands.

Although great potential has been demonstrated for various peptide-related therapeutic strategies, the enforcement of therapeutic peptides was soon dampened by the realization that the bioavailability of native L-enantiomeric peptides is limited by their short half-life under physiological conditions. This is a consequence of certain factors such as peptidases and excretory mechanisms that act as regulators of hormone homeostasis in the body but promote clearance of native peptide therapeutics when administered to the body [234]. To address this problem, chemical strategies were developed that improved half-life, serum stability, and receptor selectivity, which soon led, for example, to peptide analogs of native hormones with improved pharmaceutical properties. However, the need to inject peptides to patients due to their limited oral bioavailability remained one of the key factors making small molecule-based strategies more attractive. In addition, high-throughput screening technologies accelerated the development of small molecules designed to mimic the binding specificity of peptides while offering higher oral bioavailability and easier manufacturing.

This concept of small molecule development has been successfully applied to several application areas. However, in several cases small molecules have been shown to be less effective than the corresponding peptide ligand at certain receptors, for example, because they cannot cover the spatially challenging binding sites [235, 236]. In addition, small molecules are more frequently associated with off-targeting, drug-drug interactions and undesired side effects than peptide ligands due to their comparable lower specificity [237].

Most of the therapeutic peptides developed to date, about 60 approved compounds in total, primarily target hormone receptor proteins such as G-protein coupled receptors (GPCRs, about 40%). Non-GPCR surface receptor proteins such as natriuretic peptide receptors and cytokine receptors are also popular targets for peptide therapeutics. Antimicrobials, ion

channels, and extracellular target proteins make up the bulk of the remaining targets for peptide therapeutics [238].

### 1.3.2 Peptide optimization strategies for improved pharmacokinetics, membrane penetrance and enhanced target binding affinity and specificity

The chemical basis of peptide therapeutics is classified as native, analog or heterologous with respect to their original peptide molecules [239]. Native peptides have the same sequence as their natural product, while analog peptides are modified or substituted versions, showing improved properties compared to the natural molecule. In contrast, heterologous peptides are developed independently of the natural peptide sequences, for example, by library screening or phage display selection. The current development of optimization strategies for therapeutic peptides aims to overcome the previously mentioned drawbacks of peptide drug delivery, which mainly focus on the problem of bioavailability due to their poor half-life under physiological conditions. However, for drug candidates that target intracellular proteins, to be administered orally, or targeting proteins in the brain, another major problem arises that reduces the number of potential drug candidates during drug development: the problem of membrane penetrance. Again, various optimization strategies have been developed to lower the hurdle for peptide drug candidates to overcome membrane barriers. Nevertheless, improving target affinity and specificity remains one of the major issues in peptide drug optimization (Fig. 13).

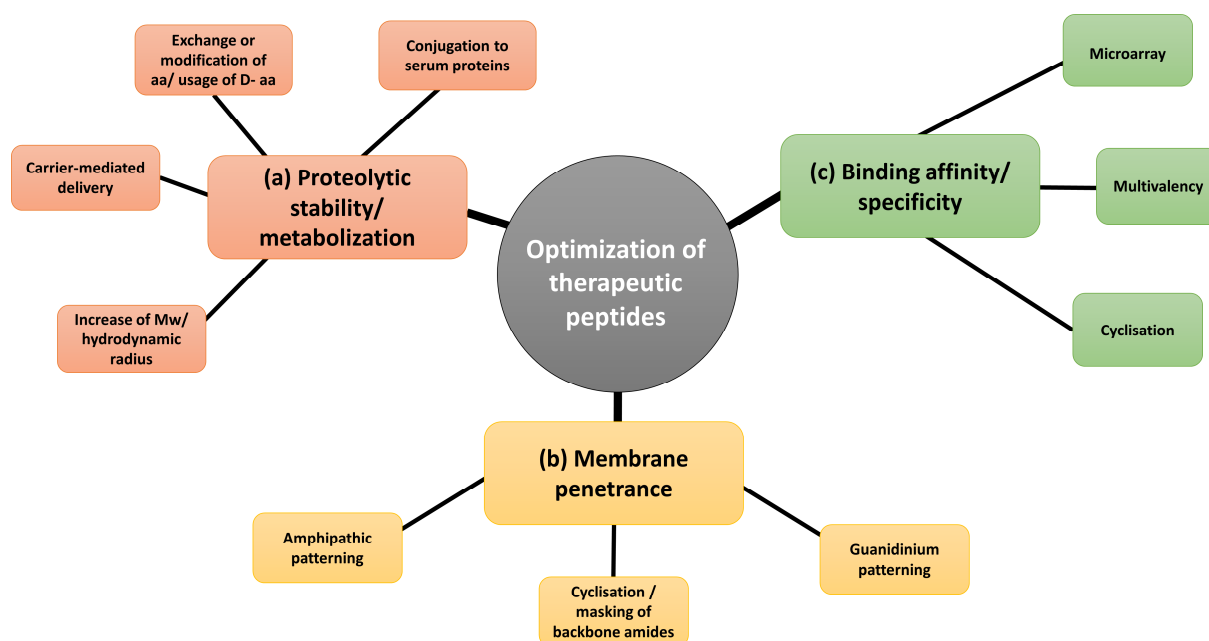


**Figure 13: Fields of peptide drug optimization and corresponding strategies.** The main concerns of peptide optimizations are (a) enhancement of proteolytic stability and reduction of metabolization under physiological conditions for improved bioavailability, (b) enhanced membrane penetrance for compounds where the intended site of action is obstructed from the site of application by one or multiple membrane barriers, and (c) improvement of binding affinity and specificity to avoid undesired off-target reactions as well as drug-drug interactions.

Several factors have been shown to contribute significantly to peptide clearance under physiological conditions, such as the renal filtration system and general protease-induced clearance during systemic circulation or metabolization in the liver by hepatocytes (Fig. 13 (a)). To avoid clearance via the kidney, strategies that increase the  $M_w$  and thus the hydrodynamic radius of a compound have proven effective [240, 241]. One way to achieve this is by conjugation to a moiety such as polyethylene glycol (PEG) or recombinant polypeptides. Conjugation of compounds to serum proteins that have a naturally high half-life, such as albumin, immunoglobulins and transferrin, has also been shown to be an efficient strategy to avoid metabolic clearance by the liver and kidneys [240]. Another approach to improve half-life is carrier-mediated delivery of peptide compounds, where binding or embedding in a carrier environment such as microspheres, liposome matrices, and micro/nanoparticles is intended to protect the compound during administration and ensure sustained release of the compound at the site of action [242].

However, all of the above strategies that rely on covalent peptide modifications will most likely negatively affect the ability of the drugs to penetrate membranes. Therefore, half-life extension strategies that enhance membrane penetration ability are the more attractive approach in certain cases. One such strategy is to manipulate or replace certain amino acids. Another approach is to completely replace an L-enantiomeric peptide sequence with its D-enantiomeric counterpart. This strategy is referred to as the "retro-inverso" approach (Fig. 14, [243]). In this process, the amino acid sequence and N-terminal charges of the peptide termini are rearranged to resemble the three-dimensional spacing and charge distribution of the L-enantiomeric derivative, thereby preserving binding affinity and specificity for the target structure. The replacement of the L- by the D-enantiomeric amino acids results in increased proteolytic resistance, as the D-enantiomers of amino acids are a less preferred target of the corresponding endogenous proteases. [244]. Another approach to realize a proteolytic more resistant all-D-enantiomeric peptide compound is the phage display selection of L-enantiomeric peptide ligands on the D-enantiomeric target protein, which yields D-enantiomeric peptide ligands that exert high affinity for the L-enantiomeric target. This technique, which will be illuminated in more detail in the following section, is called mirror-image phage display [245].

## Introduction

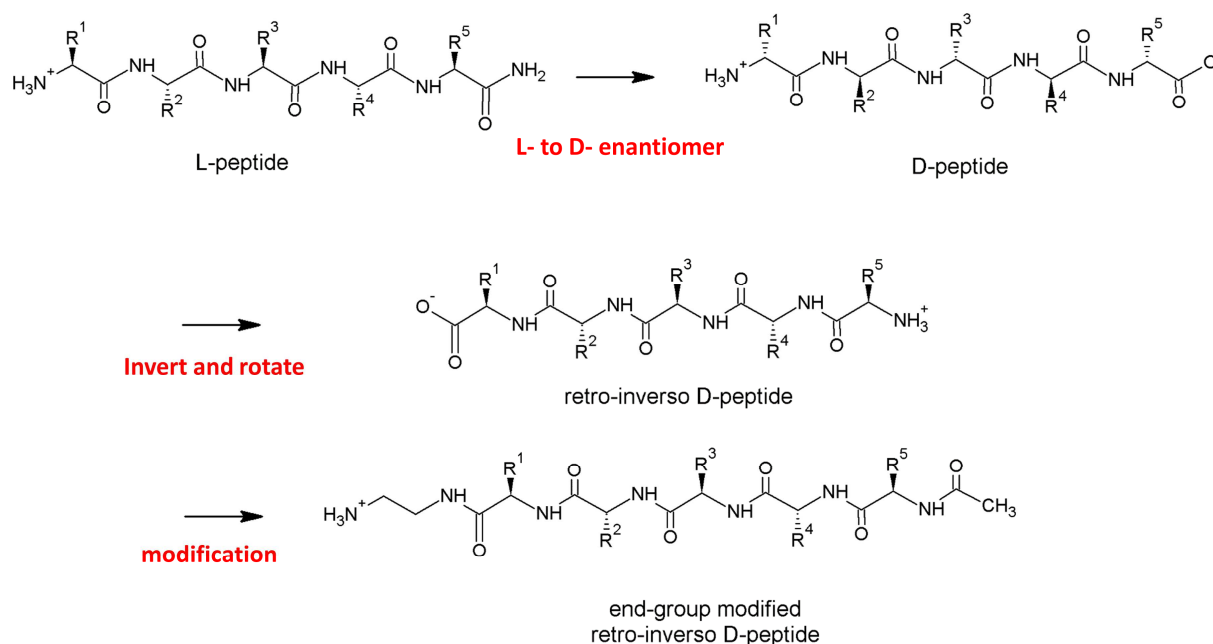


**Figure 14: Retro-inverso peptide optimization strategy for phage display derived L-enantiomeric peptide sequences.** First, the L-enantiomeric peptide sequence is converted in a D-enantiomeric sequence. The D-enantiomeric sequence is then inverted (and rotated 180° along the x-axis for better visualization). Finally, end-group modifications are introduced to achieve a charge distribution similar to that of the original L-enantiomeric peptide: acetylation of the primary amino group (resembles amidated C-terminus of the original L-peptide) and introduction of ethylenediamine at the carboxylic group (resembles N-terminal primary amino group of the original L-peptide).

Once a potential drug peptide has achieved proteolytic stability, another challenge is membrane penetration (Fig. 13 (b)). This problem must be solved for drugs whose target proteins are either localized intracellularly or for which penetration of a natural membrane barrier such as the BBB is essential to reach the intended site of action. In general, membrane crossing can occur via three different pathways: passive diffusion, direct translocation and endocytosis [246-248].

Small, relatively nonpolar molecules can pass through membranes by passive diffusion, which is characterized by concentration dependence, fast kinetics, and energy independence [249]. This mechanism is less suitable for cell-penetrating peptides (CPPs) with molecular weight ( $M_w$ ) > 1.2 kDa. An optimization strategy that primarily targets passive diffusion aims for minimizing of solvent exposed surfaces. This is done by reducing the size of the molecule via cyclization or masking of hydrogen donors, e.g., N-methylation of the backbone [250].

The most well-known mechanism for CPPs is the endocytosis-dependent mechanism. In this energy-dependent process, a CPP first attaches to the membrane surface, is endocytosed into the cell and finally released into the cytoplasm [251, 252]. Guanidinium group patterning, in which arginine is placed along the peptide sequence at defined intervals, has been shown to trigger endocytosis-dependent uptake [253]. Another strategy that relies on

endocytosis-mediated uptake is amphipathic patterning. Various covalent crosslinking modifications of the side chains, also called "stacking", have been shown to enhance membrane penetration primarily by stabilizing the secondary structure of the peptides in an  $\alpha$ -helical conformation [254-256]. This effect can be further strengthened by the combination of amphipathic patterning and guanidinium group patterning [257].

A final aspect of peptide drug optimization aims to increase the affinity of the peptide toward the target protein. Similar to the presented aspects of proteolytic stability and membrane penetrance, different techniques and combinations can be used to improve the stability of the complex and increase the binding specificity. One method, already mentioned in the context of passive diffusion, is the cyclization of peptides, in which peptide termini and/or side chains are covalently bound. The reduced conformational flexibility of the cyclized peptides should lead to a reduction in the Gibbs free energy of binding compared to the linear derivative, thus increasing the stability of the complex formed [258, 259]. Another powerful approach for optimization of binding affinities is the use of peptide micro-array screens [260, 261]. This method allows screening of different punctate amino acid substitutions and their synergistic effects with respect to target binding affinity. In addition, micro-array screens allow the reduction of the binding sequence to its minimal active portion by sequence shortening, consecutive deletions or alanine replacements [262]. This can reduce the size of the peptide sequence and improve the binding specificity. Finally, combining minimally active sequences in the form of a multivalent drug complex is a promising strategy to increase the avidity and local concentration of a drug. Here, various combinatorial techniques such as head-to-tail, tail-to-tail, head-to-head or linker-conjugated multivalent approaches represent potential strategies [263].

### 1.4 Phage display selection

Phage display technology is a powerful technique developed in 1985 [264] and awarded the 2018 Nobel Prize to George P. Smith and Gregory P. Winter [265]. Since its first application, the method has been widely used to study protein – protein [266] as well as protein – non protein interaction [267]. The method has also been successfully applied for the identification of novel pharmaceutical or biotechnological compounds, as for example for the targeting of tumor-related antigens [268, 269]. A phage library is a mixture of phage clones which display a randomized library of either peptide sequences, proteins or protein domains that are genetically fused to the phage surface proteins, typically using filamentous M13 [270] or spherical T7 [271] bacteriophages. The physical linkage of phenotype and genotype in one self-replicating phage particle allows the high-throughput screening and analysis of sequence

variants based on their biophysical behavior (Fig. 15, A). Phage display libraries are usually constructed with a target capacity of  $10^{10}$ -  $10^{11}$  displayed variants from which potential target protein binding sequences are selected and enriched within the variant pool by a repetitive process known as biopanning (Fig. 15, B and C; [272]). In this procedure, the phage library is incubated with the surface-immobilized target protein to allow binding. Subsequently, phages that bind to non-target-related surfaces are washed off by repeated washing and finally target-related variants are eluted (Fig. 15 B).

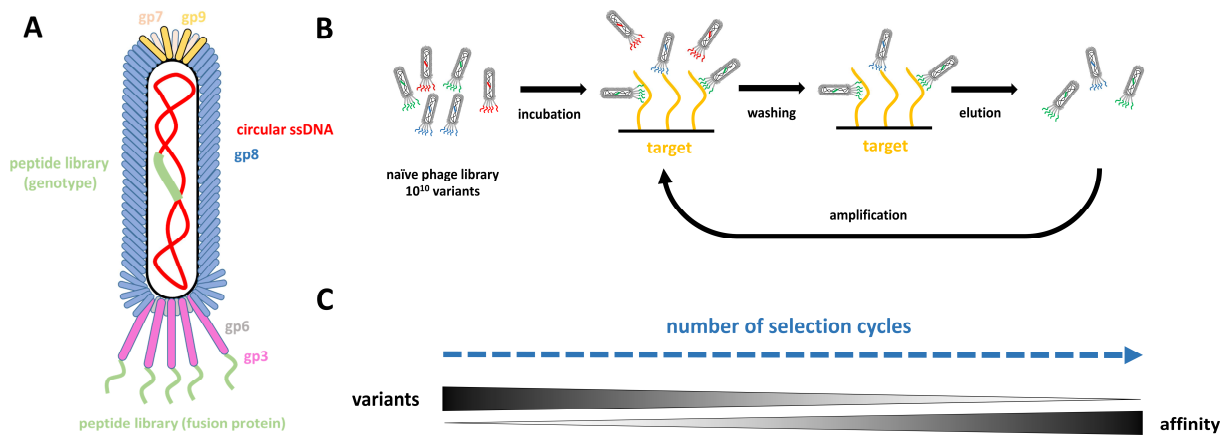


**Figure 15: Principle of M13 phage display selection.** (A) The M13 bacteriophage is composed of circular single stranded DNA (ssDNA), encapsulated by approximately 2,700 copies of the major coating protein gp8 and several copies of the minor coating proteins gp7, gp9, gp6 and gp3. In a phage display library, the minor coating protein gp3, which caps the bacteriophage with five copies, is fused to a randomized library (green). (B) Schematic depiction of the phage display selection procedure. The naïve phage library consists of  $10^{10}$  –  $10^{11}$  variants, which are screened for binding affinity towards an immobilized target protein during biopanning. After washing, phage variants with affinity for the target (green and blue) remain on the surface, while those with no or weak affinity are removed by washing (red). Bound phage variants are recovered by elution, amplified, and used as input for the subsequent selection round. (C) By performance of repetitive selection rounds, the number of variants is reduced, while their target affinity progressively increases.

There are two major pitfalls of this process. The first is that non-target related variants enrich together with target related variants during the selection process and potentially outcompete target binders in the sequence pool. Second, the preference for certain sequences in amplification by *E. coli* could lead to a biased library before and during selection. To overcome these hurdles, several strategies aim to identify typical sequence variants that are unrelated to the target [273, 274] or sequences that have an amplification advantage [275]. In addition, optimization of the selection procedure, e.g., by alternating blocking conditions and/or immobilization surface with each selection round has been shown to be beneficial [276]. In addition, deep sequencing techniques like NGS enable the identification of millions of sequences per sample, allowing the separation of target-related and non-target-related sequences in a single experiment [277, 278]. Depending on the number of sequences identified by NGS, even one selection might be sufficient to identify target-related binders [279]. Another strategy to increase the proportion of target-related variants during selection is the enhancement of the

elution specificity in comparison to unspecific elution methods like pH or ultrasound [280, 281]. This can be achieved by competitive elution methods with addition of the target protein in high excess concentrations [282] or detachment of the target related phages together with the reversibly immobilized target protein (e.g., by elution of D-desthiobiotin and streptavidin with biotin [283]).

Another more specialized phage display technique of particular interest for the development of therapeutic peptides is the mirror-image phage display method (Fig. 16, [245]). In mirror-image phage display, the selection of binding peptide sequences is performed on the D-enantiomer of the target protein. The resulting peptides are initially synthesized as D-enantiomeric variants, which in turn target the physiological L-enantiomeric protein. Due to stereoisomerism, the binding affinity and selectivity between the two isoforms of the same sequence are maintained. This selection technique allows the development of D-enantiomeric target binders that exhibit an improved proteolytic stability and therefore higher bioavailability than their L-enantiomeric counterparts. The success of the method has been shown in several publications [173, 284-286] and thus seems to be more promising than comparable strategies based on rearrangement of already identified L-enantiomeric ligands to resemble D-enantiomeric isomers (e.g. by retro-inverso, Fig. 14).

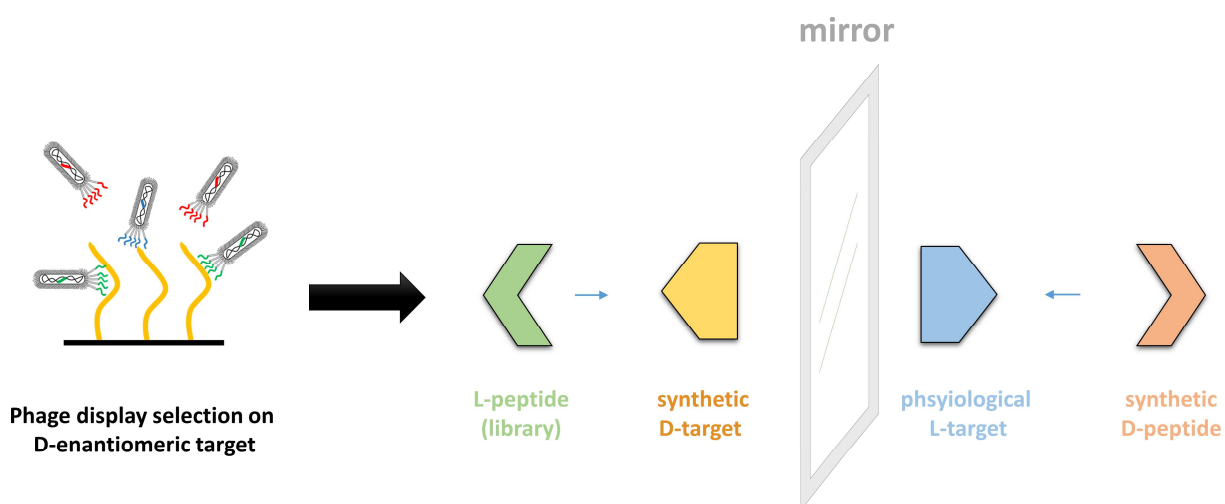


**Figure 16: Mirror-image phage display selection.** Mirror-image phage display is used for the identification of L-peptide sequences that bind a synthetic D-enantiomeric target protein (left side). The proteolytically more stable D-enantiomeric (mirrored) isomer of the same sequence can then bind the physiological L-enantiomeric target protein (right side).

### 1.5 Aim of this work

Phage display, invented towards the end of the last century, is a versatile tool for the straightforward development of high affinity ligands. The target molecules or surfaces can be freely chosen, making the method versatile for various applications.

In this work, the phage display method is used to identify peptide ligands that can bind to therapeutically relevant protein targets and thereby prevent or attenuate the progression of the corresponding diseases. Although the two target diseases mainly considered in this work, namely PD and COVID-19, represent a related pathogenic mode characterized by self-replicating particles (prions and viruses), the MoA targeted with the peptide compounds is distinct.

In neurodegenerative PD and its target protein  $\alpha$ -syn monomer, the mirror-image phage display selection should yield D-enantiomer peptides that bind to the  $\alpha$ -syn monomer, thereby stabilizing the physiological form and preventing aggregation. At the same time, the identified compounds revert aggregate formation by shifting the equilibrium from the toxic aggregated structures to the physiological monomer. The latter implies eliminating the toxic and self-replicating conformers of  $\alpha$ -syn in PD.

Second, to identify therapeutic peptides for COVID-19 treatment, a phage display procedure targeting the SARS-CoV-2 spike protein RBD should be performed. The proposed MoA aims to inhibit and reverse the association of the spike protein with its natural host cell receptor hACE2. Since the formation of the complex is the first crucial step of the viral replication cycle, the therapeutic goal is to attenuate viral replication. A basic understanding of the kinetic properties of the interaction of the SARS-CoV-2 spike protein with hACE2 is required to characterize the inhibitory potential of the selected compounds. Therefore, another aim of this work is the kinetic characterization of this specific interaction.

For both therapeutic strategies, the identified lead compounds should be further characterized with respect to their *in vitro* efficacy concerning the intended MoA. Moreover, first optimizations for improved therapeutic profiles should be realized and evaluated.

In addition to the therapeutic diseases and target proteins mentioned above, this work also includes the identification, characterization, and optimization of additional phage display-derived peptides for other therapeutic targets and MoA. The first target protein is human superoxide dismutase 1 (hSOD1), which is thought to be one of the key factors in another neurodegenerative disease, Amyotrophic lateral sclerosis (ALS). Again, the MoA aims to stabilize the physiological conformation through peptide-ligand interaction to prevent protein aggregation. Another MoA in this work addresses the inhibition of the viral SARS-CoV-2 3CL<sup>pro</sup>-main protease by therapeutic peptides. This MoA targets inhibition of the enzymatic activity thus polyprotein maturation, which is required for viral replication of SARS-CoV-2.

## Introduction

Considering the different target proteins and therapeutic applications, this work should give insights in a general strategy for the identification, evaluation, and optimization of therapeutic peptides.

## 2 Published Manuscripts

### 2.1 Direct disassembly of $\alpha$ -syn preformed fibrils into native $\alpha$ -syn monomers by an all-D-peptide

Authors: **Marc Sevenich**, Ian Gering, Madita Vollmer, Selma Aghabashlou Saisan, Markus Tusche, Tatsiana Kupreichyk, Thomas Pauly, Matthias Stoldt, Wolfgang Hoyer, Antje Willuweit, Janine Kutzsche, Nils-Alexander Lakomek, Luitgard Nagel-Steger, Lothar Gremer, Gültekin Tamgüney, Jeannine Mohrlüder and Dieter Willbold

Journal: Journal of American Chemical Society (submitted)

DOI: n.A.

Impact Factor: 15.4 (2022)

Contribution: Project outline, Phage display selection and NGS analysis, planning and performance of ThT assays, planning and performance of MST and SPR measurements, planning and sample preparation of NMR measurements, planning and sample preparation for intracellular aggregation assay, planning and sample preparation for cell viability assay, planning and performance of DLS measurements, sample preparation for AFM measurements, writing of original draft.

## Direct disassembly of $\alpha$ -syn preformed fibrils into native $\alpha$ -syn monomers by an all-D-peptide

*Marc Sevenich<sup>1,3</sup>, Ian Gering<sup>1</sup>, Madita Vollmer<sup>1</sup>, Selma Aghabashlou Saisan<sup>1,2</sup>, Markus Tusche<sup>1</sup>, Tatsiana Kupreichyk<sup>1,2</sup>, Thomas Pauly<sup>2</sup>, Matthias Stoldt<sup>1</sup>, Wolfgang Hoyer<sup>1,2</sup>, Antje Willuweit<sup>3,4</sup>, Janine Kutzsche<sup>1</sup>, Nils-Alexander Lakomek<sup>1,2</sup>, Luitgard Nagel-Steger<sup>2</sup>, Lothar Gremer<sup>1,2</sup>, Gültekin Tamgüney<sup>1,2</sup>, Jeannine Mohrlüder<sup>1</sup> and Dieter Willbold<sup>1,2,5\*</sup>*

<sup>1</sup> Institute of Biological Information Processing (IBI-7), Forschungszentrum Jülich, Jülich, Germany

<sup>2</sup> Institut für Physikalische Biologie, Heinrich-Heine-Universität Düsseldorf, Düsseldorf, Germany

<sup>3</sup> Priavoid GmbH, Düsseldorf, Germany

<sup>4</sup> Institute of Neuroscience and Medicine (INM-4), Forschungszentrum Jülich, Jülich, Germany

<sup>5</sup> JuStruct, Forschungszentrum Jülich, Jülich, Germany

\* Corresponding author: Phone: +49 2461 612100, fax: +49 2461 612023, e-mail: [d.willbold@fz-juelich.de](mailto:d.willbold@fz-juelich.de), [j.mohrlueder@fz-juelich.de](mailto:j.mohrlueder@fz-juelich.de)

**ABSTRACT**

Parkinson's disease (PD) is the most common neurodegenerative movement disorder worldwide. One of its central features is the neurodegeneration that starts in the substantia nigra and progressively tends to involve other brain regions.  $\alpha$ -Synuclein ( $\alpha$ -syn) and its aggregation during pathogenesis have been drawn into the center of attention, where especially soluble oligomeric and fibrillar structures are thought to play a key role in cell-to-cell transmission and induction of toxic effects. Here, we report the development of all-D-enantiomeric peptide ligands that bind monomeric  $\alpha$ -syn with high affinity, thereby stabilizing the physiological intrinsically disordered structure and preventing initiation of aggregation, and more important, disassembling already existing aggregates. This "anti prionic" mode of action (MoA) has the advantage over other MoAs that it eliminates the particles responsible for disease propagation directly and independently of the immune system, thereby restoring the physiological monomer. Based on mirror image phage display on the D-enantiomeric full-length  $\alpha$ -syn target, we identified SVD-1 and SVD-1a by next generation sequencing, Thioflavin-T screens and rational design. The compounds were analyzed with regard to their anti-aggregation potential and both compounds showed aggregation delaying as well as seed capacity reducing effects in *de novo* and seeded environments, respectively. High affinity towards the monomeric  $\alpha$ -syn, in the low nano- to picomolar  $K_D$  range was identified by surface plasmon resonance (SPR). SVD-1a reduced toxic effects as well as intracellular seeding capacity of  $\alpha$ -syn pre-formed fibrils (PFF) in cell culture. SVD-1a disassembled  $\alpha$ -syn PFF into monomers as identified by atomic force microscopy (AFM), time dependent dynamic light scattering (DLS) and size exclusion chromatography (SEC) analysis. The present work provides promising results on the development of lead compounds with this anti-prionic mode of action for treatment of Parkinson's disease and other synucleinopathies.

## INTRODUCTION

Fibrils consisting of  $\alpha$ -syn have been extracted from brain tissue of patients suffering from Parkinson's disease (PD). PD, dementia with Lewy bodies (DLB) and multiple system atrophy (MSA) are diseases that are collectively referred to as synucleinopathies, as they are all characterized by the accumulation of insoluble  $\alpha$ -synuclein ( $\alpha$ -syn) aggregates in neuronal cells. The majority of the filamentous proportion of these deposits is composed of the  $\alpha$ -syn protein (1, 2).  $\alpha$ -Syn, encoded by the *SNCA* gene, is a 140 amino acid, 14.6 kDa, pre-synaptically located, and intrinsically disordered protein (IDP), which is thought to be involved in synaptic vesicle trafficking, synaptic plasticity as well as modulation of neurotransmitter release including dopamine (3, 4). More than insoluble  $\alpha$ -syn fibrils, smaller soluble versions of them as well as  $\alpha$ -syn oligomers are suspected to be responsible for progression of the disease and the spreading of the pathology through the brain.

On- as well as off-pathway oligomers show a clear negative impact on many cellular processes including membrane, proteasome, mitochondria and ER function, as well as inflammation, autophagy, and synaptic transmission (5-7). In addition, recent insights suggest that aggregated species of  $\alpha$ -syn are able to self-propagate between neuronal cells in a prion-like manner and, therefore, might be the central factor of the progressive nature of disease pathology (8-10).

In this sense, the most promising mode of action for PD treatment is the destabilization and direct elimination of the toxic and self-replicating  $\alpha$ -syn species. We have therefore termed such a therapeutic strategy and the compounds that realize it, "anti-prionic" (11). This term stays in analogy to the term "antibiotic" where elimination of the self-replicating pathological species is also the desired mode of action. In contrast to antibiotics, where it is about killing bacteria by chemical intervention of bacterial enzymes, anti-prionics need to inverse a thermodynamic equilibrium that favors formation of  $\alpha$ -syn fibrils and oligomers from  $\alpha$ -syn monomers (Fig. 1). This is achieved by compounds that stabilize the IDP conformation of the  $\alpha$ -syn monomer.

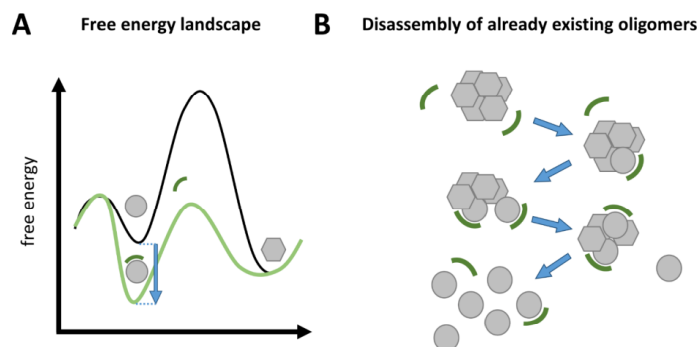


**Figure 1: Mechanistic model of the anti-prionic mode of action realized by the all-D-peptide described in the present work.** Anti-prionic all-D- peptides are designed to stabilize monomers in their native, intrinsically disordered conformation – symbolized by circles. This conformation is distinct from the yet unknown, but certainly highly defined beta-sheet-rich conformation building blocks in oligomers – symbolized by hexagons. (A) Qualitative and schematic free energy landscape for the anti-prionic mode of action. The black line represents the energy landscape in absence of the anti-prionic all-D-peptide. Monomer building blocks in oligomers are more stable than monomers. This allows the formation of oligomers from monomers thermodynamically, although there is a kinetic barrier, which is called primary nucleation and currently under intensive investigation. Stabilization of the monomer by the anti-prionic all-D-peptide is lowering the free energy of the monomer (light green line), when in complex with the all-D-peptide, by the free binding energy (blue arrow) of the complex. Because in the presence of the anti-prionic all-D-peptide, the monomer has a lower free energy as compared to the oligomer, oligomers are disassembled into monomers. (B) Mechanistic model for disassembly of already existing oligomers from top to bottom: Anti-prionic all-D- peptides – symbolized by circle segments – approach oligomers. Due to their affinity to  $\alpha$ -syn monomers, each all-D-peptide will interact with one of the  $\alpha$ -syn building blocks within the oligomer assembly and thereby pushes its conformation towards the intrinsically disordered monomer conformation. This is incompatible with the oligomer assembly and therefore destabilizing the oligomer assembly. Further destabilization by interaction of additional anti-prionic molecules with other monomer building blocks, ultimately leads to the complete disassembly of the oligomer into monomers in their native intrinsically disordered conformation. Both molecules remain disordered in this transient complex, which may therefore be called “fuzzy complex” (12). We called this mode of action “anti-prionic”, because it is ultimately disrupting prion-like behaving aggregates (11).

The success of this therapeutic strategy against the target A $\beta$  oligomers for the treatment of Alzheimer’s disease (AD) was previously demonstrated with the anti-prionic compound RD2 (13-15). RD2 is a 12-aa all-D-enantiomeric peptide that binds A $\beta$  monomers with high affinity (16). This results in the destabilization and ultimately the disassembly of oligomers into monomers. This kind of target engagement has been demonstrated *in vitro* (14), *in vivo* (13) and most recently, *ex vivo* with patient brain derived A $\beta$  oligomers (17). Moreover, the compound proofed cognitive restoration when administered to AD-mice with full-blown pathology (13), while its D-enantiomeric structure and low molecular weight confers proteolytic stability, high bioavailability and penetration of the blood-brain barrier (14, 18, 19).

In this study, we demonstrate the realization of the anti-prionic MoA for  $\alpha$ -syn. The developed all-D-enantiomeric peptides SVD-1 and SVD-1a bind monomeric  $\alpha$ -syn with high affinity, inhibit non-seeded as well as seeded  $\alpha$ -syn aggregation, and most importantly disassemble pre-formed fibrils (PFF) into monomers with high efficiency.

## MATERIAL AND METHODS

### *Recombinant expression and purification of monomeric wt and $\alpha$ -syn A140C*

N-terminal acetylated  $\alpha$ -syn wt (hereinafter referred to as  $\alpha$ -syn) and acetylated  $\alpha$ -syn-A140C were expressed in *E. coli* BL21(DE3) carrying codon-optimized  $\alpha$ -syn in pT7 vector and the pNatB vector with the N-terminal acetylation enzyme from *Schizosaccharomyces pombe* (20). Expression was performed in LB or  $^{15}\text{N}$ -supplemented M9-minimal medium with 1 mM IPTG after reaching an  $\text{OD}_{600}$  of 1.2 followed by incubation for 4 h at 37 °C. Purification was performed as described previously (21) with some modifications: The pellets from 1 l expression was resuspended in 25 ml 20 mM Tris pH 8.0 and boiled at 95 - 100 °C for 2 x 15 min. After centrifugation at 20.000 x g for 30 min at 4 °C, the supernatant was precipitated using a final concentration of 0.45 g/ml of ammonium sulfate. The protein was pelleted at 20.000 x g for 30 min and resuspended in 50 ml 20 mM Tris-HCl pH 8.0. After sterile filtration the sample was loaded on a HiPrep QFF 16/10 (Cytiva, USA, CV = 20 ml) anion exchange column. Gradient elution was performed with a target concentration of 800 mM NaCl over 20 CV. Recombinant  $\alpha$ -syn eluted at a conductivity of 28-32 mS/cm. The fractions containing recombinant  $\alpha$ -syn were pooled and precipitated using ammonium sulfate as described previously. The pellets were resuspended in 5 ml 50 mM Tris-HCl pH 7.4 50 mM NaCl and loaded on a HiLoad Superdex 60/75 pg gel filtration column (Cytiva, USA, CV = 120 ml). The expression yielded 20-30 mg/l as determined by  $A_{275}$  with an extinction coefficient of 5600  $\text{M}^{-1} \text{cm}^{-1}$ . Protein aliquots were frozen with liquid nitrogen and stored at -80 °C.

### *Mirror-image phage display selection*

In phage display, exogenous peptides are presented on phage particles by fusion with the major coating proteins. Consecutive rounds of biopanning and amplification increase the fraction of phages presenting strong target binders, which is detectable by sequencing of the variable portion of the genome (22). Using mirror-image phage display, the L-enantiomeric selection target is replaced by an otherwise identical D-enantiomeric version. This allows the

identification of D-enantiomeric peptides that show high affinity for the physiological L-target and are more resistant to metabolic degradation than their L-enantiomeric counterparts (23, 24).

For mirror-image phage display, the commercially available M13-bacteriophage library TriCo-16 (Creative Biolabs, USA) was used. The library has a capacity of  $2.6 \cdot 10^{10}$  pIII fused 16-mer peptide variants. D-enantiomeric full-length  $\alpha$ -syn carrying a C-terminally biotinylation and N-terminal acetylation was purchased as lyophilized powder from P&E (Peptides and Elephants, GE) with a purity of > 90 %. To minimize non-target related peptide enrichment, the display format was alternated between a polystyrene and polypropylene streptavidin functionalized 96-well plate surface (Maximum capacity plates, BioTeZ, GE). For target immobilization, D-enantiomeric  $\alpha$ -syn was diluted to a concentration of 2 pmol/well. Non-coupled streptavidin was quenched using biotin. The selection was performed as described previously (25-27) with some minor modifications. Briefly, three consecutive selection rounds were performed using alternating blocking conditions with bovine serum albumin (BSA) and milk powder (MP) with PBS pH 7.4 as selection buffer. Selection pressure was stepwise increased with each selection round using 5 to 10 washing repetitions. The selection was performed in three consecutive rounds on the target (*target selection* = TS). Additionally, input phages resulting from selection rounds on the target were incubated on a surface without target (*direct control* = DC), which was otherwise treated identically to the TS surface. As a second control, a consecutive selection was performed exclusively without target on otherwise identically treated surfaces (*empty selection* = ES). A concentration of  $2 \cdot 10^{12}$  CFU ml<sup>-1</sup> was used as input for all selection rounds and controls.

#### *Enrichment ELISA*

Enrichment ELISA is a method to identify enrichment of target binding phages during phage display selection. All steps were performed as described previously with some minor changes (25). Briefly, 20 pmol/well of the D-enantiomeric  $\alpha$ -syn target was immobilized on a streptavidin coated polystyrene 96-well plate (maximum capacity plates, BioTeZ, GE). Both, the target immobilized and target free surface were quenched with biotin. In total,  $2.5 \cdot 10^{11}$  phages from the TS input samples were diluted in 100  $\mu$ l washing buffer and incubated on target and control surface. The A<sub>450</sub> of the product of the peroxidase reaction product 3,3',5,5'-tetramethylbenzidine diimine was quantified after reaction stop with H<sub>2</sub>SO<sub>4</sub> by absorption measurement in a Fluorostar optima platereader (BMG labtech, GE; n = 3).

*ssDNA purification and next generation sequencing of phage input samples*

The ssDNA of the input phage suspensions resulting from mirror-image phage display selection was purified by phage precipitation and subsequent ssDNA separation as described previously (25, 28, 29). For next generation sequencing, PCR was performed adding adapter sequences to both, the 3' and 5' end of the amplification product. Amplicon next generation sequencing was performed by BMFZ-GTL Düsseldorf (GE) with a MiSeq system (Illumina, USA).

*Analysis of the next generation sequences by filtering and clustering*

Variable DNA sequences resulting from next generation sequencing (NGS) were transcribed to peptide sequences as described previously (25, 28, 29). The transcribed sequences were filtered based on their frequency increase in TS (library < TS1 < TS2 < TS3), their correlation with the presence of the target (TS2 > DC2; TS3 > DC3) and their frequency in the selection without target (TS1 > ES1; TS2 > ES2; TS3 > ES3). Sequences that passed the filter were ranked corresponding to their enrichment from library to TS3 (TS3/library = *enrichment score*) and their frequency in TS3 compared to ES3 (TS3/ES3 = *empty score*). Filtered sequences were used as input for *Hammock clustering software* (30). The input FASTA-file included all filtered sequences as ranked by their *empty score*. *Hammock clustering software* was run in full mode with sequences ranked according to their input position (-R input). Cluster motif logos were generated from initial clusters after greedy clustering using the *WebLogo 3.4* application.

*D-enantiomeric peptides*

D-enantiomeric peptides were purchased with C-terminal amidation from CASLO (CASLO, DK) as lyophilized chloride salt powder with a purity of > 95 %. SVD-1 and SVD-1a were tested in different buffer conditions including PBS pH 7.4, where UV-vis absorption measurements after 1 h incubation at 37 °C and 20.800 xg centrifugation showed that both compounds completely retained in the supernatant up to at least 1 mM initial concentration.

*Thioflavin T assay*

The Thioflavin T (ThT) assay is commonly used for the visualization of  $\alpha$ -syn fibrilization, since the dye ThT is able to bind to the amyloidogenic cross- $\beta$ -sheet proportions of fibril structures. Recombinant  $\alpha$ -syn was thawed on ice and centrifuged for 30 min at 21.000 x g and 4°C. The concentration of the supernatant was determined as described previously. Lyophilized D-peptides were thawed at RT for 1 h and dissolved in 500  $\mu$ l PBS pH 7.4. After centrifugation for 30 min at 21.000 x g the supernatant concentration was determined by UV-vis using the corresponding extinction coefficient at  $A_{280}$ . All ThT assay experiments were performed at 37 °C with 15  $\mu$ M ThT and 0.05 % sodium azide (w/v) in PBS pH 7.4 if not otherwise stated. ThT fluorescence was monitored with bottom optics at  $\lambda_{ex} = 448$  nm and  $\lambda_{em} = 482$  nm in a fluorescence plate reader with orbital averaging on 3 mm (Clariostar or Polarstar Optima, BMG labtech, GE). Prior to measurement start, 120  $\mu$ l sample solution was transferred to a non-binding 96-half area well plate with transparent flat bottom (Corning, USA). One borosilicate glass bead (d = 3.0 mm, Hilgenberg, GF) was added to each well for all *de novo* aggregation assays. For seeded aggregation assays no bead was used and samples were incubated under quiescent conditions. Wells that surrounded the sample wells were filled with the same volume of buffer to improve heat distribution. Experiments were performed with five replicates (n = 5) if not otherwise stated.

ThT assay was used for different purposes. First, *de novo* ThT aggregation assays served as screening platform for the aggregation delay with the synthetic D-peptides. Here, 50  $\mu$ M recombinant  $\alpha$ -syn was incubated with a three-fold molar excess of each D-peptide, respectively. Samples were shaken before each cycle using orbital shaking mode at 300 rpm for 30 s. Peptides that were insoluble in aqueous buffer were dissolved in 2.5  $\mu$ l DMSO (0.5 mg peptide) and gradually mixed with PBS pH 7.4 until a final concentration of 2.5 % (v/v) DMSO was reached. For these samples, the reference aggregation of  $\alpha$ -syn alone was also performed in PBS pH 7.4 with 2.5 % (v/v) DMSO. Aggregation curves of each replicate were individually fitted using a symmetric Boltzmann sigmoidal fit (OriginPro 2020, OriginLab, USA) with the following formula:  $y = \frac{A_1 - A_2}{1 + e^{(x-x_0)/dx}} + A_2$  ( $A_1$  = initial value,  $A_2$  = final value,  $x_0$  = inflection point [s],  $dx$  = time constant [1/s]). The inflection point of the fit determines the aggregation half-time  $t_{1/2}$ , whereas the lag-time was approximated with the following formula:  $t_{1/2} - 2 \cdot dt_{1/2}$ , where  $dt_{1/2}$  is defined as the slope of the fit at  $x = t_{1/2}$  in 1/s (31). Half-time and

lag-time were calculated as mean value of the separate fits. For the concentration dependency of aggregation delay, different compound concentrations were applied to 50  $\mu\text{M}$  recombinant  $\alpha\text{-syn}$ . Lag-time and  $t_{1/2}$  were calculated as described previously. For graphical representation, the fitted steady-states were normalized to 1 for all conditions and the mean error was calculated based on the fits. Statistical testing on the significance of the time shifts was performed using the two sample Welch's t-test with  $p < 0.05$  (OriginPro 2020, OriginLab, USA). For *de novo* ThT assays including sub-stoichiometric compound concentrations, 10  $\mu\text{M}$   $\alpha\text{-syn}$  was used. In contrast to the screening aggregation assay  $\alpha\text{-syn}$  samples were continuously shaken at 300 rpm using orbital shaking mode to reduce the aggregation time taking measurements every 5 min. Statistical evaluation was performed as described previously by comparing the significance of  $t_{1/2}$ , lag-time shifts and steady state reduction in the presence of the inhibitor and the same concentration of the corresponding control peptide. For seeded ThT assays, 50 nM monomer equivalent PFF oligomers were incubated ON at 37 °C under quiescent condition together with or without different concentrations of the compounds in the fluorescence plate reader. After 20 h 20  $\mu\text{M}$  monomeric  $\alpha\text{-syn}$  was added to the samples mixture to start seeding. Measurements were taken every five minutes ( $n = 3$ ).

#### *Preparation of PFF oligomers*

PFF oligomers were prepared as described previously with some modifications (32). First, insoluble PFF were produced by incubation of 300  $\mu\text{M}$  recombinant  $\alpha\text{-syn}$  in a LoBind reaction tube (Eppendorf GmbH, GE) with one borosilicate glass bead ( $d = 3.0$  mm; Hilgenberg, DE) in 20 mM NaPi pH 7.0 150 mM NaCl 0.05 % (w/v) sodium azide for one week at 37 °C. The insoluble PFF were harvested by ultracentrifugation at 100.000 x g for 30 min at 4 °C and the pellet was washed several times with 20 mM NaPi pH 7.0 150 mM NaCl. The monomer equivalent concentration was determined by measuring the  $\alpha\text{-syn}$  concentration in the supernatant after the first centrifugation and subtracting it from the start concentration for fibrilization. The insoluble PFF were resuspended in buffer and frozen at -80 °C with liquid  $\text{N}_2$ . PFF oligomers were generated by harsh sonication of 200  $\mu\text{l}$  insoluble PFF with 300  $\mu\text{M}$  monomer equivalent concentration for 3 x 15 s (1 sec. on/off) and 60 % amplitude with a tip sonifier (MS 72 micro tip, Sonopuls, Brandelin, GE). Insoluble PFF were separated by centrifugation at 100.000 x g for 1 h at 4 °C. The supernatant containing PFF oligomers was separated, aliquoted and frozen at -80 °C with liquid  $\text{N}_2$ .

*Surface plasmon resonance kinetic experiments*

Measurements were performed using an 8K Biacore device (Cytiva, USA). Interactions were measured using single cycle kinetics experiments. For all assays, the peptide compounds were immobilized as ligand on the sensor surface and recombinant  $\alpha$ -syn was injected as analyte in the flow. SVD-1 and SVD-1a were immobilized via primary amino groups on a CMD200M carboxyl dextran matrix chip (Xantec, GE). Immobilization was performed after 7 min EDC/NHS activation at 10  $\mu$ l/min with 50  $\mu$ g/ml peptide in 10 mM NaAc pH 5.0 for SVD-1 and pH 7.0 for SVD-1a until a saturation signal was reached (SVD-1: 400 RU, SVD-1a: 500 RU). Surface quenching was performed using 1 M ethanolamine pH 8.3. The kinetic experiments were performed using a flow rate of 30  $\mu$ l/min in PBS pH 7.4 if not otherwise stated. The surface was regenerated in between cycles using 30 s injections of 2 M Gua-HCl at 30  $\mu$ l/min. Data evaluation was performed using Biacore *insight evaluation software* v3.0 (Cytiva, USA).

*SVD-1a\_Cys\_MTSL spin label preparation*

The spin-labeled analogue of SVD-1a was prepared by covalent attachment of MTSL (S-(1-oxyl-2,2,5,5-tetramethyl-2,5-dihydro-1H-pyrrol-3-yl)methyl methanesulfonylthioate, Toronto Research Chemicals, USA) to the C-terminal D-cysteine residue of SVD-1a\_Cys. MTSL was dissolved in DMF (N,N-dimethylformamide) with a concentration of 20 mM and diluted in 200 mM HEPES pH 7.6 to a final concentration of 2 mM. 900  $\mu$ l of the solution was then added to 1 mg of lyophilized SVD-1a\_Cys to create a fivefold molar excess of MTSL compared to SVD-1a\_Cys. The reaction mixture was incubated for 2 h at RT and subsequently applied to a semipreparative RP-HPLC C8 column (Zorbax-300 SB, Agilent, GE) connected to an HPLC system (Agilent 1260, Agilent, GE). Purification of the spin-labeled peptide SVD-1a\_Cys\_MTSL was achieved by applying an aqueous acetonitrile (ACN) gradient (8% ACN, 0.1% trifluoroacetic acid (TFA) to 60% ACN, 0.1% TFA in Milli-Q water within 40 min), running at a flow rate of 4 ml min<sup>-1</sup> at 25 °C with a detection at 214 nm. The purified reaction product was flash-frozen with liquid N<sub>2</sub> and lyophilized (LT-105, Martin Christ, GE). The purity of the SVD-1a\_Cys\_MTSL spin labeled peptide was verified by RP-HPLC with > 98 %.

*NMR spectroscopy*

Samples were prepared at final concentrations of 25  $\mu\text{M}$   $^{15}\text{N}$ -labeled full-length acetyl- $\alpha$ -syn in the absence (reference) and presence of an equimolar amount of SVD-1a (not isotopically labeled, thus NMR-invisible) in PBS buffer, pH 7.4, with an addition of 5 %  $\text{D}_2\text{O}$  for internal reference. 2D  $^1\text{H}$ - $^{15}\text{N}$  HSQC spectra were recorded back-to-back, on a Bruker AVANCE NEO spectrometer (Bruker, USA) operating at 1200 MHz proton Larmor frequency. The experimental temperature was 10  $^\circ\text{C}$ . Spectral dimensions were 16.02 ppm ( $^1\text{H}$ ) x 30 ppm ( $^{15}\text{N}$ ), with 2048 points in the  $^1\text{H}$  dimension and 256 increments in the  $^{15}\text{N}$  dimension, resulting in an acquisition time of 53 ms for the  $^1\text{H}$  dimension and 35 ms for the  $^{15}\text{N}$  dimension. For each increment, 32 scans were recorded, with a recovery delay of 1 s between scans, resulting in an overall experimental time of 4.8 h per spectrum.

NMR Paramagnetic Relaxation Enhancement (PRE) data were recorded on 25  $\mu\text{M}$   $^{15}\text{N}$ -labeled full-length acetyl- $\alpha$ -syn in presence of 25  $\mu\text{M}$  paramagnetically labeled (but not isotopically enriched) SVD-1a\_Cys\_MTSL (using a MTSL spin-label covalently attached to the SVD-1a C-terminus), resulting in a 1:1 ratio of  $\alpha$ -syn : SVD-1a. Intensities ( $I_{\text{para}}$ ) were extracted from 2D  $^1\text{H}$ - $^{15}\text{N}$  Best-TROSY NMR spectra recorded at 600 MHz and 10  $^\circ\text{C}$ , each with 128 scans per increment, resulting in a total experimental time of 16 h per spectrum. Reference data were obtained by adding a 20-fold molar excess of ascorbic acid to the same sample, therefore quenching the paramagnetic effect of the spin-label and obtaining a diamagnetic reference sample. The diamagnetic reference spectra and intensities ( $I_{\text{dia}}$ ) were recorded back-to-back and under identical conditions as for the paramagnetic sample.

NMR data sets were processed using the Bruker TopSpin software (version 4.1.1) and visualised using *CcpNmr Analysis* (v2.4.2) (33). For the assessment of chemical shift changes of  $\alpha$ -syn resonances in presence of SVD-1a relative to the reference spectrum (without SVD-1a), peak positions were extracted using the *CcpNmr Analysis* software. From the residue specific chemical shift changes in the  $^1\text{H}$  and  $^{15}\text{N}$  dimensions, an absolute chemical shift change,  $\Delta\delta$  was calculated using the formula  $\Delta\delta = \sqrt{0.5(\delta_H^2 + (0.14 \delta_N^2))}$  (34). For analysis of the PRE data, resonance intensities of the paramagnetic sample and the diamagnetic reference sample peak intensities were extracted using *CcpNmr Analysis*.

*Size exclusion chromatography (SEC)*

Elimination of PFF oligomers was evaluated by SEC and subsequent detection of the PFF oligomer and monomer peaks. PFF oligomers were incubated with or without SVD-1a in PBS pH 7.4 for 3 d at 37 °C under quiescent condition in low retention Eppendorf tubes (Eppendorf, GE). Prior to injection, samples were centrifuged at 20.800 xg for 2 min and 100 µl sample was injected on a SEC-HPLC column (Bio SEC-3 300 Å, Agilent, USA) using an Agilent 1260 Infinity II system (Agilent, USA) with a flow rate of 1 ml/min and PBS pH 7.4 as mobile phase. Protein was detected using A<sub>214</sub>.

*Dynamic light scattering (DLS)*

Measurements were performed using a SpectroSize 300 131 (XtalConcepts, GE) instrument and a sample volume of 1 ml in a sealed quartz cuvette (Hellma Group, GE). Samples were incubated at 37 °C under quiescent conditions. Prior to measurements, all samples were centrifuged at 21.000 × g for 30 min at 4 °C in order to remove potential impurities from solution. For time dependent DLS measurements data points were recorded every 30 s. Diffusion coefficients were obtained from analysis of the decay of the scattered intensity autocorrelation function and were used to determine apparent hydrodynamic radii via the Stokes-Einstein equation.

*Atomic forced microscopy (AFM)*

Samples were prepared by dilution to 1 µM  $\alpha$ -syn monomer concentration and 5 µl was incubated and dried on a freshly cleaved mica surface. Surfaces were then three-times washed with 200 µl ddH<sub>2</sub>O and dried using a gentle stream of N<sub>2</sub>. Measurements were performed in a Nanowizard 3 system (JPK BioAFM - Bruker Nano GmbH, GE) using intermittent contact mode with 2 x 2 and 5 x 5 µm section and line rates of 0.5–2 Hz in ambient conditions using a silicon cantilever and tip with nominal spring constant of 26 N/m, average tip radius of 9±2 nm and a resonance frequency of approximately 300 kHz (Olympus OMCL-AC160TS-R3). The images were processed using JPK data processing software (version spm-5.0.84). For the

height profiles presented, a polynomial fit was subtracted from each scan line, first independently and then using limited data range.

#### *Circular dichroism (CD) spectroscopy*

Far-UV circular dichroism (CD) data were collected using a Jasco J-1100 spectropolarimeter (Jasco, GE). 350  $\mu$ l samples were pooled and loaded into a high precision quartz cuvette with a path length of 1 mm (Hellma group, GE). A scan speed of 20 nm/min with five accumulations per sample was performed using far UV wavelengths from 260 to 190 nm. Baseline was corrected by subtracting measurements of the buffer only.

#### *Cell assay for $\alpha$ -synuclein aggregation*

A construct encoding full-length A53T-mutated human  $\alpha$ -syn fused with YFP at the C-terminus was synthesized and introduced into the pMK-RQ expression vector (GeneArt; Thermo Fisher Scientific, USA). The  $\alpha$ -synA53T-YFP construct was subcloned into the pIRESpuro3 vector (Clontech; Takara Bio, JPN) using NheI (5') and NotI (3') restriction sites. HEK293T cells (American Type Culture Collection) were cultured in high glucose Dulbecco's Modified Eagle's Medium (DMEM; Sigma-Aldrich, USA) supplemented with 10 % fetal calf serum (Sigma-Aldrich, USA), and 50 units/ml penicillin as well as 50  $\mu$ g/ml streptomycin (Sigma-Aldrich, USA). Cells were cultured in a humidified atmosphere of 5 % CO<sub>2</sub> at 37 °C. Cells plated in DMEM were transfected using Lipofectamine 2000 (Invitrogen; Thermo Fisher Scientific, USA). Stable cells were selected in DMEM containing 1  $\mu$ g/ml puromycin (EMD Millipore, USA). Monoclonal lines were generated by fluorescence-activated cell sorting of a polyclonal cell population in 96-well plates using a MoFlo XDP cell sorter (Beckman Coulter, USA). Finally, the clonal cell line B5 was selected from among 24 clonal cell lines and is referred to as  $\alpha$ SynA53T-YFP cells. Peptides were incubated with 1.5 % Lipofectamine 2000 in OptiMEM for 2 h at room temperature. The  $\alpha$ -synA53T-YFP cells were plated in a 384-well plate with poly-D-lysine coating (Greiner, AT) at a density of 1,000 cells per well with 0.1  $\mu$ g/ml Hoechst 33342 (Thermo Fisher Scientific, USA) and the previously prepared transfection mix was added directly to the cells in the well. To seed cellular aggregation of  $\alpha$ -syn in  $\alpha$ -synA53T-YFP cells, 30 nM soluble  $\alpha$ -syn PFF oligomers were incubated with 1.5 % Lipofectamine in OptiMEM for 2 h at room temperature and added to each well 3 h after the first transfection. The plate was then incubated in a humidified atmosphere of 5 % CO<sub>2</sub> at

37 °C. On day 3 the cells were imaged with an IN Cell Analyzer 6500HS System (Cytiva, USA) using the blue and green fluorescence channel, and analyzed using IN Carta Image Analysis Software (Cytiva, USA) after an algorithm was established to identify intracellular aggregates in living cells. For each condition we used four wells and took 16 images per well, which were analyzed by a fully automated algorithm to avoid bias. Statistical analysis was performed using one-way ANOVA followed by Dunnett's multiple comparisons test (GraphPad Prism 9, GraphPad Software, USA). Error bars represent standard deviation.

*Cell-viability assay (CellGlo test)*

We used the CellTiter-Glo Luminescent Cell Viability Assay (Promega GmbH, GE) to determine the number of viable cells in culture based on quantitation of the ATP present, an indicator of metabolically active cells. After culturing cells in 384-well plates for three days, 35  $\mu$ l of medium was removed from the wells and 40  $\mu$ l of CellTiter-Glo Reagent directly added to each well. After mixing, luminescence was measured 10 min later using a Fluostar (BMG labtech, GE).

*Immunofluorescent cell staining*

After culturing cells for 3 days on 384-well plates, the cells were fixed in 4 % formaldehyde (Sigma-Aldrich, USA) in PBS (pH 7.4) for 15 min. After washing three times with PBS for 5 min each, the cells were permeabilized with 0.25 % Triton X-100 (Sigma-Aldrich, USA) in PBS for 10 min. After another three washes with PBS for 5 min each, the cells were blocked with 1 % bovine serum albumin (Sigma-Aldrich, USA) in PBS supplemented with 0.1 % Tween 20 (Sigma-Aldrich, USA) for 30 min. The cells were stained with CF633 (Biotium, USA) fluorescently labeled antibodies at 8  $\mu$ g/ml in 1 % bovine serum albumin in PBS supplemented with 0.1 % Tween-20 for 1–3 h at room temperature in the dark. For detecting total  $\alpha$ -syn, we used the anti- $\alpha$ -syn antibody syn211 (Abcam, UK). For detecting oligomeric and fibrillar  $\alpha$ -syn, we used the anti-aggregated  $\alpha$ -syn antibody, clone 5G4 (Sigma-Aldrich, USA). For detecting  $\alpha$ -syn phosphorylated at serine 129, we used the recombinant anti- $\alpha$ -syn (phospho S129) antibody EP1536Y (Abcam, UK). After a final three washes in PBS for 5 min each, the cells were imaged in PBS using an IN-Cell Analyzer 6500HS System and 40-fold magnification (Cytiva, USA).

*Cell viability assay (MTT test)*

The potential cell viability rescue of PC12 cells (Leibniz Institute DSMZ, GE) from  $\alpha$ -syn toxicity through addition of SVD-1, SVD-1a or SVD-1\_scrambled was measured in a MTT (3-(4,5-dimethylthiazol-2-yl)-2,5-diphenyltetrazolium bromide) cell viability test. PC12 cells (Leibniz Institute DSMZ, GE) were cultivated on collagen A-coated (Biochrom GmbH, GE) tissue culture flasks in RPMI 1640 medium supplemented with 5 % fetal calf serum and 10 % horse serum in a 95 % humidified atmosphere with 5 % CO<sub>2</sub> at 37 °C. 10.000 cells per well in a volume of 100  $\mu$ l were seeded on collagen A-coated 96-well plates (Thermo Fisher Scientific, USA) and were incubated for 24 h at 37 °C and 300 rpm in a thermo cycler. Then, final concentrations of 30 nM  $\alpha$ -syn either in the absence or after pre-incubation with 15  $\mu$ M SVD-1, SVD-1\_scrambled or 0.5  $\mu$ M SVD-1a was added to the cells. In addition, 15  $\mu$ M of the peptides alone, cell media, buffer without peptides and 0.1 % Triton X-100 (cytotoxic compound) served as controls. After further incubation in a 95 % humidified atmosphere with 5 % CO<sub>2</sub> at 37 °C for 24 h, cell viability was measured using the Cell Proliferation Kit I (MTT) (Roche Applied Science, CH) according to manufacturer's protocol. The MTT formazan product was quantified by measuring the absorbance at 570 nm corrected by subtraction of the absorbance at 660 nm in a FluoroStar Optima plate reader (BMG labtech, GE). All results were normalized to untreated cells grown in medium only. Test on significance was performed using one-way ANOVA with Bonferroni post hoc analysis (OriginPro 2020, OriginLab, USA; n = 4).

## RESULTS

A phage display selection against the mirror image of full-length  $\alpha$ -syn yielded SVD-1 as the most promising all-D-peptide for stabilization of native  $\alpha$ -syn monomers (for full description of the phage display and peptide screening procedure please see SI Fig. 1 to 6). SVD-1a is a derivative of SVD-1, with D-methionine replaced by D-leucine at position 2, D-lysine replaced by D-arginine at position 1, and addition of five D-arginines to the C-terminal end yielding the sequence shown in fig. 2.

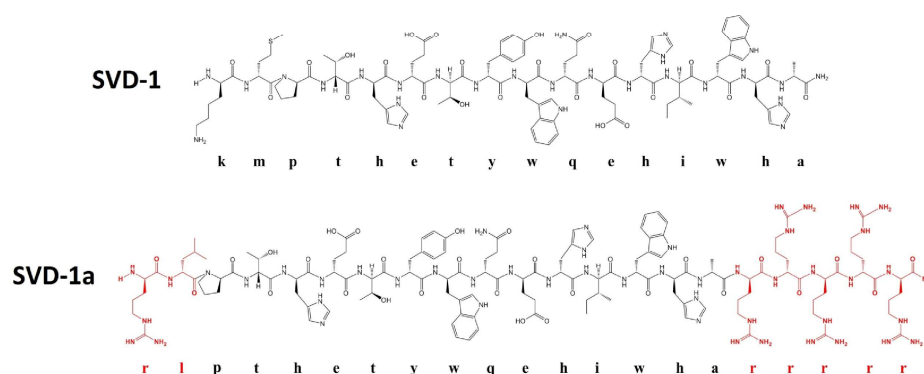


**Figure 2: Natta projection of the D-enantiomeric lead compound SVD-1 and its first optimized derivative SVD-1a.** Amino acid residues marked in red were exchanged or added for improved bioavailability, membrane penetration and inhibitory effects.

First, we characterized binding affinities of SVD-1 and SVD-1 to  $\alpha$ -syn monomer. SPR experiments allow the detection of kinetic values, thereby giving insights in time dependency of target recognition and complex rigidity. Prior to measurements, the SVD peptides were immobilized on a carboxyl dextran matrix surface via amino coupling and  $\alpha$ -syn was injected as analyte in the concentration range of 30 to 500 nM (Fig. 3 A). Likewise, a control peptide that had the same amino acid composition as SVD-1 but with random amino acid sequence (SVD-1\_scrambled) was immobilized. As control for SVD-1a, five arginines were added to the C-terminus of SVD-1 control peptide (SVD-1\_scrambled+5r; (Fig. 3 B)).

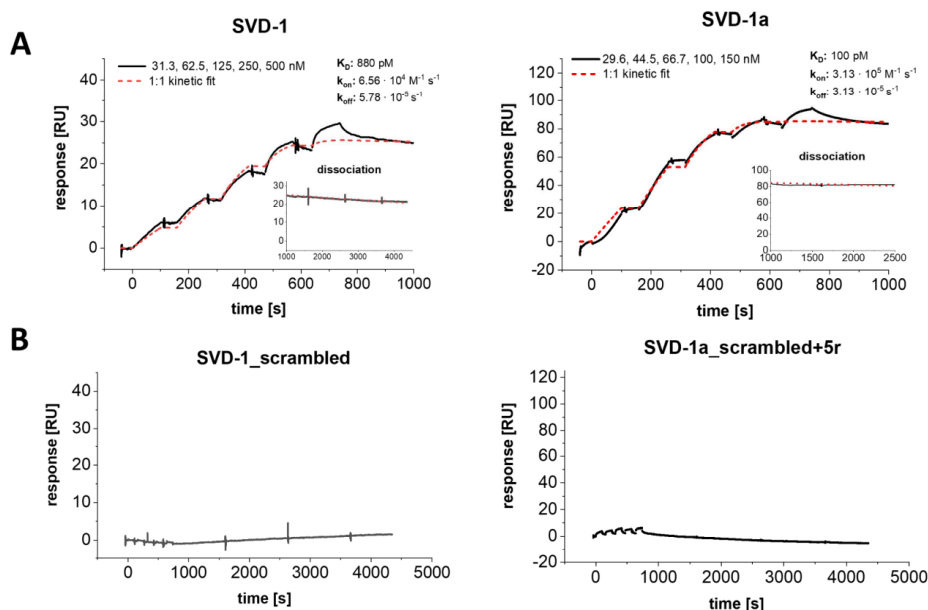


**Figure 3: Single cycle kinetic experiment with  $\alpha$ -syn and immobilized SVD-1 and SVD-1a and control peptides.** (A) SVD-1 (left) and SVD-1a (right) were immobilized on a carboxyl dextran matrix via amino coupling until saturation was reached (CMD200M, Xantec, GE).  $\alpha$ -Syn was injected for 100 s at 30  $\mu\text{l}/\text{min}$  in PBS 7.4 in a serial dilution ranging from 30 to 500 nM, followed by a dissociation time of 60 min or 30 min, respectively. The experiment was performed as individual measurement. The interaction kinetics were fitted with a 1:1 kinetic interaction model: SVD-1:  $K_D$ : 880 pM,  $k_{on}$ :  $6.56 \cdot 10^4 \text{ M}^{-1} \text{ s}^{-1}$ ,  $k_{off}$ :  $5.78 \text{ s}^{-1} \cdot 10^{-5}$ ; SVD-1a:  $K_D$ : 100 pM,  $k_{on}$ :  $3.13 \cdot 10^5 \text{ M}^{-1} \text{ s}^{-1}$ ,  $k_{off}$ :  $3.13 \cdot 10^{-5} \text{ s}^{-1}$ . The non-referenced signal of active and referenced surface is shown in SI Fig. 7. (B) SVD-1\_scrambled (left) and SVD-1a\_scrambled+5r (right) were immobilized on a carboxyl dextran matrix via amino coupling until saturation was reached (CMD200M, Xantec, GE). Full-length  $\alpha$ -syn was injected for 100 s at 30  $\mu\text{l}/\text{min}$  in PBS 7.4 in a serial dilution ranging from 15 to 250 nM, followed by a dissociation time of 60 min. Y-axis scaling was adjusted to the (A).

When applying a 1:1 Langmuir based interaction model, we obtained a  $K_D$  value of 880 pM with a  $k_{on}$  of  $6.56 \cdot 10^4 \text{ M}^{-1} \text{ s}^{-1}$  and a  $k_{off}$  of  $5.78 \cdot 10^{-5} \text{ s}^{-1}$  for SVD-1. For SVD-1a a  $K_D$  of 100 pM with a  $k_{on}$   $3.13 \cdot 10^5 \text{ M}^{-1} \text{ s}^{-1}$  and a  $k_{off}$  of  $3.13 \cdot 10^{-5} \text{ s}^{-1}$  was identified. However, the data is not fully explained by the 1:1 model, which is evident from a deviation of the fits from the data obtained for the later injections, suggesting an additional low-affinity binding mode in the higher nM range.

The inhibitory effects on amyloid formation was further verified in ThT assays under *de novo* as well as seeded conditions with several ratios of  $\alpha$ -syn and SVD-1 or SVD-1a (SI Fig. 8). For seeding assays we incubated SVD-1 or SVD-1a together with pre-formed fibrillary (PFF)

oligomers that induce fibril mass growth in the presence of monomeric  $\alpha$ -syn. In order to obtain fibril seeds with a homogeneous size and high seeding capacity, we started from mature fibrils and treated them by harsh ultra-sonication. This yielded short fibrils with a high ratio of fibril ends per mass. Eventually remaining larger fibrils were removed by ultracentrifugation as described by Kaufmann et al. ((32), SI Fig. 9). Referring to their small size, we call them “PFF oligomers” throughout the manuscript. Due to their high ratio of fibril ends per mass, added monomeric  $\alpha$ -syn is very efficiently and reproducibly elongating the seeds (35).

Sequence specificity of the effect was confirmed by comparing the inhibitory effects of SVD-1 and SVD-1a with the respective control peptides. The sequence-randomized control peptides had virtually no inhibitory effects, clearly suggesting that not the overall electrostatic charge or hydrophilicity were important, but the amino acid sequence of SVD-1 and SVD-1a (SI Fig. 8). In contrast to the sequence-randomized control peptide, SVD-1 confirmed its efficacy by a concentration dependent delay of aggregation onset as well as by a reduction of steady state levels under *de novo* aggregation conditions. Thus, SVD-1 inhibits primary nucleation of  $\alpha$ -syn. Also, in contrast to the sequence-randomized control peptide, SVD-1 was able to significantly decelerate amyloid growth in the seeded environment. Thus, SVD-1 also inhibits elongation and secondary nucleation of  $\alpha$ -syn. Similar observations were made for SVD-1a under *de novo* aggregation conditions, where at twofold molar excess aggregation was completely inhibited. When SVD-1a was present in the pre-incubation period with the PFF oligomers, a reduction of the elongation rate was observed later during the incubation period with  $\alpha$ -syn monomers already at 5  $\mu$ M SVD-1a. 20  $\mu$ M or higher SVD-1a concentrations even led to the complete inhibition of the seeding capacity. 20  $\mu$ M of the control peptide, SVD-1\_scrambled+5r, did not yield any inhibition of seeding, again underlining the SVD-1a sequence specificity for the observed effects.

It is tempting to speculate that SVD-1a was successfully reducing the amount of PFF oligomer seeds during the 20 h pre-incubation period to explain the reduction of their seeding activity. In order to investigate this further, we incubated 100 nM monomer equivalent purified PFF oligomers with increasing concentrations of SVD-1a for 72 h and analyzed then the samples by SEC, time dependent dynamic light scattering (DLS) and atomic force microscopy (AFM) (Fig. 4).

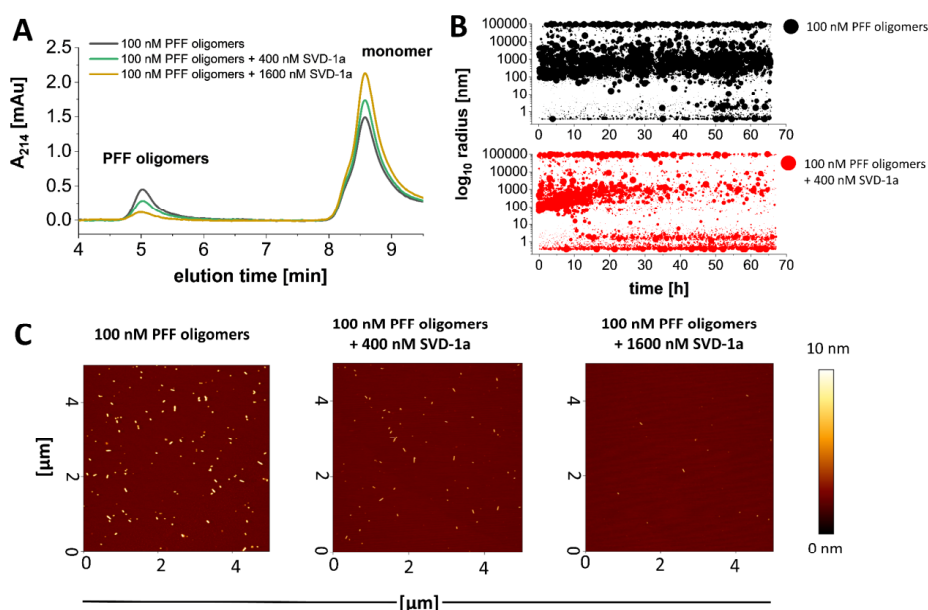


**Figure 4: SVD-1a disassembles PFF oligomers into  $\alpha$ -syn monomers.** PFF oligomers were prepared as described previously. 100 nM monomer equivalent PFF oligomers were incubated with or without 400 nM and 1600 nM SVD-1a for 3 d at 37 °C in PBS pH 7.4. (A) HPLC-SEC measurement samples were injected on a Bio SEC-3 column (300 Å, Agilent, USA). The PFF oligomers elute after approx. 5 min, while  $\alpha$ -syn monomer is detected after approx. 8.6 min. (B) Time dependent DLS measurements with 100 nM PFF oligomers in presence (red) and absence (black) of 400 nM SVD-1a. 1 ml sample was continuously measured in a sealed quartz cuvette at 37 °C under quiescent condition every 30 s for 72 h in a SpectroSize 300 instrument (XtalConcepts, GE). Data are shown as radius plot where the signal amplitude of each particle size is represented by the data point diameter. (C) For AFM analysis 5  $\mu$ l of the samples as described in (A) was rescued before centrifugation and incubated and dried on a freshly cleaved mica surface followed by washing with ddH<sub>2</sub>O and drying using a gentle stream of N<sub>2</sub>. Analysis was performed using NanoWizard 3 system (J-1100, JPK BioAFM, USA), recording multiple surface sections. The sections shown in C are representative for the observed species and particle density identified on all surface sections.

The SEC analysis yielded that the PFF oligomer preparation contains a substantial fraction of monomers in equilibrium that may occur due to the proportionally high number of fibril ends as compared to mature fibrils. Incubation of the PFF oligomers with increasing concentrations of SVD-1a (here 400 and 1600 nM) resulted in an increase of monomer concentration paralleled by a decrease in oligomer concentration (Fig. 4 A). This is supported by AFM (Fig. 4 C). In addition, the time dependent DLS measurement (Fig. 4 B) shows that SVD-1a is progressively eliminating the PFF oligomers (Fig. 4 B, red, 100 to 1000 nm radius) by disassembling them into monomeric  $\alpha$ -syn (Fig. 4 B, red, 3 nm radius). In contrast, no change

of the PFF oligomer particle size radius was observed when SVD-1a is absent (Fig. 4 B, black, 100 to 1000 nm radius).

In conclusion, the analysis of the inhibitory mechanism of SVD-1a on  $\alpha$ -syn aggregation under seeded condition has shown that (i) SVD-1a eliminates PFF oligomers in a time dependent process, (ii) stabilizes monomeric  $\alpha$ -syn in its random coil conformation and (iii) reduces the emergence of mature fibrils.

To further verify whether SVD-1a is also able to counteract the seeding potential of soluble  $\alpha$ -syn PFF oligomers in living cells,  $\alpha$ -synA53T-YFP expressing cells were transfected with soluble  $\alpha$ -syn PFF oligomers together with SVD-1a or a negative-control peptide with similar molecular weight as SVD-1a but no affinity to monomeric  $\alpha$ -syn (Fig. 5). In the  $\alpha$ -synA53T-YFP cell system, human  $\alpha$ -syn with the familial A53T mutation fused to YFP is stably expressed in HEK293T cells and enables fluorescence-based detection of intracellular aggregation of endogenously expressed  $\alpha$ -synA53T after seeding with patient-brain extracts containing PFFs as shown previously (36-39) or with PFF oligomers as shown here. To avoid interference with the fluorescence-based aggregate detection, we intentionally did not use fluorescence labelled SVD-1a or control peptide. Another reason was that fluorescence dyes can positively or negatively interfere with the transfection efficacy and possibly also with the subcellular localization of the respective peptide.

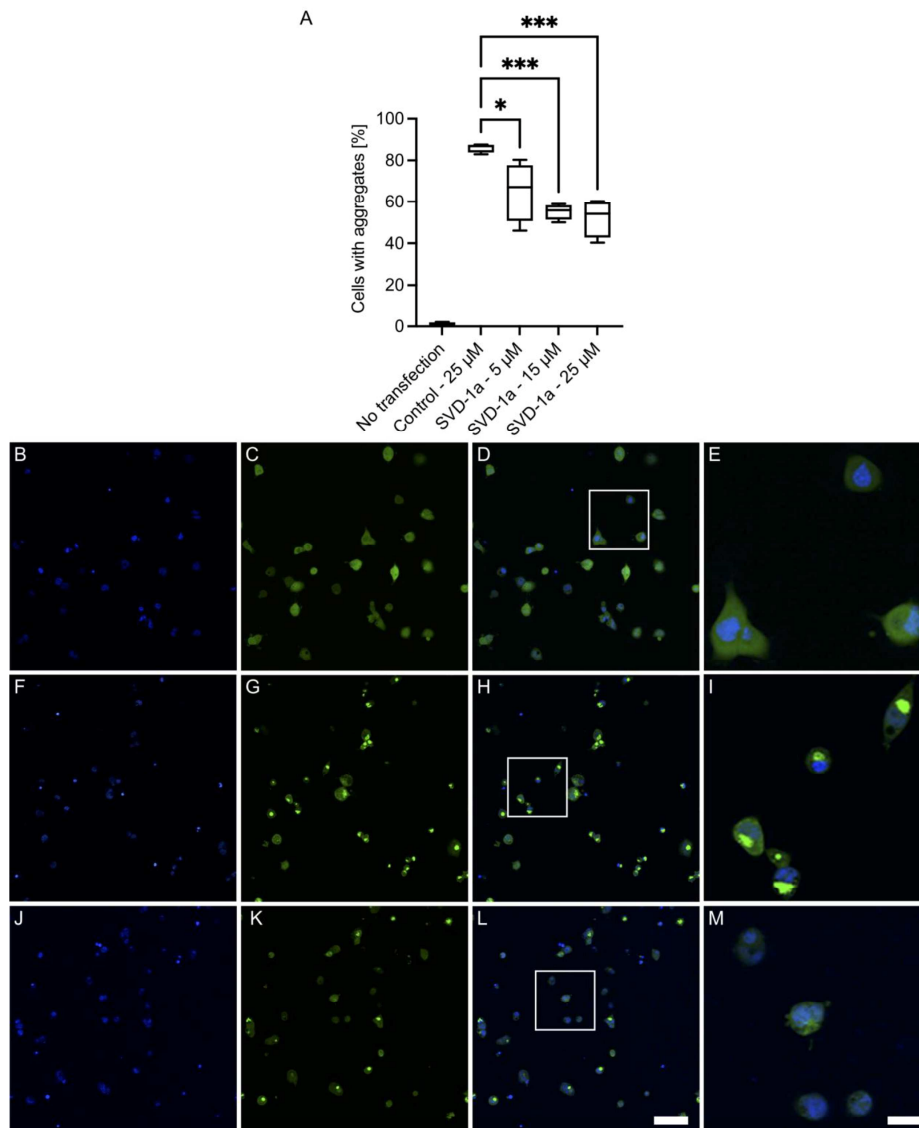


**Figure 5: SVD-1a inhibits seeded  $\alpha$ -syn aggregation in cells.** To validate the inhibitory effect of SVD-1a in cells, we used the  $\alpha$ -synA53T–YFP cell system, which stably expresses human  $\alpha$ -syn with the familial A53T mutation fused to YFP in HEK293T cells and enables fluorescence-based detection of aggregates that show up as highly fluorescent spots within the cells clear above background, intracellularly after seeding with PFF oligomers. In order to avoid interference of the peptide with the uptake of PFF oligomers, we performed a two-step transfection starting with a first transfection of peptide and a second transfection with PFF-oligomers. SVD-1a but not the negative control peptide (kgvgnleyqlwalegk-NH2) inhibited  $\alpha$ -syn aggregation in  $\alpha$ SynA53T–YFP cells in a dose-dependent manner (A). To quantify the number of cells with aggregates in our images and to avoid

experimental bias, we used a fully automated algorithm for image analysis. Significance was calculated using one-way ANOVA followed by Dunnett's multiple comparisons test. One asterisk denotes p values less than 0.05 and three asterisks a p value less than 0.001. Error bars indicate standard deviation. In contrast to unseeded cells, which did not harbor any  $\alpha$ -syn aggregates at day three after plating (B–E), seeding with soluble  $\alpha$ -syn PFF oligomer induced aggregation in 85 % of cells treated with a negative-control peptide (25  $\mu$ M) that does not bind to  $\alpha$ -syn (F–I). Treatment with increasing concentrations of SVD-1a, here imaged at 25  $\mu$ M, led to a concentration-dependent reduction in the number of cells with aggregates (J–M). Panels B, E, and H show nuclei stained with Hoechst 33342. Panels C, F, and I show  $\alpha$ SynA53T–YFP fluorescence. Panels D, G, and J show merged images. The scale bar in L represents 100  $\mu$ m and applies to panels B–D, F–H, and J–L. Panels E, I, and M represent magnifications of the insets in D, H, and L, respectively the scale bar in M applies to panels E, I and M and represents 25  $\mu$ M. The viability of the cells was not reduced by transfection with seeds or in SVD-1a as shown in SI Fig. 12. Confirmation that highly fluorescent aggregates contain  $\alpha$ -syn is shown in SI Fig. 10 by co-immunostaining with syn-211 antibody, anti- $\alpha$ -syn (phospho S129) antibody and 5G4 antibody.

Seeding with  $\alpha$ -syn PFF oligomers in the presence of a negative-control peptide induced aggregation in 85 % of the cells (Fig. 5 A, E–G). We verified that the induced intracellular, yellow-fluorescent aggregates consist of  $\alpha$ -syn by immunofluorescence staining with three different antibodies recognizing aggregated  $\alpha$ -syn,  $\alpha$ -syn phosphorylated at serine 129, and total  $\alpha$ -syn (SI Fig. 11). When SVD-1a was transfected into the cells, a concentration-dependent reduction of aggregate-positive cells was observed resulting in 64 % and 57 % aggregate-positive cells using 5 and 25  $\mu$ M of SVD-1a, respectively (Fig 13 A, H–J). Also, the viability of PFF oligomer-seeded  $\alpha$ -synA53T–YFP cells was not significantly reduced in the presence of any of the two peptides (SI Fig. 12. SVD-1aCys\_Alexa647 is crossing the membrane without transfection (SI Fig. 13). These results demonstrate that SVD-1a inhibits PFF oligomer-induced aggregation of  $\alpha$ -syn in the intracellular environment without inducing cytotoxicity. Moreover, in PC12 cells a reduction of PFF oligomer cytotoxicity was verified in presence of SVD peptides using cell viability assay (SI Fig. 14).

SVD-1 and SVD-1a have been selected and developed to specifically bind  $\alpha$ -syn monomers in order to stabilize  $\alpha$ -syn in its monomeric conformation, which is well known to be a classic example of an intrinsically disordered protein (IDP). The constant and fast sampling of a large conformational space gives IDPs the structural plasticity and adaptability to interact with and control multiple binding partners at the same time. IDPs have very characteristic NMR spectra. The amide protons of the protein backbone are solvent exposed and not involved in typical secondary structural elements like  $\beta$ -sheets or  $\alpha$ -helices. This and the high mobility of the protein backbone and the side chains on a very rapid time scale limit the chemical shift dispersion of IDPs more or less to the time averaged random coil chemical shifts of the

respective amino acid residues of the protein in aqueous solution. This is the reason, why the amide protons of IDPs have a typical chemical shift dispersion of only 0.7 ppm. In contrast, the amide protons of globularly folded proteins have a chemical shift dispersion of up to 4 ppm, and the individual chemical shift of the amide proton is dependent of its involvement in a hydrogen bond and whether its chemical environment contributes more shielding or de-shielding contributions, both of which are not averaged out over time as in IDPs (40, 41).

Of course, we were very curious to investigate, whether SVD-1 and SVD-1a have a significant impact on the IDP conformation of  $\alpha$ -syn monomers, given their high affinity based on SPR. The highly dynamic and transient interactions may for each amide proton and  $^{15}\text{N}$ -nucleus lead to many different shielding and de-shielding events in their chemical environment that become zero, when averaged over the NMR time scale. The probability, however, that each chemical shift change is averaged to exactly zero, is very low. Thus, we investigated the chemical shift changes upon binding of SVD-1a to  $\alpha$ -syn monomers at the highest available field. Figure 6 A shows the superposition of the  $^1\text{H}$ - $^{15}\text{N}$  HSQC NMR spectra of  $25\ \mu\text{M}$   $^{15}\text{N}$ -labeled full-length  $\alpha$ -syn in absence and presence of  $25\ \mu\text{M}$  SVD-1a. Careful and automated peak analysis revealed that there are indeed small chemical shift changes that are shown  $\alpha$ -syn sequence specifically in Figure 6 C with some examples displayed in Figure 6 B. Overall, the chemical shift changes are very small, with most residues showing significant chemical shift changes located in the C-terminal region but also residues in other parts of  $\alpha$ -syn are affected.

To obtain more information, which parts of the  $\alpha$ -syn molecule are involved in the highly dynamic and transient interaction, we applied paramagnetic relaxation enhancement (PRE) NMR experiments. Such NMR-PRE data have proven insightful for the study of binding interactions of amyloid- $\beta$  recently (42).

Residue-specific NMR PREs intensity ratios,  $I_{\text{para}} / I_{\text{dia}}$ , were recorded for  $^{15}\text{N}$ -labeled (NMR-visible)  $\alpha$ -syn in the presence of SVD-1a, with a paramagnetic spin-label covalently attached at its C-terminus (Fig. 6 D). Decrease of intensity ratios point to proximity of the paramagnetic spin-label of SVD-1a to the respective residue of  $\alpha$ -syn. Indeed, we observed an overall decrease of intensity ratios,  $I_{\text{para}} / I_{\text{dia}}$ , in the spectra (paramagnetic vs diamagnetic sample) for practically all residues, in the order of 15 to 20 % and with an increased reduction for the C-terminal residues of  $\alpha$ -syn (Fig 6 D). Strikingly, this coincides with the residues showing the “largest” of the very small chemical shift changes (Fig. 6 B) that were most prominent in the C-terminal region. The apparently weak transient interactions with the N-terminal 108  $\alpha$ -syn

residues, as observed by the NMR-PRE data, are in their accumulated sum effect relevant and impactful. This is indicated by the observation that the *de novo* aggregation not only of full length  $\alpha$ -syn is efficiently inhibited by SVD-1 and SVD-1a, but also that of the C-terminal deletion mutant of  $\alpha$ -syn,  $\alpha$ -syn (1-108) (SI Fig. 15).

The PRE data together with the absence of large chemical shift changes are in-line with lowly populated transient binding interactions, presumably due to an on/off hopping of SVD-1a to  $\alpha$ -syn occurring on a very fast time scale. Hence, the binding mode is potentially best described by an IDP – IDP interaction with multiple dynamic binding sites, whereas both partners retain their disordered structure (12, 43). Such fuzzy complexes have been described previously (44-50). In some cases no chemical shift changes have been reported at all (44). For several of those cases, NMR paramagnetic relaxation enhancement (PRE) measurements revealed transient interactions between the protein and the binding partner (44-50).

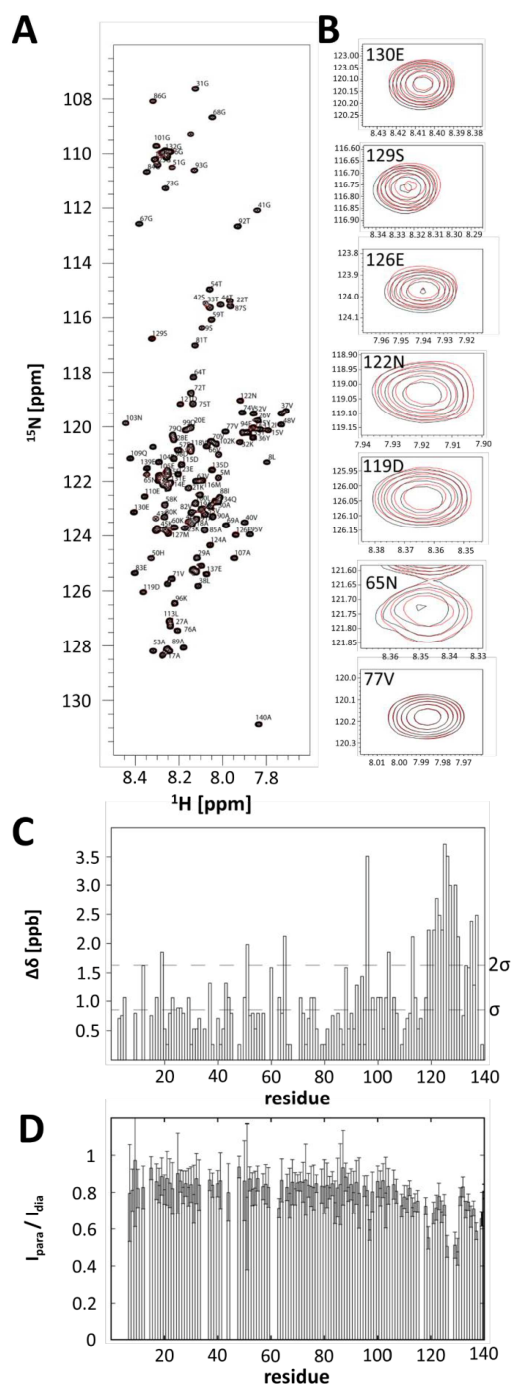


**Figure 6: NMR analysis of  $^{15}\text{N}$ -labeled  $\alpha$ -syn interacting with SVD-1a (not isotope labeled).** (A) Overlay of two-dimensional  $^1\text{H}$ - $^{15}\text{N}$  HSQC spectra of  $25\ \mu\text{M}$   $^{15}\text{N}$   $\alpha$ -syn in the presence (red) and absence (black) of an equimolar amount of SVD-1a. (B) Enlargement of several resonances in the spectra shown under (A) that show small chemical changes for residues in the presence (red) relative to the absence (black) of SVD-1a (130E, 129S, 126E, 122N, 119D, 65N); for comparison, resonance 77V is shown that does not show any chemical shift change. (C) Residue-specific absolute NMR chemical shift changes in the spectra of  $^{15}\text{N}$   $\alpha$ -syn in presence of SVD-1a relative to the absence of SVD-1a. The standard deviation,  $\sigma$ , as well as the 2-fold standard deviation,  $2\sigma$ , of the distribution of observed chemical shift changes are indicated as dashed lines. (D) NMR PRE intensity ratios of  $^{15}\text{N}$   $\alpha$ -syn in the presence of the paramagnetically-labeled SVD-1a. Residue-specific intensity ratios,  $I_{\text{para}} / I_{\text{dia}}$ , of the cross-peak intensities in the two-dimensional  $^1\text{H}$ - $^{15}\text{N}$  NMR spectra of the paramagnetic vs diamagnetic sample are shown. The lower the intensity ratios,  $I_{\text{para}} / I_{\text{dia}}$ , the closer the proximity of the paramagnetically-labeled SVD-1a to the respective residue of  $\alpha$ -syn. An intensity of one would indicate the absence of interactions. Data point to a bit more pronounced (transient) binding interaction of SVD-1a with residues in the C-terminal region of  $\alpha$ -syn, as compared to the average effect on residues in the remaining N-terminal region.

To investigate in further detail how this interaction mode functions under aggregation promoting conditions, we performed *de novo* aggregation in presence and absence of the peptide and analyzed the endpoint samples by circular dichroism spectroscopy (CD) and AFM.

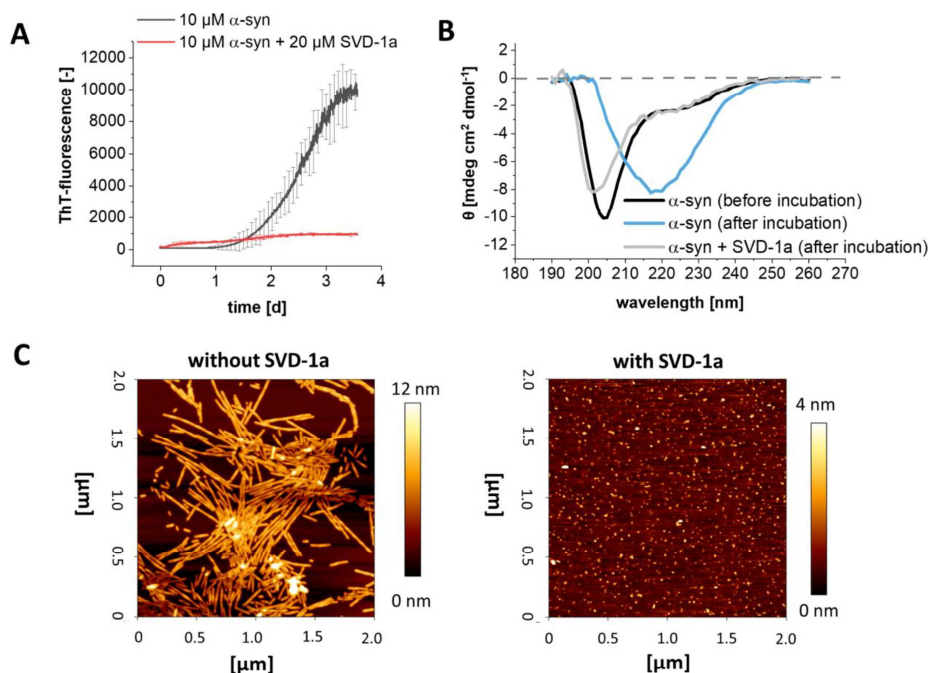


**Figure 7: *De novo* aggregation analysis of  $\alpha$ -syn in the presence and absence of SVD-1a using ThT, DGC, CD and AFM. (A) *De novo* ThT assay of 10  $\mu$ M  $\alpha$ -syn with and without 20  $\mu$ M SVD-1a. ThT fluorescence progression was measured in a 96-well non-binding half-area plate (Corning, USA) with a Fluorostar platereader (BMG labtech, GE) at  $\lambda_{ex} = 448$  nm and  $\lambda_{em} = 482$  nm with 300 rpm continuous orbital shaking between reads. Data are shown as mean values with  $\pm$  SD ( $n = 5$ ). (B) CD secondary structure analysis of *de novo* aggregation samples. Samples were incubated as described in (A) without added ThT ( $n = 3$ ) and subsequently pooled for CD analysis. Far-UV ellipticity of the samples was measured in a quartz cuvette ( $l = 10$  mm) in a J-1100 CD-spectrometer (Jasco, GE). In addition to (A), a sample with 20  $\mu$ M SVD-1a alone was incubated under identical conditions and later used as reference for the sample with  $\alpha$ -syn and SVD-1a. For this sample ( $\alpha$ -syn + SVD-1a (after incubation)) the SVD-1a reference subtracted CD spectrum is shown. (C) Samples from (A) were isolated directly after incubation and diluted in PBS pH 7.4 to a final concentration of 1  $\mu$ M  $\alpha$ -syn monomer equivalent. 5  $\mu$ l diluted sample was incubated and dried on a freshly cleaved mica surface followed by washing with ddH<sub>2</sub>O and drying using a gentle stream of N<sub>2</sub>. Analysis was performed using NanoWizard 3 system (J-1100, JPK BioAFM, USA), recording multiple surface sections. The section shown in (C) are representative for the observed species identified on all surface sections.**

CD secondary structure analysis (Fig. 7 B) of replicate samples without ThT shows that incubation of monomeric  $\alpha$ -syn results in a shift from random coil (Fig. 7 B, black line) to beta-sheet (Fig. 7 B, blue line) CD spectrum, typical for  $\alpha$ -syn fibrils (51). However, in the presence of SVD-1a, while the overall signal is slightly reduced, no spectrum shift towards a beta-sheet spectrum was observed (Fig. 7 B, grey line). In combination with the ThT measurements, the

CD measurements clearly indicate that the majority of monomeric  $\alpha$ -syn that is present at the start point of incubation, is retained in its monomeric random coil form when SVD-1a is present and is only aggregating into  $\beta$ -sheet rich fibrils when SVD-1a is not present. These observations are confirmed by AFM pictures of the samples taken from the incubation endpoints in the ThT assay of figure 11 A (Fig. 7 C). Here, the sample without SVD-1a shows mature fibrils (Fig. 7 C, left). The AFM pictures from samples that contained SVD-1a reveal small particles that are artifacts due to the drying of the samples (Fig. 7 C, right) before imaging. However, they clearly do not contain any fibrils, supporting that SVD-1a was able to inhibit fibril formation as already demonstrated by the ThT experiments.

In order to integrate the results shown into a mechanistic model (Fig. 1) of a therapeutic mode of action, the following considerations are crucial: only very small chemical shift changes were identified for unbound vs bound  $\alpha$ -syn, indicating that the presence of the compounds did not significantly change the overall  $\alpha$ -syn conformation. At first glance, this may seem counter-intuitive when compared to the classical receptor-ligand interaction studies, where one would expect chemical shift changes for the residues close to the “binding pocket”. However, the binding mode of IDPs, such as  $\alpha$ -syn, may substantially deviate from such classical picture (52, 53). Thus, we carried out NMR experiments with  $^{15}\text{N}$  isotope-labelled  $\alpha$ -syn and SVD-1a with a paramagnetic label attached. When applying paramagnetic relaxation enhancements (PRE) experiments the PRE-label associated with the peptide decreases the peak intensities around the binding site. As our PRE measurements indicate (Fig. 6 D), SVD-1a interacts with the entire  $\alpha$ -syn monomer, with the C-terminal part showing the strongest interaction. PRE data indicate a transient and highly dynamic interaction.

The binding data would be consistent with the following scenario: SVD-1 and SVD-1a encounter  $\alpha$ -syn in various conformations. Each conformation of this conformational ensemble is transient and sparsely populated, with conformations interconverting among each other on fast time scales. In sum, the accumulated high number of sparsely populated binding events will result in the observed macroscopic high affinity binding constant. Note, that the observed overall binding will not necessarily induce large chemical shift changes for the individual residues (44, 45), but leads to the observed NMR PRE effects. This is a binding mode, which comes closest to the envisioned mode of action for SVD-1 and SVD-1a, namely to stabilize  $\alpha$ -syn monomers in their highly dynamic and flexible IDP conformation.

For the majority of the  $\alpha$ -syn anti-aggregation compounds that have been developed over the last years, an essential dogma was the avoidance of a direct interference with the physiological monomeric form of  $\alpha$ -syn in order to exclude effects that might influence the physiological function of the target protein (54, 55). The following data support the conclusion that SVD-1a binds to the  $\alpha$ -syn monomer, stabilizes it in its IDP-like conformation, and keeps it monomeric in its physiological IDP conformation. Incubation of 25  $\mu$ M  $\alpha$ -syn with 25  $\mu$ M SVD-1a for 4.8 h at 10 °C for the NMR experiments shown in Figure 6 A did not yield any signs of signal loss due to precipitation. Similarly, for the PRE NMR experiments (Fig. 6 D), the observed amide cross peak intensity reduction due to the PRE label interaction with  $\alpha$ -syn residues, was fully rescued upon addition of ascorbate to quench the PRE label (which was the diamagnetic reference experiment). Thus, SVD-1a is not sequestering  $\alpha$ -syn monomers into any other conformation or state. SVD-1a is rather stabilizing  $\alpha$ -syn monomers in their IDP conformation by the free binding energy underlying the high affinity demonstrated by the SPR measurements (Fig. 3). The strong binding of SVD-1a to  $\alpha$ -syn monomers is not influencing its IDP conformation, suggesting that its physiological role in the cell might not be affected or limited by SVD-1a. Figure 1 A illustrates, why the stabilization of  $\alpha$ -syn monomers by the free binding energy of SVD-1a, is also disassembling already existing PFF oligomers (Fig. 1 B), just because SVD-1a bound  $\alpha$ -syn monomers are thermodynamically more stable than the  $\alpha$ -syn building block conformation in oligomers. This strongly supports the proposed mode of action of SVD-1a. Disassembly of PFF oligomers by SVD-1a as demonstrated by SEC analysis of PFF oligomers incubated with SVD-1a by the observed increase of  $\alpha$ -syn monomer concentration paralleled by the decrease of the PFF oligomer concentration, in an SVD-1a concentration dependent manner, also verified by DLS (Fig. 4). All these results support the mechanistic model for SVD-1a's mode of action as described in Fig. 1.

Taken together, the oligomer-elimination assay as well as the assays for which PFF oligomers were used as the pre-formed aggregate species (cell viability assay, intracellular aggregation assay, seeded aggregation assay) show that the compounds are able to eliminate soluble  $\alpha$ -syn aggregates independent of their overall structural assembly. This result appears to be in agreement with the intended anti-prionic mode of action, where the compounds stabilize the physiological IDP-like monomer structure, thereby destabilizing and disassembling the toxic aggregates. This allows the mode of action to be independent of the specific conformation of specific toxic aggregate assemblies. The physiological solution structure of monomeric  $\alpha$ -syn remains the same *in vitro* and *in vivo*, irrespective of the localization (56). This makes

monomeric  $\alpha$ -syn a more attractive target, since this mode of action is independent of the final form of the toxic component, and thus independent of any prion strain.

These results are a promising starting point for further development of an all-D-enantiomeric peptide compound is even disassembling already existing aggregates. Since the compounds presented here are predominately interacting with the physiological active monomeric form of  $\alpha$ -syn, future studies will also address the preservation of its physiological functionality in presence of the compounds. In addition, future efforts will deal with the investigation of the compound's blood-brain-barrier penetrance and pharmacokinetic profile to show the transferability of the anti-prionic mode of action *in vivo*.

#### **CONFLICT OF INTEREST**

MS, JM and DW are co-inventor of patents covering the composition of matter of SVD-peptides. DW and AW are co-founders and shareholders of the company "Priavoid GmbH, Düsseldorf, Germany", which is planning to further develop the SVD-peptides. They declare that this has not influenced to evaluation and interpretation of experiments. All other authors declare no competing interest.

#### **AUTHOR CONTRIBUTIONS**

**Conceived and designed the project outline:** MS, WH, AW, GT, JK, JM and DW. **Planned and performed experiments:** Phage display selection (MS, WH, JM, DW); ThT screening assays (MS); *de novo* and seeded ThT assays (MS); peptide optimization (MS, JM, DW); surface plasmon resonance (MS); circular dichroism spectroscopy (MS); dynamic light scattering (MS); atomic force microscopy: (MS, TK), nuclear magnetic resonance spectroscopy (MS, MS<sup>2</sup>, NAL, LG), intracellular seeding assay (MS, MV, SAS, GT); PFF oligomer elimination (MS); cell viability assay (MS, MT, JK); **wrote the manuscript:** MS, NAL, GT, JM and DW; **contribution for revision:** LNS, TP. All authors contributed to the manuscript.

#### DATA AVAILABILITY STATEMENT

The datasets generated during and/or analysed during the current study are available from the corresponding author on reasonable request.

#### RESEARCH FUNDING

The project received funding by the Michael J. Fox Research Foundation (Grant-ID: MJFF-000934).

#### ACKNOWLEDGEMENTS

The authors acknowledge access to the Jülich-Düsseldorf Biomolecular NMR Center that is jointly run by the Forschungszentrum Jülich and Heinrich-Heine-University Düsseldorf. We acknowledge Abishek Cukkemane for help with time dependent DLS experiments as well as Lena Mangels for help with AFM measurements.

#### REFERENCES

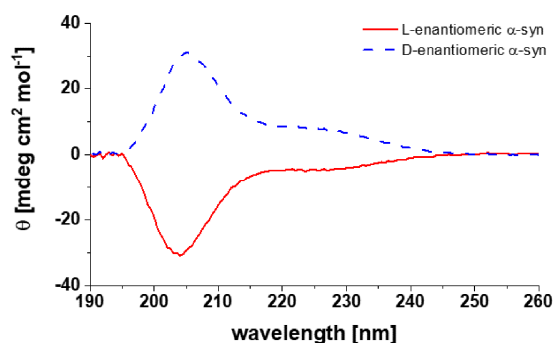
1. K. Wakabayashi *et al.*, The Lewy Body in Parkinson's Disease and Related Neurodegenerative Disorders. *Mol Neurobiol* **47**, 495-508 (2013).
2. M. G. Spillantini *et al.*, alpha-synuclein in Lewy bodies. *Nature* **388**, 839-840 (1997).
3. F. R. Cheng, G. Vivacqua, S. Yu, The role of alpha-synuclein in neurotransmission and synaptic plasticity. *J Chem Neuroanat* **42**, 242-248 (2011).
4. L. Maroteaux, J. T. Campanelli, R. H. Scheller, Synuclein - a Neuron-Specific Protein Localized to the Nucleus and Presynaptic Nerve-Terminal. *J Neurosci* **8**, 2804-2815 (1988).
5. C. R. Fields, N. Bengoa-Vergniory, R. Wade-Martins, Targeting Alpha-Synuclein as a Therapy for Parkinson's Disease. *Front Mol Neurosci* **12**, (2019).
6. N. Bengoa-Vergniory, R. F. Roberts, R. Wade-Martins, J. Alegre-Abarrategui, Alpha-synuclein oligomers: a new hope. *Acta Neuropathol* **134**, 819-838 (2017).
7. M. Ingelsson, Alpha-Synuclein Oligomers-Neurotoxic Molecules in Parkinson's Disease and Other Lewy Body Disorders. *Front Neurosci-Switz* **10**, (2016).
8. H. J. Lee, S. Patel, S. J. Lee, Intravesicular localization and exocytosis of alpha-synuclein and its aggregates. *J Neurosci* **25**, 6016-6024 (2005).
9. L. Volpicelli-Daley, P. Brundin, Editorial: Pathogenic templating proteins in Neurodegenerative Disease. *Neurobiol Dis* **109**, 175-177 (2018).

10. S. B. Prusiner *et al.*, Evidence for alpha-synuclein prions causing multiple system atrophy in humans with parkinsonism. *P Natl Acad Sci USA* **112**, E5308-E5317 (2015).
11. D. Willbold, J. Kutzsche, Do We Need Anti-Prion Compounds to Treat Alzheimer's Disease? *Molecules* **24**, (2019).
12. A. Borgia *et al.*, Extreme disorder in an ultrahigh-affinity protein complex. *Nature* **555**, 61-+ (2018).
13. S. Schemmert *et al.*, A Oligomer Elimination Restores Cognition in Transgenic Alzheimer's Mice with Full-blown Pathology. *Mol Neurobiol* **56**, 2211-2223 (2019).
14. T. van Groen *et al.*, The A beta oligomer eliminating D-enantiomeric peptide RD2 improves cognition without changing plaque pathology. *Sci Rep-Uk* **7**, (2017).
15. S. Schemmert *et al.*, Deceleration of the neurodegenerative phenotype in pyroglutamate-A beta accumulating transgenic mice by oral treatment with the A beta oligomer eliminating compound RD2. *Neurobiol Dis* **124**, 36-45 (2019).
16. T. Zhang, J. Loschwitz, B. Strodel, L. Nagel-Steger, D. Willbold, Interference with Amyloid- Nucleation by Transient Ligand Interaction. *Molecules* **24**, (2019).
17. B. Kass *et al.*, Abeta oligomer concentration in mouse and human brain and its drug-induced reduction ex vivo. *Cell Rep Med* **3**, 100630 (2022).
18. A. Elfgen *et al.*, Metabolic resistance of the D-peptide RD2 developed for direct elimination of amyloid-beta oligomers. *Sci Rep-Uk* **9**, (2019).
19. L. H. E. Leithold *et al.*, Pharmacokinetic Properties of a Novel D-Peptide Developed to be Therapeutically Active Against Toxic beta-Amyloid Oligomers. *Pharm Res-Dordr* **33**, 328-336 (2016).
20. M. Johnson, A. T. Coulton, M. A. Geeves, D. P. Mulvihill, Targeted Amino-Terminal Acetylation of Recombinant Proteins in *E. coli*. *Plos One* **5**, (2010).
21. W. Hoyer *et al.*, Dependence of alpha-synuclein aggregate morphology on solution conditions. *J Mol Biol* **322**, 383-393 (2002).
22. R. Barderas, E. Benito-Pena, The 2018 Nobel Prize in Chemistry: phage display of peptides and antibodies. *Anal Bioanal Chem* **411**, (2019).
23. S. A. Funke, D. Willbold, Mirror image phage display-a method to generate D-peptide ligands for use in diagnostic or therapeutical applications. *Mol Biosyst* **5**, 783-786 (2009).
24. K. Wiesehan, D. Willbold, Mirror-image phage display: Aiming at the mirror. *Chembiochem* **4**, 811-815 (2003).
25. K. Santur *et al.*, Ligand-Induced Stabilization of the Native Human Superoxide Dismutase 1. *Acs Chem Neurosci* **12**, 2520-2528 (2021).
26. M. Sevenich *et al.*, Phage Display-Derived Compounds Displace hACE2 from Its Complex with SARS-CoV-2 Spike Protein. *Biomedicines* **10**, (2022).
27. P. E. Kolkwitz, J. Mohrlueder, D. Willbold, Inhibition of Polyglutamine Misfolding with D-Enantiomeric Peptides Identified by Mirror Image Phage Display Selection. *Biomolecules* **12**, (2022).
28. M. Sevenich *et al.*, Phage Display-Derived Compounds Displace hACE2 from Its Complex with SARS-CoV-2 Spike Protein. *Biomedicines* **10**, (2022).
29. P. E. Kolkwitz, J. Mohrlueder, D. Willbold, Inhibition of Polyglutamine Misfolding with D-Enantiomeric Peptides Identified by Mirror Image Phage Display Selection. *Biomolecules* **12**, (2022).
30. A. Krejci, T. R. Hupp, M. Lexa, B. Vojtesek, P. Muller, Hammock: a hidden Markov model-based peptide clustering algorithm to identify protein-interaction consensus motifs in large datasets. *Bioinformatics* **32**, 9-16 (2016).

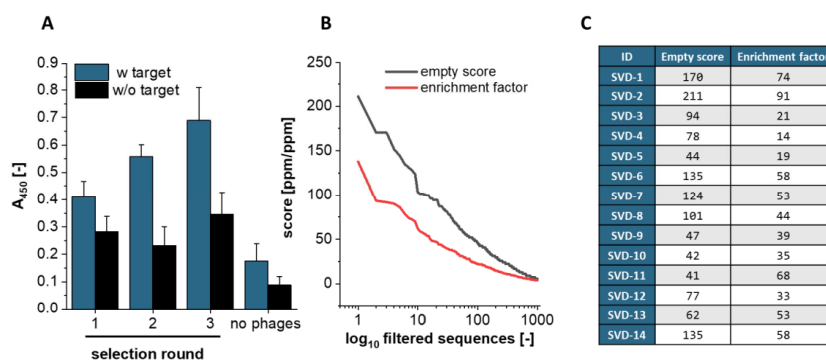
31. L. Nielsen *et al.*, Effect of environmental factors on the kinetics of insulin fibril formation: Elucidation of the molecular mechanism. *Biochemistry-US* **40**, 6036-6046 (2001).
32. T. J. Kaufmann, P. M. Harrison, M. J. E. Richardson, T. J. T. Pinheiro, M. J. Wall, Intracellular soluble alpha-synuclein oligomers reduce pyramidal cell excitability. *J Physiol-London* **594**, 2751-2772 (2016).
33. W. F. Vranken *et al.*, The CCPN data model for NMR spectroscopy: Development of a software pipeline. *Proteins* **59**, 687-696 (2005).
34. M. P. Williamson, Using chemical shift perturbation to characterise ligand binding. *Prog Nucl Mag Res Sp* **73**, 1-16 (2013).
35. A. K. Buell *et al.*, Solution conditions determine the relative importance of nucleation and growth processes in alpha-synuclein aggregation. *P Natl Acad Sci USA* **111**, 7671-7676 (2014).
36. A. L. Woerman *et al.*, Propagation of prions causing synucleinopathies in cultured cells. *Proc Natl Acad Sci U S A* **112**, E4949-4958 (2015).
37. A. L. Woerman *et al.*, alpha-Synuclein: Multiple System Atrophy Prions. *Cold Spring Harb Perspect Med* **8**, (2018).
38. A. L. Woerman *et al.*, Familial Parkinson's point mutation abolishes multiple system atrophy prion replication. *Proc Natl Acad Sci U S A* **115**, 409-414 (2018).
39. A. Aoyagi *et al.*, Abeta and tau prion-like activities decline with longevity in the Alzheimer's disease human brain. *Sci Transl Med* **11**, (2019).
40. B. Brutscher *et al.*, NMR Methods for the Study of Intrinsically Disordered Proteins Structure, Dynamics, and Interactions: General Overview and Practical Guidelines. *Adv Exp Med Biol* **870**, 49-122 (2015).
41. A. Prestel, K. Bugge, L. Staby, R. Hendus-Altenburger, B. B. Kragelund, Characterization of Dynamic IDP Complexes by NMR Spectroscopy. *Methods Enzymol* **611**, 193-226 (2018).
42. E. V. Bocharov *et al.*, All-d-Enantiomeric Peptide D3 Designed for Alzheimer's Disease Treatment Dynamically Interacts with Membrane-Bound Amyloid-beta Precursors. *J Med Chem* **64**, 16464-16479 (2021).
43. S. W. Wu *et al.*, The Dynamic Multisite Interactions between Two Intrinsically Disordered Proteins. *Angew Chem Int Edit* **56**, 7515-7519 (2017).
44. G. M. Clore, Seeing the invisible by paramagnetic and diamagnetic NMR. *Biochem Soc T* **41**, 1343-1354 (2013).
45. G. M. Clore, C. Tang, J. Iwahara, Elucidating transient macromolecular interactions using paramagnetic relaxation enhancement. *Curr Opin Struct Biol* **17**, 603-616 (2007).
46. L. Deshmukh, J. M. Louis, R. Ghirlando, G. M. Clore, Transient HIV-1 Gag-protease interactions revealed by paramagnetic NMR suggest origins of compensatory drug resistance mutations. *Proc Natl Acad Sci U S A* **113**, 12456-12461 (2016).
47. A. Di Savino *et al.*, Efficient Encounter Complex Formation and Electron Transfer to Cytochrome c Peroxidase with an Additional, Distant Electrostatic Binding Site. *Angew Chem Int Ed Engl* **59**, 23239-23243 (2020).
48. J. Iwahara, G. M. Clore, Detecting transient intermediates in macromolecular binding by paramagnetic NMR. *Nature* **440**, 1227-1230 (2006).
49. C. Tang, C. D. Schwieters, G. M. Clore, Open-to-closed transition in apo maltose-binding protein observed by paramagnetic NMR. *Nature* **449**, 1078-U1012 (2007).
50. A. N. Volkov, J. A. R. Worrall, E. Holtzmann, M. Ubbink, Solution structure and dynamics of the complex between cytochrome c and cytochrome c peroxidase determined by paramagnetic NMR. *P Natl Acad Sci USA* **103**, 18945-18950 (2006).

51. S. Nath, J. Meuvlis, J. Hendrix, S. A. Carl, Y. Engelborghs, Early Aggregation Steps in alpha-Synuclein as Measured by FCS and FRET: Evidence for a Contagious Conformational Change. *Biophys J* **98**, 1302-1311 (2010).
52. M. Arai, K. Sugase, H. J. Dyson, P. E. Wright, Conformational propensities of intrinsically disordered proteins influence the mechanism of binding and folding. *P Natl Acad Sci USA* **112**, 9614-9619 (2015).
53. H. J. Dyson, P. E. Wright, NMR illuminates intrinsic disorder. *Curr Opin Struct Biol* **70**, 44-52 (2021).
54. J. Wagner *et al.*, Anle138b: a novel oligomer modulator for disease-modifying therapy of neurodegenerative diseases such as prion and Parkinson's disease. *Acta Neuropathol* **125**, 795-813 (2013).
55. J. Pujols *et al.*, Small molecule inhibits alpha-synuclein aggregation, disrupts amyloid fibrils, and prevents degeneration of dopaminergic neurons. *P Natl Acad Sci USA* **115**, 10481-10486 (2018).
56. A. Binolfi, F. X. Theillet, P. Selenko, Bacterial in-cell NMR of human alpha-synuclein: a disordered monomer by nature? *Biochem Soc T* **40**, 950-U292 (2012).
57. R. Winkler, ESIprot: a universal tool for charge state determination and molecular weight calculation of proteins from electrospray ionization mass spectrometry data. *Rapid Commun Mass Sp* **24**, 285-294 (2010).

## SUPPLEMENTARY INFORMATION

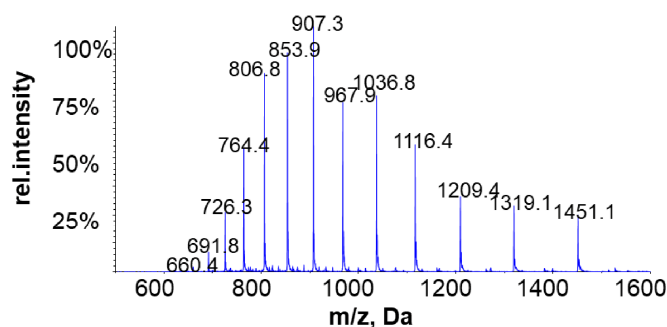


**SI Figure 1: CD-measurement of recombinant L- and synthetic D-enantiomeric full-length  $\alpha$ -syn.** The D-enantiomeric C-terminally biotinylated synthetic  $\alpha$ -syn was used as selection target. Measurements of  $20 \mu\text{g ml}^{-1}$  protein in 50 mM NaPi pH 7.4 were performed as described in the method section.

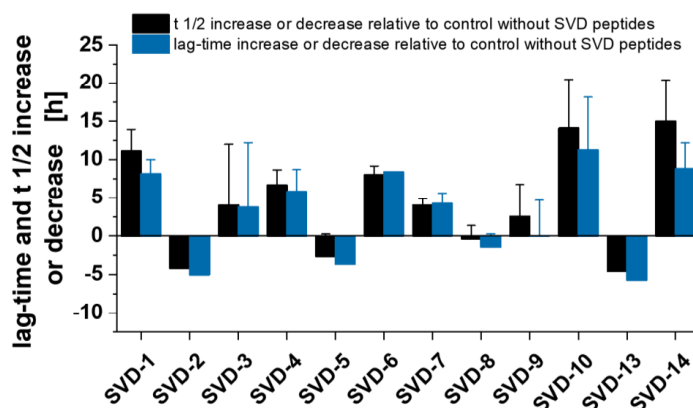


**SI Figure 2: Results of the mirror image phage display selection and NGS analysis.** Mirror-image phage display and NGS analysis was performed as described as follows: The full-length D-enantiomeric  $\alpha$ -syn target protein (SI Fig. 1) was immobilized by directed coupling on a streptavidin derivatized surface via a C-terminal biotin to ensure a homogenous interaction surface during biopanning with the 16-mer M13 phage library. In addition to incubation of the phage library with the target protein (TS = target selection), an identical parallel selection, which lacks the target immobilization (ES = empty selection), was performed. Each purified phage suspension resulting from one TS round was additionally incubated on a surface without target (DC = direct control). Enrichment of target binding phages was verified after three selection rounds by direct detection of the phage coating protein in an ELISA set-up. The purified DNA of the phage suspensions was analyzed by NGS resulting in 0.9 – 1.1 Mio total sequences per sample. Target related sequences were identified after normalization by filtering specifically for those sequences whose number increased during selection rounds (TS3 > TS2 > TS1

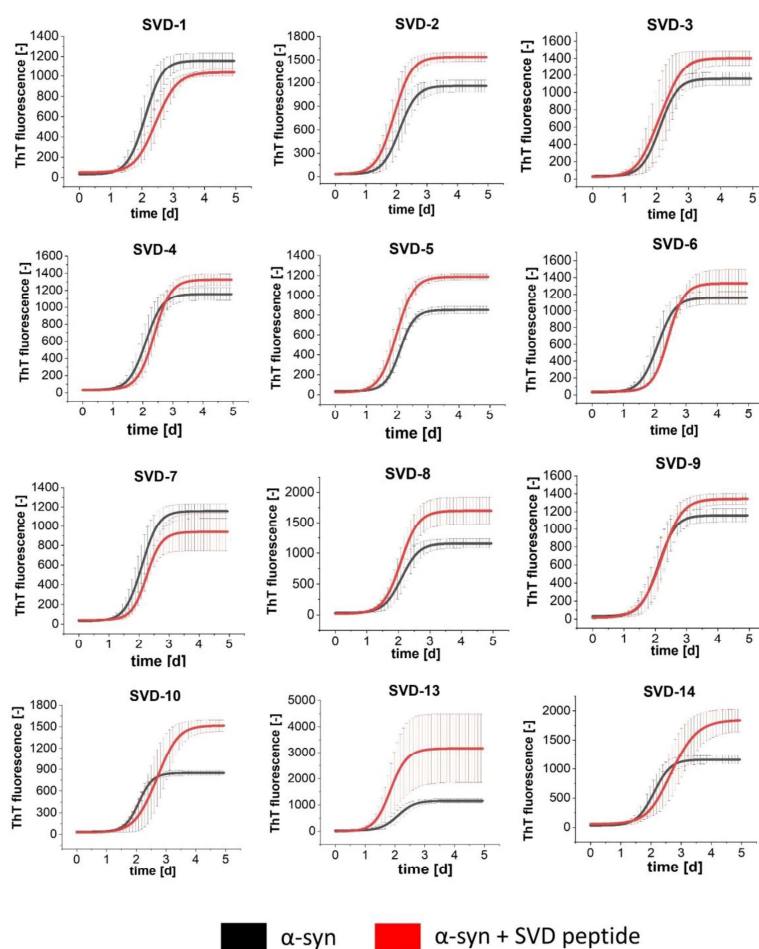
> library) and occurred with a higher frequency in TS than in the corresponding controls that miss the target (TS1 > ES1, TS2 > ES2, TS3 > ES3, TS2 > DC2, TS3 > DC3). Thus, the sequence pool was narrowed down to 140,000 sequence variants with ~ 4,000 showing more than one appearance. The sequences were ranked by a scoring system based on enrichment (enrichment factor = TS3/ library) and target related occurrence (empty score = TS3/ ES3), which allowed the identification of the sequence variants with the highest probability for a target interaction. In addition, clustering of the filtered sequences allowed the identification of motifs and possible cluster extensions. Based on these results, 14 D-enantiomeric synthetic peptides were further analyzed in in vitro experiments. (A) Enrichment ELISA of phage suspensions after amplification.  $2.5 \cdot 10^{11}$  phages were incubated with or without 20 pmol/well immobilized D-enantiomeric full-length  $\alpha$ -syn target protein (n = 3). (B) Scoring values for enrichment (empty score = TS3/ ES3) and target specificity (enrichment factor = TS3/ library) of the filtered sequences resulting from NGS sample analysis. (C) List of sequences that were selected for synthesis based on NGS-scoring, empty score and enrichment factor. These sequences were screened for aggregation delaying effects in ThT-assay as shown in SI Fig. 4.



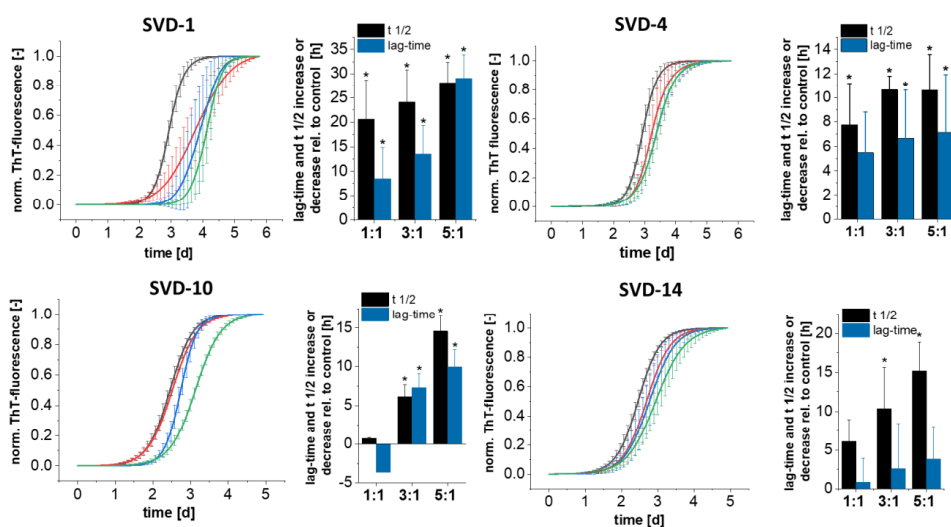
**SI Figure 3: Mass spectrometry spectrum of recombinant  $\alpha$ -syn.** An HPLC-MS method with ESI as an ionization mode with a Triple Quadrupole Qtrap6500 instrument (ABSciex, GE) coupled with an Agilent 1260 HPLC system (Agilent, GE) was used. The reversed-phase column Thermo, Accucore-150-C4 (100\*4.6 mm 2.6  $\mu$ m) was used with the following gradient: the gradient started with 5 % B for 5 min, followed by a 15 min ramp from 5 % to 9 % B followed by a hold of 95 % B for 5 min and a re-equilibration of 10 min with 5 % B. [(A: 0.1 % v/v formic acid in H<sub>2</sub>O), (B: 0.1 % v/v formic acid in ACN)] at 30°C and an injection volume of 10  $\mu$ l. Mass deconvolution was performed with ESIProt (57).



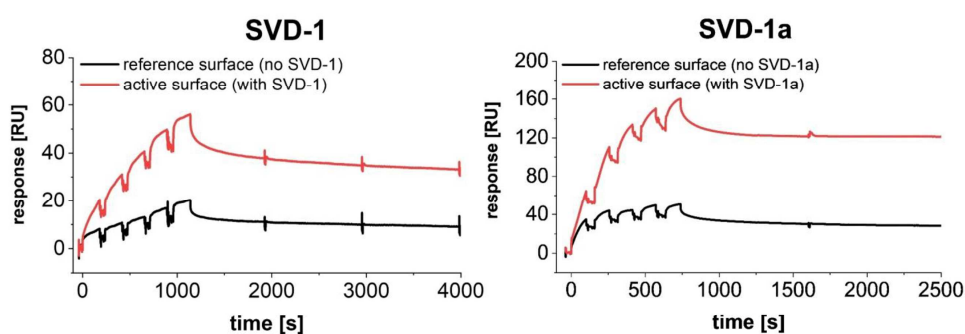
**SI Figure 4: Thioflavin-T assay with  $\alpha$ -syn and D-enantiomeric 16-mer peptides SVD-1 to SVD-14.** Monomeric  $\alpha$ -syn (SI Fig. 3) was incubated with or without a 3-fold molar excess of the D-peptides. Peptides SVD-11 and -12 were found to be insoluble in aqueous buffer and organic solvents and were therefore excluded from further analysis. The ThT positive aggregation was fitted with a symmetric Boltzmann fit and  $t_{1/2}$ - and lag-time were calculated accordingly. Since ThT signal is not always correlating with absolute amyloid mass (since different inhibitors can induce the formation of different fibril polymorphs) we decided not to evaluate the steady state in the early screening phase but rather concentrate on peptide induced  $t_{1/2}$ - and lag-time shifts. 50  $\mu$ M recombinant  $\alpha$ -syn was incubated with or without a three-fold molar excess of the respective D-peptide in PBS pH 7.4 at 37°C. ThT fluorescence progression was measured in a 96-well non-binding half-area with a Fluorostar plate reader at  $\lambda_{ex} = 448$  nm and  $\lambda_{em} = 482$  nm. Samples were shaken at 300 rpm for 30 s per cycle using orbital shaking mode  $t_{1/2}$ - and lag-time increase or decrease were calculated after Boltzmann sigmoidal fitting. The  $t_{1/2}$  is given by the inflection point of the fit and the lag-time was approximated using the formula [lag-time =  $t_{1/2} - 2dx$ ] where dx is defined as the slope of the fit at  $x = t_{1/2}$ .  $t_{1/2}$  and lag-time increase or decrease were determined based on the differences between samples with and without SVD peptide, whereas the 0-value represents the reference control without inhibitor. Mean data are shown with  $\pm$ SD (n = 3). For  $\alpha$ -syn without peptide the following  $t_{1/2}$ - and lag-times were determined:  $t_{1/2}$  50.5 h (PBS) and 50.1 h (PBS + 2.5 % DMSO); lag-time: 38.2 h (PBS) and 38.9 h (PBS + 2.5 % DMSO). Non-normalized aggregation curves are provided in SI Fig. 5. Seven out of twelve D-peptides delayed  $\alpha$ -syn aggregation (SVD- 1, 3, 4, 6, 7, 10, 14), whereas three D-peptides promoted the aggregation onset (SVD 2, -5, -13) and two D-peptides did not show significant impact on the aggregation (SVD 8 and -9). Among the peptides that delayed the aggregation, SVD-1, -4, -6, -10 and -14 showed the strongest inhibitory effects ranging from + 5 to 15 h  $t_{1/2}$ - and lag-time shifts. Next, to verify the concentration dependency of the inhibitory effect,  $\alpha$ -syn was incubated with increasing peptide concentrations, starting with equimolar concentration and continuing with a three-fold and five-fold molar excess, respectively (SI Fig. 6).



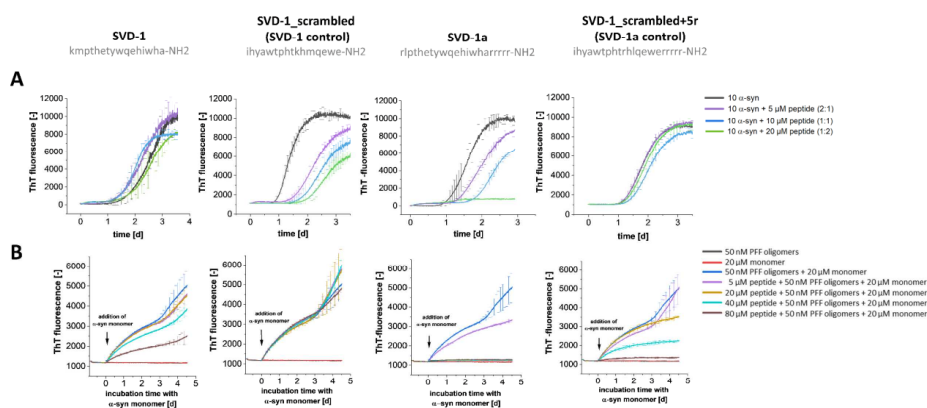
**SI Figure 5: Non-normalized ThT data of *de novo* aggregation assay screen with  $\alpha$ -syn and SVD peptides 1 to 14 as shown in SI Fig. 4.** 50  $\mu$ M recombinant full-length L- $\alpha$ -syn was incubated with or without a three-fold molar excess of the respective D-peptide in PBS pH 7.4 at 37°C. ThT fluorescence progression was measured in a 96-well non-binding half-area with a Fluorostar plate reader at  $\lambda_{\text{exc}} = 448$  nm and  $\lambda_{\text{em}} = 482$  nm. Samples were shaken at 300 rpm for 30 s per cycle using orbital shaking mode  $t_{1/2}$ - and lag-time shifts were calculated after Boltzmann sigmoidal fitting. Mean data are shown with  $\pm$ SD (n = 3). For  $\alpha$ -syn without peptide the following  $t_{1/2}$ - and lag-times were determined:  $t_{1/2}$  50.5 h (PBS) and 50.1 h (PBS + 2.5 % DMSO); lag-time: 38.2 h (PBS) and 38.9 h (PBS + 2.5 % DMSO).



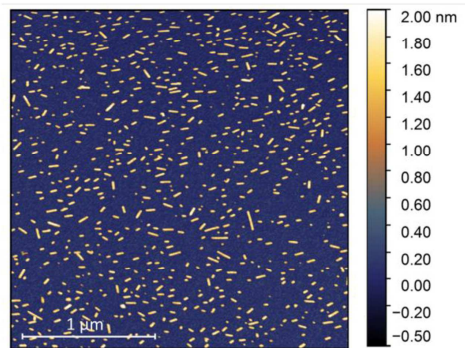
**SI Figure 6: Thioflavin-T assay with  $\alpha$ -syn and D-enantiomeric 16-mer peptides.** 50  $\mu$ M  $\alpha$ -syn was incubated with or without 50, 150 or 250  $\mu$ M D-peptide in PBS pH 7.4 (black: 0  $\mu$ M; red: 50  $\mu$ M; blue: 150  $\mu$ M; green: 250  $\mu$ M). ThT fluorescence progression was measured in a 96-well non-binding half-area plate (Corning, USA) with a Fluorostar platereader (BMG labtech, GE) at  $\lambda_{ex} = 448$  nm and  $\lambda_{em} = 482$  nm. Samples were shaken at 300 rpm for 30 s per cycle using orbital shaking mode. The five replicates of each condition were individually fitted with a Boltzmann fit. The  $t_{1/2}$  is given by the inflection point of the fit and the lag-time was approximated using the formula [lag-time =  $t_{1/2} - 2dx$ ] where  $dx$  is defined as the slope of the fit at  $x = t_{1/2}$ .  $t_{1/2}$  and lag-time increase or decrease were determined based on the differences between samples with and without peptide, whereas the 0-value the reference control without inhibitor. The significance of time-shifts was tested with a two sample Welch's t-test with  $p < 0.05$  (significant: \*). Mean data shown with  $\pm$  SD ( $n = 5$ ). For  $\alpha$ -syn without peptide the following  $t_{1/2}$ - and lag-times were determined: For SVD-1 and SVD-4:  $t_{1/2}$ : 70.4 h and lag-time 58.9 h for SVD-10 and SVD-14:  $t_{1/2}$ : 59.8 h and lag-time 49.4 h. All of the tested D-peptides decelerated  $\alpha$ -syn aggregation, with SVD-1 being most efficient, with a  $t_{1/2}$ -time shift of  $+28 \pm 4.2$  h and a lag-time shift of  $+29 \pm 4.9$  h for a five-fold molar excess. Because of these results, we decided to continue with SVD-1 for further verification of the sequence specificity of the observed effects (Fig. 2).



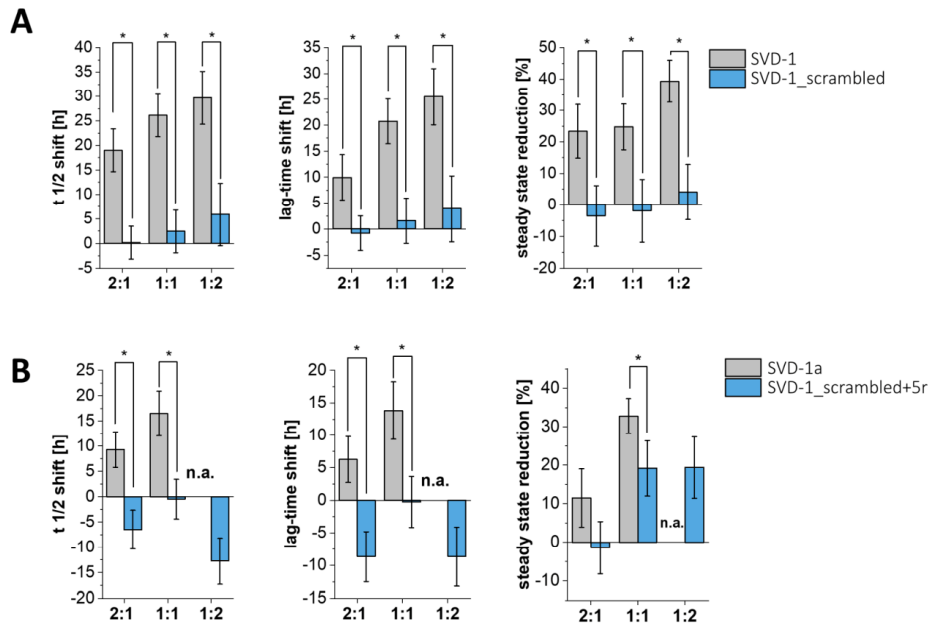
**SI Figure 7: Single cycle injections of  $\alpha$ -syn on active surface with immobilized SVD-1 and SVD-1a and the non-immobilized reference surface.** SVD-1 (left) and SVD-1a (right) were immobilized on a carboxyldextran matrix via amino coupling until saturation was reached (CMD200M, Xantec, GE). Full-length  $\alpha$ -syn was injected for 100 s for each concentration at 30  $\mu$ l/min in PBS 7.4 on the active sensor with immobilized SVD peptide (red) and on the empty reference surface (black). Injections empty reference surface (black). Injections were performed using a serial dilution in the range of 30 to 500 nM and 30 to 150 nM for SVD-1 and SVD-1a, respectively. Referenced data are shown in Fig. 7.



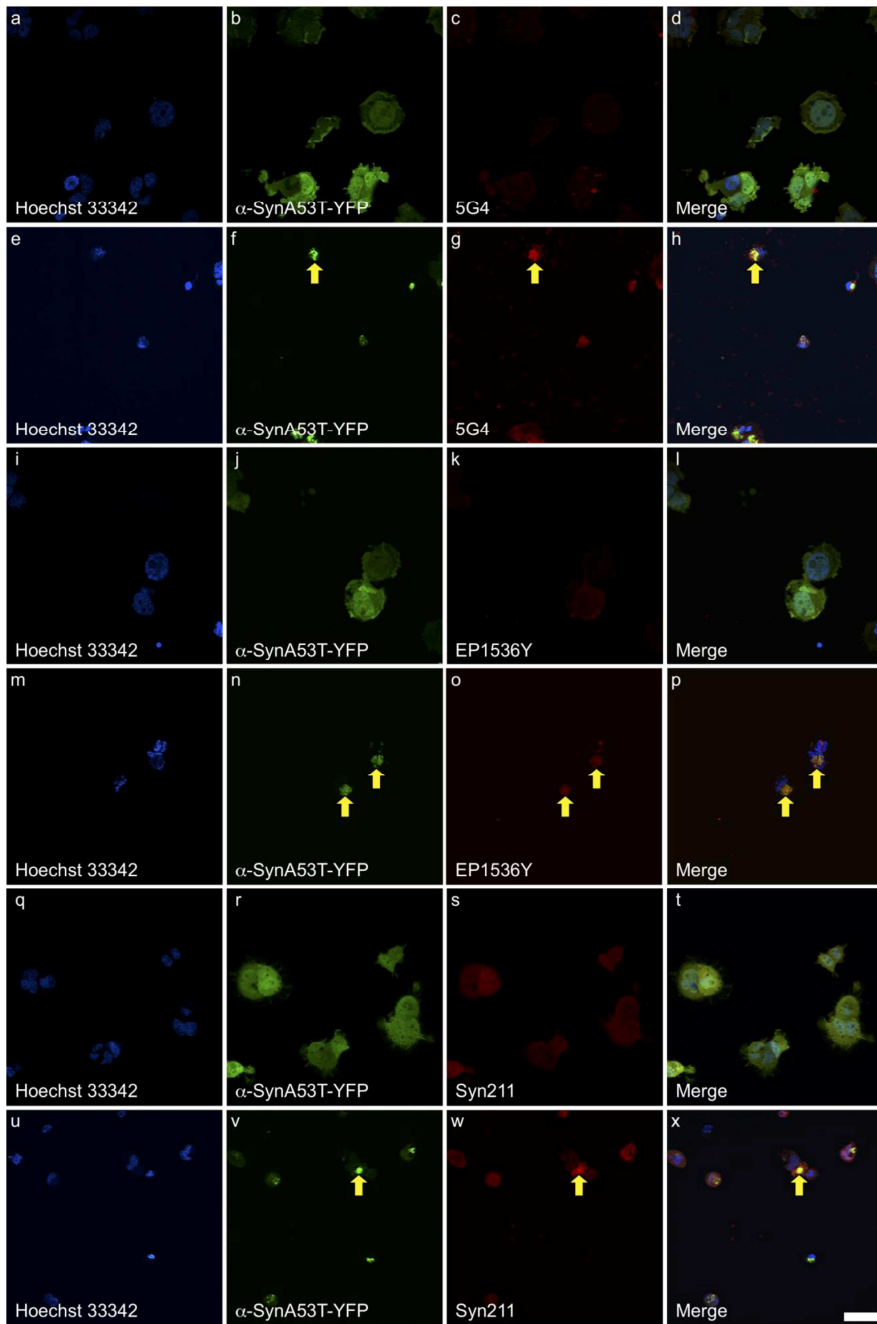
**SI Figure 8: De novo and seeded ThT aggregation with SVD-1 and SVD-1a and the respective randomized control peptides (SVD-1\_scrambled and SVD-1\_scrambled+5r).** ThT fluorescence progression was measured in a 96-well non-binding half-area plate (Corning, USA) with a Fluorostar plater reader (BMG labtech, GE) at  $\lambda_{\text{exc}} = 448$  nm and  $\lambda_{\text{em}} = 482$  nm. D-peptide sequences are shown as single letter amino acid code in grey. (A) *De novo* aggregation assay. 10  $\mu$ M  $\alpha$ -syn monomer was incubated with 5, 10 and 20  $\mu$ M peptide at 37  $^{\circ}$ C, adding one borosilicate glass bead per well ( $d = 3.0$  mm, Hilgenberg, GE) with continuous orbital shaking at 300 rpm in between reads. Mean data shown with  $\pm$  SD ( $n = 5$ ). The statistical evaluation on significance of inhibitory effects is shown in SI Fig. 10. Please note, when comparing the lag-times in this figure with those in SI figures 4 to 6, that shaking conditions were different. (B) Seeded aggregation assay. 50 nM monomer equivalent PFF oligomers as seeds were pre-incubated for 20 h with or without peptide at 37  $^{\circ}$ C under quiescent conditions. Only then, 20  $\mu$ M  $\alpha$ -syn monomer was added for induction of seeding and the incubation time with  $\alpha$ -syn monomers started. Mean data shown with  $\pm$  SD ( $n = 3$ ).



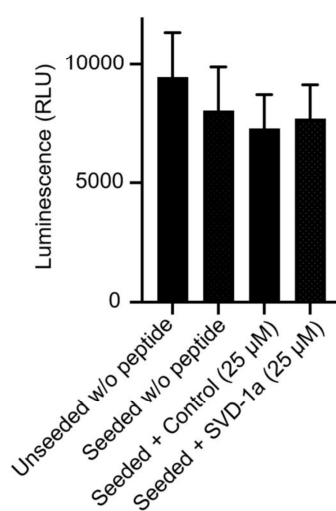
**SI Figure 9: Atomic force microscopy image of  $\alpha$ -syn PFF oligomer seed preparations.** The preparation after ultracentrifugation was diluted to a final concentrations of 5  $\mu$ M monomer equivalent in PBS pH 7.4. 5  $\mu$ l was incubated for 30 min at RT on a freshly cleaved mica, washed three times with distilled water and dried in a gentle stream of  $N_2$ . Measurements were performed in a Nanowizard 3 system (JPK Instruments AG, GE) using intermittent contact mode with  $2.5 \times 2.5 \mu$ m section and line rates of 0.5–1 Hz in ambient conditions with a silicon cantilever with nominal spring constant of 26 newtons/m and average tip radius of 7 nm (Olympus OMCL-AC160TS).



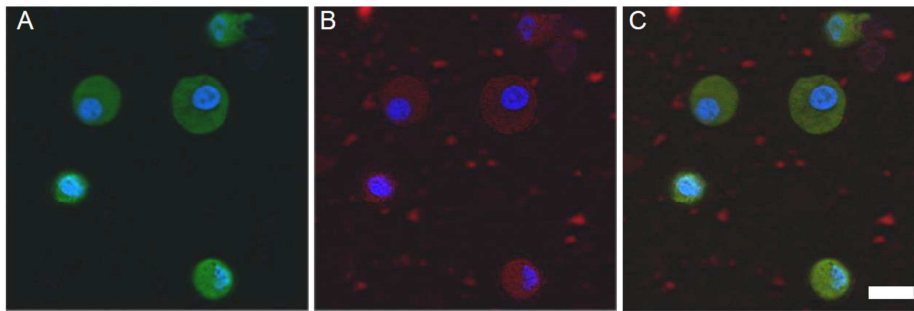
**SI Figure 10: Statistical evaluation of *de novo* aggregation  $t_{1/2}$ -, lag-time shifts as well as steady state reduction for SVD-1 and SVD-1\_scrambled as shown in SI Fig. 9** The five replicates of each condition were individually fitted with a symmetric Boltzmann fit. For each fit,  $x_{1/2}$ , lag-time and steady state response was determined in order to calculate their mean value for each condition. The  $t_{1/2}$  is given by the inflection point of the fit and the lag-time was approximated using the formula  $[\text{lag-time} = t_{1/2} - 2dx]$  where  $dx$  is defined as the slope of the fit at  $x = t_{1/2}$ .  $t_{1/2}$  and lag-time shifts were determined based on the differences between samples with and without peptide, whereas the 0-value represents the reference control without inhibitor. The 2:1 stoichiometric sample of SVD-1a was not fitted due to lacking signal intensity and thus is marked with n.a..  $\alpha$ -Syn untreated control aggregation time: SVD-1:  $t_{1/2}$  32.9 h, lag-time 23.0 h; SVD-1\_scrambled: 43.0 h; lag-time: 31.2 h; SVD-1a:  $t_{1/2}$  38.2 h; lag-time 27.2 h; SVD-1\_scrambled+5r:  $t_{1/2}$  60.8 h; lag-time: 44.5 h. The significance of time-shifts between sample and the same concentration of the according control peptide was tested with a two sample Welch's t-test with  $p < 0.05$  (significant: \*). Mean data shown with  $\pm$  SD ( $n = 5$ ).



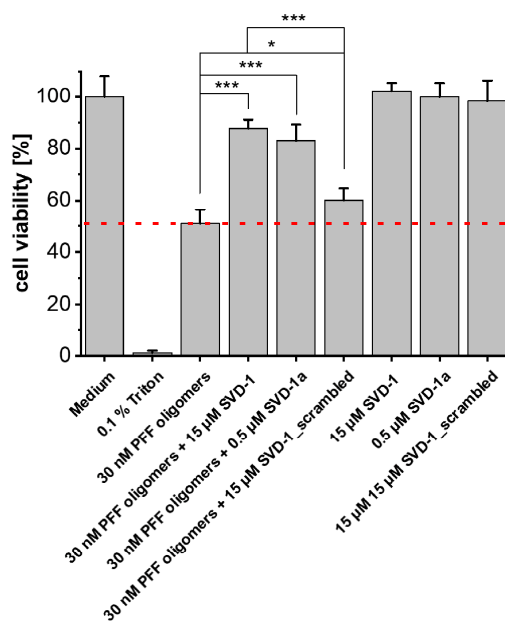
**SI Figure 11: Immunofluorescence staining of  $\alpha$ -syn aggregates in  $\alpha$ -synA53T-YFP cells.** After culturing unseeded cells (a–d, i–l, and q–t) and cells seeded with  $\alpha$ -syn PFF oligomers (e–h, m–p, and u–x) for 3 days, cells were fixed, permeabilized, and stained with fluorescently labeled antibodies (red). For detecting oligomeric and fibrillar  $\alpha$ -syn, we used the anti-aggregated  $\alpha$ -syn antibody, clone 5G4 (c, d, g, h). For detecting  $\alpha$ -syn phosphorylated at serine 129, which accumulates when  $\alpha$ -syn aggregates and forms deposits, we used the recombinant anti- $\alpha$ -syn (phospho S129) antibody EP1536Y (k, l, o, p). For detecting total  $\alpha$ -syn, we used the anti- $\alpha$ -syn antibody syn211 (s, t, w, x). Nuclei were stained with Hoechst 33342.  $\alpha$ -synA53T-YFP fluorescence is shown in green. Panels on the right represent merged images (d, h, l, p, t, x). While  $\alpha$ -synA53T-YFP fluorescence is diffusely distributed in unseeded cells, it forms foci in cells seeded with  $\alpha$ -syn PFF oligomers, indicative of  $\alpha$ -syn aggregation. Yellow arrows indicate aggregated  $\alpha$ -syn (yellow), a colocalization of antibody staining for  $\alpha$ -syn (red) and fluorescence of aggregated  $\alpha$ -synA53T-YFP (green). The scale bar indicates 100  $\mu$ m.



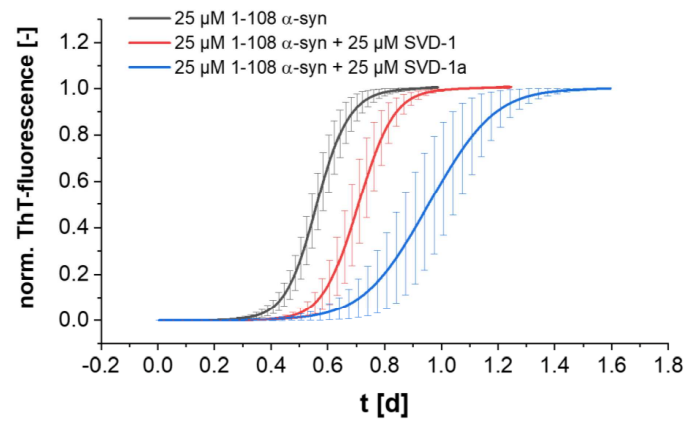
**SI Figure 12: The transfection of PFF oligomers and SVD-1a does not significantly reduce HEK293 cell viability.** CellTiter-Glo Luminescent Cell Viability Assay (Promega GmbH, GE) was used to determine the number of viable cells in culture based on quantitation of the ATP present, an indicator of metabolically active cells. After culturing cells in 384-well plates for three days, 35  $\mu$ l of medium was removed from the wells and 40  $\mu$ l of CellTiter-Glo Reagent directly added to each well. After mixing, luminescence was measured 10 min later using a Fluostar (BMG labtech, GE). The luminescence of seeded  $\alpha$ SynA53T-YFP cells was slightly lower than that of unseeded cells, however, the difference was not significant. Also, treatment with a negative-control peptide or with SVD-1a did not induce significantly different luminescence in comparison to unseeded cells or seeded cells without peptide treatment. Significance was calculated using one-way ANOVA followed by Dunnett's multiple comparisons test with  $p < 0.05$ .



**SI Figure 13: Fluorescently labeled SVD-1aCys\_Alexa647 is taken up in  $\alpha$ -synA53T-YFP cells.** Unseeded  $\alpha$ -synA53T-YFP cells were supplemented with 5  $\mu$ M of SVD-1aCys\_Alexa647 in the cell culture medium for 24 h. Confocal images of the cells show a diffuse green signal for cytoplasmic  $\alpha$ -synA53T-YFP (A), and a diffuse red signal for SVD-1aCys\_Alexa647 that was labeled with a red fluorescent dye and taken up by the cells (B). Nuclei were stained with Hoechst 33342 in blue. The last panel represents a merged image (C). The scale bar indicates 20  $\mu$ m. Because the red fluorophore signal was homogeneously distributed in the cytosol of the cells, we assume that the peptide is able to enter the cells even without transfection.



**SI Figure 14: SVD-1 and SVD-1a increase cell viability in MTT assay with PFF oligomers seeds.** SVD-1, SVD-1a SVD-1\_scrambled were incubated over night at 37 °C and 300 rpm with or without 30 nM PFF oligomers and subsequently incubated with PC12 cells in final concentrations of 15 μM (SVD-1 and SVD-1\_scrambled) or 0.5 μM (SVD-1a). While the cell viability was reduced with 30 nM PFF oligomers alone to 50 %, 89 and 82 % of cells were rescued in the presence of SVD-1 and SVD-1a, respectively. Slight increase of cell viability saving effect was also detected for 15 μM of the control peptide SVD-1\_scrambled. Test on significance was performed using one-way ANOVA with Bonferroni post hoc analysis: \*  $p \leq 0.5$ , \*\*\*  $p \leq 0.01$ . Mean data are shown with  $\pm$ SD (n = 4). While the cell viability was reduced by 50 % in the presence of 30 nM soluble  $\alpha$ -syn PFF oligomers alone, no toxic effect of the compounds on PC12 was observed. However, when the seeds were pre-incubated with SVD-1 or SVD-1a, the cell viability increased to 89 and 82 % using 15 μM or 0.5 μM compound concentrations, respectively. Thus, similar cell viability saving effects were found for SVD-1a using a 30-fold lower concentration. For the concentration of 15 μM SVD 1\_scrambled, only a slight cell viability saving effect was found which was significantly lower than the cell saving effect identified for the same concentration of SVD-1. This result shows that the efficacy of the compounds on the soluble  $\alpha$ -syn PFF is not only limited to a seeding capacity reduction, but additionally, the compounds also reduce the toxicity of the seeds in the cellular environment.



**SI Figure 15: SVD-1 and SVD-1a inhibit the aggregation of 1-108 truncated  $\alpha$ -syn.** 25  $\mu$ M monomeric 1-108  $\alpha$  syn was incubated with or without equimolar concentrations of SVD-1 and SVD-1a as described in the method section for *de novo* ThT-aggregation screening set-up. Aggregation curves were fitted with a symmetric Boltzmann fit and the steady state signal was normalized to 1. SVD-1 as well as SVD-1a show delay of 1-108 truncated  $\alpha$ -syn aggregation.

## **2.2 A so-far overlooked secondary conformation state in the binding mode of SARS-CoV-2 spike protein to human ACE2 and its conversion rate is crucial for estimating infectivity efficacy of the underlying virus variant**

Authors: **Marc Sevenich**, Ian Gering, Joop van den Heuvel, Jeannine Mohrlüder and Dieter Willbold.

Journal: Journal of Virology

DOI: <https://doi.org/10.1128/jvi.00685-22>

Impact Factor: 5.103 (2022)

Contribution: Project outline, planning and performance of SPR measurements, planning and performance of HPLC-SEC measurements, writing of original draft.



# A So-Far Overlooked Secondary Conformation State in the Binding Mode of SARS-CoV-2 Spike Protein to Human ACE2 and Its Conversion Rate Are Crucial for Estimating Infectivity Efficacy of the Underlying Virus Variant

Marc Sevenich,<sup>a,d</sup> Joop van den Heuvel,<sup>b</sup> Ian Gering,<sup>a</sup> Jeannine Mohrlüder,<sup>a</sup>  Dieter Willbold<sup>a,c,e</sup>

<sup>a</sup>Institute of Biological Information Processing (IBI-7), Forschungszentrum Jülich, Jülich, Germany

<sup>b</sup>Helmholtz Centre for Infection Research, Braunschweig, Germany

<sup>c</sup>Institut für Physikalische Biologie, Heinrich-Heine-Universität Düsseldorf, Düsseldorf, Germany

<sup>d</sup>Priavoid GmbH, Jülich, Germany

<sup>e</sup>JuStruct, Forschungszentrum Jülich, Jülich, Germany

**ABSTRACT** Since its outbreak in 2019, severe acute respiratory syndrome coronavirus 2 (SARS-CoV-2) has spread with high transmission efficiency across the world, putting health care as well as economic systems under pressure. During the course of the pandemic, the originally identified SARS-CoV-2 variant has been multiple times replaced by various mutant versions, which showed enhanced fitness due to increased infection and transmission rates. In order to find an explanation for why SARS-CoV-2 and its emerging mutated versions showed enhanced transmission efficiency compared with SARS-CoV (2002), an enhanced binding affinity of the spike protein to human angiotensin converting enzyme 2 (hACE2) has been proposed by crystal structure analysis and was identified in cell culture models. Kinetic analysis of the interaction of various spike protein constructs with hACE2 was considered to be best described by a Langmuir-based 1:1 stoichiometric interaction. However, we demonstrate in this report that the SARS-CoV-2 spike protein interaction with hACE2 is best described by a two-step interaction, which is defined by an initial binding event followed by a slower secondary rate transition that enhances the stability of the complex by a factor of  $\sim 190$  (primary versus secondary state) with an overall equilibrium dissociation constant ( $K_D$ ) of 0.20 nM. In addition, we show that the secondary rate transition is not only present in SARS-CoV-2 wild type ("wt"; Wuhan strain) but also found in the B.1.1.7 variant, where its transition rate is 5-fold increased.

**IMPORTANCE** The current SARS-CoV-2 pandemic is characterized by the high infectivity of SARS-CoV-2 and its derived variants of concern (VOCs). It has been widely assumed that the reason for its increased cell entry compared with SARS-CoV (2002) is due to alterations in the viral spike protein, where single amino acid residue substitutions can increase affinity for hACE2. So far, the interaction of a single unit of the CoV-2 spike protein has been described using the 1:1 Langmuir interaction kinetic. However, we demonstrate here that there is a secondary state binding step that may be essential for novel VOCs in order to further increase their infectivity. These findings are important for quantitatively understanding the infection process of SARS-CoV-2 and characterization of emerging SARS-CoV-2 variants of spike proteins. Thus, they provide a tool for predicting the potential infectivity of the respective viral variants based on secondary rate transition and secondary complex stability.

**KEYWORDS** SARS-CoV-2, human angiotensin converting enzyme 2, protein kinetics, spike protein, surface plasmon resonance, variants of concern

**Editor** Tom Gallagher, Loyola University Chicago

**Copyright** © 2022 Sevenich et al. This is an open-access article distributed under the terms of the [Creative Commons Attribution 4.0 International license](https://creativecommons.org/licenses/by/4.0/).

Address correspondence to Dieter Willbold, D.Willbold@fz-juelich.de.

The authors declare no conflict of interest.

**Received** 2 May 2022

**Accepted** 14 May 2022

Severe acute respiratory syndrome coronavirus 2 (SARS-CoV-2) is a beta class coronavirus that was first discovered and characterized in Wuhan, China, at the end of 2019 (1, 2). Since then, it has challenged health care systems due to its rapid spread and COVID-19 transmission throughout the world. Far more than the past coronavirus pandemic, caused by SARS-CoV in 2002, the ongoing pandemic has claimed over 6.2 million lives with over 504 million total cases so far (3–5).

The SARS-CoV-2 coronavirus replication depends on a multistep process starting with the interaction of the viral trimeric spike (S) protein and human angiotensin converting enzyme 2 (hACE2) that mediates the uptake of the viral RNA into the host-cell cytoplasm. Each monomer of the S protein consists of the two functional subunits S1 and S2. The S1 subunit comprises the receptor binding domain (RBD) that interacts via a defined motif sequence (RBM) with an N-terminally located helical structure of the hACE2. The S2 subunit, however, plays a crucial role in the membrane fusion process. While the S1-hACE2 interaction allows viral attachment to the host cell surface, the S2-site is cleaved by the human endoprotease TMPRSS2. This leads to irreversible conformational changes of the S protein that result in cell membrane fusion and viral uptake by the host cell (6). Although the viral S proteins of SARS-CoV (2002) and SARS-CoV-2 (wt; Wuhan strain) share ~76% amino acid sequence identity, SARS-CoV-2 shows an enhanced cell infectivity and human-to-human transmission efficiency compared with SARS-CoV (7, 8). Since its first appearance in 2019, the virus has undergone numerous mutational events, resulting in variants with enhanced fitness concerning their transmissibility (9, 10). A large proportion of these mutations cluster in the spike protein, where one-third of the sequence has been associated with diverse alterations (11). To date, the most widespread variants B.1.1.7 ( $\alpha$ -variant), B.1.617.2 ( $\delta$ -variant), P.1 ( $\gamma$ -variant), and B.1.1.529 ( $\omicron$ -variant) have widely replaced the originally identified SARS-CoV-2 virus due to their enhanced fitness (10, 12–17).

In order to understand why certain variants increase infectivity, the process of virus contact with the cell surface and cell uptake has been drawn into the center of attention. Although a more efficient fusion process will also impact the infectiousness of the virus (18), the interaction of the spike protein with hACE2 will provide the initial contact and therefore limit the time frame for subsequent processes. To date, the kinetics of the SARS-CoV spike-hACE2 interaction have been defined widely as a one-step binding process with a monoexponential decay using a Langmuir-based 1:1 fitting model for surface plasmon resonance or biolayer interferometry experiments (6, 19–23). However, this model fails to describe the complexity of the interaction, which becomes very apparent when looking at the heterogeneity of the complex decay.

Here, we report that the interaction of the isolated monomeric SARS-CoV-2 ectodomain with hACE2 has a two-state binding mode. The additional secondary conformational transition increases the overall stability of the prefusional state dramatically and therefore potentially enlarges the time frame for the initiation of membrane fusion and viral cell entry. In addition, we characterized the secondary interaction state in the trimeric SARS-CoV-2 B.1.1.7 ( $\alpha$ -variant) spike protein, where the conversion rate to the secondary conformational state is increased dramatically compared with the SARS-CoV-2 wild type. This observation gives insights into how the infectivity among SARS-CoV-2 mutants is modified and represents a precise and fast analysis method to predict the infectivity of novel SARS-CoV-2 variants with mutated spike protein sequences.

## RESULTS AND DISCUSSION

**The Langmuir 1:1 binding model is not sufficient to fit experimental data for spike protein binding to hACE2.** For characterization of the S1-S2 spike protein interaction with the hACE2 receptor, two different kinetic methods were applied. First, for biolayer interferometry, hACE2 was immobilized via a C-terminal biotin on a streptavidin-coated sensor surface. Incubation with a serial dilution of the S1-S2 spike protein yielded the sensograms shown in Fig. 1A. To obtain apparently good-looking fits based on a Langmuir 1:1 model, the dissociation time needed to be shortened significantly (Fig. 1B). Such incomplete fitting allowed the determination of an equilibrium

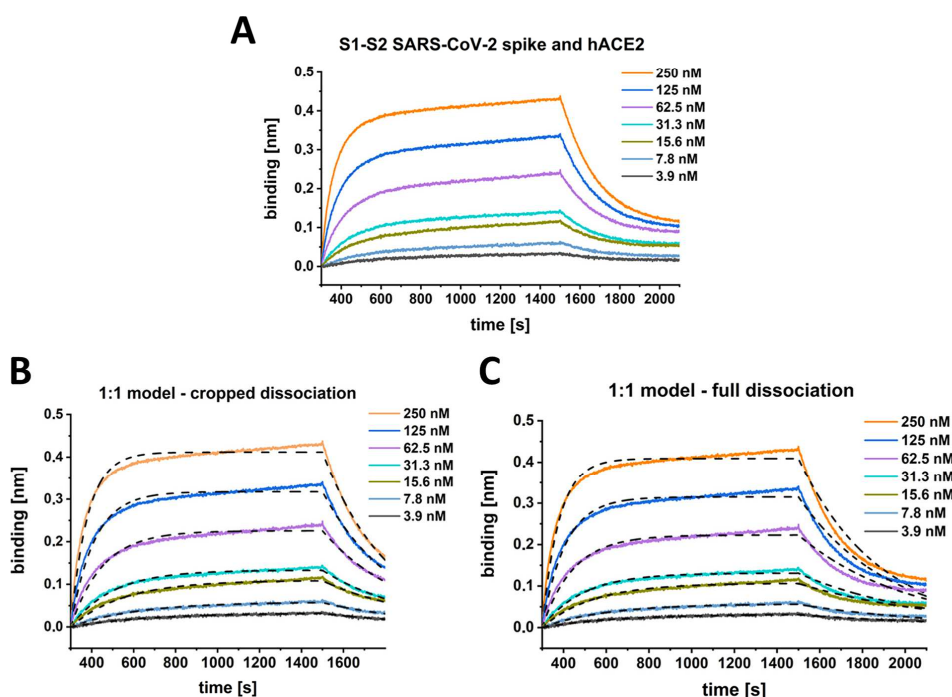


**FIG 1** BLI kinetic experiment with SARS-CoV-2 S1-S2 and hACE2. The sensogram (A) was globally fitted with a 1:1 interaction model (B and C, black dashed lines) either with a cropped dissociation time of 200 s (B) or the full dissociation time of 600 s (C). (B)  $K_D$ , 22 nM;  $k_{on}$ ,  $1.1 \times 10^5 \pm 7.5 \times 10^4$  [1/Ms];  $k_{off}$ ,  $2.4 \times 10^{-3} \pm 4.7 \times 10^{-3}$  [1/s],  $R^2$ , 0.98. (C)  $K_D$ , 11 nM;  $k_{on}$ ,  $1.7 \times 10^5 \pm 1.5 \times 10^5$  [1/Ms],  $k_{off}$ ,  $1.9 \times 10^{-3} \pm 4.7 \times 10^{-3}$  [1/s],  $R^2$ , 0.96.

dissociation constant ( $K_D$ ) and kinetic rates similar to those that have been published previously (6, 19, 22, 23). The model fails, however, to describe the dissociation phase of the interaction, which cannot be fitted satisfactorily by a monoexponential decay (Fig. 1 C).

This conclusion is confirmed by surface plasmon resonance (SPR) experiments. hACE2 was coupled via an IgG1 fc-tag on a protein A/G derivatized surface, and various concentrations of the S1-S2 spike protein were applied as analytes (Fig. 2A). Apparently satisfying fits based on a Langmuir 1:1 model are obtained only when the dissociation time is only a few hundred seconds (Fig. 2B). The inclusion of longer dissociation times into the analysis, however, clearly shows that the interaction of the viral S1-S2 spike protein and the hACE2 is not of a 1:1 Langmuir binding model (Fig. 2C).

**S1-S2 spike protein hACE2 interaction induces a time-dependent secondary state.** Because the interaction of hACE2 and S1-S2 spike protein is not matching a 1:1 Langmuir binding model, we checked for the existence of a potentially underlying second rate processes by SPR (Fig. 3A) (24, 25) and verified the monomeric status of S1-S2 and the dimeric status of hACE2 by size exclusion chromatography–high-pressure liquid chromatography (SEC-HPLC).

For a test on the secondary state by SPR (Fig. 3A), hACE2 was coupled at a constant immobilization level of 25 resonance units (RU). The S1-S2 spike protein was injected at a concentration of 500 nM. Contact times were increased gradually by increasing the injection times ranging from 150 to 600 s. For each injection, steady state was reached within a short time interval so that a constant complex concentration can be assumed during the different contact times.

The resulting plot reveals a strong dependency of incubation time and dissociation

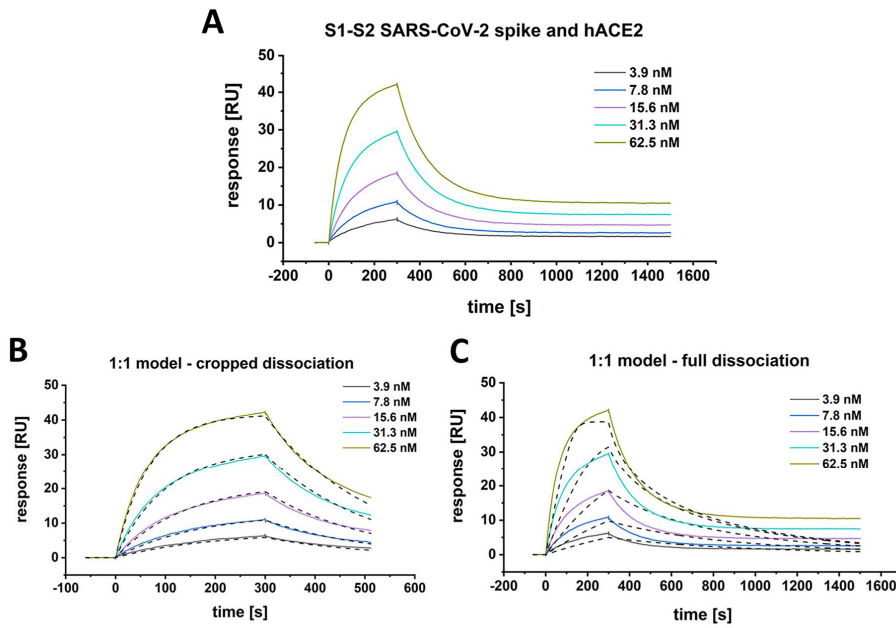


**FIG 2** SPR-multicycle kinetic experiment of SARS-CoV-2 S1-S2 and hACE2. The sensogram (A) was globally fitted with a Langmuir 1:1 interaction model (B and C, black dashed lines) either with a cropped dissociation time of 200 s (B) or the full (C) dissociation time of 1,200 s. (B)  $K_{Dp}$  28.5 nM;  $k_{off}$   $1.7 \text{ E} + 5 \pm 5.4 \text{ E} + 2$  [1/Ms];  $k_{on}$   $4.7 \text{ E}-3 \pm 1.0 \text{ E}-5$  [1/s].  $\text{Chi}^2$ , 0.28 [RU<sup>2</sup>]. (C)  $K_{Dp}$  12.2 nM;  $k_{off}$   $5.4 \text{ E} + 7 \pm 2.2 \text{ E} + 6$  [1/Ms];  $k_{on}$   $0.7 \pm 0.03$  [1/s].  $\text{Chi}^2$ , 6.6 [RU<sup>2</sup>].

rate (Fig. 3). Increasing injection times and thus increasing contact time correlate with decreasing dissociation rates. This finding cannot be expected for a single-step 1:1 interaction but clearly indicates the formation of a secondary complex state, whose proportion increases with contact time duration. This is typical for a two-step binding mode, in which the formation of the primary complex induces a conformational reorganization into a secondary complex conformation that strengthens the interaction and leads to a very low dissociation rate.

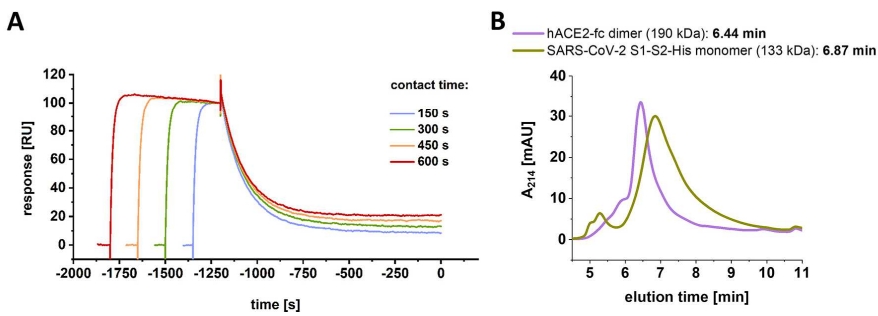


**FIG 3** SPR experiment testing for the presence of a two-state reaction. (A) A total of 500 nM SARS-CoV-2 S1-S2 spike protein was injected over a constant immobilization level of 25 RU hACE2. Injection times were gradually increased (150 to 600 s). Dissociation start point was aligned on the time scale. (B) SEC-HPLC using 5- $\mu$ g/mL injections of SARS-CoV-2 S1-S2 monomer and hACE2 dimer. Column calibration was performed using protein standards of thyroglobulin (660 kDa, 5.78 min),  $\gamma$ -globulin (150 kDa, 7.52 min), ovalbumin (45 kDa, 8.52 min), and aprotinin (6.5 kDa, 11.12 min).

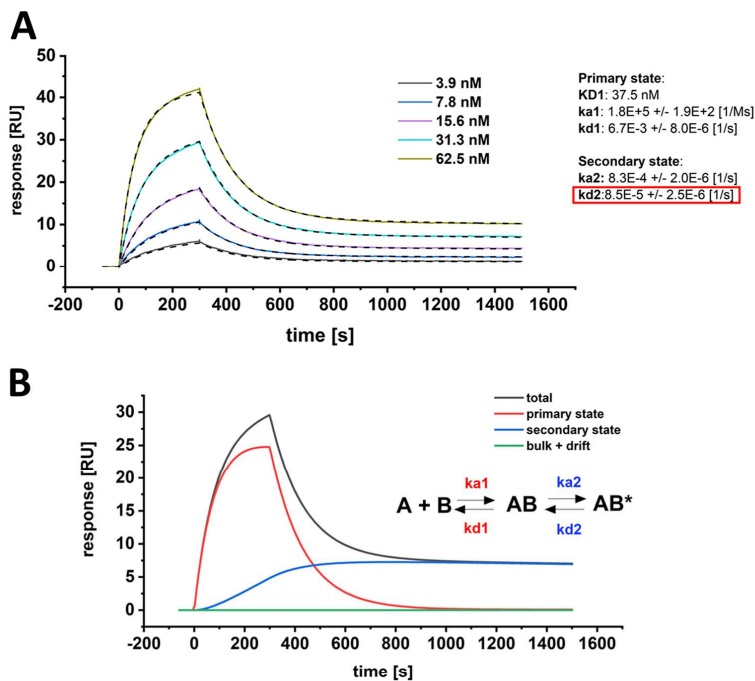


**FIG 4** SPR multicycle kinetic experiment of SARS-CoV-2 S1-S2 and hACE2. (A) The sensogram was globally fitted with a two-state kinetic model, including the full dissociation time of 1,200 s. Kinetic parameters for the first interaction were determined with  $K_{D1}$  of 37.5 nM,  $k_{a1}$  of  $1.8E+5 \pm 1.9E+2$  [1/Ms] and  $k_{d1}$  of  $6.6E-3 \pm 8.0E-6$  [1/s]. Kinetic parameters for the second interaction were determined with  $k_{a2}$  of  $8.3E-4 \pm 2.0E-6$  [1/s] and  $k_{d2}$  of  $8.5E-5 \pm 2.5E-6$  [1/s].  $\chi^2$ , 0.08 [RU<sup>2</sup>]. The overall  $K_{D-total}$  for both events was identified with 0.2 nM. The dissociation rate of the secondary state contributes significantly to the increase in overall affinity (red box). (B) Component analysis of the 31.3 nM S1-S2 spike protein binding curve as shown in A. The sensogram (total) is composed of the primary binding event (red), followed by a secondary transition event (blue) which results in a highly stable secondary complex (AB\*).

**Secondary complex state of the S1-S2 spike protein with hACE2 results in enhanced complex stability.** In order to define the secondary rate kinetics of complex transition after primary binding, the interaction of the S1-S2 spike protein and hACE2 was fitted with a secondary state model. In contrast to the previously presented attempts of the Langmuir model fitting (Fig. 1 and 2), the two-step kinetic model allows the description of the interaction with high accuracy over the complete dissociation time (Fig. 4A).

The kinetic rates of the primary binding event were identified with  $k_{a1}$  of  $1.8 \times 10^{-5} M^{-1} s^{-1}$  ( $k_a$  = association rate or on-rate) and  $k_{d1}$  of  $6.7 \times 10^{-3} s^{-1}$  ( $k_d$  = dissociation rate or off-rate) resulting in a dissociation constant ( $K_D$ ) of 37.5 nM. This result matches with previously reported kinetic values for the RBD interaction with hACE2 (6, 19, 22, 23). As soon as the first complex is formed, a secondary event increases the complex stability (Fig. 4B). This transition is most likely a structural rearrangement that decreases the complex dynamics as proposed previously (16). The kinetic data show that this secondary process is with an on-rate of  $8.3 \times 10^{-4} s^{-1}$  rather slow compared to the primary binding event but at the same time increases the complex half-life by a factor of  $\sim 80$  with an off-rate of  $8.5 \times 10^{-5} s^{-1}$ . When the kinetic values of the primary and secondary events are combined to one binding constant, the full binding process yields a total affinity that is described with  $K_{D-total}$  of 0.20 nM.

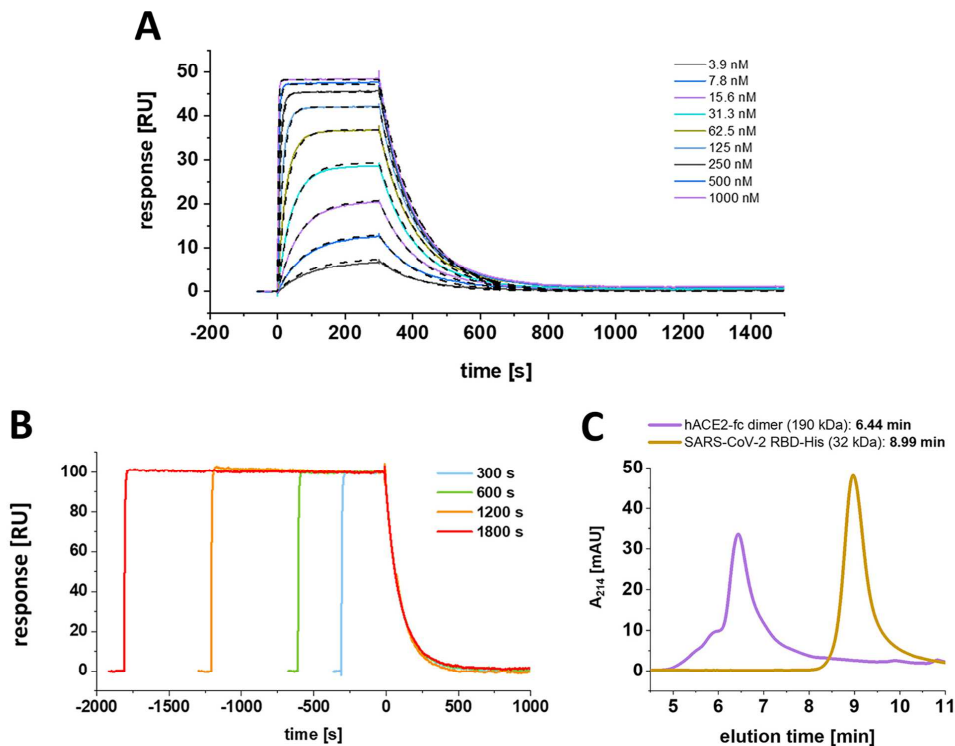


**FIG 5** The SARS-CoV-2 RBD interaction with hACE2 follows a Langmuir-based kinetic with time-independent monoexponential decay. (A) Multicycle experiment with SARS-CoV-2 RBD. hACE2-fc was immobilized on a protein A/G sensor chip, and SARS-CoV-2 RBD was injected in a concentration range of 3.9 to 1,000 nM. The  $K_D$  was globally fitted with a 1:1 Langmuir-based interaction model. The kinetic parameters were determined with a  $K_D$  of 21.3 nM,  $k_a$  of  $4.3 \text{ E} + 5 \pm 2.2 \text{ E} + 2$  [1/Ms], and  $k_d$  of  $9.1 \text{ E}-3 \pm 4.2 \text{ E}-6$  [1/s].  $\chi^2$ , 0.05 [RU<sup>2</sup>] (B) Test on secondary state reaction. hACE2 was immobilized on a protein A sensor surface, and 500 nM SARS-CoV-2 was injected at a constant concentration for increasing contact intervals. Dissociation starting point was aligned on the time scale. (C) SEC-HPLC using 5- $\mu\text{g}/\text{mL}$  injections of SARS-CoV-2 RBD and hACE2 dimer. Column calibration was performed using protein standards of thyroglobulin (660 kDa, 5.78 min),  $\gamma$ -globulin (150 kDa, 7.52 min), ovalbumin (45 kDa, 8.52 min), and aprotinin (6.5 kDa, 11.12 min).

**The SARS-CoV-2 RBD interaction with hACE2 follows a Langmuir interaction kinetic.** To verify whether the secondary transition can be obtained exclusively for the S1-S2 monomeric construct or might be associated with certain proportions of the spike protein, a SARS-CoV-2 RBD construct was assayed for the existence of an underlying secondary rate kinetic (Fig. 5A and B).

After confirmation of its monomeric status (Fig. 5C), SARS-CoV-2 RBD was analyzed in a multicycle kinetic experiment on the immobilized hACE2, where the dissociation phase showed a clear monoexponential behavior with complete baseline dissociation, which is in full agreement with a Langmuir-based 1:1 interaction model (Fig. 5A). This finding appears to be in contrast with the previously identified biphasic dissociation for the S1-S2 SARS-CoV-2 construct. Additionally, the RBD did not show a contact time-dependent alteration of the dissociation phase, when increasing contact times are applied (Fig. 5B). However, the dissociation constant as well as the on- and off-rate of the RBD and the primary binding event of the monomeric S1-S2 show high similarity. This finding implies that the primary binding event of the two-state interaction is carried out by the interaction of the RBD and hACE2 alone, whereas the context of the full S1-S2 protein is essential for the formation of the secondary complex.

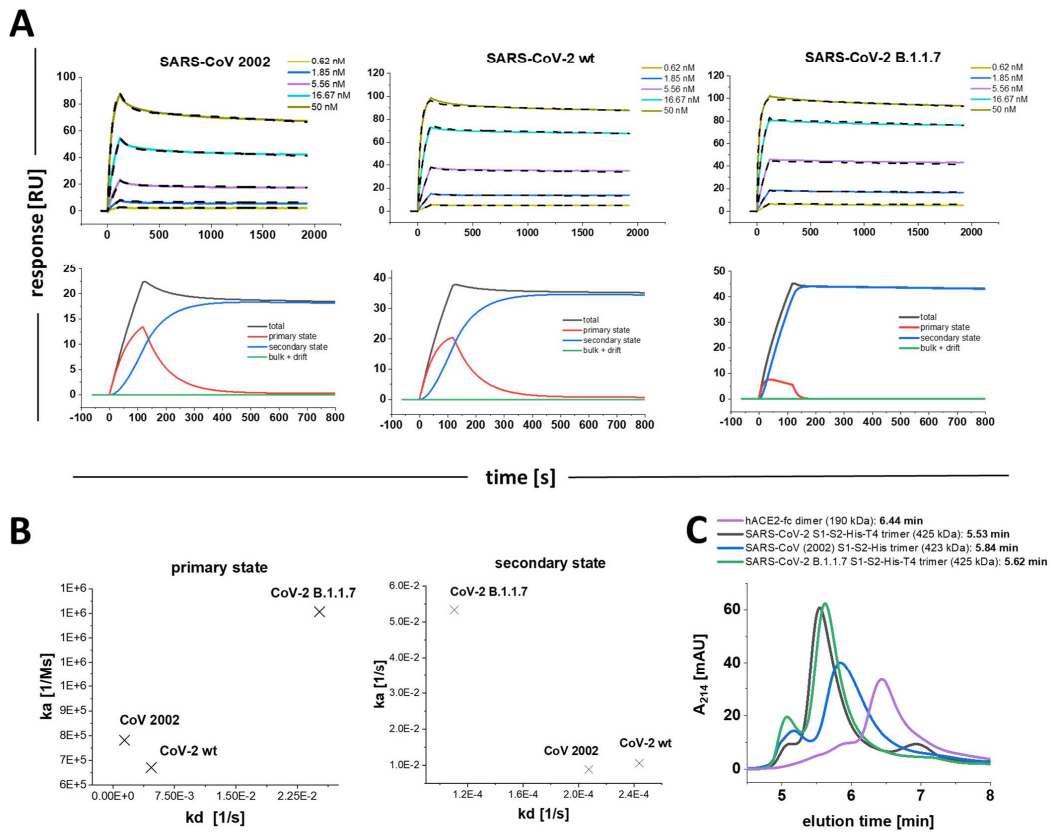


**FIG 6** Multicycle SPR experiments with SARS-CoV (2002), SARS-CoV-2 wt, and SARS-CoV-2 B.1.1.7 trimeric spike proteins. (A) hACE2-fo was immobilized on a protein A/G sensor surface, and CoV trimer proteins were injected in concentration range of 0.62 to 50 nM. The sensograms were globally fitted with the secondary state reaction model. SARS-CoV (2002):  $K_{D1}$ , 6.7 nM;  $k_{s1}$ ,  $6.72 \text{ E} + 5 \pm 4.4 \text{ E} + 3$  [1/Ms];  $k_{d1}$ ,  $4.7 \text{ E} - 3$  [1/s]  $\pm 6.9 \text{ E} - 5$ ;  $k_{s2}$ ,  $8.8 \text{ E} - 3 \pm 6.9 \text{ E} - 5$  [1/Ms];  $k_{d2}$ ,  $2.1 \text{ E} - 4 \pm 1.6 \text{ E} - 6$  [1/s];  $K_{D-total}$ , 160 pM.  $\text{Chi}^2$ , 0.6 [RU<sup>2</sup>]. SARS-CoV-2 wt:  $K_{D1}$ , 1.8 nM;  $k_{s1}$ ,  $7.8 \text{ E} + 5 \pm 1.2 \text{ E} + 3$  [1/Ms];  $k_{d1}$ ,  $1.41 \text{ E} - 3 \pm 3.75 \text{ E} - 5$  [1/s];  $k_{s2}$ ,  $1.1 \text{ E} - 2 \pm 1.8 \text{ E} - 4$  [1/Ms];  $k_{d2}$ ,  $2.4 \text{ E} - 4 \pm 3.6 \text{ E} - 6$  [1/s];  $K_{D-total}$ , 41 pM.  $\text{Chi}^2$ , 0.8 [RU<sup>2</sup>]. (SARS-CoV-2 B.1.1.7)  $K_{D1}$ , 193 nM;  $k_{s1}$ ,  $1.31 \text{ E} + 6 \pm 1.5 \text{ E} + 4$  [1/Ms];  $k_{d1}$ ,  $2.5 \text{ E} - 2 \pm 1.5 \text{ E} - 3$  [1/s];  $k_{s2}$ ,  $5.3 \text{ E} - 2 \pm 1.5 \text{ E} - 3$  [1/Ms];  $k_{d2}$ ,  $1.1 \text{ E} - 4 \pm 2.6 \text{ E} - 6$  [1/s];  $K_{D-total}$ , 40 pM;  $\text{Chi}^2$ , 0.7 [RU<sup>2</sup>]. For graphic representation of the distribution of primary and secondary state reaction, a component analysis was performed for each of the trimeric spike proteins using the injection concentration of 5.56 nM spike. The sensogram (total) is composed of the primary binding event (red), followed by a secondary transition event (blue) which results in a highly stable secondary complex (B) On-off chart for the kinetic values of the SARS-CoV spike trimers in the primary and secondary state. (C) SEC-HPLC using 5- $\mu\text{g/mL}$  injections of SARS-CoV-2 S1-S2 trimer, SARS-CoV (2002) trimer, SARS-CoV-2 B.1.1.7 trimer, and hACE2 dimer. Column calibration was performed using protein standards of thyroglobulin (660 kDa, 5.78 min),  $\gamma$ -globulin (150 kDa, 7.52 min), ovalbumin (45 kDa, 8.52 min), and aprotinin (6.5 kDa, 11.12 min).

**The secondary state transition rate is modified among SARS-CoV, SARS-CoV-2, and B.1.1.7 trimeric spike proteins.** The secondary state model was essential to fully describe the interaction of the S1-S2 monomer with hACE2. Next, we analyzed the interaction of the SARS-CoV (2002), SARS-CoV-2 wt, and SARS-CoV-2 B.1.1.7 mutant trimeric spike protein with hACE2 as described previously. After confirmation of their trimeric status by SEC-HPLC (Fig. 6C), the sensograms were again fitted using global fitting with the two-state reaction model (Fig. 6A and B).

The dissociation phases of the trimeric spike proteins (Fig. 6A) show biphasic decays as already observed for the monomeric SARS-CoV-2 S1-S2. Again, the secondary state model allowed the most accurate fit for the given sensograms. The component analysis reveals that the secondary state transition (Fig. 6A, blue line) was dominating the

complex formation after a short initial contact time. Fig. 6B shows the on-off chart of the primary and secondary interaction mode as fitted for the SARS-CoV (2002), the SARS-CoV-2 wt, and SARS-CoV-2 B.1.1.7 trimers. When the  $k_a$  and  $k_d$  values of the primary interaction are compared with those found for the SARS-CoV-2 S1-S2 and RBD constructs, the 2002 and wt trimeric spikes show values in the same range, implying that the initial binding event is not so much different among these constructs. The B.1.1.7 mutant, however, showed faster association and dissociation for the primary contact. Similarly, the kinetic values of the B.1.1.7 secondary state deviate from those identified for the 2002 and wt trimers. Here, the secondary state transition rate is of highest interest because it will directly impact the contact time that will be needed to form a complex with enhanced stability. The  $k_a$  identified for B.1.1.7 is 5.1 and 6.1 faster than the transition rate for the wt and 2002 trimer, respectively.

The significance of this finding becomes obvious when it is transferred to physiological conditions, where the probability of a potential primary contact between the viral spike and the cell surface located hACE2 is limited by the local concentration of the two interaction partners. Hence, a more rapid transition of a low- to high-affinity binding state will increase the complex half-time once a primary contact occurs and therefore increases the infection efficacy as observed for the B.1.1.7 and other mutants.

**Summary and conclusion.** This study helps to understand the basis of the enhanced infectivity that has been observed for SARS-CoV-2 and its derived mutants compared with SARS-CoV (2002). We have demonstrated that a secondary state of the SARS-CoV-2 spike-hACE2 complex exists and that the transition increases the stability of the complex by a factor of  $\sim 190$  (primary versus secondary state) with an overall  $K_D$  of 0.20 nM for the monomeric spike S1-S2 protein (for full list of all kinetic values see Table 1). Furthermore, when the isolated RBD was assayed for its affinity to hACE2, no secondary state formation was observed. This finding clearly suggests that the context of the whole ectodomain is needed to promote the secondary state within the complex after the first contact is mediated by the RBD. When the kinetics of the monomeric SARS-CoV-2 S1-S2 were compared with the trimeric variant, an increased secondary state transition was identified for the trimeric protein, suggesting cooperative effects between the subunits. These cooperative effects are best explained by the dimeric status of hACE2 (26), which results in the interaction of two RBDs in the “up” position of one trimeric spike. Using the secondary state model, a 5- to 6-fold increased secondary state transition rate was observed for the B.1.1.7 variant compared with that of the wt and 2002 trimeric spike protein. A previous cryo-electron microscopy (cryo-EM) analysis of the spike-hACE2 complex demonstrated that the RBD-hACE2 complex is dynamic relative to the remaining part of the S protein as well as exhibits intrinsic dynamics (27, 28). This structural flexibility leaves room for the here observed secondary state, which is possibly mirrored by the gradually shift of initially more flexible proportions toward a more rigid conformation. Because these conformational changes are not necessarily restricted to the direct binding interface, we refrain from speculations on what residues may be involved.

Taken together, these findings highlight the role of the SARS-CoV-2 spike protein in the context of the ongoing pandemic and stress its importance as a potential drug target. The presented SPR method for the verification of secondary state transitions within the spike protein-hACE2 complex will allow a straightforward way of predicting the infectiousness of newly appearing SARS-CoV-2 variants. To date, several studies aim for the inhibition of the spike-hACE2 interaction by targeting one of the interaction partners (29–32). However, the present study shows that an efficient inhibitor should impact both the primary as well as secondary binding state in order to obtain a significant reduction of complex formation. Since the secondary transition rate is the decisive parameter for a potentially enhanced infection rate, it is important to understand its molecular mechanism. Targeting the secondary state transition may be very efficient for the development of therapeutic compounds for COVID-19. Most importantly, we suggest that future researchers should determine the full quantitative kinetic binding

**TABLE 1** Kinetic values of spike protein constructs with hACE2<sup>a</sup>

Analyte	Expt	Fitting method	$k_{a1}$ [1/M s]	$k_{d1}$ [1/s]	$K_{D1}$ [nM]	$k_{a2}$ [1/M s]	$k_{d2}$ [1/s]	$K_{D-total}$ [nM]	R <sup>2</sup> /Chi <sup>2</sup> [-] <sup>b</sup>
SARS-Cov-2 S1-S2 monomer	BLI (cropped)	1:1 Langmuir	1.1E + 5	2.4E-3	22				0.98
SARS-Cov-2 S1-S2 monomer	BLI (full)	1:1 Langmuir	1.7E + 5	1.9E-3	11				0.96
SARS-Cov-2 S1-S2 monomer	SPR (cropped)	1:1 Langmuir	1.7E + 5	4.7E-3	28.5				0.28 RU <sup>2</sup>
SARS-Cov-2 S1-S2 monomer	SPR (full)	1:1 Langmuir	5.4E + 7	0.7	12.15				6.63 RU <sup>2</sup>
SARS-CoV-2 RBD	SPR	1:1 Langmuir	4.25E + 5	9.1E-3	21.3				0.05 RU <sup>2</sup>
SARS-Cov-2 S1-S2 monomer	SPR	Secondary state	1.8E + 5	6.6E-3	37.5	8.3E-4	8.5E-5	0.2	0.08 RU <sup>2</sup>
SARS-CoV-2 RBD	SPR	1:1 Langmuir	4.3E + 5	9.1E-3	21.3				0.05 RU <sup>2</sup>
SARS-CoV (2002) S1-S2 trimer	SPR	Secondary state	6.7E + 5	4.7E-3	6.7	8.8E-3	2.1E-4	0.16	0.06 RU <sup>2</sup>
SARS-CoV-2 wt S1-S2 trimer	SPR	Secondary state	7.8E + 5	1.4E-3	1.8	1.1E-2	2.4E-4	0.04	0.08 RU <sup>2</sup>
SARS CoV B.1.1.7 S1 S2 trimer	SPR	Secondary state	1.31 E + 6	2.5 E 2	192.7	5.3E 2	1.1E 4	0.04	0.07 RU <sup>2</sup>

<sup>a</sup>Measurements were performed using the immobilized hACE2 dimer as the ligand and spike protein constructs as analytes.

<sup>b</sup>[-] means that RU<sup>2</sup> and Chi<sup>2</sup> values have no SI unit.

behavior to hACE2 for newly appearing spike protein variants to possibly predict the infectivity efficacy of the underlying virus variant.

## MATERIALS AND METHODS

**Protein expression and purification.** Expression of SARS-CoV-2 spike protein constructs was either performed using High Five insect cells [SARS-CoV-2 RBD, SARS-CoV-2 S1-S2 monomer and trimer, SARS-CoV-2 B.1.1.7 S1-S2 trimer, SARS-CoV (2002) trimer] or HEK293-6E cells (hACE-2) via transient gene expression (33, 34). The High Five (Hi5) insect cell line (officially called BTI-Tn-5B1-4) was isolated by the Boyce Thompson Institute for Plant Research (USA). The cell line was obtained from Thermo Fisher Scientific (USA). The HEK293-6E cell line was licensed from National Research Council (NRC), Biotechnological Research Institute (BRI, Canada). Recombinant protein genes for the CoV constructs (see Fig. S2 in the supplemental material) were synthesized by Genscript (USA) or Thermo Fisher Scientific. Protein samples were purified using HisExcel columns (Cytiva) for 6× His-tagged proteins, StrepTrap HP columns (Cytiva, USA) for TwinStrep-tagged proteins (all trimeric proteins with foldon sequence were Strep- and His-tagged and were purified via StrepTrap HP column), or protein A columns (Thermo Fisher Scientific) for Fc-tagged proteins (see Table 2 for complete list of all constructs and modifications). The C-terminal introduction of a T4 bacteriophage foldon sequence (with exception of the SARS-CoV construct) was used for the induction of S1-S2 stable trimers (35). All purifications steps were performed on Äkta Start or Äkta Pure systems (Cytiva) according to the manufacturer's protocol. Depending on the protein size, size exclusion chromatography (SEC) was performed as a final polishing step using either a Superdex 200 or Superose 6 column (Cytiva) in 20 mM Tris (pH 8.0) and 150 mM NaCl as the running buffer. For verification of the oligomeric status of the spike protein constructs as well as hACE2, SEC-HPLC was performed. For SEC-HPLC, proteins were diluted to 5 µg/mL and injected on a Bio-SEC3 300 Å column using a 1260 Infinity II system (Agilent, USA) with 1 mL/min phosphate-buffered saline (PBS; pH 7.4) as the running buffer. A full list of all used protein constructs and their origin as well as included modifications are shown in Table 2.

**Kinetic experiments biolayer interferometry (BLI).** BLI kinetic experiments were performed with an Octet RED 96 BLI system using streptavidin-coated high-precision SAX-sensors (Sartorius, GE) and a shaking speed of 1,000 rpm. hACE2 was immobilized to a binding level of 1.6 nm with a concentration of 5 µg/mL. Serial dilutions of the S1-S2 SARS-CoV-2 spike protein were prepared in range of 3.9 to 250 nM in 10 mM HEPES (pH 7.4), 150 mM NaCl, 3 mM EDTA, and 0.005% Tween 20. The experiment was performed with double reference subtraction.

**Surface plasmon resonance kinetic experiments.** SPR kinetic experiments were performed with a T200-SPR Biacore system (Cytiva) using a protein A/G-coated sensor chip (PAGD-200M; Xantec) and a flow rate of 30 µL/min unless otherwise noted. hACE2 was captured to a response level of 70 RU for each cycle using a concentration of 2.5 µg/mL. The surface was regenerated with 10 mM NaOH by 2 × 30-s injections at 10 µL/min. For kinetic measurements, serial dilutions of the spike protein were prepared in range from 3.9 to 62.5 nM for the monomeric S1-S2 and 0.65 to 50 nM for the trimeric constructs in 10 mM HEPES (pH 7.4), 150 mM NaCl, 3 mM EDTA, and 0.005% Tween 20. Data fitting was

**TABLE 2** List of SARS-CoV, SARS-CoV-2 spike protein, and hACE2 constructs used in the study

Construct name	Supplier	Expression organism	Tag
SARS-CoV-2 RBD-His	In-house	High Five insect cells	6× His tag
SARS-CoV-2 S1-S2-His monomer	In-house	High Five insect cells	6× His tag
SARS-CoV (2002) S1-S2-His trimer	In-house	High Five insect cells	6× His tag
SARS-CoV-2 S1-S2-His-T4 trimer	In-house	High Five insect cells	6× His tag, T4-foldon
SARS-CoV-2 B.1.1.7 S1-S2 -His-T4 trimer	In-house	High Five insect cells	6× His tag, T4-foldon
hACE2-fc dimer	In-house	HEK293-6E cells	IgG1-Fc
hACE2-His biotin dimer	Acrobiosystems, USA (Cat. No. AC2-H82E6) <sup>a</sup>	HEK293 cells	Biotinylated Avitag, 6× His

<sup>a</sup>UniProt KB Q9BYF1.

performed using Biacore T200 data evaluation software v. 3.2. For all fits, a contribution of refractive index was excluded.

While testing for the second state interaction, hACE2 was immobilized to a response level of 25 RU for each cycle. A total of 500 nM S1-S2 spike protein was injected with contact times of 150 to 600 s. Buffer referencing was performed prior to each analyte injection cycle. The experimental evaluation was done by alignment of the dissociation start and normalization of the saturation response signal to 100% by the time point of injection phase end.

**Data availability.** The data sets generated during and/or analyzed during the current study are available from the corresponding author on reasonable request.

#### ACKNOWLEDGMENT

This research received no specific grant from any funding agency in the public, commercial, or not-for-profit sectors.

#### REFERENCES

- Huang C, Wang Y, Li X, Ren L, Zhao J, Hu Y, Zhang L, Fan G, Xu J, Gu X, Cheng Z, Yu T, Xia J, Wei Y, Wu W, Xie X, Yin W, Li H, Liu M, Xiao Y, Gao H, Guo L, Xie J, Wang J, Jiang R, Gao Z, Jin Q, Wang J, Cao B. 2020. Clinical features of patients infected with 2019 novel coronavirus in Wuhan, China. *Lancet* 395:497–506. [https://doi.org/10.1016/S0140-6736\(20\)30183-5](https://doi.org/10.1016/S0140-6736(20)30183-5).
- Li Q, Guan X, Wu P, Wang X, Zhou L, Tong Y, Ren R, Leung KSM, Lau EHY, Wong JY, Xing X, Xiang N, Wu Y, Li C, Chen Q, Li D, Liu T, Zhao J, Liu M, Tu W, Chen C, Jin L, Yang R, Wang Q, Zhou S, Wang R, Liu H, Luo Y, Liu Y, Shao G, Li H, Tao Z, Yang Y, Deng Z, Liu B, Ma Z, Zhang Y, Shi G, Lam TTY, Wu JT, Gao GF, Cowling BJ, Yang B, Leung GM, Feng Z. 2020. Early transmission dynamics in Wuhan, China, of novel coronavirus-infected pneumonia. *N Engl J Med* 382:1199–1207. <https://doi.org/10.1056/NEJMoa2001316>.
- Rabaan AA, Al-Ahmed SH, Haque S, Sah R, Tiwari R, Malik YS, Dhama K, Yattoo MI, Bonilla-Aldana DK, Rodriguez-Morales AJ. 2020. SARS-CoV-2, SARS-CoV, and MERS-CoV: a comparative overview. *Infect Med* 28:174–184.
- Lee N, Hui D, Wu A, Chan P, Cameron P, Joynt GM, Ahuja A, Yung MY, Leung CB, To KF, Lui SF, Szeto CC, Chung S, Sung JY. 2003. A major outbreak of severe acute respiratory syndrome in Hong Kong. *N Engl J Med* 348:1986–1994. <https://doi.org/10.1056/NEJMoa030685>.
- WHO Coronavirus (COVID-19) Dashboard. 2022. Available from: <https://covid19.who.int/>.
- Wang Q, Zhang Y, Wu L, Niu S, Song C, Zhang Z, Lu G, Qiao C, Hu Y, Yuen K-Y, Wang Q, Zhou H, Yan J, Qi J. 2020. Structural and functional basis of SARS-CoV-2 entry by using human ACE2. *Cell* 181:894–904.e9. <https://doi.org/10.1016/j.cell.2020.03.045>.
- Hoffmann M, Kleine-Weber H, Schroeder S, Krüger N, Herrler T, Erichsen S, Schiergens TS, Herrler G, Wu N-H, Nitsche A, Müller MA, Drosten C, Pöhlmann S. 2020. SARS-CoV-2 cell entry depends on ACE2 and TMPRSS2 and is blocked by a clinically proven protease inhibitor. *Cell* 181:271–280.e8. <https://doi.org/10.1016/j.cell.2020.02.052>.
- Xia S, Liu M, Wang C, Xu W, Lan Q, Feng S, Qi F, Bao L, Du L, Liu S, Qin C, Sun F, Shi Z, Zhu Y, Jiang S, Lu L. 2020. Inhibition of SARS-CoV-2 (previously 2019-nCoV) infection by a highly potent pan-coronavirus fusion inhibitor targeting its spike protein that harbors a high capacity to mediate membrane fusion. *Cell Res* 30:343–355. <https://doi.org/10.1038/s41422-020-0305-x>.
- Chen J, Wang R, Wang M, Wei G-W. 2020. Mutations strengthened SARS-CoV-2 infectivity. *J Mol Biol* 432:5212–5226. <https://doi.org/10.1016/j.jmb.2020.07.009>.
- Tang JW, Tambyah PA, Hui DSC. 2021. Emergence of a new SARS-CoV-2 variant in the UK. *J Infect* 82:e27–e28. <https://doi.org/10.1016/j.jinf.2020.12.024>.
- Guruprasad L. 2021. Human SARS CoV-2 spike protein mutations. *Proteins* 89:569–576. <https://doi.org/10.1002/prot.26042>.
- Plante JA, Liu Y, Liu J, Xia H, Johnson BA, Lokugamage KG, Zhang X, Muruato AE, Zou J, Fontes-Garfias CR, Mirchandani D, Scharon D, Billello JP, Ku Z, An Z, Kalveram B, Freiberg AN, Menachery VD, Xie X, Plante KS, Weaver SC, Shi PY. 2020. Spike mutation D614G alters SARS-CoV-2 fitness. *Nature* 592:116–121. <https://doi.org/10.1038/s41586-020-2895-3>.
- Mlcochova P, Kemp SA, Dhar MS, Papa G, Meng B, Ferreira IATM, Dattir R, Collier DA, Albecka A, Singh S, Pandey R, Brown J, Zhou J, Goonawardane N, Mishra S, Whittaker C, Mellan T, Marwal R, Datta M, Sengupta S, Ponnusamy K, Radhakrishnan VS, Abdullahi A, Charles O, Chattopadhyay P, Devi P, Caputo D, Peacock T, Wattal C, Goel N, Satwik A, Vaishya R, Agarwal M, Chauhan H, Dikid T, Gogia H, Lall H, Verma K, Dhar MS, Singh
- MK, Soni N, Meena N, Madan P, Singh P, Sharma R, Sharma R, Kabra S, Kumar S, Kumari S, Sharma U, The Indian SARS-CoV-2 Genomics Consortium (INSACOG), et al. 2021. SARS-CoV-2 B.1.617.2 Delta variant replication and immune evasion. *Nature* 599:114–119. <https://doi.org/10.1038/s41586-021-03944-y>.
- Karim SSA, Karim QA. 2021. Omicron SARS-CoV-2 variant: a new chapter in the COVID-19 pandemic. *Lancet* 398:2126–2128. [https://doi.org/10.1016/S0140-6736\(21\)02758-6](https://doi.org/10.1016/S0140-6736(21)02758-6).
- Tagliamonte MS, Mavian C, Zainabadi K, Cash MN, Lednický JA, Magalis BR, Riva A, Deschamps MM, Liautaud B, Rouzier V, Fitzgerald DW, Pape JW, Morris JG, Salemi M. 2021. Rapid emergence and spread of SARS-CoV-2 gamma (P.1) variant in Haiti. *Clin Infect Dis* ciab736. <https://doi.org/10.1093/cid/ciab736>.
- Brielle ES, Schneidman-Duhovny D, Linal M. 2020. The SARS-CoV-2 exerts a distinctive strategy for interacting with the ACE2 human receptor. *Viruses* 12:497. <https://doi.org/10.3390/v12050497>.
- Piantham C, Ito K. 2021. Estimating the increased transmissibility of the B.1.1.7 strain over previously circulating strains in England using fractions of GISAID sequences and the distribution of serial intervals. *medRxiv*. <https://doi.org/10.1101/2021.03.17.21253775>.
- Coutard B, Valle C, de Lamballerie X, Canard B, Seidah NG, Decroly E. 2020. The spike glycoprotein of the new coronavirus 2019-nCoV contains a furin-like cleavage site absent in CoV of the same clade. *Antiviral Res* 176:104742. <https://doi.org/10.1016/j.antiviral.2020.104742>.
- Shang J, Ye G, Shi K, Wan Y, Luo C, Aihara H, Geng Q, Auerbach A, Li F. 2020. Structural basis of receptor recognition by SARS-CoV-2. *Nature* 581:221–224. <https://doi.org/10.1038/s41586-020-2179-y>.
- Ozono S, Zhang Y, Ode H, Sano K, Tan TS, Imai K, Miyoshi K, Kishigami S, Ueno T, Iwatani Y, Suzuki T, Tokunaga K. 2021. SARS-CoV-2 D614G spike mutation increases entry efficiency with enhanced ACE2-binding affinity. *Nat Commun* 12:848. <https://doi.org/10.1038/s41467-021-21118-2>.
- Wang Y, Liu M, Gao J. 2020. Enhanced receptor binding of SARS-CoV-2 through networks of hydrogen-bonding and hydrophobic interactions. *Proc Natl Acad Sci U S A* 117:13967–13974. <https://doi.org/10.1073/pnas.2008209117>.
- Wrapp D, Wang N, Corbett KS, Goldsmith JA, Hsieh C-L, Abiona O, Graham BS, McLellan JS. 2020. Cryo-EM structure of the 2019-nCoV spike in the prefusion conformation. *Science* 367:1260–1263. <https://doi.org/10.1126/science.abb2507>.
- Lan J, Ge J, Yu J, Shan S, Zhou H, Fan S, Zhang Q, Shi X, Wang Q, Zhang L, Wang X. 2020. Structure of the SARS-CoV-2 spike receptor-binding domain bound to the ACE2 receptor. *Nature* 581:215–220. <https://doi.org/10.1038/s41586-020-2180-5>.
- Karlsson R, Falt A. 1997. Experimental design for kinetic analysis of protein-protein interactions with surface plasmon resonance biosensors. *J Immunol Methods* 200:121–133.
- Lund-Katz S, Nguyen D, Dhanasekaran P, Kono M, Nickel M, Saito H, Phillips MC. 2010. Surface plasmon resonance analysis of the mechanism of binding of apoA-I to high density lipoprotein particles. *J Lipid Res* 51:606–617. <https://doi.org/10.1194/jlr.M002055>.
- Ismail AM, Elfiky AA. 2020. SARS-CoV-2 spike behavior in situ: a Cryo-EM images for a better understanding of the COVID-19 pandemic. *Sig Transduct Target Ther* 5:252. <https://doi.org/10.1038/s41392-020-00365-7>.
- Xu C, Wang Y, Liu C, Zhang C, Han W, Hong X, Wang Y, Hong Q, Wang S, Zhao Q, Wang Y, Yang Y, Chen K, Zheng W, Kong L, Wang F, Zuo Q,

- Huang Z, Cong Y. 2021. Conformational dynamics of SARS-CoV-2 trimeric spike glycoprotein in complex with receptor ACE2 revealed by cryo-EM. *Sci Adv* 7:eabe5575. <https://doi.org/10.1126/sciadv.abe5575>.
28. Song W, Gui M, Wang X, Xiang Y. 2018. Cryo-EM structure of the SARS coronavirus spike glycoprotein in complex with its host cell receptor ACE2. *PLoS Pathog* 14:e1007236. <https://doi.org/10.1371/journal.ppat.1007236>.
29. Alagumuthu M, Rajpoot S, Baig MS. 2021. Structure-based design of novel peptidomimetics targeting the SARS-CoV-2 spike protein. *Cell Mol Bioeng* 14:177–185. <https://doi.org/10.1007/s12195-020-00658-5>.
30. Han YX, Kral P. 2020. Computational design of ACE2-based peptide inhibitors of SARS-CoV-2. *ACS Nano* 14:5143–5147. <https://doi.org/10.1021/acsnano.0c02857>.
31. Guo L, Bi W, Wang X, Xu W, Yan R, Zhang Y, Zhao K, Li Y, Zhang M, Cai X, Jiang S, Xie Y, Zhou Q, Liu L, Dang B. 2021. Engineered trimeric ACE2 binds viral spike protein and locks it in “Three-up” conformation to potently inhibit SARS-CoV-2 infection. *Cell Res* 31:98–100. <https://doi.org/10.1038/s41422-020-00438-w>.
32. Bojadzic D, Alcazar O, Buchwald P. 2020. Methylene blue inhibits the SARS-CoV-2 spike-ACE2 protein-protein interaction—a mechanism that can contribute to its antiviral activity against COVID-19. *Front Pharmacol* 11:600372. <https://doi.org/10.3389/fphar.2020.600372>.
33. Schubert M, Nimtz M, Bertoglio F, Schmelz S, Lukat P, van den Heuvel J. 2021. Reproducible and easy production of mammalian proteins by transient gene expression in high five insect cells. *Methods Mol Biol* 2305:129–140. [https://doi.org/10.1007/978-1-0716-1406-8\\_6](https://doi.org/10.1007/978-1-0716-1406-8_6).
34. Meyer S, Lorenz C, Baser B, Wördehoff M, Jäger V, van den Heuvel J. 2013. Multi-host expression system for recombinant production of challenging proteins. *PLoS One* 8:e68674. <https://doi.org/10.1371/journal.pone.0068674>.
35. Papanikolopoulou K, Forge V, Goeltz P, Mitraki A. 2004. Formation of highly stable chimeric trimers by fusion of an adenovirus fiber shaft fragment with the foldon domain of bacteriophage T4 fibrin. *J Biol Chem* 279:8991–8998. <https://doi.org/10.1074/jbc.M311791200>.

## 2.3 Phage Display-Derived Compounds that Displace hACE2 from Its Complex with SARS-CoV-2 Spike Protein

Authors: **Marc Sevenich**, Elena Thul, Nils-Alexander Lakomek, Thomas Klünemann, Maren Schubert, Federico Bertoglio, Joop van den Heuvel, Patrick Petzsch, Jeannine Mohrlüder and Dieter Willbold

Journal: Biomedicines

DOI: <https://doi.org/10.3390/biomedicines10020441>

Impact Factor: 6.081 (2020)

Contribution: Project outline, planning of phage display selection, performance of NGS analysis, planning and performance of kinetic assays, planning of peptide optimization, writing of original draft.

Article

# Phage Display-Derived Compounds Displace hACE2 from Its Complex with SARS-CoV-2 Spike Protein

Marc Sevenich <sup>1,2</sup>, Elena Thul <sup>3</sup>, Nils-Alexander Lakomek <sup>1,4</sup>, Thomas Klünemann <sup>5</sup>, Maren Schubert <sup>6</sup>, Federico Bertoglio <sup>6</sup>, Joop van den Heuvel <sup>5</sup>, Patrick Petzsch <sup>7</sup>, Jeannine Mohrlüder <sup>1,\*</sup> and Dieter Willbold <sup>1,4,8,\*</sup>

<sup>1</sup> Institute of Biological Information Processing (IBI-7), Forschungszentrum Jülich, 52425 Jülich, Germany; m.sevenich@fz-juelich.de (M.S.); n.lakomek@fz-juelich.de (N.-A.L.)

<sup>2</sup> Priavoid GmbH, 40225 Düsseldorf, Germany

<sup>3</sup> Medizinische Fakultät, Westfälische Wilhelms Universität Münster, 48149 Münster, Germany; e\_thul01@uni-muenster.de

<sup>4</sup> Institut für Physikalische Biologie, Heinrich-Heine-Universität Düsseldorf, 40225 Düsseldorf, Germany

<sup>5</sup> Helmholtz Centre for Infection Research, 38124 Braunschweig, Germany;

thomas.kluenemann@helmholtz-hzi.de (T.K.); joop.vandenheuvel@helmholtz-hzi.de (J.v.d.H.)

<sup>6</sup> Institut für Biochemie, Biotechnologie und Bioinformatik – Abteilung Biotechnologie, Technische Universität Braunschweig, 38106 Braunschweig, Germany; m.bleckmann@tu-bs.de (M.S.); f.bertoglio@tu-bs.de (F.B.)

<sup>7</sup> Biologisch-Medizinisches Forschungszentrum (BMFZ), Heinrich-Heine-Universität Düsseldorf, 40225 Düsseldorf, Germany; patrick.petzsch@uni-duesseldorf.de

<sup>8</sup> JuStruct, Forschungszentrum Jülich, 52425 Jülich, Germany

\* Correspondence: j.mohrlueder@fz-juelich.de (J.M.); d.willbold@fz-juelich.de (D.W.); Tel.: +49-2461-612100 (D.W.)

**Citation:** Sevenich, M.; Thul, E.; Lakomek, N.-A.; Klünemann, T.; Schubert, M.; Bertoglio, F.; van den Heuvel, J.; Petzsch, P.; Mohrlüder, J.; Willbold, D. Phage Display-Derived Compounds Displace hACE2 from Its Complex with SARS-CoV-2 Spike Protein. *Biomedicines* **2022**, *10*, 441. <https://doi.org/10.3390/biomedicines10020441>

Academic Editor: Dong-Yan Jin

Received: 19 January 2022

Accepted: 11 February 2022

Published: 14 February 2022

**Publisher's Note:** MDPI stays neutral with regard to jurisdictional claims in published maps and institutional affiliations.



**Copyright:** © 2022 by the authors. Licensee MDPI, Basel, Switzerland. This article is an open access article distributed under the terms and conditions of the Creative Commons Attribution (CC BY) license (<http://creativecommons.org/licenses/by/4.0/>).

**Abstract:** Severe respiratory syndrome coronavirus-2 (SARS-CoV-2) is a highly contagious beta-class coronavirus. Although vaccinations have shown high efficacy, the emergence of novel variants of concern (VOCs) has already exhibited traits of immune evasion. Thus, the development of tailored antiviral medications for patients with incomplete, inefficient, or non-existent immunization, is essential. The attachment of viral surface proteins to the cell surface is the first crucial step in the viral replication cycle, which for SARS-CoV-2 is mediated by the high affinity interaction of the viral trimeric spike with the host cell surface-located human angiotensin converting enzyme-2 (hACE2). Here, we used a novel and efficient next generation sequencing (NGS) supported phage display strategy for the selection of a set of SARS-CoV-2 receptor binding domain (RBD)-targeting peptide ligands that bind to the target protein with low  $\mu\text{M}$  dissociation constants. Compound CVRBDL-3 inhibits the SARS-CoV-2 spike protein association to hACE2 in a concentration-dependent manner for pre- as well as post-complex formation conditions. Further rational optimization yielded a CVRBDL-3 based divalent compound, which demonstrated inhibitory efficacy with an  $\text{IC}_{50}$  value of 47 nM. The obtained compounds were not only efficient for the different spike constructs from the originally isolated “wt” SARS-CoV-2, but also for B.1.1.7 mutant trimeric spike protein. Our work demonstrates that phage display-derived peptide ligands are potential fusion inhibitors of viral cell entry. Moreover, we show that rational optimization of a combination of peptide sequences is a potential strategy in the further development of therapeutics for the treatment of acute COVID-19.

**Keywords:** SARS-CoV-2; coronavirus; spike protein; phage display; acute COVID-19 treatment; spike-hACE2 inhibitor

## 1. Introduction

SARS-CoV-2 is a beta class coronavirus with the ability for human-to-human transmission that was initially discovered and characterized in Wuhan, China, at the end

of 2019 [1,2]. Since then, it has challenged health care systems due to its rapid spread and the transmission of COVID-19 throughout the world. Far more than the past coronavirus pandemics, caused by SARS-CoV in 2002 and MERS-CoV in 2012, the ongoing pandemic has claimed over 5.7 million lives with over 386 million total cases across the world [3–6].

The coronavirus replication depends on a multi-step process starting with the interaction of the viral trimeric spike protein (S) and the human angiotensin converting enzyme (hACE2) receptor that mediates uptake of the viral RNA into the host-cell cytoplasm. Each monomer of the spike protein consists of the two functional subunits S1 and S2. The S1 subunit comprises the receptor binding domain (RBD) that interacts via a defined motif sequence (RBM) with an N-terminally located helical structure of the hACE2. In accordance with previous observations from SARS-CoV, the SARS-CoV-2 RBD has been found to exist in two conformational states, from which the 'up' state initiates interaction with hACE2 and the 'down' state's main function is the shielding of receptor binding relevant proportions from immune reactions [7]. The S2 subunit plays a crucial role in the membrane fusion process. While the S1-hACE2 interaction allows viral attachment to the host cell surface, the S2 site is cleaved by the human endoprotease TMPRSS2. Together with cooperative actions of other tissue specific endogenous proteases, proteolytic cleavage results in irreversible conformational changes of the S protein that eventually results in cell membrane fusion and endocytic host-cell uptake [8].

Although the viral S proteins of SARS-CoV and SARS-CoV-2 share ~73% amino acid sequence identity, SARS-CoV-2 shows significantly enhanced transmission efficiency when compared to SARS-CoV [9,10]. Structural studies suggest that alterations at the furin cleavage site, located at the boundary between S1 and S2 subunits, may result in reduced stability of the S protein, which facilitates the conformational adaptation that is required for receptor binding [11]. In addition, SARS-CoV-2 specific amino acid residues identified within the RBM were shown to enhance the binding affinity of the SARS CoV-2 spike protein and hACE2 as compared to SARS-CoV [12–14].

Since its first appearance in 2019, the virus has undergone numerous mutational events, resulting in variants of concern (VOCs) with enhanced fitness regarding their transmissibility and disease severity [15,16]. A large proportion of these mutations cluster in the spike protein, influencing its binding affinity towards hACE2 [13,17–20]. To date, the most widespread mutants such as B.1.617.2 ( $\delta$ -variant), P.1 ( $\gamma$ -variant) and B.1.1.529 ( $\omicron$ -variant) have widely replaced the originally identified SARS-CoV-2 virus due to their enhanced fitness [21–25]. Interestingly, most of the circulating variants that have enhanced infectivity as compared to the ancestral strain carry a D614G substitution in the S1 domain of the spike protein. Several indications suggest that the mutation may be directly linked to the enhanced transmissibility [21,24].

Although mRNA-based vaccines in particular turned out as a successful strategy for controlling the pandemic spread of SARS-CoV-2, vaccinations have already been shown to be partially less effective for certain VOCs [19,25]. The selection pressure created by different immunization strategies in combination with naturally occurring spontaneous mutations consequently leads to the enforcement of variants with increased immune evasive traits, making adaptation of vaccines as well as repetitive renewal of immunization mandatory. This situation, which resembles the status quo of the influenza virus [26], requires the development of antiviral medication, especially for cases where either no sufficient immunity is present or already existing immunity is circumvented by novel viral strains.

Hence, various research efforts have either focused on the development of novel drug candidates for a causative treatment such as Paxlovid (Pfizer), repurposing approved compounds such as Molnupiravir (Merck), or even screening components from natural sources [27–33]. However, there are no generally proven effective antiviral treatment options for SARS-CoV-2 infections. In this study, we present a novel phage display based strategy for the development of SARS-CoV-2 RBD-targeting peptide ligands. The resulting lead compounds show high binding affinity for the RBD in the nanomolar scale

and binding selectivity for the SARS-CoV-2 RBD, as well as for the B.1.1.7 mutant ( $\alpha$ -variant). Moreover, when analyzed in binding experiments with the isolated proteins, one of the selected peptide sequences reduced the SARS-CoV-2 spike protein binding towards the cellular receptor hACE2 when added before complex formation on one side, but was also able to displace the spike protein from the already formed complex. In addition, a first optimization of the most promising lead compound resulted in an even more efficient compound.

## 2. Materials and Methods

### 2.1. Phage Display Selection

In phage display, exogenous peptides are presented on phage particles as fusion constructs with coat proteins. Consecutive rounds of biopanning and amplification increase the fraction of phages presenting strong target binders, which can be identified by sequencing of the variable portion of the genome [34].

For biopanning, the commercially available M13-bacteriophage library TriCo-16 (Creative Biolabs, Shirley, USA) was used. The library had a capacity of  $2.6 \times 10^{10}$  pIII fused 16-mer peptide variants. The biotinylated SARS-CoV-2 RBD target protein (positions 319 to 541) was purchased as lyophilized powder from Acrobiosystems (# QHD43416, USA) with a purity of >95%. The protein carries a C-terminal His-Tag for Ni-NTA purification followed by an Avitag sequence (SPD-C82E9, [35]) for BirA catalyzed transfer of biotin. The protein was expressed in HEK293 cells and had a Mw of 28.2 kDa with additional 5 to 8 kDa due to glycosylation. For surface immobilization, the target protein was incubated on a streptavidin-functionalized polystyrene 96-well plate (High capacity, Thermo Fisher Scientific, Waltham, USA) for 1 h at RT using 70 pmol/well of target protein in 25 mM HEPES, pH 7.4, 150 mM NaCl, 100  $\mu$ M EDTA (selection buffer). Non-coupled streptavidin was quenched by 10 min incubation with 100  $\mu$ L of 10  $\mu$ M biotin. Subsequent surface blocking was performed for 1 h by incubation with either 1% (*w/v*) BSA or nonfat milk powder in selection buffer. For the first selection round, 10  $\mu$ L of the phage library ( $6 \times 10^{11}$  phages/well) was diluted in 90  $\mu$ L selection buffer with 0.2% (*w/v*) BSA or milk powder and incubated for 20 min. The subsequent washing steps with 200  $\mu$ L washing buffer (0.05% (*v/v*) Tween-20 and either 0.2% (*w/v*) bovine serum albumin (BSA) or milk powder in selection buffer) were gradually increased from 5 to 15 repetitions with the number of selection rounds. Phage elution was performed using 10 min incubation with 100  $\mu$ L of 0.2 M glycine-HCl (pH 2.2), followed by neutralization in 25  $\mu$ L of 1 M Tris-HCl (pH 9.1). Eluted phages were amplified for 4.5 h in 20 mL of LB-cultured *E. coli* K12 ER2783 with a starting OD<sub>600</sub> of 0.1. The pelleted cells were discarded after 20 min centrifugation at 5000 $\times$  g and the phages were precipitated by addition of 7 mL 20% (*w/v*) PEG-8000, 2.5 M NaCl followed by overnight (ON) incubation at 4  $^{\circ}$ C. Phages were pelleted by centrifugation at 5000 $\times$  g for 1 h at 4  $^{\circ}$ C and resuspended in 1 mL PBS (pH 7.4). After additional centrifugation at 10,000 rpm for 10 min, the supernatant was mixed with 200  $\mu$ L of 20% (*w/v*) PEG-8000, 2.5 M NaCl and incubated for 1 h at 4  $^{\circ}$ C. The phages were pelleted in a last purification step for 1 h at 5000 rpm and the pellet was suspended in 100  $\mu$ L selection buffer. Phage concentration of the purified phages was determined by serial dilution of the phage suspension and incubation with *E. coli* K12 ER2783 on IPTG/X Gal-LB titer plates ON at 37  $^{\circ}$ C. The concentration of input phages was calculated based on the serial dilution and a concentration of  $6 \times 10^{12}$  phage forming units ml<sup>-1</sup> (PFU) was used as the input for all selection rounds and controls. The selection was performed for three consecutive rounds on the target (target selection = TS). Additionally, input phages resulting from selection rounds on the target were applied to a parallel selection (direct control = DC) on a surface without target, which was otherwise treated identically to the TS surface. As a second control, a consecutive selection was performed exclusively without target on otherwise identically treated surfaces (empty selection = ES).

## 2.2. Enrichment ELISA

Enrichment-ELISA is a method to identify enrichment of target binding phages during phage display selection. All steps were carried out at RT. A total of 20 pmol/well of the biotinylated SARS-CoV-2 RBD target protein was immobilized on a streptavidin-functionalized polystyrene 96-well plate (High capacity, Thermo Fisher, USA). Both the target-immobilized and target-free surfaces were quenched with biotin as described previously. The surfaces were blocked with 1% (*w/v*) BSA in selection buffer for 1 h and washed with washing buffer (0.2% (*w/v*) BSA, 0.05% Tween-20 in selection buffer). A total of  $2.5 \times 10^{11}$  phages from the TS input samples or library were diluted in 100  $\mu$ L washing buffer and incubated on target and control surfaces for 1 h. After washing with 200  $\mu$ L washing buffer, the anti-M13 gpVIII monoclonal HRP-antibody (Sino Biologicals, Beijing, CHN) was diluted to a final concentration of 0.4 mg ml<sup>-1</sup> in washing buffer and 100  $\mu$ L per well was incubated for 1 h. After six-fold washing with washing buffer, 100  $\mu$ L of 3,3',5,5'-3,3,5,5-Tetramethylbenzidin (Sigma-Aldrich, St. Louis, MO, USA) substrate solution was incubated for 20 min and stopped by addition of an equal volume of 2 M H<sub>2</sub>SO<sub>4</sub>. The signal intensity was quantified by absorption measurement in a Fluorostar optima platereader at 450 nm (BMG Labtech, Ortenberg, GE; n = 3).

## 2.3. ssDNA Purification and next Generation Sequencing (NGS) of Phage Samples

The ssDNA of the phage suspensions resulting from each phage display selection round was purified by phage precipitation, as described before, followed by resuspending in 200  $\mu$ L of a 10:1 mixture of 3 M sodium acetate pH 5.2:1  $\times$  TE-buffer and addition of 500  $\mu$ L of 99% ethanol. ssDNA was precipitated at 14,000 rpm for 10 min at 4 °C and the supernatant was discarded. After pellet purification by the addition of 250  $\mu$ L of 70% EtOH and repeated centrifugation at 10,000 rpm, the pellet was dried and the DNA concentration was determined by signal quantification at A<sub>260</sub>. For next generation sequencing, a polymerase chain reaction (PCR) was used to add adapter sequences to both the 3' and 5' end of the amplification product. Success of the amplification was determined by agarose gel separation with ethidium bromide staining. Amplicon next generation sequencing was performed with a MiSeq system (Illumina, San Diego, CA, USA).

## 2.4. Analysis of next Generation Obtained Sequences

Variable DNA sequences resulting from next generation sequencing (NGS) were transcribed into peptide sequences, as described previously [36]. The transcribed sequences were filtered based on their relative frequency increase within the TS (library < TS1 < TS2 < TS3), the relative frequency of a sequence observed in one TS compared to its abundance within the respective DC (TS2 > DC2; TS3 > DC3) and the relative frequency of one sequence observed in one TS round compared to its abundance within the respective ES round (TS1 > ES1; TS2 > ES2; TS3 > ES3). Sequences of the last TS round that passed the filter were ranked corresponding to their enrichment from library to TS3 (TS3/library = enrichment factor) and their relative frequencies in TS3 compared to ES3 (TS3/ES3 = empty score). Filtered sequences were used as inputs for the Hammock clustering software [37]. The input FASTA-file included all filtered sequences as ranked by their empty score. The Hammock clustering software was performed in full mode with sequences ranked according to their input position (-R input). Cluster motif logos were generated from initial clusters after greedy clustering using the WebLogo 3.4 application.

## 2.5. CVRBDL Compounds

CVRBDL peptides were purchased with C-terminal amidation from CASLO (Copenhagen, DK) as lyophilized chloride salt powder with a purity of >95%.

### 2.6. SARS-CoV-2 Spike Protein and hACE2 Sample Preparation

Expression of SARS-CoV-2 spike protein constructs was either performed using High Five insect cells (SARS-CoV-2 RBD, SARS-CoV-2 S1S2 monomer and trimer, SARS-CoV-2 B.1.1.7 S1S2 trimer, SARS-CoV (2002) trimer, and SARS-CoV-2 “closed” S1S2 trimer) or HEK293-6E cells (hACE-2) via transient gene expression [38,39]. The High Five (Hi5) insect cell line (officially called BTI-Tn-5B1-4) was isolated by the Boyce Thompson Institute for Plant Research (Ithaca, NY, USA); the cell line can be acquired from Thermo Fisher Scientific (USA). The HEK293-6E cell line was licensed from National Research Council (NRC), Biotechnological Research Institute (BRI, CAN). Recombinant protein genes for the CoV constructs (Figure A1) were synthesized by Genscript (Piscataway Township, NJ, USA) or Thermo Fisher Scientific (Waltham, MA, USA). Protein samples were purified using HisExcel columns (Cytiva, Marlborough, MA, USA) for 6xHis tagged proteins, StrepTrap HP columns (Cytiva, MA, USA) for TwinStrep tagged proteins (all trimeric proteins with fold-on sequences were Strep and His-tagged and purified via StrepTrap HP columns) or protein A columns (Thermo Fisher Scientific, USA) for Fc-tagged proteins (see Table A1 for complete list of all constructs and modifications). A C-terminal introduction of a T4 bacteriophage fold-on sequence (with exception of the SARS-CoV construct) was used for the induction of S1S2 stable trimers [40]. All purifications were performed on Äkta Start or Äkta Pure systems (Cytiva, USA) according to the manufacturer’s protocol. Depending on the protein size, size exclusion chromatography (SEC) was performed as a final polishing step using either a Superdex 200 or Superose 6 column (Cytiva, USA) in 20 mM Tris (pH 8.0), 150 mM NaCl as running buffer. The SARS-CoV-2 nuclear magnetic resonance (NMR) sample was additionally purified via 10/300 Superdex 200 Increase SEC (Cytiva, USA) in 20 mM 2-(*N*-morpholino)ethanesulfonic acid (MES) (pH 6.5), 100 mM NaCl. The oligomerization state and purity of each construct was verified by SEC—multiangle light scattering (SEC-MALS).

### 2.7. NMR Sample Preparation

SARS-CoV-2 RBD protein was expressed in HighFive insect cells as described previously. The NMR sample was prepared using 0.85 mM (25.7 mg/mL) SARS-CoV-2 RBD, dissolved in 20 mM MES (pH 6.5), 100mM NaCl sample buffer. After recording the reference NMR spectrum of the RBD domain alone (see below), CVRBDL-3 was added to a final concentration of 1 mM, resulting in a molar stoichiometry of 1.1:1 for the peptide vs. RBD domain.

### 2.8. NMR Spectroscopy

Two dimensional  $^1\text{H}$ - $^{15}\text{N}$  HMQC (heteronuclear multiple quantum coherence) spectra of the isolated RBD domain (natural abundance) were recorded on a Bruker Avance Neo 1.2 GHz spectrometer, equipped with a 3 mm HCN cryoprobe. Spectral dimensions were 16.02 ppm ( $^1\text{H}$ )  $\times$  32.89 ppm ( $^{15}\text{N}$ ); 1024 and 27 complex points were recorded in the direct ( $^1\text{H}$ ) and indirect ( $^{15}\text{N}$ ) dimension, resulting in acquisition times of 53.2 ms and 6.8 ms in the direct and indirect dimension, respectively. To compensate for the low sensitivity of the natural abundance sample ( $^{15}\text{N}$  natural abundance of 0.37%), 8192 scans were recorded for each increment in the indirect dimension. The recovery delay between experiments was set to 1 s, resulting in a total experimental time of 5 d 15 h per spectrum. The experimental temperature was 20 °C. Spectra of the RBD domain in the presence of the peptide, as well as for the isolated peptide, were recorded back-to-back, under identical conditions as for the reference spectrum of the RBD domain alone. Spectra were processed using the Bruker Topsin 4 software (Billerica, MA, USA) and analyzed using the CCPN Analysis 2.3 software (Collaborative Computing Project for NMR; [41]).

### 2.9. Surface Plasmon Resonance (SPR) Experiments

SPR experiments were performed with a Biacore T200 device (Cytiva, USA) using 10 mM HEPES (pH 7.4), 150 mM NaCl, 3 mM EDTA, 0.005% (v/v) Tween-20 as assay buffer. SPR experiments were performed at a flow rate of 30  $\mu$ L/min and RT if not otherwise stated.

### 2.10. SPR Affinity Measurements

Affinity screening for CVRBDL peptides -1 to -5 was performed by immobilization of the biotinylated SARS-CoV-2 RBD selection target (Acrobiosystems, Newark, NY, USA) on a streptavidin-functionalized sensor surface (SA sensor, Cytiva, USA). CVRBDL peptides were injected for 300 s in a concentration range of 11.1 to 0.01  $\mu$ M, followed by 600 s of dissociation phase detection. For affinity measurements on SARS-CoV-2 and COVID (2002) RBD, S1S2 monomer and S1S2 trimer constructs, the proteins were immobilized on a polycarboxylate sensor surface using EDC/sulfo-NHS chemistry at pH 5.5 (HC200M, Xantec, GE). Injections were performed for 60 s association and 100 s dissociation using CVRBDL-3 and -3\_3 concentration ranges of 5 to 0.04  $\mu$ M. For both setups, regeneration was performed using 2  $\times$  30 s injections of 20 mM glycine-HCl (pH 3.5). Data evaluation was performed using Biacore T200 Evaluation Software v3.2 (Cytiva, USA).

### 2.11. SPR Inhibition Assay

The SPR inhibition assay was performed by immobilization of hACE2-fc on a Protein A functionalized sensor surface by injecting 6  $\mu$ g/mL protein for 45 s at 10  $\mu$ L/min (Protein A, Cytiva, USA). Next, 50 nM of the SARS-CoV-2 S1S2 monomer was injected for 300 s with or without compound concentrations in the range of 100  $\mu$ M to 6.4 nM and 5  $\mu$ M to 20 nM for CVRBDL-3 and -3\_3, respectively. All injections including compound were referenced with the corresponding injections of compound only on the immobilized hACE2, while the S1S2 injection without compound (before and after the concentration row) was referenced with a buffer only injection. For IC<sub>50</sub> validation, the responses at injection times of  $t = 750$  s were plotted against the log<sub>10</sub> of the used compound concentration. Data fitting was performed using a Boltzmann fit model (OriginPro 2020, OriginLab, Northampton, MA, USA):  $y = (A1 - A2)/(1 + e^{-(x - x_0)/dx}) + A2$  with A1 = initial value, A2 = final value,  $x_0$  = inflection point = IC<sub>50</sub>, and dx = time constant.

### 2.12. SPR Displacement Assay

The displacement assay was performed by hACE2-fc immobilization as described in the previous section. Next, 50 nM SARS-CoV-2 wt S1S2 was injected for 300 s at 30  $\mu$ L/min, followed by a dissociation recording of 1200 s. During dissociation, different concentrations of CVRBDL-3 and -3\_3 were injected in the range of 2  $\mu$ M to 0.63  $\mu$ M for 300 s. These injections were referenced with compound-only injections using the same concentration on the immobilized hACE2-fc. Data evaluation was performed by plotting the response at  $t = 1050$  s against the corresponding compound concentration. Displacement effects were fitted using a mono exponential decay model (OriginPro 2020, OriginLab, Northampton, MA, USA):  $y = y_0 + A e^{-x/t}$  with  $y_0$  = offset, A = amplitude, t = time constant, and  $t \frac{1}{2} = DC_{50} = t \ln(2)$ .

## 3. Results

### 3.1. Phage Display Selection on the SARS-CoV-2 RBD Target Protein

For identification of RBD binding peptide sequences, M13 phage display selection was performed on the biotinylated SARS-CoV-2 RBD target protein in three consecutive selection rounds (TS = target selection). The control selections on “empty” surfaces (same surfaces but without RBD) were either derived from selection rounds on the target (DC = direct control) or from a selection starting from the original library that was exclusively performed without target protein (ES = empty selection; Figure 1A).

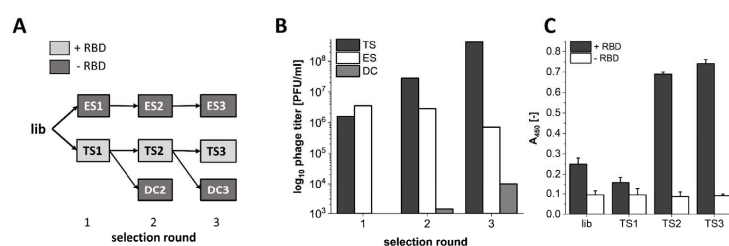


**Figure 1.** M13 phage display selection on SARS-CoV-2 RBD in three consecutive selection rounds. (A) Selection scheme: lib = naïve library; TS = target selection on RBD; DC = direct control; ES = empty selection. Samples are derived from each other in the direction of the connecting arrow starting with the naïve phage display library (lib). For TS, the selection target SARS-CoV-2 RBD was immobilized on a streptavidin-functionalized surface, while no target protein was immobilized for ES and DC. (B) Output phage titer in PFU/mL for selection samples of TS, ES and DC as measured past phage elution after biopanning. (C) Enrichment ELISA with input titer samples on the immobilized SARS-CoV-2 RBD selection target protein. Phage concentration was adjusted based on  $A_{265}$  UV-vis measurements to a total input of  $2.5 \times 10^{10}$  phages for all samples.

During the selection process, the success of target-related sequence enrichment was verified by determination of the PFU concentration in phage elution suspensions after biopanning (Figure 1B). Here, a 270-fold increase of the output titer was observed for the TS3 as compared to TS1, while an output titer reduction by a factor of ~5 was observed when no target was present during biopanning (ES3 compared to ES1). Likewise, the titer of TS derived samples decreased when a surface without target was used for the subsequent selection round (DC). In addition, the enrichment ELISA with the input titer phage samples showed a ~5-fold increase in end-point signal on the selection target, while a low signal was identified when no selection target was present (Figure 1C).

### 3.2. Analysis of Sequences Derived from NGS Sequencing

NGS sequencing of phage-isolated ssDNA yielded about 500,000 to 600,000 sequence reads per sample. In order to identify sequences that were enriched during phage display selection due to specific binding to the target protein, the TS3 sequences were filtered according to their enrichment on the target during the selection (lib < TS1, TS2 < TS3), their frequency in the target selection as compared to selections missing the target protein (TS1 > ES1, TS2 > ES2, TS3 > ES3), and the relative frequency decrease when a target-selection-derived sequence was subjected to a surface without target (TS2 > DC2, TS3 > DC3). In total, 90,000 unique sequences were identified that passed the filtering process. Analysis of the sequence enrichment (enrichment score [TS3/lib]) revealed that 18 unique sequences were enriched by a factor of 1000 or more. More than 50% of the total number of all sequence reads that passed the filter are represented by these 18 variants (Figure 2A). Additionally, 14 of the 18 sequences were identified with an ES of at least 1000 (empty score [TS3/ES3]), which underlines the target specificity of these sequences.

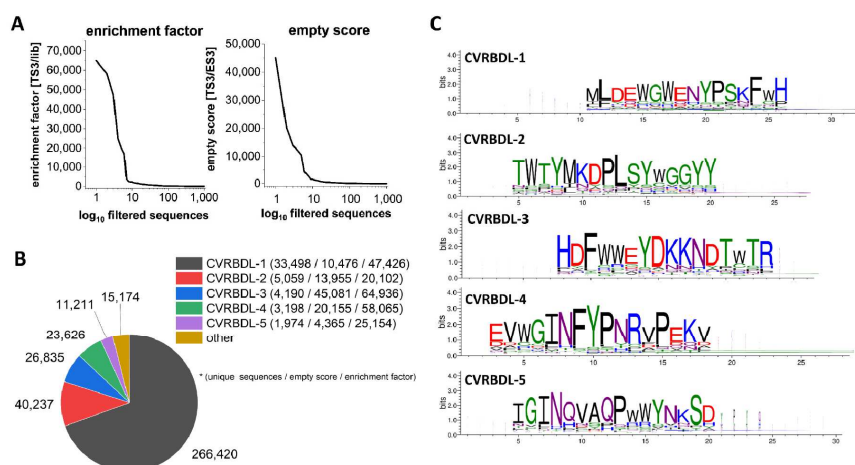


**Figure 2.** NGS sequence filtering and clustering reveals five main sequence motifs. (A) Evaluation of the enrichment factors (TS3/lib) and empty scores (TS3/ES3) of the first 1000 sequences as ranked by their enrichment factor or empty score, respectively. Sequences were filtered according to their enrichment on the target (lib > TS1 > TS2 > TS3), their frequency in the target selection as compared to the empty selection (TS1 > ES1; TS2 > ES2; TS3 > ES3) as well as their frequency decrease when the target selection was subjected to a surface without target (TS2 > DC2; TS3 > DC3). (B) Cluster distribution of the filtered sequences after three consecutive rounds of cluster extension and merging. The pie chart depicts the total number of sequences that were assigned to one cluster including multiple occurrences of identical sequences. The legend shows the number of unique sequences that were assigned to each cluster. Additionally, for each main sequence of the cluster, the specific empty score and enrichment factor is listed. (C) Conserved cluster motifs resulting from cluster assignments as shown in (B) derived by Hammock clustering software.

Next, the sequences were clustered according to their sequence homology in three consecutive rounds of cluster alignment and extension using Hammock clustering software (37). Clustering resulted in 16 clusters containing 57,712 unique and 383,503 total sequences, where ~96% of total sequence reads that passed the filter were assigned to five main clusters. The clusters were named CVRBDL-1 to -5, corresponding to the descending order of their total number of assigned sequence reads. The largest proportion by far, with over 70% of total sequence reads, was assigned to CVRBDL-1, followed by 10, 7, 6 and 3% for CVRBDL-2 to -5 (Figure 2B). Based on the sequence alignments, motifs were generated for each of the main clusters (Figure 2C), revealing five highly conserved sequence motifs, including amino acid residue variations, which can be used for potential sequence optimization steps. The amino acid residues with the highest occurrence at each position determined the peptide sequence of the peptides together with three C-terminally introduced arginines for enhanced solubility and C-terminal amidation: CVRBDL-1: MLDEWGWENYPskFwHRRR-NH<sub>2</sub>; CVRBDL-2: TWYMKDPLSYwGGYYRRR-NH<sub>2</sub>; CVRBDL-3: HDFWWEYDKKNDTwTRRRR-NH<sub>2</sub>; CVRBDL-4: EVwGINFYpNRvPEKvRRR-NH<sub>2</sub>; CVRBDL-5: IGINQVAQPwwYnkSDRRR-NH<sub>2</sub>.

### 3.3. Affinity of CVRBDL Peptides towards the SARS-CoV-2 RBD

To verify whether the compounds showed affinity towards the selection target, the biotinylated SARS-CoV-2 RBD, as already used for phage display selection, was immobilized on a streptavidin-derivatized sensor surface and the compounds CVRBDL-1 to -5 were injected as analytes in a multicycle SPR experiment, which was subsequently evaluated by steady-state analysis.

All of the tested peptides showed affinity towards the immobilized SARS-CoV-2 RBD in the low  $\mu\text{M}$  range as determined by steady-state analysis. As typical for peptides interacting with a folded binding partner, a transient binding behavior was detected for most of the compounds (Figure 3). However, the transient binding proportion CVRBDL-1 and -2 showed a partially slower complex decay, which can be recognized by a non-mono-exponential complex decay during the dissociation phase. This suggests that multiple binding sites for these peptides may exist, which would be a reasonable explanation for these sequences to be assigned as main sequences of the most prominent clusters as shown previously (Figure 2). Interestingly, the lowest affinity constant and therefore highest complex stability was identified for CVRBDL-3 with a  $K_D$  of  $1.3 \mu\text{M}$ , showing a  $\sim 70$ -fold higher affinity than the least stable interaction with CVRBDL-5.

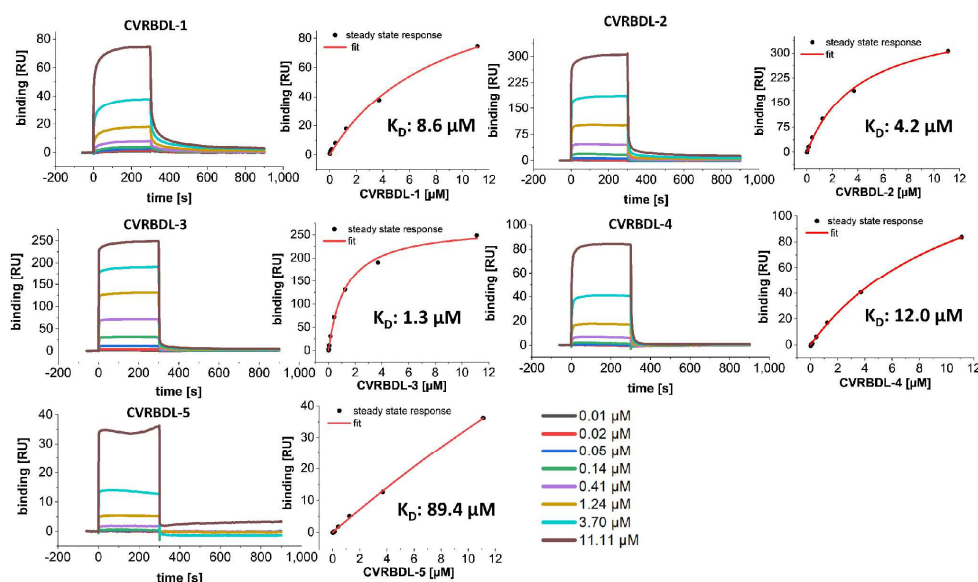


**Figure 3.** SPR affinity measurement of compounds CVRBDL-1 to -5 on the immobilized SARS-CoV-2 RBD selection target. The C-terminally biotinylated SARS-CoV-2 RBD was immobilized on a streptavidin-derivatized sensor surface in a T200 SPR device (SA, Cytiva, USA). The compounds were injected for 300 s with  $30 \mu\text{L}/\text{min}$  in a range of  $0.01$  to  $11.11 \mu\text{M}$  in  $10 \text{ mM}$  HEPES (pH 7.4),  $150 \text{ mM}$  NaCl,  $3 \text{ mM}$  EDTA,  $0.005\%$  (*v/v*) Tween-20. Surface regeneration in between cycles was performed using  $30 \text{ s}$  injections of an acidic regeneration cocktail (pH 5.0), ( $0.15 \text{ M}$  oxalic acid,  $0.15 \text{ M}$   $\text{H}_3\text{PO}_4$ ,  $0.15 \text{ M}$  formic acid,  $0.15 \text{ M}$  malonic acid). The  $K_D$  was determined by steady state fit as follows: CVRBDL-1:  $8.6 \mu\text{M} \pm 1.3 \mu\text{M}$ ; CVRBDL-2:  $4.2 \mu\text{M} \pm 0.38 \mu\text{M}$ ; CVRBDL-3:  $1.3 \mu\text{M} \pm 0.12 \mu\text{M}$ ; CVRBDL-4:  $12.0 \mu\text{M} \pm 0.87 \mu\text{M}$ ; CVRBDL-5:  $89.4 \mu\text{M} \pm 32.0 \mu\text{M}$ .  $K_D$  evaluation was performed using the Biacore T200 data evaluation software v. 3.2 with offset set to zero.

Further, binding properties of the peptide CVRBDL-3 to the RBD domain were investigated by solution NMR spectroscopy. Two-dimensional  $^1\text{H}$ - $^{15}\text{N}$  HMQC (Heteronuclear Multiple Quantum Coherence) spectra of an 0.85 mM RBD domain sample (unlabeled, natural abundance) were recorded using a Bruker AvanceNeo 1.2 GHz spectrometer (Figure 4), as described in the Material and Methods section. Figure 4A shows the  $^1\text{H}$ - $^{15}\text{N}$  correlation spectrum of the RBD domain. Roughly, every resonance in the spectrum corresponds to one amino acid residue of the protein sequence, with the nitrogen resonance correlated to the proton resonance of the backbone amide group. Therefore, the HMQC spectrum serves as a “fingerprint” of the protein. Because of the natural abundance of the  $^{15}\text{N}$  isotope of only 0.37%, the “NMR active” concentration of the 0.85 mM RBD sample corresponds to about 3  $\mu\text{M}$ . Therefore, presumably only the most intense (most dynamic) residues of the RBD domain are visible in the spectra, while the more rigid regions stay below the detection threshold and thus remain invisible.

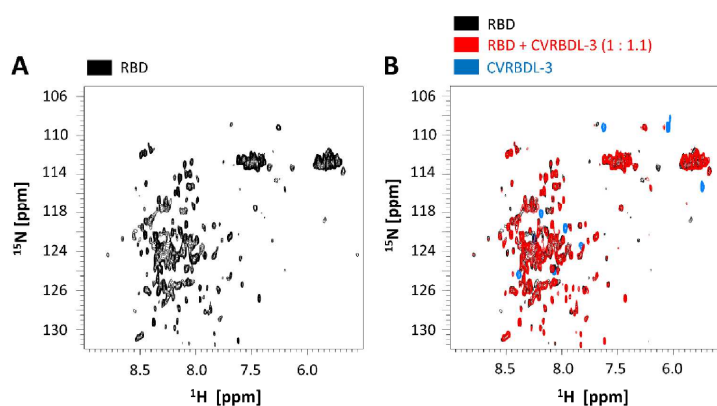


**Figure 4.** Two-dimensional  $^1\text{H}$ - $^{15}\text{N}$  HMQC spectra (at 1.2 GHz proton frequency) of the RBD domain (natural abundance) in absence (A) and presence (B) of the peptide CVRBDL-3. (A) Reference spectrum of the RBD alone. (B) The spectrum of the RBD domain alone (black) is overlaid with the spectra of the RBD in presence of the peptide (red), as well as the isolated peptide (blue).

Next, the CVRBDL-3 peptide was added to the RBD domain at a molar ratio of about 1.1:1 (peptide: RBD domain). The resulting spectrum showed decreased intensities for several resonances of the RBD domain (Figure 4B, red spectrum), compared to the reference spectrum of the unbound RBD (black). A possible explanation is that residues involved in the binding become more rigidified upon peptide interaction, leading to decreased intensities, as a result of faster transverse relaxation. A second reference spectrum of the peptide only was recorded (blue, Figure 4B). Interestingly, the resonances of the peptide (natural abundance, 1.1 higher concentration than the RBD domain) disappear in the spectra of the RBD plus peptide sample (Figure 4B, red spectrum), clearly indicating binding. Presumably, the peptide binds to the more rigid (invisible) region of the RBD and therefore becomes invisible as well (as it assumes the same NMR relaxation properties as the invisible part of the RBD).

#### 3.4. Inhibition of the SARS-CoV-2 S1S2 Spike Protein Interaction with hACE2

Phage display selection was combined with NGS to identify peptides that target the SARS-CoV-2 RBD with medium to low  $\mu\text{M}$  affinities. To further verify whether the CVRBDL peptides are able to interfere with the association of the spike protein towards

hACE2, SPR-based inhibition assays were performed. hACE2-fc was immobilized on a protein A-derivatized sensor surface and the monomeric SARS-CoV-2 S1S2 protein (ectodomain of the spike protein) was injected as an analyte together with or without a 100-fold molar excess of one of the CVRBDL peptides.

Three out of five peptides (CVRBDL-2, -3 and -4) were able to interfere with association of the monomeric S1S2 spike protein to hACE2 in our experimental setup, which can be recognized by a reduction in the binding signal of the S1S2 protein to hACE2 in the steady-state phase upon compound addition (Figure 5A). Here, CVRBDL-3 showed the strongest inhibitory effect by a steady-state reduction of ~33% as compared to the setup without compound. CVRBDL-2 and -4 reduced the steady-state signal only by ~10 and 5%, respectively (Figure 5B). To verify whether the effect observed for CVRBDL-3 was concentration-dependent, compound concentrations in the range of 6.4 nM to 100  $\mu$ M were applied to the inhibition setup.

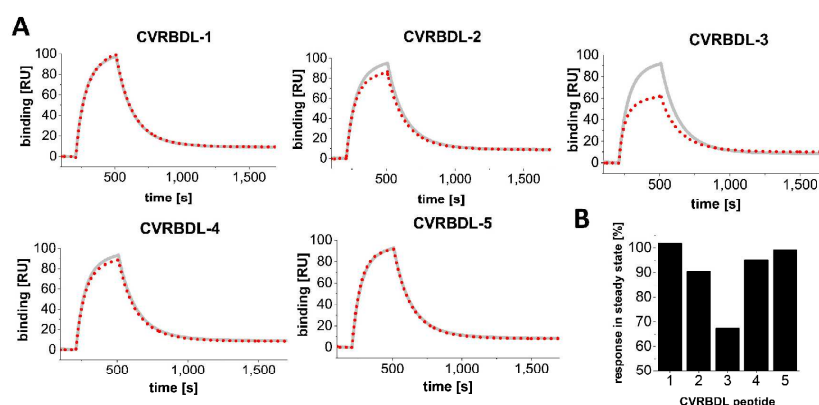


**Figure 5.** SPR inhibition assay of SARS-CoV-2 S1S2 spike interaction to hACE2 with and without compounds CVRBDL-1 to -5. (A) hACE2-fc was immobilized on a protein A/G derivatized sensor surface in a T200 SPR device (Cytiva, USA). 50 nM SARS-CoV-2 S1S2 was injected with (red dotted line) or without (solid grey line) 5  $\mu$ M of compounds CVRBDL-1 to -5. Prior to each injection of S1S2 with compound, a separate injection without compound was performed. All injections with compound were referenced with compound-only injections on the hACE2 immobilized surface. Injections were performed with a flow rate of 30  $\mu$ L/min in 10 mM HEPES (pH 7.4), 150 mM NaCl, 3 mM EDTA, 0.005% (v/v) Tween-20. (B) Relative steady state responses of the injections with compound as detected 270 s after injection start. CVRBDL-3 shows the strongest inhibitory effect with a steady-state reduction of ~33% as compared to SARS-CoV-2 S1S2 injection without compound.

When CVRBDL-3 is applied with increasing molar ratios concerning the SARS-CoV-2 S1S2 protein, a concentration-dependent inhibition of the S1S2-hACE2 complex formation can be observed (Figure 6A). Surprisingly, the compound was not able to inhibit the complex formation completely, which can be attributed either to an insufficient steric inhibition of the hACE2 accessibility or to an inherent heterogeneity of the S1S2-hACE2 complex. The latter has already been described by us previously [42], where we identified the S1S2-hACE2 complex formation as undergoing a two-state reaction binding behavior. In this context, the compound CVRBDL-3 is able to block the primary association of the RBD with hACE2 but possibly not the secondary state transition, which is inherent to the already formed complex. However, although CVRBDL-3 is not able to completely suppress the spike protein association to hACE2, the inhibitory effect can be characterized

with an  $IC_{50}$  of 532 nM by Boltzman sigmoidal fitting, showing a maximum inhibitory saturation level of ~58% (Figure 6B).

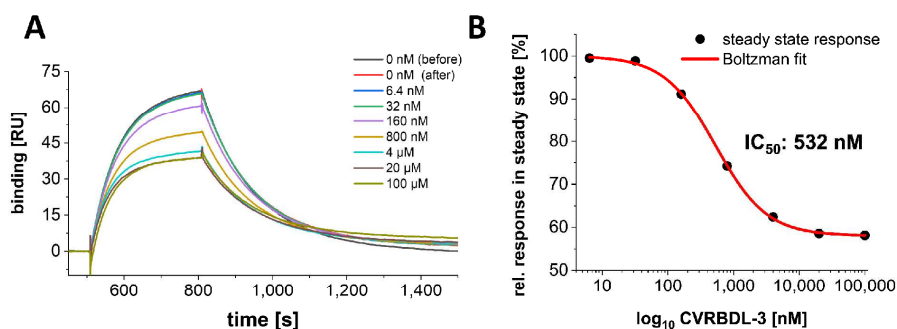


**Figure 6.** Concentration dependency of the inhibitory effect of CVRBDL-3 on the SARS-CoV-2 S1S2 interaction with hACE2. (A) hACE2-fc was immobilized on a protein A/G derivatized sensor surface in a T200 SPR device (Cytiva, USA). 50 nM SARS-CoV-2 S1S2 was injected with or without 6.4 nM to 100  $\mu$ M CVRBDL-3. Injections without compound were performed prior and after the concentration row to demonstrate reproducibility of the S1S2 binding level. All injections with compound were referenced with the corresponding concentration of compound only injections on the hACE2 immobilized surface. Injections were performed with a flow rate of 30  $\mu$ L/min in 10 mM HEPES pH 7.4, 150 mM NaCl, 3 mM EDTA, 0.005% (*v/v*) Tween-20. (B) Relative response in steady as detected at  $t = 750$  s. The inhibitory effect of CVRBDL-3 saturates at ~58% of the S1S2 binding level without compound. The  $IC_{50}$  was determined by a Boltzman sigmoidal fit to be 532 nM (OriginPro, OriginLab, USA).

### 3.5. Tail-To-Tail Construct Design: CVRBDL-3\_3

In order to further increase the compound affinity towards the SARS-CoV-2 spike protein, we created a tail-to-tail construct of the compound CVRBD-3 leading to a divalent compound. This construct, named CVRBDL-3\_3, consists of a lysine with two CVRBDL-3 molecules covalently linked with their C-termini to the  $\alpha$ - and  $\epsilon$ -amino groups of the lysine via linkers each consisting of  $\gamma$ -aminobutyric acid (Abu) and arginine (Figure 7). The tail-to-tail connection was expected to retain the availability of the N-termini of the CVRBDL-3 moieties, which was also exposed during phage display selection as the N-terminal extension of the M13-phage coating protein pIII.

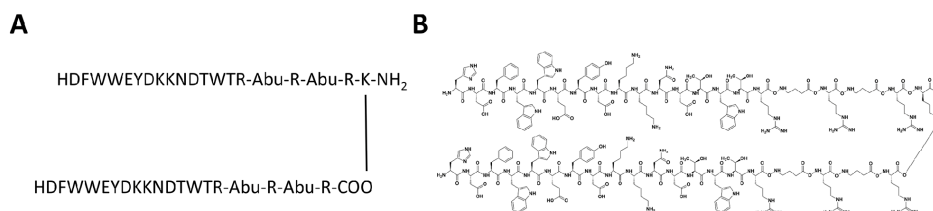


**Figure 7.** Amino acid single letter sequence and Natta projection of peptide construct CVRBDL-3\_3. CVRBDL-3\_3 was created by C-terminal attachment of two CVRBDL-3 sequences via the side chain primary amino group of a C-terminal introduced lysine. Each of the peptides carries a C-terminal [-Abu-R-Abu-R-] spacer region for increased binding flexibility and spacing of binding regions (Abu =  $\gamma$ -amino butyric acid). (A) Single letter amino acid CVRBDL-3\_3 sequence. (B) Natta projection of the CVRBDL-3\_3 sequence.

### 3.6. CVRBDL-3\_3 Shows Increased Affinity for the CoV-2 Spike Protein Compared with CVRBDL-3

We compared the affinity of the single peptide CVRBDL-3 and the tail-to-tail combination CVRBDL-3\_3 to the poly-His tagged spike protein constructs of SARS-CoV-2 RBD, S1S2 monomer and the S1S2 trimer using SPR analysis. SARS-CoV-2 RBD, S1S2 monomer and S1S2 trimer were immobilized via primary amino group coupling on a polycarboxylate sensor surface and the compounds were injected in a multicycle experiment using concentrations in the range of 0.04 to 5  $\mu$ M. The subsequent evaluation was performed by steady-state analysis (Figure 8).

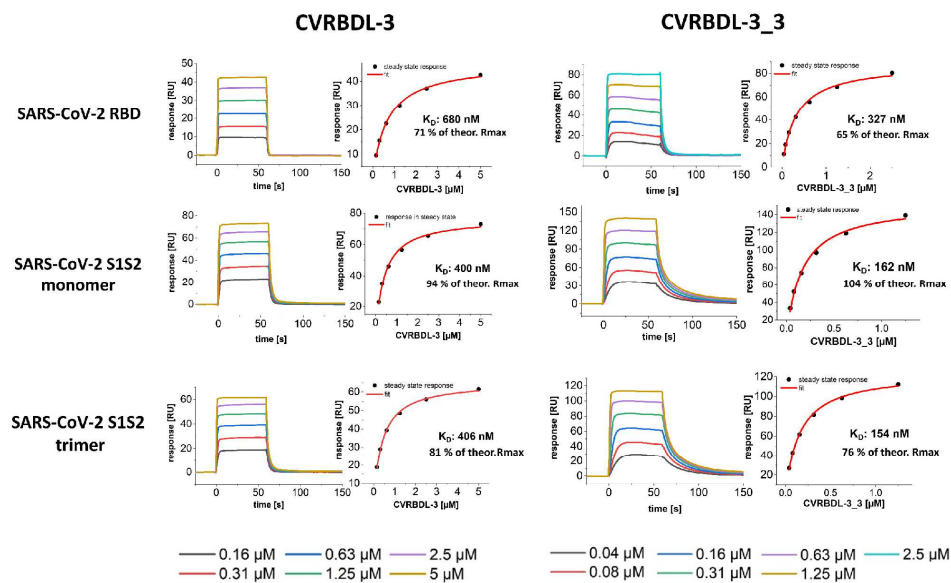


**Figure 8.** SPR affinity measurement of CVRBDL-3 and CVRBDL-3\_3 on the SARS-CoV-2 RBD, S1S2 monomer and trimeric spike constructs. The spike constructs were immobilized on a polycarboxylate matrix by coupling via primary amino groups with sulfo-NHS ester at pH 5.5 (200 HCM, Xantec, GE). Measurements were performed in 10 mM HEPES (pH 7.4), 150 mM NaCl, 3 mM EDTA, 0.005% Tween-20 solution in a T200 device (Cytiva, USA). Six concentrations of each compound were injected for 60 s with a 1:1 serial dilution, with 5  $\mu$ M being the highest concentration for CVRBDL-3 and 2.5  $\mu$ M for CVRBDL-3\_3.  $K_D$  evaluation was performed using Biacore T200 data evaluation software v. 3.2 with an offset of zero. The theoretical  $R_{max}$  was calculated based on the molecular weight ratio of the interactants and the immobilization level after quenching.

The interaction of CVRBDL-3 towards the SARS-CoV-2 RBD was identified to be ~two-fold more affine than for the original biotinylated selection target ( $K_D$ : 680 nM vs. 1.3  $\mu$ M, respectively), whereas slightly higher affinities were determined for the S1S2 monomer and the trimeric S1S2 ( $K_D$ : 400 and 406 nM, respectively). As already observed during affinity measurement on the selection target protein, CVRBDL-3 shows again a transient binding behavior for all of the tested spike protein constructs. Additionally, the identified  $R_{max}$  was found to be lower than the theoretical  $R_{max}$  for all measurements, which indicates a 1:1 binding stoichiometry. Notably, the CVRBDL-3 binding is not influenced

when the RBD is presented in the context of the monomeric and trimeric spike ectodomain. This implies that the interaction of CVRBDL-3 with the RBD binding epitope is not significantly disturbed by the RBD switch between “up-” and “down-” conformations.

CVRBDL-3\_3 shows increased binding affinity as compared to the single peptide alone. The complex stability increased by a factor of ~2 towards the RBD ( $K_D$ : 327 nM) and by a factor of ~2.5 towards the monomeric and trimeric S1S2 ( $K_D$ : 162 and 154 nM, respectively). The binding kinetics changed for CVRBDL-3\_3 as compared to CVRBDL-3 from a transient binding mode with fast dissociation to a more stable complex with partially slower dissociation. However, the kinetics cannot be described with a 1:1 stoichiometric Langmuir binding behavior, indicating a distinct binding mode. Moreover, the bivalent analyte model was not able to sufficiently describe the interaction’s heterogeneity. A possible explanation could be that the aforementioned continuous position switching between ‘up’ and ‘down’ conformations of the SARS-CoV-2 RBD does not influence the interaction with CVRBDL-3 on the one side, but potentially restricts the association of CVRBDL-3\_3 on the other site. This interference possibly hinders the assignment of a clear kinetic model to the observed sensograms. However, since the binding kinetics of CVRBDL-3\_3 appears almost identical for monomeric and trimeric S1S2, a simultaneous binding of two RBD located epitopes with an increased avidity seems implausible, leaving room for further optimization of the linker length.

### *3.7. CVRBDL-3 and CVRBDL-3\_3 Show High Affinity for the B.1.1.7 Mutant Spike Trimer and Bind the SARS-CoV (2002) and SARS-CoV-2 “Closed” RBD Trimer with Reduced Affinity*

We have previously shown that the compounds CVRBDL-3 and -3\_3 show high affinity with nM binding constants towards the SARS-CoV-2 RBD, S1S2 monomer and trimer. Here, we additionally verify whether the binding specificity of the compounds is limited to the “wt” of SARS-CoV-2 spike protein or can also be extended to mutant versions, where some have been found to show enhanced affinity for the cellular receptor hACE2. Therefore, we analyzed the binding affinity of the compounds towards the SARS-CoV-2 B.1.1.7 S1S2 trimeric spike mutant ( $\alpha$ -variant) as a model for other emerging variants of the spike protein. In total, seven amino acid sequence positions differ between SARS-CoV-2 “wt” spike protein and the B.1.1.7 variant, whereas four mutations are located at intermolecular interaction sites of the subunits and one mutation, namely N501Y, is found in the RBM of the RBD [43]. This amino acid residue substitution has been shown to increase the binding affinity for the hACE2, which may be one of the reasons for the observed four to six-fold increase in transmissibility in cooperation with other mutations that do not directly interfere with receptor binding but enhance binding e.g., by increasing RBD flexibility such as D614G [44–46].

The affinity measurement on the trimeric B.1.1.7 (Figure 9) shows clearly that the binding affinity of neither CVRBDL-3 nor -3\_3 is influenced by the mutation sites of the B.1.1.7 variant. Similar binding constants as already identified for the SARS-CoV-2 “wt” S1S2 spike protein were identified (528 and 243 nM for -3 and -3\_3), whereas the binding kinetics shows a clear transient binding mode for CBRBDL-3 and higher complex stability with slower complex decay for CVRBDL-3\_3. Since the SARS-CoV 2002 RBD shares 73% sequence identity and high structural similarity with the SARS-CoV-2 “wt” RBD [47], we speculated that the compounds are also able to bind the COVID 2002 trimeric spike protein with high affinity.

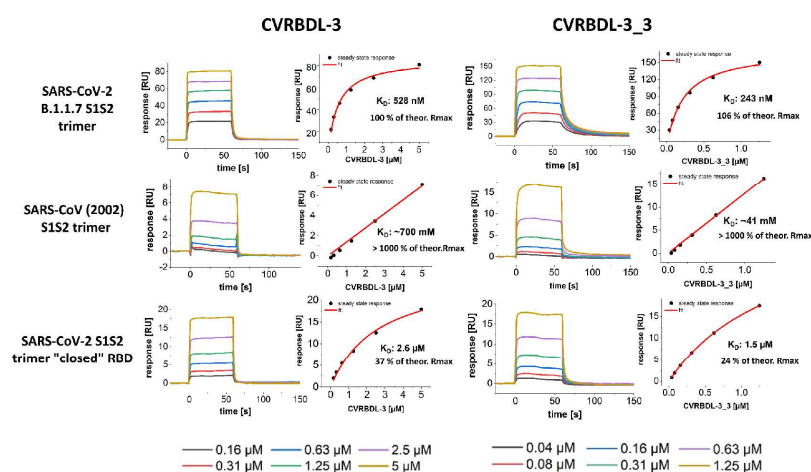


**Figure 9.** SPR affinity measurement of CVRBDL-3 and tail-to-tail construct CVRBDL-3\_3 on the SARS-CoV-2 B.1.1.7 trimer spike, SARS-CoV (2002) trimer and the SARS-CoV-2 “closed” RBD trimeric spike. The spike constructs were immobilized on a polycarboxylate matrix by coupling via primary amino groups with sulfo-NHS ester at pH 5.5 (200 HCM, Xantec, GE). Measurements were performed in 10 mM HEPES (pH 7.4), 150 mM NaCl, 3 mM EDTA, 0.005% Tween-20 in a T200 device (Cytiva, USA). Six concentrations of each compound were injected for 60 s with a 1:1 serial dilution, with 5  $\mu$ M being the highest concentration for CVRBDL-3 and 1.25  $\mu$ M for CVRBDL-3\_3.  $K_D$  evaluation was performed using Biacore T200 data evaluation software v. 3.2 with the offset set to zero. The theoretical  $R_{max}$  was calculated based on the molecular weight ratio of the interactants and the immobilization level after quenching.

The affinity measurements, however, show that CVRBDL-3 and -3\_3 do not have any affinity for this construct (both  $K_D$ 's in high mM range). Next, we verified the binding affinity towards the “closed” SARS-CoV-2 trimer [48]. For construct design, the spike protein was manipulated by the replacement of amino acid residues at positions 383 and 985 with cysteines in order to form a disulfide bond that fixes the RBD in its “down” position. Hence, the relevant positions for interaction with hACE2 are masked in this construct. When the compounds' affinities were determined for this RBD “down” fixed S1S2 construct, significantly decreased affinities were observed. Additionally, the experimental  $R_{max}$  reached only 32 and 24% of the theoretical  $R_{max}$  for CVRBDL-3 and -3\_3, respectively.

### 3.8. CVRBDL-3\_3 Efficiently Inhibits the Spike-hACE2 Complex Formation and Displaces the Spike Protein from the Pre-Formed Complex

The tail-to-tail combination of the two CVRBDL-3 peptides achieved (CVRBDL-3\_3) increased binding affinities and decreased dissociation rates for the different SARS-CoV-2 constructs. Moreover, CVRBDL-3\_3 retained its target specificity and the high binding affinity towards the SARS-CoV-2 B.1.1.7 mutant spike protein. Here, we compared CVRBDL-3 and CVRBDL-3\_3 concerning their ability to (i) inhibit complex formation of the SARS-CoV-2 S1S2 monomer with hACE2 and (ii) displace the spike protein from the pre-formed complex, consisting of the S1S2 monomer and hACE2. Two experimental set-ups allowed a complete evaluation of the compound's effectiveness in either pre- or post-complex formation conditions.

We injected constant concentrations of the monomeric S1S2 spike protein with or without increasing CVRBDL-3\_3 concentrations on the immobilized hACE2 receptor.

As already observed for CVRBDL-3, CVRBDL-3\_3 also shows a concentration-dependent reduction of the SARS-CoV-2 S1S2 association towards hACE2 (Figure 10A). Interestingly, the inhibition saturates at 58% of the binding level without compound, which is identical with the saturation level that was previously identified for CVRBDL-3. Evaluation of the  $IC_{50}$  (Figure 10B) shows that the inhibition efficiency of complex formation increased by a factor of ~11 as compared to CVRBDL-3 (532 nM as compared to 47 nM for CVRBDL-3 and CVRBDL-3\_3, respectively).

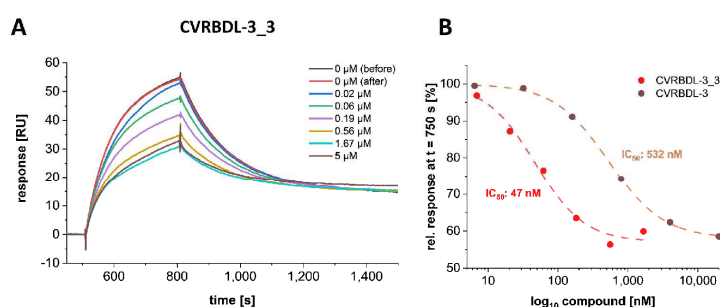


**Figure 10.** CVRBDL-3\_3 much more efficiently inhibits the SARS-CoV-2 S1S2 spike protein interaction with hACE2 as compared to CVRBDL-3. (A) hACE2-fc was immobilized on a Protein A/G-derivatized sensor surface in a T200 SPR device (Cytiva, USA). 50 nM SARS-CoV-2 S1S2 was injected with or without 6.4 nM to 100 μM CVRBDL-3\_3. Injections without compound were performed prior and after the concentration row to verify reproducibility of the S1S2 binding level. All injections with compound and spike protein were referenced with the corresponding concentration of compound only injections on the hACE2 immobilized surface. Injections were performed with 30 μL/min in 10 mM HEPES (pH 7.4), 150 mM NaCl, 3 mM EDTA, 0.005% (*v/v*) Tween-20. (B) Relative response in steady state as detected 270 s after injection start (for CVRBDL-3 see Figure 6). The inhibitory effect of CVRBDL-3 and CVRBDL-3\_3 saturates at ~58% of the S1S2 binding level without compound. The  $IC_{50}$  was determined by Boltzman sigmoidal fit to be 532 nM (OriginPro, OriginLab, USA).

Next, we analyzed the effectiveness of CVRBDL-3 and -3\_3 in displacing SARS-CoV-2 S1S2 monomers from the pre-formed complex with hACE2. For this assay, a constant concentration of monomeric S1S2 was injected on pre-immobilized hACE2 for all injection cycles. During dissociation, increasing concentrations of the compounds were applied to the pre-formed complex.

The sensogram course during compound injection indicates whether the compound presence accelerates the complex decay by shifting the equilibrium between hACE2 bound and unbound spike protein to the dissociated form (Figure 11A,B). For both compounds, the effect of spike protein displacement was observed by a concentration-dependent acceleration of signal reduction during the compound injection phase. When the remaining signal at  $t = 1050$  s was plotted against the injected compound concentration, the concentration dependent effect is best described with a mono-exponential decay function (Figure 11C). Here, again CVRBDL-3\_3 shows an enhanced effect as compared to CVRBDL-3. Although the concentration needed for reaching 50% of the maximum displacement just slightly differs between the two compounds ( $DC_{50}$ : 510 and 417 nM for CVRBDL-3 and 3\_3, respectively), the maximum displacement of CVRBDL-3\_3 surpasses the one observed for CVRBDL-3 by a factor of 1.6 ( $y_{0}$ : 84 and 74% for CVRBDL-3 and 3\_3, respectively).

Further analysis in an SPR-based experiment using the isolated SARS-CoV-2 S1S2 spike and hACE2 proteins demonstrated that CVRBDL-3 inhibits the complex formation when it is injected together with the monomeric S1S2 spike protein on the immobilized hACE2 (Figure 5). CVRBDL-3 also displaced hACE2 from the spike protein when the complex was already preformed (Figure 11). These two experimental SPR set-ups resemble physiological conditions where the virus has either not attached to the cell surface or the spike protein is already attached to the cellular receptor. A potent inhibitor targeting fusion inhibition can be expected to interfere with pre- as well as post-complex formation states. Because CVRBDL-3 is efficient in both, the targeted binding site of CVRBDL-3 on the RBD surface appears to be critical for its complex formation with hACE2 and remains at least partially accessible for CVRBDL-3 once the complex with hACE2 has been formed.

The divalent version of CVRBDL-3, CVRBDL-3\_3, had a two- to three-fold higher affinity for the SARS-CoV-2 spike protein (RBD, S1S2 monomer, S1S2 trimer) as compared to CVRBDL-3. The dissociation rates for the interaction of CVRBDL-3\_3 with monomeric and trimeric S1S2 were substantially decreased for CVRBDL-3\_3. Because there was no difference between the  $K_D$  values of CVRBDL-3\_3 and monomeric and trimeric SARS-CoV-2 S1S2 spike protein (Figure 8), we conclude that the designed divalent binding mode was realized, but the increased affinity is much more likely due to the increased local concentration of the CVRBDL-3 moiety leading to decreased dissociation rates due to enhanced rebinding effects [49]. This leaves room for much more enhanced affinities by optimizing the linker length within CVRBDL-3\_3 in the future. Nevertheless, CVRBDL-3\_3 demonstrated increased binding affinity as compared to CVRBDL-3 in pre- as well as in post-complex formation conditions (Figures 10 and 11).

To further verify the binding specificity of CVRBDL-3 and CVRBDL-3\_3, we tested their affinity towards the trimeric spike protein constructs of SARS-CoV-2 B.1.1.7, SARS-CoV (2002) and a “closed” SARS-CoV-2 spike, for which the RBD was fixed in a “down” position. CVRBDL-3 and CVRBDL-3\_3 bind the B.1.1.7 mutant spike protein as efficiently as the “wt” spike trimer. This finding supports the idea that inhibitory binding sites do not necessarily overlap with the typical VOC mutational sites and thus future emerging variants may still be vulnerable to the compounds. On the other hand, the spike protein of the “old” SARS-CoV virus from the year 2002 did not show efficient binding by CVRBDL-3 and CVRBDL-3\_3. This result indicates that the binding site and the observed inhibitory effect of CVRBDL-3 and CVRBDL-3\_3 is specific for SARS-CoV-2 and probably not interchangeable with other SARS coronaviruses. The binding affinity, as well as the fraction of the theoretical  $R_{max}$  that is achieved towards the “closed” RBD trimeric CoV-2 constructs, is substantially decreased compared to the non-manipulated “wt” version. This result points to a decisive role of the inaccessible regions in the “closed” trimer for interaction with the compounds.

In conclusion, affinity measurements clearly show that the CVRBDL-3 and CVRBDL-3\_3 compounds target a binding site of the RBD that (i) is specific to SARS-CoV-2, (ii) is conserved in a mutant version, (iii) shows reduced accessibility in the “closed” conformation, and finally (iv) is critical for the interaction with hACE2. Phage display is an appropriate strategy for the identification of potent SARS-CoV-2 fusion inhibitors. This concept is not limited to coronaviruses only, but is transferable to other viruses, opening an option for a general and straightforward identification of drug compounds against novel emerging VOCs. The presented compound selection strategy yields small peptide compounds that are not template-protein-derived and thus are less likely prone to exhibit undesired side effects under physiological conditions. This can, for example, be expected for hACE2-template-based peptides [50,51]. The expected poor bioavailability of such L-enantiomeric peptide therapeutics may be overcome by their conversion into D-enantiomeric derivatives, for example by “retro-inverso” strategies [52] that endow all-D-enantiomeric peptide compounds with enhanced proteolytic stability [53] but conserve binding

specificity and affinity. After optimization of proteolytic stability and binding affinity, future studies will first address testing of the optimized compounds in viral proliferation assays to ensure transferability of the observed effects to the cellular level.

**Author Contributions:** Conceived and designed the project outline: M.S. (Marc Sevenich), J.M. and D.W.; planned and performed experiments: phage display (M.S. (Marc Sevenich), E.T. and J.M.); next-generation sequencing (M.S. (Marc Sevenich) and P.P.); expression and purification of COVID and hACE-2 constructs (T.K., M.S. (Marc Sevenich), F.B. and J.v.d.H.); nuclear magnetic resonance (M.S. (Marc Sevenich) and N.-A.L.); surface plasmon resonance (M.S. (Marc Sevenich)); wrote the manuscript: M.S. (Marc Sevenich) and D.W. with the help of all other authors. All authors have read and agreed to the published version of the manuscript.

**Funding:** N.-A.L. thanks the German Science Foundation (DFG, grant project number 433700474) for funding as well as support by the project “Virological and immunological determinants of COVID-19 pathogenesis – lessons to get prepared for future pandemics (KA1-Co-02 “COVIPA”)", a grant from the Helmholtz Association's Initiative and Networking Fund.

**Institutional Review Board Statement:** Not applicable.

**Informed Consent Statement:** Not applicable.

**Data Availability Statement:** The data presented in this study are available on request from the corresponding author.

**Acknowledgments:** Computational support of the Zentrum für Informations- und Medientechnologie, especially the HPC (High Performance Computing) team at the Heinrich Heine University Düsseldorf is acknowledged.

**Conflicts of Interest:** M.S., J.M. and D.W. are co-inventor of patents covering the composition of matter of CVRBDL-peptides. All other authors declare no competing interest.

## Appendix A

**Table A1.** SARS-CoV, SARS-CoV-2 spike protein and hACE2 constructs used in the study including organism used for expression, introduced tags for multimerization and purification, molecular weight (MW) and experimental usage.

Construct Name	Expression Organism	Tag	Mw Monomer [kDa]	Experimental Usage
SARS-CoV-2 RBD (Acrobiosystems)	HEK293 cells	Avitag, 6xHis-tag	28.2	Phage display screening, affinity screening
SARS-CoV-2 RBD	High Five insect cells	6x His-tag	31.8	Affinity measurement with CVRBDL-3 and CVRBDL-3_3, NMR
SARS-CoV-2 S1S2-His	High Five insect cells	6x His-tag	133.13	Inhibition and displacement analysis with CVRBDL-3 and CVRBDL-3_3
SARS-CoV (2002) S1S2-His trimer	High Five insect cells	6x His-tag	132.4	Affinity measurement with CVRBDL-3 and CVRBDL-3_3
SARS CoV-2 S1S2 trimer	High Five insect cells	6x His-tag, T4-foldon	141.9	Affinity measurement with CVRBDL-3 and CVRBDL-3_3
SARS CoV-2 B.1.1.7 S1S2	High Five insect cells	6x His-tag, T4-foldon	141.6	Affinity measurement with CVRBDL-3 and CVRBDL-3_3
hACE2	HEK293-6E cells	IgG1-Fc	95.2	Inhibition and displacement analysis with CVRBDL-3 and CVRBDL-3_3

SARS-CoV-2 S1S2-His monomer (M<sub>w</sub>: 133.13 kDa)

```

10      20      30      40      50      60
MAQCWLTTR TQLPFAVYNS FTRGVYYPDK VFRSSVLHST QDLFLPFFSN VVWFHAI SGT
70      80      90      100     110     120
NGTKRRFMFV LPFNDGVYFA STEKSNIIIRG WIFGTTLDSK TQSLLLVNNNA TNVWIKVCEP
130     140     150     160     170     180
QFCMDFTLGV YHKNNKSRME SEFRVYSSAN NCTFTVYVSP FLMDLGGKQG NFKMLREYVF
190     200     210     220     230     240
KNIDGYFKIY SKHTFINLVR DLPQGFSALE PLVDLEIGIN ITRFQTLLAL HRSYLTFGDS
250     260     270     280     290     300
SSGWTAGAAA YVGVYLOPRT FLLKYNENGT ITDAVDCALD PLSETRKTLK SFTVEKGIYQ
310     320     330     340     350     360
TSNERVQPTF SIVRFENITN LCPFGEVFNA TRPASVYAMN RKRISNCVAD YSVLYNSASF
370     380     390     400     410     420
STFKCYGVSP TKLNDLCFTN VYADSFVIRG DEVRQIAPGQ TGIADYNYK LPDDFTFGCVI
430     440     450     460     470     480
AMNSNLDLSE VGGNYRFLYR LFRKSNLKEP ERDISTEIIYQ AGSTPCNGVE GFNCYFTLQS
490     500     510     520     530     540
YGFQPTYGVG YQPYRVVLS FELLHAPATV CGPKKSNLV KMKCVNFINN GLTGTGVLTE
550     560     570     580     590     600
SNKRFLFPQQ FGRDIDTTD AVRDFQTLEI LDITPCSPGG VSVITFGTNT SNQVAVLYQG
610     620     630     640     650     660
VNCTEYFVAI HADQLTFTMR VYSTGSNVFO TRAGCLIGAE HVNMSYCDI PIGAGLGSY
670     680     690     700     710     720
QPTNSHGSA SVASQSIIA YIMSLGAENS VAYSNNISAI PINFTISVIT EILFVSMTRK
730     740     750     760     770     780
SVDCVTYICG DSTECNMLLL QVGSFCTQLN RALITGLAVED DMKQVDFVQ VKQIYKTFPI
790     800     810     820     830     840
KDFGFGNFSC ILEDFSKPSK RSPFIEDLLEN KVTLDAGFI KQVGDCLGDI AARDLICQKR
850     860     870     880     890     900
ENGLTVLPLF LTDEMLAQYT SALLAGTITS GWTFGAAGAL QIFFAMQMY RFNGIGVTQN
910     920     930     940     950     960
VLYENKDLIA NQFNSLGIKI QSLSSSTASA LGLKLDVNVQ NAQALATLVK QLSLSNFAIS
970     980     990     1000    1010    1020
SVINDILARL DPPEAEVQID RLITGRLQSL QTVVYQQLIR AAARASANL AATRMSECVL
1030    1040    1050    1060    1070    1080
GQSKRVDFCG KGYHLSFFQ SAPHGVTFLH VTYVFAQERN FTTAPAIQCHD GRAHFFREGV
1090    1100    1110    1120    1130    1140
FVSNGTNHFV TQRNFYEQI ITHNTVEVSG NCDVVIQVNV NTVYDELOPE LDSFKEELDK
1150    1160    1170    1180    1190    1200
YFKNHTSPDV DLGDISGINA SVVNIQKEID RLNEVARNLN ESLIDLQELG KYEQAAA

```

SARS-CoV (2002) S1S2-His trimer without foldon sequence (M<sub>w</sub> monomer: 132.4 kDa)

```

10      20      30      40      50      60
MGSDLRCTT FDDVQAPNYT QHTSMRGVY YPDEI FRSDT LVLTDLFLP FYSNVTFHT
70      80      90      100     110     120
INHYTEENVI PFKDGIYFAA TEKSNVGRGW VFGSTNNKKS QSVILINHSI NVVIRAGNFE
130     140     150     160     170     180
LCDNPFPAVS KFMGTQTHM IFDNAFNCTF EYISDAFSLD VSEKSGNFKH LREFVFNKD
190     200     210     220     230     240
GFLYVYKGIQ PIDVNRLEFS GFNLIKRFIFK LPLGIMTINF RALLTAESFA QDTWTSAAA
250     260     270     280     290     300
YFVGYLKPIT FMLKYDENGIT IDAVDCSQN PLAEKCSVK SFEIDKGIYQ TSNFRVPSG
310     320     330     340     350     360
DVVRFPHITN LCPFGEVFNA TKFPSVVAWE RKKISNCVAD YSVLYNSTFF STFKCYGVA
370     380     390     400     410     420
TKLNDLSESN VYADSFVIRG DEVRQIAPGQ TGVIAADYNYK LPDDFTFGCVL AMNTRMLDAT
430     440     450     460     470     480
STGNVNYKYR YLRHGKLRPF ERDISNVFSS PDGKPCPPA LNCVPLNDY GPYTTTIGIY
490     500     510     520     530     540
QPYRVVLSYK ELLNAFATVC GFKLSTDLIK NQCVNFRNG LTFGVLTFPS SKREYFFKQY
550     560     570     580     590     600
GRDVSDFPSS VRDPKTSSEI DISPCSFGV SVITPQNAS SEAVVLYQDV NCTDVSTAIH
610     620     630     640     650     660
ADQLTEPARI YSTGNVYFQT QAGCLIGAEH VDTSYECDIP IGAGICASYH TVSLRSTSSQ
670     680     690     700     710     720
KSIVAVTMSL GADSSIAYSN NTIAIFNFS ISITTEVMPV SMAKTSVDCN MYICGUSTEC
730     740     750     760     770     780
ANLLQYGSF CTQLNRALSG IAABQDRNTR EVFAQVKQMY KPTPTLYFGG FNFSQILPDP
790     800     810     820     830     840
LKPTKRSFIE DLLFNKTLA DAGMFKVGE GLGDIARBL ICAQNFNGIT VLPPLTDDM
850     860     870     880     890     900
IAAYTAALVS GTATAGWTFG AGAALQIPFA MQMAYRNFGI GTQNVLYEN QKQIANQFNK
910     920     930     940     950     960
AISQIQESLT TTSTALGKIQ DVVWQNAQAL NTLVKQLSSN FGAISSVIND ILSRLDKVEA
970     980     990     1000    1010    1020
EVOIDRLITG RLQSLQTYVT QQLIRADEIR ASANLAATRM SECVLQSKR VDFCGKGYHL
1030    1040    1050    1060    1070    1080
MSFPQAAPHG VVFLVYVYV SQERNFTTAP AICHEGKAYF PREGVVFVNG TSWFITQRNF
1090    1100    1110    1120    1130    1140
FSPQIITTDN TFVSGNCDVV IGIINNTVYD PLQELDFSK EELDKYFKMH TSPDLDLSDI
1150    1160    1170    1180    1190
SGINASVVNI QKEIDRLNEV AKNLNESLID LQELGKYEQY IKWPAAR

```

SARS-CoV-2 RBD-His (M<sub>w</sub>: 31.8 kDa)

```

10      20      30      40      50      60
MARVQPTESI VRFNITNLCPFGEVFNATR FASVVAWNRK RISNCVADYS VLNSASFSST
70      80      90      100     110     120
FKCYGVSPK LNDLCFTNVY ADSFVIRGDE VRQIAFGQTG KIADYNYKLE DDFGTGCVIAW
130     140     150     160     170     180
NSNNLDSKVG GNYNYLYRLF RKSNLKPFER DISTEIVQAG STPCNGVEGF NCFYFLQSYG
190     200     210     220     230     240
FQPTNGVGYQ PYRVVLSFE LLHAPATVCG PPKSTNLVKN KCVNFPNGL TGTGVLTESN
250     260     270     280
KKFLFPQQFG RDIADTTDAV RDPQTLEILD ITPCSAAAHHHHH
    
```

SARS CoV-2 S1S2 trimer with foldon sequence (M<sub>w</sub> monomer: 141.9 kDa)

```

10      20      30      40      50      60
MAQCWHLTR TQLPPAVTNS FTRGVVYEDK VFRSSVLHST QDLFLPFFSN VTWFHAIHVS
70      80      90      100     110     120
GTNGTKRFDN EVLEFNDGVY FAGTEKGNLI RGMIFGTLLD GHTQGLLVN NATNVVHKVC
130     140     150     160     170     180
EFQFCNDPFL GVIYHKNNKS WMESEFRVYS SANNCTEYEV SQPFLMDLEG KQGNFKMLRE
190     200     210     220     230     240
FVFKNIDGYF KIYSKHTPIN LVLDLQGGFS ALEPLVDLPI GINITRFQTL LALHRSYLTTP
250     260     270     280     290     300
GDSSSGWTAG AAAYVGYLQ PRTFLKLYNE NGTITDAVDC ALDPLSETKC TLKSFVTEKGG
310     320     330     340     350     360
IYQTSNFRVQ PTESIVRFPN ITNLCPFGEV FNATRFASVY AMNRKRISNC VADYSVLVNS
370     380     390     400     410     420
ASFSTFKCYG VSPKLDLDC FTNVVADSFV IRGDEVQRQA PGQTGKIADY NYKLPDDFTG
430     440     450     460     470     480
CVIAWNSNLI DSKVGGNYNY LYRLEFRKSNL KPFERDISTE IYQAGSTPCN GVEGFNCYFE
490     500     510     520     530     540
LQSYGFQPTN GVGYPYRVV VLSFELLHAF ATVCGPKKST NLVKNKCVNF NFNGLTGTGV
550     560     570     580     590     600
LFSNKKFLP FQQFGRDIAD TTDVDRDQQT LEILDITPCS FGGVSVITPG TNSNQAVL
610     620     630     640     650     660
YQDVNCTEVF VAIHADQLTF TWRVYSTGSN VFQTRAGCLI GAHVNSNYSY CDIPIGAGIC
670     680     690     700     710     720
ASYQTQNSP GSASSVASQS IIAVTMSLGA ENSVAYSNNNS IAIPTNPTIS VTTEILPVSM
730     740     750     760     770     780
TKTSDVCTMY ICGDSTECSN LLLQYGSFCT QLNRAITGIA VEQDKNTQEV FAQVKQIYKT
790     800     810     820     830     840
PPIKDFGGFN FSQILPDPK PSKRSFIEDL LFNKVTLADA GFIKQFGDCL GDIAARDLIC
850     860     870     880     890     900
AQKFNGLTVL PPLLTDEMIÄ QYTSALLAGT ITSGWTFGAG AALQIPFAMQ MAYRENGIGV
910     920     930     940     950     960
TONVLYENQR LIANQFNSAI GKIQDSLST ASALGKIQDV VNQNAQALNT LVKQLSNFNG
970     980     990     1000    1010    1020
AISSVLNDIL SRLDPPEAEV QIDRLITGRL QSLQTVVTQQ LIRAAEIRAS ANLAATKMSSE
1030    1040    1050    1060    1070    1080
CVLGQSKRVD FCGKGYHIMS FQSAFHGVV FLHVTYVPAQ EKNFTTAPAI CHDGKAHPPR
1090    1100    1110    1120    1130    1140
EGVFSVNGTH WFTVQRNFYE PQIITDNTF VSGNCDVVIG IVNNTVYDPL QPELDSFKREE
1150    1160    1170    1180    1190    1200
LDKYFKNHTS PDVDLGDISG INASVNIQR EIDRLNEVAK NLNESLIDLQ ELGKYEQAATA
1210    1220    1230    1240    1250    1260
LVPRGSPGS YIPEAPRDQ AYVFKDGEWV LLSTELVENVL YFQGGSAWSH PQFEKGGSSG
1270    1280
GGSGGSAWSH PQFEKLEHHHHH
    
```

SARS CoV-2 B.1.1.7 S1S2 trimer with foldon sequence (M<sub>w</sub> monomer: 141.6 kDa)

```

10      20      30      40      50      60
MAQCVALLTR TQLPFAATNS FTRGVYYPDK VFRSSVLHST QDLFLFFFSN VTWFHAIISGT
70      80      90     100     110     120
NGTKRFDNPV LPFNDGVYFA STEKSNIIRG WIFGTTLDSE TQSLLIWNNA TNVVIKVCFF
130     140     150     160     170     180
QFCNDPFLGV YHKNNKSWME SEFRVYSSAN NCTFEVYSQP FLMDLEGKQG NFNKLRREFVF
190     200     210     220     230     240
KNIDGYFKIY SKHTPIINLVR DLPGGFSALE PLVDLPIGIN ITRFOTLLAL HRSYLTFGDS
250     260     270     280     290     300
SSGWTASAAA YVGTGLQFRT FLKKHENGST ITDAVDCALD PLSEFKCTLK SFTVERGIYQ
310     320     330     340     350     360
TSNFRVQPTF SIVRFENITN LCPFGVEVFNA TRFASVYAMN RKRIISNCVAD YSVLYNSASF
370     380     390     400     410     420
STFKCYGVSP TKLNDLCFTN VYADSEVIRG DEVRQIAPQG TGKIADYNYK LPDDFTGCVI
430     440     450     460     470     480
AMNSNNLDSK VGGNYNYLYR LFRKSNLKPF ERDISEIYQ AGSTPCNGVE GFNCYFPLQS
490     500     510     520     530     540
YGFQPTGVG YQPYRVVWLS FELLHAFATV CGFRKSTNLV ANKCVNFMFN GLTGTGVLTTE
550     560     570     580     590     600
SNKKFLPFQQ FGRDIDVTD AVRPDQTLLEI LDITFCSPFG VSVITFGTNT SNQVAVLYQG
610     620     630     640     650     660
VNCTEVPVAIHADQLTPTR VYSTGSNVFQ TRAGCLIGAE HVNNSYECDDI PIGAGICASY
670     680     690     700     710     720
QTQTSHGSA SSVASQSIIA YTMSLGAENS VAYSNNSIAI PINFTISVTT ELLFVSMTKT
730     740     750     760     770     780
SVDCTMYICG DSTECSNLLI QYGSFCTQLN RALTGIAVEEQ DKNTQVEVFAQ VKQIYKTFPT
790     800     810     820     830     840
KDFGGFNFQF ILPDPKSKSK RSFIEDLLEFN KVTLADAGST KQYGDCLIGDI AARDLICAKK
850     860     870     880     890     900
ENGLIVLPLI LTDEMIAGYT SALLAGTITS GWTFGAGAAI QIPFAMQMAI RENIGVITQI
910     920     930     940     950     960
VLYENQKLIH NQFNSAIGKI QDLSLSTASA LGKLDQVNVQ NAQALNTLVK QLSNFGAIS
970     980     990     1000    1010    1020
SVLNDILARL DPFEAEVVID KLITGRLOSL QTYVTQQLIR AAERIRASANL AATKMSKCVL
1030    1040    1050    1060    1070    1080
GQSKRVDFDG KGYHLMSPFC SAPHGVVLEF VTYVFAQEKH FTTAFAICHD GKAHFPRECV
1090    1100    1110    1120    1130    1140
FVSNQTHWFV TQRNEVEPQT ITTHNTFVSG NCDVVIQIVN NTVYDPLQPE LDSFKEELDK
1150    1160    1170    1180    1190    1200
YFKNHTSPDV DLGDISGINA SVVNIQKIID RLNEVAKNLN ESLIDLQELG KYEQAALVF
1210    1220    1230    1240    1250    1260
RGSFGSGYIF EAPRDCAAVV RKGDEWLLS TFLVNIYFQ GGSANSHQF EKGGGSGGGG
1270    1280
GGSAWSPQF EKLEHHHHHH HH

```

hACE2-fc (M<sub>w</sub>: 95.2 kDa)

```

10      20      30      40      50      60
MQSTIEEQAK TFLDKFNHEA EDLFYQSSLA SWNYNTNITE ENVQNMNAG DKWSAFLKEQ
70      80      90     100     110     120
STLAQMYPLQ EIQNLTVKLQ LQALQQNGSS VLSEDKSKRL NTLNNTMSTI YSTGKVCNPF
130     140     150     160     170     180
NPQECILLEF GLNEIMANSL DYNERLWAVE SWRSEVGGQL RPLYEEVYVL KNEMARAMHY
190     200     210     220     230     240
EDYGDYWRGD YEVNGVDGYD YSRGQLIEDV EHTFEEIKPL YEHLHAYVRA KLMNAYPSYI
250     260     270     280     290     300
SPIGCLPAHL LGDMWGREWT NLYSLTVFPFQ QKPNIDVTDV MVDQAWDAQR IFKAEAEKFF
310     320     330     340     350     360
SVGLENMTCG FWENSMITDF GNVQKAVCHP TAWDLGKGF RILMCTRVTM DDFLTAHHEM
370     380     390     400     410     420
GHIQYDMAYA AQPFLLRNGA NEGPFHEAVGE IMSLSAATPK HLRSIGLLEP DFQEDNTEEI
430     440     450     460     470     480
NFLKQALTI VGTLPFTYML EKNRMMVFKG EIPKQDMKKK WWMKKREIVG VVEPVPHEDT
490     500     510     520     530     540
YCDPASLFHV SNDYSFIRYV TRTLYQFQFQ EALCQAAKHE GPLHKCDISN STEAGQKLEN
550     560     570     580     590     600
MLRLGKSEPW TLALENVVA GKNMVRPLL N YFEPLFTWLK DQNKNSFVGV STDWSPYADA
610     620     630     640     650     660
AASDKTHTCF PCPAPELLGG PSVLFPPEK KDTLMSISIT EVTCVVVDYS HEDPEKRRNW
670     680     690     700     710     720
YVDGVNHRH KTKPREEQYN STYRWVSLT VLRQDWLNGK EYKCKYSNKA LEAPLEKTIIS
730     740     750     760     770     780
KAKGQPREPQ VYTLPPSRDE LTKNQVSLTLC LVKGFYPSDI AVEWESNGQP ENNYKTTFPF
790     800     810     820     830
LDSGSEFLY SKLTVDKSRW QQGNVFCSCV MHEALHNHYT QKSLSLSPGR

```

Figure A1. Single letter amino acid sequence of the SARS-CoV spike protein and hACE2 constructs used for SPR experiments. T4 fold-on sequences are marked in yellow, Poly-His sequences are marked in green and fc-tags are marked in turquoise.

## References

- Huang, C.; Wang, Y.; Li, X.; Ren, L.; Zhao, J.; Hu, Y.; Zhang, L.; Fan, G.; Xu, J.; Gu, X.; et al. Clinical features of patients infected with 2019 novel coronavirus in Wuhan, China. *Lancet* **2020**, *395*, 497–506.
- Li, Q.; Guan, X.; Wu, P.; Wang, X.; Zhou, L.; Tong, Y.; Ren, R.; Leung, K.S.; Lau, E.H.; Wong, J.Y.; et al. Early Transmission Dynamics in Wuhan, China, of Novel Coronavirus-Infected Pneumonia. *N. Engl. J. Med.* **2020**, *382*, 1199–1207.
- Rabaan, A.A.; Al-Ahmed, S.H.; Haque, S.; Sah, R.; Tiwari, R.; Malik, Y.S.; Dhama, K.; Yattoo, M.I.; Bonilla-Aldana, D.K.; Rodriguez-Morales, A.J. SARS-CoV-2, SARS-CoV, and MERS-CoV: A comparative overview. *Infez Med.* **2020**, *28*, 174–184.
- Lee, N.; Hui, D.; Wu, A.; Chan, P.; Cameron, P.; Joynt, G.M.; Ahuja, A.; Yung, M.Y.; Leung, C.; To, K.; et al. A major outbreak of severe acute respiratory syndrome in Hong Kong. *N. Engl. J. Med.* **2003**, *348*, 1986–1994.
- Hänel, K.; Willbold, D. SARS-CoV accessory protein 7a directly interacts with human LFA-1. *Biol. Chem.* **2007**, *388*, 1325–1332.
- WHO Coronavirus (COVID-19) Dashboard. Available online: <https://covid19.who.int/> (accessed on 7 February 2022).
- Wang, Q.; Zhang, Y.; Wu, L.; Niu, S.; Song, C.; Zhang, Z.; Lu, G.; Qiao, C.; Hu, Y.; Yuen, K.Y.; et al. Structural and Functional Basis of SARS-CoV-2 Entry by Using Human ACE2. *Cell* **2020**, *181*, 894–904.e899.
- Koch, J.; Uckele, Z.M.; Doldan, P.; Stanifer, M.; Boulant, S.; Lozach, P.Y. TMPRSS2 expression dictates the entry route used by SARS-CoV-2 to infect host cells. *Embo J.* **2021**, *40*, e107821.
- Chen, J.; Wang, R.; Wang, M.; Wei, G.W. Mutations Strengthened SARS-CoV-2 Infectivity. *J. Mol. Biol.* **2020**, *432*, 5212–5226.
- Choe, H.; Farzan, M. How SARS-CoV-2 first adapted in humans. *Science* **2021**, *372*, 466–467.
- Shang, J.; Ye, G.; Shi, K.; Wan, Y.; Luo, C.; Aihara, H.; Geng, Q.; Auerbach, A.; Li, F. Structural basis of receptor recognition by SARS-CoV-2. *Nature* **2020**, *581*, 221–224.
- Wan, Y.S.; Shang, J.; Graham, R.; Baric, R.S.; Li, F. Receptor Recognition by the Novel Coronavirus from Wuhan: An Analysis Based on Decade-Long Structural Studies of SARS Coronavirus. *J. Virol.* **2020**, *94*, e00127–20.
- Letko, M.; Marzi, A.; Munster, V. Functional assessment of cell entry and receptor usage for SARS-CoV-2 and other lineage B betacoronaviruses. *Nat. Microbiol.* **2020**, *5*, 562–569.
- Tang, J.W.; Tambyah, P.A.; Hui, D.S. Emergence of a new SARS-CoV-2 variant in the UK. *J. Infect.* **2021**, *82*, e27–e28.
- Guruprasad, L. Human SARS CoV-2 spike protein mutations. *Proteins* **2021**, *89*, 569–576.
- Huang, Y.; Yang, C.; Xu, X.F.; Xu, W.; Liu, S.W. Structural and functional properties of SARS-CoV-2 spike protein: Potential antiviral drug development for COVID-19. *Acta Pharmacol. Sin.* **2020**, *41*, 1141–1149.
- Yi, C.; Sun, X.; Ye, J.; Ding, L.; Liu, M.; Yang, Z.; Lu, X.; Zhang, Y.; Ma, L.; Gu, W.; et al. Key residues of the receptor binding motif in the spike protein of SARS-CoV-2 that interact with ACE2 and neutralizing antibodies. *Cell Mol. Immunol.* **2020**, *17*, 621–630.
- Lan, J.; Ge, J.; Yu, J.; Shan, S.; Zhou, H.; Fan, S.; Zhang, Q.; Shi, X.; Wang, Q.; Zhang, L.; et al. Structure of the SARS-CoV-2 spike receptor-binding domain bound to the ACE2 receptor. *Nature* **2020**, *581*, 215–220.
- Harvey, W.T.; Carabelli, A.M.; Jackson, B.; Gupta, R.K.; Thomson, E.C.; Harrison, E.M.; Ludden, C.; Reeve, R.; Rambaut, A.; Peacock, S.J.; et al. SARS-CoV-2 variants, spike mutations and immune escape. *Nat. Rev. Microbiol.* **2021**, *19*, 409–424.
- Volz, E.; Mishra, S.; Chand, M.; Barrett, J.C.; Johnson, R.; Geidelberg, L.; Hinsley, W.R.; Laydon, D.J.; Dabrera, G.; O’Toole, Á.; Amato, R. Assessing transmissibility of SARS-CoV-2 lineage B.1.1.7 in England. *Nature* **2021**, *593*, 266–269.
- Mlcochova, P.; Kemp, S.A.; Dhar, M.S.; Papa, G.; Meng, B.; Ferreira, I.A.T.M.; Datir, R.; Collier, D.A.; Albecka, A.; Singh, S.; et al. SARS-CoV-2 B.1.617.2 Delta variant replication and immune evasion. *Nature* **2021**, *599*, 114–119.
- Karim, S.S.A.; Karim, Q.A. Omicron SARS-CoV-2 variant: A new chapter in the COVID-19 pandemic. *Lancet* **2021**, *398*, 2126–2128.
- Tagliamonte, M.S.; Mavian, C.; Zainabadi, K.; Cash, M.N.; Lednický, J.A.; Magalis, B.R.; Riva, A.; Deschamps, M.M.; Liautaud, B.; Rouzier, V.; et al. Rapid emergence and spread of SARS-CoV-2 gamma (P.1) variant in Haiti. *Clin. Infect. Dis.* **2021**. doi: 10.1093/cid/ciab736.
- Arora, P.; Pohlmann, S.; Hoffmann, M. Mutation D614G increases SARS-CoV-2 transmission. *Signal Transduct. Target. Ther.* **2021**, *6*, 101.
- Thomson, E.C.; Rosen, L.E.; Shepherd, J.G.; Spreafico, R.; da Silva Filipe, A.; Wojcechowskyj, J.A.; Davis, C.; Piccoli, L.; Pascall, D.J.; Dillen, J.; et al. Circulating SARS-CoV-2 spike N439K variants maintain fitness while evading antibody-mediated immunity. *Cell* **2021**, *184*, 1171–1187.
- Couch, R.B. Seasonal inactivated influenza virus vaccines. *Vaccine* **2008**, *26* (Suppl. 4), D5–D9.
- Bolarin, J.A.; Oluwatoyosi, M.A.; Orege, J.I.; Ayeni, E.A.; Ibrahim, Y.A.; Adeyemi, S.B.; Tiamiyu, B.B.; Gbadegesin, L.A.; Akinyemi, T.O.; Odoh, C.K.; et al. Therapeutic drugs for SARS-CoV-2 treatment: Current state and perspective. *Int. Immunopharmacol.* **2021**, *90*, 107228.
- Mohapatra, S.; Nath, P.; Chatterjee, M.; Das, N.; Kalita, D.; Roy, P.; Satapathi, S. Repurposing therapeutics for COVID-19: Rapid prediction of commercially available drugs through machine learning and docking. *PLoS ONE* **2020**, *15*, e0241543.
- Eberle, R.J.; Olivier, D.S.; Amaral, M.S.; Gering, I.; Willbold, D.; Arni, R.K.; Coronado, M.A. The Repurposed Drugs Suramin and Quinacrine Cooperatively Inhibit SARS-CoV-2 3CL(pro) In Vitro. *Viruses* **2021**, *13*, 873.

30. Loschwitz, J.; Jäckering, A.; Keutmann, M.; Olagunju, M.; Eberle, R.J.; Coronado, M.A.; Olubiyi, O.O.; Strodel, B. Novel inhibitors of the main protease enzyme of SARS-CoV-2 identified via molecular dynamics simulation-guided in vitro assay. *Bioorg. Chem.* **2021**, *111*, 104862.
31. Gordon, C.J.; Tchesnokov, E.P.; Schinazi, R.F.; Gotte, M. Molnupiravir promotes SARS-CoV-2 mutagenesis via the RNA template. *J. Biol. Chem.* **2021**, *297*, 100770.
32. Mahase, E. Covid-19: Pfizer's paxlovid is 89% effective in patients at risk of serious illness, company reports. *BMJ* **2021**, *375*, n2713.
33. Ibrahim, M.A.; Abdelrahman, A.H.; Hussien, T.A.; Badr, E.A.; Mohamed, T.A.; El-Seedi, H.R.; Pare, P.W.; Efferth, T.; Hegazy, M.E.F. In silico drug discovery of major metabolites from spices as SARS-CoV-2 main protease inhibitors. *Comput. Biol. Med.* **2020**, *126*, 104046.
34. Barderas, R.; Benito-Pena, E. The 2018 Nobel Prize in Chemistry: Phage display of peptides and antibodies. *Anal. Bioanal. Chem.* **2019**, *411*, 2475–2479.
35. Cronan, J.E., Jr. Biotinylation of proteins in vivo. A post-translational modification to label, purify, and study proteins. *J. Biol. Chem.* **1990**, *265*, 10327–10333.
36. Santur, K.; Reinartz, E.; Lien, Y.; Tusche, M.; Altendorf, T.; Sevenich, M.; Tamgüney, G.; Mohrlüder, J.; Willbold, D. Ligand-Induced Stabilization of the Native Human Superoxide Dismutase 1. *ACS Chem. Neurosci.* **2021**, *12*, 2520–2528.
37. Krejci, A.; Hupp, T.R.; Lexa, M.; Vojtesek, B.; Muller, P. Hammock: A hidden Markov model-based peptide clustering algorithm to identify protein-interaction consensus motifs in large datasets. *Bioinformatics* **2016**, *32*, 9–16.
38. Schubert, M.; Nimtz, M.; Bertoglio, F.; Schmelz, S.; Lukat, P.; Heuvel, J.V.D. Reproducible and Easy Production of Mammalian Proteins by Transient Gene Expression in High Five Insect Cells. *Methods Mol. Biol.* **2021**, *2305*, 129–140.
39. Meyer, S.; Lorenz, C.; Başer, B.; Wördehoff, M.; Jäger, V.; Heuvel, J.V.D. Multi-Host Expression System for Recombinant Production of Challenging Proteins. *PLoS ONE* **2013**, *8*, e68674.
40. Papanikolopoulou, K.; Forge, V.; Goeltz, P.; Mitraki, A. Formation of highly stable chimeric trimers by fusion of an adenovirus fiber shaft fragment with the foldon domain of bacteriophage T4 fibrillin. *J. Biol. Chem.* **2004**, *279*, 8991–8998.
41. Vranken, W.; Boucher, W.; Stevens, T.J.; Fogh, R.H.; Pajon, A.; Llinas, M.; Ulrich, E.L.; Markley, J.L.; Ionides, J.; Laue, E.D. The CCPN data model for NMR spectroscopy: Development of a software pipeline. *Proteins* **2005**, *59*, 687–696.
42. Sevenich, M.; van den Heuvel, J.; Gering, I.; Mohrlüder, J.; Willbold, D. Conversion rate to the secondary conformation state in the binding mode of SARS-CoV-2 spike protein to human ACE2 may predict infectivity efficacy of the underlying virus mutant. *bioRxiv* **2021**.
43. Ostrov, D.A. Structural Consequences of Variation in SARS-CoV-2 B.1.1.7. *J. Cell Immunol.* **2021**, *3*, 103–108.
44. Starr, T.N.; Greaney, A.J.; Hilton, S.K.; Ellis, D.; Crawford, K.H.; Dingens, A.S.; Navarro, M.J.; Bowen, J.E.; Tortorici, M.A.; Walls, A.C.; et al. Deep Mutational Scanning of SARS-CoV-2 Receptor Binding Domain Reveals Constraints on Folding and ACE2 Binding. *Cell* **2020**, *182*, 1295–1310.
45. Khan, A.; Zia, T.; Suleman, M.; Khan, T.; Ali, S.S.; Abbasi, A.A.; Mohammad, A.; Wei, D.Q. Higher infectivity of the SARS-CoV-2 new variants is associated with K417N/T, E484K, and N501Y mutants: An insight from structural data. *J. Cell Physiol.* **2021**, *236*, 7045–7057.
46. Zhang, L.; Jackson, C.B.; Mou, H.; Ojha, A.; Peng, H.; Quinlan, B.D.; Rangarajan, E.S.; Pan, A.; Vanderheiden, A.; Suthar, M.S.; et al. SARS-CoV-2 spike-protein D614G mutation increases virion spike density and infectivity. *Nat. Commun.* **2020**, *11*, 6031.
47. Brielle, E.S.; Schneidman-Duhovny, D.; Linial, M. The SARS-CoV-2 Exerts a Distinctive Strategy for Interacting with the ACE2 Human Receptor. *Viruses* **2020**, *12*, 497.
48. Xiong, X.; Qu, K.; Ciazynska, K.A.; Hosmillo, M.; Carter, A.P.; Ebrahimi, S.; Ke, Z.; Scheres, S.H.; Bergamaschi, L.; Grice, G.L.; et al. A thermostable, closed SARS-CoV-2 spike protein trimer. *Nat. Struct. Mol. Biol.* **2020**, *27*, 934–941.
49. Vauquelin, G. Effects of target binding kinetics on in vivo drug efficacy: K(off), k(on) and rebinding. *Br. J. Pharmacol.* **2016**, *173*, 2319–2334.
50. Larue, R.C.; Xing, E.; Kenney, A.D.; Zhang, Y.; Tuazon, J.A.; Li, J.; Yount, J.S.; Li, P.K.; Sharma, A. Rationally Designed ACE2-Derived Peptides Inhibit SARS-CoV-2. *Bioconjugate Chem.* **2021**, *32*, 215–223.
51. Panda, S.K.; Gupta, P.S.S.; Biswal, S.; Ray, A.K.; Rana, M.K. ACE-2-Derived Biomimetic Peptides for the Inhibition of Spike Protein of SARS-CoV-2. *J. Proteome Res.* **2021**, *20*, 1296–1303.
52. Rai, J. Peptide and protein mimetics by retro and retroinverso analogs. *Chem. Biol. Drug Des.* **2019**, *93*, 724–736.
53. Elfgen, A.; Hupert, M.; Bochinsky, K.; Tusche, M.; González de San Román Martín, E.; Gering, I.; Sacchi, S.; Pollegioni, L.; Huesgen, P.F.; Hartmann, R.; et al. Metabolic resistance of the D-peptide RD2 developed for direct elimination of amyloid-beta oligomers. *Sci. Rep.* **2019**, *9*, 5715.

## **2.4 Development of an $\alpha$ -synuclein fibril and oligomer specific tracer peptide for diagnosis of Parkinson's disease, dementia with Lewy bodies and multiple system atrophy**

Authors: **Marc Sevenich**, Dominik Honold, Antje Willuweit, Jeanine Kutzsche, Jeannine Mohrlüder and Dieter Willbold

Journal: Neurochemistry International

DOI: <https://doi.org/10.1016/j.neuint.2022.105422>

Impact Factor: 4.3 (2022)

Contribution: Project outline, planning and performance of phage display selection and sequence analysis, planning and performance of kinetic assays, planning of immunohistochemical staining, writing of original draft.



Contents lists available at ScienceDirect

Neurochemistry International

journal homepage: [www.elsevier.com/locate/neuint](http://www.elsevier.com/locate/neuint)

## Development of an $\alpha$ -synuclein fibril and oligomer specific tracer for diagnosis of Parkinson's disease, dementia with Lewy bodies and multiple system atrophy

Marc Sevenich<sup>a,b</sup>, Dominik Honold<sup>b</sup>, Antje Willuweit<sup>a,c</sup>, Janine Kutzsche<sup>b</sup>,  
Jeannine Mohrlüder<sup>b</sup>, Dieter Willbold<sup>b,d,e,\*</sup>

<sup>a</sup> Priavoid GmbH, Düsseldorf, Germany

<sup>b</sup> Institute of Biological Information Processing (IBI-7), Forschungszentrum Jülich, Jülich, Germany

<sup>c</sup> Institute of Neuroscience and Medicine (INM-4), Forschungszentrum Jülich, Jülich, Germany

<sup>d</sup> Institut für Physikalische Biologie, Heinrich-Heine-Universität Düsseldorf, Düsseldorf, Germany

<sup>e</sup> JuStruct, Forschungszentrum Jülich, Jülich, Germany

### ARTICLE INFO

#### Keywords:

Tracer  
Diagnosis  
Alpha synuclein  
Parkinson's disease  
Multiple system atrophy  
Dementia with Lewy bodies  
Synucleinopathies  
Phage display

### ABSTRACT

The development of specific disease-associated PET tracers is one of the major challenges, the realization of which in neurodegenerative diseases would enable not only the efficiency of diagnosis but also support the development of disease-modifying therapeutics. Parkinson's disease (PD) is the most common neurodegenerative movement disorder and is characterized by neuronal fibrillary inclusions composed of aggregated  $\alpha$ -synuclein ( $\alpha$ -syn). However, these deposits are not only found in PD, but also in other related diseases such as multiple system atrophy (MSA) and dementia with Lewy bodies (DLB), which are grouped under the term synucleinopathies. In this study, we used NGS-guided phage display selection to identify short peptides that bind aggregated  $\alpha$ -syn. By surface plasmon resonance (SPR)-based affinity screening, we identified the peptide SVLfib-5 that recognizes aggregated  $\alpha$ -syn with high complex stability and sequence specificity. Further analysis SPR showed that SVLfib-5 is not only specific for aggregated  $\alpha$ -syn, but in particular recognizes fibrillary and oligomeric structures. Moreover, fluorescence microscopy of human brain tissue sections from PD, MSA, and DLB patients with SVLfib-5 allowed specific recognition of  $\alpha$ -syn and a clear discrimination between diseased and non-diseased samples. These findings provide the basis for the further development of an  $\alpha$ -syn PET tracer for early diagnosis and monitoring of disease progression and therapy progress.

### 1. Introduction

Abnormal intra-neuronal deposition of  $\alpha$ -synuclein ( $\alpha$ -syn) is the hallmark of many neurodegenerative diseases such as Parkinson's disease (PD), dementia with Lewy bodies (DLB), and multiple system atrophy (MSA) (Spillantini et al., 1997a; Poewe et al., 2017). These intraneuronal inclusions, termed Lewy bodies (LB) or Lewy neurites (LN) depending on their intracellular location (soma or neurite, respectively), are found mainly in the substantia nigra of PD patients, whereas they are largely distributed in the cerebral cortex of DLB patients. In contrast to PD and DLB, MSA patients show filamentous inclusions not only in neurons but also to a higher extent in oligodendrocytes, where they are referred to as Papp-Lantos bodies

(Papp et al., 1989; Spillantini et al., 1998). Initial indications that these abnormal deposits are likely to be associated with disease progression were provided by the finding that they are mainly consisting of insoluble fibrillary biopolymers of physiologically monomeric  $\alpha$ -syn and that certain mutations in the SNCA region, encoding for  $\alpha$ -syn, are linked to certain types of familial PD (Chartier-Harlin et al., 2004; Alcalay et al., 2010; Nuytemans et al., 2010). Moreover, structural analysis of fibrils extracted from brain homogenates of diseased patients has shown that the different synucleinopathies are associated with different fibril polymorphs that have distinct capacities to induce aggregation in the presence of monomeric  $\alpha$ -syn. This led to the hypothesis that the fibril polymorph is not only decisive for the pathophenotype, but also for disease progression (Peng et al., 2018; Yamasaki et al., 2019).

\* Corresponding author. Institute of Biological Information Processing (IBI-7), Forschungszentrum Jülich, Jülich, Germany.  
E-mail address: [d.willbold@tz-juelich.de](mailto:d.willbold@tz-juelich.de) (D. Willbold).

<https://doi.org/10.1016/j.neuint.2022.105422>

Received 7 July 2022; Received in revised form 26 September 2022; Accepted 2 October 2022

Available online 15 October 2022

0197-0186/© 2022 Elsevier Ltd. All rights reserved.

Among the various fibrillary conformers of  $\alpha$ -syn aggregates formed during autocatalytic self-amplification of seeding species, soluble oligomeric non-fibrillary structures are considered to be the major toxic component causing neuronal cell death in PD and other synucleinopathies (Bengoa-Vergniory et al., 2017; Winner et al., 2011). Similar to fibrils, oligomeric  $\alpha$ -syn structures occur with a high degree of structural diversity, which, together with their transient nature, complicates their biophysical characterization and detection (Alam et al., 2019; Giehm et al., 2011; Lorenzen et al., 2014).

Recent progress was made in quantitating soluble  $\alpha$ -syn oligomers in CSF of PD patients and patients from other synucleinopathies (Blomeke et al., 2022). However, currently, there is no reliable method to visualize  $\alpha$ -syn aggregates in patients, which not only hinders early detection of the disease and thus appropriate therapeutic intervention, but also impedes the development of new causative treatments. Positron emission tomography (PET) has the potential to reveal the pathogenesis of brain diseases and to evaluate the effect of novel therapeutics if appropriate tracer molecules are available (Barc and Kuzma-Kozakiewicz, 2019). However, in the absence of suitable disease-related tracers, imaging of dopaminergic neurons remains the most important application for evaluating the success of disease-modifying PD treatments. In fact, in most patients, the disease begins much earlier, before dopaminergic neurons degenerate, and the loss of dopaminergic neurons is a consequence of disease progression rather than its cause (Olanow and Brundin, 2013). A specific tracer molecule that recognizes disease-related  $\alpha$ -syn aggregates in the central nervous system (CNS) would therefore be crucial.

One of the major challenges in the development of  $\alpha$ -syn PET-tracers is that the absolute concentration of  $\alpha$ -syn aggregates found in the CNS is significantly lower than for other neurodegenerative disease markers such as A $\beta$  or tau aggregates (Mathis et al., 2017). Therefore, tracer molecules with the highest specificity and selectivity are needed for identification of disease-related  $\alpha$ -syn aggregates. Moreover, structure-based design is complicated not only by the polymorphism of  $\alpha$ -syn aggregates but also by the limited availability of high-resolution structures of fibrils or oligomers.

In the present work, we took a different approach from the structure-guided design by using phage display selection with subsequent next generation sequencing (NGS) analysis (Sevenich et al., 2022) for the development of an anti- $\alpha$ -syn tracer molecule that specifically recognizes aggregated  $\alpha$ -syn. The resulting 16-mer peptide SVLfib-5 does not only bind fibrillary  $\alpha$ -syn with high sequence specificity, but also recognizes off-pathway oligomer structures, while showing no affinity for monomeric  $\alpha$ -syn. Moreover, when applied to brain samples derived from PD, DLB and MSA patients, staining with SVLfib-5 allowed an accurate discrimination between patient and control samples.

Thus, SVLfib 5 represents a promising candidate for a specific PET tracer for PD, DLB, and MSA. In addition, the described method can be extended to other neurodegenerative diseases such as Alzheimer's diseases for the straightforward identification of peptide-based PET tracers.

## 2. Methods

### 2.1. Expression and purification of monomeric wt and $\alpha$ -syn A140C

Expression of N-terminal acetylated full-length wt  $\alpha$ -syn and acetylated full length  $\alpha$ -syn-A140C was performed in *E. coli* BL21(DE3). Acetylation was achieved by introducing a pT7 vector encoding for N-terminal acyltransferase (pNatB) from *Schizosaccharomyces pombe* (Johnson et al., 2010). For expression in LB-medium, 1 mM IPTG was added in mid-log phase following incubation for 4 h at 37 °C. Purification was performed as described previously (Hoyer et al., 2002) with the following modifications: cells from 1 l expression were pelleted and resuspended in 25 ml 20 mM Tris pH 8.0. Cell lysis was performed by boiling the cells at 95–100 °C for 2  $\times$  15 min. After centrifugation, a final concentration of 0.45 g/ml of ammonium sulfate was added for protein

precipitation. The protein was pelleted and resuspended in 50 ml buffer. Subsequently, the sample was loaded on a HiPrep QFF 16/10 (Cytiva, USA, CV = 20 ml) anion exchange column.  $\alpha$ -syn was recovered by applying a gradient elution with a target concentration of 800 mM NaCl over 20 CV.  $\alpha$ -syn containing fractions were pooled and precipitated as described previously. A final chromatography step was performed by purifying monomeric  $\alpha$ -syn with a HiLoad Superdex 60/75 pg gel filtration column (Cytiva, USA, CV = 120 ml). Protein aliquots were frozen with liquid nitrogen and stored at  $-80$  °C.

### 2.2. Biotinylation and purification of 140C $\alpha$ -syn

For biotinylation of  $\alpha$  syn 250  $\mu$ M  $\alpha$  syn 140C was incubated with a ten-fold excess of TCEP at RT for 30 min. The labeling reaction was performed in 25 mM NaPi pH 7.0 by incubation with a ten-fold excess of PEG<sub>2</sub>-biotin maleimide (Thermo Fisher, USA) for 2 h at RT. Labeled biotinylated 140C-PEG<sub>2</sub>-biotin  $\alpha$ -syn was purified using an Agilent 1260 Infinity II system and C8 RP-HPLC column (Zorbax 300 SB-C8, Agilent, USA) at 80 °C. Mobile phases consisted of A: Water +0.1% TFA and B: Acetonitrile +0.1% TFA. Elution of labeled peptides and proteins was performed with a gradient of 5–40% (v/v) B within 30 min. Fractions containing the labeled protein were united and lyophilized. Lyophilized protein was stored at  $-20$  °C until usage.

### 2.3. Preparation of biotinylated $\alpha$ -syn fibrils for selection

Preparation of  $\alpha$ -syn fibrils was performed as described previously (Heise et al., 2005) with the following modifications: for preparation of 10% biotinylated  $\alpha$ -syn fibrils, wt and biotinylated 140C  $\alpha$ -syn was mixed in a 10:1 M ratio. A total volume of 500  $\mu$ l with a concentration of 400  $\mu$ M in 25 mM Tris-HCl pH 7.4, 0.05% (w/v) Na<sub>2</sub>S<sub>2</sub>O<sub>8</sub> was incubated at 37 °C in a quartz cuvette and continuously stirred at 200 rpm using a teflon bar. To monitor fibrillation, 5  $\mu$ l sample was removed, mixed with 95  $\mu$ l Tris buffer and 10  $\mu$ M ThT (20  $\mu$ M monomer equivalent  $\alpha$ -syn) and transferred to a Greiner half area non-binding 96-well plate (Greiner Bio-one, GE). ThT fluorescence was monitored with bottom optics at  $\lambda_{exc}$  = 448 nm and  $\lambda_{em}$  = 482 nm in a fluorescence plate reader with orbital averaging on 3 mm (Clariostar or Polarstar Optima, BMG labtech, GE). After 6 d of incubation, the whole sample was centrifuged at 175,000  $\times$ g for 30 min at 4 °C. The supernatant was removed, and the pellet was washed several times with buffer and finally resuspended in 500  $\mu$ l Tris-HCl pH 7.4. After 3  $\times$  45 s sonification with a microtip (10% max. amplitude, 50% cycle, Ultrasonics sonifier 250, Branson, USA), the sample was aliquoted to 10  $\mu$ l and flash frozen with liquid nitrogen. Samples were stored at  $-80$  °C until further usage.

### 2.4. Saturation ELISA

Saturation ELISA was performed to verify the successful immobilization of the fibrils on the streptavidin derivatized selection surface. Biotinylated  $\alpha$ -syn fibrils were thawed on ice, diluted to 20  $\mu$ M in 20 mM Tris-HCl pH 7.4 (Tris-buffer) and subsequently sonified as described previously. 100  $\mu$ l/well of 2.5, 5, 10 and 20  $\mu$ M monomer equivalent of fibrils was incubated for 1 h at RT in a High Capacity streptavidin coated 96-well plate (Thermo Fisher Scientific, USA). Afterwards, the surface was quenched using 100  $\mu$ l of saturated biotin solution. Subsequently, the surface was blocked using 100  $\mu$ l of BSA (bovine serum albumin) blocking solution (1% (w/v) BSA in 25 mM Tris-HCl pH 7.4). The surface was washed three times with 200  $\mu$ l washing solution (Tris-buffer + 0.1% (v/v) Tween-20). The primary anti-aggregated monoclonal  $\alpha$ -syn antibody (clone 5G4, Merck, USA) was diluted to a final concentration of 1  $\mu$ g/ml in Tris-buffer and 100  $\mu$ l was incubated for 1 h at RT. The surface was washed five times with 200  $\mu$ l washing buffer. The secondary antibody (goat anti-mouse-IgG-HRP antibody, Thermo Fisher, USA) was diluted to 0.2  $\mu$ g/ml in Tris-buffer, 100  $\mu$ l was added to the wells and incubated for 1 h at RT. After washing six times with 200  $\mu$ l

washing buffer, the TMB substrate (3,3',5,5'-Tetramethylbenzidine, Sigma Aldrich, USA) was incubated for 4 min and the reaction was stopped by adding equal volumes of 2 M sulfuric acid. The absorption was quantified at A<sub>450</sub> using a platereader (Clariostar, BMG Labtech, GE).

### 2.5. Phage display selection

Phage display was performed as described previously (Sevenich et al., 2022) with some modifications: For selection, 25 mM Tris-HCl pH 7.4 50 mM NaCl was used as selection buffer. All other buffers such as blocking, incubation and washing buffer were modified by addition of the corresponding substance as described previously. Fibrils were homogenized by sonication as previously described and 100 µl was added to a High Capacity streptavidin 96-well plate (Thermo Fisher Scientific, USA) in 10 µM monomer equivalents (1000 pmol/well). Selection was performed using either the commercially available NEB-12 (New England Biolabs, USA) or Trico-16 (Creative Biolabs, USA) libraries. For the first selection round, the phage library titer was determined by absorption at A<sub>269</sub>, and 2x10<sup>11</sup> total phages were used as input. Three consecutive selection rounds were performed using alternating blocking conditions with either MP (milk powder) or BSA and 10-fold washing repetitions for each selection round.

### 2.6. Enrichment ELISA

Enrichment ELISA was performed as described previously (Sevenich et al., 2022) with the following modifications: for target immobilization either 0.2 µM sonified biotinylated α-syn fibrils or 140C PEG<sub>2</sub>-biotin-α-syn monomer was incubated. All steps were performed using 25 mM Tris-HCl pH 7.4, 50 mM NaCl (blocking buffer: addition of 1% (w/v) BSA; washing buffer: addition of 0.5% (w/v) BSA and 0.05% Tween-20).

### 2.7. Next generation sequencing (NGS) and cluster evaluation

DNA sample preparation and NGS sequencing was performed as described previously (Sevenich et al., 2022). Hammock clustering software (Krejci et al., 2016) was used with default settings except for -U set as "input". Decision for synthesis of peptide variants was made based on empty score, enrichment factor values, cluster size and sequence motif conservation.

### 2.8. SVLfib peptide synthesis

L-enantiomeric SVLfib peptides were purchased with C-terminal amidation from CASLO (CASLO, DK) as lyophilized chloride salt powder with a purity of >95%.

### 2.9. Surface plasmon resonance (SPR) screening

SPR experiments were used to screen the interaction of the SVLfib peptides with aggregated α-syn, to verify binding specificity (monomer, fibrils, oligomers), and to kinetically characterize the interaction with the target molecules. All measurements were performed using a Biacore T200 device and Biacore insight evaluation software v3.0 for kinetic evaluation (Cytiva, USA). For affinity screening of whole aggregate pool samples, wt α-syn was aggregated and purified as previously described for the preparation of biotinylated fibrils. The resulting aggregated sample was immobilized on a carboxymethyl dextran matrix using EDC/NHS chemistry (CM5 or CM3 sensor surfaces, Cytiva, USA). SVLfib peptides were dissolved in DMSO and diluted to a final concentration of 2.5% (v/v) in 25 mM Tris-HCl pH 7.4 50 mM NaCl. Multicycle injections without regeneration were performed using peptide concentrations of 8.4–135 µM with a flow rate of 30 µl/min. For kinetic characterization of SVLfib-5 peptide with the whole aggregate pool sample, measurements were either performed as multicycle injections without regeneration or

as single cycle injections. Both experiments were performed in 25 mM Tris pH 7.4, 50 mM NaCl at RT using flow rates of 60 µl/min for the association phase and 30 µl/min for dissociation phase. SVLfib-5 was diluted in running buffer at a concentration range from 1.3–135 µM. Biotinylated α-syn monomers were immobilized on streptavidin derivatized SA sensor surfaces (Cytiva, USA). Data fitting was performed using a 1:1 kinetic interaction model (Biacore T200 data evaluation software v. 3.2, Cytiva, USA). For comparison of SVLfib-5<sub>original</sub>, CP1, CP2 and short interaction with the whole aggregate pool and interaction with off-pathway oligomers, identical experimental conditions were used as described previously. Biotinylated α-syn off-pathway oligomers were immobilized on a streptavidin derivatized SA-sensor surface (SA, Cytiva, USA). Peptides were injected using concentration ranges from 6.25 to 100 µM.

### 2.10. Preparation of biotinylated α-syn off-pathway oligomers

α-syn off-pathway oligomers were prepared as described by Giehlm et al. (2011) with some modifications: wt α-syn monomer was mixed with 5% biotinylated 140C-α-syn monomer before incubation. Biotinylated off-pathway oligomers were purified using a Superdex 200 10/300 column (Cytiva, USA) in 25 mM Tris 125 mM NaCl pH 7.0 as running buffer (SI Fig. 1).

### 2.11. CF633 fluorophore labeling of SVLfib-5Cys

Fluorophore labeling of the peptide was achieved by covalently linking the CF633 maleimide labeling reagent (Sigma-Aldrich, USA) and the C-terminally introduced cysteine of the peptide SVLfib-5Cys. Briefly, CF633 was dissolved in DMSO to a final stock concentration of 10 mM. 100 µM SVLfib-5Cys was reduced by incubation with a 10-fold molar excess of TCEP in 10 mM NaPi pH 7.0 for 30 min at RT. Subsequently, a 20-fold molar excess of the CF633 maleimide labeling reagent was added followed by incubation ON at 4 °C. Labeled SVLfib-5-CF633 was purified using a RP-HPLC C18 column (Zorbax 300 SB-C18, Agilent, USA) with isocratic elution at 18.5% (v/v) Acetonitrile and 0.1% (v/v) TFA in ddH<sub>2</sub>O for 40 min at RT (SI Fig. 2). Samples were flash frozen in liquid N<sub>2</sub>, lyophilized and stored at -20 °C. The concentration of dissolved labeled product was determined by absorbance at A<sub>280</sub> and A<sub>633</sub> as described in the manufacturer's protocol.

### 2.12. Preparation of brain sections

Brain tissue samples were obtained from the Netherlands Brain Bank (nbb; NL). Menzel Superfrost slides (Thermo Fisher, USA) were frozen at -20 °C for preparation of brain sections in the cryostat (Leica CM3050S, GE). After the temperature of the cryostat was set at -20 °C and the temperature of the preparation head was set at 14 °C, the brain sections were attached to the preparation head with TissueTek O.C.T. medium (Science Services, GE). Sections were cut into 20 µm thick slices, transferred to slides, and thawed at RT, followed by drying on a hot plate at 37 °C for 30 min. Long-term storage was performed at -80 °C until further use.

### 2.13. Immunostaining of brain sections with SVLfib-5<sub>CF633</sub> and the monoclonal antibody 211<sub>CF488</sub>

The monoclonal antibody syn-211 (Thermo Fisher, USA) was labeled with CF488 succinimidyl ester (Sigma Aldrich, USA) via primary amino groups and then purified according to the manufacturer's protocol (DOL: 3.16). For staining, brain sections were thawed at RT for 5 min and then fixed in 4% paraformaldehyde (Sigma-Aldrich, USA) in Tris-buffered saline (TBS) for 10 min. The sections were then washed 3 × 3 min in TBS-T (TBS + 1% (w/v) Triton X 100). syn-211 mAb was diluted to a final concentration of 1 µg/ml and SVLfib-5-CF633 was diluted to a final concentration of 0.65 µg/ml (MW: 2612 g/mol) in TBS-

T containing 1% (w/v) BSA, followed by incubation on the brain sections ON at 4 °C. After incubation, the sections were washed  $3 \times 3$  min in TBS-T and incubated with DAPI (0.1  $\mu\text{g}/\text{ml}$  in TBS, Thermo Fisher, USA) for 5 min. After  $3 \times 3$  min washing in TBS, samples were covered with Fluoromount G Mounting Medium (Thermo Fisher, USA) and dried until the next day. Fluorescence images were acquired with identical exposure times for the different sections at 420 nm (DAPI), 488 nm (211\_Cf488) and 568 nm (SVLfib\_5\_Cf633) excitation wavelength (*Leica Application Suite v4.0*).

### 3. Results and discussion

#### 3.1. Preparation and validation of the aggregated $\alpha$ -syn selection target

Biotinylated  $\alpha$ -syn fibrils were prepared by incubation of 5% biotinylated  $\alpha$ -syn monomer with wt monomer, followed by incubation for 6 d at 37 °C under aggregation promoting conditions (Heise et al., 2005).

During the incubation process, formation of ThT-positive  $\alpha$ -syn aggregates was monitored by probing the sample at different time points (Fig. 1A). After 6 d of incubation, insoluble aggregates were harvested and separated from remaining free  $\alpha$ -syn monomer by centrifugation. The identity of the  $\alpha$ -syn aggregates and the status of biotinylation were subsequently verified by saturation ELISA using the anti-aggregated  $\alpha$ -syn monoclonal antibody 5G4 as the primary detection antibody to detect biotinylated  $\alpha$ -syn aggregates, which were immobilized in 96-well plate derivatized with streptavidin (Fig. 1B). Additional AFM sample analysis shows fibrillary polymorphs, which were detected together with smaller species, probably induced by sonication of the sample prior to surface immobilization. The biotinylated  $\alpha$ -syn fibrils were further used as target for the following phage display selection procedure.

#### 3.2. Phage display selection

To identify peptide ligands that bind to aggregated  $\alpha$ -syn species, phage display selection on aggregated  $\alpha$ -syn was performed in three consecutive selection rounds using either NEB 12-mer or Trico 16-mer M13 phage libraries (New England Biolabs and creative Biolabs, USA, respectively). The selection procedure, including positive and negative control surfaces, was performed as described previously (Sevenich et al., 2022; Kolkwitz et al., 2022; Santur et al., 2021).

To verify the successful enrichment of the target-specific binding sequences during the selection process, output titer after phage elution

(Fig. 2A) and the enrichment of the binding phages on the target protein and the monomeric  $\alpha$ -syn control were determined (Fig. 2B). The output titer analysis for the Trico-16 selection shows a slight increase from  $4$  to  $7 \cdot 10^7$  PFU/ml when the target was present during the selection process (target selection = TS), while a titer decrease from  $1 \cdot 10^8$  to  $7 \cdot 10^7$  PFU/ml was observed when the target was absent (empty selection = ES; Fig. 2A, left). Similar, the enrichment ELISA of amplified phages shows progressive signal increase on the fibril target with each selection round, while the third selection round additionally shows a higher signal on the fibril target as compared to the monomer target (Fig. 2B, left). These results indicate that the selection with the Trico-16 library resulted in an enrichment of peptide variants that exhibit affinity for aggregated  $\alpha$ -syn, but reduced affinity for the  $\alpha$ -syn monomer.

In contrast to the Trico-16 selection, the output titer of the NEB-12 selection decreases from the first to the third selection round from  $2 \cdot 10^8$  to  $6 \cdot 10^7$  PFU/ml (Fig. 2A, right). While the output titer of TS, ES, and DC of the third selection round (DC = direct control; TS-derived input is exposed to an empty surface) show titer values in the same range (Fig. 2A, right), a higher signal was detected for the fibril target compared to the monomer-coated surface for the third selection round in the ELISA assay (Fig. 2B, right).

Since both selections show a specific target-related signal in the third selection round, both selections were further analyzed by NGS.

#### 3.3. NGS and sequence clustering yield SVLfib peptide sequences

NGS sequencing resulted in identification of  $\sim 250,000$  and  $\sim 173,000$  sequence variants per sample for the NEB-12 and Trico-16 phage display selections, respectively. By applying an automated filter system, which sorts for target specific, enriching variants, the total number of variants was reduced to  $\sim 150,000$  for the NEB-12 selection and  $\sim 110,000$  for the Trico-16 selection. Sequence ranking by empty score (TS3/ES3) and enrichment factor (TS3/lib), combined with motif clustering using *Hammock clustering software* (Krejci et al., 2016), allowed the identification of five sequence variants per selection, that showed an increase of its relative frequency, when subjected to the target in TS, and decrease, if the target was not present (DC). Moreover, motif clustering reveals, that the majority of the sequence positions is highly conserved (Fig. 3A and B). Interestingly, the majority of the sequences that emerged from Trico-16 selection showed a pronounced accumulation of amino acids with acidic isoelectric point, such as aspartic acid and glutamic acid, toward the C-terminus of the sequence, which may indicate a general function of negative charges for

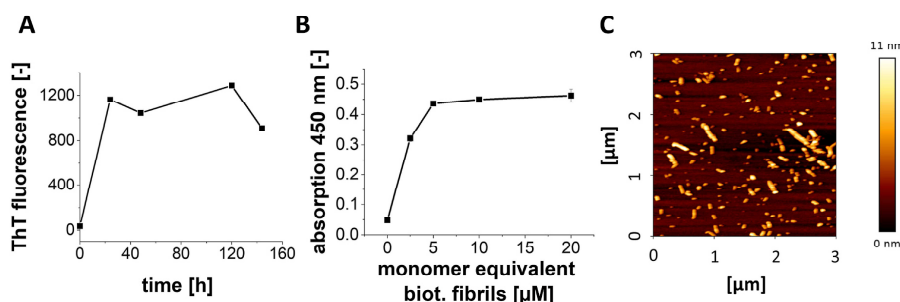


**Fig. 1. Preparation and characterization of biotinylated  $\alpha$ -syn fibrils.** (A) ThT monitoring of biotinylated  $\alpha$ -syn fibril formation. Biotinylated fibrils were prepared by incubation of 400  $\mu\text{M}$  5%  $\alpha$ -syn 140C\_PEG2-biotin with 95 % wt  $\alpha$ -syn at 37 °C under continuous stirring with a teflon coated micro bar at 200 rpm (in 25 mM Tris pH 7.5, 0.01%  $\text{NaN}_3$ ). (B) Saturation ELISA with 2.5–20  $\mu\text{M}$  freshly sonicated biotinylated  $\alpha$ -syn fibrils. Biotinylated fibrils were incubated on streptavidin coated 96-well plates. Fibrils were detected using 5G4 anti-aggregated  $\alpha$ -syn as primary antibody and anti-IgG-HRP fusion secondary antibody (error bars show SD;  $n = 3$ ). (C) Atomic force microscopy (AFM) measurement of biotinylated  $\alpha$ -syn fibrils. The fibrils were diluted to a final concentration of 1  $\mu\text{M}$   $\alpha$ -syn monomer equivalent. 5  $\mu\text{l}$  diluted sample was incubated and dried on a freshly cleaved mica surface followed by washing with  $\text{ddH}_2\text{O}$  and drying using a gentle stream of  $\text{N}_2$ . Analysis was performed using a NanoWizard 3 system (J-1100, JPK BioAFM, USA).

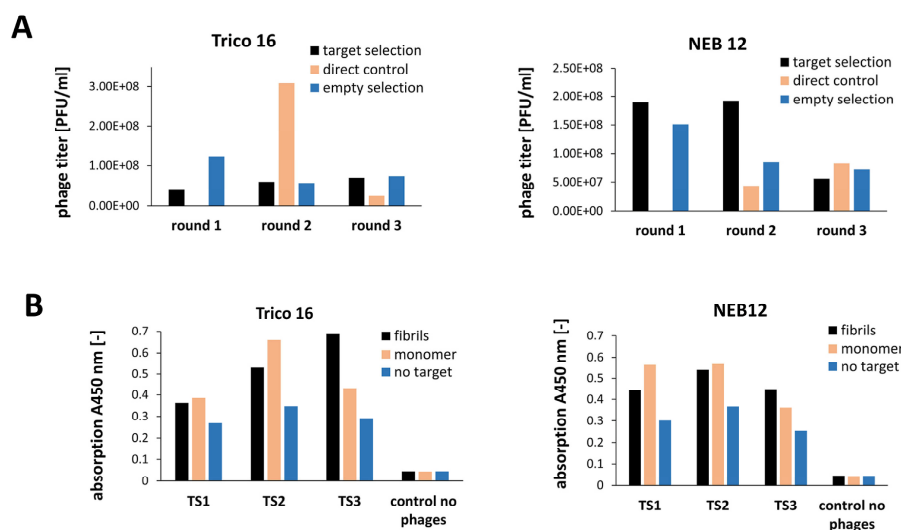


Fig. 2. Selection on  $\alpha$ -syn fibrils using Trico-16 and NEB libraries. Selection on biotinylated  $\alpha$ -syn fibrils was performed in three consecutive selection rounds using either Trico 16 or NEB12 phage libraries. (A) Output phage titer of phage forming units (PFU)/ml were determined by blue-white screening. Please note that in round 1 the direct control is identical to the empty selection and this is not shown separately. (B) Enrichment ELISA using input phage samples from Trico and NEB12 selections. Streptavidin derivatized surfaces were coated using biotinylated  $\alpha$ -syn monomer or biotinylated fibrils to verify the target specificity of the enriched phages.

interaction with the aggregated  $\alpha$ -syn target protein.

Based on the NGS filter and motif clustering results, the 10 synthetic peptides SVLfib-1 to -10 (5 sequences per selection, Fig. 3A and B, tables) were evaluated in the following assays to investigate their interaction with the selection target.

#### 3.4. Identification of lead peptide sequence SVLfib-5 by affinity screening

The synthetic peptides SVLfib-1 to -10 were analyzed for their interaction with the selection target. For this purpose, wt  $\alpha$ -syn was fibrillated without biotin tag and then purified as described previously. Subsequently, the aggregated  $\alpha$ -syn sample was sonicated and immobilized on a carboxyl dextran sensor surface. Elongation capacity of the immobilized species was verified by injection of monomeric  $\alpha$ -syn, and identity was proven via recognition by the anti-aggregation  $\alpha$ -syn monoclonal antibody 5G4 (SI Fig. 2). For subsequent affinity screening, the solubility of SVLfib peptides was tested by diluting DMSO dissolved samples to a target concentration of 2.5% DMSO in 25 mM Tris pH 7.4 50 mM NaCl. SVLfib-1 and -6 precipitated during the procedure and were therefore excluded from further analysis. The remaining SVLfib peptides were injected onto aggregated  $\alpha$ -syn-immobilized sensor surfaces (Fig. 4) (see Fig. 5).

Multicycle injections of the SVLfib peptides on the immobilized aggregated  $\alpha$ -syn revealed transient interaction profiles for SVLfib-3, -4, -9 and -10, whereas a stable interaction was identified for sequence SVLfib-5 (Fig. 4).

To further characterize the interaction with the aggregated  $\alpha$ -syn species kinetically, SVLfib-5 was injected in multicycle as well as single cycle kinetic experiments on carboxymethyl dextran derivatized surfaces immobilized with aggregated  $\alpha$ -syn as described previously (Fig. 6A and C). In addition, the peptide was injected on a streptavidin surface immobilized with biotinylated  $\alpha$ -syn monomer as control (Fig. 6B).

Kinetic analysis of SVLfib-5 interaction with aggregated and

monomeric  $\alpha$ -syn shows that the interaction is specific for the aggregated sample, while the monomer is not bound by the peptide. This result is consistent with the enrichment ELISA, which showed lower specificity for  $\alpha$ -syn monomer compared to the aggregated sample (Fig. 2B). Fitting of multicycle and single-cycle kinetic experiments yields kinetic rates in the same range. Interestingly, a rather slow association rate without signal curvature was obtained for both experiments, probably indicating mass transport limitation. This is likely due to the high ligand immobilization level. Because the mass transport limitation is not satisfactorily reduced by increasing the flow rate, the interaction kinetics presented here must be considered as indicative rather than absolute kinetic parameters. Moreover, the heterogeneity of the immobilized pool of aggregated  $\alpha$ -syn species might make it difficult to assign a unique kinetic model for the interaction.

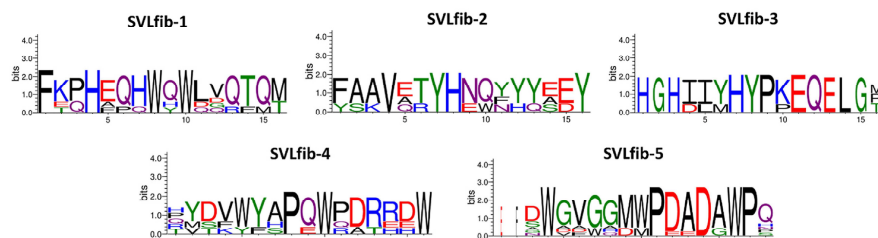
However, since most of the above experimental constraints should lead to an underestimation of the association rate, the actual  $K_D$  is most likely in the nM range.

#### 3.5. SVLfib-5 recognizes $\alpha$ -syn oligomers and fibrils with high sequence specificity

Previous experiments have led to the identification of lead sequence SVLfib-5, exhibiting high affinity towards the whole immobilized pool of  $\alpha$ -syn aggregates. Since the immobilized aggregate sample consists of various fibrillary as well as non-fibrillary conformers, we decided to additionally analyze the affinity towards a purified, non-fibrillar conformer. For immobilization on a streptavidin derivatized sensor surface, we prepared biotinylated off-pathway oligomers. To further verify the sequence specificity of the observed interactions we designed the two randomized control peptides SVLfib.CP1 and CP2 (CP1: AAVGGDWPQDWWMPD-NH<sub>2</sub>; CP2: DDPGWPAQDAGMVGW-NH<sub>2</sub>) as well as a hypothetical binding region, which comprises the C-terminal part of SVLfib-5, containing the previously mentioned negatively charged aspartate residues: SVLfib-5<sub>short</sub> (WPDADAWP-NH<sub>2</sub>). All

A

ID	Sequence	TS3	ES3	DC3	TS2	ES2	DC2	TS1	ES1	lib	empty score	enrichment score
SVLfib-1	FKPHEQHQQWLVQTQM	61.33	0.62	34.66	6.42	0.67	2.51	1.36	0.70	1.14	98.78	53.62
SVLfib-2	FAAVETYNQYYEY	37.33	0.62	23.10	26.98	6.66	26.37	12.21	8.41	6.86	60.13	5.44
SVLfib-3	HGHITTYHYPKEQLG	29.33	0.62	16.17	6.42	0.67	3.77	4.07	1.40	2.29	47.24	12.82
SVLfib-4	CYDVWYAPQWDRRDW	28.00	0.62	2.31	8.99	0.67	3.77	2.71	0.70	1.14	45.09	24.48
SVLfib-5	DWVGGMWPDADAWPQ	44.00	1.24	41.59	19.27	0.67	12.56	2.71	1.40	1.14	35.43	38.47



B

ID	Sequence	TS3	ES3	DC3	TS2	ES2	DC2	TS1	ES1	lib	empty score	enrichment score
SVLfib-6	DYITNPSPFHQ	96.36	0.79	93.98	10.14	0.83	7.98	0.81	0.83	0.75	121.80	128.13
SVLfib-7	SNHLNPHPSHG	38.21	0.79	30.81	8.69	0.83	7.98	1.62	0.83	0.75	48.30	50.81
SVLfib-8	SSNHDSLPTRF	31.57	0.79	7.70	5.80	0.83	3.19	3.25	0.83	0.75	39.90	41.97
SVLfib-9	GTWSRPSDSHA	31.57	0.79	15.41	11.59	0.83	1.60	6.49	0.83	0.75	39.90	41.97
SVLfib-10	AWASSVPSGLR	29.90	0.79	16.95	14.49	0.83	12.77	3.25	0.83	0.75	37.80	39.76

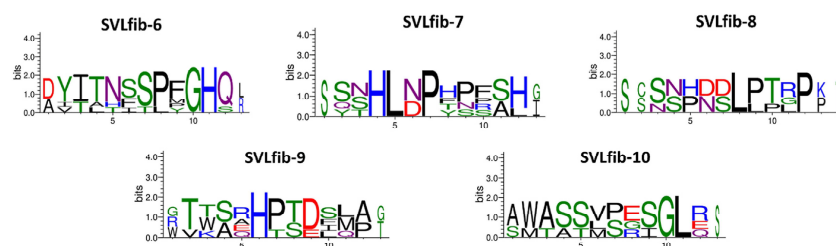


**Fig. 3.** NGS sequencing and motif clustering of Trico 16 and NEB phage display selections on  $\alpha$ -syn fibrils. NGS sequencing and cluster motif generation was performed as described previously (Sevenich et al., 2022) for Trico 16 (A) and NEB12 (B) phage display selection. Based on empty score and enrichment score, 5 peptides of each selection were selected for synthesis and further evaluation steps (SVLfib-1 to –10). Cluster motifs were generated with *Hammock clustering software* (Krejci et al., 2016), where the corresponding NGS-identified sequence built the cluster core. This means that the sequence shown in the motif can partially deviate from the one identified by NGS.

variants were injected on sensor surfaces, which were previously immobilized either with the whole  $\alpha$ -syn aggregate pool (Fig. 7A) or purified biotinylated  $\alpha$ -syn off-pathway oligomers (Fig. 7B).

Both experiments show that SVLfib-5<sub>original</sub> recognizes aggregated  $\alpha$ -syn with high sequence specificity. While no binding signal of the control peptides SVLfib\_CP1 and \_CP2 was observed for the oligomeric  $\alpha$ -syn (Fig. 7B), binding with substantially slower association rate and faster dissociation rate as compared to SVLfib-5<sub>original</sub> was identified on the whole aggregate ligand (Fig. 7A). Interestingly, SVLfib<sub>short</sub>, which encompasses the hypothetical binding region, shows no affinity for either sample, similar to SVLfib\_CP1 and \_CP2. These results show clearly, that the recognition of SVLfib-5 is highly sequence specific and that the complete 16-mer sequence is required for target interaction. Regarding the identity of the target conformer, the results indicate that SVLfib-5 binding is not only restricted to fibrillary conformers (Fig. 7A),

but might be specific for binding sites that are shared by certain types of fibrillary and oligomeric polymorphs (Fig. 7B).

### 3.6. Staining with SVLfib-5<sub>CF633</sub> overlaps with anti- $\alpha$ -syn specific staining of PD, MSA and DLB tissue samples

SVLfib-5 has shown high specificity for certain aggregated  $\alpha$ -syn species in previous experiments. To further verify, whether this specificity is also valid for human samples with actual disease-associated structures, immunofluorescence double staining was performed with the anti- $\alpha$ -syn monoclonal antibody syn-211<sub>CF488</sub> (green channel) and labeled SVLfib-5<sub>CF633</sub> (red channel) to confirm co-localization (Fig. 8). Syn-211 binds a C-terminal epitope (positions 121 to 125 (Giasson et al., 2000) of  $\alpha$ -syn and, therefore, recognizes  $\alpha$ -syn in both its monomeric and aggregated forms (oligomeric and fibrillary (Kumar et al., 2020),

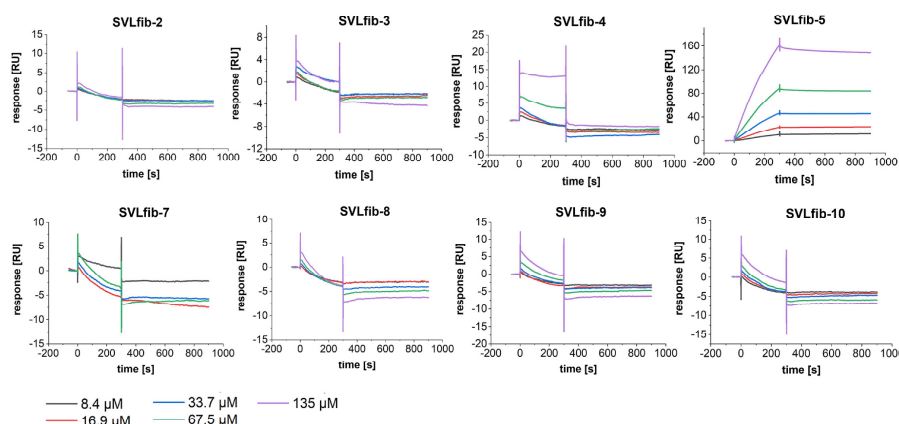


**Fig. 4.** SPR multicycle screening of SVLfib peptides on immobilized non-biotinylated  $\alpha$ -syn fibrils.  $\alpha$ -syn fibrils were prepared as described previously without the addition of biotinylated  $\alpha$ -syn monomer. Fibrils were immobilized via primary amino group coupling on a carboxyl derivatized matrix (CM5, Cytiva, USA) using EDC/NHS chemistry. SVLfib peptides were injected in TBS pH 7.4, 50 mM NaCl, 2.5% DMSO using 30  $\mu$ l/min in a Biacore T200 device (Cytiva, USA). No regeneration was performed in between cycles to avoid fibril disruption. Peptides SVLfib-2 and -6 were not soluble in the assay buffer and therefore excluded from the screening.

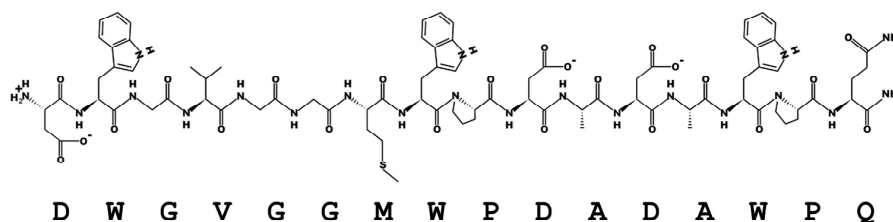


**Fig. 5.** Natta projection and single letter amino acid code of the lead compound sequence SVLfib-5.

although accumulated signal will most likely indicate aggregated  $\alpha$ -syn species.

For staining, sections from PD, MSA, and DLB patients as well as age matched non-demented controls (for sample specifications see [SI Table 1](#)) were prepared and incubated with the syn-211\_CF488 as well as SVLfib-5\_CF633 probes ([Fig. 8](#)).

Subsequent fluorescence detection showed clear differences between diseased and non-diseased control samples. Co-localization of SVLfib-5 and syn-211 are evident in larger areas in the diseased samples, but not in the non-demented controls. In the samples of the non-demented controls, the fluorescent signal is mainly green and only a small fraction yellow, suggesting that the signal detected here originates from nonspecific binding of syn-211 or auto-fluorescence rather than from co-localization with SVLfib-5. In addition, the size of the co-localized areas shows a marked difference between the diseased sample and the corresponding controls. Although, due to the fact that syn-211 recognizes both monomeric and aggregated species, no concluding statement can be made about the morphologic identity of the co-localizing signal accumulations, it is tempting to speculate that they are indeed fibrillary or oligomeric  $\alpha$ -syn in the form of Lewy bodies, Lewy neurites, or Papp-Lantos inclusions. This assumption is supported in particular by the striking structure and size of these areas, which has been described previously numerous times ([Spillantini et al., 1997b](#); [Kanazawa et al., 2008](#); [Jellinger and Lantos, 2010](#)).

More importantly, SVLfib-5 is recognizing only structures that are

also stained by monoclonal antibody syn-211 and the majority of the larger structures can be clearly assigned to the diseased samples.

#### 4. Summary and outlook

In this study, we presented a novel phage display and NGS-based method for the straightforward identification of PET tracer peptides tailored for PD and other synucleinopathies. The development of tracer molecules for these diseases is of utmost importance, as there is currently no approved disease-associated tracer.

SPR-based affinity screening led to the identification of the lead sequence SVLfib-5, which exhibited low micromolar to nanomolar dissociation constants for the entire immobilized aggregate pool, whereas no affinity for the monomeric  $\alpha$ -syn was detected. Further analysis using randomized control peptides showed not only that the interaction is highly sequence specific, but also that  $\alpha$ -syn off-pathway oligomer preparations were recognized with similar affinity as compared to the entire aggregate pool. Finally, comparison of immunofluorescence staining of PD, MSA, and DLB brain samples with the corresponding non-diseased controls showed that SVLfib-5 specifically recognizes  $\alpha$ -syn containing structures that are also recognized by syn-211.

Taken together, all experimental results show that SVLfib-5 recognizes aggregated  $\alpha$ -syn structures (oligomer and or fibrillary) with high affinity and specificity. One of the fundamental advantages of using

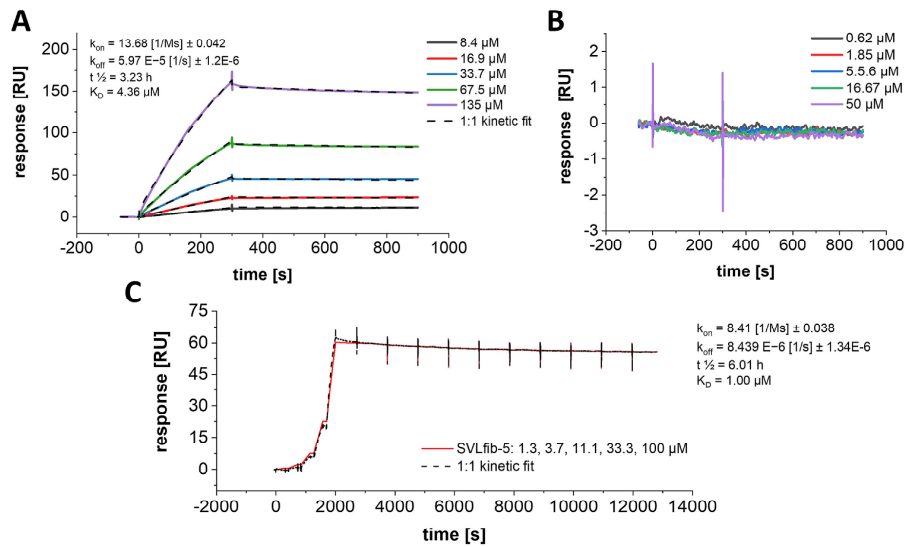


**Fig. 6.** Kinetic analysis of SVLfib-5 interaction with aggregated and monomeric  $\alpha$ -syn. (A/C) Kinetic multicycle (A) and single cycle (C) analysis of SVLfib-5 on immobilized  $\alpha$ -syn fibrils.  $\alpha$ -syn fibrils were prepared as described previously without the addition of biotinylated  $\alpha$ -syn monomer. Fibrils were immobilized via primary amino group coupling on a carboxyl-derivatized matrix (CM5, Cytiva, USA) using EDC/NHS chemistry. SVLfib-5 was injected in TBS pH 7.4, 50 mM NaCl using 60  $\mu$ l/min for association phase and 30  $\mu$ l/min for dissociation phase at RT. Fitting was performed using a 1:1 kinetic interaction model (Biacore insight evaluation software v3.0 (Cytiva, USA)). (B) Multicycle injection of SVLfib-5 on  $\alpha$ -syn monomer. 140C-PEG<sub>2</sub>-biotin  $\alpha$ -syn was immobilized on a streptavidin derivatized SA-sensor surface (Cytiva, USA).

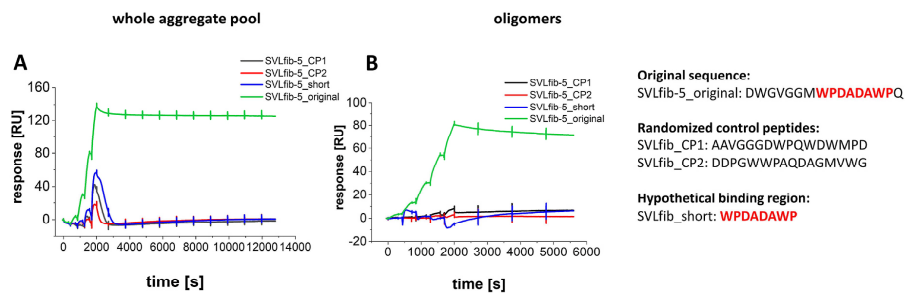


**Fig. 7.** Single cycle kinetic experiment with SFLfib-5 and its control peptides on the whole immobilized aggregate pool or off pathway oligomers. (A) For immobilization of the whole aggregate pool, non-biotinylated  $\alpha$ -syn aggregates were immobilized via primary amino group coupling on a carboxyl methyl-derivatized matrix (CM5, Cytiva, USA) using EDC/NHS chemistry. SFLfib-5, \_CP1, \_CP2 and \_short were injected in TBS pH 7.4, 50 mM NaCl using 6.25, 12.5, 25, 50 and 100  $\mu$ M concentrations at 60  $\mu$ l/min with 300 s association, followed by 3 h dissociation at 30  $\mu$ l/min. (B) Biotinylated  $\alpha$ -syn off-pathway oligomers were immobilized on a streptavidin functionalized SA-Sensor Chip (Cytiva, USA), followed by quenching with biotin. SFLfib-5, \_CP1, \_CP2 and \_short were injected in TBS pH 7.4, 50 mM NaCl using 6.25, 12.5, 25, 50 and 100  $\mu$ M concentrations at 60  $\mu$ l/min with 300 s association, followed by 1 h dissociation at 30  $\mu$ l/min.

peptides as tracer molecules is their high penetration rate of the blood-brain barrier compared to antibodies (Zhou et al., 2021). However, since L-enantiomeric peptides such as SVLfib-5 are rapidly degraded by proteases when administered to the body, further optimization steps regarding their stability may be required in the future. Here, the retro-inverso strategy could be used to create D-enantiomeric peptides with higher proteolytic resistance (Vaissiere et al., 2017). On the other hand, *ex vivo* detection of  $\alpha$ -syn oligomers in body fluids such as blood, cerebrospinal fluid or saliva for PD, MSA and DLB diagnosis could be another promising application for SVLfib-5. Methods based on the identification of single aggregate particles, such as the sFIDA assay

(Herrmann et al., 2017), in combination with tailored high-affinity all-D-peptide tracers, would be a promising strategy for the early diagnosis of these diseases. Although staining of brain tissue from PD, MSA, and DLB patients has shown that SVLfib-5 is rather a general marker for aggregated  $\alpha$ -syn species and not able to distinguish polymorphic subtypes, the histopathological distribution of aggregates and the spread of pathology should allow differentiation between PD, MSA, and DLB.

In conclusion, the presented data show promising initial results on the development of a  $\alpha$ -syn specific tracer peptide for PD and other synucleinopathies. In particular, the transfer of the described methods to other neurodegenerative disease such as Alzheimer's, Tauopathies and

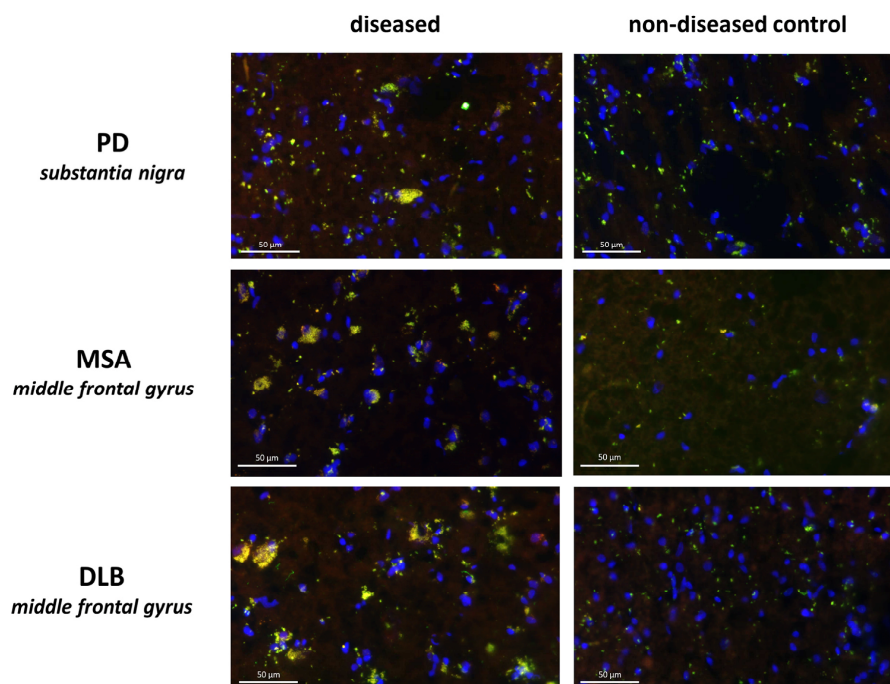


**Fig. 8.** Co-staining of brain tissue samples using SVLfib-5\_Cf633 (red) and mAb syn-211\_Cf488 (green). Brain tissue samples (obtained from Netherlands Brain Bank) were selected based on diagnosis and affected brain region (substantia nigra for PD and middle frontal gyrus for MSA and DLB, respectively). Immunofluorescence was performed on 20 µm frozen brain sections, which were subsequently incubated ON with SVLfib-5\_Cf633 and syn-211\_Cf488. For visualization of cell nuclei, counterstaining with DAPI (blue) was performed and fluorescence images were recorded with identical exposure time for each sample and fluorescence channel. The sections shown here are representative for multiple recorded sections.

Poly-Q diseases could be a promising starting point for the development of further disease-specific tracer peptides.

#### Research funding

DW received funding from the German Research Foundation, CRC 1208, Project B02.

#### Author contributions

**Conceptualization:** MS, AW, JM and DW; **Formal analysis:** MS, AW, JK, JM and DW; **Investigation:** MS and DH; **Methodology:** MS and DH; **Project administration:** MS, JM and DW; **Validation:** MS and DH; **Visualization:** MS and DH; **Writing - original draft:** MS; **Review & editing:** MS, AW, JK, JM and DW.

#### Declaration of competing interest

MS, JM and DW are co-inventor of patents covering the composition of matter of SVLfib-5 peptide. They declare that this has not influenced to evaluation and interpretation of experiments. All other authors declare no competing interest.

#### Data availability

Data will be made available on request.

#### Appendix A. Supplementary data

Supplementary data to this article can be found online at <https://doi.org/10.1016/j.neuint.2022.105422>.

#### References

- Alam, P., et al., 2019. alpha-synuclein oligomers and fibrils: a spectrum of species, a spectrum of toxicities. *J. Neurochem.* 150 (5), 522–534.
- Alcalay, R.N., et al., 2010. Frequency of known mutations in early-onset Parkinson disease. *Arch. Neurol.* 67 (9), 1116–1122.
- Bare, K., Kuzma-Kozakiewicz, M., 2019. Positron emission tomography neuroimaging in neurodegenerative diseases: Alzheimer's disease, Parkinson's disease, and amyotrophic lateral sclerosis. *Neurol. Neurochir. Pol.* 53 (2), 99–112.
- Bengoa-Vergniory, N., et al., 2017. Alpha-synuclein oligomers: a new hope. *Acta Neuropathol.* 134 (6), 819–838.
- Blomeke, L., et al., 2022. Quantitative detection of alpha-Synuclein and Tau oligomers and other aggregates by digital single particle counting. *NPJ Parkinsons Dis* 8 (1), 68.
- Chartier-Harlin, M.C., et al., 2004. alpha-synuclein locus duplication as a cause of familial Parkinson's disease. *Lancet* 364 (9440), 1167–1169.
- Giasson, B.L., et al., 2000. A panel of epitope-specific antibodies detects protein domains distributed throughout human alpha-synuclein in Lewy bodies of Parkinson's disease. *J. Neurosci. Res.* 59 (4), 528–533.
- Giehm, L., et al., 2011. Low-resolution structure of a vesicle disrupting alpha-synuclein oligomer that accumulates during fibrillation. *Proc. Natl. Acad. Sci. U.S.A.* 108 (8), 3246–3251.
- Heise, H., et al., 2005. Molecular-level secondary structure, polymorphism, and dynamics of full-length alpha-synuclein fibrils studied by solid-state NMR. *Proc. Natl. Acad. Sci. U.S.A.* 102 (44), 15871–15876.
- Herrmann, Y., et al., 2017. sFIDA automation yields sub-femtomolar limit of detection for Aβ aggregates in body fluids. *Clin. Biochem.* 50 (4–5), 244–247.

- Hoyer, W., et al., 2002. Dependence of alpha-synuclein aggregate morphology on solution conditions. *J. Mol. Biol.* 322 (2), 383–393.
- Jellinger, K.A., Lantos, P.L., 2010. Papp-Lantos inclusions and the pathogenesis of multiple system atrophy: an update. *Acta Neuropathol.* 119 (6), 657–667.
- Johnson, M., et al., 2010. Targeted amino-terminal acetylation of recombinant proteins in *E. coli*. *PLoS One* 5 (12).
- Kanazawa, T., et al., 2008. Three-layered structure shared between Lewy bodies and Lewy neurites - three-dimensional reconstruction of triple-labeled sections. *Brain Pathol.* 18 (3), 415–422.
- Kolkwitz, P.E., Mohrlueder, J., Willbold, D., 2022. Inhibition of polyglutamine misfolding with D-enantiomeric peptides identified by mirror image phage display selection. *Biomolecules* 12 (2).
- Krejci, A., et al., 2016. Hammock: a hidden Markov model-based peptide clustering algorithm to identify protein-interaction consensus motifs in large datasets. *Bioinformatics* 32 (1), 9–16.
- Kumar, S.T., et al., 2020. How specific are the conformation-specific alpha-synuclein antibodies? Characterization and validation of 16 alpha-synuclein conformation-specific antibodies using well-characterized preparations of alpha-synuclein monomers, fibrils and oligomers with distinct structures and morphology. *Neurobiol. Dis.* 146.
- Lorenzen, N., et al., 2014. The role of stable alpha-synuclein oligomers in the molecular events underlying amyloid formation. *J. Am. Chem. Soc.* 136 (10), 3859–3868.
- Mathis, C.A., et al., 2017. Small-molecule PET tracers for imaging proteinopathies. *Semin. Nucl. Med.* 47 (5), 553–575.
- Nuytemans, K., et al., 2010. Genetic etiology of Parkinson disease associated with mutations in the SNCA, PARK2, PINK1, PARK7, and LRRK2 genes: a mutation update. *Hum. Mutat.* 31 (7), 763–780.
- Olanow, C.W., Brundin, P., 2013. Parkinson's disease and alpha synuclein: is Parkinson's disease a prion-like disorder? *Mov. Disord.* 28 (1), 31–40.
- Papp, M.I., Kahn, J.E., Lantos, P.L., 1989. Glial cytoplasmic inclusions in the CNS of patients with multiple system Atrophy (Striatonigral degeneration, olivopontocerebellar atrophy and Shy-Drager Syndrome). *J. Neurol. Sci.* 94 (1–3), 79–100.
- Peng, C., et al., 2018. Cellular milieu imparts distinct pathological alpha-synuclein strains in alpha-synucleinopathies. *Nature* 557 (7706), 558–563.
- Poewe, W., et al., 2017. Parkinson disease. *Nat. Rev. Dis. Prim.* 3.
- Santur, K., et al., 2021. Ligand-induced Stabilization of the native human Superoxide Dismutase 1. *ACS Chem. Neurosci.* 12 (13), 2520–2528.
- Sevenich, M., et al., 2022a. Phage display-derived compounds Displace hACE2 from its complex with SARS-CoV-2 Spike protein. *Biomedicines* 10 (2).
- Spillantini, M.G., et al., 1997a. alpha-synuclein in Lewy bodies. *Nature* 388 (6645), 839–840.
- Spillantini, M.G., et al., 1997b. Alpha-synuclein in Lewy bodies. *Nature* 388 (6645), 839–840.
- Spillantini, M.G., et al., 1998. Filamentous alpha-synuclein inclusions link multiple system atrophy with Parkinson's disease and dementia with Lewy bodies. *Neurosci. Lett.* 251 (3), 205–208.
- Vaissiere, A., et al., 2017. A retro-inverso cell-penetrating peptide for siRNA delivery. *J. Nanobiotechnol.* 15 (1), 34.
- Winner, B., et al., 2011. In vivo demonstration that alpha-synuclein oligomers are toxic. *Proc. Natl. Acad. Sci. U.S.A.* 108 (10), 4194–4199.
- Yamasaki, T.R., et al., 2019. Parkinson's disease and multiple system atrophy have distinct alpha synuclein seed characteristics. *J. Biol. Chem.* 294 (3), 1045–1058.
- Zhou, X., Smith, Q.R., Liu, X.L., 2021. Brain penetrating peptides and peptide-drug conjugates to overcome the blood-brain barrier and target CNS diseases. *Wiley Interdisciplinary Reviews-Nanomedicine and Nanobiotechnology* 13 (4).

## 2.5 Discovery of all-D-peptide inhibitors of SARS-CoV-2 3C-like protease

Authors: Raphael Eberle, **Marc Sevenich**, Ian Gering, Lara Scharbert, Birgit Strodel, Nils A. Lakomek, Karoline Santur, Jeannine Mohrlüder, Mônica A. Coronado and Dieter Willbold

Journal: ACS Chemical Biology

DOI: <https://doi.org/10.1021/acscchembio.2c00735>

Impact Factor: 5.1 (2022)

Contribution: Planning and performance of SPR assays, sample preparation for NMR measurements, writing of SPR method section, results and discussion, manuscript editing.

## Discovery of All-D-Peptide Inhibitors of SARS-CoV-2 3C-like Protease

Raphael J. Eberle, Marc Sevenich, Ian Gering, Lara Scharbert, Birgit Strodel, Nils A. Lakomek, Karoline Santur, Jeannine Mohrlüder, Mônica A. Coronado,\* and Dieter Willbold\*

 Cite This: <https://doi.org/10.1021/acscchembio.2c00735>

Read Online

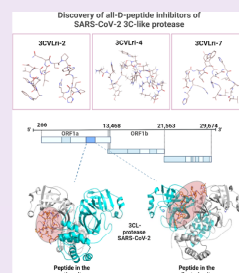
ACCESS |

Metrics &amp; More

Article Recommendations

Supporting Information

**ABSTRACT:** During the replication process of SARS-CoV-2, the main protease of the virus [3-chymotrypsin-like protease (3CL<sup>pro</sup>)] plays a pivotal role and is essential for the life cycle of the pathogen. Numerous studies have been conducted so far, which have confirmed 3CL<sup>pro</sup> as an attractive drug target to combat COVID-19. We describe a novel and efficient next-generation sequencing (NGS) supported phage display selection strategy for the identification of a set of SARS-CoV-2 3CL<sup>pro</sup> targeting peptide ligands that inhibit the 3CL protease, in a competitive or noncompetitive mode, in the low  $\mu\text{M}$  range. From the most efficient L-peptides obtained from the phage display, we designed all-D-peptides based on the retro-inverso (ri) principle. They had IC<sub>50</sub> values also in the low  $\mu\text{M}$  range and in combination, even in the sub-micromolar range. Additionally, the combination with Remdesivir decreases 10-fold the IC<sub>50</sub> value of the competitive inhibitor. The inhibition modes of these D-ri peptides were the same as their respective L-peptide versions. Our results demonstrate that retro-inverso obtained all-D-peptides interact with high affinity and inhibit the SARS-CoV-2 3CL protease, thus reinforcing their potential for further development toward therapeutic agents. The here described D-ri peptides address limitations associated with current L-peptide inhibitors and are promising lead compounds. Further optimization regarding pharmacokinetic properties will allow the development of even more potent D-peptides to be used for the prevention and treatment of COVID-19.



## 1. INTRODUCTION

The spread of Coronavirus disease 2019 (COVID-19) caused by severe acute respiratory syndrome coronavirus 2 (SARS-CoV-2), with increasing levels of infectivity and transmissibility, has strained human health and public safety worldwide.<sup>1</sup> By May 2022, the COVID-19 pandemic has resulted in more than 524 million confirmed cases and more than 6.2 million confirmed deaths, according to the World Health Organization (WHO).<sup>2</sup> To date, vaccination is considered the key strategy for ending the pandemic<sup>3</sup> and the worldwide vaccination campaign using clinical safe and efficient vaccines against SARS-CoV-2 have controlled the number of death. However, not yet the spread of the diseases.<sup>4–7</sup> So far, more than 11.8 billion vaccine doses have been administered.<sup>2</sup> Remdesivir, Dexamethasone, Favipiravir, Lopinavir/Ritonavir, Nirmatrelvir/Ritonavir (Main protease inhibitor), and Darunavir have been approved for emergency use to inhibit SARS-CoV-2 infection and replication.<sup>8–12</sup> Given a considerable limitation of direct-acting antivirals for COVID-19 and an increasing presence of SARS-CoV-2 variants (B.1.1.529, B.1.617.2, B.1.1.7, B.1.351, A.23.1, B.1.525, B.1.526 and P.1),<sup>13</sup> it remains a strategic priority to develop new drug candidates with minimal side effects and also targeting the new variants.

For the expression and replication of the CoV gene, proteases play essential roles involving the proteolytic processing of replicase polyproteins, which makes them attractive targets for drug development.<sup>14,15</sup> The main protease, also called 3CL protease (3CL<sup>pro</sup>), is the 3-chymotrypsin-like cysteine protease

that features a His41-Cys145 catalytic dyad. A glutamine (Gln) residue is commonly located at the P1 site on the protease substrate. No known human cysteine protease cleaves after Gln, thus offering potential selectivity for this viral target over human proteases.<sup>16,17</sup> Viral proteases have been attractive targets for oral small-molecule therapies in treating HIV and HCV.<sup>18,19</sup> The use of SARS-CoV-2 3CL<sup>pro</sup> as a drug target has several advantages over other virus proteins: (i) its essential role in the viral replication process, (ii) its potential for mechanistic safety, and (iii) the expected lack of variant resistance challenges.<sup>8</sup> 3CL<sup>pro</sup> inhibition represents an attractive approach for a safe and orally available antiviral therapy to treat COVID-19.

Drugs are conventionally classified into two molecule weight classes: “small-molecule” drugs (<500 Da) and protein/peptide-based drugs (>1000 Da).<sup>20</sup> Besides the obvious advantages of small molecules like favorable oral bioavailability and a rational design,<sup>21</sup> they often have low target selectivity, ultimately resulting in side effects. In comparison, peptides were often neglected as potential molecules for drug development, despite binding to their target proteins with high affinity and specificity. They are smaller than proteins and can be obtained synthetically

Received: September 22, 2022

Accepted: December 1, 2022

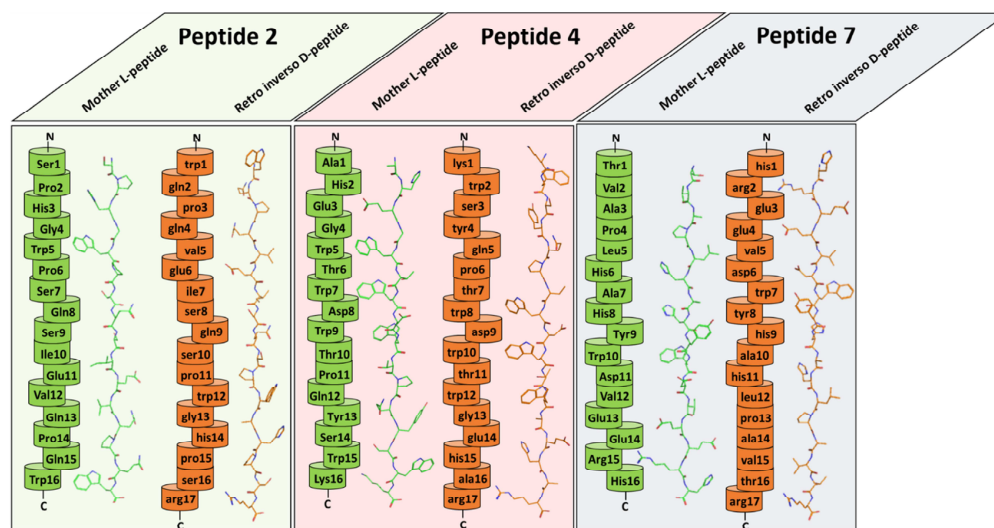


Figure 1. Schematic overview of the investigated D-ri peptides and their mother L-peptides.

by well-established and cost-efficient methods.<sup>22</sup> The disadvantages of peptide drugs are their potential immunogenicity and low bioavailability due to degradation and short half-lives. Several approaches have been developed to approach these problems. D-Enantiomeric amino acid residues effectively enhance the resistance to degradation since most proteolytic enzymes have substrate specificity for L-peptide bonds, allowing oral administration of D-enantiomeric peptides.<sup>23,24</sup> Furthermore, all-D-peptides are less immunogenic.<sup>25</sup>

Several studies described the development of the first all-D-peptide designed to treat Alzheimer's disease, and it proved to be efficient in animal models and safe in humans.<sup>26–28</sup> In the case of SARS-CoV-2, several studies describe the identification of D-peptide inhibitors against SARS-CoV-2 Spike protein and 3CL<sup>pro</sup>.<sup>29–32</sup> Of particular interest are all-D-peptides composed of D-amino acid residues. However, many peptide-based drug development strategies, like phage display selection, end up with L-peptides. So-called D-retro-inverso (D-ri) peptides are composed solely of D-amino acid residues in the reverse sequence of their parental L-peptide (Figure 1). Such a peptide assembled in reversed sequence from D-amino acid residues will have almost the same structure, stability, and bioactivity as its parent peptide made of L-amino acid residues, but with the advantage of being more resistant to proteolytic degradation. This combination makes D-ri peptides attractive drug candidates.<sup>33</sup> The overall orientation of the side chains of the D-ri peptides is very similar to the original L-peptides, which, however, does not lead to perfect D-ri peptides, which is undoubtedly one reason why the retro-inverso approach was not successful in every case.<sup>34–36</sup>

However, in this paper, we demonstrate the inhibition potential of L-peptides selected using phage display targeting SARS-CoV-2 3CL<sup>pro</sup>. Subsequently, its retro-inverso versions were explored, also in combination.

## 2. RESULTS

### 2.1. Characterization of SARS-CoV-2 3CL<sup>pro</sup> Inhibition by L- and D-Retro-Inverso Peptides.

All experiments were performed with recombinant produced SARS-CoV-2 3CL<sup>pro</sup> protein (Supporting Information, Figure S1). To select binding L-peptides to the 3CL<sup>pro</sup>, M13 phage display selection was performed (Figure 2A). Detailed information about the phage display process is described in Supporting Information, Text S1, Figures S2 and S3, and Tables S1–S3. To verify whether the selected peptides showed inhibition toward the target protein, they were primary tested using a final concentration of 10  $\mu\text{M}$  of each peptide, separately, in an enzyme-based fluorescence assay (Figure 2B). With more than 60% inhibition, the peptides 3CVL-2 (SPHGWPSQSIEVQPQW), 3CVL-4 (AHEGWTWDWTPQYSWK), and 3CVL-7 (TVAPLHAHYWDVEERH) were selected for further analysis (Figure 2C–E). Concerning their potential to inhibit 100% of the protease activity, determination of the IC<sub>50</sub> was performed using 0–140  $\mu\text{M}$  (3CVL-2), 0–120  $\mu\text{M}$  (3CVL-4), and 0–100 (3CVL-7). The 3CVL-2 at a final concentration of 140  $\mu\text{M}$  showed 100% inhibition of the protease (Supporting Information, Figure S4A) with a calculated IC<sub>50</sub> value of  $4.90 \pm 0.8 \mu\text{M}$  (Table 1 and Figure 2C). In a similar concentration range, the tested 3CVL-4 inhibited 100% of the protease activity at a final concentration of 120  $\mu\text{M}$  (Supporting Information, Figure S4C), presenting an IC<sub>50</sub> value of  $2.44 \pm 0.6 \mu\text{M}$  (Table 1 and Figure 2D). The selected peptide 3CVL-7 performs even better and inhibits 100% of the recombinant SARS-CoV-2 protease activity at a final concentration of 80  $\mu\text{M}$  (Supporting Information, Figure S4E) with an IC<sub>50</sub> value of  $0.98 \pm 0.2 \mu\text{M}$  (Table 1 and Figure 2E). Further inhibition mode assays identified 3CVL-2 and 3CVL-7 as competitive inhibitors. These peptides compete with the substrate for the active and/or binding sites of the protease (Supporting Information, Figure S4B,F). Remarkably, the inhibition mode has shown that 3CL<sup>pro</sup> can be allosterically inhibited by 3CVL-4, which discloses a

B

<https://doi.org/10.1021/acscchembio.2c00735>  
ACS Chem. Biol. XXXX, XXX, XXX–XXX

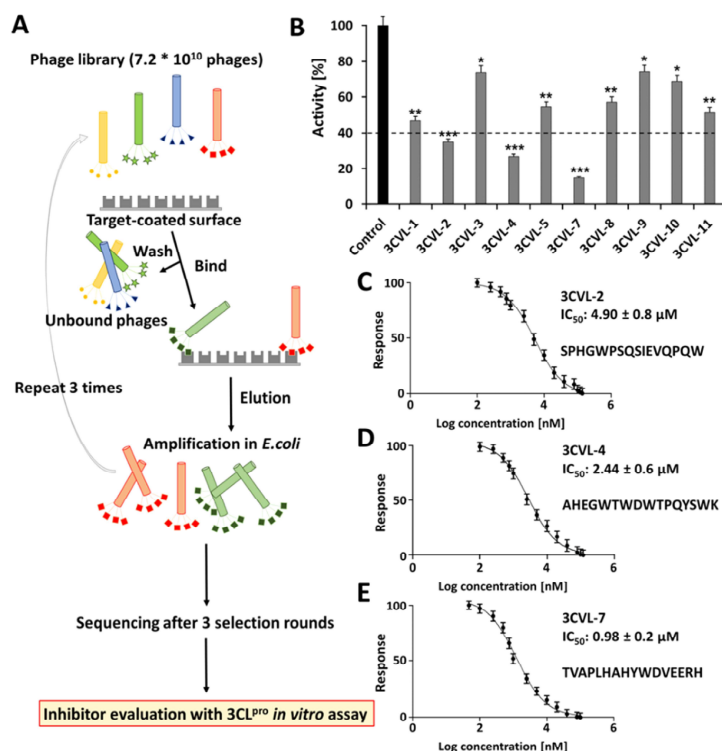


**Figure 2.** Phage display scheme and screening of phage display L-peptides against SARS-CoV-2 3CL<sup>pro</sup> activity. (A) Schematic diagram of the phage display process. (B) Primary screen of the 11 selected peptides (10  $\mu$ M) against SARS-CoV-2 3CL<sup>pro</sup> activity. 3CVL-2, 3CVL-4, and 3CVL-7 inhibit the virus protease activity by more than 60%. (C–E) Selected peptide inhibiting SARS-CoV-2 3CL<sup>pro</sup>. Dose–response curves for IC<sub>50</sub> values of 3CVL-2 (C), 3CVL-4 (D), and 3CVL-7 (E) were determined by nonlinear regression. Data shown are the mean  $\pm$  standard deviation (SD) from three independent measurements ( $n = 3$ ). Asterisks mean that the data differ from the control (0  $\mu$ M inhibitor) significantly at  $p < 0.05$  (\*),  $p < 0.01$  (\*\*), and  $p < 0.001$  (\*\*\*) levels according to analyses of variance (ANOVA) and Tukey's test.

**Table 1. Summary of the SARS-CoV-2 3CL<sup>pro</sup> Inhibition Experiments by 3CVL-2, -4, and -7**

peptide	IC <sub>50</sub> ( $\mu$ M)	inhibition mode
3CVL-2	$4.90 \pm 0.8$	competitive
3CVL-4	$2.44 \pm 0.6$	noncompetitive
3CVL-7	$0.98 \pm 0.2$	competitive

noncompetitive inhibition mode (Supporting Information, Figure S4D).

To improve the poor proteolytic stability of L-enantiomeric peptides without losing affinity and binding specificity to their target protein, the peptides 3CVL-2, 3CVL-4, and 3CVL-7 were synthesized in retro-inverse D-enantiomeric (D-ri) form and designated as 3CVLri-2, 3CVLri-4, and 3CVLri-7, respectively. Glycine does not have a chiral center that was the reason that the D-ri peptides have identical amino acid sequences, except for glycine, which was replaced by alanine. Additionally, an arginine was added to the C-termini of each D-ri peptide to increase the permeability of the peptides. The representative scheme is shown in Figure 3A,B.

Like the L-peptides, the D-ri-peptides were tested using a concentration range of up to 140  $\mu$ M (3CVLri-2 and 3CVLri-4) and up to 100  $\mu$ M (3CVLri-7), which showed 100% inhibition of the protease by the corresponding used final concentration (Supporting Information, Figure S5A,C,E). Based on the enzymatic assay, the IC<sub>50</sub> values were determined for each D-ri peptide, displaying for 3CVLri-2 ( $9.09 \pm 0.5 \mu$ M), 3CVLri-4 ( $5.36 \pm 1.7 \mu$ M) and 3CVLri-7 ( $1.57 \pm 0.2 \mu$ M) an increase of the IC<sub>50</sub> values of about 2-fold compared to the L-peptides (Figure 3C–E and Table 2). The mode of inhibition of the D-ri peptides was maintained, displaying a competitive mode of 3CVLri-2 and -7 and an allosteric mode of inhibition for 3CVLri-7 (Supporting Information, Figure S5B,D,F). A sequence analysis between the preferred 3CL<sup>pro</sup> cleavage sequence pattern at the substrate-binding site and the identified inhibitors demonstrated that the competitive inhibitors have a higher similarity (ranging from 62.5 to 12.5%) compared to the noncompetitive inhibitors (no similarity) (Supporting Information, Figure S6).

**2.2. Competitive and Noncompetitive D-Retro-Inverso Peptides Act Cooperatively to Inhibit SARS-CoV-2 3CL<sup>pro</sup>.** To presume the effect of the competitive (3CVLri-2

C

<https://doi.org/10.1021/acscchembio.2c00735>  
ACS Chem. Biol. XXXX, XXX, XXX–XXX

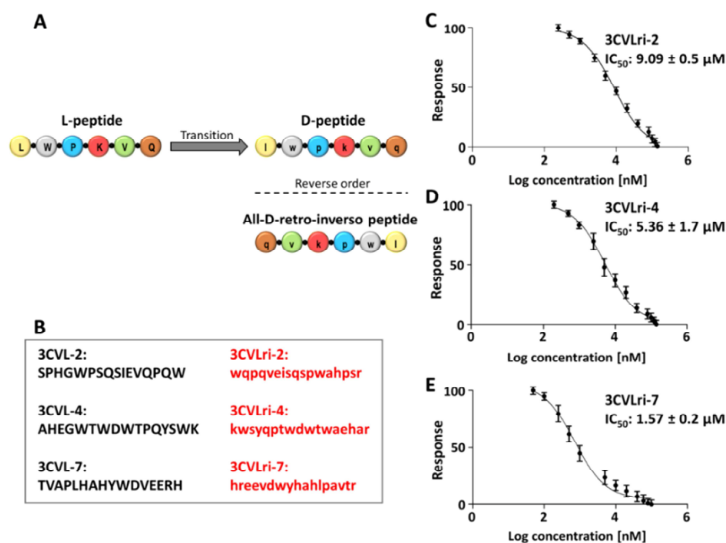


**Figure 3.** Principle for obtaining D-retro-inverso peptides and inhibitory effect against SARS-CoV-2 3CL<sup>pro</sup> activity. (A) Schematic diagram of D-retro-inverso (D-ri) peptides. (B) Sequences of 3CVLri-2, -4, -7 and their mother L-peptides. In the D-ri peptides, glycine (G) was replaced by alanine (a). (C–E) All-D-ri peptides inhibit SARS-CoV-2 3CL<sup>pro</sup> activity. Dose–response curves for  $IC_{50}$  values of 3CVLri-2 (C), 3CVLri-4 (D), and 3CVLri-7 (E) were determined by nonlinear regression. Data shown are the mean  $\pm$  SD from three independent measurements ( $n = 3$ ).

**Table 2.** Summary of the SARS-CoV-2 3CL<sup>pro</sup> Inhibition Experiments by 3CVLri-2, -4 and -7

peptide	$IC_{50}$ ( $\mu\text{M}$ )	inhibition mode
3CVLri-2	$9.09 \pm 0.5$	competitive
3CVLri-4	$5.36 \pm 1.7$	noncompetitive
3CVLri-7	$1.57 \pm 0.2$	competitive

and 3CVLri-7) and noncompetitive (3CVLri-4) D-retro-inverso peptides, a combined inhibitory assay was performed (3CVLri-2 + 3CVLri-4 and 3CVLri-7 + 3CVLri-4). Both peptides were mixed in a 1:1 volume ratio and tested against the protease activity (Figure 4).

The calculated  $IC_{50}$  values for the 3CVLri-2 + 3CVLri-4 combination and the 3CVLri-7 + 3CVLri-4 combination were  $0.87 \pm 0.3$  and  $0.39 \pm 0.1 \mu\text{M}$  (Figure 4A,B).

**2.3. Cooperative Inhibition of SARS-CoV-2 3CL<sup>pro</sup> by Rupintrivir and 3CVLri-4.** Rupintrivir is a known inhibitor of the 3C cysteine protease family but showed a weak inhibitory potential against the SARS-CoV-2 3CL<sup>pro</sup>.<sup>37–39</sup> The determined  $IC_{50}$  value for Rupintrivir was  $109 \pm 14.40 \mu\text{M}$  (Figure 5A) and is in agreement with published data.<sup>34,35</sup> The  $IC_{50}$  value for the Rupintrivir/3CVLri-4 combination was  $15.10 \pm 1.60 \mu\text{M}$  (Figure 5B).

**2.4. Binding Affinities of Selected 3CL<sup>pro</sup>- and D-Peptide Inhibitors.** The interaction kinetics of 3CVLri-2, -4, and -7 with 3CL<sup>pro</sup> and its D-ri form was determined using surface plasmon resonance (SPR) experiments. 3CL<sup>pro</sup> was immobilized via covalent primary amino group coupling, and 3CVL and 3CVLri peptides were injected as analytes. Supporting Information Figures S9 and S10 show the SPR sensorgrams for 3CVL peptides at assay concentrations of 50,

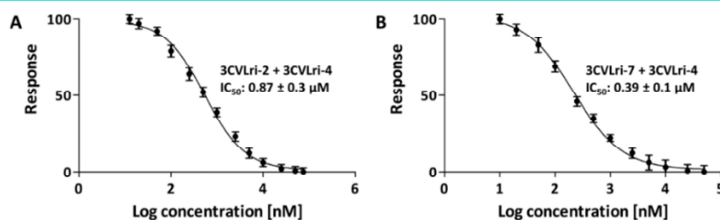


**Figure 4.** SARS-CoV-2 3CL<sup>pro</sup> inhibition by a combination of competitive and noncompetitive D-retro-inverso peptides simultaneously. Dose–response curves for  $IC_{50}$  values of the combination were determined by nonlinear regression. Data shown are the mean  $\pm$  SD from three independent measurements ( $n = 3$ ). The corresponding normalized activity and inhibition plots of SARS-CoV-2 3CL<sup>pro</sup> under the influence of the combined peptides are shown in the Supporting Information, Figure S7. (A) Dose–response curve of the 3CVLri-2 + 3CVLri-4 combination. (B) Dose–response curve of the 3CVLri-7 + 3CVLri-4 combination.

D

<https://doi.org/10.1021/acscchembio.2c00735>  
ACS Chem. Biol. XXXX, XXX, XXX–XXX

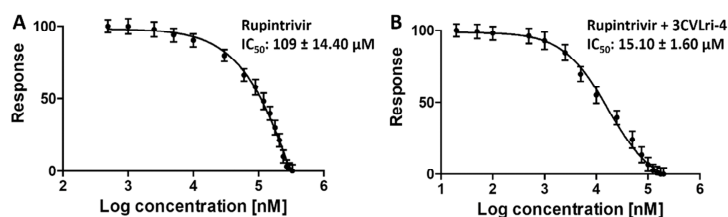


**Figure 5.** SARS-CoV-2 3CL<sup>pro</sup> inhibition by Rupintrivir and Rupintrivir/3CVLri-4 combination. Dose–response curves of the IC<sub>50</sub> values were determined by nonlinear regression. Data shown are the mean ± SD from three independent measurements (*n* = 3). The corresponding normalized activity and inhibition plots of SARS-CoV-2 3CL<sup>pro</sup> under the influence of the combined peptides are shown in Supporting Information, Figure S8. (A) Dose–response curve of Rupintrivir. (B) Dose–response curve of the Rupintrivir/3CVLri-4 combination.

25, 12.5, 6.25, 3.12, 1.56, 0.78, and 0.39  $\mu\text{M}$  on 3CL<sup>pro</sup> immobilized on the CMS sensor chip. The fit for the competitive inhibitors was made using a heterogeneous ligand model in which the two binding sites on the dimer are assumed to behave differently, as described for the 3CL<sup>pro</sup> dimer active sites.<sup>40–42</sup> The fit for the noncompetitive inhibitor was made using a 1:1 stoichiometric kinetic fitting.

Heterogeneous ligand fitting revealed dissociation constants from the low  $\mu\text{M}$  to low nM range for the higher affine binding site. Global 1:1 fitting showed dissociation constants in the low  $\mu\text{M}$  range (Supporting Information, Figures S9 and S10 and Table 3).

**Table 3.**  $K_D$  Values Determined by SPR Experiments

heterogeneous ligand fitting		
peptide	$K_D1$	$K_D2$
3CVL-2	0.5 nM	6.5 $\mu\text{M}$
3CVL-7	1.8 $\mu\text{M}$	7.8 $\mu\text{M}$
3CVLri-2	46.8 $\mu\text{M}$	1.7 $\mu\text{M}$
3CVLri-7	2.4 nM	35 $\mu\text{M}$
1:1 ligand fitting		
peptide	$K_D$	
3CVL-4	5.1 $\mu\text{M}$	
3CVLri-4	25.2 $\mu\text{M}$	

The binding kinetic parameters of the association rate  $k_a$ , dissociation rate  $k_d$ , and dissociation constant  $K_D$  ( $k_d/k_a$ ) for the interaction of 3CL<sup>pro</sup> with peptides 3CVL-2, -4, -7, and 3CVLri-2, -4, and -7 are shown in Supporting Information, Figures S9 and S10.

**2.5. 24 h Stability and Promiscuous Assays of 3CVLri Peptides.** Peptide-based inhibitors targeting active proteolytic proteases can lose their inhibitory effect over time. Based on our focus, the retro-inverso peptides were tested regarding their stability over 24 h. The results demonstrated a constant inhibition of SARS-CoV-2 3CL<sup>pro</sup> over time, showing that the peptides are not prone to the 3CL protease digestion (Supporting Information, Figure S11). Furthermore, a detergent-based control was carried out to exclude peptide inhibitors that possibly act as an aggregator of 3CL<sup>pro</sup>, so-called “promiscuous” inhibitors. The experiment was performed by adding 0.001, 0.01, and 0.1% of Triton X-100 detergent to the reaction. Suppose that a molecule exhibits significant inhibition of 3CL<sup>pro</sup>, but this is diminished by detergent; it may act as an aggregation-based inhibitor. This was not observed for the tested 3CVLri peptides (Supporting Information, Figure S12).

**2.6. Metabolic Stability of 3CVLri Peptides.** To investigate the 3CVLri-2, 3CVLri-4, and 3CVLri-7 peptides’ resistance against enzymatic degradation, the peptides were incubated in media simulating the gastrointestinal tract, blood, and liver, and the unmetabolized peptides were quantified by reversed-phase high-performance liquid chromatography (RP-HPLC). In simulated gastric fluid (SGF), the resistance of 3CVLri-2, 3CVLri-4, and 3CVLri-7 was monitored over 8 h. The results showed that the 3CVLri-4 and -7 peptides are relatively stable ( $\geq 80 \pm 3\%$ ) within 8 h. In contrast, 3CVLri-2 was remarkably metabolized ( $\sim 75 \pm 2\%$ ) (Figure 6A). The resistance of the D-ri peptides was also investigated using a simulated intestinal fluid (SIF). The peptides 3CVLri-2 and 3CVLri-4 remained rather stable over the selected time ( $\geq 90 \pm 1.5\%$ ), as well as 3CVLri-7 ( $\geq 85 \pm 5\%$ ) (Figure 6B). In human plasma, the stability of 3CVLri-2 and 3CVLri-7 was monitored for 48 h, with approximately 5% being metabolized ( $\geq 95 \pm 4.5\%$ ). In contrast, the 3CVLri-4 showed about  $21 \pm 5.6\%$  of degradation within 48 h (Figure 6C). Furthermore, human liver microsomes were monitored for 24 h, and 3CVLri-2 and 3CVLri-7 were about  $5 \pm 1.1\%$  metabolized. However, 3CVLri-7 was almost 50% metabolized ( $\geq 45 \pm 3.7\%$ ) in the same period (Figure 6D). The corresponding HPLC profiles of the stability tests are shown in Supporting Information, Figures S13–S16.

**2.7. In Silico Structural Properties of 3CVL and 3CVLri Peptides and Their Similar Interaction Mode with SARS-CoV-2 3CL<sup>pro</sup>.** Protease-peptide docking and subsequent molecular dynamics (MD) simulations were performed to investigate the possible binding interface between 3CL<sup>pro</sup>-L and D-ri-peptide complexes. The secondary structure of the three-dimensional (3D) models of the L-peptides (3CVL-2, -4, and -7) and their D-ri counterparts corroborates with circular dichroism (CD) spectroscopy results.

The models are supported by the results of the inhibition assay. The inhibition mode assay identified two peptides as competitive inhibitors, which requires interaction in the active site and/or in the substrate-binding site. Another peptide was identified as a noncompetitive inhibitor, which requires interaction with an allosteric site. Indeed, the two competitive inhibitors docked in the active site formed a very stable interaction during the MD simulations. The noncompetitive inhibitor was docked in an allosteric site, which was described previously and showed a stable interaction through MD simulation.

During the 1  $\mu\text{s}$  MD simulations of the unbound peptides, they mainly contained a random coiled secondary structure. However, the L- and D-ri-3CVL-4 peptides also frequently formed an  $\alpha$ -helix (Supporting Information, Figure S17A–C).

E

<https://doi.org/10.1021/acscchembio.2c00735>  
ACS Chem. Biol. XXXX, XXX, XXX–XXX

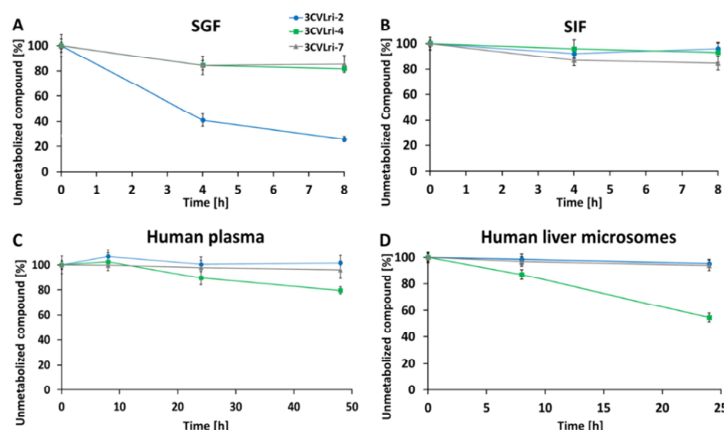


**Figure 6.** Stability of 3CVLri-2, 3CVLri-4, and 3CVLri-7 peptides incubated in SGF, SIF, human plasma, and human liver microsomes. (A) SGF, (B) SIF, (C) human plasma, and (D) human liver microsomes. Unmetabolized peptides were quantified by P-HPLC. The peak areas of the unmetabolized peptides after different incubation times were normalized to the peptides' peak areas after direct extraction from the media. Data are presented as mean  $\pm$  SD ( $n = 3$ ).

The atomic coordinates of SARS-CoV-2 3CL<sup>pro</sup> dimer (PDB entry: 6M2N) and ten representative structures per peptide from the peptide simulations were submitted for docking using AutoDock Vina.<sup>43</sup>

The competitive peptides 3CVL-2/3CVLri-2 and 3CVL-7/3CVLri-7 were docked into the active site and substrate-binding site of the protease (Supporting Information, Table S4). The noncompetitive peptides 3CVL-4 and 3CVLri-4 were docked in a potential allosteric binding site (Supporting Information, Table S4). Previous studies have indicated that only one active site of the dimer is functional.<sup>40,42</sup> Based on that information, 200 ns control MD simulation of the dimer without ligands was performed to identify a potentially less stable protomer or collapsing binding sites. Based on the volume of the active sites, we did not identify any differences between both protomers (Supporting Information, Figure S18). Therefore, we docked the competitive peptides into the active site of chain A. After docking, 100 ns MD simulations with 3 different initial structures of the 3CL<sup>pro</sup>/peptide complexes obtained from docking were conducted to further assess their stabilities. The initial structures were selected based on the calculated binding free energy and the distance to the critical catalytic dyad residues (Cys145 and His41). The flexibility of the peptides in complex with the protease was monitored by calculating the root-mean-square deviation (RMSD), root-mean-square fluctuations (RMSF), and  $\Delta H$  as the enthalpy of binding (Supporting Information, Figures S19–S21). In all three simulations of each 3CL<sup>pro</sup>/peptide complex, the peptide maintained its overall conformation in the binding pocket and no unbinding event was detected. Representative structures for all three simulations of each L- and D-ri-peptide are shown in Supporting Information, Figures S22 and S23. To investigate the 3CL<sup>pro</sup> peptide interactions in more detail, we selected one of the three MD simulations per peptide based on several criteria, such as the RMSD, RMSF, and the binding free energy, elongated the simulations to 200 ns and conducted them in triplicate. Each replica of the elongated simulations showed a stable interaction

between the L- and D-ri-3CVL peptides and their respective binding site of the 3CL<sup>pro</sup> dimer throughout the simulation.

To identify the most popular binding modes sampled during the elongated simulations, we applied conformational clustering but considered only the nonflexible/interacting residues (RMSF  $\leq 5$  Å) of the peptides (Supporting Information, Figure S24).

Interactions between the residues of the peptides and the protease were analyzed by calculating the minimum distance between them for the first three clusters per complex (Table 4).

**Table 4. Summary of MD Simulation Triplicates Considering Nonflexible/Interacting Residues of Peptides**

peptide	#cluster	representative frames first 3 clusters (%)
3CVL-2	8	97
3CVL-4	12	88
3CVL-7	25	80
3CVLri-2	12	83
3CVLri-4	10	99
3CVLri-7	14	93

Analysis of the 3CL<sup>pro</sup>-peptide complexes provides valuable information on the interaction interface similarities between 3CVL and 3CVLri peptides. Structural representation (Figure 7) demonstrated that 3CVL-2 extends along with S1', S1, and S3 subpockets of the protease substrate-binding site (Figure 7A).

In contrast, the 3CVLri-2 interacts with the substrate-binding site differently. However, it extends along with S1', S1, S2, and S3 (Figure 7B), which shows that one of the D-Gln residues of the 3CVLri-2 is very well accommodated. The 3CVL-7 and 3CVLri-7 interaction areas comprise residues of the S1', S1, S2 and S3 subsites (Figure 7C,D). The graphs in Figure 7 that show the minimum distance between peptide and 3CL<sup>pro</sup> residues reveal that all analyzed peptides formed several interactions with 3CL<sup>pro</sup> active/binding site residues. The localization in the substrate-binding region of the 3CVL peptides and their D-ri counterparts, even when it does not interact with the catalytic

F

<https://doi.org/10.1021/acscchembio.2c00735>  
ACS Chem. Biol. XXXX, XXX, XXX–XXX

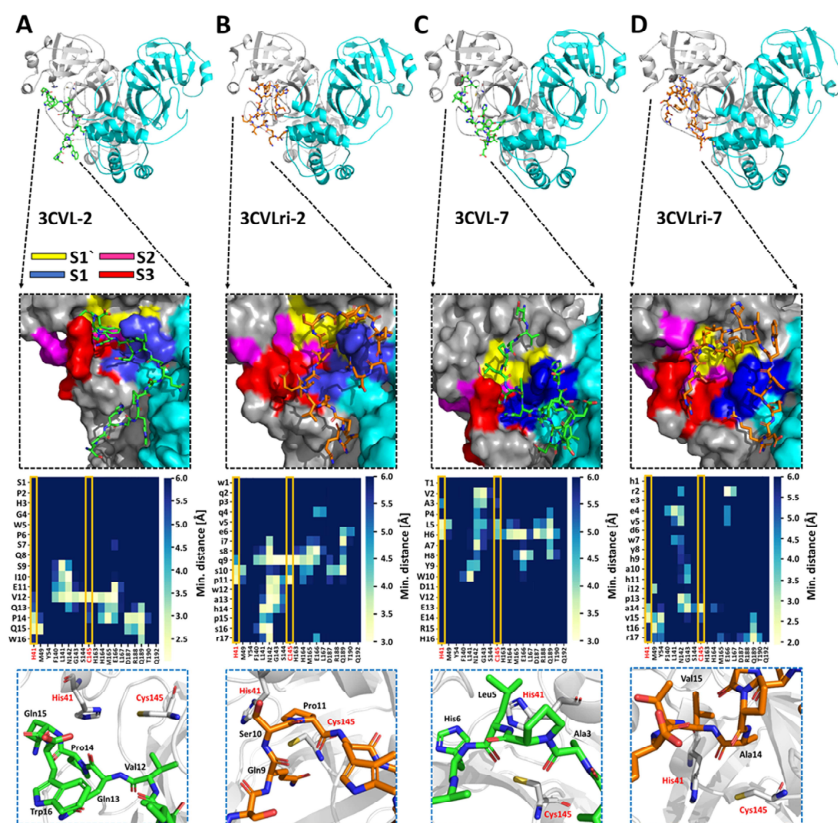


**Figure 7.** Comparison of the competitive 3CVL and 3CVLri peptide inhibitors binding position in the 3CVL<sup>P70</sup> active and substrate-binding site. 3CVL<sup>P70</sup> is shown in ribbon view: chain A (gray) and chain B (turquoise). The 3CVL (green) and 3CVLri (orange) peptides are shown as sticks. The surface view demonstrates a preferred position of the peptide in the substrate-binding region, and the single subsites are marked by different colors (S1': yellow; S1: blue; S2: pink; S3: red). The distance between the 3CVL<sup>P70</sup> substrate-binding site residues and the peptides shows that active site residues His41 and Cys145 are blocked by the inhibitors: (A) 3CVL-2, (B) 3CVLri-2, (C) 3CVL-7, (D) 3CVLri-7.

dyad (His41 and Cys145), showed the potential to block the entrance of the substrate.

To investigate the impact of the competitive inhibitors 3CVL-2, 3CVLri-2, 3CVL-7, and 3CVLri-7, two-dimensional NMR 1H-15N correlation spectra of 100  $\mu$ M 15N 3CVL<sup>P70</sup> were recorded in the presence of an equimolar amount of the respective peptides (1:1 ratio). Supporting Information, Figure S25A shows the reference spectrum of 15N 3CVL<sup>P70</sup> in the absence of the peptides. Spectral resonances are well resolved and display the properties of a globular protein containing both  $\beta$ -sheets and  $\alpha$ -helices. Several other 15N 3CVL<sup>P70</sup> resonances appear in the presence of 3CVL-2 (orange spectrum) compared to the reference spectrum (black) (Supporting Information, Figure S25B). That could point either to a second 3CVL<sup>P70</sup> conformation becoming visible or previously invisible parts of 3CVL<sup>P70</sup> becoming more dynamic and visible in the presence of the peptide. The effect seems less intense for 3CVLri-2 (Supporting Information, Figure S25C, light blue spectrum).

The NMR spectra of 15N 3CVL<sup>P70</sup> in the presence of 3CVL-7 (Supporting Information, Figure S26B) look very similar to those for 3CVL-2; several new resonances of 15N 3CVL<sup>P70</sup> appear in the presence of 3CVL-7 and 3CVLri-7 (Supporting Information, Figure S26B,C), indicating higher conformational or overall dynamics.

Contrary, the noncompetitive inhibitors 3CVL-4 and 3CVLri-4 were docked in a suggested allosteric site at the interface of the protomers. Structural representation of the interfaces of 3CVL<sup>P70</sup> in complex with the 3CVL-4 and 3CVLri-4 peptides are shown in Figure 8A,B.

Analysis of the distance between residues of the allosteric site of each protomer demonstrated that several residues of both protomer chains interact with the protease, in particular Lys12, 97, and 100 (Figure 8).

MD simulations of 3CVL-4 and 3CVLri-4 in a proposed allosteric site showed that this interaction induces conformational changes in the protease's active site.

G

<https://doi.org/10.1021/acchembio.2c00735>  
ACS Chem. Biol. XXXX, XXX, XXX–XXX

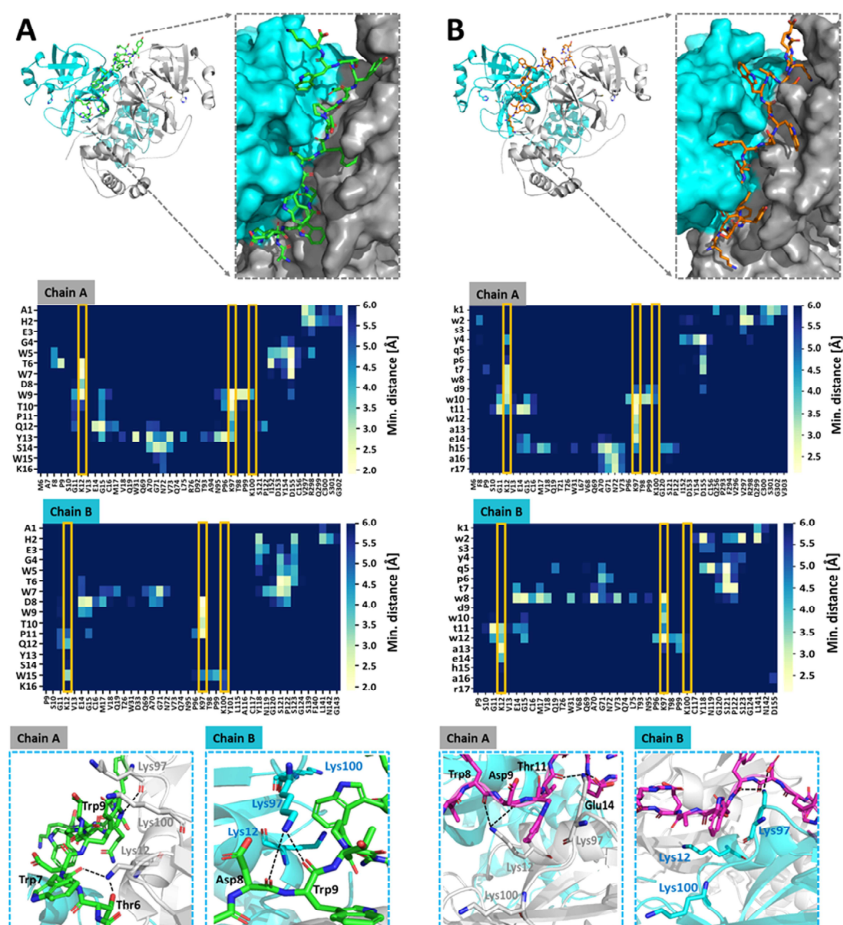


**Figure 8.** Comparison of the noncompetitive 3CVL-4 and 3CVLri-4 peptide inhibitors in a supposed 3CL<sup>Pro</sup> allosteric site. 3CL<sup>Pro</sup> is shown in ribbon view, and each protomer is colored differently: chain A (gray) and chain B (turquoise). 3CVL (green) and 3CVLri (orange) peptides are shown as sticks. The surface view demonstrates a preferred position of the peptide in the proposed allosteric site in a cleft between both protease protomers: (A) 3CVL-4 and (B) 3CVLri-4.

Determination of B-chain active site volume demonstrates a reduction compared to the control simulation due to the binding of 3CVL-4 and 3CVLri-4, respectively (Figure 9A–C and Supporting Information, Figure S27).

To determine the contribution of specific residues of the 3CVL and 3CVLri peptides to the interaction with 3CL<sup>Pro</sup> we performed a mutational analysis using alanine scanning. Alanine mutations that result in positive  $\Delta\Delta H$  values relative to the parent structure suggest loss of binding, which indicates that the mutated amino acid was involved in an overall favorable network of electrostatic interactions. Mutations that result in negative  $\Delta\Delta H$  suggest gain of binding, which indicates that the mutated amino acid was involved in an overall unfavorable network of electrostatic interactions.

In the case of 3CVLri-2 and its parental L-peptide Gln9 and Gln8, respectively, are important for the interaction with 3CL<sup>Pro</sup>. The Ser8 residue (Ser7 in the L-peptide) situated at the P2 position seems to have a weak effect on the interaction with 3CL<sup>Pro</sup> (Supporting Information, Figure S28A). The glutamine residues are in the P1 position of the peptides, as in the substrate already described for the protease, the P2 site has a preference for hydrophobic residues (Supporting Information, Figure S6). Important residues in the interaction between 3CVLri-7 (3CVL-7) and 3CL<sup>Pro</sup> are His9 (His6) and His11 (His8), unfavorable residues are Asp6 (Asp11) and Ala10 (Ala7) (Supporting Information, Figure S28A). In the case of the noncompetitive inhibitors, 3CVLri-4 (3CVL-4), Trp8 (Trp9), and Tyr4 (Tyr13) are mainly involved in the interaction with the virus protease. Interestingly, Asp8 in the mother L-peptide

H

<https://doi.org/10.1021/acscchembio.2c00735>  
ACS Chem. Biol. XXXX, XXX, XXX–XXX

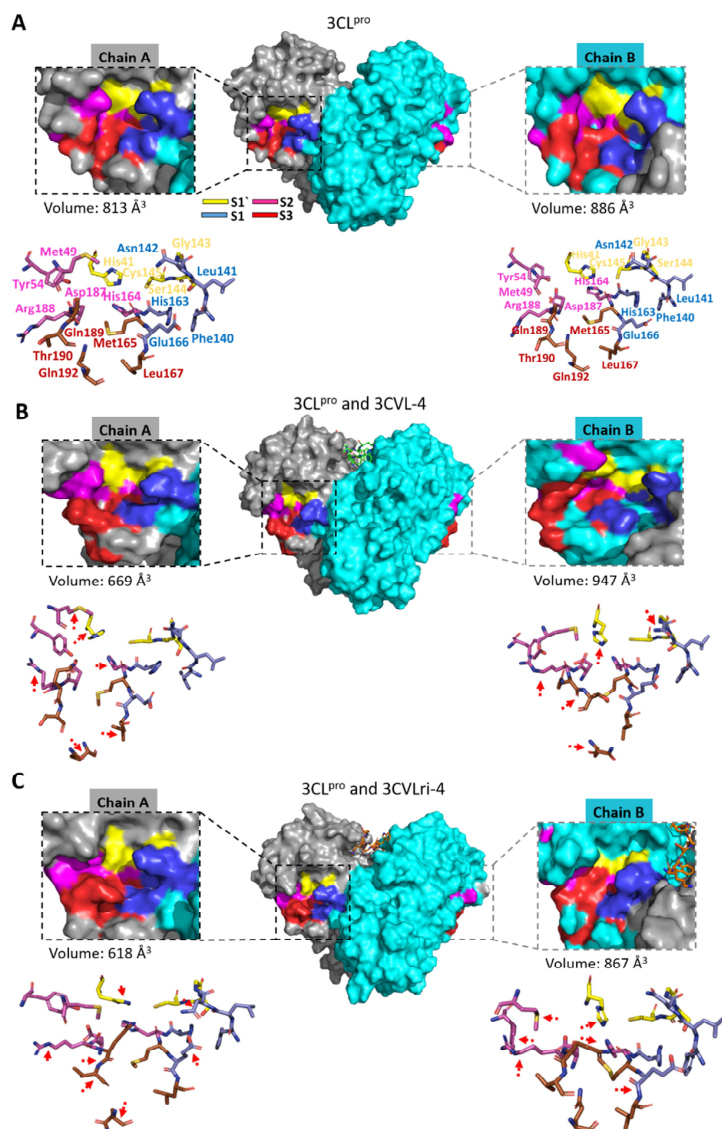


**Figure 9.** Comparison of the active site volumes of control and after binding of the noncompetitive  $3\text{CVL-4}$  and  $3\text{CVLri-4}$  peptide inhibitors in a supposed  $3\text{CL}^{\text{pro}}$  allosteric site.  $3\text{CL}^{\text{pro}}$  is shown in surface view, and each protomer is colored differently: chain A (gray) and chain B (turquoise). The substrate-binding subsites are colored differently. The active sites and substrate-binding sites of each protomer are shown enlarged with the corresponding volume in Å<sup>3</sup>. Amino acids forming the active site and substrate-binding site are shown in sticks, red arrows demonstrate the change of the position of the residues because of the conformational change induced by the noncompetitive inhibitors: (A)  $3\text{CL}^{\text{pro}}$ , (B)  $3\text{CL}^{\text{pro}}$  and  $3\text{CVL-4}$ , (C)  $3\text{CL}^{\text{pro}}$  and  $3\text{CVLri-4}$ .

(Supporting Information, Figure S28B) is unfavorable for the interaction, but the corresponding residue in the D-ri peptide is involved in the interaction with  $3\text{CL}^{\text{pro}}$ .

### 3. DISCUSSION AND CONCLUSIONS

Even with the development of several vaccines against SARS-CoV-2, the development of suitable therapeutics against COVID-19 is important since no causative therapy is known.

I

<https://doi.org/10.1021/acchembio.2c00735>  
ACS Chem. Biol. XXXX, XXX, XXX–XXX

Instead of inhibiting the interaction of the spike protein with the cell receptors,<sup>44,45</sup> we intend to target one of the most important proteases in virus replication, the 3CL protease, by D-enantiomeric peptide ligands preventing the cleavage function of 3CL<sup>pro</sup>. To this end, a phage display selection was performed. The identified L-peptides showed a strong inhibitory effect in the enzyme activity assay, with IC<sub>50</sub> values varying between 0.9 and 9 μM. As we demonstrated experimentally, 3CVL-4 is a noncompetitive inhibitor with an IC<sub>50</sub> value of 2.4 μM, which was maintained in its D-enantiomer retro-inverso form; however, with an increased IC<sub>50</sub> value of about 2-fold (5.4 μM). A 1:1 molar combination of the competitive and noncompetitive D-ri-peptides reduced the IC<sub>50</sub> values remarkably. 3CVLri-2 + 3CVLri-4 combination reduces the IC<sub>50</sub> value to 0.9 μM and the combination of 3CVLri 7 + 3CVLri 4 to 0.4 μM. It was clearly demonstrated that a combination of competitive and non-competitive inhibitors improved the inhibitory potential of all D-peptides. Similarly, in combination with Rupintrivir, a weak SARS-CoV-2 3CL<sup>pro</sup> competitive inhibitor (IC<sub>50</sub> > 100 μM), the inhibitory effect improved after the combination with the noncompetitive 3CVLri-4 (IC<sub>50</sub> of 15.10 ± 1.60 μM). The cooperative inhibition of SARS-CoV-2 3CL<sup>pro</sup> by competitive and noncompetitive inhibitors was also observed for Quinacrine/Suramin.<sup>42</sup> The structural analysis of 3CL<sup>pro</sup> in complex with the studied peptides by docking followed by molecular dynamics simulation predicted a stable conformation for each complex, indicating significant intermolecular interaction. Of note, when not directly interacting with the catalytic dyad, amino acid residues of the peptide are located close to the pocket entry, blocking the substrate entrance. The predicted structures of 3CL<sup>pro</sup> in complex with 3CVLri-2 indicate the occurrence of significant intermolecular interaction between the D-glutamine of the all-D-ri peptide and amino acid residues of the S1 subpocket, which explains the strong preference for D-glutamine at P1.<sup>46</sup>

A combination of competitive and noncompetitive D-ri-peptides (3CVLri-2/3CVLri-4 and 3CVLri-7/3CVLri-4) increased the inhibitory effect against 3CL<sup>pro</sup>.

The all-D-peptides 3CVLri-2 and -7 showed a remarkable resistance against metabolism over 8 h.

Two-dimensional 1H-15N TROSY-NMR correlation spectra of 15N 3CL<sup>pro</sup> with 3CVL-2/3CVLri-2 and 3CVL-7/3CVLri-7 demonstrated the appearance of new and similar resonances, which may indicate the same binding region for the peptides.

Our study yielded all-D-peptides with a promising potential for further development toward therapeutic use against SARS-CoV-2 3CL<sup>pro</sup>.

#### 4. MATERIALS AND METHODS

**4.1. Peptides.** All peptides were purchased from Caslo (Lyngby, Denmark) as a lyophilized powder with >98% purity. Peptides 3CVL 1–10 consist of 16 amino acid residues in L-configuration with amidated C-termini. The D-retro-inverso (D-ri) peptides 3CVLri-2, 3CVLri-4, and 3CVLri-7 have identical amino acid sequences, except for glycine, which was replaced by alanine in the case of 3CVLri-2 and 3CVLri-4. All amino acid residues in D-configuration and with a reversal peptide bond. Additionally, an arginine was added to the C-termini of each ri-peptide resulting in 17 amino acid residues. The C-termini of the D-ri-peptides are amidated, and the N-termini are acetylated. An analysis certificate from Caslo (Lyngby, Denmark) demonstrated the purity of each peptide (Supporting Information, Figures S29–S32 and Table S5). High-performance liquid chromatography (HPLC) analysis was performed with a C18 column. For the mass spectrometry

certificate, the matrix-assisted laser desorption ionization time-of-flight (MALDI-TOF) method was used.

**4.2. Protein Expression and Purification.** SARS-CoV-2 3CL<sup>pro</sup> (Uniprot entry: PODTD1, virus strain: hCoV-19/Wuhan/WIV04/2019) was cloned, expressed, and purified as described previously.<sup>41</sup>

**4.3. Phage Display.** Two independent phage display selections (selection A and B), each with three rounds, were performed to obtain peptides that bind 3CL<sup>pro</sup>. Therefore, in both selections, 100 μg/mL purified 3CL<sup>pro</sup> diluted in 100 μL of 20 mM potassium phosphate buffer pH 7.5 with 150 mM sodium chloride were immobilized on an amino plate (Nunc Amino Immobilizer 96-well plates, polystyrene; Thermo Scientific, Waltham). After 30 min at room temperature (RT), the 3CL<sup>pro</sup> solution was removed, and the surface was quenched with 1 M ethanolamine pH 8.5 (Cytiva; Chicago) for 1 h at RT. Additionally, the surface was blocked with 200 μL of 10 mg/mL BSA in 20 mM potassium phosphate buffer pH 7.5 with 150 mM sodium chloride in the first round and with 200 μL of 10 mg/mL milk powder in 20 mM potassium phosphate buffer pH 7.5 with 150 mM sodium chloride in the second round to reduce unspecific binding events. In the third round, the surface was not additionally blocked to vary the selection conditions. The surface was washed six times with 200 μL of washing buffer (20 mM potassium phosphate buffer pH 7.5 with 150 mM sodium chloride and 0.05% tween-20). During the first and second rounds, 2 mg/mL BSA or milk powder was added to the washing buffer, respectively. Then, 7.2 × 10<sup>10</sup> phages (TriCo-16 phage display peptide library; Creative Biolabs, New York) in 100 μL of the corresponding washing buffer were added and incubated for 20 min at RT with the exception of the third round of selection B. Here, the incubation time was extended to 30 min. After removing of nonbinding phages, the well was washed with 200 μL of the respective washing buffer of the corresponding round. The number of washing steps was varied in each selection round (selection A: 2-5-5; selection B: 5-8-10). Elution of phages was performed by incubation with 100 μL of 0.2 M Glycine-HCl pH 2.2 for 10 min at RT. The phage-containing solution was then removed from the plate and neutralized by transferring it to a tube containing 25 μL of 1 M Tris-HCl pH 9.1. To determine the output titer, 5 μL of eluted phages were used. Therefore, a dilution series from 10<sup>-2</sup> to 10<sup>-8</sup> was prepared with the eluted phages in a total volume of 100 μL of LB medium. Each dilution was mixed with 100 μL of *Escherichia coli* K12 ER2738 (OD600 of 0.6) and plated with 800 μL of top agar on plates (35 × 10 mm; Sarstedt, Nümbrecht, Germany) containing LB-Agar-IPGTG-XGal. After overnight incubation at 37 °C, the plaques were counted to determine the output titer.

The remaining eluted phages (120 μL) were amplified in 20 mL of *E. coli* K12 ER2738, starting with an OD<sub>600</sub> of 0.1 for 3.5 h at 37 °C and 120 rpm. The culture was then centrifuged for 20 min at 2700g and 4 °C. The pellet was discarded, and the supernatant was incubated with 7 mL of PEG-8000/2.5 M sodium chloride overnight at 4 °C for phage precipitation. Subsequently, the solution was centrifuged for 1 h at 4 °C, and 2700g. The phage-containing pellet was dissolved in 1 mL of 1 × phosphate-buffered saline (PBS) before another centrifugation step at 4 °C and 11,000g for 5 min to get rid of residual bacterial components. Afterward, the supernatant was added to 200 μL of PEG-8000/2.5 M sodium chloride and incubated for 1 h on ice, followed by final centrifugation for 45 min at 2700g and 4 °C. The phage-containing pellet was properly resuspended in 100 μL of 1 × PBS. The input titer was determined by spectrophotometry<sup>40</sup> in 1 × PBS using a 1:10 dilution. The resulting phages were then used in the next selection round with the same phage amount as before and further used for an enrichment enzyme-linked immunosorbent assay (ELISA) and prepared for next-generation sequencing (NGS) analysis.

Besides the primary selection with 3CL<sup>pro</sup> as the target (Target Selection, TS), two control selections were performed as described before<sup>46</sup> to enable an efficient evaluation of the selection success and to facilitate further the identification of target-binding peptides over those peptides that have accumulated, e.g., because of an affinity to the surface. The first control selection, called Empty Selection (ES), was performed in the same way as TS but without 3CL<sup>pro</sup>. During immobilization, 20 mM potassium phosphate buffer pH 7.5 with 150 mM sodium chloride was used instead of 3CL<sup>pro</sup>. One further control,

J

<https://doi.org/10.1021/acscchembio.2c00735>  
ACS Chem. Biol. XXXX, XXX, XXX–XXX

Direct Control (DC), was performed starting from the second round without 3CL<sup>pro</sup>, but in contrast to ES, the phages resulting from each round of TS were used for the following selection rounds.

**4.4. Enrichment ELISA.** An enrichment ELISA was performed to validate the success of the phage display selection. Therefore, 100  $\mu\text{g}/\text{mL}$  3CL<sup>pro</sup> diluted in 100  $\mu\text{L}$  of 20 mM potassium phosphate buffer pH 7.5 with 150 mM sodium chloride was immobilized on an amino plate (Nunc Immobilizer Amino 96-well plate, polystyrene; Thermo Scientific, Waltham) for 30 min at RT. Noncoated wells (20 mM potassium phosphate buffer pH 7.5 with 150 mM sodium chloride without 3CL<sup>pro</sup>) were used as a control for each selection round. The solution was removed, and the surface was quenched with 200  $\mu\text{L}$  of 1 M ethanolamine pH 8.5 (Cytiva; Chicago) for 1 h at RT, followed by a blocking step with 200  $\mu\text{L}$  of blocking solution (10 mg/mL BSA in 20 mM potassium phosphate buffer pH 7.5 with 150 mM sodium chloride) for 15 min at RT. After three washing steps with 200  $\mu\text{L}$  of washing buffer (150 mM sodium chloride, 0.05% Tween-20, 2 mg/mL BSA in 20 mM potassium phosphate buffer pH 7.5), the amplified and purified phages of each target selection round were diluted in washing buffer to a total amount of  $5 \times 10^{10}$  phages in 100  $\mu\text{L}$ . The wells immobilized with 3CL<sup>pro</sup> and noncoated wells were incubated with the corresponding phage solution for 1 h at RT. Unbound phages were removed by five washing steps with 150  $\mu\text{L}$  of washing buffer. The anti-M13 antibody (HRP conjugated mouse monoclonal antibacteriophage M13 antibody; Sino Biological, Peking, China) was diluted in washing buffer to a final concentration of 0.35 ng/ $\mu\text{L}$ , and 100  $\mu\text{L}$  was added to each well for 1 h at RT. After 6 washing steps with 150  $\mu\text{L}$  of washing buffer, the supernatant was removed entirely, and 100  $\mu\text{L}$  of the 3,3',5,5'-tetramethylbenzidine (TMB) solution (TMB was previously dissolved in 1 mL of dimethyl sulfoxide (DMSO) and diluted with 9 mL of 0.05 M phosphate citrate buffer pH 5) were added into each well. After 2.5 min incubation at RT, the reaction was stopped with 100  $\mu\text{L}$  of 2 M H<sub>2</sub>SO<sub>4</sub>. The absorption was quantified at 450 nm using a microplate reader (BMG Labtech, Ortenberg, Germany).

In addition to the samples from the target selection (TS1, TS2, TS3), the library and the wild-type phage without peptides were analyzed. The measurement was performed in single determination to save protein samples. Noncoated wells that were incubated with washing buffer without phages were used as a control for the background signal.

**4.5. Sequence Analysis.** Extraction and the amplification of the single-stranded phage DNA from each sample from the phage display selection were purified and prepared for NGS analysis as described previously.<sup>46</sup> NGS analysis was performed by the Biologisch-Medizinisches Forschungszentrum at the Heinrich Heine University Düsseldorf, Germany. The resulting sequences were further processed and evaluated with the targeted sequencing analysis tool (TSAT) and the open-source software Hammock for subsequent sequence alignment.<sup>47,48</sup>

**4.6. SARS-CoV-2 3CL<sup>pro</sup> Activity Assay.** SARS-CoV-2 3CL<sup>pro</sup> activity assay was performed as described previously.<sup>42,49–51</sup> A fluorogenic substrate DABCYL-KTSAVLQJSGFRKME-EDANS (Bachem, Bubendorf, Switzerland) was used, and the assay buffer contained 20 mM Tris pH 7.2, 200 mM NaCl, 1 mM ethylenediaminetetraacetic acid (EDTA), and 1 mM tris(2-carboxyethyl)-phosphine (TCEP). The reaction mixture was pipetted in a Corning 96-Well plate (Merck, Darmstadt, Germany) consisting of 0.5  $\mu\text{M}$  3CL<sup>pro</sup>. The assay was initiated with the addition of the substrate at a final concentration of 50  $\mu\text{M}$ . The fluorescence intensities were measured at 60 s intervals over 30 min using an Infinite 200 PRO plate reader (Tecan, Männedorf, Switzerland), and the temperature was set to 37 °C. The excitation and emission wavelengths were 360 and 460 nm, respectively.

**4.7. SARS-CoV-2 3CL<sup>pro</sup> Inhibition Assay.** Inhibition of SARS-CoV-2 3CL<sup>pro</sup> activity by 3CVL-1 to 10 and 3CVLri-2, -4, and -7 was investigated using the described activity assay. The L-Peptides (10  $\mu\text{M}$ ) were used for a preliminary screening test. For the final inhibition assays, 0.5  $\mu\text{M}$  protein was incubated with 0–140  $\mu\text{M}$  3CVL-2, 0–120  $\mu\text{M}$  3CVL-4, and 0–100  $\mu\text{M}$  3CVL-7. The corresponding 3CVLri peptides were incubated with the same inhibitor concentrations, except for 3CVLri-4 (0–140  $\mu\text{M}$ ). The mixtures were incubated for 30 min at

RT. When the substrate with a final concentration of 50  $\mu\text{M}$  was added to the mixture, the fluorescence intensities were measured at 60 s intervals over 30 min using an Infinite 200 PRO plate reader (Tecan, Männedorf, Switzerland). The temperature was set to 37 °C, and the excitation and emission wavelengths were 360 and 460 nm, respectively. Inhibition assays were performed as triplicates.

For the 3CVLri-2 + 3CVLri-4 and 3CVLri-4 + 3CVLri-7 combination tests, a 1:1 stock solution of the molecules was prepared. Protein (0.5  $\mu\text{M}$ ) was incubated with 0–75  $\mu\text{M}$  (3CVLri-2 + 3CVLri-4) and 0–50  $\mu\text{M}$  (3CVLri-4 + 3CVLri-7) of the combined molecules. The IC<sub>50</sub> values were calculated by plotting the initial velocity against various concentrations of the peptides using a dose–response curve in GraphPad Prism software version 8 (San Diego, CA). Data are presented as mean  $\pm$  SD.

**4.8. Determination of Inhibition Mode.** The inhibition mode was determined using different final concentrations of the inhibitors and substrate. Briefly, 0.5  $\mu\text{M}$  SARS-CoV-2 3CL<sup>pro</sup> was incubated with the inhibitor, in various concentrations, for 30 min at RT. Subsequently, the reaction was initiated by adding the corresponding concentration series of the substrate. The data were analyzed using a Lineweaver–Burk plot; therefore, the reciprocal of velocity (1/V) vs the reciprocal of the substrate concentration (1/[S]) was compared.<sup>52,53</sup> All measurements were performed in triplicate, and data are presented as mean  $\pm$  SD.

**4.9. Inhibitor Stability over 24 h.** Stable inhibition of SARS-CoV-2 3CL<sup>pro</sup> by 3CVLri-2, -4, and -7 was followed via a 24 h inhibition experiment. Briefly, 0.5  $\mu\text{M}$  SARS-CoV-2 3CL<sup>pro</sup> was incubated with 5  $\mu\text{M}$  (D-ri peptides 2 and 4) and 20  $\mu\text{M}$  (D-ri peptide 7) and incubated for 1/2, 1, 2, 3, 4, 5, and 24 h at RT. The control was performed with 3CL<sup>pro</sup> without the peptides and measured together after each time point. Subsequently, the reaction was initiated by the addition of the substrate. All measurements were performed in triplicate, and data are presented as mean  $\pm$  SD.

**4.10. Assay to Exclude D-ri Peptides as Promiscuous Inhibitors.** A detergent-based control assay was performed to exclude inhibitors that possibly act as promiscuous aggregators of the 3CL<sup>pro</sup> by adding 0.001, 0.01, and 0.1% of Triton X-100 to the reaction.<sup>54</sup> Four concentrations of 3CVLri 2 (1, 5, 10, and 20  $\mu\text{M}$ ), 3CVLri 4 (1, 5, 10, and 20  $\mu\text{M}$ ), and 3CVLri-7 (0.25, 0.5, 1, and 5  $\mu\text{M}$ ) were tested. All measurements were performed in triplicate, and data are presented as mean  $\pm$  SD.

**4.11. Circular Dichroism Spectroscopy.** Circular dichroism (CD) measurements were carried out with a Jasco J-1100 spectropolarimeter (Jasco, Germany). Far-UV spectra were measured between 190 to 260 nm using 5  $\mu\text{M}$  3CL<sup>pro</sup> in 20 mM K<sub>2</sub>HPO<sub>4</sub>/KH<sub>2</sub>PO<sub>4</sub> pH 7.4 and a single peptide concentration of 30  $\mu\text{M}$  in H<sub>2</sub>O. The secondary structure of 3CVL-2, 3CVL-4, 3CVL-7, and the related D-ri peptides was checked. A 1 mm path length cell was used for the measurements; 15 repeat scans were obtained for each sample, and five scans were conducted to establish the respective baselines. The averaged baseline spectrum was subtracted from the averaged sample spectrum. The results are presented as molar ellipticity [ $\theta$ ], according to eq 1

$$[\theta]\lambda = \theta / (c \cdot 0.001 \cdot l \cdot n) \quad (1)$$

where  $\theta$  is the ellipticity measured at the wavelength  $\lambda$  (deg),  $c$  is the peptide concentration (mol/L), 0.001 is the cell path length (cm), and  $n$  is the number of amino acids.

**4.12. Surface Plasmon Resonance Measurements.** Surface plasmon resonance (SPR) measurements with 3CVL peptides and SARS-CoV-2 3CL<sup>pro</sup> were performed using a Biacore 8K device (GE Healthcare, Uppsala, Sweden). Recombinant 3CL<sup>pro</sup> was immobilized on a CM5 sensor surface (GE Healthcare, Uppsala, Sweden) via covalent coupling of primary amino groups. The protease was diluted to a final concentration of 15  $\mu\text{g}/\text{mL}$  in 10 mM NaAc pH 5.5 and injected for 600 s at 10  $\mu\text{L}/\text{min}$  to reach a final immobilization level of 2700 to 3000 RU. After quenching with Ehanolamine at pH 8.5, kinetic experiments were performed as parallel injections on all eight flow channels. 3CVL and 3CVLri peptides were diluted in 20 mM Tris pH 7.4, 100 mM NaCl, 1 mM EDTA and 0.05% Tween-20 in the

K

<https://doi.org/10.1021/acscchembio.2c00735>  
ACS Chem. Biol. XXXX, XXX, XXX–XXX

concentration range of 0.03–50  $\mu\text{M}$  with a 1:1 dilution series and injected at 30  $\mu\text{L}/\text{min}$ . Surface regeneration was performed after dissociation ended for  $2 \times 45$  s at 30  $\mu\text{L}/\text{min}$  using an acidic regeneration solution consisting of 150 mM oxalic acid, 150 mM phosphoric acid, 150 mM formic acid, and 150 mM malonic acid at pH 5.0. Data evaluation was performed using a heterogeneous ligand fit model for the competitive inhibitors with Biacore Insight Evaluation Software v3.0.12 (GE Healthcare, Uppsala, Sweden). The heterogeneous ligand model assumes analyte binding at two independent ligand sites. Each ligand site binds the analyte independently and with a different rate constant. A global 1:1 kinetic fit model was used for the noncompetitive inhibitor.

**4.13. Nuclear Magnetic Resonance.** Two-dimensional 1H-15N TROSY-NMR correlation spectra<sup>55</sup> of 100  $\mu\text{M}$  15N 3CL<sup>PRO</sup> dissolved in 20 mM MES pH 6.5 buffer containing 150 mM NaCl were recorded in the presence and absence of 3CVL-2 and 3CVLri-2 as well as 3CVL-7 and 3CVLri-7 peptides. Experiments for 3CVL-4 and 3CVLri-4 could not be performed because of the peptide's instability at pH 6.5. Spectra were recorded on a Bruker 1.2 GHz AVANCE neo spectrometer equipped with a triple-resonance 1H,15N,13C cryogenic probe. The experimental temperature was 25 °C. Spectral dimensions were 16.02 ppm (1H)  $\times$  32.89 ppm (15N), with 1024 complex points recorded in the 1H dimension and 64 complex points recorded in the 15N dimension, and the Echo/Anti-echo scheme used for quadrature detection, resulting in an acquisition time of 53.2 ms in the 1H dimension and 16 ms in the 15N dimension. The carrier was positioned at 4.7 ppm in the 1H dimension and 117 ppm in the 15N dimension; 512 scans were recorded for each increment, with a recovery delay of 1 s between scans, resulting in an overall experimental time of 19.7 h per spectrum.

To study the interaction between 3CL<sup>PRO</sup> and the various peptides, only the protease was 15N-labeled and, therefore, NMR-visible, while the peptides were unlabeled and invisible in the 1H-15N correlation spectra. For the interaction study, 100  $\mu\text{M}$  15N-labeled 3CL<sup>PRO</sup> was mixed with an equimolar amount of the respective peptide. Spectra were overlaid and compared to the reference spectrum of 3CL<sup>PRO</sup> (equal final concentration, in the absence of the peptide). Spectra analysis was performed using the software Bruker Topspin 4.1.3. and CCPN Analysis 3.0.<sup>56</sup>

**4.14. Metabolic Stability.** Metabolic stability experiments of the 3CVLri peptides were performed as described before.<sup>57,58</sup> Solutions simulating gastric and intestinal fluid (SGF and SIF) were prepared according to the European Pharmacopoeia 7.0. Human plasma samples were purchased from Innovative Research (Novi, Michigan), and human liver microsomes were purchased from Sekisui XenoTech (Kansas City; H1000). The liver microsomes were diluted in an NADPH regenerating system (NRS). For the stability tests, 150  $\mu\text{M}$  3CVLri peptides were incubated in SGF, SIF, human plasma, and human liver microsomes in triplicate at 37 °C with slight shaking for different periods. The peptides were extracted by precipitating the proteins with a solution containing acetonitrile and 0.5% formic acid. Afterward, the mixture was mixed and heated for 5 min at 95 °C. The sample was subsequently centrifuged at 14,000g for 10 min at 4 °C. The extracted peptides are in the supernatant and were analyzed by reversed-phase high-performance liquid chromatography (RP-HPLC). The RP-HPLC system (Agilent Technologies, Santa Clara; 1260 series) consisted of an autosampler, quaternary pump, a thermostatted column compartment, and a variable-wavelength detector. Chromatography was performed with a C18 column (Agilent Technologies, Santa Clara; ZORBAX 300SB-C18 5  $\mu\text{m}$ , 4.6  $\times$  250 mm) at 25 °C and 214 nm with a flow rate of 1 mL/min. The sample injection volume was 20  $\mu\text{L}$ . Chromatograms were recorded and analyzed with the Agilent software OpenLab version 2–5. Mobile phases were acetonitrile + 0.1% trifluoroacetic acid (TFA) (A) and water + 0.1% TFA (B) for sample analysis from stability tests. The samples were measured with an initial isocratic step at 15% solvent A for 3 min followed by a gradient elution to 45% A in 15 min. All measurements were performed in triplicate, and data are presented as mean  $\pm$  SD.

**4.15. Statistical Analysis.** All data are expressed as the mean  $\pm$  standard deviations (SDs). The statistical significance of the mean

values' differences was assessed with one-way analyses of variance (ANOVA), followed by Tukeys' multiple comparison test. Significant differences were considered at  $p < 0.05$  (\*),  $p < 0.01$  (\*\*), and  $p < 0.001$  (\*\*\*)). All statistical analyses were performed with GraphPad Prism software version 8 (San Diego, CA).

**4.16. Docking and Molecular Dynamics.** **4.16.1. Peptide and Protein Structure Preparation.** The peptide models were constructed as linear chains using the python module PeptideBuilder.<sup>59</sup> To obtain D-retro-inverso (D-ri) peptides, the peptides were first generated as L-retro-inverso molecules, followed by the inversion of their stereochemical configuration by flipping the structure files with cartesian coordinates along the x-axis. The sequences of the peptides are shown in Table 5.

**Table 5. Sequences of 3CVL and 3CVLri Peptide Models**

peptide	sequence
3CVL-2	SPHGWPSQSVIEVQWQW
3CVL-4	AHEGWTDWDTPTQYSWK
3CVL-7	TVAPLHAHYWDVEERH
3CVLri-2	wqppqviesqspwahpsr
3CVLri-4	kwsyqptwdtwtwaeahar
3CVLri-7	hreevdwyhahlpavtr

The initial structural data of the 3CL<sup>PRO</sup> dimer were obtained from a crystal structure (PDB: 6M2N).

**4.16.2. Docking of the Peptides against the 3CL<sup>PRO</sup> Dimer.** 3CVL-2, 3CVL-7, 3CVLri-2, and 3CVLri-7 were docked against the active site of chain A of the 3CL<sup>PRO</sup> dimer (PDB: 6M2N), which can be defined by the residues His41, Met49, Tyr54, Phe140, Leu141, Asn142, Gly143, Ser144, Cys145, His163, His164, Met165, Glu166, Leu167, Asp187, Arg188, Glu189, Thr190, and Gln192.<sup>60</sup>

3CVL-4 and 3CVLri-4 bind 3CL<sup>PRO</sup> allosterically, and both peptides were docked against the potential binding site residues Lys12, Lys97, Lys100, Tyr101, Lys102, Phe103, Val104, and Arg105.<sup>36</sup> Autodock Tools<sup>61,62</sup> were used to generate a docking grid around the positions of the binding site residues of the 3CL<sup>PRO</sup> dimer. The grid was centered at x,y,z-position of -33.572, -62.854, 40.9 (Active site) and -49.16, -47.323, 38.911 (Allosteric binding site). After adding hydrogen atoms to the 3CL<sup>PRO</sup> dimer and the peptides, Gasteiger partial charges were computed and added to the dimer and the peptides using AutoDock Tool. The protein and peptide models were saved in the PDBQT format. The docking was then performed using AutoDock Vina,<sup>63</sup> which treats the ligand as flexible while keeping the receptor rigid.

**4.16.3. Simulation Setup and Production Run.** All MD simulations and analyses were performed with GROMACS 2021.4.<sup>63</sup> AMBER14SB<sup>64</sup> was used as a force field, and the TIP3P water model<sup>65</sup> for explicit water simulation. The peptides and the protein-peptide complexes were centered in a dodecahedron box with 240.8–370.5 and 872.5 nm<sup>3</sup>, solvated with water, and neutralized with Na<sup>+</sup> and Cl<sup>-</sup> ions resulting in a system size of ~23,500–36,000 and ~86,000 atoms, respectively.

The systems' energy was minimized using the steepest descent algorithm.<sup>66</sup> The systems were then equilibrated in two steps. First, a 0.1 ns simulation was performed in the NVT ensemble, and second, a 1 ns simulation in the NpT ensemble at 310 K—velocity-rescaling thermostat<sup>67</sup> and 1.0 bar—Berendsen barostat.<sup>68</sup> First, 1  $\mu\text{s}$  peptide MD simulations were performed. After the peptides were docked against the 3CL<sup>PRO</sup> dimer, we performed 100 ns of protein-peptide complexes with the temperature set to 310 K (Nosé–Hoover thermostat)<sup>69</sup> and the pressure set to 1 bar (Parinello–Rahman barostat).<sup>70</sup> One selected simulation of each protein-peptide complex was then extended to 200 ns and ran in triplicates.

Electrostatic interactions were processed with the particle-mesh Ewald method,<sup>71,72</sup> combined with periodic boundary conditions and a real-space cutoff of 12 Å. The same cutoff was applied to Lennard-Jones (LJ) interactions. The leapfrog stochastic dynamics integrator was used with a time step of 2 fs to integrate the equations of motion. During the

L

<https://doi.org/10.1021/acscchembio.2c00735>  
ACS Chem. Biol. XXXX, XXX, XXX–XXX

MD simulations, all bond lengths were constrained using the LINCS algorithm.<sup>73</sup>

**4.16.4. Molecular Dynamics Analysis.** The peptide's root means square deviation (RMSD) indicates how flexible the ligand is within the binding site. The protein structures sampled during the MD simulations were aligned to the MD starting structure, and then the RMSD was calculated for the ligand using *gmx rms*.

To investigate the effect of the allosteric peptides and the occupation of the peptides that bind to the active site, we used the VMD plugin Epoch 1.0.5 to evaluate the pocket volume of both active sites of the dimer for 1000 snapshots of the whole MD simulation after fitting the protein to the starting structure.<sup>74</sup> The following simulations were conducted for the second half of the MD simulations: The root-mean-square fluctuation (RMSF) was determined for each peptide with *gmx rmsf* to identify the flexible and rigid areas of the peptide within the protein–peptide complex, and the average minimum distance between specific residues of the protein and peptide was determined using *gmx mindist*.

We used the MM/PBSA method as implemented in *gmx\_mmpbsa* to calculate the binding free energy  $\Delta G_{\text{bind}}$  between the protein and the peptide and to perform alanine scanning.<sup>75</sup> The linear PB equation was solved using the level set function to build the dielectric interface between the solvent and solute.<sup>76</sup> The ionic strength was set to 150 mM. The total nonpolar solvation free energy was modeled as a single term linearly proportional to the solvent-accessible surface area.<sup>77</sup> Here, the binding free energy is defined as

$$\Delta G_{\text{bind}} = \langle G_{\text{complex}} \rangle - \langle G_{\text{receptor}} \rangle - \langle G_{\text{ligand}} \rangle$$

with  $\langle \rangle$  indicating the average of over 500 snapshots. The free energy for each entity is given as

$$\langle G_i \rangle = \langle E_{\text{bonded}} \rangle + \langle E_{\text{nonbonded}} \rangle + \langle G_{\text{polar}} \rangle + \langle G_{\text{nonpolar}} \rangle - \langle TS \rangle$$

where  $E_{\text{bonded}}$  describes the bonded interactions,  $E_{\text{nonbonded}}$  indicates the nonbonded, i.e., the Coulomb and Lennard-Jones interactions, and  $G_{\text{polar}}$  and  $G_{\text{nonpolar}}$  are the polar and nonpolar contributions to the solvation free energy, respectively. The  $TS$  term includes the absolute temperature,  $T$ , and the entropy,  $S$ .

$\Delta G_{\text{bind}}$  can also be stated as

$$\Delta G_{\text{bind}} = \Delta H - T\Delta S$$

with  $\Delta H$  the enthalpy of binding and  $-T\Delta S$  the conformational entropy after ligand binding. To determine the entropic component, *gmx\_mmpbsa* provides different methods, such as quasi-harmonic (QH) approximation, interaction entropy (IE), or C2 entropy approach. However, these methods were inappropriate for our system, as they either required a large number of snapshots ( $\geq 3N$ ,  $N$  = number of complex atoms) or a standard deviation of the interaction energy (sIE) of  $< 3.6$  kcal/mol to obtain realistic entropies. Thus, we decided to omit the entropic term, as  $\Delta H$  is usually sufficient to compare a set of similar ligands by their relative binding free energies.<sup>78</sup> To elucidate the contribution of each peptide residue to the binding free energy, we performed alanine scanning using *gmx\_mmpbsa*. Each residue of the 3CVL and 3CVL-r1 peptides (Except Gly and Pro) was substituted by Ala and the enthalpy of binding difference  $\Delta\Delta H^{X \rightarrow A}$  upon alanine mutation was calculated in the following way

$$\Delta\Delta H^{X \rightarrow A} = \Delta H^A - \Delta H^X$$

To identify the peptide structures with the most populated configuration or binding pose in the protein–peptide complex, the algorithm of Daura et al. was used as implemented in GROMACS (*gmx cluster*).<sup>78</sup>

The cutoff for clustering the peptide configurations was set to 3.5 Å, and the average structures of the 10 most populated clusters were used for docking against the dimer of the main protease. The binding poses of the peptides in the elongated protein–peptide complex simulations were clustered using a cutoff of 3.0 Å. To avoid biasing of nonbinding flexible areas of the peptide, only those peptide residues with an RMSF of  $< 6$  Å were considered for clustering. The three most prominent

clusters were then analyzed for interacting residues by generating a contact map.

## ■ ASSOCIATED CONTENT

### Supporting Information

The Supporting Information is available free of charge at <https://pubs.acs.org/doi/10.1021/acscchembio.2c00735>.

Additional experiments and supplementary figures (phage display outcome, inhibitor tests, SPR analysis, HPLC profiles, NMR spectra, and MD analysis) and tables (analysis of peptide sequences selected by phage display and list of amino acids forming the 3CL<sup>pro</sup> substrate-binding site and allosteric site) (PDF)

## ■ AUTHOR INFORMATION

### Corresponding Authors

**Mónika A. Coronado** – Institute of Biological Information Processing, Structural Biochemistry (IBI-7), Forschungszentrum Jülich, S2425 Jülich, Germany; Email: [m.coronado@fz-juelich.de](mailto:m.coronado@fz-juelich.de)

**Dieter Willbold** – Institute of Biological Information Processing, Structural Biochemistry (IBI-7), Forschungszentrum Jülich, S2425 Jülich, Germany; Institut für Physikalische Biologie, Heinrich-Heine-Universität Düsseldorf, 40225 Düsseldorf, Germany; [orcid.org/0000-0002-0065-7366](https://orcid.org/0000-0002-0065-7366); Email: [d.willbold@fz-juelich.de](mailto:d.willbold@fz-juelich.de)

### Authors

**Raphael J. Eberle** – Institute of Biological Information Processing, Structural Biochemistry (IBI-7), Forschungszentrum Jülich, S2425 Jülich, Germany; Institut für Physikalische Biologie, Heinrich-Heine-Universität Düsseldorf, 40225 Düsseldorf, Germany; [orcid.org/0000-0002-8763-3884](https://orcid.org/0000-0002-8763-3884)

**Marc Sevenich** – Institute of Biological Information Processing, Structural Biochemistry (IBI-7), Forschungszentrum Jülich, S2425 Jülich, Germany; Institut für Physikalische Biologie, Heinrich-Heine-Universität Düsseldorf, 40225 Düsseldorf, Germany; Priavoid GmbH, 40225 Düsseldorf, Germany

**Ian Gering** – Institute of Biological Information Processing, Structural Biochemistry (IBI-7), Forschungszentrum Jülich, S2425 Jülich, Germany

**Lara Scharbert** – Institute of Biological Information Processing, Structural Biochemistry (IBI-7), Forschungszentrum Jülich, S2425 Jülich, Germany; Institut für Physikalische Biologie, Heinrich-Heine-Universität Düsseldorf, 40225 Düsseldorf, Germany

**Birgit Strodel** – Institute of Biological Information Processing, Structural Biochemistry (IBI-7), Forschungszentrum Jülich, S2425 Jülich, Germany; Institut für Physikalische Biologie, Heinrich-Heine-Universität Düsseldorf, 40225 Düsseldorf, Germany; [orcid.org/0000-0002-8734-7765](https://orcid.org/0000-0002-8734-7765)

**Nils A. Lakomek** – Institute of Biological Information Processing, Structural Biochemistry (IBI-7), Forschungszentrum Jülich, S2425 Jülich, Germany; Institut für Physikalische Biologie, Heinrich-Heine-Universität Düsseldorf, 40225 Düsseldorf, Germany

**Karoline Santur** – Institute of Biological Information Processing, Structural Biochemistry (IBI-7), Forschungszentrum Jülich, S2425 Jülich, Germany; Institut für Physikalische Biologie, Heinrich-Heine-Universität Düsseldorf, 40225 Düsseldorf, Germany

M

<https://doi.org/10.1021/acscchembio.2c00735>  
ACS Chem. Biol. XXXX, XXX, XXX–XXX

Jeannine Mohrlüder – Institute of Biological Information Processing, Structural Biochemistry (IBI-7), Forschungszentrum Jülich, S2425 Jülich, Germany; [orcid.org/0000-0002-9922-2986](https://orcid.org/0000-0002-9922-2986)

Complete contact information is available at: <https://pubs.acs.org/10.1021/acscchembio.2c00735>

#### Author Contributions

Conceptualization: R.J.E., J.M., and M.A.C.; methodology: R.J.E., M.S., I.G., L.S., B.S., N.A.L., K.B.S., J.M., and M.A.C.; validation: R.J.E., M.S., I.G., L.S., B.S., N.A.L., K.B.S., J.M., and M.A.C.; formal analysis: R.J.E., M.S., I.G., L.S., B.S., N.A.L., K.B.S., J.M., and M.A.C.; investigation: R.J.E. and M.A.C.; resources: B.S. and D.W.; writing—original draft preparation: R.J.E. and M.A.C.; writing—review and editing: R.J.E., M.S., I.G., L.S., B.S., N.A.L., K.B.S., J.M., M.A.C., and D.W. All authors have read and agreed to the published version of the manuscript.

#### Funding

D.W. received funding from the Deutsche Forschungsgemeinschaft (DFG, German Research Foundation), Project-ID 267205415, SFB 1208. B.S. and L.S. received funding from the VolkswagenStiftung for that project (project number 99761). N.A.L. thanks the German Science Foundation (DFG, grant project number 433700474) for funding as well as support by the project “Virological and immunological determinants of COVID 19 pathogenesis—lessons to get prepared for future pandemics (KAI-Co-02 “COVIPA””, a grant from the Helmholtz Association’s Initiative and Networking Fund.

#### Notes

The authors declare no competing financial interest.

#### ACKNOWLEDGMENTS

Dedicated to Karl-Erich Jaeger for his pioneering contributions in the field of molecular enzyme technology. The authors thank the support of the Institute of Biological Information Processing (IBI-7) Forschungszentrum Jülich, Germany. L.S. and B.S. gratefully acknowledge the computing time granted by the JARA Vergabegremium and provided under project “3cldtp” on the JARA Partition part of the supercomputer JURECA at Forschungszentrum Jülich.

#### REFERENCES

- Hu, B.; Guo, H.; Zhou, P.; Shi, Z. L. Characteristics of SARS-CoV-2 and COVID-19. *Nat. Rev. Microbiol.* **2021**, *19*, 141–154.
- WHO. *Coronavirus Disease 2019 (COVID-19) Dashboard*; World Health Organization, 2022.
- Mathieu, E.; Ritchie, H.; Ortiz-Ospina, E.; Roser, M.; Hasell, J.; Appel, C.; Giattino, C.; Rod s-Guirao, L. A global database of COVID-19 vaccinations. *Nat. Hum. Behav.* **2021**, *5*, 947–953.
- Polack, F. P.; Thomas, S. J.; Kitchen, N.; Absalon, J.; Gurtman, A.; Lockhart, S.; Perez, J. L.; Marc, G. P.; Moreira, E. D.; Zerbini, C.; Bailey, R.; Swanson, K. A.; Gruber, W. C.; et al. Safety and efficacy of the BNT162b2 mRNA Covid-19 vaccine. *N. Engl. J. Med.* **2020**, *383*, 2603–2615.
- Baden, L. R.; El Sahly, H. M.; Essink, B.; Kotloff, K.; Frey, S.; Novak, R.; Diemert, D.; Spector, S. A.; Rouphael, N.; Creech, C. B.; McGettigan, J.; Khetan, S.; Zaks, T.; et al. Efficacy and safety of the mRNA-1273 SARS-CoV-2 vaccine. *N. Engl. J. Med.* **2021**, *384*, 403–416.
- Voysey, M.; Clemens, S. A. C.; Madhi, S. A.; Weckx, L. Y.; Folegatti, P. M.; Aley, P. K.; Bijkler, E.; et al. Safety and efficacy of the ChAdOx1 nCoV-19 vaccine (AZD1222) against SARS-CoV-2: an interim analysis of four randomised controlled trials in Brazil, South Africa, and the UK. *Lancet* **2021**, *397*, 99–111.
- Livingston, E. H.; Malani, P. N.; Creech, C. B. The Johnson & Johnson Vaccine for COVID-19. *JAMA* **2021**, *325*, 1575.
- Owen, D. R.; Allerton, C. M.; Anderson, A. S.; Aschenbrenner, L.; Avery, M.; Berritt, S.; Boras, B.; Cardin, R. D.; Carlo, A.; Coffman, K. J.; Dantonio, A.; et al. An oral SARS-CoV-2 Mpro inhibitor clinical candidate for the treatment of COVID-19. *Science* **2021**, *374*, 1586–1593.
- Madsen, L. W. Remdesivir for the Treatment of Covid-19-Final Report. *N. Engl. J. Med.* **2020**, *338*, 1813–1826.
- Hosseinzadeh, M. H.; Shamshirian, A.; Ebrahimzadeh, M. A. Dexamethasone Vs. COVID-19: An Experimental Study in Line with the Preliminary Findings of a Large Trial. *Int. J. Clin. Pract.* **2020**, *75*, No. e13943.
- Nangaku, M.; Kadowaki, T.; Yotsuyanagi, H.; Ohmagari, N.; Egi, M.; Sasaki, J.; Sakamoto, T.; Hasegawa, Y.; Ogura, T.; Chiba, S.; Node, K.; Suzuki, R.; Yamaguchi, Y.; Murashima, A.; Ikeda, N.; Morishita, E.; Yuzawa, K.; Moriuchi, H.; Hayakawa, S.; Nishi, D.; Irisawa, A.; Miyamoto, T.; Suzuki, H.; Sone, H.; Fujino, Y. The Japanese Medical Science Federation COVID-19 Expert Opinion English Version. *JMA J.* **2021**, *4*, 148–162.
- Italian Society of Infectious and Tropical Diseases (SIMIT). *Guidelines for the Treatment and Support Management of Patients with COVID-19 Coronavirus Infection*, 2nd ed.; Italian Society of Infectious and Tropical Diseases (SIMIT): Italy, 2020.
- Rambaut, A.; Holmes, E. C.; O’Toole, A.; Hill, V.; McCrone, J. T.; Ruis, C.; du Plessis, L.; Pybus, O. G. A dynamic nomenclature proposal for SARS-CoV-2 lineages to assist genomic epidemiology. *Nat. Microbiol.* **2020**, *5*, 1403–1407.
- Pillaiyar, T.; Manickam, M.; Namasivayam, V.; Hayashi, Y.; Jung, S. H. An overview of Severe Acute Respiratory Syndrome-Coronavirus (SARS-CoV) 3CL protease inhibitors: Peptidomimetics and small molecule chemotherapy. *J. Med. Chem.* **2016**, *59*, 6595–6628.
- Jin, Z.; Du, X.; Xu, Y.; Deng, Y.; Liu, M.; Zhao, Y.; Zhang, B.; Li, X.; Zhang, L.; Peng, C.; Duan, Y.; Yu, J.; Wang, L.; Yang, K.; Liu, F.; Jiang, R.; Yang, X.; You, T.; Liu, X.; Yang, X.; Bai, F.; Liu, H.; Liu, X.; Guddat, L. W.; Xu, W.; Xiao, G.; Qin, C.; Shi, Z.; Jiang, H.; Rao, Z.; Yang, H. Structure of Mpro from SARS-CoV-2 and discovery of its inhibitors. *Nature* **2020**, *582*, 289–293.
- Rut, W.; Groborz, K.; Zhang, L.; Sun, X.; Zmudzinski, M.; Pawlik, B.; Wang, X.; Jochmans, D.; Neyts, J.; Mlynarski, W.; Hilgenfeld, R.; Drag, M. SARS-CoV-2 Mpro inhibitors and activity-based probes for patient-sample imaging. *Nat. Chem. Biol.* **2021**, *17*, 222–228.
- Anand, K.; Ziebuhr, J.; Wadhwani, P.; Mesters, J. R.; Hilgenfeld, R. Coronavirus main proteinase (3CLpro) structure: Basis for design of anti-SARS drugs. *Science* **2003**, *300*, 1763–1767.
- Ghosh, A. K.; Osswald, H. L.; Prato, G. Recent progress in the development of HIV-1 protease inhibitors for the treatment of HIV/AIDS. *J. Med. Chem.* **2016**, *59*, 5172–5208.
- Cannalire, R.; Barreca, M. L.; Manfroni, G.; Cecchetti, V. A journey around the medicinal chemistry of Hepatitis C virus inhibitors targeting NS4B: From target to preclinical drug candidates. *J. Med. Chem.* **2016**, *59*, 16–41.
- Craik, D. J.; Fairlie, D. P.; Liras, S.; Price, D. The future of peptide-based drugs. *Chem. Biol. Drug Des.* **2013**, *81*, 136–147.
- Mikitsh, J. L.; Chacko, A. M. Pathways for small molecule delivery to the central nervous system across the blood-brain barrier. *Perspect. Med. Chem.* **2014**, *6*, 11–24.
- Goodwin, D.; Simerska, P.; Toth, I. Peptides as therapeutics with enhanced bioactivity. *Curr. Med. Chem.* **2012**, *19*, 4451–4461.
- Jiang, N.; Leithold, L. H.; Post, J.; Ziehm, T.; Mauler, J.; Gremer, L.; Cremer, M.; Schartmann, E.; Shah, N. J.; Kutzsche, J.; Langen, K. J.; et al. Preclinical pharmacokinetic studies of the tritium labelled D-enantiomeric peptide D3 developed for the treatment of Alzheimer’s disease. *PLoS One* **2015**, *10*, No. e0128553.
- Leithold, L. H. E.; Jiang, N.; Post, J.; Ziehm, T.; Schartmann, E.; Kutzsche, J.; Shah, N. J.; Breikreutz, J.; Langen, K. J.; Willuweit, A.; Willbold, D. Pharmacokinetic properties of a novel D-peptide developed to be therapeutically active against toxic  $\beta$ -amyloid oligomers. *Pharm. Res.* **2016**, *33*, 328–336.

N

<https://doi.org/10.1021/acscchembio.2c00735>  
ACS Chem. Biol. XXXX, XXX, XXX–XXX

- (25) Chong, P.; Sia, C.; Tripet, B.; James, O.; Klein, M. Comparative immunological properties of enantiomeric peptides. *Letf. Pept. Sci.* **1996**, *3*, 99–106.
- (26) Zhang, T.; Gering, I.; Kutzsche, J.; Nagel-Steger, L.; Willbold, D. Toward the mode of action of the clinical stage all-D-enantiomeric peptide RD2 on A $\beta$ 42 aggregation. *ACS Chem. Neurosci.* **2019**, *10*, 4800–4809.
- (27) Kutzsche, J.; Jürgens, D.; Willuweit, A.; Adermann, K.; Fuchs, C.; Simons, S.; Windisch, M.; Hümpel, M.; Rossberg, W.; Wolzt, M.; Willbold, D. Safety and pharmacokinetics of the orally available antiprionic compound PRI-002: A single and multiple ascending dose phase I study. *Alzheimer's Dement.* **2020**, *6*, No. e12001.
- (28) Schemmert, S.; Camargo, L. C.; Honold, D.; Gering, I.; Kutzsche, J.; Willuweit, A.; Willbold, D. In Vitro and In Vivo Efficacies of the Linear and the Cyclic Version of an All-d Enantiomeric Peptide Developed for the Treatment of Alzheimer's Disease. *Int. J. Mol. Sci.* **2021**, *22*, 6553.
- (29) Valiente, P. A.; Wen, H.; Nim, S.; Lee, J.; Kim, H. J.; Kim, J.; Perez-Riba, A.; Paudel, Y. P.; Hwang, I.; Kim, K. D.; Kim, S.; Kim, P. M. Computational Design of Potent D-Peptide Inhibitors of SARS-CoV-2. *J. Med. Chem.* **2021**, *64*, 14955–14967.
- (30) Valiente, P. A.; Nim, S.; Lee, J.; Kim, S.; Kim, P. M. Targeting the Receptor-Binding Motif of SARS-CoV-2 with D-Peptides Mimicking the ACE2 Binding Helix: Lessons for Inhibiting Omicron and Future Variants of Concern. *J. Chem. Inf. Model.* **2022**, *62*, 3618–3626.
- (31) Hernández González, J. E.; Eberle, R. J.; Willbold, D.; Coronado, M. A. A computer-aided approach for the discovery of D-peptides as inhibitors of SARS-CoV-2 main protease. *Front. Mol. Biosci.* **2022**, *8*, No. 816166.
- (32) Eberle, R. J.; Gering, I.; Tusche, M.; Ostermann, P. N.; Müller, L.; Adams, O.; Schaal, H.; Olivier, D. S.; Amaral, M. S.; Arni, R. K.; Willbold, D.; Coronado, M. A. Design of D-Amino Acids SARS-CoV-2 Main Protease Inhibitors Using the Cationic Peptide from Rattlesnake Venom as a Scaffold. *Pharmaceuticals* **2022**, *15*, 540.
- (33) Cardoso, M. H.; Cândido, E. S.; Oshiro, K. G. N.; Rezende, S. B.; Franco, O. L. *Peptide Applications in Biomedicine, Biotechnology and Bioengineering*, Koutsoopoulos, S., Ed.; Woodhead Publishing, 2018.
- (34) Fischer, P. M. The design, synthesis and application of stereochemical and directional peptide isomers: a critical review. *Curr. Protein Pept. Sci.* **2003**, *4*, 339–356.
- (35) Li, C.; Pazgier, M.; Li, J.; Li, C.; Liu, M.; Zou, G.; Li, Z.; Chen, J.; Tarasov, S. G.; Lu, W. Y.; Lu, W. Limitations of peptide retro-inverso isomerisation in molecular mimicry. *J. Biol. Chem.* **2010**, *285*, 19572–19581.
- (36) Li, C.; Zhan, C.; Zhao, L.; Chen, X.; Lu, W. Y.; Lu, W. Functional consequences of retro-inverso isomerisation of a miniature protein inhibitor of the p53–MDM2 interaction. *Bioorg. Med. Chem.* **2013**, *21*, 4045–4050.
- (37) Cheng, L.; Boland, S.; Scholle, M. D.; Bardiotti, D.; Marchand, A.; Chaltin, P.; Blatt, L. M.; Beigelman, L.; Symons, J. A.; Raboisson, P.; Gurard-Levin, Z. A.; Vandyck, K.; Deval, J. Dual inhibition of SARS-CoV-2 and human rhinovirus with protease inhibitors in clinical development. *Antiviral Res.* **2021**, *187*, No. 105020.
- (38) Antonopoulou, I.; Sapountzaki, E.; Rova, U.; Christakopoulos, P. Inhibition of the main protease of SARS-CoV-2 (Mpro) by repurposing/designing drug-like substances and utilising nature's toolbox of bioactive compounds. *Comput. Struct. Biotechnol. J.* **2022**, *20*, 1306–1344.
- (39) Lockbaum, G. J.; Henes, M.; Lee, J. M.; Timm, J.; Nalivaika, E. A.; Thompson, P. R.; Yilmaz, K. N.; Schiffer, C. A. Pan-3C Protease Inhibitor Rupintrivir Binds SARS-CoV-2 Main Protease in a Unique Binding Mode. *Biochemistry* **2021**, *60*, 2925–2931.
- (40) Chen, H.; Wei, P.; Huang, C.; Tan, L.; Liu, Y.; Lai, L. Only one protomer is active in the dimer of SARS 3C-like proteinase. *J. Biol. Chem.* **2006**, *281*, 13894–13898.
- (41) Kidera, A.; Moritsugu, K.; Ekimoto, T.; Ikeguchi, M. Allosteric regulation of 3CL protease of SARS-CoV-2 and SARS-CoV observed in the crystal structure ensemble. *J. Mol. Biol.* **2021**, *433*, No. 167324.
- (42) Eberle, R. J.; Olivier, D. S.; Amaral, M. S.; Gering, I.; Willbold, D.; Arni, R. K.; Coronado, M. A. The Repurposed Drugs Suramin and Quinacrine Cooperatively Inhibit SARS-CoV-2 3CLpro In Vitro. *Viruses* **2021**, *13*, 873.
- (43) Trott, O.; Olson, A. AutoDock Vina: Improving the speed and accuracy of docking with a new scoring function, efficient optimisation, and multithreading. *J. Comput. Chem.* **2010**, *31*, 455–461.
- (44) Bojadzic, D.; Alcazar, O.; Chen, J.; Chuang, S. T.; Capcha, J. M. C.; Shehadeh, L. A.; Buchwald, P. Small-Molecule Inhibitors of the Coronavirus Spike: ACE2 Protein–Protein Interaction as Blockers of Viral Attachment and Entry for SARS-CoV-2. *ACS Infect. Dis.* **2021**, *7*, 1519–1534.
- (45) Sevenich, M.; Thul, E.; Lakomek, N. A.; Klünemann, T.; Schubert, M.; Bertoglio, F.; van den Heuvel, J.; Pertsch, P.; Mohrlüder, J.; Willbold, D. Phage Display Derived Compounds Displace hACE2 from Its Complex with SARS-CoV-2 Spike Protein. *Biomedicines* **2022**, *10*, 441.
- (46) Singh, E.; Khan, R. J.; Jha, R. K.; Amera, G. M.; Jain, M.; Singh, R. P.; Muthukumaran, J.; Singh, A. K. A comprehensive review on promising antiviral therapeutic candidates identified against main protease from SARS-CoV-2 through various computational methods. *J. Genet. Eng. Biotechnol.* **2020**, *18*, 1–12.
- (47) Santur, K.; Reinartz, E.; Lien, Y.; Tusche, M.; Altendorf, T.; Sevenich, M.; Tamguiney, G.; Mohrlüder, J.; Willbold, D. Ligand-Induced Stabilisation of the Native Human Superoxide Dismutase 1. *ACS Chem. Neurosci.* **2021**, *12*, 2520–2528.
- (48) Krejci, A.; Hupp, T. R.; Lexa, M.; Vojtesek, B.; Müller, P. Hammock: A hidden Markov model-based peptide clustering algorithm to identify protein-interaction consensus motifs in large datasets. *Bioinformatics* **2016**, *32*, 9–16.
- (49) Zhang, L.; Lin, D.; Sun, X.; Curth, U.; Drosten, C.; Sauerhering, L.; Becker, S.; Rox, K.; Hilgenfeld, R. Crystal structure of SARS-CoV-2 main protease provides a basis for design of improved  $\alpha$ -ketoamide inhibitors. *Science* **2020**, *368*, 409–412.
- (50) Zhang, L.; Lin, D.; Kusov, Y.; Nian, Y.; Ma, Q.; Wang, J.; De Wilde, A.; et al.  $\alpha$ -Ketoamides as broad-spectrum inhibitors of coronavirus and enterovirus replication: Structure-based design, synthesis, and activity assessment. *J. Med. Chem.* **2020**, *63*, 4562–4578.
- (51) Ma, C.; Sacco, M. D.; Hurst, B.; Townsend, J. A.; Hu, Y.; Szeto, T.; Zhang, X.; Tarbet, B.; Marty, M. T.; Chen, Y.; Wang, J. Boceprevir, GC-376, and calpain inhibitors II, XII inhibit SARS-CoV-2 viral replication by targeting the viral main protease. *Cell Res.* **2020**, *30*, 678–692.
- (52) Roy, A.; Lim, L.; Srivastava, S.; Lu, Y.; Song, J. Solution conformations of Zika NS2B-NS3pro and its inhibition by natural products from edible plants. *PLoS One* **2017**, *12*, No. e0180632.
- (53) Motulsky, H.; Christopoulos, A. *Fitting Models to Biological Data Using Linear and Nonlinear Regression: A Practical Guide to Curve Fitting*; Oxford University Press, 2004.
- (54) Feng, B. Y.; Shoichet, B. K. A detergent-based assay for the detection of promiscuous inhibitors. *Nat. Protoc.* **2006**, *1*, 550–553.
- (55) Pervushin, K.; Riek, R.; Wider, G.; Wüthrich, K. Attenuated T2 relaxation by mutual cancellation of dipole-dipole coupling and chemical shift anisotropy indicates an avenue to NMR structures of very large biological macromolecules in solution. *Proc. Natl. Acad. Sci. U.S.A.* **1997**, *94*, 12366–12371.
- (56) Skinner, S. P.; Fogh, R. H.; Boucher, W.; Ragan, T. J.; Mureddu, L. G.; Vuister, G. W. CcpNmr AnalysisAssign: a flexible platform for integrated NMR analysis. *J. Biomol. NMR* **2016**, *66*, 111–124.
- (57) Elfgen, A.; Santiago-Schübel, B.; Gremer, L.; Kutzsche, J.; Willbold, D. Surprisingly high stability of the A $\beta$  oligomer eliminating all-d-enantiomeric peptide D3 in media simulating the route of orally administered drugs. *Eur. J. Pharm. Sci.* **2017**, *107*, 203–207.
- (58) Elfgen, A.; Hupert, M.; Bochinsky, K.; Tusche, M.; González de San Román, M. E.; Gering, I.; Sacchi, S.; Pollegioni, L.; Huesgen, P. F.; Hartmann, R.; Santiago-Schübel, B.; et al. Metabolic resistance of the D-peptide RD2 developed for direct elimination of amyloid- $\beta$  oligomers. *Sci. Rep.* **2019**, *9*, No. 5715.

- (59) Tien, M. Z.; Sydykova, D. K.; Meyer, A. G.; Wilke, C. O. PeptideBuilder: A simple Python library to generate model peptides. *Peer J.* **2013**, *1*, No. e80.
- (60) Tang, B.; He, F.; Liu, D.; Fang, M.; Wu, Z.; Xu, D. *AI-Aided Design of Novel Targeted Covalent Inhibitors against SARS-CoV-2*; bioRxiv, 2020.
- (61) Goodsell, D.; Morris, G.; Olson, A. Automated docking of flexible ligands: Applications of AutoDock. *J. Mol. Recognit.* **1996**, *9*, 1–5.
- (62) Santos-Martins, D.; Forli, S.; Ramos, M.; Olson, A. AutoDock4Zn: An Improved AutoDock Force Field for Small-Molecule Docking to Zinc Metalloproteins. *J. Chem. Inf. Model.* **2014**, *54*, 2371–2379.
- (63) Abraham, M. J.; Murtola, T.; Schulz, R.; Páll, S.; Smith, J.; Hess, B.; Lindahl, E. GROMACS: High performance molecular simulations through multi-level parallelism from laptops to supercomputers. *SoftwareX* **2015**, *1–2*, 19–25.
- (64) Maier, J. A.; Martinez, C.; Kasavajhala, K.; Wickstrom, L.; Hauser, K. E.; Simmerling, C. ff14sb: Improving the accuracy of protein side chain and backbone parameters from ff99sb. *J. Chem. Theory Comput.* **2015**, *11*, 3696–3713.
- (65) Jorgensen, W. L.; Chandrasekhar, J.; Madura, J.; Impey, R.; Klein, M. Comparison of simple potential functions for simulating liquid water. *J. Chem. Phys.* **1983**, *79*, 926–935.
- (66) Cauchy, M. A. Méthode générale pour la résolution des systèmes d'équations simultanées. *C. R. Hebd. Seances Acad. Sci.* **1847**, *25*, 536–538.
- (67) Bussi, G.; Donadio, D.; Parrinello, M. Canonical sampling through velocity rescaling. *J. Chem. Phys.* **2007**, *126*, No. 014101.
- (68) Berendsen, H. J. C.; Postma, J. P. M.; van Gunsteren, W. F.; DiNola, A.; Haak, J. R. Molecular dynamics with coupling to an external bath. *J. Chem. Phys.* **1984**, *81*, 3684–3690.
- (69) Nosé, S. Molecular-dynamics method for simulations in the canonical ensemble. *Mol. Phys.* **1984**, *52*, 255–268.
- (70) Parrinello, M.; Rahman, A. Polymorphic transitions in single-crystals—a new molecular-dynamics method. *Mol. Phys.* **1981**, *52*, 7182–7190.
- (71) Darden, T.; York, D.; Pedersen, L. Particle Mesh Ewald—an N. Log(N) method for ewald sums in large systems. *J. Chem. Phys.* **1993**, *98*, 10089–10092.
- (72) Essmann, U.; Perera, L.; Berkowitz, M.; et al. A smooth particle mesh ewald method. *J. Chem. Phys.* **1995**, *103*, 8577–8593.
- (73) Hess, B.; Bekker, H.; Berendsen, H.; Fraaije, J. LINCS: A linear constraint solver for molecular simulations. *J. Comput. Chem.* **1997**, *18*, 1463–1472.
- (74) Laurent, B.; Chavent, M.; Cragolini, T.; Dahl, A. C. E.; Pasquali, S.; Derreumaux, P.; Sansom, M. S. P.; Baaden, M. Epock: rapid analysis of protein pocket dynamics. *Bioinformatics.* **2015**, *31*, 1478–1480.
- (75) Valdés-Tresanco, M. S.; Valdés-Tresanco, M. E.; Valiente, P. A.; Moreno, E. gmx\_MMPBSA: a new tool to perform end state free energy calculations with GROMACS. *J. Chem. Theory Comput.* **2021**, *17*, 6281–6291.
- (76) Wang, J.; Cai, Q.; Xiang, Y.; Luo, R. Reducing grid dependence in finite-difference Poisson–Boltzmann calculations. *J. Chem. Theory Comput.* **2012**, *8*, 2741–2751.
- (77) Tan, C.; Tan, Y. H.; Luo, R. Implicit nonpolar solvent models. *J. Phys. Chem. B* **2007**, *111*, 12263–12274.
- (78) Daura, X.; Gademann, K.; Jaun, B.; Seebach, D.; van Gunsteren, W.; Mark, A. E. Peptide folding: when simulation meets experiment. *Angew. Chem., Int. Ed.* **1999**, *38*, 236–240.

## Recommended by ACS

### Comprehensive Peptide Cyclization Examination Yields Optimized APP Scaffolds with Improved Affinity toward Mint2

Christian R. O. Bartling, Kristian Strømgaard, et al.  
FEBRUARY 07, 2023  
JOURNAL OF MEDICINAL CHEMISTRY

READ 

### Mutation Effects on Structure and Dynamics: Adaptive Evolution of the SARS-CoV-2 Main Protease

Elizabeth M. Diessner, Carter T. Butts, et al.  
JANUARY 19, 2023  
BIOCHEMISTRY

READ 

### Potential Self-Peptide Inhibitors of the SARS-CoV-2 Main Protease

Arkadeep Banerjee and Shachi Gosavi  
JANUARY 23, 2023  
THE JOURNAL OF PHYSICAL CHEMISTRY B

READ 

### Site-Selective Tyrosine Phosphorylation in the Activation of the p50 Subunit of NF-κB for DNA Binding and Transcription

Shengxi Chen, Sidney M. Hecht, et al.  
DECEMBER 19, 2022  
ACS CHEMICAL BIOLOGY

READ 

Get More Suggestions >

P

<https://doi.org/10.1021/acscchembio.2c00735>  
ACS Chem. Biol. XXXX, XXX, XXX–XXX

## 2.6 Ligand-Induced Stabilization of the Native Human Superoxide Dismutase 1

Authors: Karoline Santur, Elke Reinartz, Yi Lien, Markus Tusche, Tim Altendorf, Marc Sevenich, Gültekin Tamgüney, Jeannine Mohrlüder and Dieter Willbold

Journal: ACS Chemical Neuroscience

DOI: <https://doi.org/10.1021/acscemneuro.1c00253>

Impact Factor: 4.418 (2022)

Contribution: Development of phage display selection and NGS analysis method.



# Ligand-Induced Stabilization of the Native Human Superoxide Dismutase 1

Karoline Santur, Elke Reinartz, Yi Lien, Markus Tusche, Tim Altendorf, Marc Sevenich, Gültekin Tamgüney, Jeannine Mohrlüder,\* and Dieter Willbold\*

Cite This: *ACS Chem. Neurosci.* 2021, 12, 2520–2528

Read Online

ACCESS |

Metrics & More

Article Recommendations

**ABSTRACT:** A common characteristic of familial (fALS) and sporadic amyotrophic lateral sclerosis (sALS) is the accumulation of aberrant proteinaceous species in the motor neurons and spinal cord of ALS patients—including aggregates of the human superoxide dismutase 1 (hSOD1). hSOD1 is an enzyme that occurs as a stable dimeric protein with several post-translational modifications such as the formation of an intramolecular disulfide bond and the acquisition of metal cofactors that are essential for enzyme activity and further contribute to protein stability. Some mutations and/or destabilizing factors promote hSOD1 misfolding, causing neuronal death. Aggregates containing misfolded wild-type hSOD1 have been found in the spinal cords of sALS as well as in non-hSOD1 fALS patients, leading to the hypothesis that hSOD1 misfolding is a common part of the ALS pathomechanism. Therefore, stabilizing the native conformation of SOD1 may be a promising approach to prevent the formation of toxic hSOD1 species and thus ALS pathogenesis. Here, we present the 16-mer peptide S1VL-21 that interferes with hSOD1 aggregation. S1VL-21 was identified by phage display selection with the native conformation of hSOD1 as a target. Several methods such as microscale thermophoresis (MST) measurements, aggregation assays, and cell viability assays revealed that S1VL-21 has a micromolar binding affinity to native hSOD1 and considerably reduces the formation of hSOD1 aggregates. This present work therefore provides the first important data on a potential lead compound for hSOD1-related drug development for ALS therapy.

**KEYWORDS:** ALS, SOD1, aggregate elimination, treatment strategy, native conformation stabilization, phage display selection

## INTRODUCTION

Amyotrophic lateral sclerosis (ALS) is a fatal adult-onset neurodegenerative disorder that causes degeneration of upper and lower motor neurons in the primary cortex, brain stem, and spinal cord. Death occurs typically within 3–5 years after diagnosis due to respiratory failure. Approximately 90% of all ALS cases are considered sporadic (sALS), whereas familial ALS cases (fALS) account for the remaining ~10%.<sup>1–3</sup> However, despite widespread research, there is still no efficient treatment for ALS. The only available FDA approved drugs are riluzole and radicava, which extend survival by only 2–3 months<sup>4</sup> or decelerate the rate of decline in physical functions by 33%,<sup>5</sup> respectively.

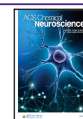
Mutations in the gene coding for the human superoxide dismutase 1 (hSOD1) are found in ~1% of all ALS cases<sup>6</sup> and account for ~20% of fALS cases.<sup>5</sup> Since 1993, when the first ALS-associated mutations in hSOD1 were found,<sup>7</sup> more than 200 mutations in hSOD1 have been identified (<https://alsod.ac.uk/>). The human SOD1 is an enzyme that converts toxic superoxide radicals to hydrogen peroxide and oxygen. The mature protein is a 32 kDa homodimer with one copper and

one zinc ion per monomer that are important for the activity and stability, respectively. An intramolecular disulfide bond in each subunit further contributes to protein stability.<sup>8</sup> All post-translational modifications, including the dimerization, the coordination of the metals, and the disulfide bond, lead to one of the most stable proteins known.<sup>9,10</sup> However, mutations and/or altered post-translational modifications are linked to the pathogenesis of ALS, whereas the underlying mechanism behind hSOD1-mediated toxicity is still unclear. Loss of hSOD1 function may lead to an accumulation of toxic radicals and thus be a possible reason for the disease, but SOD1 knockout mice do not exhibit an ALS-like phenotype.<sup>11</sup> Some studies have suggested a toxic gain-of-function of mutant hSOD1 as a result of protein misfolding and aggregation,<sup>8,12,13</sup>

Received: April 20, 2021

Accepted: June 1, 2021

Published: June 17, 2021



and the pathogenicity of mutant hSOD1 is proportional to the amount of toxic hSOD1 species.<sup>14</sup> Indeed, aggregates containing mutant and misfolded hSOD1 have been found in the spinal cord of sALS and hSOD1-fALS patients.<sup>15–17</sup> In addition, misfolded wild-type hSOD1 was also detected in non-hSOD1 fALS patients leading to the hypothesis that hSOD1 misfolding is a common part of the ALS pathomechanism.<sup>18</sup> Moreover, aggregated hSOD1 has been shown to induce aggregation of mutant and wild-type SOD1 *in vitro*<sup>19</sup> as well as in cell culture<sup>20</sup> with a prion-like behavior<sup>21</sup> and the overexpression of wild-type hSOD1 in mice led to an ALS-like phenotype.<sup>13</sup> Lacking one or several post-translational hSOD1 modifications destabilizes the native protein and generates an apo monomer, whose thermal stability is significantly reduced, and that has been shown to be the precursor for aggregation.<sup>22,23</sup>

In order to investigate whether the destabilization of the hSOD1 holoenzyme is crucial to ALS pathology, we want to explore whether stabilization of the native hSOD1 conformation by specifically binding ligands is able to interfere with hSOD1 aggregation. Such ligands should then be able to inhibit formation of hSOD1 aggregates *in vitro* and *in vivo*. In addition, elimination of pre-existing hSOD1 aggregates might also become feasible.

A similar approach has been applied in the transthyretin (TTR)-associated amyloidosis. It has been shown that the tetrameric protein dissociates into monomers before misfolding and aggregation.<sup>24</sup> However, binding of small specific molecules stabilized the native conformation of the protein and increased the kinetic barrier to tetrameric dissociation, thus preventing amyloidosis.<sup>25</sup> The efficacy of specific ligands in interfering with protein aggregation was also successfully demonstrated for amyloid- $\beta$  protein ( $A\beta$ ), whose toxic species are involved in the pathogenesis of Alzheimer's disease. *In vitro* data revealed that the D-enantiomeric peptide RD2 binds monomeric  $A\beta$ (1–42) and inhibits concentration-dependent formation of  $A\beta$  fibrils. In addition, RD2 was able to eliminate pre-existing toxic  $A\beta$  oligomers,<sup>26</sup> and mouse studies demonstrated a significant reduction of  $A\beta$  oligomers as well as an improvement of cognitive properties.<sup>26–28</sup> Thus, stabilizing the wild-type hSOD1 native conformation by specifically binding ligands may be a beneficial approach in ALS treatment.

Here, we report the identification of a hSOD1-binding peptide selected by phage display and its analysis regarding its potential to stabilize native hSOD1 and thus inhibit hSOD1 aggregation.

## RESULTS AND DISCUSSION

**hSOD1-Binding Peptides Were Enriched during Phage Display Selection.** To identify peptide ligands that are able to stabilize the native conformation of hSOD1, the TriCo-16 phage display peptide library was used in a phage display selection. After four selection rounds, the success of the selection was analyzed by an enrichment ELISA.

As shown by ELISA analysis (Figure 1), the phage display selection enriched phages that bind to hSOD1-coated wells (Figure 1; dark green) more than to noncoated wells (Figure 1; light green). The weak binding of the wild-type phage to hSOD1 with an intensity similar to the control without phages indicates that the measured values result from the binding of the presented peptides and not from that of the phage itself. The signal intensity of the wells with and without hSOD1 are

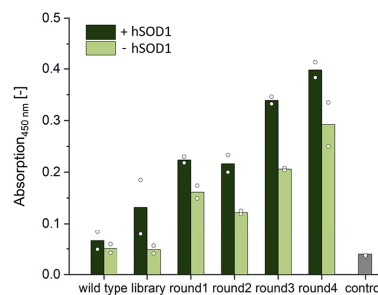


**Figure 1.** hSOD1-binding peptides were enriched during phage display selection. Enrichment ELISA of the hSOD1 phage display was performed to verify the enrichment of hSOD1-binding peptides during the selection. Relative binding affinities of the phage samples ( $5 \times 10^{10}$  phages) of the wild type, library, and each selection round to immobilized hSOD1 (dark green) and to empty wells without hSOD1 (light green) were investigated in a double determination (points: corresponding values) as well as a control without hSOD1 and phages (gray).

not considerably different. As shown by the increased signal intensity with each selection round starting from the library, hSOD1-binding peptides accumulated during the selection. The library already contains hSOD1-binding peptides as indicated by the higher signal intensity for hSOD1-coated wells compared to noncoated wells.

**Sequence Analysis Led to the Identification of hSOD1-Binding Peptide S1VL-21.** Next-generation sequencing (NGS) analysis followed by processing via the Target Sequencing Analysis Tool (TSAT) and Hammock led to the identification of the peptide S1VL-21. In total, 60 937 sequences were identified during this selection after analysis. The sequence at position 1 in the scoring according to the parameter Empty Score (EmS) exhibited a value of 83 but displayed an Enrichment Factor (EnF) value of only 6. In contrast, another sequence with an EnF value of 271 was most enriched, whereby this sequence was also highly present in the controls (EmS of 6). S1VL-21 was ranked at position 25 in the scoring according to the parameter EmS (value of 23) and at position 38 according to the parameter EnF (value of 25). Moreover, it formed the largest cluster in sequence alignment with 2469 sequences including 2393 unique sequences of the remaining 60 751 sequences. Thus, the peptide S1VL-21 and its three randomized control peptides S1VL-21\_Rdm1, S1VL-21\_Rdm2, and S1VL-21\_Rdm3 were further investigated according to their potential to bind and stabilize native hSOD1 as well as their potential to prevent hSOD1 from aggregation.

**S1VL-21 Exhibits Micromolar Binding Affinity to hSOD1.** Microscale thermophoresis (MST) measurements were used to determine the equilibration dissociation constant ( $K_D$ ) of hSOD1 to the selected peptide S1VL-21. As a control for the sequence specificity of the binding affinity, three peptides with the same amino acid residues, but in randomized sequence order, were also measured for affinity to hSOD1 (Figure 2A). Therefore, 250 nM hSOD1 labeled with CF633 was used, whereas nonlabeled peptide was added with different concentrations. The S1VL-21 exhibits the strongest binding affinity to hSOD1 with a resulting  $K_D$  of  $5.3 \pm 0.3 \mu\text{M}$  (Figure

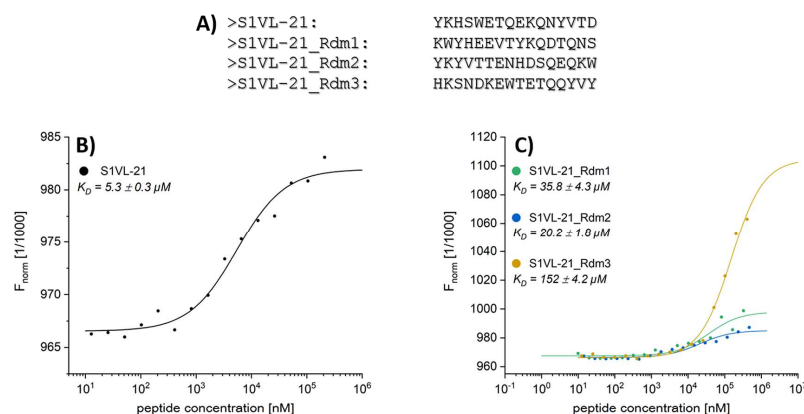


**Figure 2.** S1VL-21 exhibits a micromolar binding affinity to hSOD1. (A) Sequences of the selected peptide S1VL-21 and its randomized control peptides S1VL-21\_Rdm1, S1VL-21\_Rdm2, and S1VL-21\_Rdm3, which were measured for affinity to hSOD1. (B) MST measurement of hSOD1-CF633 (250 nM) and S1VL-21 as well as (C) its randomized control peptides with increasing concentrations (10 nM–470  $\mu\text{M}$ ) in 50 mM sodium acetate buffer pH 6 containing 150 mM NaCl and 0.05% Tween-20 were performed at 25 °C with an LED power of 40%. Changes in thermophoresis at 40% MST power were plotted against the peptide concentrations and evaluated through thermophoresis for determining the  $K_D$  values of  $5.3 \pm 0.3 \mu\text{M}$  for S1VL-21 (B) and  $35.8 \pm 4.3 \mu\text{M}$  (C; green),  $20.2 \pm 1.9 \mu\text{M}$  (C; blue), and  $152 \pm 4.2 \mu\text{M}$  (C; orange) for the randomized control peptides S1VL-21\_Rdm1, S1VL-21\_Rdm2, and S1VL-21\_Rdm3, respectively.

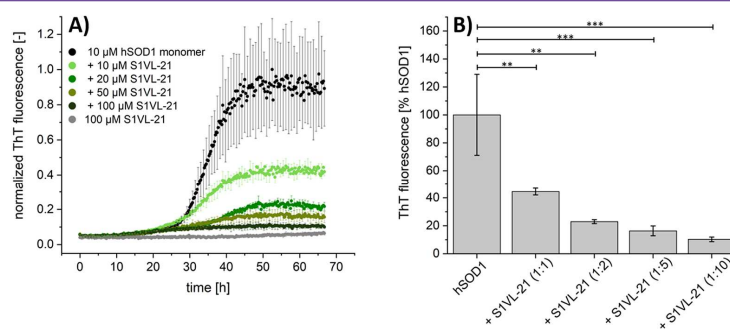


**Figure 3.** S1VL-21 exhibits an influence on the formation of amyloid-like hSOD1 aggregates. The ThT assay was performed to investigate the influence of S1VL-21 on amyloid-like hSOD1 aggregation. All samples containing 5  $\mu\text{M}$  dimeric hSOD1 with and without the corresponding peptide concentration as well as peptide alone were incubated in 50 mM sodium acetate buffer pH 6 with 10 mM TCEP, 5 mM EDTA, 150 mM sodium chloride, and 5  $\mu\text{M}$  ThT for 15 min at 37 °C before the fluorescence progression measurement was started in a 96-well half-area flat-bottom microplate (Corning, New York, USA) containing one stainless steel bead (3.2 mm). The progression of fluorescence intensity was measured every 15 min at  $\lambda_{\text{ex}} = 448 \text{ nm}$  and  $\lambda_{\text{em}} = 482 \text{ nm}$  with 30 s of agitation at 400 rpm before every measurement using a microplate reader (BMG Labtech, Ortenberg, Germany). The ThT fluorescence intensity was normalized to the highest value and plotted against the time. (A) The ThT assay of hSOD1 (black) and with different concentrations of S1VL-21 (green colors) in 3- to 5-fold determination. Gray: 100  $\mu\text{M}$  S1VL-21 without hSOD1. The ThT fluorescence is decreased with S1VL-21. (B) Comparison of the ThT fluorescence intensity (Figure 3A) of all samples present in A after 52.5 h. S1VL-21-containing samples were normalized to the fluorescence intensity of the sample with hSOD1 alone. One-way ANOVA (analysis of variance) with Fisher post hoc analysis was used for statistical analysis. \*\*  $p \leq 0.01$ ; \*\*\*  $p \leq 0.001$ . The ThT fluorescence was significantly reduced by 90% by addition of a 10-fold molar excess of S1VL-21.

2B). In contrast, the measurements with the randomized control peptides S1VL-21\_Rdm1, S1VL-21\_Rdm2, and S1VL-21\_Rdm3 led to  $K_D$  values of 36, 20, and 152  $\mu\text{M}$ , respectively (Figure 2C). Thus, the selected S1VL-21 has an enhanced affinity with a 4- to 30-fold lower  $K_D$  value for the hSOD1 interaction compared to the randomized control peptides.

**S1VL-21 Exhibits an Influence on the Formation of Amyloid-Like hSOD1 Aggregates.** To investigate the

influence of S1VL-21 on amyloid-like hSOD1 aggregation, a thioflavin T (ThT) assay was performed. Briefly, 5  $\mu\text{M}$  dimeric hSOD1 was incubated with and without the corresponding peptide in 50 mM sodium acetate buffer pH 6 containing 10 mM TCEP, 5 mM EDTA, 150 mM sodium chloride, and 5  $\mu\text{M}$  ThT for 15 min at 37 °C before the fluorescence progression measurement was started in a microplate containing one 3.2 mm stainless steel bead per well. The

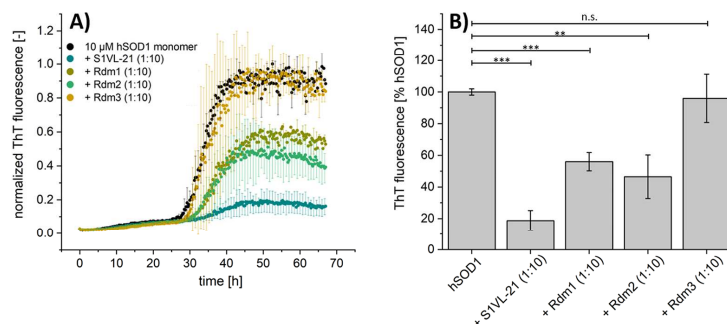


**Figure 4.** Randomized control peptides S1VL-21\_Rdm1–3 revealed to be less effective in the inhibition of amyloid-like hSOD1 aggregation compared to S1VL-21. The ThT assay was performed to investigate the influence of S1VL-21 as well as its randomized control peptides S1VL-21\_Rdm1–3 on amyloid-like hSOD1 aggregation. All samples containing 5  $\mu$ M dimeric hSOD1 with and without the corresponding peptide were incubated in 50 mM sodium acetate buffer pH 6 with 10 mM TCEP, 5 mM EDTA, 150 mM sodium chloride, and 5  $\mu$ M ThT for 15 min at 37  $^{\circ}$ C before the fluorescence progression measurement was started in a 96-well half-area flat-bottom microplate (Corning, New York, USA) containing one stainless steel bead (3.2 mm). The progression of fluorescence intensity was measured every 15 min at  $\lambda_{ex}$  = 448 nm and  $\lambda_{em}$  = 482 nm with 30 s of agitation at 400 rpm before every measurement using a microplate reader (BMG Labtech, Ortenberg, Germany). The ThT fluorescence intensity was normalized to the highest value and plotted against the time. (A) The ThT assay of hSOD1 (black) related to the monomeric concentration of hSOD1. The peptides alone showed no increase in fluorescence (data not shown). The ThT fluorescence is most reduced with S1VL-21. (B) Comparison of the ThT samples after 52.5 h. Samples containing peptides are normalized to the fluorescence of the sample with hSOD1 alone. One-way ANOVA (analysis of variance) with Fisher post hoc analysis was used for statistical analysis. \*\*  $p \leq 0.01$ ; \*\*\*  $p \leq 0.001$ ; n.s. not significant ( $p > 0.05$ ). The ThT fluorescence was significantly reduced by 44 and 53% with a 10-fold molar excess of S1VL-21\_Rdm1 and S1VL-21\_Rdm2, respectively. S1VL-21\_Rdm3 did not reduce the ThT fluorescence.

effect of S1VL-21 on hSOD1 aggregation was determined by adding increasing concentrations of S1VL-21 to the fibrillation samples. Furthermore, the randomized control peptides were also analyzed for their influence on amyloid-like hSOD1 aggregate formation. In order to exclude aggregation of the peptide itself, the respective peptide was also investigated under the given conditions without hSOD1. Due to the high concentrations of TCEP and EDTA, which reduces the disulfide bond and complexes the metal ions, respectively, and the given stainless steel bead that causes mechanical agitation and thus fragmentation, hSOD1 unfolds and aggregates.<sup>29</sup>

The results were analyzed by comparing the relative fluorescence emission after 52.5 h, where the control (without peptide) reached its fluorescence maximum (Figure 3A; black). As shown in Figure 3A, the maximal fluorescence emission was decreased by addition of S1VL-21, and this effect was more evident the more peptide was added. With a 10-fold molar excess, the fluorescence was reduced by 90% (Figure 3B).

Compared to S1VL-21, its randomized peptides S1VL-21\_Rdm1, S1VL-21\_Rdm2, and S1VL-21\_Rdm3 indicated less influence on ThT fluorescence and thus on the formation of amyloid-like hSOD1 aggregates as shown in Figure 4. While S1VL-21\_Rdm1 and S1VL-21\_Rdm2 reduced the plateau of the hSOD1 aggregation-dependent ThT fluorescence by about 44 and 53%, respectively, S1VL-21\_Rdm3 did not exhibit any effect at all (Figure 4B). Thus, the randomized control peptides with the same amino acid composition but in a different sequence order were less effective in inhibition of amyloid-like hSOD1 aggregation compared to S1VL-21.

**Incubation of hSOD1 with S1VL-21 during Aggregation Resulted in hSOD1 Species That Were Significantly**

**Less Toxic to Neuro2a Cells than Non-peptide-Treated hSOD1 Aggregates.** In order to confirm that resulting hSOD1 species are less toxic to Neuro2a cells when hSOD1 was incubated with S1VL-21 under reducing conditions during the aggregation assay, a cell viability assay using the reduction of MTT was performed in a 5-fold determination (Figure 5). Therefore, Neuro2a cells were treated with samples that have been collected after 65 h of hSOD1 aggregation incubated with and without increasing concentrations of S1VL-21.

The cell proliferation was normalized to the mean value of cells treated with medium. Subsequently, the rate of cells that were rescued due to the initial addition of S1VL-21 during hSOD1 aggregation was determined by normalizing the proliferation level to that of cells treated with hSOD1 aggregates. Cells treated with hSOD1 that has been incubated with different concentrations of S1VL-21 during the aggregation assay yielded a concentration-dependent increase in rescue rate (Figure 5; 1:1:14  $\pm$  6%; 1:5:35  $\pm$  7%; 1:10:48  $\pm$  8). Notably, compared to cells treated with hSOD1 aggregates, 48% of cells have been rescued after treatment with hSOD1 species, where hSOD1 was initially incubated with a 10-fold molar excess of S1VL-21. Thus, the incubation of hSOD1 with S1VL-21 during the aggregation assay resulted in hSOD1 species that were significantly less toxic to Neuro2a cells than non-peptide-treated hSOD1 aggregates.

## CONCLUSION

It has been shown that destabilizing of hSOD1 by mutations and/or post-translational modifications possibly leads to hSOD1 misfolding and aggregation, whereas *in vitro* and *in vivo* studies revealed an important role of hSOD1 aggregates in the progression of ALS. These aggregates containing mutant and misfolded wild-type hSOD1 were found in sALS patients

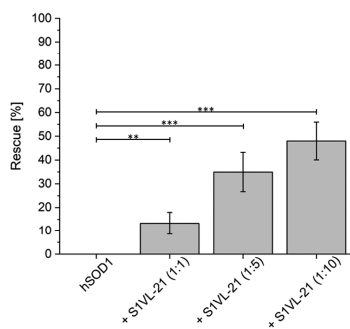


**Figure 5.** Incubation of hSOD1 with S1VL-21 during aggregation resulted in significantly less toxic hSOD1 species to Neuro2a cells than non-peptide-treated hSOD1 aggregates. A cell viability assay was performed in Neuro2a cells (2500 cells/well) cultured in flat-bottomed 96-well plates in DMEM including 10% FBS and 1% streptomycin and penicillin. After 6 h, the cells were treated with the pellet of samples containing hSOD1 alone and hSOD1 that was incubated with increasing concentrations of S1VL-21 during 65 h under aggregating conditions as described in Figure 3. Therefore, the samples were centrifuged at 100 000g for 1 h at 4 °C, and the pellet was solvated and diluted (1:1) in medium. After 3 days, the cell viability was measured using the cell proliferation Kit I according to the manufacturer's instructions (Roche, Basel, Switzerland) in a 5-fold determination. The proliferation was normalized to the mean value of the medium-treated cells. The rate of cells that could be rescued due to the initial addition of S1VL-21 during hSOD1 aggregation was determined by normalizing the proliferation level to that of cells treated with hSOD1 aggregates. One-way ANOVA (analysis of variance) with Fisher post hoc analysis was used for statistical analysis. \*\*  $p \leq 0.01$ ; \*\*\*  $p \leq 0.001$ . Cells treated with hSOD1 that has been incubated with different concentration of S1VL-21 during aggregation led to a concentration-dependent increase in the rescue rate compared to non-peptide-treated hSOD1 aggregates.

as well as in hSOD1-fALS and non-hSOD1 fALS patients.<sup>8,16,18</sup>

Our intention was to explore whether stabilization of the native hSOD1 conformation by specifically binding ligands is able to interfere with hSOD1 aggregation.

Here, we report a 16-mer peptide S1VL-21 selected by phage display that was identified as a ligand to stabilize the native conformation of hSOD1. MST measurements revealed a micromolar binding affinity of S1VL-21 to native hSOD1. ThT assays were used to investigate the inhibition efficacy of S1VL-21 on hSOD1 aggregation. As the emission at 482 nm is proportional to the amount of amyloid fibrils and amyloid-like aggregates, the aggregation of hSOD1 was followed by measuring the ThT fluorescence.<sup>30</sup> We observed that coinubation of hSOD1 with S1VL-21 during the aggregation assay resulted in a concentration-dependent inhibition of the ThT fluorescence emission increase. For example, incubation of hSOD1 with an equimolar amount of S1VL-21 under hSOD1-aggregating conditions resulted in a reduced formation of amyloid-like hSOD1 aggregates by 55%, whereas with a 10-fold molar excess of S1VL-21, the formation of amyloid-like hSOD1 aggregates was reduced by even 90%. Additionally, we were able to show that these remaining species are less toxic to Neuro2 cells than non-peptide-treated hSOD1 aggregates, also in a concentration-dependent manner, probably due to the

lower amount of aggregates. Although the mechanism of hSOD1 aggregation has not yet been clearly elucidated, Chattopadhyay et al. demonstrated *in vitro* that even small amounts of metal-free and reduced monomeric hSOD1 can initiate the formation of amyloid species in disulfide-bridge-intact forms of hSOD1 and that elongation is driven by recruitment of apo or partially metalated, dimeric, disulfide-intact hSOD1.<sup>31</sup> We suggest that the specific binding of S1VL-21 to the native hSOD1 leads to a reduction or even a prevention in the formation of misfolded, ThT-positive hSOD1 species. Moreover, the effect of S1VL-21 is sequence-specific as indicated by the analyses using sequence randomized control peptides. Whereas Rdm1 and Rdm2 also showed a reducing but considerably smaller effect on the formation of amyloid-like hSOD1 aggregates compared to S1VL-21, Rdm3 did not exhibit an influence in interfering with hSOD1 aggregation. It cannot be excluded that there are still similarities in parts of the sequences between the two randomized control peptides and S1VL-21 (e.g., amino acid combinations/positions or charge distributions) that may explain the existing influence on hSOD1 aggregate formation. However, compared to S1VL-21, the randomized control peptides showed a lower affinity to native hSOD1 and significantly less inhibition of aggregate formation.

In summary, we used phage display including control selections and NGS analysis for the identification of peptide ligands for native hSOD1. In this way and together with subsequent characterization methods, we were able to identify S1VL-21 and we showed that this peptide has an impact on hSOD1 aggregation. Further investigations to figure out the binding site of S1VL-21 to hSOD1 are necessary to understand the mechanism of impairment of hSOD1 aggregation. S1VL-21 will be further optimized in order to reduce the required concentration at which the same inhibition rate of aggregate formation is achieved as with S1VL-21 to become a potential lead for drug development.

## MATERIALS & METHODS

**Protein Expression, Purification, and Reconstitution.** Heterologous expression of human SOD1 (hSOD1) in *E. coli* and its purification and fully reconstitution to natively folded dimeric holoenzyme was performed as described previously in Santur et al.<sup>31</sup>

**Peptides.** Peptide S1VL-21 (YKHSWETQEKQNYVTD-NH<sub>2</sub>) as well as its randomized control peptides (S1VL-21\_Rdm1: KQYHE-EVYKQDTQNS-NH<sub>2</sub>; S1VL-21\_Rdm2: YKYVTTENHD-SQEQKW-NH<sub>2</sub>; S1VL-21\_Rdm3: HKSNDKEWTETQYVY-NH<sub>2</sub>) were purchased from Caslo (Lyngby, Denmark) with >98% purity. They are C-terminal-amidated and consist of 16 L-enantiomeric amino acid residues with a molecular mass of 2055 Da.

**Phage Display.** Phage display with four selection rounds was performed to obtain peptides that specifically bind to native hSOD1. Therefore, 25 μg/mL of dimeric hSOD1 diluted in 100 μL of 50 mM sodium acetate pH 6 was immobilized on a NHS-activated surface (3D-NHS 96-well plate, 100 μL functionalization volume, polystyrene; PolyAn, Berlin, Germany) for 1 h at RT. In all selection rounds, the surface was quenched after the hSOD1 solution was removed with 200 μL of quenching solution (50 mM ethanolamine and 100 mM Tris in 10 mM sodium phosphate pH 9) for 1 h at RT followed by five washing steps with 200 μL of washing buffer (150 mM sodium chloride and 0.05% Tween-20 in 50 mM sodium acetate pH 6). In addition before washing, the surface was blocked with 200 μL of 10 mg/mL of bovine serum albumin (BSA) in 50 mM sodium acetate pH 6 in the second round and with 200 μL of 10 mg/mL of milk powder in 50 mM sodium acetate pH 6 in the third round for 15 min at RT to reduce unspecific binding events. During those rounds, 2

mg/mL of BSA or milk powder was added to the washing buffer, respectively. In the first as well as in the fourth round, the surface was not additionally blocked to vary the selection conditions. Then,  $2.8 \times 10^{11}$  phages (TriCo-16 phage display peptide library; Creative Biolabs, New York, USA) in 50 mM sodium acetate pH 6 were added and incubated for 30 min at RT in each round. After the nonbinding phages were removed, the well was washed with 200  $\mu$ L of the respective washing buffer of the corresponding round. The number of washing steps after phage incubation was increased until round 3 (5/10/15/15). Elution of phages was done by incubation with 100  $\mu$ L of 0.2 M glycine-HCl pH 2.2 for 10 min at RT. The phage containing solution was then removed from the plate and neutralized by transferring it to a tube containing 25  $\mu$ L of 1 M Tris-HCl pH 9.1. To determine the output titer, 5  $\mu$ L of eluted phages were used. Therefore, a dilution series from  $10^{-2}$  to  $10^{-8}$  was prepared with the eluted phages in a total volume of 100  $\mu$ L in lysogeny broth (LB) medium. Each dilution was mixed with 100  $\mu$ L of *E. coli* K12 ER2738 (OD<sub>600</sub> of 0.6) and plated together with 800  $\mu$ L of top agar on plates (35  $\times$  10 mm; Sarstedt, Nümbrecht, Germany) containing LB-Agar-IPTG-XGal. After overnight incubation at 37 °C, the plaques were counted to determine the output titer.

The remaining eluted phages (120  $\mu$ L) were amplified in 20 mL of *E. coli* K12 ER2738, starting with an OD<sub>600</sub> of 0.1, for 4 h at 37 °C. Subsequently, the culture was centrifuged for 20 min at 2700g at 4 °C. For phage precipitation, the supernatant was added to 7 mL of PEG-8000/2.5 M sodium chloride, incubated overnight at 4 °C, and centrifuged at 2700g at 4 °C for 1 h. The supernatant was discarded, while the phage-containing pellet was dissolved in 1 mL of 1X PBS before another centrifugation at 4 °C and 11 000g for 5 min to get rid of residual bacterial components. Afterward, the supernatant was added to 200  $\mu$ L of PEG-8000/2.5 M sodium chloride and incubated for 1 h on ice followed by a final centrifugation step for 45 min at 2700g and 4 °C. The phage-containing pellet was properly resuspended in 100  $\mu$ L of 1X PBS. The input titer was determined by spectrophotometry<sup>32</sup> in 1X PBS using a 1:10 dilution. The resulting phages were then used in the next selection round with the same phage amount as before and further used for an enrichment ELISA as well as prepared for next-generation sequencing (NGS) analysis.

Besides the main selection with hSOD1 as a target (target selection, TS), two control selections were performed as illustrated in Figure 6

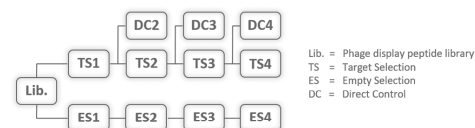


**Figure 6.** Schematic overview of the phage display selection with target (target selection, TS) and the corresponding control selections empty selection (ES) and direct control (DC) without target. In the first round, the phages from the peptide library are used for the target selection (TS) as well as for the control selection without target called empty selection (ES). One further control without target is performed from the second selection round called direct control (DC), where in contrast to ES, the phages resulting from previous TS are used.

to improve the sequence evaluation efficiency after NGS analysis. The first control selection, called empty selection (ES), was performed in the same way as TS but without hSOD1. During immobilization, 50 mM sodium acetate pH 6 was used instead of hSOD1. All further steps are the same as for TS so that in the end two separate selections with enriched phages were present. One further control was performed starting from the second selection round (direct control, DC). In contrast to ES, here the phages resulting from each round of TS were used for the next selection round that was performed without target protein. After four rounds, four samples for TS and ES (TS1–TS4 and ES1–ES4) and three for DC (DC2–DC4) with enriched

phages were present, which were subsequently used together with the phage display peptide library for further analysis.

**Enrichment ELISA.** An enrichment ELISA was performed to validate the success of the phage display selection. Therefore, 25  $\mu$ g/mL of dimeric hSOD1 diluted in 100  $\mu$ L of 50 mM sodium acetate pH 6 was immobilized on an amino plate (Nunc Immobilizer Amino 96-well plate, polystyrene; Thermo Scientific, Waltham, USA) for 1 h at RT. Noncoated wells (50 mM sodium acetate pH 6 without hSOD1) were used as a control for each selection round. The solution was removed, and the surface was quenched with 200  $\mu$ L of quenching solution (50 mM ethanolamine and 100 mM Tris in 10 mM sodium phosphate pH 9) for 1 h at RT followed by a blocking step with 200  $\mu$ L of blocking solution (10 mg/mL BSA in 50 mM sodium acetate pH 6) for 15 min at RT. After three washing steps with 200  $\mu$ L of washing buffer (150 mM sodium chloride, 0.05% Tween-20, 2 mg/mL of BSA in 50 mM sodium acetate pH 6), the amplified and purified phages of each target selection round were diluted in washing buffer to a total amount of  $5 \times 10^{10}$  phages in 100  $\mu$ L. The wells immobilized with hSOD1 as well as noncoated wells were incubated with the corresponding phage solution for 1 h at RT. Unbound phages were removed by three washing steps with 150  $\mu$ L of washing buffer. The anti-M13 antibody (horseradish peroxidase (HRP)-conjugated mouse monoclonal antibacteriophage M13 antibody; Sino Biological, Peking, China) was diluted 1:2500 in washing buffer, and 100  $\mu$ L was added into each well for 1 h at RT. After six washing steps with 150  $\mu$ L of washing buffer, the supernatant was completely removed, 100  $\mu$ L of the 3,3',5,5'-tetramethylbenzidine (TMB) solution (TMB was previously dissolved in 1 mL of DMSO and diluted with 9 mL of 0.05 M phosphate citrate buffer pH 5) was added into each well, and after 10 min of incubation at RT, the reaction was stopped with 100  $\mu$ L of 2 M H<sub>2</sub>SO<sub>4</sub>. The absorption was quantified at 450 nm using a microplate reader (BMG Labtech, Ortenberg, Germany).

In addition to the samples from the target selection (TS1, TS2, TS3, TS4), the library as well as the wild-type phage without peptide were analyzed. The measurement was performed in double determination. Noncoated wells that were incubated with washing buffer without phages were used as a control for background signal.

**Extraction and Amplification of ssM13 DNA for Sequencing.** The single-stranded phage DNA from each sample from the phage display selection (all samples from TS, ES, and DC containing enriched phages in 1X PBS as well as the library) were purified and prepared for next-generation sequencing (NGS). Therefore, 10  $\mu$ L of each input sample was diluted in 600  $\mu$ L of 1X PBS and incubated with 200  $\mu$ L of PEG-8000/2.5 M sodium chloride for 20 min at RT after the samples were inverted eight times. The samples were then centrifuged at 20 800g for 10 min at 4 °C. The supernatant was removed, and the pellet was carefully resuspended in 200  $\mu$ L of a 10:1 mixture of 3 M sodium acetate (pH 5.2) and TE. The samples were incubated with 500  $\mu$ L of 99% ethanol for 15 min at RT before centrifugation at 20 800g and 4 °C for 10 min. The supernatant was discarded, and the pellet was washed with 250  $\mu$ L of 70% ethanol. After a final centrifugation step for again 10 min at 20 800g and 4 °C, the supernatant was removed, and the pellet was dried at 30 °C for 8 min before being resuspended in 40  $\mu$ L of 10 mM Tris pH 8. The concentration of the DNA was determined by the absorption at 260 nm.

The ssDNA was amplified using the KAPA HiFi HotStart ReadyMixPCR Kit (Kapa Biosystems, Wilmington, USA) and the polymerase chain reaction (PCR) for the subsequent NGS. For each 25 ng of phage DNA, 5  $\mu$ M primers (forward: 5'-TCGTCGGCAG-CGTCAGATGTGTATAAGAGACAGCGCAATTCCCTTAGTGG-TACC-3', reverse: 5'-GTCTCGTGGCTCGGAGATGTGTAT-AAGAGACAGCCCTCATAGTTAGCGTAACG-3') and 12.5  $\mu$ L of KAPA HiFi Hot Start Ready Mix were added and filled up to 25  $\mu$ L with ddH<sub>2</sub>O. The PCR protocol was composed as follows: initial step at 95 °C for 3 min, followed by 25 cycles with denaturation of DNA at 95 °C for 30 s, annealing at 55 °C for 30 s, and extension at 72 °C for 30 s. A final step of the extension at 72 °C was done for 5 min. The concentration of the amplified DNA was measured by the absorption

at 260 nm and the success of the PCR was evaluated using a 1% agarose gel. Further sample processing and NGS analysis was performed by the Biologisch-Medizinisches Forschungszentrum at the Heinrich Heine University in Düsseldorf, Germany.

**Sequence Analysis.** The resulting sequencing from the NGS analysis was processed and evaluated with the Target Sequencing Analysis Tool (TSAT), an evaluation software that has been developed by our research group. The use of advanced controls during the phage display selection as well as the establishment of NGS analysis including further sequencing processing via TSAT enabled a high throughput for the identification of target-specific binders.

TSAT is a program that is based on a Python script with front-end access for user. The following modules were used during its creation: Tkinter,<sup>33</sup> Bio,<sup>34</sup> base64,<sup>35</sup> re,<sup>36</sup> collections,<sup>37</sup> sqlite3,<sup>38</sup> time,<sup>39</sup> datetime,<sup>40</sup> sys,<sup>41</sup> and threading.<sup>42</sup>

TSAT screens a given document for the fixed regions directly upstream and downstream of the randomized peptide coding region in the phage genome. The peptide coding sequence is excised and checked for its length. If the length of the nucleotides is dividable by 3, it is translated into the corresponding amino acids. Otherwise, the code is discarded and listed in a document of incomplete sequences. The translated sequences are temporarily saved in a dictionary, which documents the amino acid composition and the total count of each single sequence. For further analysis, the resulting data are transferred to and saved in a data bank. The frequencies of each translated sequence are then normalized to the total number of all translated sequences of the corresponding selection and converted into a parts per million (ppm) format to allow easier comparison between different selections. This is done for each sample of the selection rounds containing the target selection (TS), direct control (DC), and the empty selection (ES) as described in 0. Subsequently, the resulting data from each selection round are compared with each other, whereby only those sequences are considered at the end that have accumulated during the selection starting from the library and that are more or equally frequently present in the TS than in the corresponding ES and DC, respectively. Thus, enriched unspecific binders such as plate binders are removed from the evaluation by directly comparing the selection with target with those without target. The filtered sequences are then assigned two parameters called empty score (EmS) and enrichment factor (EnF). EnF is the frequency of a sequence in the last target selection round divided by the frequency of the same sequence in the library, whereas EmS represents the frequency of a sequence in the last target selection round divided by the frequency of the same sequence in the last empty selection round. As a last step, a scoring list is created based on the EmS values, and the sequences are saved in a FASTA format for the subsequent sequence alignment using the open source software Hammock<sup>43</sup> using default parameters expect that sequence input was done sorted by the EmS values.

**Labeling of Native hSOD1 with Fluorophore CF633.** CF633 succinimidyl ester (Sigma-Aldrich, St. Louis, USA) was used for labeling native hSOD1 according to the manufacturer's instructions with a few modifications. Therefore, 10  $\mu$ L of a 50 mM dye stock solution in anhydrous DMSO was added to 190  $\mu$ L of 180  $\mu$ M hSOD1 (monomeric concentration) in 50 mM sodium acetate pH 6, which corresponds to a dye/protein molar ratio of 15:1 and results in a final concentration of 5% DMSO. All further steps were performed as described in the manufacturer's manual. Free dye was removed by dialysis against 50 mM sodium acetate pH 6. The concentration of labeled CF633-hSOD1 was determined by Bradford assay.<sup>44</sup>

**Microscale Thermophoresis Measurements for  $K_D$  Determination.** In order to determine the equilibration dissociation constant ( $K_D$ ) of hSOD1 to the selected peptide, microscale thermophoresis (MST) measurements were performed using a Monolith NT.115 blue/red instrument (Nanotemper Technologies, Munich, Germany). Fluorescently labeled hSOD1 (CF633-hSOD1; DOL of 0.5) with a final dimeric concentration of 250 nM was added to samples containing increasing concentrations of unlabeled peptide. Therefore, a 1:1 serial dilution of peptide and a 500 nM CF33-hSOD1 stock

solution were prepared in 50 mM sodium acetate pH 6 containing 150 mM sodium chloride and 0.05% Tween-20. The 16 samples were then transferred into specialized glass capillaries (Monolith NT.155 premium capillaries MO-K025; Nanotemper Technologies, Munich, Germany). The measurement was performed at 25 °C using the blue/red channel with an MST and LED power of 40% leading to fluorescence levels between 700 and 900 units. For all experiments, standard parameters were used as recommend by the manufacturer (delay time of heating period of 30 s and re-equilibration period of 5 s). The data were evaluated through the thermophoresis effect using the manufacturer supplied NT analysis software (version 1.5.41).

**Thioflavin T Assay.** Thioflavin T (ThT) assay was performed to analyze the influence of peptide on hSOD1 fibrillation and/or amyloid-like aggregation. Lyophilized peptides were solved in filtered ddH<sub>2</sub>O. Buffers and solutions were then sterile filtered (for larger volumes: Minisart-Plus syringe filter, 0.2  $\mu$ m, Sartorius, Göttingen, Germany; for smaller volumes: Anotop 10 syringe filter, 0.2  $\mu$ m, Cytiva, Chicago, USA), while the hSOD1 stock solution in 50 mM sodium acetate buffer pH 6 was centrifuged for 10 min at 20 800g and 21 °C to remove larger particles. Before pipetting together, all components were prewarmed for 1 h at 37 °C. Then, 5  $\mu$ M dimeric hSOD1 was mixed with 5  $\mu$ M ThT, 10 mM TCEP, 5 mM EDTA, 150 mM sodium chloride, and the corresponding concentration of peptide (protein/peptide molar ratios of 1:1, 1:2, 1:5, and 1:10 related to the monomeric concentration of hSOD1) in 50 mM sodium acetate buffer pH 6. As controls, a sample with hSOD1 and without peptide and a sample without hSOD1 and with peptide were used. All prepared samples were incubated for 15 min at 37 °C without agitation. Then, 120  $\mu$ L of each sample was transferred into a well of a 96-well half-area flat-bottom microplate (Corning, New York, USA) containing one 3.2 mm stainless steel bead (Biospec Products, Bartlesville, USA), and the plate was sealed with a foil for 96-well microplates (Thermo Fisher Scientific, Waltham, USA). The progression of fluorescence intensity was measured using a microplate reader (BMG Labtech, Ortenberg, Germany) at 37 °C every 15 min at  $\lambda_{ex}$  = 448–10 nm and  $\lambda_{em}$  = 482–10 nm with 30 s of agitation at 400 rpm before every measurement. The measurements were performed in a 3- to 5-fold determination.

**Cell Viability Assay.** A cell viability assay using the reduction of 3-(4,5-dimethylthiazol-2-yl)-2,5-diphenyltetrazolium bromide (MTT) was performed to investigate the cytotoxicity of hSOD1 species that were previously incubated with and without S1VL-21 under aggregating conditions. Therefore, Neuro2a cells were cultivated in DMEM medium supplemented with 10% fetal bovine serum (FBS) and 1% penicillin and streptomycin. A total of 2500 cells per well in a volume of 100  $\mu$ L were seeded on flat-bottomed 96-well plates (VWR, Radnor, USA) and incubated in a 95% humidified atmosphere with 5% CO<sub>2</sub> at 37 °C for 6 h. Aggregates of hSOD1 alone and hSOD1 incubated with increasing concentrations of S1VL-21 (1:1; 1:5; 1:10) under aggregating conditions were prepared as described in 0. The samples were collected after 65 h and centrifuged for 1 h at 4 °C and 100 000g. The supernatant was completely removed, whereas the pellet was dissolved in the same volume of cell culture medium (DMEM containing 10% FBS and 1% penicillin and 1% streptomycin) and diluted to 1:1. Neuro2a cells were then treated with 30  $\mu$ L of each sample and were further incubated for 3 days in a 95% humidified atmosphere with 5% CO<sub>2</sub> at 37 °C. Cell viability was measured using the Cell Proliferation Kit I according to the manufacturer's instructions (Roche, Basel, Switzerland) in a 5-fold determination. The absorbance of the formazan product was determined by measuring the absorption at 570 nm subtracted by the absorbance at 690 nm in a microplate reader (BMG Labtech, Ortenberg, Germany). The results were normalized to the mean value of cells treated with medium only. As a positive control for cytotoxicity, 10% DMSO diluted in medium was used.

## AUTHOR INFORMATION

### Corresponding Authors

**Jeannine Mohrlüder** – Institute of Biological Information  
Processing: Structural Biochemistry (IBI-7),  
Forschungszentrum Jülich, 52425 Jülich, Germany;  
orcid.org/0000-0002-9922-2986; Phone: +49-2461-  
613518; Email: j.mohrlueder@fz-juelich.de

**Dieter Willbold** – Institute of Biological Information  
Processing: Structural Biochemistry (IBI-7),  
Forschungszentrum Jülich, 52425 Jülich, Germany; Institut  
für Physikalische Biologie, Heinrich-Heine-Universität  
Düsseldorf, 40225 Düsseldorf, Germany; orcid.org/0000-  
0002-0065-7366; Phone: +49-2461-612100;  
Email: d.willbold@fz-juelich.de

### Authors

**Karoline Santur** – Institute of Biological Information  
Processing: Structural Biochemistry (IBI-7),  
Forschungszentrum Jülich, 52425 Jülich, Germany; Institut  
für Physikalische Biologie, Heinrich-Heine-Universität  
Düsseldorf, 40225 Düsseldorf, Germany

**Elke Reinartz** – Institut für Physikalische Biologie, Heinrich-  
Heine-Universität Düsseldorf, 40225 Düsseldorf, Germany

**Yi Lien** – Institute of Biological Information Processing:  
Structural Biochemistry (IBI-7), Forschungszentrum Jülich,  
52425 Jülich, Germany

**Markus Tusche** – Institute of Biological Information  
Processing: Structural Biochemistry (IBI-7),  
Forschungszentrum Jülich, 52425 Jülich, Germany

**Tim Altendorf** – Institute of Biological Information  
Processing: Structural Biochemistry (IBI-7),  
Forschungszentrum Jülich, 52425 Jülich, Germany; Institut  
für Physikalische Biologie, Heinrich-Heine-Universität  
Düsseldorf, 40225 Düsseldorf, Germany

**Marc Sevenich** – Institute of Biological Information  
Processing: Structural Biochemistry (IBI-7),  
Forschungszentrum Jülich, 52425 Jülich, Germany; Institut  
für Physikalische Biologie, Heinrich-Heine-Universität  
Düsseldorf, 40225 Düsseldorf, Germany

**Gültekin Tamgüney** – Institute of Biological Information  
Processing: Structural Biochemistry (IBI-7),  
Forschungszentrum Jülich, 52425 Jülich, Germany; Institut  
für Physikalische Biologie, Heinrich-Heine-Universität  
Düsseldorf, 40225 Düsseldorf, Germany

Complete contact information is available at:  
<https://pubs.acs.org/10.1021/acchemneuro.1c00253>

### Author Contributions

K.S. contributed to the design of the TSAT software, contributed to the design of experiments, performed most of the experiments, analyzed data, and wrote the initial draft of the manuscript; E.R. contributed to the design of experiments and provided feedback on experimental results; Y.L. and M.T. performed cell cultivation; T.A. contributed to the design of TSAT and edited the manuscript; M.S. contributed to the design of TSAT; G.T. contributed to the design of the cell viability assay as well as provided feedback on experimental results; J.M. contributed to the study conception and design and edited the manuscript; D.W. designed the overall study and edited the manuscript. All authors contributed to the preparation of this manuscript as well as read and approved the final manuscript.

### Notes

The authors declare no competing financial interest.

### ACKNOWLEDGMENTS

The authors wish to express their thanks to the Biologisch-Medizinisches Forschungszentrum of the Heinrich Heine University Düsseldorf for performing the NGS analysis.

### REFERENCES

- (1) Bento-Abreu, A., Van Damme, P., Van Den Bosch, L., and Robberecht, W. (2010) The neurobiology of amyotrophic lateral sclerosis. *Eur. J. Neurosci* 31, 2247–2265.
- (2) Sreedharan, J., and Brown, R. H., Jr (2013) Amyotrophic lateral sclerosis: problems and prospects. *Ann. Neurol.* 74, 309–316.
- (3) Grad, L. I., Rouleau, G. A., Ravits, J., and Cashman, N. R. (2017) Clinical spectrum of amyotrophic lateral sclerosis (ALS). *Cold Spring Harbor Perspect. Med.* 7, a024117.
- (4) Gordon, P. H. (2013) Amyotrophic lateral sclerosis: an update for 2013 clinical features, pathophysiology, management and therapeutic trials. *Aging Dis* 04, 295–310.
- (5) Zhao, B., Marciniuk, K., Gibbs, E., Yousefi, M., Napper, S., and Cashman, N. R. (2019) Therapeutic vaccines for amyotrophic lateral sclerosis directed against disease specific epitopes of superoxide dismutase 1. *Vaccine* 37, 4920–4927.
- (6) Baskoylu, S. N., Yersak, J., O'Hern, P., Grosser, S., Simon, J., Kim, S., Schuch, K., Dimitriadis, M., Yanagi, K. S., Lins, J., et al. (2018) Single copy/knock-in models of ALS SOD1 in *C. elegans* suggest loss and gain of function have different contributions to cholinergic and glutamatergic neurodegeneration. *PLoS Genet.* 14, No. e1007682.
- (7) Rosen, D. R., Siddique, T., Patterson, D., Figlewicz, D. A., Sapp, P., Hentati, A., Donaldson, D., Goto, J., O'Regan, J. P., Deng, H. X., et al. (1993) Mutations in Cu/Zn superoxide-dismutase gene are associated with familial amyotrophic-lateral-sclerosis. *Nature* 362, 59–62.
- (8) Valentine, J. S., Doucette, P. A., and Zittin Potter, S. (2005) Copper-zinc superoxide dismutase and amyotrophic lateral sclerosis. *Annu. Rev. Biochem.* 74, 563–593.
- (9) Roe, J. A., Butler, A., Scholler, D. M., Valentine, J. S., Marky, L., and Breslauer, K. J. (1988) Differential scanning calorimetry of Cu,Zn-superoxide dismutase, the apo-protein, and its zinc-substituted derivatives. *Biochemistry* 27, 950–958.
- (10) Rodriguez, J. A., Valentine, J. S., Eggers, D. K., Roe, J. A., Tiwari, A., Brown, R. H., Jr, and Hayward, L. J. (2002) Familial amyotrophic lateral sclerosis-associated mutations decrease the thermal stability of distinctly metallated species of human copper/zinc superoxide dismutase. *J. Biol. Chem.* 277, 15932–15937.
- (11) Reaume, A. G., Elliott, J. L., Hoffman, E. K., Kowall, N. W., Ferrante, R. J., Sivek, D. F., Wilcox, H. M., Flood, D. G., Beal, M. F., Brown, R. H., Jr, et al. (1996) Motor neurons in Cu/Zn superoxide dismutase-deficient mice develop normally but exhibit enhanced cell death after axonal injury. *Nat. Genet.* 13, 43–47.
- (12) Jonsson, P. A., Graffmo, K. S., Brannstrom, T., Nilsson, P., Andersen, P. M., and Marklund, S. L. (2006) Motor neuron disease in mice expressing the wild type-like D90A mutant superoxide dismutase-1. *J. Neuropathol. Exp. Neurol.* 65, 1126–1136.
- (13) Graffmo, K. S., Forsberg, K., Bergh, J., Birve, A., Zetterstrom, P., Andersen, P. M., Marklund, S. L., and Brannstrom, T. (2013) Expression of wild-type human superoxide dismutase-1 in mice causes amyotrophic lateral sclerosis. *Hum. Mol. Genet.* 22, 51–60.
- (14) van Zundert, B., and Brown, R. H., Jr (2017) Silencing strategies for therapy of SOD1-mediated ALS. *Neurosci. Lett.* 636, 32–39.
- (15) Bosco, D. A., Morfini, G., Karabacak, N. M., Song, Y., Gros-Louis, F., Pasinelli, P., Goolsby, H., Fontaine, B. A., Lemay, N., McKenna-Yasek, D., et al. (2010) Wild-type and mutant SOD1 share an aberrant conformation and a common pathogenic pathway in ALS. *Nat. Neurosci.* 13, 1396–1403.

- (16) Forsberg, K., Jonsson, P. A., Andersen, P. M., Bergemalm, D., Graffino, K. S., Hultdin, M., Jacobsson, J., Rosquist, R., Marklund, S. L., and Brannstrom, T. (2010) Novel antibodies reveal inclusions containing non-native SOD1 in sporadic ALS patients. *PLoS One* 5, No. e11552.
- (17) Forsberg, K., Andersen, P. M., Marklund, S. L., and Brannstrom, T. (2011) Glial nuclear aggregates of superoxide dismutase-1 are regularly present in patients with amyotrophic lateral sclerosis. *Acta Neuropathol.* 121, 623–634.
- (18) Grad, L. I., Yerbury, J. J., Turner, B. J., Guest, W. C., Pokrishevsky, E., O'Neill, M. A., Yanai, A., Silverman, J. M., Zeineddine, R., Corcoran, L., et al. (2014) Intercellular propagated misfolding of wild-type Cu/Zn superoxide dismutase occurs via exosome-dependent and -independent mechanisms. *Proc. Natl. Acad. Sci. U. S. A.* 111, 3620–3625.
- (19) Chia, R., Tattum, M. H., Jones, S., Collinge, J., Fisher, E. M., and Jackson, G. S. (2010) Superoxide dismutase 1 and tgSOD1 mouse spinal cord seed fibrils, suggesting a propagative cell death mechanism in amyotrophic lateral sclerosis. *PLoS One* 5, No. e10627.
- (20) Furukawa, Y., Kaneko, K., Watanabe, S., Yamanaka, K., and Nukina, N. (2013) Intracellular seeded aggregation of mutant Cu,Zn-superoxide dismutase associated with amyotrophic lateral sclerosis. *FEBS Lett.* 587, 2500–2505.
- (21) Grad, L. I., Pokrishevsky, E., Silverman, J. M., and Cashman, N. R. (2014) Exosome-dependent and independent mechanisms are involved in prion-like transmission of propagated Cu/Zn superoxide dismutase misfolding. *Prion* 8, 331–335.
- (22) Rakhit, R., Crow, J. P., Lepock, J. R., Kondejewski, L. H., Cashman, N. R., and Chakrabarty, A. (2004) Monomeric Cu,Zn-superoxide dismutase is a common misfolding intermediate in the oxidation models of sporadic and familial amyotrophic lateral sclerosis. *J. Biol. Chem.* 279, 15499–15504.
- (23) Ding, F., Furukawa, Y., Nukina, N., and Dokholyan, N. V. (2012) Local unfolding of Cu, Zn superoxide dismutase monomer determines the morphology of fibrillar aggregates. *J. Mol. Biol.* 421, 548–560.
- (24) Lai, Z., Colon, W., and Kelly, J. W. (1996) The acid-mediated denaturation pathway of transthyretin yields a conformational intermediate that can self-assemble into amyloid. *Biochemistry* 35, 6470–6482.
- (25) Wiseman, R. L., Johnson, S. M., Kelker, M. S., Foss, T., Wilson, I. A., and Kelly, J. W. (2005) Kinetic stabilization of an oligomeric protein by a single ligand binding event. *J. Am. Chem. Soc.* 127, 5540–5551.
- (26) van Groen, T., Schemmert, S., Brener, O., Gremer, L., Ziehlm, T., Tusche, M., Nagel-Steger, L., Kadish, I., Schartmann, E., Elfgen, A., et al. (2017) The Abeta oligomer eliminating D-enantiomeric peptide RD2 improves cognition without changing plaque pathology. *Sci. Rep.* 7, 16275.
- (27) Kutzsche, J., Schemmert, S., Tusche, M., Neddens, J., Rabl, R., Jurgens, D., Brener, O., Willuweit, A., Hutter-Paier, B., and Willbold, D. (2017) Large-scale oral treatment study with the four most promising D3-derivatives for the treatment of Alzheimer's disease. *Molecules* 22, 1693.
- (28) Schemmert, S., Schartmann, E., Zafiu, C., Kass, B., Hartwig, S., Lehr, S., Bannach, O., Langen, K. J., Shah, N. J., Kutzsche, J., et al. (2019) Abeta oligomer elimination restores cognition in transgenic Alzheimer's mice with full-blown pathology. *Mol. Neurobiol.* 56, 2211–2223.
- (29) Abdolvahabi, A., Shi, Y. H., Rasouli, S., Croom, C. M., Chuprin, A., and Shaw, B. F. (2017) How do gyrating beads accelerate amyloid fibrillization? *Biophys. J.* 112, 250–264.
- (30) Naiki, H., Higuchi, K., Hosokawa, M., and Takeda, T. (1989) Fluorometric-determination of amyloid fibrils invitro using the fluorescent dye, thioflavine-T. *Anal. Biochem.* 177, 244–249.
- (31) Santur, K. B., Sevenich, M. M., Schwarten, M., Nischwitz, V., Willbold, D., and Mohrluder, J. (2018) In vitro reconstitution of the highly active and natively folded recombinant human superoxide dismutase 1 holoenzyme. *Chemistryselect* 3, 7627–7632.
- (32) Casadevall, A., and Day, L. A. (1982) DNA packing in the filamentous viruses fd, Xf, Pfl and Pf3. *Nucleic Acids Res.* 10, 2467–2481.
- (33) Lundh, F. (1999) An introduction to Tkinter, <https://docs.python.org/3/library/tkinter.html>.
- (34) Cock, P. J. A., Antao, T., Chang, J. T., Chapman, B. A., Cox, C. J., Dalke, A., Friedberg, I., Hamelryck, T., Kauff, F., Wilczynski, B., et al. (2009) Biopython: freely available Python tools for computational molecular biology and bioinformatics. *Bioinformatics* 25, 1422–1423.
- (35) base64 — Base16, Base32, Base64, Base85 Data Encodings, <https://docs.python.org/3/library/base64.html?highlight=base64#module-base64>.
- (36) re — regular expression operations, <https://docs.python.org/3/library/re.html?highlight=re#module-re>.
- (37) collections — container datatypes, <https://docs.python.org/3/library/collections.html?highlight=collections#module-collections>.
- (38) Hipp, D. R. (2020) SQLite, <https://www.sqlite.org/index.html>.
- (39) time — time access and conversions, <https://docs.python.org/3/library/time.html>.
- (40) datetime — basic date and time types, <https://docs.python.org/3/library/datetime.html?highlight=datetime#module-datetime>.
- (41) sys — system-specific parameters and functions, <https://docs.python.org/3/library/sys.html?highlight=sys#module-sys>.
- (42) threading — thread-based parallelism, <https://docs.python.org/3/library/threading.html>.
- (43) Krejci, A., Hupp, T. R., Lexa, M., Vojtesek, B., and Muller, P. (2016) Hammock: a hidden Markov model-based peptide clustering algorithm to identify protein-interaction consensus motifs in large datasets. *Bioinformatics* 32, 9–16.
- (44) Bradford, M. M. (1976) A rapid and sensitive method for the quantitation of microgram quantities of protein utilizing the principle of protein-dye binding. *Anal. Biochem.* 72, 248–254.

## **2.7 In vitro reconstitution of the highly active and natively folded human superoxide dismutase 1 (hSOD1)**

Authors: Karoline B. Santur\*, **Marc M. Sevenich**\*, Melanie Schwarten, Volker Nischwitz, Dieter Willbold, Jeannine Mohrlüder (\*shared first authors)

Journal: Chemistry Select

DOI: <https://doi.org/10.1002/slct.201801319>

Impact Factor: 2.109 (2020)

Contribution: Establishment of the hSOD1 expression and purification procedure, establishment of the reconstitution procedure, manuscript editing.

## ■ Biological Chemistry & Chemical Biology

# In Vitro Reconstitution of the Highly Active and Natively Folded Recombinant Human Superoxide Dismutase 1 Holoenzyme

Karoline B. Santur,<sup>+, [a, b]</sup> Marc M. Sevenich,<sup>+, [a, b]</sup> Melanie Schwarten,<sup>[a]</sup> Volker Nischwitz,<sup>[c]</sup> Dieter Willbold,<sup>\*, [a, b]</sup> and Jeannine Mohrlüder<sup>\*, [a]</sup>

SOD1 is an antioxidant enzyme that exists as a highly stable dimer in healthy humans. Each subunit contains an intramolecular disulfide bond and coordinates one zinc and one copper ion. The dimer is destabilized in the absence of the ions and disruption of the disulfide bond, which leads to the formation of small oligomers and subsequently larger insoluble aggregates. An acquired toxic function of destabilized SOD1 is postulated to be associated with amyotrophic lateral sclerosis (ALS), which is a neurodegenerative disease characterized by

peripheral and central paralysis and by 3- to 5-year median survival after diagnosis. In this study, we present a protocol for heterologous expression of human SOD1 in *E. coli* and total reconstitution of the holoenzyme, which exhibits the highest reported specific activity (four-fold higher) of recombinant hSOD1. Biophysical characterization confirms the native state of this protein. The presented protocol provides highly active hSOD1 that will benefit *in vitro* investigations of this protein.

## Introduction

Amyotrophic lateral sclerosis (ALS) is a fatal adult-onset motor neuron disease affecting both upper and lower motor neurons. Patients suffering from ALS generally die within 5 years of diagnosis because of respiratory failure.<sup>[1]</sup> ALS predominantly occurs sporadically (sALS) with ~10% of cases appearing within families (fALS), and thus arise more than once in a family lineage and are usually inherited in an autosomal dominant manner.<sup>[2]</sup> Approximately 20% of the disease causing mutations are located in the gene coding for the enzyme superoxide dismutase 1 (SOD1).<sup>[3]</sup> Aggregates of human SOD1 have been detected in the

spinal cord of mutant-SOD1 ALS patients and in non-SOD1 sALS, leading to the hypothesis that SOD1 misfolding is part of a pathomechanism that is common to all types of ALS.<sup>[4]</sup>

The native conformation of the metalloenzyme Cu,Zn-SOD1 is a stable homodimer and functions in the conversion of superoxide to peroxide. Posttranslational modification of SOD1 includes formation of an intramolecular disulfide bond, and coordination of a zinc ion in the zinc loop and a copper ion in the active site of each subunit. A consistent pattern of glutathionylation and phosphorylation occurs in close proximity to the dimer interface of endogenous SOD1 derived from human erythrocytes.<sup>[5]</sup> All posttranslational modifications affect the monomer-dimer equilibrium of SOD1. Metal binding and an intact intramolecular disulfide bond promote dimer formation, whereas glutathionylation facilitates dissociation.<sup>[5]</sup> Natively folded human SOD1 (hSOD1) is an extremely thermostable protein. Depending on its metal content, melting temperatures up to 83 °C have been reported.<sup>[6]</sup> Structural integrity and enzymatic activity of bovine SOD is maintained in 8 M urea or in the presence of 4% SDS.<sup>[7]</sup> Protein destabilization by mutations, oxidation or deprivation of metal ions renders hSOD1 prone to dissociation and oligomerization. The resulting soluble oligomers subsequently form amorphous aggregates or even fibrils.<sup>[8]</sup> In particular, the small soluble oligomers are hypothesized to exhibit neurotoxic properties in ALS.<sup>[9]</sup>

Studies have focused on the structure and function of hSOD1 in health and disease for many years. *In vitro* approaches examining the aggregation propensity of hSOD1 and success of therapeutic agents are crucial for the development of therapeutic strategies to treat ALS. Experiments critically rely on the native fold of recombinantly expressed hSOD1. Currently, *in vitro* preparation of hSOD1 produced in *E. coli* often results in incomplete metalation levels, and strategies to improve the

[a] K. B. Santur,<sup>+</sup> M. M. Sevenich,<sup>+</sup> Dr. M. Schwarten, Prof. D. Willbold, Dr. J. Mohrlüder  
Institute of Complex Systems (ICS-6)  
Forschungszentrum Jülich  
Germany  
phone: +49 2461 612100  
fax: +49 2461 612023  
E-mail: d.willbold@fz-juelich.de  
j.mohrlueder@fz-juelich.de

[b] K. B. Santur,<sup>+</sup> M. M. Sevenich,<sup>+</sup> Prof. D. Willbold  
Institut für Physikalische Biologie  
Heinrich-Heine-Universität Düsseldorf  
Germany

[c] Dr. V. Nischwitz  
Central Institute for Engineering, Electronics and Analytics (ZEA-3)  
Forschungszentrum Jülich  
Germany

[†] Both authors contributed equally to this work.

Supporting information for this article is available on the WWW under <https://doi.org/10.1002/slct.201801319>

© 2019 The Authors. Published by Wiley-VCH Verlag GmbH & Co. KGaA. This is an open access article under the terms of the Creative Commons Attribution Non-Commercial License, which permits use, distribution and reproduction in any medium, provided the original work is properly cited and is not used for commercial purposes.

metal content of recombinant hSOD1 have been proposed.<sup>[5,10]</sup> Documented specific activities of the heterologous expressed enzyme have not exceeded values of ~5,600 U/mg.<sup>[11]</sup>

Here, we report a procedure for total reconstitution of recombinant hSOD1 expressed in *E. coli* without using the human copper chaperone for SOD1 (hCCS). The applied reconstitution procedure partly follows established protocols.<sup>[10a,12]</sup> Notably, the oxidation state, incubation time and temperature during holoenzyme reconstitution were identified as crucial factors for ensuring an optimal metal load. The resulting isolated holoenzyme displayed the highest reported specific activity of recombinant hSOD1.

## Results and Discussion

### Yields and findings of the hSOD1 purification and reconstitution

Protein expression was performed in *E. coli* BL21 (DE3) (Figure 1A) and yielded about 4 g cell pellet per liter culture. The

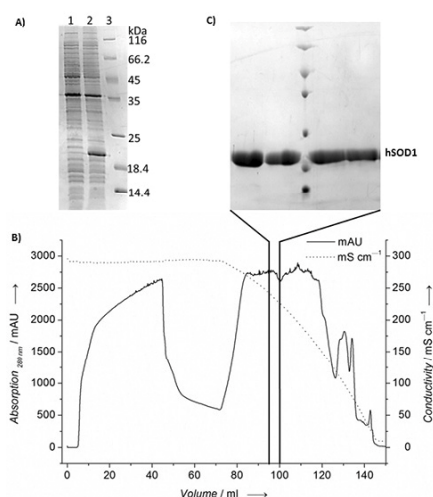


**Figure 1. Expression and purification of hSOD1.** A: Heterologous expression of tagless hSOD1 in *E. coli* BL21 (DE3) before (lane 1) and after induction with 1 mM IPTG and incubation overnight at 37 °C (lane 2). The molecular weight marker (26610, Thermo Fisher Scientific) is shown in lane 3. Human SOD1 migrates at about 20 kDa. B: Elution profile of the hydrophobic interaction chromatography purification of hSOD1 from the cell lysate after ammonium sulfate precipitation. Human SOD1 elutes at about 230–250 mS/cm. C: SDS PAGE of fractions containing hSOD1 with a purity of more than 98%. Marker bands correspond to Figure 1A.

tagless hSOD1 was purified via ammonium sulfate precipitation and hydrophobic interaction chromatography. Human SOD1

was released from the Source 15PHE column at ~45% buffer B (235–224 mS/cm) (Figure 1B) and fractions containing hSOD1 with a purity of more than 98% were pooled (Figure 1C), supplemented with an equimolar amount of zinc sulfate and stored at –80 °C. The amount of purified hSOD1 obtained per gram wet cell pellet was 1.3 mg. Between 5 and 6 mg purified hSOD1 (2.5–3 mg/mL) were applied to the reconstitution protocol, which gave a final yield of 0.35–2 mg of the reconstituted holoenzyme. The SEC run (Figure 2A) resulted in a considerable loss of protein because oligomeric and monomeric species of hSOD1 are separated from the dimeric protein and could not be used in further experiments. In addition, during renaturation and copper loading a constant loss of hSOD1 was observed, which might arise from adhesion of the protein to the dialysis membrane or to the test tubes.

Holoenzyme reconstitution partly followed established protocols. Notably, reduction of hSOD1 before copper loading was crucial for improved protein renaturation. We found the incubation temperature and time of the copper loading procedure to be important factors for increasing the copper content of hSOD1 significantly. By adjusting the incubation temperature to 37 °C and by extending the incubation time to seven days we were able to reach metal loading states of ~0.7 equivalents Cu as well as ~0.7 equivalents Zn per hSOD1 monomer, as determined by ICP-MS (Table 1).

	Reconstitution #1	Reconstitution #2	Reconstitution #3
Cu equivalents per hSOD1 monomer	0.70 ± 0.04	0.73 ± 0.05	0.62 ± 0.01
Zn equivalents per hSOD1 monomer	0.86 ± 0.06	0.71 ± 0.05	0.64 ± 0.01
Specific activity [U/mg]	15966 ± 1888	14949 ± 594	11952 ± 1932
Normalized activity [U/mg/Cu]	22808 ± 2697	20478 ± 814	19277 ± 3116
Melting temperature [°C]	86.01	85.20	83.62

### Reconstituted recombinant Cu-Zn-hSOD1 is a dimer exhibiting long time stability without the tendency to aggregate

SEC analysis with reconstituted hSOD1 was performed to investigate protein stability. Destabilized hSOD1 dissociates to monomers and these monomeric species are known to aggregate.<sup>[13]</sup> The elution profile and retention volume of the analytical SEC run indicated a homogenous hSOD1 dimer in the reconstituted sample without the presence of any mono- or oligomeric species (Figure 2B). Repetition of the experiment with a lower protein amount after sample storage for 14 weeks at 4 °C resulted in a very similar elution profile (Figure 3), which provides evidenced of a well-folded holoenzyme that exhibits

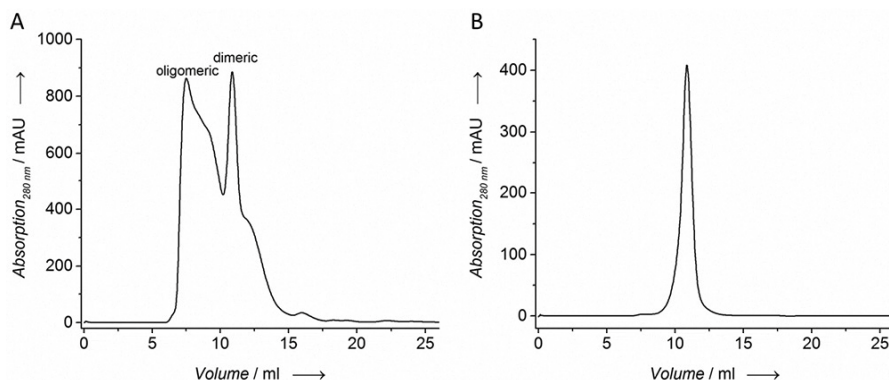


**Figure 2.** Isolation of the hSOD1 dimer via SEC. A: Reconstituted human SOD1 was loaded onto a superdex 75 10/30 HR column pre-equilibrated with 50 mM sodium acetate, pH 6.0, and a flow rate of 0.25 mL/min. The dimeric enzyme eluted at about 10.8 mL. Fractions containing dimeric hSOD1 (elution volume of 10.5–11.2 mL) were pooled. Oligomeric species (6–10 mL retention volume) and hSOD1 that eluted after 11.2 mL were discarded. B: 80  $\mu$ L of hSOD1 (237  $\mu$ M dimer) was applied to a superdex 75 10/30 HR column immediately after reconstitution. A homogenous peak with a retention volume of about 10.8 mL representing the dimeric state of hSOD1 was observed.

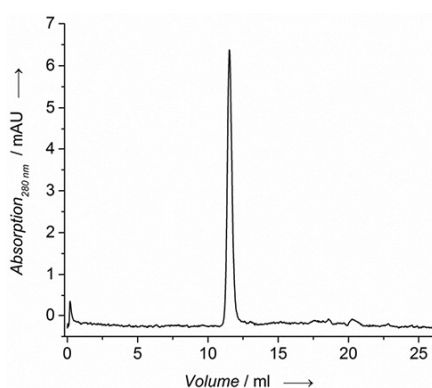


**Figure 3.** SEC analysis of reconstituted hSOD1. After sample storage for 14 weeks at 4 °C, 70  $\mu$ L of hSOD1 (3  $\mu$ M) was applied to a superdex 75 increase 10/300 GL column. A homogenous peak with a retention volume of about 11.5 mL was observed, indicating that the dimeric stoichiometry of hSOD1 showed no tendency to form monomers or oligomeric species.

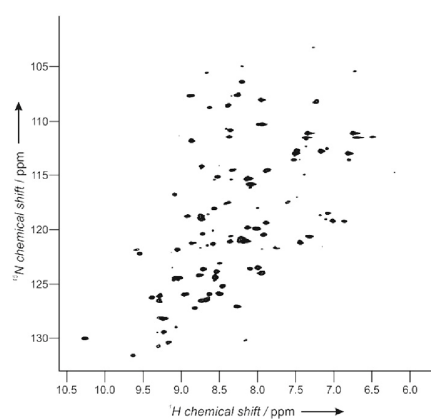


**Figure 4.** NMR spectrum of hSOD1. 2D  $^1\text{H}$ - $^{15}\text{N}$ -HSQC spectrum of 16  $\mu$ M [ $U$ - $^{15}\text{N}$ ]-hSOD1 recorded at 25 °C.

longtime stability without any tendency to aggregate Structural information about the reconstituted hSOD1 holoenzyme was collected via NMR spectroscopy. The 2D  $^1\text{H}$ - $^{15}\text{N}$  HSQC spectrum of hSOD1 showed a well-dispersed set of signals, indicating a well-folded protein (Figure 4). Several resonance signals showed low signal intensity, possibly due to the presence of the paramagnetic  $\text{Cu}^{2+}$  in close proximity.

#### Cu-Zn-hSOD1 displays high dimer stability

Human SOD1 retains its homodimeric integrity, enzymatic activity and metal binding ability in the presence of 1% SDS.<sup>[14]</sup> We used semi-native SDS-PAGE (0.4% SDS) to investigate the dimer stability of fully reconstituted Cu-Zn-hSOD1<sup>5-5</sup>. For this purpose we incubated the protein for 30 min with the above mentioned loading buffers at 37 °C. The samples were subjected to a conventional SDS gel and run for 2 h at 80 V. After

staining and destaining, the hSOD1 dimer was detected at about 45 kDa while the monomeric protein was detected at about 20 kDa.<sup>[14]</sup>

In the absence of DTT and EDTA in the loading buffer, hSOD1 migrated as a single band at about 45 kDa (Figure 5,

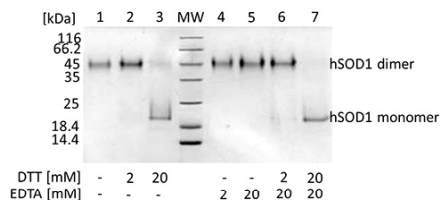


**Figure 5. Dimer stability of human SOD1 investigated by partially denaturing SDS-PAGE.** Reconstituted hSOD1 was pre-incubated for 30 min at 37 °C in loading buffer consisting of 62 mM Tris, pH 6.8, 10% glycerol, 0.05% bromophenol blue and different amounts of DTT and EDTA as indicated. The protein molecular weight marker was boiled before loading. 2 µg hSOD1 was applied per lane and the 15% gel was run at 80 V for 2 h with the standard gel running buffer. The gel was stained with pre-warmed Coomassie staining solution at RT. After destaining, migration of hSOD1 was documented using a ChemIDoc MP Imaging System (Bio-Rad). Dimeric hSOD1 migrates at ~45 kDa, whereas the monomeric hSOD1 can be detected at ~20 kDa.

lane 1), thus indicating the purely dimeric assembly. Addition of 2 mM DTT in the loading buffer did not facilitate dimer dissociation (Figure 5, lane 2), whereas buffer supplement with 20 mM DTT caused considerable dissociation of hSOD1 (Figure 5, lane 3). The dimer destabilizing effect of DTT was further strengthened by addition of 20 mM EDTA (Figure 5, lanes 4–7). This is in accordance to data published for endogenous hSOD1 isolated from human erythrocytes<sup>[14]</sup> and demonstrated high

dimer stability of the recombinantly expressed and reconstituted hSOD1 holoenzyme.

Rodrigues et al. determined the melting point of purified hSOD1 by differential scanning calorimetry. Dependent on the protein metal content three melting points of about 60 °C (E<sub>2</sub>ZnE SOD1), 72 to 76 °C (E<sub>2</sub>Zn<sub>2</sub> SOD1) and 83 °C (CuE<sub>2</sub>Zn<sub>2</sub> SOD1) were reported.<sup>[6a]</sup> We performed thermal melting point analysis of reconstituted hSOD1 via circular dichroism (CD) spectroscopy. Melting curves were monitored at 260–190 nm and increasing temperatures (Figure 6A). The resulting  $T_m$  of about 86 °C (Figure 6B) indicated a well-folded, metal coordinated protein. Measurements of hSOD1 derived from two independent reconstitution procedures resulted in similar melting temperatures (84 to 85 °C) and are provided in Table 1. Thus, reconstitution of human SOD1 that has been recombinantly expressed in *E. coli* yields protein with high thermal stability, as specified for the hSOD1 holoenzyme.

#### ***E. coli* produced and reconstituted Cu-Zn-hSOD1 displays the highest specific activity reported for recombinantly produced hSOD1**

Specific activity of hSOD1 critically relies on coordination of copper in the active site of the enzyme; however, the specific activity of hSOD1 is commonly reported as units per mg protein without regard to its copper loading state. Specific activities of 3000 to 6000 U/mg have been documented for recombinant hSOD1<sup>[11,15]</sup> and normalization of specific activity to the copper loading state of hSOD1 has rarely been reported. The maximal theoretical specific activity for the purified protein has been estimated to be between 7000 and 8000 U/mg protein/Cu for wild-type hSOD1.<sup>[11]</sup> There is a sole publication that determined the specific activity of endogenous hSOD1 assayed in red blood cell lysates to be as high as 23,700 U/mg.<sup>[16]</sup>

The SOD determination kit (Sigma) was used according to manufacturer's instructions. Human SOD1 from three inde-

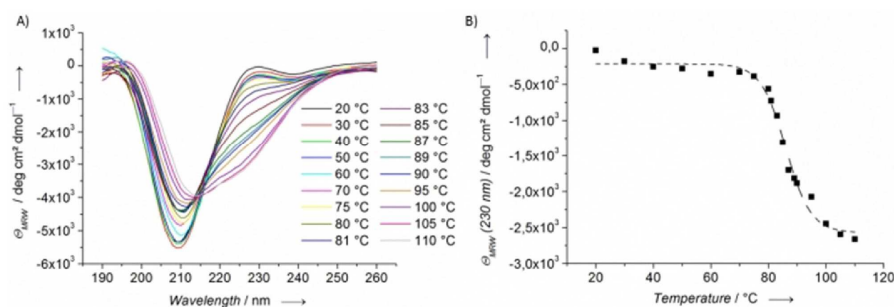


**Figure 6. Thermal stability of reconstituted hSOD1 determined via CD spectroscopy.** A: Spectra with 0.26 to 0.28 mg/mL hSOD1 in 50 mM sodium acetate, pH 6.0, were recorded in a temperature interval measurement (20 to 110 °C) at 260 to 190 nm with a scan speed of 20 nm/min. Five accumulations per measurement were performed and a buffer sample was subtracted from all protein containing spectra. Data were processed to mean molar ellipticity. B: The apparent melting temperature of about 86 °C was determined from data recorded at 230 nm via a Boltzmann sigmoidal fit (Origin 8).

pendent reconstitution events with slightly varying copper and zinc contents were compared with hSOD1 from a previous preparation that mainly followed published protocols.<sup>[10a,17]</sup> The latter protein preparation (containing 0.68 equivalents Zn and 0.04 equivalents Cu per monomer) displayed a specific activity of ~500–1000 U/mg. Fully reconstituted hSOD1 derived by the protocol described herein contained about 0.6 to 0.7 equivalents Cu and 0.64 to 0.86 equivalents Zn per monomer and exhibited a specific activity of ~14,300 U/mg, which is the highest specific activity reported for recombinant and purified hSOD1 (Table 1). Normalization to the copper loading state of hSOD1 resulted in a maximal theoretical specific activity of about 20,900 U/mg/Cu, which is in very good agreement to the data published for endogenous hSOD1 assayed in red blood cell lysates.

Repetition of activity determination after eight months of storage at 4 °C yielded 12,300 ± 260 U/mg for reconstitution #2, which demonstrates the high stability of reconstituted hSOD1.

## Conclusions

The production and reconstitution of recombinantly expressed hSOD1 is crucial to many studies that aim to elucidate the molecular pathomechanism of ALS, and to create therapeutic strategies for efficient disease prevention and cure. The present work describes a reproducible procedure for total reconstitution of hSOD1 expressed in *E. coli* without requiring hCCS. In brief, the protein was purified via ammonium sulfate precipitation and hydrophobic interaction chromatography and supplemented with zinc. SOD1 was reduced and subsequently denatured in guanidine hydrochloride. Renaturation was performed in the presence of zinc via dialysis against buffers containing decreasing concentrations of guanidine hydrochloride. The protein was supplemented with Cu<sup>2+</sup> and incubated at 37 °C for 7 days. The dimeric hSOD1 holoenzyme was finally isolated via SEC. Extensive analysis indicated that the natively folded holoenzyme was produced, which exhibits high thermal stability and the highest reported specific activity of recombinantly expressed and purified hSOD1. In particular, reduction of hSOD1 before copper loading and increasing the incubation temperature and time during copper loading lead to elevated copper levels of the reconstituted protein. The final dimer purification step using SEC increased the yield of pure hSOD1 dimer. Together with the high copper loading a drastically increased specific activity of hSOD1 was reached.

Published protocols document the importance of the copper chaperone for hSOD1 integrity. Many enzymes, especially chaperones, increase the efficiency of the reaction. Here, the coordination of a copper ion into the respective copper ion-binding site is mediated. In organisms, hCCS activity might be essential because the free copper ion concentration is far below the concentrations used in our reconstitution.

In preliminary experiments we did include hCCS in the assay. Comparison of the results that included this protein versus the protocol herein showed no clear differences concerning the metal coordination level. Consequently, and to

simplify the protocol, the purification and ion loading procedure in the absence of hCCS was used.

The present reconstitution procedure will be a valuable tool for prospective investigations, which critically rely on the structural integrity of the hSOD1 holoenzyme.

## Supporting Information Summary

The supporting information describes hSOD1 expression and purification, the reconstitution procedure and all analytical methods (e.g., ICP-MS, NMR, SEC runs, enzyme activity assay, semi-native PAGE and melting point determination via CD) in detail.

## Acknowledgments

This study was partially funded by the "Deutsche Gesellschaft für Muskelkranke e.V." to Jeannine Mohrlüder (Mo6/1). The authors acknowledge access to the Jülich-Düsseldorf Biomolecular NMR Center that is jointly run by Forschungszentrum Jülich and Heinrich Heine University Düsseldorf.

## Conflict of Interest

The authors declare no conflict of interest.

**Keywords:** enzyme activity · metalloenzyme · reconstitution · SOD1 · thermostability

- [1] L. J. Haverkamp, V. Appel, S. H. Appel, *Brain* **1995**, *118* ( Pt 3), 707–719.
- [2] T. Siddique, S. Ajroud-Driss, *Acta Myol* **2011**, *30*, 117–120.
- [3] A. Chio, B. J. Traynor, F. Lombardo, M. Fimognari, A. Calvo, P. Ghiglione, R. Mutani, G. Restagno, *Neurology* **2008**, *70*, 533–537.
- [4] L. I. Grad, J. J. Yerbury, B. J. Turner, W. C. Guest, E. Pokrishevsky, M. A. O'Neill, A. Yanai, J. M. Silverman, R. Zeineddine, L. Corcoran, J. R. Kumita, L. M. Luheshi, M. Yousefi, B. M. Coleman, A. F. Hill, S. S. Plotkin, I. R. Mackenzie, N. R. Cashman, *Proc. Natl. Acad. Sci. U. S. A.* **2014**, *111*, 3620–3625.
- [5] K. C. Wilcox, L. Zhou, J. K. Jordan, Y. Huang, Y. Yu, R. L. Redler, X. Chen, M. Caplow, N. V. Dokholyan, *J. Biol. Chem.* **2009**, *284*, 13940–13947.
- [6] a) J. A. Rodriguez, J. S. Valentine, D. K. Eggers, J. A. Roe, A. Tiwari, R. H. Brown, Jr., L. J. Hayward, *J. Biol. Chem.* **2002**, *277*, 15932–15937; b) J. S. Valentine, P. A. Doucette, S. Zittin Potter, *Annu. Rev. Biochem.* **2005**, *74*, 563–593.
- [7] a) H. J. Forman, I. Fridovich, *J. Biol. Chem.* **1973**, *248*, 2645–2649; b) D. P. Malinowski, I. Fridovich, *Biochem.* **1979**, *18*, 5909–5917.
- [8] a) L. Banci, I. Bertini, A. Durazo, S. Girotto, E. B. Gralla, M. Martinelli, J. S. Valentine, M. Vieru, J. P. Whitelegge, *Proc. Natl. Acad. Sci. U. S. A.* **2007**, *104*, 11263–11267; b) S. S. Leal, J. S. Cristovao, A. Biesemeier, I. Cardoso, C. M. Gomes, *Metallomics* **2015**, *7*, 333–346.
- [9] a) T. E. Brotherton, Y. Li, J. D. Glass, *Neurobiol. Dis.* **2013**, *49*, 49–56; b) E. A. Proctor, L. Fee, Y. Tao, R. L. Redler, J. M. Fay, Y. Zhang, Z. Lv, I. P. Mercer, M. Deshmukh, Y. L. Lyubchenko, N. V. Dokholyan, *Proc. Natl. Acad. Sci. U. S. A.* **2016**, *113*, 614–619.
- [10] a) L. Banci, I. Bertini, F. Cantini, T. Kozyreva, C. Massagni, P. Palumaa, J. T. Rubino, K. Zovo, *Proc. Natl. Acad. Sci. U. S. A.* **2012**, *109*, 13555–13560; b) M. Ahl, M. J. Lindberg, L. A. Tibell, *Protein Expr. Purif.* **2004**, *37*, 311–319.
- [11] V. K. Bhogaraju, M. S. Levi, R. L. Reed, J. P. Crow, *Amyotroph Lateral Scler* **2010**, *11*, 283–288.
- [12] L. J. Hayward, J. A. Rodriguez, J. W. Kim, A. Tiwari, J. J. Goto, D. E. Cabelli, J. S. Valentine, R. H. Brown, Jr., *J. Biol. Chem.* **2002**, *277*, 15923–15931.

- [13] R. L. Redler, L. Fee, J. M. Fay, M. Caplow, N. V. Dokholyan, *Biochem.* **2014**, *53*, 2423–2432.
- [14] A. Tiwari, L. J. Hayward, *J. Biol. Chem.* **2003**, *278*, 5984–5992.
- [15] a) N. Fujiwara, M. Nakano, S. Kato, D. Yoshihara, T. Ookawara, H. Eguchi, N. Taniguchi, K. Suzuki, *J. Biol. Chem.* **2007**, *282*, 35933–35944; b) L. T. Benov, W. F. Beyer, Jr., R. D. Stevens, I. Fridovich, *Free Radic. Biol. Med.* **1996**, *21*, 117–121; c) J. C. Stevens, R. Chia, W. T. Hendriks, V. Bros-Facer, J. van Minnen, J. E. Martin, G. S. Jackson, L. Greensmith, G. Schiavo, E. M. Fisher, *PLoS ONE* **2010**, *5*, e9541.
- [16] T. Saito, K. Ito, M. Kurasaki, S. Fujimoto, H. Kaji, K. Saito, *Clin. Sci.* **1982**, *63*, 251–255.
- [17] G. S. Wright, S. S. Hasnain, J. G. Grossmann, *Biochem J* **2011**, *439*, 39–44.

Submitted: May 3, 2018

Accepted: June 25, 2018

## **2.8 Alpha-Synuclein-specific naturally occurring antibodies prevent aggregation in vitro and in vivo**

Authors: Anne K. Braczynski, **Marc Sevenich**, Ian Gering, Tatsiana Kupreichyk, Emil D. Agerschou, Yannick Kronimus, Pardes Habib, Matthias Stoldt, Dieter Willbold, Jörg B. Schulz, Jan-Philipp Bach, Björn H. Falkenburger, Wolfgang Hoyer

Journal: Biomolecules

DOI: 10.3390/biom12030469

Impact Factor: 4.569 (2022)

Contribution: Planning and performance of SPR measurements, manuscript editing.

Article

# Alpha-Synuclein-Specific Naturally Occurring Antibodies Inhibit Aggregation In Vitro and In Vivo

Anne K. Braczynski <sup>1,2</sup>, Marc Sevenich <sup>3,4</sup>, Ian Gering <sup>3</sup>, Tatsiana Kupreichyk <sup>2,3</sup>, Emil D. Agerschou <sup>2</sup>, Yannick Kronimus <sup>5</sup>, Pardes Habib <sup>1,6</sup>, Matthias Stoldt <sup>2,3</sup>, Dieter Willbold <sup>2,3</sup>, Jörg B. Schulz <sup>1,7</sup>, Jan-Philipp Bach <sup>1</sup>, Björn H. Falkenburger <sup>1,8,\*</sup> and Wolfgang Hoyer <sup>2,3,\*</sup>

- <sup>1</sup> Department of Neurology, RWTH University Hospital, 52074 Aachen, Germany; abraczynski@ukaachen.de (A.K.B.); phabib@ukaachen.de (P.H.); jschulz@ukaachen.de (J.B.S.); j\_pbach@yahoo.de (J.-P.B.)
- <sup>2</sup> Institut für Physikalische Biologie, Heinrich-Heine University Düsseldorf, 40225 Düsseldorf, Germany; tatsiana.kupreichyk@hhu.de (T.K.); emil.agerschou@hhu.de (E.D.A.); m.stoldt@fz-juelich.de (M.S.); d.willbold@fz-juelich.de (D.W.)
- <sup>3</sup> Institute of Biological Information Processing (IBI-7: Structural Biochemistry), Forschungszentrum Jülich, 52428 Jülich, Germany; m.sevenich@fz-juelich.de (M.S.); i.gering@fz-juelich.de (I.G.)
- <sup>4</sup> Priavoid GmbH, 40225 Düsseldorf, Germany
- <sup>5</sup> Department of Geriatric Medicine, University Hospital Essen, University Duisburg-Essen, 47057 Duisburg, Germany; yannickk89@web.de
- <sup>6</sup> Institute of Biochemistry and Molecular Immunology, Medical Faculty, RWTH Aachen University, 52074 Aachen, Germany
- <sup>7</sup> JARA-Institute Molecular Neuroscience and Neuroimaging, Jülich Aachen Research Alliance, FZ Jülich and RWTH University, 52428 Jülich, Germany
- <sup>8</sup> Department of Neurology, University Hospital Carl Gustav Carus, 01307 Dresden, Germany
- \* Correspondence: bjoern.falkenburger@dzne.de (B.H.F.); w.hoyer@fz-juelich.de (W.H.)



**Citation:** Braczynski, A.K.;

Sevenich, M.; Gering, I.;

Kupreichyk, T.; Agerschou, E.D.;

Kronimus, Y.; Habib, P.; Stoldt, M.;

Willbold, D.; Schulz, J.B.; et al.

Alpha-Synuclein-Specific Naturally

Occurring Antibodies Inhibit

Aggregation In Vitro and In Vivo.

*Biomolecules* **2022**, *12*, 469. <https://doi.org/10.3390/biom12030469>

Academic Editor: Declan P. McKernan

Received: 14 February 2022

Accepted: 15 March 2022

Published: 18 March 2022

**Publisher's Note:** MDPI stays neutral with regard to jurisdictional claims in published maps and institutional affiliations.



**Copyright:** © 2022 by the authors. Licensee MDPI, Basel, Switzerland. This article is an open access article distributed under the terms and conditions of the Creative Commons Attribution (CC BY) license (<https://creativecommons.org/licenses/by/4.0/>).

**Abstract:** Parkinson's disease (PD) is associated with motor and non-motor symptoms and characterized by aggregates of alpha-synuclein ( $\alpha$ Syn). Naturally occurring antibodies (nAbs) are part of the innate immune system, produced without prior contact to their specific antigen, and polyreactive. The abundance of nAbs against  $\alpha$ Syn is altered in patients with PD. In this work, we biophysically characterized nAbs against  $\alpha$ Syn (nAbs- $\alpha$ Syn) and determined their biological effects. nAbs- $\alpha$ Syn were isolated from commercial intravenous immunoglobulins using column affinity purification. Biophysical properties were characterized using a battery of established in vitro assays. Biological effects were characterized in HEK293T cells transiently transfected with fluorescently tagged  $\alpha$ Syn. Specific binding of nAbs- $\alpha$ Syn to monomeric  $\alpha$ Syn was demonstrated by Dot blot, ELISA, and Surface Plasmon Resonance. nAbs- $\alpha$ Syn did not affect viability of HEK293T cells as reported by Cell Titer Blue and LDH Assays. nAbs- $\alpha$ Syn inhibited fibrillation of  $\alpha$ Syn reported by the Thioflavin T aggregation assay. Altered fibril formation was confirmed with atomic force microscopy. In cells transfected with EGFP-tagged  $\alpha$ Syn we observed reduced formation of aggresomes, perinuclear accumulations of  $\alpha$ Syn aggregates. The results demonstrate that serum of healthy individuals contains nAbs that specifically bind  $\alpha$ Syn and inhibit aggregation of  $\alpha$ Syn in vitro. The addition of nAbs- $\alpha$ Syn to cultured cells affects intracellular  $\alpha$ Syn aggregates. These findings help understanding the role of the innate immune systems for the pathogenesis of PD and suggest that systemic  $\alpha$ Syn binding agents could potentially affect neuronal  $\alpha$ Syn pathology.

**Keywords:** aggregation; Parkinson's disease; intravenous immunoglobulins (IVIG); naturally occurring antibodies; alpha-synuclein

## 1. Introduction

Parkinson's disease (PD) is the second-most common neurodegenerative disorder. The characteristic pathological changes consist of dopaminergic neuronal loss in the substantia

nigra, gliosis, and intraneuronal alpha-synuclein ( $\alpha$ Syn) pathology, comprising Lewy bodies and Lewy neurites [1].  $\alpha$ Syn is the predominant protein in Lewy body inclusions [2].  $\alpha$ Syn pathology spreads along anatomical connections with gut and olfactory bulb constituting putative entry points into the nervous system [3,4]. The theory of multiorgan spreading of  $\alpha$ Syn along the “gut-brain-axis” is supported by a large body of evidence from patient cohorts and animal experiments [5–10]. Consistent with the origin of  $\alpha$ Syn pathology in the periphery,  $\alpha$ Syn deposits were also found in glands [11], skin [12,13], and gastrointestinal tissue [14,15].

$\alpha$ Syn is a natively unfolded protein of 140 amino acids encoded by the gene *SNCA* and localized in presynaptic terminals [16].  $\alpha$ Syn consists of three domains: The N-terminus (aa 1–60) contains the positions of the six mutations that cause hereditary PD and sites for post-translational modifications [17,18]. The hydrophobic non-amyloid component (NAC) region (aa 61–95) is important for aggregation, oligomerization, and for building  $\beta$ -sheet containing structures including fibrils [19]. The C-terminal domain (aa 96–140) is proline- and aspartate/glutamate-rich, contains phosphorylation sites [20,21], and is the epitope to most antibodies tested as therapeutic strategies against PD [22].

The discovery of  $\alpha$ Syn pathology in PD led to a plethora of immunization studies [22,23]. Different animal models have consistently illustrated the potential of passive [24–26] and active [27,28] immunization to reduce brain  $\alpha$ Syn pathology and improve motor outcome. Clinical studies are on their way [22,29].

Naturally occurring antibodies (nAbs) are part of the innate immune system, produced without contact to the specific antigen they recognize and polyreactive [30]. The majority of reported nAbs are IgM and IgG [31] and seem to play a role in neurodegenerative disorders [32,33], but also in other diseases, such as chronic inflammatory diseases or atherosclerosis [34]. Although their mechanism of action is fairly unclear, nAbs have been shown to identify apoptotic debris and initiate its phagocytic removal [34,35]. There are also nAbs against  $\alpha$ Syn (nAbs- $\alpha$ Syn) [36]. Their abundance is altered in PD patients [37–39]. The field is, however, still uncertain about the direction of change of nAbs- $\alpha$ Syn in PD. Several groups described decreased nAbs- $\alpha$ Syn in the serum of patients with PD as compared to healthy controls [36,37,40]. Yet, other groups described no changes [38], or even increased levels [39,41–44]. Interestingly, nAbs- $\alpha$ Syn are already present in early childhood with levels comparable to healthy adult controls [45]. The binding of nAbs to  $\alpha$ Syn monomers, oligomers, and fibrils could be confirmed using dot blot, surface plasmon resonance (SPR) and enzyme-linked immunosorbent assay (ELISA) [26,46]. nAbs- $\alpha$ Syn purified from commercial intravenous immunoglobulins (IVIg) using  $\alpha$ Syn oligomers inhibit aggregation of  $\alpha$ Syn as reported by thioflavin T (ThT) fluorescence [26].

Intracellular  $\alpha$ Syn aggregates are transported towards the perinuclear aggresome and degraded by autophagy [47,48]. In this process, the aggresome is a steady-state structure that grows whenever generation and transport of aggregates exceeds the capacity of autophagic clearance [49].  $\alpha$ Syn affects cellular homeostasis by different mechanism and nAbs- $\alpha$ Syn attenuated toxicity resulting from  $\alpha$ Syn oligomers in N2a cells [26].

Given the importance of better understanding PD pathogenesis and providing effective therapies for patients, reproducing findings is of particular importance in Translational Neurosciences [50]. Basic research lately could not translate into the development of therapeutics to cure diseases despite promising findings; the reasons for this reproducibility crisis are numerous and reviewed in [50]. We, therefore, characterized in this study nAbs against  $\alpha$ Syn derived from IVIg preparations that are commercially available in Germany, using a standard battery of Dot blot, ELISA, SPR, and biophysical methods including Thioflavin T (ThT) aggregation assay and Atomic Force Microscopy (AFM). Furthermore, we determined their effects in a cellular model of  $\alpha$ Syn pathology [51].

## 2. Materials and Methods

### 2.1. Gravity Flow Affinity Purification of nAbs

nAbs- $\alpha$ Syn were isolated from IVIG as previously described [46]. Briefly, we used purified intravenous immunoglobulin G (IgG) (Gamunex 10%, 100 mg/mL, Grifols, Barcelona, Spain). Then, 96% of protein represents normal human IgG (IgA < 0.2 mg (0.02%); IgM < 0.1 mg (0.01%)). IgG subclasses are fully represented (IgG 1, 65%; IgG 2, 30%; IgG 3, 3%; IgG 4, 2%). Recombinant  $\alpha$ Syn (rPeptides, Bogart, GA, USA) was coupled to aldehyde-activated agarose support (Aminolink Plus Coupling Resin; Thermo Scientific, Waltham, MA, USA). A total of 20 mL of 2.5% IVIG was added to the column in fractions of 3.5 mL, followed by incubation at room temperature for 60 min per fraction. After washing with PBS, the bound antibodies were eluted from the column with  $10 \times 0.5$  mL 0.1 M glycine buffer, and pH 2.8. Each fraction was collected in a microreaction tube containing 35  $\mu$ L 1 M Tris-HCl, pH 9. IVIg depleted of nAbs- $\alpha$ Syn, termed flowthrough (FT), was also collected and used as a negative control in experimental settings. To maintain the integrity of the antibodies, a neutral pH was adjusted immediately after elution by adding the appropriate amount of Tris-HCl or glycine buffer. nAbs- $\alpha$ Syn of several purification rounds were concentrated with Vivaspin concentration device (Vivaspin 20, 5 k, Sartorius, Goettingen, Germany) according to the manufacturer's instructions. A total of 25 purification batches resulted in ca. 250  $\mu$ L of nAbs- $\alpha$ Syn at a concentration of ca. 180  $\mu$ M nAbs- $\alpha$ Syn. Protein concentration was measured with the DC Protein Assay (Bio-Rad, Dreieich, Germany) in a 96-well-plate (Falcon, Corning, Glendale, AZ, USA) against a standard calibration curve. Absorbance at 756 nm was measured after 15 min incubation on a microplate reader (Infinite 200 PRO Microplate Reader, Tecan, Crailsheim, Germany).

### 2.2. Dot Blot

The indicated amounts of recombinant  $\alpha$ Syn were spotted onto nitrocellulose membranes (Amersham Protan 0.2  $\mu$ M, Chalfont St. Giles, Great Britain), dried for 15 min and blocked for 1 hour at 20 °C once in RotiBlock (Carl Roth, Karlsruhe, Germany). Each dot blot was incubated with either 0.2  $\mu$ g/mL nAbs- $\alpha$ Syn, FT or anti- $\alpha$ Syn antibody (1:2000, Syn 211, Thermo Scientific, Rockford, USA) over night at 4 °C and washed 3 times with Tris buffered saline with 0.05% Tween-20 (TBS-T) for 30 min. As secondary antibody, horse reddish peroxidase (HRP) coupled to anti-human IgG antibodies (Peroxidase conjugated Affinity Pure Anti-Human IgG, Jackson Immunoresearch, Ely, United Kingdom) was used to detect the antibodies of human source (nAbs- $\alpha$ Syn and FT). Anti-mouse antibodies (Peroxidase conjugated Affinity Pure Goat anti-mouse IgG H + L, Jackson Immunoresearch, Ely, United Kingdom) were used to detect the anti- $\alpha$ Syn antibody. Blots were developed with Super Signal West Femto Max Sensitivity Substrate (Thermo Scientific, Waltham, MA, USA) on Bio-Rad ChemiDoc. (Bio-Rad, Munich, Germany). The experimental setup is schematically depicted in Figure 1a.

### 2.3. Enzyme-Linked Immunosorbent Assay (ELISA)

Wells of high-binding 96-well ELISA plates (Immulon Microtiter Plates 2HB "U" Bottom, Thermo Scientific, Waltham, MA, USA) were coated with 50  $\mu$ L of 3  $\mu$ g/mL recombinant  $\alpha$ Syn (Analytic Jena, Jena, Germany) in phosphate-buffered saline (PBS). After 24 h at 4 °C, wells were blocked with 180  $\mu$ L blocking buffer (1  $\times$  Rotiblock + 0.1% Tween-20, Carl Roth, Karlsruhe, Germany) for additional 24 h at 4 °C. Antibodies were added to the wells in a series of decreasing concentrations starting from 4  $\mu$ g/mL. Plates were incubated with samples for 1 h at 20 °C and shaken on an orbital platform shaker (Unimax 1010, Heidolph, Schwabach, Germany) at 100 rpm. Afterwards, 50  $\mu$ L/well biotinylated goat anti-human detection antibody was added to the wells (Dianova GmbH, Hamburg, Germany, 1:20,000 in blocking buffer). After 1 h at 20 °C and 100 rpm, the samples were incubated with 50  $\mu$ L/well of streptavidin-peroxidase (Streptavidin-HRP, R&D Systems, Minneapolis, MN, USA, 1:200 in blocking buffer) and shaken for 20 min at 20 °C and 100 rpm. The assay was developed using 50  $\mu$ L/well Tetramethylbenzidine (TMB) (Merck,

Darmstadt, Germany). After 20 min, the reaction was stopped by adding 25  $\mu\text{L}$ /well of 5% sulfuric acid (Carl Roth, Karlsruhe, Germany). Absorbance at 450 nm was measured using a microplate reader (Infinite 200 PRO Microplate Reader, Tecan, Crailsheim, Germany). All incubation steps were performed in the dark. After each step up to and including TMB addition, the wells were washed three times with 300  $\mu\text{L}$   $1 \times$  PBS + 0.05% Tween-20 using an Amersham Biotrak II Plate Washer (GE Healthcare, Chicago, IL, USA).

#### 2.4. Surface Plasmon Resonance (SPR)

SPR measurements were performed using a Biacore T200 instrument (GE Healthcare, GE Healthcare, Chicago, IL, USA) at 25  $^{\circ}\text{C}$  with PBS/0.05% Tween-20, pH 7.4 as running buffer. For preparation of the flow cells, a CM5 sensor chip (GE Healthcare, Chicago, IL, USA) was activated with 1-ethyl-3-(3-dimethylaminopropyl) carbodiimide (EDC)/N-hydroxysuccinimide (NHS) (0.2 M/0.05 M). Recombinant full-length  $\alpha\text{Syn}$  (200 ng/mL) was diluted in 10 mM sodium acetate, pH 4.0. It was immobilized to a final level of 125 reactive units (RU), and the flow cell was deactivated with 1 M ethanolamine-HCl, pH 8.5. A reference flow cell was activated and deactivated only. Afterwards, IVIG, FT and nAbs- $\alpha\text{Syn}$  at concentrations ranging from 39 nM to min. 5  $\mu\text{M}$  were injected once followed by 5 cycles of regeneration with 5 M urea. All samples were injected over the flow cells for 300 s, followed by a dissociation step of 900 s. The sensorgrams were double referenced. Evaluation was performed by plotting the respective response levels against the applied nAbs- $\alpha\text{Syn}$  concentrations in a steady-state fit. For data evaluation, the sensorgrams were calculated in the Biacore T200 Evaluation Software 3.1 (version 3.1, proprietary software of GE Healthcare).

#### 2.5. Thioflavin T Aggregation Assay

ThT aggregation assays were conducted as described before [52] in Corning half area 96-well plates with non-binding surface (Corning No. 3881, Glendale, AZ, USA). For the assays starting from monomeric  $\alpha\text{Syn}$ , 25  $\mu\text{M}$  of wild type (WT)  $\alpha\text{Syn}$  was used. Aggregation assays were run for 60 h with measurement of ThT fluorescence every 20 min ( $\lambda_{\text{Ex}} = 450$  nm, bandwidth 5 nm;  $\lambda_{\text{Em}} = 482$  nm, bandwidth 10 nm) with 15 s of orbital shaking before the measurement in a plate reader (BMG Clariostar Plus, Ortenberg, Germany). The assays were conducted at 37  $^{\circ}\text{C}$  in 25 mM K-phosphate buffer at pH 7.3, 100 mM KCl, 1 mM  $\text{MgCl}_2$ , 10  $\mu\text{M}$  ThT, and 0.05%  $\text{NaN}_3$ , reflecting intracellular potassium and magnesium concentration, as well as intracellular pH and ionic strength. A glass ball of 2.85–3.45 mm size was added per well to improve mixing. Per well, a sample volume of 125  $\mu\text{L}$  sample was used. For evaluation, the mean of triplicate measurements was referenced to the highest fluorescence of 25  $\mu\text{M}$  WT  $\alpha\text{Syn}$ .

#### 2.6. Atomic Force Microscopy

AFM images were taken with a Nanowizard 3 atomic force microscope (JPK, Berlin, Germany) in intermittent contact mode (AC mode) in air, using silicon cantilever and tip (OMCL-AC160TS-R3, Olympus, Hamburg, Germany) with a typical tip radius of  $9 \pm 2$  nm, a force constant of 26 N/m and a resonance frequency of approximately 300 kHz. The images derive from a manual observer-blind estimation, and provide qualitative characteristics. The image processing was performed using JPK data processing software (version spm-5.0.84): for each of the presented height profiles, a polynomial fit was subtracted from each scan line first independently and then using limited data range. For the sample preparation, solutions containing fibrils were diluted to a concentration of 1  $\mu\text{M}$  (in monomer equivalents) in water and 5  $\mu\text{L}$  samples of the diluted solution were deposited on freshly cleaved muscovite mica and left to dry for at least 30 min. The samples were carefully washed with 50  $\mu\text{L}$  of double distilled  $\text{H}_2\text{O}$  and then dried again with a stream of  $\text{N}_2$  gas before imaging.

### 2.7. Cell Culture

HEK293T (RRID: CVCL\_0063) cells were cultured in Dulbecco's modified Eagle's medium supplemented with 10% fetal calf serum and 1% penicillin-streptomycin. 'HEK' cells are listed in version 8.0 of the Database of Cross-Contaminated or Misidentified Cell Lines. Our HEK293T cells were validated in November 2017 by analysis of 21 genetic loci (Promega, Madison, WI, USA, PowerPlex 21 PCR Kit carried out by Eurofins Medigenomix Forensik, Ebersberg, Germany). Cells were plated on poly-L-lysine-coated glass cover slips or on plastic plates. Transfection was performed 18–20 h after plating using Metafectene (Biontex Laboratories, Munich, Germany). Unless noted otherwise, subsequent analysis was completed 24 h after transfection.

### 2.8. LDH Release

CytoTox 96 Non-Radioactive Cytotoxicity Assay (Promega, Madison, WI, USA) was performed according to the manufacturer's protocol to measure release of lactate dehydrogenase (LDH) as a marker of cellular viability, as described before [53]. HEK293T were seeded on a 96-well plate 48 h prior to treatment with nAbs- $\alpha$ Syn. After 1 h/3 h/6 h/24 h incubation time, 50  $\mu$ L of each well was transferred to a fresh 96-well plate. In addition to a no-treatment-cell control, a no-cell control, and a control containing HEK293T lysed with Triton X-100 were used. CytoTox 96 Reagent (Promega, Madison, WI, USA) was added to each well, and the absorbance was recorded at 490 nm by Infinite M200 (Tecan, Männedorf, Switzerland). Data are presented as a percentage of maximum LDH release (100%), which was determined by HEK293T lysed with 1% Triton X-100.

### 2.9. Metabolic Activity Assay

To assess metabolic activity a CellTiter-Blue (CTB) Cell Viability Assay was performed according to manufacturer's protocol as described before [53]. HEK293T were seeded on a 96-well plate 48 h prior to treatment with nAbs- $\alpha$ Syn. After 1 h/3 h/6 h/24 h incubation time, CellTiter-Blue Reagent (Promega, Madison, WI, USA) was added to each well. After 2.5–3 h, a color switch (reduction in resazurin) was observed and fluorescence was recorded at 560Ex/590Em by Infinite M200 (Tecan, Männedorf, Switzerland).

### 2.10. Plasmids

A53T- $\alpha$ Syn was flexibly tagged with EGFP by using the interaction of a PDZ domain (post synaptic density protein (PSD95), *Drosophila* disc large tumor suppressor (Dlg1), and zonula occludens-1 protein (zo-1)) with its six amino acid-binding motifs. PDZ-EGFP was coexpressed with  $\alpha$ Syn to which a six amino acid PDZ binding domain was added at the C-terminus [51].

### 2.11. Microscopy of Fixed Cells

Analysis of cells expressing EGFP-tagged  $\alpha$ Syn was carried out as previously described [51,54]. For the classification of EGFP distribution patterns, cells were grown and transfected on coverslips. Then, 24 hours after transfection, cells were washed three times in cold PBS and fixed with paraformaldehyde solution (PFA, 4% paraformaldehyde, 5% sucrose in PBS) for 10 min. Coverslips were mounted with Fluoromount g (Cat# 0100-01 Southern Biotech, Birmingham, AL, USA). Using standard fluorescence microscopy (BX51 microscope, 60 $\times$  oil immersion objective, NA 1.35, Olympus, Hamburg, Germany) focal depth was sufficient to see the entire cell in focus. The EGFP distribution pattern was classified manually into the following categories: 'homogenous', 'one aggresome' (large, round, perinuclear aggregate), 'aggresome and aggregates' and 'unhealthy' (round, condensed cells). Z-Stacks were not acquired. A blinded investigator classified at least 100 cells per coverslip. In each experiment, three coverslips were evaluated per experimental group and the results averaged by calculating mean. Depicted graphs summarize data (mean standard error of the mean (SEM)) from three independent experiments with 'n' equal to the number of independent experiments summarized.

### 2.12. Statistics

The study was not pre-registered. For assignment of experimental groups, no special randomization methods were employed. Sample sizes were determined by past experience and not by a statistical sample size calculation (Figure 3: at least 100 cells were analyzed). For statistical analysis and data presentation, we used GraphPad Prism 5.0 and 6.0 (RRID: SCR\_002798, GraphPad Software, LaJolla, CA, USA). Graphs represent mean SEM. The tests used for comparison in each graph are noted in the figure legend (Figure 3: one-way ANOVA). The experiments were replicated independently at least three times with three replicates, representative graphs are shown.  $P < 0.05$  was considered significant. In graphs,  $p$ -values are depicted as  $*p < 0.05$ ,  $**p < 0.01$ ,  $***p < 0.001$ ,  $****p < 0.0001$ .

## 3. Results

### 3.1. Experimental Work

#### 3.1.1. Binding Characteristics of nAbs- $\alpha$ Syn

nAbs- $\alpha$ Syn were isolated from commercial human IVIG preparations using gravity flow affinity purification as described previously [46]. nAbs- $\alpha$ Syn are not very abundant, so several purification batches were pooled to obtain a sufficient amount of nAbs- $\alpha$ Syn protein. The flow through (FT) of the affinity purification was used as negative control.

First, we analyzed binding of nAbs- $\alpha$ Syn to monomeric  $\alpha$ Syn protein by dot blot. In a dot blot, the bait protein is immobilized to a solid surface (nitrocellulose) and incubated with the prey protein (the indicated probes containing antibodies) in the fluid phase (as depicted in the scheme, Figure 1a). Dependent on the species of the prey protein, the detection system varies. We observed concentration-dependent immunoreactivity against Fc termini using either a commercial  $\alpha$ Syn antibody (Figure 1a, top) or nAbs- $\alpha$ Syn (Figure 1a, bottom), but not using FT (Figure 1a, middle). Specific binding of nAbs- $\alpha$ Syn to monomeric  $\alpha$ Syn protein was confirmed in ELISA measurements (Figure 1b).  $\alpha$ Syn was detected by all nAbs- $\alpha$ Syn with different avidities even at low concentrations of nAbs- $\alpha$ Syn (0.5  $\mu$ g/mL). Furthermore, nAbs were significantly higher in their avidity in comparison to the reference control FT or PBS, resulting in a higher binding signal. In SPR measurement nAbs- $\alpha$ Syn interacted strongly with  $\alpha$ Syn. Due to the polyreactive nature of nAbs- $\alpha$ Syn, the dissociation constant ( $K_D$ ) was not determined from the binding kinetics but from a steady state fit, yielding a value of  $K_D = (4.22 \pm 0.95) \times 10^{-6}$  M. nAbs- $\alpha$ Syn showed a higher affinity than IVIG and FT (Figure 1c–f), confirming that binding agents with specificity for  $\alpha$ Syn were enriched during nAbs- $\alpha$ Syn preparation. nAbs- $\alpha$ Syn binding to  $\alpha$ Syn could be confirmed with all three methods.

#### 3.1.2. nAbs- $\alpha$ Syn Interfere with $\alpha$ Syn Amyloid Formation and Alter $\alpha$ Syn Fibril Morphology as Visualized with Atomic Force Microscopy

We performed a ThT fibrillation assay to assess de novo  $\alpha$ Syn amyloid formation in absence and presence of nAbs- $\alpha$ Syn. In the absence of nAbs- $\alpha$ Syn, the typical sigmoidal kinetics of nucleated polymerization of  $\alpha$ Syn monomers into amyloid fibrils was observed (Figure 2a). Although there was some variability between experimental repeats in the shapes of the time traces and in the final ThT fluorescence intensities, the lag-time of aggregation, i.e., the time after which amyloid formation is detectable by ThT fluorescence for the first time, was quite uniform with a value of  $\sim 15$  h. FT or IVIG at a protein concentration of 0.1  $\mu$ M were not able to interfere with amyloid formation of 25  $\mu$ M  $\alpha$ Syn as assessed by lag-times and ThT fluorescence intensities (Figure 2b,c). In contrast, in the presence of 0.1  $\mu$ M nAbs- $\alpha$ Syn there was either no increase in ThT fluorescence during the 60 h experiment, or a weak fluorescence increase after a prolonged lag-time (Figure 2d). We corroborated the effects seen in the fibrillation assay by AFM. Samples from the fibrillation assay were prepared for AFM, and representative images are shown in Figure 2e–l. A substantially lower amount of fibrils was observed in images of nAbs- $\alpha$ Syn-containing samples (Figure 2h,l) compared to samples that were either untreated (Figure 2e,i) or supplemented with IVIG (Figure 2f,j) or FT (Figure 2g,k). Moreover, the  $\alpha$ Syn fibrils in the

sample treated with nAbs- $\alpha$ Syn appeared to be thinner and exhibited a lower tendency to cluster than those in the other samples (Figure S1).

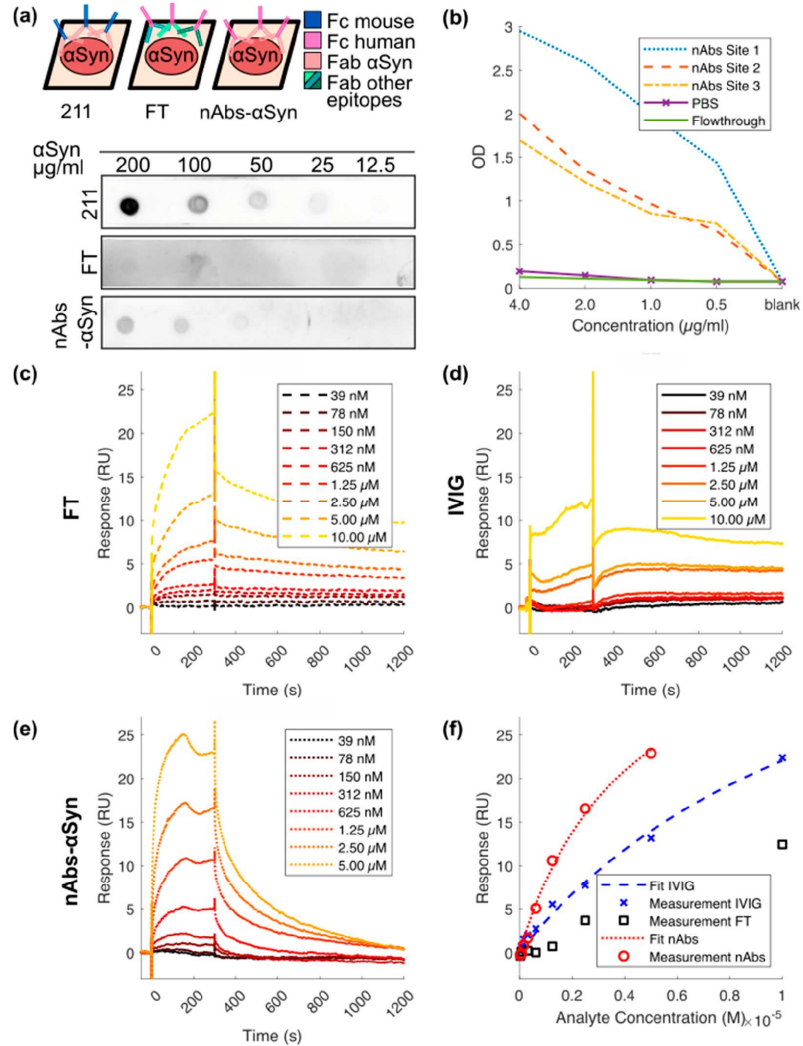


**Figure 1.** Binding characteristics of nAbs- $\alpha$ Syn in dot blot, ELISA, and SPR. (a) nAbs- $\alpha$ Syn recognize  $\alpha$ Syn on a dot blot:  $\alpha$ Syn at different concentrations were spotted on a nitrocellulose membrane and then probed with flow through and nAbs- $\alpha$ Syn. Anti- $\alpha$ Syn antibody was used as a control. Although the control antibody (211) is a mouse antibody, FT and nAbs- $\alpha$ Syn are of human origin (see scheme). Each dot blot requires a different secondary antibody (either anti-mouse or anti-human) (b) nAbs- $\alpha$ Syn recognize  $\alpha$ Syn in an ELISA: nAbs- $\alpha$ Syn from three different project sites were tested in an ELISA, to determine their capacity to bind to  $\alpha$ Syn in vitro. (c–f) nAbs- $\alpha$ Syn recognize  $\alpha$ Syn in SPR: SPR curves of nAbs- $\alpha$ Syn (e) binding to recombinant  $\alpha$ Syn. IVIG (c) and FT (d) were used as controls. A concentration range of 39 nM–5  $\mu$ M of nAbs- $\alpha$ Syn was applied in SPR. The binding affinity was determined from three replicates.

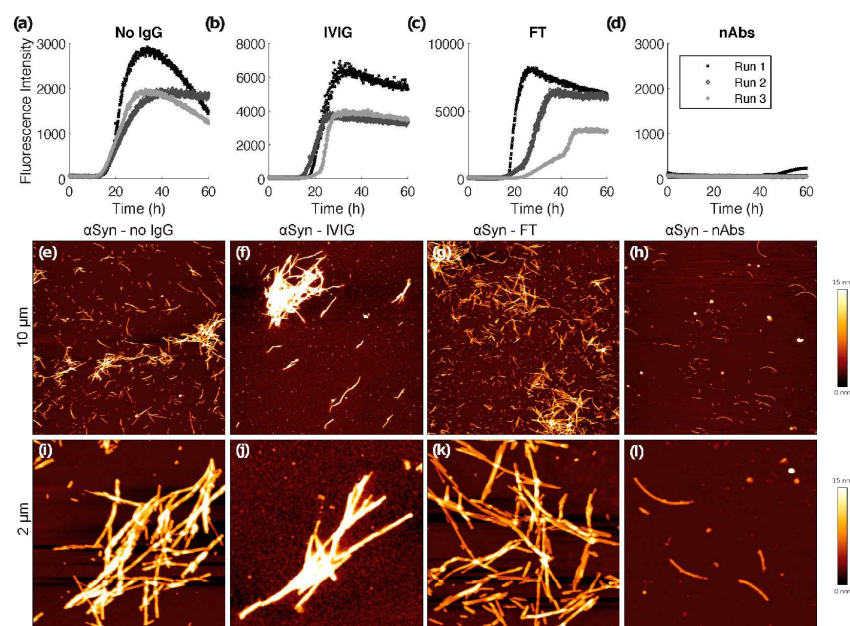


**Figure 2.** ThT fibrillation assay and atomic force microscopy. De novo fibrillation of 25  $\mu\text{M}$   $\alpha\text{Syn}$  in the absence (a) and presence of 0.1  $\mu\text{M}$  IVIG (b), FT (c) and nAbs- $\alpha\text{Syn}$  (d) followed by ThT fluorescence. Three replicates are shown per condition. At the end of the 60 h time course, samples were imaged via AFM (e–l). Representative overview images of the samples showing  $10 \times 10 \mu\text{m}$  areas (e–h) and  $2 \times 22 \mu\text{m}$  close-ups (i–l).

### 3.1.3. Treatment with nAbs- $\alpha\text{Syn}$ Decreases Occurrence of Aggregates in Cells

As a first test, we tested whether nAbs- $\alpha\text{Syn}$  affected cell viability in untransfected HEK293T cells. We observed no alteration in cell viability as assessed for LDH-release or metabolic activity (CTB assay) (Figure S2). Next, we tested whether nAbs- $\alpha\text{Syn}$  added to the culture medium can affect the behavior of intracellular  $\alpha\text{Syn}$ . We transfected HEK293T cells with EGFP-tagged  $\alpha\text{Syn}$  as previously reported [51,54,55]. The  $\alpha\text{Syn}$  construct is modified only by addition of 6 amino acids to the C-terminus of  $\alpha\text{Syn}$ . This is a small modification given that the C-terminus is relatively flexible. We, therefore, assume that the aggregation properties are not changed much. This  $\alpha\text{Syn}$  construct is tagged by EGFP by the interaction of this 6 amino acid PDZ binding motif with its PDZ domain, which is coexpressed fused to EGFP. We cannot exclude that even the reversible binding of  $\alpha\text{Syn}$  to PDZ-EGFP changes the aggregation properties, but to lesser extent than a direct fusion of  $\alpha\text{Syn}$ -EGFP would alter the aggregation properties. In addition to the EGFP- $\alpha\text{Syn}$  transfection, cells were treated with nAbs- $\alpha\text{Syn}$  or FT for 24 h. Based on the subcellular GFP distribution, we classified cells as unhealthy cells, cells with homogenous GFP fluorescence and cells with one aggregate or aggregates. nAbs- $\alpha\text{Syn}$  significantly reduced the number of cells with a visible aggregate (Figure 3d, quantified in Figure 3h). At the same time, the number of cells with small aggregates was higher in cells treated with nAbs- $\alpha\text{Syn}$  than in cells with FT (Figure 3g). We also observed more unhealthy cells with nAbs- $\alpha\text{Syn}$  treatment than without any treatment (Figure 3e), but since there was no significant difference between cells treated with nAbs and FT, we consider this effect nonspecific.

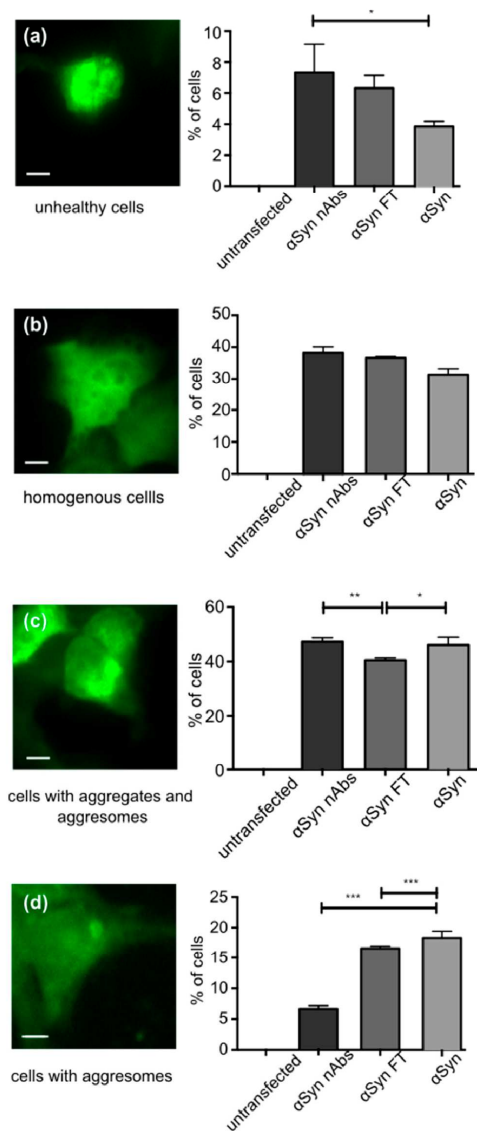


**Figure 3.** Effect of nAbs- $\alpha$ Syn on GFP-tagged  $\alpha$ Syn in HEK293T cells. HEK293T cells were transfected with  $\alpha$ Syn flexibly tagged by GFP, grown for 24 h and then treated with nAbs- $\alpha$ Syn for another 24 h. (a–d) First row, example images of cells in the following categories into which cells were manually classified: Unhealthy cells (a), cells with homogenous GFP fluorescence (b), cells with aggresomes and aggregates (c), cells with aggresomes (d). Scale bar represents 5  $\mu$ m. (a–d) Second row, quantification of  $n = 3$  experiments with at least 100 cells classified for each condition. FT: flow through. Bars represent p values from three replicates as calculated with one-way ANOVA. \*  $p < 0.05$ , \*\*  $p < 0.01$ , \*\*\*  $p < 0.001$ .

#### 4. Discussion

In this work, we characterized nAbs for  $\alpha$ Syn that were purified from commercial immunoglobulin preparations using biophysical methods and cultured cell lines. nAbs- $\alpha$ Syn bound  $\alpha$ Syn specifically and were able to affect the subcellular distribution of  $\alpha$ Syn, suggesting that they can be taken up by cells.

nAbs- $\alpha$ Syn can be isolated from IVIG preparations, as we and others have demonstrated [26,45,46]. IVIG are typically derived from young, healthy plasma donors without any past medical history. Although it cannot be formally excluded that some donors have a neurodegenerative disease or will develop one in the near future, the more likely hypothesis is that this is not the case. The presence of nAbs- $\alpha$ Syn in IVIG preparation, therefore, suggests that nAbs- $\alpha$ Syn are ubiquitously present in healthy individuals. Indeed, nAbs- $\alpha$ Syn were also observed in serum samples of children [45]. nAbs- $\alpha$ Syn, thus, are part of the innate immune system and not an acquired response to the presence of  $\alpha$ Syn pathology.

nAbs- $\alpha$ Syn were isolated from IVIG using gravity flow affinity purification, i.e., they are defined by binding recombinant  $\alpha$ Syn protein. In order to obtain an estimate of the affinity of nAbs- $\alpha$ Syn for  $\alpha$ Syn, we measured the association and dissociation by SPR. Although the Langmuir model used previously to calculate the  $K_D$  [46] is perfectly suitable for monoclonal reactants, we employed a steady state fit to better model the polyreactive nature of nAbs. The obtained apparent  $K_D$  of 4  $\mu$ M is an order of magnitude higher than the value previously determined from the binding kinetics [46]. It should be noted, however, that the obtained value results from the superposition of binding of different molecular species that might substantially differ in their affinities.

Binding of nAbs- $\alpha$ Syn to  $\alpha$ Syn is further confirmed by the fact that they inhibit aggregation of  $\alpha$ Syn in vitro (Figure 3). Importantly, this effect is neither observed with the standard IVIG preparation, which contains only small quantities of nAbs- $\alpha$ Syn, nor with the FT. nAbs- $\alpha$ Syn are polyreactive, so they likely bind to different epitopes on the  $\alpha$ Syn protein. Our data do not reveal whether all nAbs- $\alpha$ Syn species contribute equally to the inhibition of  $\alpha$ Syn aggregation, or whether some species are particularly potent. In this context, it is interesting to note that antibodies and other binding proteins to a variety of  $\alpha$ Syn sequence regions, including N-terminus, NAC region, and C-terminus were shown to inhibit aggregation [55–62].

Our study focuses on the behavior of nAbs- $\alpha$ Syn. In addition, more than 50 non-naturally occurring antibodies against  $\alpha$ Syn have been established and described, including engineered antibodies and antibody fragments to target  $\alpha$ Syn for various purposes in the field of research, diagnostics, therapeutic approaches, and biomarkers [63]. These antibodies recognize epitopes that are as versatile as the protein  $\alpha$ Syn itself: They do not only recognize different  $\alpha$ Syn sequences (see above), different  $\alpha$ Syn conformations (oligomers, fibrils), and, also, different post-translational modifications [63–65]. The anti-aggregation effect of many of these antibodies was shown in various studies [23–28].

With regard to the potential mechanism of aggregation inhibition, we have shown here that binding of  $\alpha$ -synuclein monomers can lead to potent, substoichiometric inhibition of aggregation, in the case when the 1:1 complex of  $\alpha$ -synuclein and binding protein acts as an inhibitor of nucleation processes [57]. Moreover, nAbs- $\alpha$ Syn may potentially interfere with aggregation also by interacting with higher-order oligomeric or fibrillar species [26]. Interestingly, we observe in AFM that nAbs- $\alpha$ Syn not only reduce the amount of fibrillar aggregates, but also decrease fibril clustering. This might indicate that nAbs- $\alpha$ Syn alter the properties of  $\alpha$ Syn fibril surfaces. However, the reduced formation of higher-order aggregate clusters might also simply stem from the lower fibril concentration in presence of nAbs- $\alpha$ Syn.

In order to test whether inhibition of  $\alpha$ Syn aggregation observed in vitro translates to an effect in living cells, we used the HEK293T cell line. Adding nAbs- $\alpha$ Syn to these cells did not alter viability (Figure S1). We analyzed the effect of nAbs- $\alpha$ Syn addition to the cell culture medium on the subcellular distribution of EGFP-tagged  $\alpha$ Syn (Figure 3). nAbs- $\alpha$ Syn specifically decrease the fraction of cells with a visible aggresome. Aggresomes

are formed by retrograde transport of protein aggregates to the microtubule organizing center by dynein motors and cleared by autophagy [47,49]. We cannot know from our findings whether nAbs- $\alpha$ Syn reduce aggresome formation or increase clearance, but nAbs- $\alpha$ Syn are certainly able to affect intracellular processing of  $\alpha$ Syn aggregates. These findings should be confirmed in future studies. Additional approaches to study this issue are immunostaining for  $\alpha$ Syn [66], pS129  $\alpha$ Syn [64,65], or p62 [67,68]. Analytically, these stainings followed by the puncta per cell quantification together with integrated intensity would nicely complement the EGFP visualization of  $\alpha$ Syn and grant clearer insights into its subcellular distribution.

## 5. Conclusions

In summary, we confirmed the presence of nAbs that specifically bind  $\alpha$ Syn monomers in IVIG preparations obtained from healthy donors. These nAbs alter  $\alpha$ Syn aggregation and fibril conformation in vitro and affect intracellular  $\alpha$ Syn processing. Collectively, these findings are consistent with an involvement of the innate immune system in the pathogenesis of PD and with potential therapeutic effects of antibody preparations in patients with PD. Yet, several important questions remain unsolved, such as the effects of nAbs on microglia and astrocytes in the brain, the role of peripheral  $\alpha$ Syn as opposed to central  $\alpha$ Syn deposits for PD pathogenesis, and the species or epitopes of  $\alpha$ Syn that are targeted by nAbs.

**Supplementary Materials:** The following supporting information can be downloaded at: <https://www.mdpi.com/article/10.3390/biom12030469/s1>, Figure S1: Height distribution of  $\alpha$ Syn aggregates formed in presence or absence of nAbs. Figure S2: nAbs- $\alpha$ Syn do not affect viability of untransfected HEK293T cells.

**Author Contributions:** Conceptualization, A.K.B., J.-P.B., B.H.F. and W.H.; methodology, A.K.B., J.-P.B., B.H.F. and W.H.; SPR measurements, A.K.B., I.G. and M.S. (Marc Sevenich); AFM measurements, A.K.B. and T.K.; ThT Assays, A.K.B. and E.D.A.; ELISA measurements, Y.K.; Metabolic measurements, A.K.B. and P.H.; NMR measurements, M.S. (Matthias Stoldt); writing original draft preparation, A.K.B.; writing review and editing, A.K.B., B.H.F., W.H., P.H. and J.B.S.; visualization, A.K.B.; resource, D.W.; supervision, J.-P.B., B.H.F., W.H. and D.W.; funding acquisition, A.K.B. and W.H. All authors have read and agreed to the published version of the manuscript.

**Funding:** This research was funded by the START program (grant 29/17) and the rotation program of the Medical Faculty of RWTH Aachen University to A.K.B. Support by a European Research Council (ERC) Consolidator Grant (grant agreement no. 726368, to W.H.) is acknowledged.

**Institutional Review Board Statement:** Not applicable.

**Informed Consent Statement:** Not applicable.

**Data Availability Statement:** Not applicable.

**Acknowledgments:** Access to the Biomolecular NMR Centre, jointly run by Forschungszentrum Jülich and Heinrich-Heine-Universität Düsseldorf, is acknowledged. We thank Susanne Stei, Neurology Department, Marburg University Hospital for technical support and teaching AKB the method of nAbs- $\alpha$ Syn purification. We thank Barbara Schulten, Institut für Physikalische Biologie, HHU Düsseldorf, and Sabine Hamm, Neurology Department, University Hospital Aachen, for Assistance with the purification of nAbs- $\alpha$ Syn. We thank Alexander Loewer, Systems Biology of the stress response, Biology, TU Darmstadt and Petra Snyder for using the fluorescence microscopy imaging facility.

**Conflicts of Interest:** The authors declare no conflict of interest. The funders had no role in the design of the study; in the collection, analyses, or interpretation of data; in the writing of the manuscript, or in the decision to publish the results.

## References

1. Obeso, J.A.; Stamelou, M.; Goetz, C.G.; Poewe, W.; Lang, A.E.; Weintraub, D.; Burn, D.; Halliday, G.M.; Bezdard, E.; Przedborski, S.; et al. Past, present, and future of Parkinson's disease: A special essay on the 200th Anniversary of the Shaking Palsy. *Mov. Disord.* **2017**, *32*, 1264–1310. [CrossRef]

2. Spillantini, M.G.; Crowther, R.A.; Jakes, R.; Hasegawa, M.; Goedert, M. alpha-Synuclein in filamentous inclusions of Lewy bodies from Parkinson's disease and dementia with lewy bodies. *Proc. Natl. Acad. Sci. USA* **1998**, *95*, 6469–6473. [[CrossRef](#)] [[PubMed](#)]
3. Braak, H.; Del Tredici, K.; Rub, U.; de Vos, R.A.; Jansen Steur, E.N.; Braak, E. Staging of brain pathology related to sporadic Parkinson's disease. *Neurobiol. Aging* **2003**, *24*, 197–211. [[CrossRef](#)]
4. Surmeier, D.J.; Obeso, J.A.; Halliday, G.M. Parkinson's Disease Is Not Simply a Prion Disorder. *J. Neurosci. Off. J. Soc. Neurosci.* **2017**, *37*, 9799–9807. [[CrossRef](#)] [[PubMed](#)]
5. Braak, H.; de Vos, R.A.; Bohl, J.; Del Tredici, K. Gastric alpha-synuclein immunoreactive inclusions in Meissner's and Auerbach's plexuses in cases staged for Parkinson's disease-related brain pathology. *Neurosci. Lett.* **2006**, *396*, 67–72. [[CrossRef](#)] [[PubMed](#)]
6. Luk, K.C.; Kehm, V.; Carroll, J.; Zhang, B.; O'Brien, P.; Trojanowski, J.Q.; Lee, V.M. Pathological alpha-synuclein transmission initiates Parkinson-like neurodegeneration in nontransgenic mice. *Science* **2012**, *338*, 949–953. [[CrossRef](#)] [[PubMed](#)]
7. Shannon, K.M.; Keshavarzian, A.; Mutlu, E.; Dodiya, H.B.; Daian, D.; Jaglin, J.A.; Kordower, J.H. Alpha-synuclein in colonic submucosa in early untreated Parkinson's disease. *Mov. Disord.* **2012**, *27*, 709–715. [[CrossRef](#)]
8. Holmqvist, S.; Chutna, O.; Bousset, L.; Aldrin-Kirk, P.; Li, W.; Bjorklund, T.; Wang, Z.Y.; Roybon, L.; Melki, R.; Li, J.Y. Direct evidence of Parkinson pathology spread from the gastrointestinal tract to the brain in rats. *Acta Neuropathol.* **2014**, *128*, 805–820. [[CrossRef](#)]
9. Pan-Montojo, F.; Schwarz, M.; Winkler, C.; Arnhold, M.; O'Sullivan, G.A.; Pal, A.; Said, J.; Marsico, G.; Verbavatz, J.M.; Rodrigo-Angulo, M.; et al. Environmental toxins trigger PD-like progression via increased alpha-synuclein release from enteric neurons in mice. *Sci. Rep.* **2012**, *2*, 898. [[CrossRef](#)]
10. Svensson, E.; Horvath-Puho, E.; Thomsen, R.W.; Djurhuus, J.C.; Pedersen, L.; Borghammer, P.; Sorensen, H.T. Vagotomy and subsequent risk of Parkinson's disease. *Ann. Neurol.* **2015**, *78*, 522–529. [[CrossRef](#)]
11. Vilas, D.; Iranzo, A.; Tolosa, E.; Aldecoa, I.; Berenguer, J.; Vilaseca, I.; Marti, C.; Serradell, M.; Lomena, F.; Alos, L.; et al. Assessment of alpha-synuclein in submandibular glands of patients with idiopathic rapid-eye-movement sleep behaviour disorder: A case-control study. *Lancet Neurol.* **2016**, *15*, 708–718. [[CrossRef](#)]
12. Doppler, K.; Jentschke, H.M.; Schulmeyer, L.; Vadasz, D.; Janzen, A.; Luster, M.; Hoffken, H.; Mayer, G.; Brumberg, J.; Booi, J.; et al. Dermal phospho-alpha-synuclein deposits confirm REM sleep behaviour disorder as prodromal Parkinson's disease. *Acta Neuropathol.* **2017**, *133*, 535–545. [[CrossRef](#)] [[PubMed](#)]
13. Antelmi, E.; Donadio, V.; Incensi, A.; Plazzi, G.; Liguori, R. Skin nerve phosphorylated alpha-synuclein deposits in idiopathic REM sleep behavior disorder. *Neurology* **2017**, *88*, 2128–2131. [[CrossRef](#)] [[PubMed](#)]
14. Sprenger, F.S.; Stefanova, N.; Gelpi, E.; Seppi, K.; Navarro-Otano, J.; Offner, F.; Vilas, D.; Valldeoriola, F.; Pont-Sunyer, C.; Aldecoa, I.; et al. Enteric nervous system alpha-synuclein immunoreactivity in idiopathic REM sleep behavior disorder. *Neurology* **2015**, *85*, 1761–1768. [[CrossRef](#)]
15. Stokholm, M.G.; Danielsen, E.H.; Hamilton-Dutoit, S.J.; Borghammer, P. Pathological alpha-synuclein in gastrointestinal tissues from prodromal Parkinson disease patients. *Ann. Neurol.* **2016**, *79*, 940–949. [[CrossRef](#)] [[PubMed](#)]
16. Singleton, A.B.; Hardy, J.A.; Gasser, T. The Birth of the Modern Era of Parkinson's Disease Genetics. *J. Parkinsons Dis.* **2017**, *7*, S87–S93. [[CrossRef](#)] [[PubMed](#)]
17. Dehay, B.; Bourdenx, M.; Gorry, P.; Przedborski, S.; Vila, M.; Hunot, S.; Singleton, A.; Olanow, C.W.; Merchant, K.M.; Bezard, E.; et al. Targeting alpha-synuclein for treatment of Parkinson's disease: Mechanistic and therapeutic considerations. *Lancet Neurol.* **2015**, *14*, 855–866. [[CrossRef](#)]
18. Vicente Miranda, H.; Szego, E.M.; Oliveira, L.M.A.; Breda, C.; Darendelioglu, E.; de Oliveira, R.M.; Ferreira, D.G.; Gomes, M.A.; Rott, R.; Oliveira, M.; et al. Glycation potentiates alpha-synuclein-associated neurodegeneration in synucleinopathies. *Brain* **2017**, *140*, 1399–1419. [[CrossRef](#)]
19. Giasson, B.I.; Murray, I.V.; Trojanowski, J.Q.; Lee, V.M. A hydrophobic stretch of 12 amino acid residues in the middle of alpha-synuclein is essential for filament assembly. *J. Biol. Chem.* **2001**, *276*, 2380–2386. [[CrossRef](#)]
20. George, J.M. The synucleins. *Genome Biol.* **2002**, *3*, 1–6.
21. Iwai, A.; Masliah, E.; Yoshimoto, M.; Ge, N.; Flanagan, L.; de Silva, H.A.; Kittel, A.; Saitoh, T. The precursor protein of non-A beta component of Alzheimer's disease amyloid is a presynaptic protein of the central nervous system. *Neuron* **1995**, *14*, 467–475. [[CrossRef](#)]
22. Braczynski, A.K.; Schulz, J.B.; Bach, J.P. Vaccination strategies in tauopathies and synucleinopathies. *J. Neurochem.* **2017**, *143*, 467–488. [[CrossRef](#)] [[PubMed](#)]
23. Fleming, S.M.; Davis, A.; Simons, E. Targeting alpha-synuclein via the immune system in Parkinson's disease: Current vaccine therapies. *Neuropharmacology* **2022**, *202*, 108870. [[CrossRef](#)] [[PubMed](#)]
24. Masliah, E.; Rockenstein, E.; Adame, A.; Alford, M.; Crews, L.; Hashimoto, M.; Seubert, P.; Lee, M.; Goldstein, J.; Chilcote, T.; et al. Effects of alpha-synuclein immunization in a mouse model of Parkinson's disease. *Neuron* **2005**, *46*, 857–868. [[CrossRef](#)] [[PubMed](#)]
25. Masliah, E.; Rockenstein, E.; Mante, M.; Crews, L.; Spencer, B.; Adame, A.; Patrick, C.; Trejo, M.; Ubhi, K.; Rohn, T.T.; et al. Passive immunization reduces behavioral and neuropathological deficits in an alpha-synuclein transgenic model of Lewy body disease. *PLoS ONE* **2011**, *6*, e19338. [[CrossRef](#)] [[PubMed](#)]
26. Huang, Y.R.; Xie, X.X.; Ji, M.; Yu, X.L.; Zhu, J.; Zhang, L.X.; Liu, X.G.; Wei, C.; Li, G.; Liu, R.T. Naturally occurring autoantibodies against alpha-synuclein rescues memory and motor deficits and attenuates alpha-synuclein pathology in mouse model of Parkinson's disease. *Neurobiol. Dis.* **2019**, *124*, 202–217. [[CrossRef](#)] [[PubMed](#)]

27. Mandler, M.; Valera, E.; Rockenstein, E.; Weninger, H.; Patrick, C.; Adame, A.; Santic, R.; Meindl, S.; Vigi, B.; Smrzka, O.; et al. Next-generation active immunization approach for synucleinopathies: Implications for Parkinson's disease clinical trials. *Acta Neuropathol.* **2014**, *127*, 861–879. [[CrossRef](#)] [[PubMed](#)]
28. Ghochikyan, A.; Petrushina, I.; Davtyan, H.; Hovakimyan, A.; Saing, T.; Davtyan, A.; Cribbs, D.H.; Agadjanyan, M.G. Immunogenicity of epitope vaccines targeting different B cell antigenic determinants of human alpha-synuclein: Feasibility study. *Neurosci. Lett.* **2014**, *560*, 86–91. [[CrossRef](#)]
29. Nimmo, J.T.; Kelly, L.; Verma, A.; Carare, R.O.; Nicoll, J.A.R.; Dodart, J.C. Amyloid-beta and alpha-Synuclein Immunotherapy: From Experimental Studies to Clinical Trials. *Front. Neurosci.* **2021**, *15*, 733857. [[CrossRef](#)]
30. Kasaian, M.T.; Casali, P. Autoimmunity-prone B-1 (CD5 B) cells, natural antibodies and self recognition. *Autoimmunity* **1993**, *15*, 315–329. [[CrossRef](#)]
31. Reyneveld, G.I.; Savelkoul, H.F.J.; Parmentier, H.K. Current Understanding of Natural Antibodies and Exploring the Possibilities of Modulation Using Veterinary Models. A Review. *Front. Immunol.* **2020**, *11*, 2139. [[CrossRef](#)] [[PubMed](#)]
32. Bach, J.P.; Dodel, R. Naturally occurring autoantibodies against beta-Amyloid. *Adv. Exp. Med. Biol.* **2012**, *750*, 91–99. [[CrossRef](#)] [[PubMed](#)]
33. Kronimus, Y.; Albus, A.; Balzer-Geldsetzer, M.; Straub, S.; Semler, E.; Otto, M.; Klotsche, J.; Dodel, R.; Consortium, L.; Mengel, D. Naturally Occurring Autoantibodies against Tau Protein Are Reduced in Parkinson's Disease Dementia. *PLoS ONE* **2016**, *11*, e0164953. [[CrossRef](#)] [[PubMed](#)]
34. Chou, M.Y.; Fogelstrand, L.; Hartvigsen, K.; Hansen, L.F.; Woelkers, D.; Shaw, P.X.; Choi, J.; Perkmann, T.; Backhed, F.; Miller, Y.I.; et al. Oxidation-specific epitopes are dominant targets of innate natural antibodies in mice and humans. *J. Clin. Investig.* **2009**, *119*, 1335–1349. [[CrossRef](#)] [[PubMed](#)]
35. Chen, Y.; Park, Y.B.; Patel, E.; Silverman, G.J. IgM antibodies to apoptosis-associated determinants recruit C1q and enhance dendritic cell phagocytosis of apoptotic cells. *J. Immunol.* **2009**, *182*, 6031–6043. [[CrossRef](#)] [[PubMed](#)]
36. Besong-Agbo, D.; Wolf, E.; Jessen, F.; Oechsner, M.; Hametner, E.; Poewe, W.; Reindl, M.; Oertel, W.H.; Noelker, C.; Bacher, M.; et al. Naturally occurring alpha-synuclein autoantibody levels are lower in patients with Parkinson disease. *Neurology* **2013**, *80*, 169–175. [[CrossRef](#)] [[PubMed](#)]
37. Brudek, T.; Winge, K.; Folke, J.; Christensen, S.; Fog, K.; Pakkenberg, B.; Pedersen, L.O. Autoimmune antibody decline in Parkinson's disease and Multiple System Atrophy; a step towards immunotherapeutic strategies. *Mol. Neurodegener.* **2017**, *12*, 44. [[CrossRef](#)] [[PubMed](#)]
38. Maetzler, W.; Apel, A.; Langkamp, M.; Deuschle, C.; Dilger, S.S.; Stirnkorb, J.G.; Schulte, C.; Schleicher, E.; Gasser, T.; Berg, D. Comparable autoantibody serum levels against amyloid- and inflammation-associated proteins in Parkinson's disease patients and controls. *PLoS ONE* **2014**, *9*, e88604. [[CrossRef](#)]
39. Shalash, A.; Salama, M.; Makar, M.; Roushdy, T.; Elrassas, H.H.; Mohamed, W.; El-Balkimy, M.; Abou Donia, M. Elevated Serum alpha-Synuclein Autoantibodies in Patients with Parkinson's Disease Relative to Alzheimer's Disease and Controls. *Front. Neurol.* **2017**, *8*, 720. [[CrossRef](#)]
40. Ishii, R.; Tokuda, T.; Tatebe, H.; Ohmichi, T.; Kasai, T.; Nakagawa, M.; Mizuno, T.; El-Agnaf, O.M. Decrease in plasma levels of alpha-synuclein is evident in patients with Parkinson's disease after elimination of heterophilic antibody interference. *PLoS ONE* **2015**, *10*, e0123162. [[CrossRef](#)]
41. Papachroni, K.K.; Ninkina, N.; Papanagioutou, A.; Hadjigeorgiou, G.M.; Xiromerisiou, G.; Papadimitriou, A.; Kalofoutis, A.; Buchman, V.L. Autoantibodies to alpha-synuclein in inherited Parkinson's disease. *J. Neurochem.* **2007**, *101*, 749–756. [[CrossRef](#)] [[PubMed](#)]
42. Gruden, M.A.; Sewell, R.D.; Yanamandra, K.; Davidova, T.V.; Kucheryanu, V.G.; Bocharov, E.V.; Bocharova, O.A.; Polyschuk, V.V.; Sherstnev, V.V.; Morozova-Roche, L.A. Immunoprotection against toxic biomarkers is retained during Parkinson's disease progression. *J. Neuroimmunol.* **2011**, *233*, 221–227. [[CrossRef](#)] [[PubMed](#)]
43. Yanamandra, K.; Kfoury, N.; Jiang, H.; Mahan, T.E.; Ma, S.; Maloney, S.E.; Wozniak, D.F.; Diamond, M.I.; Holtzman, D.M. Anti-tau antibodies that block tau aggregate seeding in vitro markedly decrease pathology and improve cognition in vivo. *Neuron* **2013**, *80*, 402–414. [[CrossRef](#)] [[PubMed](#)]
44. Akhtar, R.S.; Licata, J.P.; Luk, K.C.; Shaw, L.M.; Trojanowski, J.Q.; Lee, V.M. Measurements of auto-antibodies to alpha-synuclein in the serum and cerebral spinal fluids of patients with Parkinson's disease. *J. Neurochem.* **2018**, *145*, 489–503. [[CrossRef](#)] [[PubMed](#)]
45. Kuhn, I.; Rogosch, T.; Schindler, T.I.; Tackenberg, B.; Ziemlin, M.; Maier, R.F.; Dodel, R.; Kronimus, Y. Serum titers of autoantibodies against alpha-synuclein and tau in child- and adulthood. *J. Neuroimmunol.* **2018**, *315*, 33–39. [[CrossRef](#)] [[PubMed](#)]
46. Albus, A.; Gold, M.; Bach, J.P.; Burg-Roderfeld, M.; Jordens, M.; Kirchhein, Y.; Kronimus, Y.; Mengel, D.; Zerr, I.; Dodel, R. Extending the functional characteristics of naturally occurring autoantibodies against beta-Amyloid, Prion Protein and alpha-Synuclein. *PLoS ONE* **2018**, *13*, e0202954. [[CrossRef](#)] [[PubMed](#)]
47. Dinter, E.; Saridakis, T.; Diederichs, L.; Reichmann, H.; Falkenburger, B.H. Parkinson's disease and translational research. *Transl. Neurodegener.* **2020**, *9*, 43. [[CrossRef](#)]
48. Panicker, N.; Ge, P.; Dawson, V.L.; Dawson, T.M. The cell biology of Parkinson's disease. *J. Cell Biol.* **2021**, *220*. [[CrossRef](#)] [[PubMed](#)]
49. Kopito, R.R. Aggresomes, inclusion bodies and protein aggregation. *Trends Cell Biol.* **2000**, *10*, 524–530. [[CrossRef](#)]

### 3 Global discussion

Phage display selection is a versatile tool for rapid and straightforward identification of protein compounds that interact with a target of choice. In this PhD thesis, a unique NGS-supported phage display selection strategy was developed to identify peptide ligands with therapeutic or diagnostic purpose.

#### 3.1 Optimization of the phage display selection protocol

Phage display selection is a powerful tool for the identification of novel ligands. However, the biopanning-based selection procedure is prone to yield and enrich sequence variants that are not target-related due to interaction with other components of the selection (e.g., the plate surface or blocking agents) or have an advantage during the amplification process [275]. For this reason, great efforts have been made in the past for the elimination of target-unrelated sequence variants i.e. by collecting large numbers of selection-derived target-unrelated sequences in data bases like SAROTUP [274], innovative amplification strategies that minimize amplification advantage [287] or specific elution methods that reduce elution of target-unrelated sequences [283]. Despite the efforts to limit the selection of target-irrelevant sequences, experience has shown that the appearance of target-unspecific sequences at the end of a selection cannot be completely avoided.

Thus, the focus was not primarily on reducing the enrichment of variants unrelated to the target (although appropriate measures such as changing immobilization surfaces and blocking conditions were taken), but rather on filtering out those sequences that depleted when the target was not present during panning. Therefore, negative controls were introduced during the selection process, which are necessary to track the frequency and target relationship of each sequence variant during the selection process. To cope with the enormous number of sequence variants, the high throughput method NGS was used. Although NGS can identify only 0.005 - 0.1 % of the total library capacity, the implemented filtering system reduces the number of sequence variants to 20 % of the input, making it highly efficient in identifying and excluding off-target sequences after selection. Moreover, the introduction of a scoring system allowed the ranking of sequences based on their enrichment and target-associated occurrence.

Sequences that passed the filter are inserted in a final processing step using *Hammock clustering software* [288]. The program clusters sequences with iterative cycles of cluster extension and merging steps by aligning sequences with a high degree of identity. This procedure not only minimizes the total number of sequence variants, but also provides

valuable information on possible amino acid substitutions and hypothetical minimal active sequences, which in turn can be used especially when a sequence needs to be optimized with respect to proteolytic stability, membrane permeability, and affinity (Fig. 13).

Together with the sequence-specific scoring values, the clustering enables the identification of positive hits by reducing the total number of variants to a few sequence motifs. The success of the data processing method was demonstrated throughout this dissertation with the target proteins  $\alpha$ -syn (monomer),  $\alpha$ -syn (fibril), SARS-CoV-2 RBD, SARS-CoV-2 3CL<sup>pro</sup> and hSOD1. In particular, the phage display selection on the SARS-CoV-2 RBD demonstrated that coupling of phage display with NGS and the subsequent extensive data processing is a powerful tool for identifying high affinity peptide ligands. In this project, a final number of five cluster motifs was identified after cluster analysis, each comprising approx. 2,000 to 35,000 unique sequence variants. In contrast, selections on other targets such as monomeric and fibrillary  $\alpha$ -syn did not yield as high enrichment values and cluster motif sizes as the selection on the SARS-CoV-2 RBD. Here, the analysis method is crucial to identify positive hits that otherwise would not have been found at all.

In conclusion, the phage display selection protocol was successfully extended by NGS and the subsequent data analysis procedure. Possible further optimization steps lie in the comparison of multiple selections on different targets. On the one hand, this extension should enable faster and data-based identification of non-target-related sequences, but on the other hand, it should also facilitate the identification of similar or identical target-related peptide sequences selected on different targets.

### 3.2 *In vitro* screening and characterization

The previously described process of phage display selection and NGS-based data analysis allows the identification of a set of peptide sequences that enriched during phage display in the presence of the target protein as well as the identification of their cluster motifs. However, a critical step in the development of therapeutic or diagnostic phage display derived peptide sequences is the *in vitro* screening for mode of action (MoA) -related effects.

Regardless of the subsequent use of the selected peptides, analytical methods to determine target affinity should always be one of the initial experiments of the *in vitro* screening process, as phage display selection enriches sequence variants based on their target affinity. In this context, it is important to note that the way in which peptides are presented during phage display differs substantially from the way in which both interaction partners interact freely in solution. First, the peptide library used in this work uses 16-mer sequences fused to the pIII minor-coating protein, presenting five copies of each sequence variant in close spatial proximity. This implies the possibility of multivalent binding if the binding valences of the

target protein are localized at similar distances. Consequently, the density at which a target protein is immobilized for biopanning, is critical for the affinity of the selected peptide sequences. Another aspect deals with the restricted structural flexibility of peptides fused to phage particles. In particular, the N-terminal part of the peptides can be expected to behave with higher flexibility in solution than the phage-fused version. These limitations explain, why, on the one hand, certain sequence variants are highly enriched during phage display selection, but, on the other hand, exhibit lower affinity in solution compared to less enriched variants. In this work, this observation was made when selecting on the SARS-CoV-2 RBD target protein. Here, the most enriched sequence CVRBDL-1, which also represented the largest cluster, showed only low binding affinity compared to other, less enriched variants when tested in solution.

Once the affinity screening process is complete, the next critical step for further evaluation of positive hits in therapeutic peptide development is to assess MoA-related effects *in vitro*. This step of lead compound identification is highly variable and should be tailored for each target protein. Most importantly, peptide variants that have shown high affinity interactions in the previous interaction-based screen do not necessarily have to exert MoA-related effects. This is most likely due to their heterogeneity concerning the interaction sites on the target but also their interaction kinetics. Therefore, the step of MoA-related *in vitro* screening is crucial for the identification of therapeutic lead compounds.

Due to the variability and complexity of the aggregation cascade,  $\alpha$ -syn was the target with the most challenging MoA in this work. In general, the intended MoA, which aims for IDP monomer stabilization, implies two major features: (i) inhibition of  $\alpha$ -syn aggregation at all stages where incorporation of  $\alpha$ -syn monomers into  $\alpha$ -syn aggregates is required, and (ii) the elimination of already existing aggregates, which should lead to restoration of the physiological monomer. To detect MoA-related effects, *in vitro* conditions were created in which the growth of  $\alpha$ -syn fibrils originates either from pure monomer (primary nucleation) or from monomer supplemented with seeds (seeded aggregation). In addition, it was also tested, whether pre-formed aggregates disintegrate in the presence of the compounds by observing changes in particle size distribution during the incubation period. Finally, to further verify the specificity of the observed effects, we recreated the experimental set-up in cellular environments using both intracellular fibril formation and cell viability as readouts. Cellular screening systems are in particular critical for lead compound identification, since they verify specificity of compound-target interactions in a highly protein-enriched environment, revealing compounds primarily interacting with ubiquitous protein structures or sequences. A useful addition to MoA-related set of screening experiments, which was not implemented in the current work, is the study of oligomer formation and elimination during aggregation. Here, the establishment of the QIAD assay, originally developed for A $\beta$  [174], would be conceivable, although the heterogeneity of the primary nucleation of  $\alpha$ -syn could pose a problem for the reproducibility of this assay. Another more straightforward option is to calculate the flux from

monomer to oligomeric species based on global kinetic fitting as demonstrated by Vendruscolo et al. [289]. Since secondary nucleation has been shown to be fundamental as a catalyst for the formation of oligomers compared to primary nucleation [290], the influence of compounds on this aggregation step should be carefully monitored.

Another MoA targeted in this work is the inhibition of the SARS-CoV-2-hACE2 complex formation as a potential therapeutic treatment for COVID-19. In contrast to the previously discussed MoA, which aimed to inhibit self-association of an IDP target protein, this MoA aims to inhibit the interaction of two different proteins, both exhibiting a well-defined globular fold. *In vitro* screening for MoA-related effects was primarily performed by interaction measurements in presence and absence of the peptide variants. Here, compound screening led to the identification of sequence variants that inhibited SARS-CoV-2 S1S2 monomer spike protein association with hACE2. Moreover, the compound was able to displace hACE2 from the spike protein when the complex has already formed. Although the compound already showed inhibitory effects in kinetic experiments, additional analysis will be required to complete the *in vitro* screening. First, the spike protein is homotrimeric in the physiological state. Consequently, further screening steps need to test for inhibition of hACE2 association using the physiologically active trimer. In addition, a cellular assay is required to validate the specificity of the observed effect. Here, viral proliferation assays in the presence of the compound would be a desirable approach [291].

The exact design of the MoA-related *in vitro* screening of phage display derived peptides depends on the targeted MoA of the compound. It is essential to precisely define the physiologically desired mechanism of action and to reproduce it under *in vitro* conditions using cellular as well as cell-free systems. Regardless, determining target affinity is critical and should precede all subsequent analytical steps.

### **3.3 A general procedure for the identification of D-enantiomeric peptide compounds by phage display selection**

In this work, a phage display based system for the straightforward identification and subsequent *in vitro* screening of D-enantiomeric peptides for therapeutic and diagnostic purposes was developed. Repeated application in different projects ( $\alpha$ -syn monomer,  $\alpha$ -syn fibril, SARS-CoV-2 RBD, SARS-CoV-2 3CL<sup>pro</sup>, hSOD1) has shown that the elaborated selection and screening process is applicable to different target proteins with different MoA. This work therefore provides a general protocol for the identification and *in vitro* characterization of D-enantiomeric peptides for therapeutic and diagnostic applications. Fig. 17 summarizes the

experimental steps required for the development of highly efficient D-enantiomeric peptide compounds starting from a naïve phage display library.

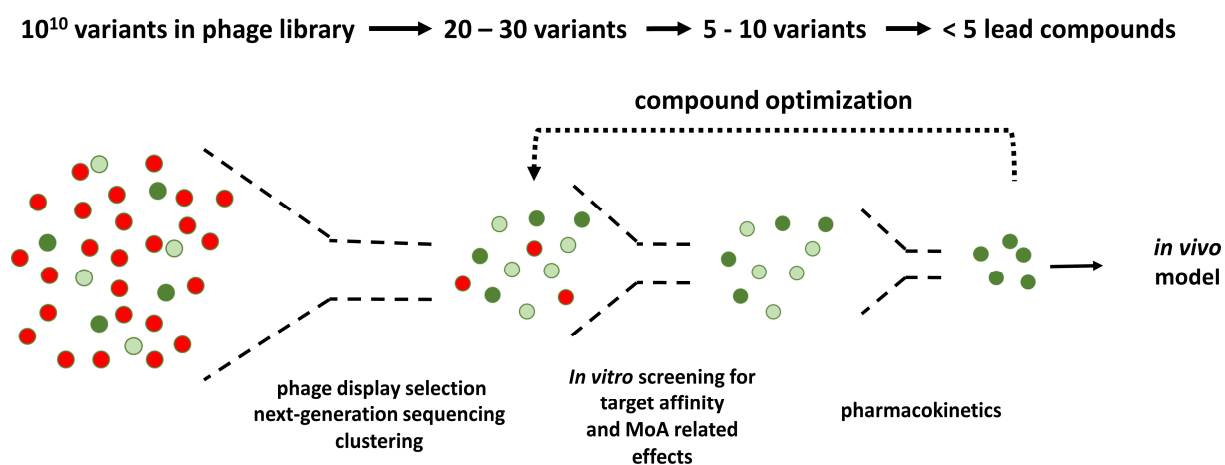


**Figure 17: Schematic representation for the development of therapeutic and diagnostic peptide compounds.**

The development of therapeutic peptides starts with the identification of target binders by phage display selection. Here, a large-scale library with  $> 10^{10}$  sequence variants is screened to yield a set of sequence variants that interact with the desired target (red ball: no interaction with target; light green ball: low affinity interaction with target; dark green ball: high affinity interaction with target). Subsequent NGS and clustering analysis reduce the number of potential compounds to approx. 20 to 30. Next, *in vitro* screening strategies are required for the identification of actual compound – target binding affinity and functional therapeutic effects that correspond with the intended MoA. This bottleneck will reduce the sequence pool to approx. five to ten sequence variants. Finally, pharmacokinetic studies will further reduce the number of lead compounds to less than five. Most likely, rational and semi-rational compound optimization strategies are needed at this point, such as strategies to improve membrane penetrance, proteolytic stability and binding affinity to further increase target selectivity, stability and membrane penetrance (if required). As optimization creates a larger pool of lead compound derivatives, these compounds must in turn overcome the last two bottlenecks. Finally, the feed-back loop consisting of optimization and screening will yield highly active and specific peptide compounds that can be used for screening in *in vivo* disease models.

The strength of the described development process lies in the initial diversity of variants provided by phage display selection. Compared to chemical synthesized small molecule screening libraries, phage display libraries offer up to  $10^6$ -fold higher capacities [292].

In the development process outlined, phage display selection is followed by an NGS-based screening process, which is coupled with clustering-based motif identification. This process allows the reduction of potential binding sequences to approx. 20 to 30 variants. The next critical step includes *in vitro* assays that screen for target affinity in combination with MoA-related effects. This step requires the development of a set of experiments that recreate the targeted disease-related mechanism under *in vitro* conditions. Experience has shown that this

screening step requires the combination of multiple experimental setups, which shed light on different aspects of the targeted disease mechanism and the corresponding compound effect.

The next critical screening step, not yet considered in the present work, is the pharmacokinetic characterization of the remaining sequence variants. Depending on the intended site of action and route of administration, a potential drug candidate must fulfill certain criteria to achieve a sufficient bioavailability. Again, the combination of multiple *in vitro* and *in vivo* experiments are required to obtain a complete picture of pharmacokinetics. Such experiments can be performed by investigation of the peptide stability in isolated blood plasma as well as in liver microsomes [293], permeability in BBB [294] and intestinal barrier cell models [295], and time-resolved quantification of tissue and fluid distribution in mouse studies [296].

Since most of the drug candidates that have reached stage of development most likely do not have sufficient properties in terms of pharmacokinetics or certain aspects of MoA-related effects, an iterative process consisting of compound optimization is required. This process consists of a combination of rational design and semi-rational design elements. Rational design, for example includes the introduction or replacement of certain amino acids to improve certain traits like proteolytic stability or membrane permeability based on existing knowledge, whereas semi-rational approaches, i.e., focus on construction and screening of large libraries. The latter could be realized i.e., by array slide analysis to optimize target affinities.

The repeated cycles of compound screening and rational as well as semi-rational drug design will ultimately result in an optimized compound that has a high chance of success in the subsequent testing in *in vivo* disease models for proof-of-concept (PoC) studies.

## 4 Summary

Based on the phage display method, peptide ligands for therapeutically relevant target proteins were identified in this work. To identify variants with high affinity, the phage display method was extended to include positive and negative controls and coupled with NGS and subsequent cluster analysis. The resulting screening system was then successfully applied to several projects with different target proteins. The obtained sequence variants were analyzed with respect to binding affinities, but also screened *in vitro* for MoA-related effects. In this way, lead sequences were identified and partially optimized by rational design. Screening for MoA-related effects allowed the identification of the most promising candidates for future therapeutic or diagnostic applications.

In the first project, a mirror-phage display selection was performed on the target protein  $\alpha$ -syn for the neurodegenerative disease PD. Fourteen peptides were identified using the NGS-based analysis system and screened for inhibitory effects using ThT-aggregation assay. The identified lead compound SVD-1 was modified in a first rational optimization (SVD-1a) and showed improved inhibitory effects under both, *de novo* and seeded aggregation conditions, while monomeric  $\alpha$ -syn was stabilized in presence of the compound. Moreover, the addition of SVD-1a was shown to destabilize PFF  $\alpha$ -syn oligomers, leading to the recovery and stabilization of the physiological monomer. Finally, SPR and MST measurements were used to demonstrate a high affinity interaction of the compounds with the monomer. In addition,  $^1\text{H}$ - $^{15}\text{N}$  HSQC and NMR-PRE-measurements demonstrated that the interaction occurs along the entire  $\alpha$ -syn monomer, with a focus on the C-terminal region. This study not only provides insight into the development of anti-prionic compounds for PD, but also provides a general understanding of how peptide compounds interact with and stabilize IDP targets.

In the second project, which focused on SARS-CoV-2, the interaction of the spike protein with hACE2 was elucidated in detail by kinetic characterization. This led to the finding that the interaction consists of a transition of the primary complex to a secondary state, which may be a critical factor for the transmission efficiency of the virus and may be modulated between different VOCs. Following these findings, phage display selection with the RBD protein of the SARS-CoV-2 spike protein was performed, resulting in the identification of five highly conserved peptide ligand sequences. Screening for inhibition of the association of the spike protein with the cellular receptor hACE2 led to the identification of the CVRBDL-3 lead sequence, which was then optimized using a divalent approach. The optimization resulted not only in improved target affinity, but also in improved inhibitory activity under conditions before and after hACE2-spike protein complex formation.

In addition to the above projects, the developed phage display and NGS screening protocol has been successfully applied to other disease-related target proteins such as

## Summary

SARS-CoV-2 3CL<sup>pro</sup> and hSOD1. For both proteins, peptide ligands were identified that not only exhibited high affinities in *in vitro* experiments, but also showed aggregation-reducing (hSOD1) or enzymatic activity-inhibiting (SARS-CoV-2 3CL<sup>pro</sup>) properties when screened for MoA-related effects. To improve proteolytic stability, SARS-CoV-2 3CL<sup>pro</sup> peptide ligands were also optimized using a retro-inverso strategy. Here, it was demonstrated that the binding site of the retro-inverso peptides is conserved compared to the L-enantiomeric counterpart. This result confirms that the retro-inverso strategy in combination with phage display is an efficient method to generate high-affinity D-enantiomeric peptide ligands.

In the final project,  $\alpha$ -syn fibrils were used as a target structure for phage display. In contrast to the above projects, peptide ligands with potential use for PD diagnostic were identified. The resulting lead sequence SVLfib-5 showed binding affinity primarily toward aggregated  $\alpha$ -syn fractions with lower  $M_w$ , potentially targeting oligomeric conformers.

In conclusion, this work provides a strategy for identifying, characterizing, and optimizing peptide ligands for therapeutic and diagnostic applications starting from phage display libraries. Using the described selection and screening strategy, high-affinity and proteolytically stable peptide ligands can be generated, which will represent a new and highly efficient drug class in the therapy of various diseases in the future.

## 5 References

1. Tysnes, O.B. and A. Storstein, *Epidemiology of Parkinson's disease*. Journal of Neural Transmission, 2017. **124**(8): p. 901-905.
2. Elbaz, A., et al., *Risk tables for parkinsonism and Parkinson's disease*. Journal of Clinical Epidemiology, 2002. **55**(1): p. 25-31.
3. Elbaz, A., et al., *Epidemiology of Parkinson's disease*. Revue Neurologique, 2016. **172**(1): p. 14-26.
4. Ma, C.L., et al., *The prevalence and incidence of Parkinson's disease in China: a systematic review and meta-analysis*. Journal of Neural Transmission, 2014. **121**(2): p. 123-134.
5. Dorsey, E.R., et al., *Projected number of people with Parkinson disease in the most populous nations, 2005 through 2030*. Neurology, 2007. **68**(5): p. 384-386.
6. Poewe, W., et al., *Parkinson disease*. Nature Reviews Disease Primers, 2017. **3**.
7. Xia, R.P. and Z.H. Mao, *Progression of motor symptoms in Parkinson's disease*. Neuroscience Bulletin, 2012. **28**(1): p. 39-48.
8. Tolosa, E., G. Wenning, and W. Poewe, *The diagnosis of Parkinson's disease*. Lancet Neurology, 2006. **5**(1): p. 75-86.
9. Alcalay, R.N., et al., *Frequency of Known Mutations in Early-Onset Parkinson Disease*. Archives of Neurology, 2010. **67**(9): p. 1116-1122.
10. Marsden, C.D., *Parkinson's disease*. Lancet, 1990. **335**(8695): p. 948-52.
11. Fearnley J.M., L.A.J., *Ageing and Parkinson's disease: substantia nigra regional selectivity*. Brain Research, 1991. **114**: p. 2283-2301.
12. Stacy, M., *Nonmotor Symptoms in Parkinson's Disease*. International Journal of Neuroscience, 2011. **121**: p. 9-17.
13. Hawkes, C.H., *The Prodromal Phase of Sporadic Parkinson's Disease: Does It Exist and If So How Long Is It?* Movement Disorders, 2008. **23**(13): p. 1799-1807.
14. Guzman, J.N., et al., *Robust Pacemaking in Substantia Nigra Dopaminergic Neurons*. Journal of Neuroscience, 2009. **29**(35): p. 11011-11019.
15. Braak, H., et al., *Staging of brain pathology related to sporadic Parkinson's disease*. Neurobiology of Aging, 2003. **24**(2): p. 197-211.
16. Goedert, M., et al., *100 years of Lewy pathology*. Nature Reviews Neurology, 2013. **9**(1): p. 13-24.
17. Good, P.F., et al., *Protein nitration in Parkinson's disease*. Journal of Neuropathology and Experimental Neurology, 1998. **57**(4): p. 338-342.
18. Kuzuhara, S., et al., *Lewy Bodies Are Ubiquitinated - a Light and Electron-Microscopic Immunocytochemical Study*. Acta Neuropathologica, 1988. **75**(4): p. 345-353.
19. Billingsley, K.J., et al., *Genetic risk factors in Parkinson's disease*. Cell and Tissue Research, 2018. **373**(1): p. 9-20.
20. Nalls, M.A., et al., *Large-scale meta-analysis of genome-wide association data identifies six new risk loci for Parkinson's disease*. Nature Genetics, 2014. **46**(9): p. 989-+.
21. Domingo, A. and C. Klein, *Genetics of Parkinson disease*. Handb Clin Neurol, 2018. **147**: p. 211-227.

## References

22. Maroteaux, L., J.T. Campanelli, and R.H. Scheller, *Synuclein - a Neuron-Specific Protein Localized to the Nucleus and Presynaptic Nerve-Terminal*. Journal of Neuroscience, 1988. **8**(8): p. 2804-2815.
23. Ueda, K., et al., *Molecular-Cloning of Cdna-Encoding an Unrecognized Component of Amyloid in Alzheimer-Disease*. Proceedings of the National Academy of Sciences of the United States of America, 1993. **90**(23): p. 11282-11286.
24. Clayton, D.F. and J.M. George, *The synucleins: a family of proteins involved in synaptic function, plasticity, neurodegeneration and disease*. Trends in Neurosciences, 1998. **21**(6): p. 249-254.
25. Weinreb, P.H., et al., *NACP, a protein implicated in Alzheimer's disease and learning, is natively unfolded*. Biochemistry, 1996. **35**(43): p. 13709-13715.
26. Burre, J., M. Sharma, and T.C. Sudhof, *Cell Biology and Pathophysiology of alpha-Synuclein*. Cold Spring Harbor Perspectives in Medicine, 2018. **8**(3).
27. Cheng, F.R., G. Vivacqua, and S. Yu, *The role of alpha-synuclein in neurotransmission and synaptic plasticity*. Journal of Chemical Neuroanatomy, 2011. **42**(4): p. 242-248.
28. Ulmer, T.S., et al., *Structure and dynamics of micelle-bound human alpha-synuclein*. Journal of Biological Chemistry, 2005. **280**(10): p. 9595-9603.
29. Fusco, G., et al., *Direct observation of the three regions in alpha-synuclein that determine its membrane-bound behaviour*. Nature Communications, 2014. **5**.
30. Fusco, G., et al., *Structural basis of synaptic vesicle assembly promoted by alpha-synuclein (vol 7, 12563, 2016)*. Nature Communications, 2017. **8**.
31. Segrest, J.P., et al., *Amphipathic Helix Motif - Classes and Properties*. Proteins-Structure Function and Genetics, 1990. **8**(2): p. 103-117.
32. George, J.M., et al., *Characterization of a Novel Protein Regulated during the Critical Period for Song Learning in the Zebra Finch*. Neuron, 1995. **15**(2): p. 361-372.
33. Davidson, W.S., et al., *Stabilization of alpha-synuclein secondary structure upon binding to synthetic membranes*. Journal of Biological Chemistry, 1998. **273**(16): p. 9443-9449.
34. Park, S.M., et al., *Distinct roles of the N-terminal-binding domain and the C-terminal-solubilizing domain of alpha-synuclein, a molecular chaperone*. Journal of Biological Chemistry, 2002. **277**(32): p. 28512-28520.
35. Souza, J.M., et al., *Chaperone-like activity of synucleins*. Febs Letters, 2000. **474**(1): p. 116-119.
36. Robotta, M., et al., *Alpha-Synuclein Binds to the Inner Membrane of Mitochondria in an alpha-Helical Conformation*. Chembiochem, 2014. **15**(17): p. 2499-2502.
37. Oikawa, T., et al., *alpha-Synuclein Fibrils Exhibit Gain of Toxic Function, Promoting Tau Aggregation and Inhibiting Microtubule Assembly*. Journal of Biological Chemistry, 2016. **291**(29): p. 15046-15056.
38. Tuttle, M.D., et al., *Solid-state NMR structure of a pathogenic fibril of full-length human alpha-synuclein*. Nature Structural & Molecular Biology, 2016. **23**(5): p. 409-415.
39. Binolfi, A., F.X. Theillet, and P. Selenko, *Bacterial in-cell NMR of human alpha-synuclein: a disordered monomer by nature?* Biochemical Society Transactions, 2012. **40**: p. 950-U292.
40. Bartels, T. and D.J. Selkoe, *Properties of native brain alpha-synuclein Reply*. Nature, 2013. **498**(7453): p. E6-E7.

## References

41. Fauvet, B., et al., *alpha-Synuclein in Central Nervous System and from Erythrocytes, Mammalian Cells, and Escherichia coli Exists Predominantly as Disordered Monomer*. Journal of Biological Chemistry, 2012. **287**(19): p. 15345-15364.
42. Theillet, F.X., et al., *Structural disorder of monomeric alpha-synuclein persists in mammalian cells*. European Biophysics Journal with Biophysics Letters, 2017. **46**: p. S396-S396.
43. Mehra, S., S. Sahay, and S.K. Maji, *alpha-Synuclein misfolding and aggregation: Implications in Parkinson's disease pathogenesis*. Biochim Biophys Acta Proteins Proteom, 2019. **1867**(10): p. 890-908.
44. Ferreon, A.C.M., et al., *Interplay of alpha-synuclein binding and conformational switching probed by single-molecule fluorescence*. Proceedings of the National Academy of Sciences of the United States of America, 2009. **106**(14): p. 5645-5650.
45. Frimpong, A.K., et al., *Characterization of intrinsically disordered proteins with electrospray ionization mass spectrometry: Conformational heterogeneity of alpha-synuclein*. Proteins-Structure Function and Bioinformatics, 2010. **78**(3): p. 714-722.
46. Lassen, L.B., et al., *Protein Partners of alpha-Synuclein in Health and Disease*. Brain Pathology, 2016. **26**(3): p. 389-397.
47. Linse, S., *Secondary nucleation in amyloid formation*. Febs Open Bio, 2019. **9**: p. 3-4.
48. Alam, P., et al., *alpha-synuclein oligomers and fibrils: a spectrum of species, a spectrum of toxicities*. Journal of Neurochemistry, 2019. **150**(5): p. 522-534.
49. Kollmer, M., et al., *Cryo-EM structure and polymorphism of A beta amyloid fibrils purified from Alzheimer's brain tissue*. Nature Communications, 2019. **10**.
50. Nordstedt, C., et al., *The Alzheimer a-Beta-Peptide Develops Protease Resistance in Association with Its Polymerization into Fibrils*. Journal of Biological Chemistry, 1994. **269**(49): p. 30773-30776.
51. Owen, M.C., et al., *Effects of in vivo conditions on amyloid aggregation*. Chemical Society Reviews, 2019. **48**(14): p. 3946-3996.
52. Buell, A.K., et al., *Solution conditions determine the relative importance of nucleation and growth processes in alpha-synuclein aggregation*. Proceedings of the National Academy of Sciences of the United States of America, 2014. **111**(21): p. 7671-7676.
53. Gaspar, R., et al., *Secondary nucleation of monomers on fibril surface dominates alpha-synuclein aggregation and provides autocatalytic amyloid amplification*. Q Rev Biophys, 2017. **50**: p. e6.
54. Meisl, G., et al., *Molecular mechanisms of protein aggregation from global fitting of kinetic models*. Nature Protocols, 2016. **11**(2): p. 252-272.
55. Polymeropoulos, M.H., et al., *Mutation in the alpha-synuclein gene identified in families with Parkinson's disease*. Science, 1997. **276**(5321): p. 2045-2047.
56. Ohgita, T., et al., *Mechanisms of enhanced aggregation and fibril formation of Parkinson's disease-related variants of alpha-synuclein*. Sci Rep, 2022. **12**(1): p. 6770.
57. Wang, C.S., et al., *alpha-Synuclein in alpha-helical conformation at air-water interface: implication of conformation and orientation changes during its accumulation/aggregation*. Chemical Communications, 2010. **46**(36): p. 6702-6704.
58. Campioni, S., et al., *The Presence of an Air-Water Interface Affects Formation and Elongation of alpha-Synuclein Fibrils*. Journal of the American Chemical Society, 2014. **136**(7): p. 2866-2875.
59. Antony, T., et al., *Cellular polyamines promote the aggregation of alpha-synuclein*. Journal of Biological Chemistry, 2003. **278**(5): p. 3235-3240.

## References

60. Galvagnion, C., et al., *Lipid vesicles trigger alpha-synuclein aggregation by stimulating primary nucleation*. Nature Chemical Biology, 2015. **11**(3): p. 229-U101.
61. Giehm, L., et al., *SDS-Induced Fibrillation of alpha-Synuclein: An Alternative Fibrillation Pathway*. Journal of Molecular Biology, 2010. **401**(1): p. 115-133.
62. Ischiropoulos, H., *Oxidative modifications of alpha-synuclein*. Parkinson's Disease: The Life Cycle of the Dopamine Neuron, 2003. **991**: p. 93-100.
63. Cremades, N., et al., *Direct Observation of the Interconversion of Normal and Toxic Forms of alpha-Synuclein*. Cell, 2012. **149**(5): p. 1048-1059.
64. Lashuel, H.A., et al., *alpha-synuclein, especially the Parkinson's disease-associated mutants, forms pore-like annular and tubular protofibrils*. Journal of Molecular Biology, 2002. **322**(5): p. 1089-1102.
65. Cremades, N., S.W. Chen, and C.M. Dobson, *Structural Characteristics of alpha-Synuclein Oligomers*. Early Stage Protein Misfolding and Amyloid Aggregation, 2017. **329**: p. 79-143.
66. Andersen, C.B., et al., *How epigallocatechin gallate binds and assembles oligomeric forms of human alpha-synuclein*. J Biol Chem, 2021. **296**: p. 100788.
67. Pieri, L., K. Madiona, and R. Melki, *Structural and functional properties of prefibrillar alpha-synuclein oligomers*. Scientific Reports, 2016. **6**.
68. Ruesink, H., et al., *Stabilization of alpha-synuclein oligomers using formaldehyde*. PLoS One, 2019. **14**(10): p. e0216764.
69. Hayden, E.Y., et al., *Heme Stabilization of alpha-Synuclein Oligomers during Amyloid Fibril Formation*. Biochemistry, 2015. **54**(30): p. 4599-610.
70. Fischer, A.F. and K.M. Matera, *Stabilization of Alpha-Synuclein Oligomers In Vitro by the Neurotransmitters, Dopamine and Norepinephrine: The Effect of Oxidized Catecholamines*. Neurochem Res, 2015. **40**(7): p. 1341-9.
71. Hong, D.P., A.L. Fink, and V.N. Uversky, *Structural Characteristics of alpha-Synuclein Oligomers Stabilized by the Flavonoid Baicalein*. Journal of Molecular Biology, 2008. **383**(1): p. 214-223.
72. Lorenzen, N., et al., *The Role of Stable alpha-Synuclein Oligomers in the Molecular Events Underlying Amyloid Formation*. Journal of the American Chemical Society, 2014. **136**(10): p. 3859-3868.
73. Paslawski, W., N. Lorenzen, and D.E. Otzen, *Formation and Characterization of alpha-Synuclein Oligomers*. Protein Amyloid Aggregation: Methods and Protocols, 2016. **1345**: p. 133-150.
74. Campioni, S., et al., *The presence of an air-water interface affects formation and elongation of alpha-Synuclein fibrils*. J Am Chem Soc, 2014. **136**(7): p. 2866-75.
75. Celej, M.S., et al., *Toxic prefibrillar alpha-synuclein amyloid oligomers adopt a distinctive antiparallel beta-sheet structure*. Biochem J, 2012. **443**(3): p. 719-26.
76. Chen, T., et al., *[Effect of curcumin on oligomer formation and mitochondrial ATP-sensitive potassium channels induced by overexpression or mutation of alpha-synuclein]*. Zhonghua Yi Xue Yi Chuan Xue Za Zhi, 2015. **32**(4): p. 462-7.
77. Zijlstra, N., et al., *Molecular composition of sub-stoichiometrically labeled alpha-synuclein oligomers determined by single-molecule photobleaching*. Angew Chem Int Ed Engl, 2012. **51**(35): p. 8821-4.
78. Gallea, J.I. and M.S. Celej, *Structural insights into amyloid oligomers of the Parkinson disease-related protein alpha-synuclein*. J Biol Chem, 2014. **289**(39): p. 26733-26742.

## References

79. van Rooijen, B.D., M.M. Claessens, and V. Subramaniam, *Lipid bilayer disruption by oligomeric alpha-synuclein depends on bilayer charge and accessibility of the hydrophobic core*. *Biochim Biophys Acta*, 2009. **1788**(6): p. 1271-8.
80. Paslawski, W., et al., *High stability and cooperative unfolding of alpha-synuclein oligomers*. *Biochemistry*, 2014. **53**(39): p. 6252-63.
81. Giehm, L., et al., *Low-resolution structure of a vesicle disrupting alpha-synuclein oligomer that accumulates during fibrillation*. *Proceedings of the National Academy of Sciences of the United States of America*, 2011. **108**(8): p. 3246-3251.
82. Chen, S.W., et al., *Structural characterization of toxic oligomers that are kinetically trapped during alpha-synuclein fibril formation*. *Protein Science*, 2015. **24**: p. 136-136.
83. Sharon, R., et al., *The formation of highly soluble oligomers of alpha-synuclein is regulated by fatty acids and enhanced in Parkinson's disease*. *Neuron*, 2003. **37**(4): p. 583-595.
84. Tofaris, G.K., et al., *Ubiquitination of alpha-synuclein in Lewy bodies is a pathological event not associated with impairment of proteasome function*. *Journal of Biological Chemistry*, 2003. **278**(45): p. 44405-44411.
85. Giasson, B.I., et al., *Neuronal alpha-synucleinopathy with severe movement disorder in mice expressing A53T human alpha-synuclein*. *Neuron*, 2002. **34**(4): p. 521-33.
86. Chen, L., et al., *Oligomeric alpha-synuclein inhibits tubulin polymerization*. *Biochem Biophys Res Commun*, 2007. **356**(3): p. 548-53.
87. Danzer, K.M., et al., *Different species of alpha-synuclein oligomers induce calcium influx and seeding*. *J Neurosci*, 2007. **27**(34): p. 9220-32.
88. Nasstrom, T., et al., *The lipid peroxidation products 4-oxo-2-nonenal and 4-hydroxy-2-nonenal promote the formation of alpha-synuclein oligomers with distinct biochemical, morphological, and functional properties*. *Free Radic Biol Med*, 2011. **50**(3): p. 428-37.
89. Tetzlaff, J.E., et al., *CHIP targets toxic alpha-Synuclein oligomers for degradation*. *J Biol Chem*, 2008. **283**(26): p. 17962-8.
90. Karpinar, D.P., et al., *Pre-fibrillar alpha-synuclein variants with impaired beta-structure increase neurotoxicity in Parkinson's disease models*. *EMBO J*, 2009. **28**(20): p. 3256-68.
91. Volles, M.J., et al., *Vesicle permeabilization by protofibrillar alpha-synuclein: implications for the pathogenesis and treatment of Parkinson's disease*. *Biochemistry*, 2001. **40**(26): p. 7812-9.
92. Volles, M.J. and P.T. Lansbury, Jr., *Vesicle permeabilization by protofibrillar alpha-synuclein is sensitive to Parkinson's disease-linked mutations and occurs by a pore-like mechanism*. *Biochemistry*, 2002. **41**(14): p. 4595-602.
93. Burre, J., *The Synaptic Function of alpha-Synuclein*. *J Parkinsons Dis*, 2015. **5**(4): p. 699-713.
94. Diogenes, M.J., et al., *Extracellular alpha-synuclein oligomers modulate synaptic transmission and impair LTP via NMDA-receptor activation*. *J Neurosci*, 2012. **32**(34): p. 11750-62.
95. Kaufmann, T.J., et al., *Intracellular soluble alpha-synuclein oligomers reduce pyramidal cell excitability*. *Journal of Physiology-London*, 2016. **594**(10): p. 2751-2772.
96. Klucken, J., et al., *Alpha-synuclein aggregation involves a bafilomycin A 1-sensitive autophagy pathway*. *Autophagy*, 2012. **8**(5): p. 754-66.
97. Bliederhaeuser, C., et al., *Age-dependent defects of alpha-synuclein oligomer uptake in microglia and monocytes*. *Acta Neuropathol*, 2016. **131**(3): p. 379-91.

## References

98. Parihar, M.S., et al., *Alpha-synuclein overexpression and aggregation exacerbates impairment of mitochondrial functions by augmenting oxidative stress in human neuroblastoma cells*. Int J Biochem Cell Biol, 2009. **41**(10): p. 2015-24.
99. Di Maio, R., et al., *alpha-Synuclein binds to TOM20 and inhibits mitochondrial protein import in Parkinson's disease*. Science Translational Medicine, 2016. **8**(342).
100. Colla, E., et al., *Accumulation of Toxic alpha-Synuclein Oligomer within Endoplasmic Reticulum Occurs in alpha-Synucleinopathy In Vivo*. Journal of Neuroscience, 2012. **32**(10): p. 3301-3305.
101. Zhang, W., et al., *Aggregated alpha-synuclein activates microglia: a process leading to disease progression in Parkinson's disease*. FASEB J, 2005. **19**(6): p. 533-42.
102. Wilms, H., et al., *Suppression of MAP kinases inhibits microglial activation and attenuates neuronal cell death induced by alpha-synuclein protofibrils*. Int J Immunopathol Pharmacol, 2009. **22**(4): p. 897-909.
103. Spillantini, M.G., et al., *Filamentous alpha-synuclein inclusions link multiple system atrophy with Parkinson's disease and dementia with Lewy bodies*. Neuroscience Letters, 1998. **251**(3): p. 205-208.
104. Spillantini, M.G., et al., *alpha-synuclein in filamentous inclusions of Lewy bodies from Parkinson's disease and dementia with Lewy bodies*. Proceedings of the National Academy of Sciences of the United States of America, 1998. **95**(11): p. 6469-6473.
105. Vilar, M., et al., *The fold of alpha-synuclein fibrils*. Proc Natl Acad Sci U S A, 2008. **105**(25): p. 8637-42.
106. Peng, C., et al., *Cellular milieu imparts distinct pathological alpha-synuclein strains in alpha-synucleinopathies*. Nature, 2018. **557**(7706): p. 558-563.
107. Bousset, L., et al., *Structural and functional characterization of two alpha-synuclein strains*. Nature Communications, 2013. **4**.
108. Peelaerts, W., et al., *alpha-Synuclein strains cause distinct synucleinopathies after local and systemic administration*. Nature, 2015. **522**(7556): p. 340-+.
109. Der-Sarkissian, A., et al., *Structural organization of alpha-synuclein fibrils studied by site-directed spin labeling*. J Biol Chem, 2003. **278**(39): p. 37530-5.
110. Rodriguez, J.A., et al., *Structure of the toxic core of alpha-synuclein from invisible crystals*. Nature, 2015. **525**(7570): p. 486-90.
111. Li, B., et al., *Cryo-EM of full-length alpha-synuclein reveals fibril polymorphs with a common structural kernel*. Nat Commun, 2018. **9**(1): p. 3609.
112. Flavin, W.P., et al., *Endocytic vesicle rupture is a conserved mechanism of cellular invasion by amyloid proteins*. Acta Neuropathol, 2017. **134**(4): p. 629-653.
113. Gustot, A., et al., *Amyloid fibrils are the molecular trigger of inflammation in Parkinson's disease*. Biochem J, 2015. **471**(3): p. 323-33.
114. Hoffmann, A., et al., *Alpha-synuclein activates BV2 microglia dependent on its aggregation state*. Biochem Biophys Res Commun, 2016. **479**(4): p. 881-886.
115. Ramos, J.M.P., et al., *Peripheral Inflammation Regulates CNS Immune Surveillance Through the Recruitment of Inflammatory Monocytes Upon Systemic alpha-Synuclein Administration*. Frontiers in Immunology, 2019. **10**.
116. Gribaudo, S., et al., *Propagation of alpha-Synuclein Strains within Human Reconstructed Neuronal Network*. Stem Cell Reports, 2019. **12**(2): p. 230-244.
117. Brettschneider, J., et al., *Spreading of pathology in neurodegenerative diseases: a focus on human studies*. Nat Rev Neurosci, 2015. **16**(2): p. 109-20.

## References

118. Luk, K.C., et al., *Pathological alpha-synuclein transmission initiates Parkinson-like neurodegeneration in nontransgenic mice*. *Science*, 2012. **338**(6109): p. 949-53.
119. Mougenot, A.L., et al., *Prion-like acceleration of a synucleinopathy in a transgenic mouse model*. *Neurobiol Aging*, 2012. **33**(9): p. 2225-8.
120. Prusiner, S.B., *Novel proteinaceous infectious particles cause scrapie*. *Science*, 1982. **216**(4542): p. 136-44.
121. Prusiner, S.B., *Biology and genetics of prions causing neurodegeneration*. *Annu Rev Genet*, 2013. **47**: p. 601-23.
122. Johnson, R.T., *Prion diseases*. *Lancet Neurology*, 2005. **4**(10): p. 635-642.
123. Imran, M. and S. Mahmood, *An overview of animal prion diseases*. *Virology*, 2011. **8**: p. 493.
124. Imran, M. and S. Mahmood, *An overview of human prion diseases*. *Virology*, 2011. **8**: p. 559.
125. Prusiner, S.B., *Prions*. *Proc Natl Acad Sci U S A*, 1998. **95**(23): p. 13363-83.
126. Jucker, M. and L.C. Walker, *Self-propagation of pathogenic protein aggregates in neurodegenerative diseases*. *Nature*, 2013. **501**(7465): p. 45-51.
127. Meyer-Luehmann, M., et al., *Exogenous induction of cerebral beta-amyloidogenesis is governed by agent and host*. *Science*, 2006. **313**(5794): p. 1781-4.
128. Goedert, M., et al., *Prion-like mechanisms in the pathogenesis of tauopathies and synucleinopathies*. *Curr Neurol Neurosci Rep*, 2014. **14**(11): p. 495.
129. Pearce, M.M.P. and R.R. Kopito, *Prion-Like Characteristics of Polyglutamine-Containing Proteins*. *Cold Spring Harb Perspect Med*, 2018. **8**(2).
130. Polymenidou, M. and D.W. Cleveland, *The seeds of neurodegeneration: prion-like spreading in ALS*. *Cell*, 2011. **147**(3): p. 498-508.
131. Kordower, J.H., et al., *Lewy body-like pathology in long-term embryonic nigral transplants in Parkinson's disease*. *Nat Med*, 2008. **14**(5): p. 504-6.
132. Kordower, J.H., et al., *Transplanted dopaminergic neurons develop PD pathologic changes: a second case report*. *Mov Disord*, 2008. **23**(16): p. 2303-6.
133. Li, J.Y., et al., *Lewy bodies in grafted neurons in subjects with Parkinson's disease suggest host-to-graft disease propagation*. *Nat Med*, 2008. **14**(5): p. 501-3.
134. Luk, K.C., et al., *Intracerebral inoculation of pathological alpha-synuclein initiates a rapidly progressive neurodegenerative alpha-synucleinopathy in mice*. *J Exp Med*, 2012. **209**(5): p. 975-86.
135. Sorrentino, Z.A., et al., *Intrastriatal injection of alpha-synuclein can lead to widespread synucleinopathy independent of neuroanatomic connectivity*. *Mol Neurodegener*, 2017. **12**(1): p. 40.
136. Braak, H. and K. Del Tredici, *Potential Pathways of Abnormal Tau and alpha-Synuclein Dissemination in Sporadic Alzheimer's and Parkinson's Diseases*. *Cold Spring Harb Perspect Biol*, 2016. **8**(11).
137. Kim, S., et al., *Transneuronal Propagation of Pathologic alpha-Synuclein from the Gut to the Brain Models Parkinson's Disease*. *Neuron*, 2019. **103**(4): p. 627-641 e7.
138. El-Agnaf, O.M., et al., *Alpha-synuclein implicated in Parkinson's disease is present in extracellular biological fluids, including human plasma*. *FASEB J*, 2003. **17**(13): p. 1945-7.
139. El-Agnaf, O.M., et al., *Detection of oligomeric forms of alpha-synuclein protein in human plasma as a potential biomarker for Parkinson's disease*. *FASEB J*, 2006. **20**(3): p. 419-25.

## References

140. Lee, H.J., S. Patel, and S.J. Lee, *Intravesicular localization and exocytosis of alpha-synuclein and its aggregates*. J Neurosci, 2005. **25**(25): p. 6016-24.
141. Blomeke, L., et al., *Quantitative detection of alpha-Synuclein and Tau oligomers and other aggregates by digital single particle counting*. Npj Parkinsons Disease, 2022. **8**(1).
142. Jang, A., et al., *Non-classical exocytosis of alpha-synuclein is sensitive to folding states and promoted under stress conditions*. J Neurochem, 2010. **113**(5): p. 1263-74.
143. Ahn, K.J., et al., *Amino acid sequence motifs and mechanistic features of the membrane translocation of alpha-synuclein*. J Neurochem, 2006. **97**(1): p. 265-79.
144. Lee, H.J., et al., *Assembly-dependent endocytosis and clearance of extracellular alpha-synuclein*. Int J Biochem Cell Biol, 2008. **40**(9): p. 1835-49.
145. Cotzias, G.C., P.S. Papavasiliou, and R. Gellene, *Modification of Parkinsonism--chronic treatment with L-dopa*. N Engl J Med, 1969. **280**(7): p. 337-45.
146. Muller, T., *Catechol-O-Methyltransferase Inhibitors in Parkinson's Disease*. Drugs, 2015. **75**(2): p. 157-174.
147. Elmer, L.W. and J.M. Bertoni, *The increasing role of monoamine oxidase type B inhibitors in Parkinson's disease therapy*. Expert Opin Pharmacother, 2008. **9**(16): p. 2759-72.
148. McColl, C.D., et al., *Motor response to levodopa and the evolution of motor fluctuations in the first decade of treatment of Parkinson's disease*. Mov Disord, 2002. **17**(6): p. 1227-34.
149. <978-1-4939-7816-8.pdf>.
150. Seppi, K., et al., *The Movement Disorder Society Evidence-Based Medicine Review Update: Treatments for the non-motor symptoms of Parkinson's disease*. Mov Disord, 2011. **26 Suppl 3**: p. S42-80.
151. Mao, X., et al., *Pathological alpha-synuclein transmission initiated by binding lymphocyte-activation gene 3*. Science, 2016. **353**(6307).
152. Fountaine, T.M. and R. Wade-Martins, *RNA interference-mediated knockdown of alpha-synuclein protects human dopaminergic neuroblastoma cells from MPP(+)-toxicity and reduces dopamine transport*. J Neurosci Res, 2007. **85**(2): p. 351-63.
153. Mittal, S., et al., *beta2-Adrenoreceptor is a regulator of the alpha-synuclein gene driving risk of Parkinson's disease*. Science, 2017. **357**(6354): p. 891-898.
154. Fields, C.R., N. Bengoa-Vergniory, and R. Wade-Martins, *Targeting Alpha-Synuclein as a Therapy for Parkinson's Disease*. Front Mol Neurosci, 2019. **12**: p. 299.
155. Decressac, M., et al., *TFEB-mediated autophagy rescues midbrain dopamine neurons from alpha-synuclein toxicity*. Proc Natl Acad Sci U S A, 2013. **110**(19): p. E1817-26.
156. Maiese, K., et al., *mTOR: on target for novel therapeutic strategies in the nervous system*. Trends in Molecular Medicine, 2013. **19**(1): p. 51-60.
157. Webb, J.L., et al., *Alpha-Synuclein is degraded by both autophagy and the proteasome*. J Biol Chem, 2003. **278**(27): p. 25009-13.
158. Crews, L., et al., *Selective molecular alterations in the autophagy pathway in patients with Lewy body disease and in models of alpha-synucleinopathy*. PLoS One, 2010. **5**(2): p. e9313.
159. Bove, J., M. Martinez-Vicente, and M. Vila, *Fighting neurodegeneration with rapamycin: mechanistic insights*. Nat Rev Neurosci, 2011. **12**(8): p. 437-52.
160. Klucken, J., et al., *A single amino acid substitution differentiates Hsp70-dependent effects on alpha-synuclein degradation and toxicity*. Biochem Biophys Res Commun, 2004. **325**(1): p. 367-73.

## References

161. Cox, D., et al., *Small Heat-shock Proteins Prevent alpha-Synuclein Aggregation via Transient Interactions and Their Efficacy Is Affected by the Rate of Aggregation*. J Biol Chem, 2016. **291**(43): p. 22618-22629.
162. Jankovic, J., et al., *Safety and Tolerability of Multiple Ascending Doses of PRX002/RG7935, an Anti-alpha-Synuclein Monoclonal Antibody, in Patients With Parkinson Disease: A Randomized Clinical Trial*. JAMA Neurol, 2018. **75**(10): p. 1206-1214.
163. Zella, S.M.A., et al., *Emerging Immunotherapies for Parkinson Disease*. Neurol Ther, 2019. **8**(1): p. 29-44.
164. Wagner, J., et al., *Anle138b: a novel oligomer modulator for disease-modifying therapy of neurodegenerative diseases such as prion and Parkinson's disease*. Acta Neuropathologica, 2013. **125**(6): p. 795-813.
165. Levin, J., et al., *The oligomer modulator anle138b inhibits disease progression in a Parkinson mouse model even with treatment started after disease onset*. Acta Neuropathol, 2014. **127**(5): p. 779-80.
166. Deeg, A.A., et al., *Anle138b and related compounds are aggregation specific fluorescence markers and reveal high affinity binding to alpha-synuclein aggregates*. Biochim Biophys Acta, 2015. **1850**(9): p. 1884-90.
167. Price, D.L., et al., *The small molecule alpha-synuclein misfolding inhibitor, NPT200-11, produces multiple benefits in an animal model of Parkinson's disease*. Sci Rep, 2018. **8**(1): p. 16165.
168. Oelschlegel, A.M. and C. Weissmann, *Acquisition of Drug Resistance and Dependence by Prions*. Plos Pathogens, 2013. **9**(2).
169. Ghaemmaghami, S., et al., *Continuous quinacrine treatment results in the formation of drug-resistant prions*. PLoS Pathog, 2009. **5**(11): p. e1000673.
170. Yin, R.H., et al., *Prion-like Mechanisms in Alzheimer's Disease*. Current Alzheimer Research, 2014. **11**(8): p. 755-764.
171. Willbold, D. and J. Kutzsche, *Do We Need Anti-Prion Compounds to Treat Alzheimer's Disease?* Molecules, 2019. **24**(12).
172. van Groen, T., et al., *The A beta oligomer eliminating D-enantiomeric peptide RD2 improves cognition without changing plaque pathology*. Scientific Reports, 2017. **7**.
173. Wiesehan, K., et al., *Selection of D-Amino-Acid peptides that bind to Alzheimer's disease amyloid peptide A beta(1-42) by mirror image phage display*. Chembiochem, 2003. **4**(8): p. 748-753.
174. Brener, O., et al., *QIAD assay for quantitating a compound's efficacy in elimination of toxic A beta oligomers*. Scientific Reports, 2015. **5**.
175. Schemmert, S., et al., *A Oligomer Elimination Restores Cognition in Transgenic Alzheimer's Mice with Full-blown Pathology*. Molecular Neurobiology, 2019. **56**(3): p. 2211-2223.
176. Gorbalenya, A.E., et al., *The species Severe acute respiratory syndrome-related coronavirus: classifying 2019-nCoV and naming it SARS-CoV-2*. Nature Microbiology, 2020. **5**(4): p. 536-544.
177. Corman, V.M., et al., *Hosts and Sources of Endemic Human Coronaviruses*. Advances in Virus Research, Vol 100, 2018. **100**: p. 163-188.
178. Rabaan, A.A., et al., *SARS-CoV-2, SARS-CoV, and MERS-COV: A comparative overview*. Infez Med, 2020. **28**(2): p. 174-184.

## References

179. Lu, R.J., et al., *Genomic characterisation and epidemiology of 2019 novel coronavirus: implications for virus origins and receptor binding*. *Lancet*, 2020. **395**(10224): p. 565-574.
180. van Groen, T., et al., *Treatment with D3 Removes Amyloid Deposits, Reduces Inflammation, and Improves Cognition in Aged A beta PP/PS1 Double Transgenic Mice*. *Journal of Alzheimers Disease*, 2013. **34**(3): p. 609-620.
181. Wang, Z.Y., et al., *Transmission and prevention of SARS-CoV-2*. *Biochemical Society Transactions*, 2020. **48**(5): p. 2307-2316.
182. Rothe, C., et al., *Transmission of 2019-nCoV Infection from an Asymptomatic Contact in Germany*. *New England Journal of Medicine*, 2020. **382**(10): p. 970-971.
183. Muller, C.P., *Do asymptomatic carriers of SARS-COV-2 transmit the virus?* *Lancet Regional Health-Europe*, 2021. **4**.
184. Polidori, M.C., et al., *COVID-19 mortality as a fingerprint of biological age*. *Ageing Research Reviews*, 2021. **67**.
185. Billah, M.A., M.M. Miah, and M.N. Khan, *Reproductive number of coronavirus: A systematic review and meta-analysis based on global level evidence*. *Plos One*, 2020. **15**(11).
186. Standl, F., et al., *Comparing SARS-CoV-2 with SARS-CoV and influenza pandemics*. *Lancet Infectious Diseases*, 2021. **21**(4): p. E77-E77.
187. Li, Q., et al., *Early Transmission Dynamics in Wuhan, China, of Novel Coronavirus-Infected Pneumonia*. *N Engl J Med*, 2020. **382**(13): p. 1199-1207.
188. Lin, L., et al., *Hypothesis for potential pathogenesis of SARS-CoV-2 infection-a review of immune changes in patients with viral pneumonia*. *Emerging Microbes & Infections*, 2020. **9**(1): p. 727-732.
189. Tay, M.Z., et al., *The trinity of COVID-19: immunity, inflammation and intervention*. *Nature Reviews Immunology*, 2020. **20**(6): p. 363-374.
190. Domingo, P., et al., *The four horsemen of a viral Apocalypse: The pathogenesis of SARS-CoV-2 infection (COVID-19)*. *Ebiomedicine*, 2020. **58**.
191. Alhazzani, W., et al., *Surviving Sepsis Campaign: Guidelines on the Management of Critically Ill Adults with Coronavirus Disease 2019 (COVID-19)*. *Critical Care Medicine*, 2020. **48**(6): p. E440-E469.
192. Hoffmann, M., et al., *SARS-CoV-2 Cell Entry Depends on ACE2 and TMPRSS2 and Is Blocked by a Clinically Proven Protease Inhibitor*. *Cell*, 2020. **181**(2): p. 271-280 e8.
193. Wang, Q., et al., *Structural and Functional Basis of SARS-CoV-2 Entry by Using Human ACE2*. *Cell*, 2020. **181**(4): p. 894-904 e9.
194. Hoffmann, M., H. Kleine-Weber, and S. Pohlmann, *A Multibasic Cleavage Site in the Spike Protein of SARS-CoV-2 Is Essential for Infection of Human Lung Cells*. *Molecular Cell*, 2020. **78**(4): p. 779-+.
195. Cantuti-Castelvetri, L., et al., *Neuropilin-1 facilitates SARS-CoV-2 cell entry and infectivity*. *Science*, 2020. **370**(6518): p. 856-860.
196. Zhu, W., et al., *Viral Proteases as Targets for Coronavirus Disease 2019 Drug Development*. *Journal of Pharmacology and Experimental Therapeutics*, 2021. **378**(2): p. 166-172.
197. Perlman, S. and J. Netland, *Coronaviruses post-SARS: update on replication and pathogenesis*. *Nature Reviews Microbiology*, 2009. **7**(6): p. 439-450.
198. V'kovski, P., et al., *Determination of host proteins composing the microenvironment of coronavirus replicase complexes by proximity-labeling*. *Elife*, 2019. **8**.

## References

199. Sola, I., et al., *Continuous and Discontinuous RNA Synthesis in Coronaviruses*. Annual Review of Virology, Vol 2, 2015. **2**: p. 265-288.
200. de Haan, C.A.M. and P.J.M. Rottier, *Molecular interactions in the assembly of coronaviruses*. Virus Structure and Assembly, 2005. **64**: p. 165-230.
201. Redondo, N., et al., *SARS-CoV-2 Accessory Proteins in Viral Pathogenesis: Knowns and Unknowns*. Frontiers in Immunology, 2021. **12**.
202. Kopecky-Bromberg, S.A., et al., *Severe acute respiratory syndrome coronavirus open reading frame (ORF) 3b, ORF 6, and nucleocapsid proteins function as interferon antagonists*. Journal of Virology, 2007. **81**(2): p. 548-557.
203. Wrapp, D., et al., *Cryo-EM structure of the 2019-nCoV spike in the prefusion conformation*. Science, 2020. **367**(6483): p. 1260-1263.
204. Ismail, A.M. and A.A. Elfiky, *SARS-CoV-2 spike behavior in situ: a Cryo-EM images for a better understanding of the COVID-19 pandemic*. Signal Transduction and Targeted Therapy, 2020. **5**(1).
205. Gupta, D., et al., *Structural and functional insights into the spike protein mutations of emerging SARS-CoV-2 variants*. Cellular and Molecular Life Sciences, 2021. **78**(24): p. 7967-7989.
206. V'kovski, P., et al., *Coronavirus biology and replication: implications for SARS-CoV-2*. Nature Reviews Microbiology, 2021. **19**(3): p. 155-170.
207. Cai, Y.F., et al., *Distinct conformational states of SARS-CoV-2 spike protein*. Science, 2020. **369**(6511): p. 1586-+.
208. Patel, S., et al., *Renin-angiotensin-aldosterone (RAAS): The ubiquitous system for homeostasis and pathologies*. Biomedicine & Pharmacotherapy, 2017. **94**: p. 317-325.
209. Lan, J., et al., *Structure of the SARS-CoV-2 spike receptor-binding domain bound to the ACE2 receptor*. Nature, 2020. **581**(7807): p. 215-220.
210. Korber, B., et al., *Tracking Changes in SARS-CoV-2 Spike: Evidence that D614G Increases Infectivity of the COVID-19 Virus*. Cell, 2020. **182**(4): p. 812-+.
211. Zhang, L., et al., *The D614G mutation in the SARS-CoV-2 spike protein reduces S1 shedding and increases infectivity*. bioRxiv, 2020.
212. Tian, F., et al., *N501Y mutation of spike protein in SARS-CoV-2 strengthens its binding to receptor ACE2*. Elife, 2021. **10**.
213. Khan, A., et al., *Higher infectivity of the SARS-CoV-2 new variants is associated with K417N/T, E484K, and N501Y mutants: An insight from structural data*. Journal of Cellular Physiology, 2021. **236**(10): p. 7045-7057.
214. Thomson, E.C., et al., *Circulating SARS-CoV-2 spike N439K variants maintain fitness while evading antibody-mediated immunity*. Cell, 2021. **184**(5): p. 1171-+.
215. Singh, A., et al., *Serine 477 plays a crucial role in the interaction of the SARS-CoV-2 spike protein with the human receptor ACE2*. Scientific Reports, 2021. **11**(1).
216. Alenquer, M., et al., *Signatures in SARS-CoV-2 spike protein conferring escape to neutralizing antibodies*. Plos Pathogens, 2021. **17**(8).
217. Wise, J., *Covid-19: The E484K mutation and the risks it poses*. Bmj-British Medical Journal, 2021. **372**.
218. Kullappan, M., et al., *Elucidating the role of N440K mutation in SARS-CoV-2 spike - ACE-2 binding affinity and COVID-19 severity by virtual screening, molecular docking and dynamics approach*. J Biomol Struct Dyn, 2021: p. 1-18.
219. Li, Q.Q., et al., *The Impact of Mutations in SARS-CoV-2 Spike on Viral Infectivity and Antigenicity*. Cell, 2020. **182**(5): p. 1284-+.

## References

220. Lubinski, B., et al., *Functional evaluation of the P681H mutation on the proteolytic activation of the SARS-CoV-2 variant B.1.1.7 (Alpha) spike*. *iScience*, 2022. **25**(1): p. 103589.
221. Altuntas, F., et al., *Convalescent plasma therapy in patients with COVID-19*. *Transfusion and Apheresis Science*, 2021. **60**(1).
222. Chen, R.E., et al., *In vivo monoclonal antibody efficacy against SARS-CoV-2 variant strains*. *Nature*, 2021. **596**(7870): p. 103-+.
223. Vangeel, L., et al., *Remdesivir, Molnupiravir and Nirmatrelvir remain active against SARS-CoV-2 Omicron and other variants of concern*. *Antiviral Res*, 2022. **198**: p. 105252.
224. Mahase, E., *Covid-19: Pfizer's paxlovid is 89% effective in patients at risk of serious illness, company reports*. *Bmj-British Medical Journal*, 2021. **375**.
225. Gordon, C.J., et al., *Molnupiravir promotes SARS-CoV-2 mutagenesis via the RNA template*. *Journal of Biological Chemistry*, 2021. **297**(1).
226. Agostini, M.L., et al., *Coronavirus Susceptibility to the Antiviral Remdesivir (GS-5734) Is Mediated by the Viral Polymerase and the Proofreading Exoribonuclease*. *Mbio*, 2018. **9**(2).
227. Sevenich, M., et al., *Phage Display-Derived Compounds Displace hACE2 from Its Complex with SARS-CoV-2 Spike Protein*. *Biomedicines*, 2022. **10**(2).
228. Markham, A., *Fostemsavir: First Approval*. *Drugs*, 2020. **80**(14): p. 1485-1490.
229. Yang, J.Z., et al., *Successful virologic outcomes over time among HAART-treated HIV-infected patients*. *Aids Care-Psychological and Socio-Medical Aspects of Aids/Hiv*, 2021.
230. Banting, F.G., et al., *Pancreatic Extracts in the Treatment of Diabetes Mellitus*. *Can Med Assoc J*, 1922. **12**(3): p. 141-6.
231. Bainbridge, M.H., et al., *Synthetic oxytocin*. *Br Med J*, 1956. **1**(4976): p. 1133-5.
232. Vavra, I., et al., *Effect of a synthetic analogue of vasopressin in animals and in patients with diabetes insipidus*. *Lancet*, 1968. **1**(7549): p. 948-52.
233. Pimenta, A.M. and M.E. De Lima, *Small peptides, big world: biotechnological potential in neglected bioactive peptides from arthropod venoms*. *J Pept Sci*, 2005. **11**(11): p. 670-6.
234. Di, L., *Strategic approaches to optimizing peptide ADME properties*. *AAPS J*, 2015. **17**(1): p. 134-43.
235. Hollenstein, K., et al., *Insights into the structure of class B GPCRs*. *Trends in Pharmacological Sciences*, 2014. **35**(1): p. 12-22.
236. Agoulnik, A.I., et al., *Synthetic non-peptide low molecular weight agonists of the relaxin receptor 1*. *Br J Pharmacol*, 2017. **174**(10): p. 977-989.
237. Rao, M.S., et al., *Novel Computational Approach to Predict Off-Target Interactions for Small Molecules*. *Front Big Data*, 2019. **2**: p. 25.
238. Lau, J.L. and M.K. Dunn, *Therapeutic peptides: Historical perspectives, current development trends, and future directions*. *Bioorg Med Chem*, 2018. **26**(10): p. 2700-2707.
239. Cabri, W., et al., *Therapeutic Peptides Targeting PPI in Clinical Development: Overview, Mechanism of Action and Perspectives*. *Front Mol Biosci*, 2021. **8**: p. 697586.
240. Strohl, W.R., *Fusion Proteins for Half-Life Extension of Biologics as a Strategy to Make Biobetters*. *BioDrugs*, 2015. **29**(4): p. 215-39.
241. Jevsevar, S., M. Kunstelj, and V.G. Porekar, *PEGylation of therapeutic proteins*. *Biotechnology Journal*, 2010. **5**(1): p. 113-128.

## References

242. Sun, J. and M. Michaels, *Novel Constructs-Half-Life Extensions*. Challenges in Protein Product Development, 2018. **38**: p. 527-544.
243. Vaissiere, A., et al., *A retro-inverso cell-penetrating peptide for siRNA delivery*. J Nanobiotechnology, 2017. **15**(1): p. 34.
244. Feng, Z. and B. Xu, *Inspiration from the mirror: D-amino acid containing peptides in biomedical approaches*. Biomol Concepts, 2016. **7**(3): p. 179-87.
245. Wiesehan, K. and D. Willbold, *Mirror-image phage display: Aiming at the mirror*. ChemBiochem, 2003. **4**(9): p. 811-815.
246. Bechara, C. and S. Sagan, *Cell-penetrating peptides: 20 years later, where do we stand?* Febs Letters, 2013. **587**(12): p. 1693-1702.
247. Komin, A., et al., *Peptide-based strategies for enhanced cell uptake, transcellular transport, and circulation: Mechanisms and challenges*. Advanced Drug Delivery Reviews, 2017. **110**: p. 52-64.
248. Stanzl, E.G., et al., *Fifteen Years of Cell-Penetrating Guanidinium-Rich Molecular Transporters: Basic Science, Research Tools, and Clinical Applications*. Accounts of Chemical Research, 2013. **46**(12): p. 2944-2954.
249. Matsson, P., et al., *Cell permeability beyond the rule of 5*. Adv Drug Deliv Rev, 2016. **101**: p. 42-61.
250. Nielsen, D.S., et al., *Orally Absorbed Cyclic Peptides*. Chem Rev, 2017. **117**(12): p. 8094-8128.
251. Richard, A. and L. Bourel-Bonnet, *Internalization of a peptide into multilamellar vesicles assisted by the formation of an alpha-oxo oxime bond*. Chemistry, 2005. **11**(24): p. 7315-21.
252. Nakase, I., et al., *Interaction of arginine-rich peptides with membrane-associated proteoglycans is crucial for induction of actin organization and macropinocytosis*. Biochemistry, 2007. **46**(2): p. 492-501.
253. Daniels, D.S. and A. Schepartz, *Intrinsically cell-permeable miniature proteins based on a minimal cationic PPII motif*. J Am Chem Soc, 2007. **129**(47): p. 14578-9.
254. Walensky, L.D. and G.H. Bird, *Hydrocarbon-stapled peptides: principles, practice, and progress*. J Med Chem, 2014. **57**(15): p. 6275-88.
255. Cromm, P.M., J. Spiegel, and T.N. Grossmann, *Hydrocarbon stapled peptides as modulators of biological function*. ACS Chem Biol, 2015. **10**(6): p. 1362-75.
256. Lau, Y.H., et al., *Peptide stapling techniques based on different macrocyclisation chemistries*. Chem Soc Rev, 2015. **44**(1): p. 91-102.
257. Mitra, S., et al., *Stapled peptide inhibitors of RAB25 target context-specific phenotypes in cancer*. Nat Commun, 2017. **8**(1): p. 660.
258. Hummel, G., U. Reineke, and U. Reimer, *Translating peptides into small molecules*. Mol Biosyst, 2006. **2**(10): p. 499-508.
259. Joo, S.H., *Cyclic Peptides as Therapeutic Agents and Biochemical Tools*. Biomolecules & Therapeutics, 2012. **20**(1): p. 19-26.
260. Lin, J., et al., *Development of a novel peptide microarray for large-scale epitope mapping of food allergens*. Journal of Allergy and Clinical Immunology, 2009. **124**(2): p. 315-322.
261. Klein, A.N., et al., *Optimization of the All-D Peptide D3 for A beta Oligomer Elimination*. Plos One, 2016. **11**(4).
262. Blondelle, S.E. and K. Lohner, *Optimization and high-throughput screening of antimicrobial peptides*. Curr Pharm Des, 2010. **16**(28): p. 3204-11.

## References

263. Liu, S.P., et al., *Multivalent Antimicrobial Peptides as Therapeutics: Design Principles and Structural Diversities*. International Journal of Peptide Research and Therapeutics, 2010. **16**(3): p. 199-213.
264. Smith, G.P., *Filamentous fusion phage: novel expression vectors that display cloned antigens on the virion surface*. Science, 1985. **228**(4705): p. 1315-7.
265. Barderas, R. and E. Benito-Pena, *The 2018 Nobel Prize in Chemistry: phage display of peptides and antibodies*. Analytical and Bioanalytical Chemistry, 2019. **411**(12).
266. Sidhu, S.S., W.J. Fairbrother, and K. Deshayes, *Exploring protein-protein interactions with phage display*. ChemBiochem, 2003. **4**(1): p. 14-25.
267. Yu, L., et al., *Phage display screening against a set of targets to establish peptide-based sugar mimetics and molecular docking to predict binding site*. Bioorg Med Chem, 2009. **17**(13): p. 4825-32.
268. Shadidi, M. and M. Sioud, *Selective targeting of cancer cells using synthetic peptides*. Drug Resistance Updates, 2003. **6**(6): p. 363-371.
269. Frenzel, A., T. Schirrmann, and M. Hust, *Phage display-derived human antibodies in clinical development and therapy*. MAbs, 2016. **8**(7): p. 1177-1194.
270. McConnell, S.J., et al., *Construction and screening of M13 phage libraries displaying long random peptides*. Mol Divers, 1996. **1**(3): p. 165-76.
271. Rosenberg, A.H., et al., *Selection, identification, and genetic analysis of random mutants in the cloned primase/helicase gene of bacteriophage T7*. Journal of Biological Chemistry, 1996. **271**(43): p. 26819-26824.
272. Nagano, K. and Y. Tsutsumi, *Phage Display Technology as a Powerful Platform for Antibody Drug Discovery*. Viruses-Basel, 2021. **13**(2).
273. Adey, N.B., et al., *Characterization of Phage That Bind Plastic from Phage-Displayed Random Peptide Libraries*. Gene, 1995. **156**(1): p. 27-31.
274. Huang, J., et al., *SAROTUP: scanner and reporter of target-unrelated peptides*. J Biomed Biotechnol, 2010. **2010**: p. 101932.
275. Derda, R., et al., *Diversity of Phage-Displayed Libraries of Peptides during Panning and Amplification*. Molecules, 2011. **16**(2): p. 1776-1803.
276. Willats, W.G.T., *Phage display: practicalities and prospects*. Plant Molecular Biology, 2002. **50**(6): p. 837-854.
277. Juds, C., et al., *Combining Phage Display and Next-Generation Sequencing for Materials Sciences: A Case Study on Probing Polypropylene Surfaces*. J Am Chem Soc, 2020. **142**(24): p. 10624-10628.
278. Santur, K., et al., *Ligand-Induced Stabilization of the Native Human Superoxide Dismutase 1*. Acs Chemical Neuroscience, 2021. **12**(13): p. 2520-2528.
279. 't Hoen, P.A.C., et al., *Phage display screening without repetitious selection rounds*. Analytical Biochemistry, 2012. **421**(2): p. 622-631.
280. Donatan, S., et al., *Physical elution in phage display selection of inorganic-binding peptides*. Materials Science & Engineering C-Biomimetic and Supramolecular Systems, 2009. **29**(1): p. 14-19.
281. Lunder, M., et al., *Ultrasound in phage display: a new approach to nonspecific elution*. Biotechniques, 2008. **44**(7): p. 893-900.
282. Eisenhardt, S.U., et al., *Subtractive single-chain antibody (scFv) phage-display: tailoring phage-display for high specificity against function-specific conformations of cell membrane molecules*. Nat Protoc, 2007. **2**(12): p. 3063-73.

283. Hirsch, J.D., et al., *Easily reversible desthiobiotin binding to streptavidin, avidin, and other biotin-binding proteins: uses for protein labeling, detection, and isolation*. Analytical Biochemistry, 2002. **308**(2): p. 343-357.
284. Zhou, X., et al., *A Novel d-Peptide Identified by Mirror-Image Phage Display Blocks TIGIT/PVR for Cancer Immunotherapy*. Angew Chem Int Ed Engl, 2020. **59**(35): p. 15114-15118.
285. Malhis, M., et al., *Potent Tau Aggregation Inhibitor D-Peptides Selected against Tau-Repeat 2 Using Mirror Image Phage Display*. Chembiochem, 2021.
286. Diaz-Perlas, C., et al., *Protein Chemical Synthesis Combined with Mirror-Image Phage Display Yields d-Peptide EGF Ligands that Block the EGF-EGFR Interaction*. Chembiochem, 2019. **20**(16): p. 2079-2084.
287. Wang, J., et al., *Highly paralleled emulsion droplets for efficient isolation, amplification, and screening of cancer biomarker binding phages*. Lab Chip, 2021. **21**(6): p. 1175-1184.
288. Krejci, A., et al., *Hammock: a hidden Markov model-based peptide clustering algorithm to identify protein-interaction consensus motifs in large datasets*. Bioinformatics, 2016. **32**(1): p. 9-16.
289. Staats, R., et al., *Screening of small molecules using the inhibition of oligomer formation in alpha-synuclein aggregation as a selection parameter*. Communications Chemistry, 2020. **3**(1).
290. Michaels, T.C.T., et al., *Chemical Kinetics for Bridging Molecular Mechanisms and Macroscopic Measurements of Amyloid Fibril Formation*. Annual Review of Physical Chemistry, Vol 69, 2018. **69**: p. 273-298.
291. Kissler, S.M., et al., *Viral dynamics of acute SARS-CoV-2 infection and applications to diagnostic and public health strategies*. Plos Biology, 2021. **19**(7).
292. Moret, N., et al., *Cheminformatics Tools for Analyzing and Designing Optimized Small-Molecule Collections and Libraries*. Cell Chemical Biology, 2019. **26**(5): p. 765-+.
293. Gajula, S.N.R., N. Nadimpalli, and R. Sonti, *Drug metabolic stability in early drug discovery to develop potential lead compounds*. Drug Metabolism Reviews, 2021. **53**(3): p. 459-477.
294. Wolff, A., et al., *In Vitro Blood-Brain Barrier Models-An Overview of Established Models and New Microfluidic Approaches*. Journal of Pharmaceutical Sciences, 2015. **104**(9): p. 2727-2746.
295. Schoultz, I. and A.V. Keita, *The Intestinal Barrier and Current Techniques for the Assessment of Gut Permeability*. Cells, 2020. **9**(8).
296. Leblanc, A.F., et al., *Murine Pharmacokinetic Studies*. Bio-Protocol, 2018. **8**(20).

### Acknowledgements

Mein Dank gilt zunächst Prof. Dieter Willbold dafür, dass er mir dieses außerordentlich spannende Promotionsthema überlassen hat. Auch möchte ich ihm für das Vertrauen in mich und meine Arbeit sowie die Unterstützung über die gesamte Zeit danken. Des Weiteren möchte ich mich bei meinem Mentor Prof. Wolfgang Hoyer für die Übernahme des Koreferates bedanken und dafür, dass er mir in vielen Punkten wertvolle Ratschläge gegeben hat.

Weiterhin bedanke ich mich bei Dr. Jeannine Mohrlüder für ihre hervorragende Betreuung über die letzten Jahre und dafür, dass sie mir immer mit Rat und Tat zur Seite gestanden hat. Auch möchte ich der ganzen AG Mohrlüder für die großartige Zusammenarbeit danken. Namentlich sind hier Tim Altendorf, Dr. Pauline Kolkwitz, Dr. Karoline Santur und Lena Mangels zu nennen. Ich denke, eine Gruppe, die so kollegial zusammenarbeitet, ist selten und ich bin mir sicher, dass wir mit unserer gemeinsamen Arbeit etwas auf den Weg gebracht haben, das auch noch in den nächsten Jahren seine Früchte tragen wird.

Ein besonderer Dank geht auch an alle Mitglieder der Priavoid GmbH, die es mir über die letzten Jahre ermöglicht haben an diesem wirklich spannenden Thema bei ihnen zu forschen. Insbesondere geht mein Dank an Dr. Antje Willuweit und Dr. Nadine Rösener. Die Problematik der neurodegenerativen Erkrankungen, die die Priavoid GmbH angehen möchte, haben eine enorme Wichtigkeit und deswegen freue ich mich darauf auch in der Zukunft die Forschung in diesem Bereich fortsetzen zu dürfen.

Nicht zuletzt möchte ich mich bei dem ganzen IBI-7 bedanken. Mir hat es immer sehr viel Spaß gemacht mit euch zusammen zu arbeiten. Basis jeder Forschungsarbeit ist ein funktionierendes Labor und damit die Menschen, die sich darum kümmern, dass alles rund läuft. Hier sind unter vielen anderen Ian Gering, Markus Tusche und Anne Cousin zu nennen. Auch möchte ich mich bei Dr. Nils-Alexander Lakomek, Prof. Erdem Tamgüney sowie Dr. Raphael Eberle für die großartige Zusammenarbeit auf so manchem Projekt bedanken. Mein Dank geht auch an Dr. Joop van den Heuvel vom Helmholtz Zentrum für Infektionsforschung für die Zusammenarbeit auf den Corona-Projekten, die ansonsten in dieser Form nicht hätten stattfinden können.

Zudem bedanke ich mich für die Zusammenarbeit mit dem ganzen IPB Düsseldorf. Die Arbeit mit euch hat mir immer viel Spaß gemacht. Hier möchte ich mich insbesondere bei Dr. Lothar Gremer sowie Tatsiana Kupreichyk bedanken.

Abschließend gilt ein entscheidender Dank meiner Frau Nadine sowie meiner ganzen Familie, die mich auf dem gesamten Weg von Studienbeginn bis zu diesem Punkt immer unterstützt haben. Insbesondere möchte ich mich bei meinen Eltern dafür bedanken, dass sie mir diesen Weg ermöglicht haben. Denn für mich gibt es nichts Spannenderes als die Forschung.

## Eidesstattliche Erklärung

Ich versichere an Eides Statt, dass die Dissertation von mir selbständig und ohne unzulässige fremde Hilfe unter Beachtung der „Grundsätze zur Sicherung guter wissenschaftlicher Praxis an der Heinrich-Heine-Universität Düsseldorf“ erstellt worden ist.

Ferner erkläre ich, dass ich in keinem anderen Dissertationsverfahren mit oder ohne Erfolg versucht habe, diese Dissertation einzureichen.

---

Ort, Datum

---

Marc Michael Sevenich

## Printing Permissions



This is a License Agreement between Marc Sevenich ("User") and Copyright Clearance Center, Inc. ("CCC") on behalf of the Rightsholder identified in the order details below. The license consists of the order details, the Marketplace Permissions General Terms and Conditions below, and any Rightsholder Terms and Conditions which are included below. All payments must be made in full to CCC in accordance with the Marketplace Permissions General Terms and Conditions below.

Order Date	16-Feb-2023	Type of Use	Republish in a thesis/dissertation
Order License ID	1324645-1	Publisher	John Wiley & Sons
ISSN	2365-6549	Portion	Chapter/article

### LICENSED CONTENT

Publication Title	ChemistrySelect	Rightsholder	John Wiley & Sons - Books
Article Title	In Vitro Reconstitution of the Highly Active and Natively Folded Recombinant Human Superoxide Dismutase 1 Holoenzyme	Publication Type	e-Journal
Author/Editor	ChemPubSoc Europe,	Start Page	7627
Date	01/01/2016	End Page	7632
Language	English	Issue	26
Country	Germany	Volume	3

### REQUEST DETAILS

Portion Type	Chapter/article	Rights Requested	Main product
Page Range(s)	1-6	Distribution	Worldwide
Total Number of Pages	6	Translation	Original language of publication
Format (select all that apply)	Electronic	Copies for the Disabled?	No
Who Will Republish the Content?	Academic institution	Minor Editing Privileges?	No
Duration of Use	Life of current and all future editions	Incidental Promotional Use?	No
Lifetime Unit Quantity	Up to 499	Currency	EUR

### NEW WORK DETAILS

Title	Identification, characterization and optimization of peptide ligands for therapeutic applications	Institution Name	Heinrich-Heine Universität Düsseldorf
Instructor Name	Marc Sevenich	Expected Presentation Date	2023-02-19

### ADDITIONAL DETAILS

The Requesting Person/Organization to Appear on the License	Marc Sevenich
---	---------------

### REQUESTED CONTENT DETAILS

Title, Description or Numeric Reference of the Portion(s)	1	Title of the Article/Chapter the Portion Is From	In Vitro Reconstitution of the Highly Active and Natively Folded Recombinant Human Superoxide Dismutase 1 Holoenzyme
Editor of Portion(s)	Santur, Karoline B.; Sevenich, Marc M.; Schwarten, Melanie; Nischwitz, Volker; Willbold, Dieter; Mohrlüder, Jeannine	Author of Portion(s)	Santur, Karoline B.; Sevenich, Marc M.; Schwarten, Melanie; Nischwitz, Volker; Willbold, Dieter; Mohrlüder, Jeannine
Volume of Serial or Monograph	3	Publication Date of Portion	2018-07-13
Page or Page Range of Portion	7627-7632		

## Printing Permissions



This is a License Agreement between Marc Sevenich ("User") and Copyright Clearance Center, Inc. ("CCC") on behalf of the Rightsholder identified in the order details below. The license consists of the order details, the Marketplace Permissions General Terms and Conditions below, and any Rightsholder Terms and Conditions which are included below. All payments must be made in full to CCC in accordance with the Marketplace Permissions General Terms and Conditions below.

Order Date	16-Feb-2023	Type of Use	Republish in a thesis/dissertation
Order License ID	1324632-1	Publisher	ELSEVIER LTD.
ISSN	0197-0186	Portion	Chapter/article

### LICENSED CONTENT

Publication Title	Neurochemistry international	Rightsholder	Elsevier Science & Technology Journals
Article Title	Development of an $\alpha$ -synuclein fibril and oligomer specific tracer for diagnosis of Parkinson's disease, dementia with Lewy bodies and multiple system atrophy	Publication Type	Journal
Date	01/01/1980	Start Page	105422
Language	English	Volume	161
Country	United Kingdom of Great Britain and Northern Ireland		

### REQUEST DETAILS

Portion Type	Chapter/article	Rights Requested	Main product
Page Range(s)	1 - 10	Distribution	Worldwide
Total Number of Pages	10	Translation	Original language of publication
Format (select all that apply)	Electronic	Copies for the Disabled?	No
Who Will Republish the Content?	Academic institution	Minor Editing Privileges?	No
Duration of Use	Life of current edition	Incidental Promotional Use?	No
Lifetime Unit Quantity	Up to 499	Currency	EUR

### NEW WORK DETAILS

Title	Identification, characterization and optimization of peptide ligands for therapeutic applications	Institution Name	Heinrich-Heine Universität Düsseldorf
Instructor Name	Marc Sevenich	Expected Presentation Date	2023-02-19

### ADDITIONAL DETAILS

Order Reference Number	N/A	The Requesting Person/Organization to Appear on the License	Marc Sevenich
------------------------	-----	---	---------------

### REQUESTED CONTENT DETAILS

Title, Description or Numeric Reference of the Portion(s)	1	Title of the Article/Chapter the Portion Is From	Development of an $\alpha$ -synuclein fibril and oligomer specific tracer for diagnosis of Parkinson's disease, dementia with Lewy bodies and multiple system atrophy
Editor of Portion(s)	Sevenich, Marc; Honold, Dominik; Willuweit, Antje; Kutzsche, Janine; Mohrlüder, Jeannine; Willbold, Dieter	Author of Portion(s)	Sevenich, Marc; Honold, Dominik; Willuweit, Antje; Kutzsche, Janine; Mohrlüder, Jeannine; Willbold, Dieter
Volume of Serial or Monograph	161	Issue, if Republishing an Article From a Serial	N/A
Page or Page Range of Portion	105422	Publication Date of Portion	2022-12-01

## Printing Permissions



This is a License Agreement between Marc Sevenich ("User") and Copyright Clearance Center, Inc. ("CCC") on behalf of the Rightsholder identified in the order details below. The license consists of the order details, the Marketplace Permissions General Terms and Conditions below, and any Rightsholder Terms and Conditions which are included below. All payments must be made in full to CCC in accordance with the Marketplace Permissions General Terms and Conditions below.

Order Date	20-Feb-2023	Type of Use	Republish in a thesis/dissertation
Order License ID	1325729-1	Publisher	AMERICAN SOCIETY FOR MICROBIOLOGY
ISSN	1098-5514	Portion	Chapter/article

### LICENSED CONTENT

Publication Title	Journal of virology : JVI	Rightsholder	American Society for Microbiology - Journals
Article Title	A So-Far Overlooked Secondary Conformation State in the Binding Mode of SARS-CoV-2 Spike Protein to Human ACE2 and Its Conversion Rate Are Crucial for Estimating Infectivity Efficacy of the Underlying Virus Variant	Publication Type	e-Journal
Author/Editor	American Society for Microbiology.	Issue	13
Date	01/01/1971	Volume	96
Language	English	URL	<a href="https://journals.asm.org/journal/jvi">https://journals.asm.org/journal/jvi</a>
Country	United States of America		

### REQUEST DETAILS

Portion Type	Chapter/article	Rights Requested	Main product
Page Range(s)	1-11	Distribution	Worldwide
Total Number of Pages	11	Translation	Original language of publication
Format (select all that apply)	Electronic	Copies for the Disabled?	No
Who Will Republish the Content?	Academic institution	Minor Editing Privileges?	No
Duration of Use	Life of current edition	Incidental Promotional Use?	No
Lifetime Unit Quantity	Up to 499	Currency	EUR

### NEW WORK DETAILS

Title	Identification, characterization and optimization of peptide ligands for therapeutic applications	Institution Name	Heinrich-Heine Universität Düsseldorf
Instructor Name	Marc Sevenich	Expected Presentation Date	2023-02-19

### ADDITIONAL DETAILS

Order Reference Number	N/A	The Requesting Person/Organization to Appear on the License	Marc Sevenich
------------------------	-----	---	---------------

### REQUESTED CONTENT DETAILS

Title, Description or Numeric Reference of the Portion(s)	1	Title of the Article/Chapter the Portion Is From	A So-Far Overlooked Secondary Conformation State in the Binding Mode of SARS-CoV-2 Spike Protein to Human ACE2 and Its Conversion Rate Are Crucial for Estimating Infectivity Efficacy of the Underlying Virus Variant
Editor of Portion(s)	Sevenich, Marc; van den Heuvel, Joop; Gering, Ian; Mohrlöder, Jeannine; Willbold, Dieter	Author of Portion(s)	Sevenich, Marc; van den Heuvel, Joop; Gering, Ian; Mohrlöder, Jeannine; Willbold, Dieter
Volume of Serial or Monograph	96	Issue, if Republishing an Article From a Serial	13
Page or Page Range of Portion	11	Publication Date of Portion	2022-07-13